



# University of HUDDERSFIELD

## University of Huddersfield Repository

Griffiths, Hollie Bethany Saffron

Investigation of emerging cancer cell molecular vulnerabilities linked to the NAD(H) metabolome and opportunities for novel therapeutics

### Original Citation

Griffiths, Hollie Bethany Saffron (2020) Investigation of emerging cancer cell molecular vulnerabilities linked to the NAD(H) metabolome and opportunities for novel therapeutics. Doctoral thesis, University of Huddersfield.

This version is available at <http://eprints.hud.ac.uk/id/eprint/35355/>

The University Repository is a digital collection of the research output of the University, available on Open Access. Copyright and Moral Rights for the items on this site are retained by the individual author and/or other copyright owners. Users may access full items free of charge; copies of full text items generally can be reproduced, displayed or performed and given to third parties in any format or medium for personal research or study, educational or not-for-profit purposes without prior permission or charge, provided:

- The authors, title and full bibliographic details is credited in any copy;
- A hyperlink and/or URL is included for the original metadata page; and
- The content is not changed in any way.

For more information, including our policy and submission procedure, please contact the Repository Team at: [E.mailbox@hud.ac.uk](mailto:E.mailbox@hud.ac.uk).

<http://eprints.hud.ac.uk/>

**Investigation of emerging cancer  
cell molecular vulnerabilities  
linked to the NAD(H) metabolome  
and opportunities for novel  
therapeutics**

**Hollie Bethany Saffron Griffiths**

A thesis submitted to the University of Huddersfield in partial fulfilment of the  
requirements for the degree of Doctor of Philosophy

**January 2020**

Copyright statement:

- i. The author of this thesis (including any appendices and/ or schedules to this thesis) owns any copyright in it (the "Copyright") and s/he has given The University of Huddersfield the right to use such Copyright for any administrative, promotional, educational and/or teaching purposes.
- ii. Copies of this thesis, either in full or in extracts, may be made only in accordance with the regulations of the University Library. Details of these regulations may be obtained from the Librarian. This page must form part of any such copies made.
- iii. The ownership of any patents, designs, trademarks and any and all other intellectual property rights except for the Copyright (the "Intellectual Property Rights") and any reproductions of copyright works, for example graphs and tables ("Reproductions"), which may be described in this thesis, may not be owned by the author and may be owned by third parties. Such Intellectual Property Rights and Reproductions cannot and must not be made available for use without permission of the owner(s) of the relevant Intellectual Property Rights and/or Reproductions.

## Acknowledgements

To begin I would like to thank my supervisor Dr Simon Allison, his excellent teaching, support, patience and encouragement are what really made this PhD journey an enjoyable experience (Diolch yn fawr iawn!). He was always there when I had silly questions and was always willing to help when needed. His supervision has helped me gain a lot of essential skills and experience which will help me in the future. I'd like to thank my fellow PhD researcher Courtney for making my time in the lab entertaining, especially when we both had our early starts and long days where heart radio and its competitions kept us company. My extended research group, under the supervision of Roger Phillips, also need thanking for just 'being there' in the lab, which include Emma, Sam, Omar, Suliman and Scott. My family, especially my parents, although they still don't quite fully understand the whole PhD process, are always encouraging and offer support when I need it, which I really appreciate. Thanks to my partner, Adam, for not getting annoyed when I've been in a world of my own whilst writing, especially the last few weeks where you've been having conversations with yourself. A big thanks to Kartheek and the members of 'girl street' – Kim, Sophie, Zoe, Naomi, Carla, Megan and Courtney, for being there for a chat and for the supply of cake, biscuits and tea. I'd also like to thank Ellie and her Leeds University access for supplying me with papers when I didn't have access.

# Abstract

**Introduction:** Traditional anti-cancer drugs target proliferating cells and are generally potent but have poor selectivity towards cancer cells leading to dose limiting toxicities. Targeted therapies offer cancer selectivity but may be effective only against cancers with particular lesions and the development of resistance can be a problem. The focus of this PhD research has been on the essential metabolite NAD<sup>+</sup> and NAD<sup>+</sup> dependent cellular processes. An emerging hallmark of cancers is deregulated cellular metabolism and it was hypothesised that differences between cancer and non-cancer cells in NAD<sup>+</sup> metabolism and function may offer potential novel therapeutic opportunities that are both cancer selective and potent.

**Aims:** The aim was to evaluate specific putative cancer cell molecular vulnerabilities linked to the NAD<sup>+</sup> metabolome. Four key hypotheses were investigated, a) that inhibition of NAD<sup>+</sup> salvage enzyme NAMPT could reduce activity of NAD<sup>+</sup>-dependent PARP DNA repair enzymes selectively in cancer cells, b) that inhibition of NAD<sup>+</sup>-dependent deacetylase SIRT1 is preferentially cytotoxic towards cancer cells and that it can modulate non-cancer and cancer cell differentiation, c) that inhibition of glycolytic enzyme LDH-A affects cancer cell epigenetics and d) that small molecule KHS101 has selective activity against cancer cells through metabolic effects and perturbation of NAD<sup>+</sup>/NADH balance.

**Methods:** Small molecule inhibitors of the indicated cellular targets, or their knock-down by RNAi, were utilised to analyse effects on a panel of cancer cell lines and non-cancer cell models *in vitro*. Cytotoxicity was analysed by chemosensitivity and image cytometry-based assays. Metabolic effects were analysed using a Seahorse XFp analyser and NAD(H) assays. mRNA expression was analysed by qPCR and protein expression by immunoblotting and IF, with colorimetric/fluorometric-based enzyme assays used to analyse effects on PARP1, SIRT1 and GPD2 activity.

**Results:** KHS101 and NAMPT inhibitor FK866 both showed promising *in vitro* activity towards the cancer cell line panel and, for the most part, were more active towards the cancer cells than the non-cancer cell models tested. Short term NAMPT inhibition by FK866 at non-toxic doses preferentially depleted NAD(H) levels in cancer cells which was independent of p53 status and was sufficient to induce a cancer selective decrease in PARP activity. Consistent with this, FK866 was able to potentiate several DNA damaging agents, in particular temozolomide, selectively in cancer cells. Preferential activity of SIRT1 inhibitor EX-527 towards

cancer cell lines than non-cancer cells over 96 hours was modest but depended on the cell line. Phenotypically, EX-527 induced a neuronal-like phenotype in two non-cancer cell models suggesting the cells undergo neuronal transdifferentiation. This was accompanied by changes in mRNA levels of stem cell factors and neuronal markers and was also observed in a glioblastoma stem cell-like model. LDH-A suppression led to alterations in the epigenetic state of cancer cells with global levels of H3K9me3 and H3K9Ac changing and mRNA levels of the epigenetically silenced TSG E-cadherin increasing. KHS101 mechanism of action studies revealed depletion of mitochondrial respiratory function and cancer cell ATP levels. Autophagy was induced by KHS101 in both cancer and non-cancer cells. Activity of mitochondrial G3P shuttle enzyme GPD2 was decreased and NAD<sup>+</sup>/NADH balance perturbed in cancer cells.

**Discussion and Conclusions:** *In vitro* proof of principle is provided that through NAMPT suppression, NAD<sup>+</sup>-dependent PARP activity can be reduced preferentially in cancer cells and certain DNA damaging chemotherapeutic agents can be potentiated selectively in cancer cells. This raises the possibility of widening the therapeutic window of clinically used drugs if such effects can be translated into *in vivo*. SIRT1 can affect cell fate or differentiation status, its inhibition promoting neuronal (trans)differentiation of non-cancer cells and of GBM stem-like cells, indicating potential to target cancer stem cells and as a differentiation therapy. LDH-A suppression affected global levels of histone H3K9 acetylation and methylation. Whilst effects at specific gene promoters have yet to be investigated, this identifies LDH-A as a novel target for selective modification of the cancer cell epigenome. Future work will investigate whether it can promote re-expression of epigenetically silenced tumour suppressors without adverse epigenetic effects on non-cancer cells. Cancer cells were unable to sufficiently metabolically compensate in response to small molecule KHS101 with *in vitro* results suggesting selective activity against multiple cancer cell types. Overall, these results suggest a number of potential therapeutic opportunities linked to the NAD<sup>+</sup> metabolome that warrant further preclinical investigation.

# Abbreviations

<b>2-DG</b>	2-Deoxyglucose
<b>2HG</b>	2-Hydroxyglutarate
<b>5hmC</b>	5-Hydroxymethylcytosine
<b>5mC</b>	5-Methylcytosine
<b>AMD</b>	Age-related macular degeneration
<b>AMPK</b>	Adenosine monophosphate-activated protein kinase
<b>AP</b>	Apurinic/Apyrimidinic
<b>AROS</b>	Active regulator of SIRT1
<b>BCA</b>	Bicinchoninic acid
<b>BER</b>	Base excision repair
<b>BRCA1/2</b>	Breast cancer gene 1/2
<b>BSA</b>	Bovine serum albumin
<b>CER</b>	Cytoplasmic extraction reagent
<b>CHOP</b>	C/EBP homologous protein
<b>CPT</b>	Camptothecin
<b>CSC</b>	Cancer stem cell
<b>DAPI</b>	4',6-diamidino-2-phenylindole
<b>DBC</b>	Deleted in breast cancer
<b>DCA</b>	Dichloroacetate
<b>DCPIP</b>	2,6-Dichlorophenolindophenol
<b>DHAP</b>	Dihydroxyacetone phosphate
<b>DMEM</b>	Dulbecco's modified eagle medium
<b>DMSO</b>	Dimethyl sulfoxide
<b>DNMT</b>	DNA methyltransferase
<b>DOX</b>	Doxorubicin
<b>DSB</b>	Double strand break
<b>ECAR</b>	Extracellular acidification rate
<b>EDTA</b>	Ethylenediaminetetraacetic acid
<b>ELISA</b>	Enzyme-linked immunosorbent assay
<b>EMA</b>	European medicines agency
<b>EMT</b>	Epithelial-mesenchymal transition
<b>EX-527</b>	6-Chloro-2,3,4,9-tetrahydro-1H-Carbazole-1-carboxamide
<b>FAD</b>	Flavin adenine dinucleotide
<b>FBS</b>	Foetal bovine serum
<b>FCCP</b>	Carbonyl cyanide-p-trifluoromethoxyphenylhydrazine
<b>FDA</b>	U.S food and drug administrations
<b>FH</b>	Fumarate hydratase
<b>FK866</b>	(E)-N-[4-(1-benzoylpiperidin-4-yl)butyl]-3-(pyridin-3-yl)acrylamide
<b>FL</b>	Full length
<b>FOXO</b>	Forkhead box protein
<b>G3P</b>	Glycerol-3-phosphate
<b>GAPDH</b>	Glyceraldehyde 3-phosphate dehydrogenase
<b>GBM</b>	Glioblastoma

<b>GLUT1</b>	Glucose transporter 1
<b>GPD1/2</b>	Glycerol-3-phosphate dehydrogenase 1/2
<b>HDAC</b>	Histone deacetylase
<b>HIF-1<math>\alpha</math></b>	Hypoxia inducible factor 1-alpha
<b>HK</b>	Hexokinase
<b>HMT</b>	Histone methyltransferase
<b>HR</b>	Homologous recombination
<b>HRP</b>	Horseradish peroxidase
<b>HSPD1</b>	Mitochondrial heat shock protein 1
<b>IDH</b>	Isocitrate dehydrogenase
<b>iPSC</b>	Induced pluripotent stem cell
<b>KDM</b>	Histone lysine demethylase
<b>KHS101</b>	N4-isobutyl-N2-((2-phenylthiazol-4-yl)methyl)pyrimidine-2,4-diamine
<b>LDH</b>	Lactate dehydrogenase
<b>MC</b>	Myrtucommulone
<b>MDH</b>	Malate dehydrogenase
<b>MGMT</b>	O <sup>6</sup> -Methylguanine-DNA-methyltransferase
<b>MMR</b>	Mismatch repair
<b>MTT</b>	Thiazolyl blue tetrazolium bromide
<b>NA</b>	Nicotinic acid
<b>NAAD</b>	Nicotinic acid adenine dinucleotide
<b>NAD</b>	Nicotinamide adenine dinucleotide
<b>NADP</b>	Nicotinamide adenine dinucleotide phosphate
<b>NADS</b>	Nicotinamide adenine dinucleotide synthase
<b>Nam</b>	Nicotinamide
<b>NAMN</b>	Nicotinic acid mononucleotide
<b>NAMPT</b>	Nicotinamide phosphoribosyltransferase
<b>NAPRT</b>	Nicotinate phosphoribosyltransferase
<b>NC-3000</b>	NucleoCounter 3000
<b>NER</b>	Nucleotide excision repair
<b>NHEJ</b>	Non-homologous end joining
<b>NHI-2</b>	1-Hydroxy-6-phenyl-4-(trifluoromethyl)-1H-Indole-2-carboxylic acid methyl ester
<b>NMN</b>	Nicotinamide mononucleotide
<b>NMNAT</b>	Nicotinamide mononucleotide adenyltransferase
<b>NR</b>	Nicotinamide riboside
<b>NRK</b>	Nicotinamide riboside kinase
<b>OCR</b>	Oxygen consumption rate
<b>PAR</b>	Poly (ADP-ribose)
<b>PARP</b>	Poly (ADP-ribose) polymerase
<b>PBS</b>	Phosphate buffered saline
<b>PBS-T</b>	PBS - 0.1% Tween 20
<b>PDH</b>	Pyruvate dehydrogenase
<b>PDK</b>	Pyruvate dehydrogenase kinase
<b>PFK</b>	Phosphofructokinase
<b>PFKB3</b>	6-phosphofructo-2-kinase/fructose-2,6-biphosphatase 3

<b>PI</b>	Propidium iodide
<b>PPP</b>	Pentose phosphate pathway
<b>qPCR</b>	Quantitative polymerase chain reaction
<b>RIPA</b>	Radioimmunoprecipitation assay buffer
<b>ROCK</b>	RHO-associated serine/threonine kinase
<b>RPE</b>	Retinal pigment epithelia
<b>RPMI</b>	Roswell Park Memorial Institute
<b>SAM</b>	S-adenosylmethionine
<b>SDH</b>	Succinate dehydrogenase
<b>SDS-PAGE</b>	Sodium dodecyl sulphate polyacrylamide gel electrophoresis
<b>SI</b>	Selectivity index
<b>SIRT</b>	Sirtuin
<b>SRB</b>	Sulforhodamine B
<b>SSB</b>	Single strand break
<b>TACC3</b>	Transforming acidic coiled-coil containing protein 3
<b>TBS-T</b>	Tris buffered saline - 0.1% Tween 20
<b>TCA</b>	Tricarboxylic acid
<b>TET</b>	Ten eleven translocation
<b>TME</b>	Tumour microenvironment
<b>TMZ</b>	Temozolomide
<b>Topo1/2</b>	Topoisomerase 1/2
<b>TSG</b>	Tumour suppressor gene
<b>UPR</b>	Unfolded protein response
<b>VEGF</b>	Vascular endothelial growth factor
<b>X-gal</b>	5-bromo-4-chloro-3-indolyl- $\beta$ -D-galactopyranoside
<b>XRCC1</b>	X-ray repair cross-complementing protein 1
<b><math>\alpha</math>-KG</b>	$\alpha$ -Ketoglutarate

# Contents

Acknowledgements .....	3
Abstract .....	4
Abbreviations .....	6
List of tables.....	16
List of figures .....	17
Publications .....	25
Presentations and conferences .....	26
1. Introduction.....	27
1.1 Cancer as a genetic disease and its current treatment.....	27
1.1.1 Brief definition of cancer.....	27
1.1.2 Cancer incidence and mortality .....	27
1.1.3 The genetic basis of cancer.....	29
1.1.4 The hallmarks of cancer .....	29
1.1.5 Current treatments .....	31
1.1.5.1 Traditional chemotherapeutic agents.....	32
1.1.5.2 Targeted approaches/agents in clinical use .....	35
1.2 Metabolic differences between cancer and non-cancer cells.....	39
1.2.1 Glucose metabolism in non-cancer cells and the role of NAD <sup>+</sup> /NADH.....	39
1.2.2 Glucose metabolism in cancer cells.....	44
1.2.3 Other cancer cell metabolic alterations .....	46
1.2.3.1 Glutamine addiction .....	46
1.2.3.2 Lipid metabolism .....	46
1.2.3.3 Pentose phosphate pathway .....	47
1.2.3.4 Dependency on serine .....	47
1.2.4 Regulation of metabolism and its dysregulation in cancer cells .....	47
1.2.5 Therapeutically targeting altered glucose metabolism.....	50
1.3 What is NAD <sup>+</sup> and how is it produced? .....	54
1.3.1 What is NAD <sup>+</sup> ? .....	54
1.3.2 Sources of NAD <sup>+</sup> .....	55

1.3.2.1	Oxidation of NADH to NAD <sup>+</sup> .....	55
1.3.2.2	Dephosphorylation of NADP <sup>+</sup> to NAD <sup>+</sup> .....	55
1.3.2.3	Biosynthesis of NAD <sup>+</sup> .....	55
1.4	NAD <sup>+</sup> consuming enzymes.....	58
1.4.1	Poly (ADP-ribose) polymerase .....	58
1.4.1.1	Clinical use of PARP inhibitors as a single agent – induction of synthetic lethality .....	61
1.4.1.2	Combination treatments with PARP inhibitors.....	65
1.4.2	Sirtuins .....	69
1.4.2.1	The role of SIRT1 in cancer development.....	70
1.4.2.2	SIRT1 splice variants .....	71
1.5	NAD <sup>+</sup> as a therapeutic target.....	74
1.5.1	Targeting NAD <sup>+</sup> via enzymes involved in the NAD <sup>+</sup> salvage pathway .....	74
1.6	Metabolism, NAD <sup>+</sup> and epigenetics .....	75
1.6.1	The rate of one-carbon metabolism alters DNA and histone methylation.....	76
1.6.2	TCA cycle metabolites affect histone and DNA demethylation .....	77
1.6.2.1	Hypoxia induces L-2HG .....	78
1.6.3	Acetyl-CoA and histone acetylation .....	78
1.7	Rationale and aims of thesis .....	79
2.	Materials and methods.....	81
2.1	Cell culture.....	81
2.1.1	General cell culture .....	81
2.1.2	Sub-culturing of cell lines .....	82
2.1.3	Sub-culturing of GBM and NP1 cells .....	83
2.1.4	Cryopreservation of cells.....	83
2.1.5	Reviving cells from cryopreservation .....	83
2.1.6	β-galactosidase senescence assay .....	83
2.2	<i>In vitro</i> chemosensitivity analysis of drugs .....	85
2.2.1	MTT chemosensitivity assay .....	85
2.2.2	Rescue of FK866 toxicity studies.....	87

2.2.3 Combination studies.....	87
2.3 Analysis of cells using the NucleoCounter® NC-3000™ image cytometer.....	88
2.3.1 Quantification of cell number and viability.....	88
2.3.2 Quantification of apoptotic cells.....	88
2.3.3 Quantification of autophagy positive cells by image cytometry.....	89
2.3.4 Cell cycle analysis.....	89
2.4 Metabolic flux analysis.....	91
2.4.1 Cell energy phenotype.....	91
2.4.2 Rescue studies.....	92
2.4.3 Mitochondria stress test after direct drug injection.....	92
2.4.4 Glycolysis stress test after direct drug injection.....	93
2.5 Cellular ATP assay.....	94
2.6 siRNA transfection.....	95
2.7 Metabolic analysis of siRNA transfected cells.....	96
2.8 Gene expression analysis.....	97
2.8.1 RNA extraction from cell pellets.....	97
2.8.2 Quantification of RNA and reverse transcription.....	97
2.8.3 qPCR using TaqMan™ probes.....	98
2.8.4 SYBR™ Green qPCR.....	99
2.9 NAD(H) assay.....	100
2.9.1 Determination of total cellular NAD(H).....	100
2.9.2 Nuclear and cytoplasmic quantification of NAD(H).....	101
2.10 Mitochondrial GPD2 activity assay.....	102
2.11 Quantification of protein expression.....	103
2.11.1 Preparation of cell lysates.....	103
2.11.2 Preparation and running of SDS-PAGE gels.....	103
2.11.3 Immunoblotting.....	104
2.11.4 Immunoblotting using the LI-COR system.....	105
2.11.5 Immunoblotting using enhanced chemi-luminescence.....	105
2.12 Quantification of cellular PARP activity.....	106
2.13 Quantification of SIRT1 activity.....	107

2.14 Immunofluorescent and autophagy staining and imaging .....	108
2.14.1 Analysis of double strand break DNA damage marker, phosphorylated $\gamma$ H2AX...108	
2.14.2 MAP2 cellular staining .....	109
2.14.3 Live CYTO-ID® imaging of autophagic cells .....	109
2.14.4 Detection of 5hmC, a marker of demethylation of DNA .....	110
2.15 Statistical analysis.....	111
3. Investigation of NAMPT suppression as a potential strategy to decrease PARP activity selectively in cancer cells .....	112
3.1 Introduction.....	112
3.2 Results.....	115
3.2.1 Validation of non-cancer cell models .....	115
3.2.2 Activity and cancer cell selectivity of the NAMPT inhibitor FK866.....	119
3.2.3 Relationship between chemosensitivity to FK866 and cellular NAMPT expression	126
3.2.4 Cancer selective metabolic effects of NAMPT inhibition.....	130
3.2.5 Ability of NAD <sup>+</sup> precursors to rescue the effects of FK866.....	135
3.2.6 Effects of FK866 on cellular NAD(H) .....	137
3.2.7 Effects of FK866 on NAD(H) in the nucleus .....	139
3.2.8 Assessment of effects of FK866 on PARP activity .....	139
3.2.9 Can FK866 potentiate current chemotherapeutic drugs? .....	143
3.2.10 Effect of FK866 in combination with microtubule targeting chemotherapeutic agent paclitaxel .....	155
3.2.11 Potentiation of temozolomide by PARP1 knock-down is not selective to cancer cells .....	157
3.2.12 Reduction in NAD(H) and PARP activity and temozolomide potentiation in GBM1 cancer stem cell-like cells .....	161
3.2.13 Does FK866 treatment lead to an impairment in DNA repair? .....	171
3.2.14 Effects of FK866 on SIRT1 activity .....	174
3.3 Discussion and Conclusions.....	177
3.3.1 Chemosensitivity to FK866 and correlation with NAMPT/NAPRT expression and cellular NAD <sup>+</sup> -consuming activity.....	177
3.3.2 NAMPT inhibition preferentially depletes cellular NAD <sup>+</sup> and NADH from cancer cells independent of cancer cell p53 status and is able to deplete the nuclear NAD(H) pool ..	179

3.3.3 Reduction of PARP DNA repair activity selectively in cancer cells and improving the selectivity of current chemotherapeutic agents .....	180
3.3.4 Conclusion.....	184
4. NAD <sup>+</sup> -dependent protein deacetylase SIRT1 as a potential anti-cancer therapeutic target and constitutive repressor of a neuronal-like phenotype switch in non-cancer and cancer cells	186
4.1 Introduction.....	186
4.2 Results.....	189
4.2.1 SIRT1 knock-down induces cancer cell death <i>in vitro</i> .....	189
4.2.2 Selectivity and activity of the small molecule inhibitor EX-527.....	190
4.2.3 EX-527 induces cell death by apoptosis .....	198
4.2.4 SIRT1-FL knock-down by siRNA and effects on neural stem cell and pluripotency markers .....	200
4.2.5 Small molecule chemical inhibition of SIRT1 via EX-527 induces neuronal trans-differentiation of ARPE-19 and CCD 841 CoN non-cancer cells .....	207
4.2.6 Effects of EX-527 treatment on cancer cell ‘stemness’ in the GBM1 cancer stem cell model. ....	212
4.2.7 Increase in MAP2 protein expression with EX-527 treatment.....	215
4.2.8 Metabolic effects of SIRT1 knock-down/inhibition .....	216
4.3 Discussion and Conclusions.....	219
4.3.1 Preferential cytotoxic activity of the SIRT1 inhibitor EX-527 towards cancer cells <i>in vitro</i> , partially mimicking the effects of SIRT1-full length knock-down by RNAi .....	219
4.3.2 SIRT1 inhibitor EX-527 induces neuronal trans-differentiation of ARPE-19 and CCD 841 CoN non-cancer cells.....	221
4.3.3 Effects of SIRT1-FL and SIRT1-Δ8 targeting on expression of stem cell and pluripotent/somatic reprogramming factors.....	223
4.3.4 Inhibition of SIRT1 reduces ‘stemness’ of GBM1 cancer stem cell-like cells.....	224
4.3.5 Metabolic effects of suppressing SIRT1.....	225
4.3.6 Conclusions .....	226
5. Epigenetic effects of suppressing LDH-A and the therapeutic potential to re-express epigenetically silenced tumour suppressor genes .....	227
5.1 Introduction.....	227
5.2 Results.....	231

5.2.1 LDH-A knock-down in HCT116 p53 <sup>+/+</sup> cancer cells leads to alterations in histone modifications .....	231
5.2.2 Effects of LDH-A inhibition on levels of 5-hydroxymethylcytosine (5hmC), a marker of DNA demethylation.....	234
5.2.3 Epigenetic effects of targeting LDH-A in other cancer cell lines.....	238
5.2.4 SIRT1 inhibitor EX-527 induces re-expression of epigenetically silenced E-cadherin in MDA-MB-231 cancer cells .....	241
5.2.5 E-cadherin re-expression with EX-527 treatment in hypoxic MDA-MB-231 cancer cells .....	244
5.2.6 Effects of targeting LDH-A on E-cadherin expression .....	245
5.2.7 Effect of EX-527 treatment combined with LDH-A knock-down on E-cadherin expression under hypoxic conditions.....	250
5.2.8 EX-527 treatment of MDA-MB-231 cancer cells induces expression of neuronal markers- an effect that is partially mirrored by LDH-A knock-down .....	251
5.3 Discussion and conclusions .....	254
5.3.1 Suppressing LDH-A increases global levels of acetylated K9 of histone H3 and reduces global levels of trimethylated H3K9 but with cancer cell heterogeneity .....	254
5.3.2 Re-expression of epigenetically silenced E-cadherin is induced by SIRT1 inhibitor EX-527 under normoxic and hypoxic conditions and by LDH-A silencing under normoxic conditions .....	257
5.3.3 LDH-A knock-down induces expression of neural stem cell factor Nestin and neuronal marker MAP1a in MDA-MB-231 breast cancer cells.....	259
5.3.4 Future work.....	259
5.3.5 Conclusions .....	260
6. Effects of small molecule KHS101 on glioblastoma cells <i>in vitro</i> and its therapeutic potential for selective targeting of other cancer types.....	262
6.1 Introduction.....	262
6.2 Results.....	265
6.2.1 Vacuolisation induction and metabolic effects of KHS101 .....	265
6.2.2 KHS101 induces GBM1 cancer cell death by apoptosis.....	267
6.2.3 Mechanism of action of KHS101 in glioblastoma cells .....	269
6.2.4 HSPD1 inhibitor myrtocommulone recapitulates the GBM-selective lethal effects of KHS101.....	271
6.2.5 Investigation of KHS101 activity against other cancer cell types .....	272

6.2.6 Mechanism(s) of action of KHS101 towards other cancer cell types.....	278
6.2.7 Does KHS101 produce differential effects on cellular metabolism in other cancer and non-cancer cells? .....	285
6.2.8 Differential effects linked to aerobic glycolysis of KHS101 treatment of HCT116 and GBM1 cancer cells.....	289
6.2.9 KHS101 treatment differentially affects ATP levels in cancer and non-cancer cells .....	290
6.2.10 Expression of potential downstream targets of KHS101 in a cell line screen .....	291
6.2.11 Action of KHS101 on GPD2 activity and NAD(H) in HCT116 p53 <sup>+/+</sup> cancer cells.	294
6.2.12 Cytoplasmic ‘speckles’/particulates induced by KHS101 .....	295
6.2.13 KHS101 induces neuronal differentiation of ARPE-19 non-cancer cells .....	300
6.3 Discussion and conclusions .....	303
6.3.1 Induction of apoptotic cell death by KHS101 and HSPD1 inhibitor myrtoicommulone in GBM cell models .....	303
6.3.2 Decrease in GPD2 activity with acute KHS101 exposure and perturbation of cellular NADH/NAD <sup>+</sup> balance .....	304
6.3.3 Cancer selective activity of KHS101 towards other cancer cell types .....	305
6.3.4 Induction of autophagy by KHS101 in HCT116 cancer cells and ARPE-19 non-cancer cells.....	306
6.3.5 Glycolytic compensation and differential effects on cellular ATP levels of KHS101 treatment in HCT116 p53 <sup>+/+</sup> and ARPE-19 cells .....	308
6.3.6 Decreased GPD2 activity in HCT116 cells and differential HSPD1 expression.....	309
6.3.7 Cytoplasmic protein aggregates induced by KHS101.....	310
6.3.8 Induction of neuronal differentiation by KHS101 in ARPE-19 retinal epithelial non-cancer cells .....	310
6.3.9 Conclusions .....	311
7. Summary and perspectives.....	313
8. References .....	321
9. Appendix .....	357

# List of tables

Table 1.1: Summary of clinically approved PARP inhibitors for single agent use. ....	64
Table 2.1: Cell line summary. ....	82
Table 2.2: Cell seeding density of a 96 well plate.....	85
Table 2.3: Dose range of drugs used for chemosensitivity. ....	86
Table 2.4: Appropriate seeding density of cell lines for annexin V analysis.....	88
Table 2.5: Appropriate conditions for XFp seahorse metabolic analysis .....	91
Table 2.6: Cell number seeding per T25 flask for siRNA transfection. ....	95
Table 2.7: siRNAs used for transfection.....	95
Table 2.8: TaqMan™ probes for qPCR.....	98
Table 2.9: Primer sequences for SYBR™ Green qPCR.....	99
Table 2.10: Appropriate seeding density of cells for cellular NAD(H) determination.....	100
Table 2.11: Antibody dilutions and conditions for immunoblotting.....	104
Table 2.12: Secondary antibody conditions for Immunoblotting.....	105
Table 2.13: Seeding densities for PARP ELISA assay.....	106
Table 3.1: IC <sub>50</sub> values of FK866 towards multiple human cell lines of different tissue origin. ....	120
Table 4.1: IC <sub>50</sub> values of EX-527 towards multiple human cell lines of different tissue origin. .	190
Table 6.1: IC <sub>50</sub> values of KHS101 towards multiple human cell lines of different tissue origin.	273
Table 9.1: Constituents for 4% and 15% SDS-PAGE gels for Immunoblotting.....	358
Table 9.2: IC <sub>50</sub> values of cisplatin in CP70/A2780cis and A2780 cancer cells.....	358
Table 9.3: IC <sub>50</sub> values of FDA-approved platinates in HCT116 p53 <sup>+/+</sup> cancer cells and CCD 841 CoN non-cancer cells.....	359
Table 9.4: IC <sub>50</sub> values of doxorubicin in HCT116 p53 <sup>+/+</sup> cancer cells under normoxic and hypoxic conditions. ....	359

# List of figures

Figure 1.1: The eight hallmarks and two enabling characteristics of cancer.....	30
Figure 1.2: The concept of a small or larger therapeutic index. ....	34
Figure 1.3: Targeted therapies being developed that target specific hallmarks of cancer.....	36
Figure 1.4: Glycolysis in non-cancer cells.....	40
Figure 1.5: The tricarboxylic acid cycle.....	42
Figure 1.6: The electron transport chain and oxidative phosphorylation. ....	43
Figure 1.7: Key events in glucose catabolism in non-cancer and cancer cells. ....	45
Figure 1.8: Chemical structure of NAD <sup>+</sup> and NADH.....	54
Figure 1.9: NAD <sup>+</sup> biosynthesis pathways. ....	56
Figure 1.10: Consumption of NAD <sup>+</sup> by PARP.....	58
Figure 1.11: Recruitment of PARP1 during BER.....	60
Figure 1.12: Schematic of synthetic lethality. ....	62
Figure 1.13: The primary cytotoxic mechanism of action of temozolomide. ....	66
Figure 1.14: Recycling of NAD <sup>+</sup> by SIRT1.....	69
Figure 1.15: Splice variants of SIRT1. ....	72
Figure 2.1: Mitochondrial assay injections. ....	92
Figure 2.2: Drug treatment set up for DNA damage marker analysis.....	108
Figure 3.1: Schematic briefly outlining PARPs involvement in cancer cell survival.....	113
Figure 3.2: Schematic of potential cancer selective inhibition of PARP.....	114
Figure 3.3: Basal cellular energetics of non-cancer cell models compared to cancer cell lines. .....	116
Figure 3.4: Cell images of CCD 841 CoN cells at different passage numbers following staining for $\beta$ -galactosidase activity as a marker of cellular senescence. ....	117
Figure 3.5: Cell cycle distribution of sub-confluent and confluent CCD 841 CoN cells. ....	118
Figure 3.6: Cell cycle distribution of sub-confluent and confluent ARPE-19 cells.....	119
Figure 3.7: Summary of FK866 cytotoxicity towards a panel of non-cancer and cancer cells and determination of a lack of cross-resistance with cisplatin. ....	121
Figure 3.8: Preferential cytotoxic activity of FK866 towards cancer cells compared to non-cancer cell models.....	123
Figure 3.9: Cancer cell selectivity of FK866 compared to FDA approved platinate based compounds. ....	124
Figure 3.10: The effect of hypoxia on doxorubicin and FK866 cytotoxicity towards HCT116 p53 <sup>+/+</sup> cells. ....	125
Figure 3.11: Protein expression of NAMPT and associated proteins in human non-cancer and cancer cell lines. ....	126
Figure 3.12: Densitometric quantification of cellular protein expression.....	127

Figure 3.13: Protein expression of NAMPT and NAPRT compared to cellular FK866 chemosensitivity (IC <sub>50</sub> ). .....	128
Figure 3.14: Cell energy phenotype of HCT116 p53 <sup>+/+</sup> cancer cells treated with NAMPT inhibitor FK866. ....	132
Figure 3.15: Cell energy phenotype of ARPE-19 non-cancer cells treated with NAMPT inhibitor FK866. ....	134
Figure 3.16: Cell energy phenotype of CCD 841 CoN non-cancer cells treated with 10nM FK866. ....	134
Figure 3.17: Chemosensitivity dose response for FK866 in HCT116 p53 <sup>+/+</sup> cancer cells in the presence or absence of NA and NMN. ....	135
Figure 3.18: Cell energy phenotype of HCT116 p53 <sup>+/+</sup> cancer cells after FK866 treatment ± NA/NMN. ....	136
Figure 3.19: Total cellular NAD(H) reduction in cells treated with FK866. ....	137
Figure 3.20: Fold reduction in NAD(H) levels in multiple non-cancer and cancer cell lines after 10nM FK866 treatment. ....	138
Figure 3.21: Reduction of nuclear and cytoplasmic NAD(H) pools by FK866. ....	139
Figure 3.22: Quantification of PARP activity after cellular FK866 treatment. ....	140
Figure 3.23: Decreased protein PARylation in MDA-MB-436 cancer cells following 24 hours FK866 treatment. ....	141
Figure 3.24: Densitometric quantification of protein PARylation levels in MDA-MB-436 cells after 24 hours FK866 treatment. ....	142
Figure 3.25: Partial rescue of decreased PARP activity, caused by FK866 treatment, by co-treatment with NAD <sup>+</sup> precursor NMN. ....	143
Figure 3.26: Quantification of PARP activity after PARP inhibitor or FK866 treatment. ....	144
Figure 3.27: Total cell number and viability after 48 hours camptothecin treatment of non-cancer and cancer cell lines in the presence or absence of FK866 or PARP inhibitor rucaparib. ....	145
Figure 3.28: Quantification of annexin V positive cells after treatment with camptothecin in the presence or absence of FK866 or PARP inhibitor rucaparib. ....	146
Figure 3.29: Total cell number and viability after non-cancer and cancer cell line treatment with doxorubicin in the presence or absence of FK866 or PARP inhibitor rucaparib. ....	147
Figure 3.30: Quantification of annexin V positive cells after treatment with doxorubicin in the presence or absence of FK866 or PARP inhibitor rucaparib. ....	148
Figure 3.31: Cell micrographs of HCT116 p53 <sup>+/+</sup> cancer cells after 48 hours treatment of temozolomide in the absence or presence of FK866 or PARP inhibitor rucaparib. ....	149
Figure 3.32: Total cell number and viability after 48 hours temozolomide treatment of non-cancer and cancer cell lines in the presence or absence of FK866 or PARP inhibitor rucaparib. ....	150
Figure 3.33: Quantification of annexin V positive cells after treatment with temozolomide in the presence or absence of FK866 or PARP inhibitor rucaparib. ....	151
Figure 3.34: Total cell number and viability of isogenic HCT116 p53 <sup>+/+</sup> and HCT116 p53 <sup>-/-</sup> cancer cells after combination treatments of DNA-damaging chemotherapeutic agents with FK866. .	152

Figure 3.35: Quantification of annexin V positive cells after combination treatments of DNA-damaging chemotherapeutic agents with FK866 in HCT116 p53 <sup>-/-</sup> cancer cells.....	153
Figure 3.36: Total cell number and viability in other cancer cells after 48 hours treatment with temozolomide in the presence or absence of FK866 or rucaparib. ....	154
Figure 3.37: Quantification of annexin V positive cells after 48 hours treatment with temozolomide in the presence or absence of FK866 or PARP inhibitor rucaparib. ....	155
Figure 3.38: Cell number and viability after 48 hours treatment of cancer and non-cancer cells with paclitaxel in the presence or absence of FK866.....	156
Figure 3.39: Quantification of annexin V positive cells after treatment with paclitaxel in the presence or absence of FK866.....	157
Figure 3.40: RNAi mediated PARP1 silencing in HCT116 p53 <sup>+/+</sup> cancer cells.....	158
Figure 3.41: Cell micrographs after 48 hours temozolomide treatment following transfection with control or PARP1 siRNA. ....	159
Figure 3.42: Cell number and viability after RNAi-mediated PARP1 knock-down and temozolomide treatment.....	160
Figure 3.43: Quantification of annexin V positive cells after RNAi-mediated PARP1 knock-down and temozolomide treatment. ....	161
Figure 3.44: Cell energy phenotype of NP1 and GBM1 cells following 24 hours 2.5nM FK866 treatment. ....	162
Figure 3.45: Fold reduction in NP1 and GBM1 total cellular NAD(H) levels with 24 hours FK866 treatment. ....	163
Figure 3.46: Quantification of PARP activity after 24 hours FK866 treatment. ....	163
Figure 3.47: Chemosensitivity dose response to temozolomide in the presence or absence of FK866 or rucaparib in NP1 and GBM1 cells.....	165
Figure 3.48: Total cell number and viability after 48 hours temozolomide treatment in GBM1 cells in the presence or absence of FK866. ....	166
Figure 3.49: Quantification of annexin V positive GBM1 cells after treatment with 400µM temozolomide in the absence or presence of 1nM FK866 for 48 hours. ....	167
Figure 3.50: Cell micrographs of NP1 cells after 48 hours treatment with temozolomide in the absence or presence of FK866 or PARP inhibitor rucaparib.....	169
Figure 3.51: Total cell number and viability after 48 hours temozolomide treatment in NP1 cells in the presence or absence of FK866 or rucaparib. ....	170
Figure 3.52: Cell cycle analysis after combination treatment. ....	171
Figure 3.53: Expression of phosphorylated gamma H2AX as a marker of DSB DNA damage in HCT116 p53 <sup>+/+</sup> cancer cells after FK866 pre-treatment and temozolomide exposure. ....	172
Figure 3.54: Expression of phosphorylated gamma H2AX as a marker of DSB DNA damage in ARPE-19 non-cancer cells after FK866 or rucaparib pre-treatment and temozolomide exposure. ....	173
Figure 3.55: Effect of FK866 on SIRT1 activity in HCT116 p53 <sup>+/+</sup> cancer cells.....	174

Figure 3.56: Total cell number and viability of HCT116 p53 <sup>-/-</sup> cells after 48 hours treatment with temozolomide in the absence of presence of SIRT1 inhibitor EX-527.....	175
Figure 3.57: Quantification of apoptosis in HCT116 p53 <sup>-/-</sup> cancer cells after treatment of temozolomide in the presence and absence of SIRT1 inhibitor EX-527.....	176
Figure 4.1: RNAi mediated SIRT1 silencing and phenotypic effects in HCT116 p53 <sup>+/+</sup> cancer cells. ....	189
Figure 4.2: Summary of EX-527 cytotoxicity towards a panel of non-cancer and cancer cells and determination of a lack of cross-resistance with cisplatin. ....	191
Figure 4.3: Preferential cytotoxicity activity of EX-527 towards cancer cells compared to non-cancer cell models. ....	192
Figure 4.4: Cancer selectivity of EX-527 compared to FDA approved platinate based compounds. ....	193
Figure 4.5: The effect of hypoxia on doxorubicin and EX-527 cytotoxicity towards HCT116 p53 <sup>+/+</sup> cells. ....	194
Figure 4.6: Protein expression of SIRT1 compared to cellular EX-527 chemosensitivity (IC <sub>50</sub> ). ....	195
Figure 4.7: Cell micrographs of ARPE-19 non-cancer cells, HCT116 p53 <sup>+/+</sup> cancer cells under normoxic and hypoxic conditions and cancer stem cell-like model GBM1 after EX-527 treatment. ....	196
Figure 4.8: Total cell number and viability after 48 hours EX-527 treatment. ....	197
Figure 4.9: Annexin V assay dot plots showing induction of apoptosis by SIRT1 inhibitor EX-527 in cancer cells and not in ARPE-19 non-cancer cells. ....	199
Figure 4.10: Quantification of annexin V positive cells in response to treatment with SIRT1 inhibitor EX-527. ....	200
Figure 4.11: Schematic summarising the current model for the proposed roles of SIRT1-FL and SIRT1-Δ8 in ARPE-19 neuronal differentiation. ....	201
Figure 4.12: Cell micrographs of ARPE-19 non-cancer cells after siRNA transfections to selectively deplete SIRT1-FL and/or SIRT1-Δ8 mRNA. ....	202
Figure 4.13: qPCR analysis of SIRT1-FL and SIRT1-Δ8 mRNA after siRNA transfection in ARPE-19 non-cancer cells. ....	203
Figure 4.14: mRNA expression of stem cell and pluripotency markers following splice variant specific siRNA mediated silencing of SIRT1 in ARPE-19 cells. ....	204
Figure 4.15: qPCR analysis of SIRT1-FL and SIRT1-Δ8 mRNA after siRNA transfection in CCD 841 CoN non-cancer cells. ....	204
Figure 4.16: Cell micrographs of CCD 841 CoN non-cancer cells after siRNA transfection to selectively deplete SIRT1-FL and/or SIRT1-Δ8 mRNA. ....	205
Figure 4.17: mRNA expression of neuronal marker MAP1a following splice variant specific siRNA mediated silencing of SIRT1 in CCD 841 CoN. ....	206
Figure 4.18: qPCR analysis of stem cell and pluripotency markers following splice variant specific siRNA mediated silencing of SIRT1 in CCD 841 CoN. ....	206

Figure 4.19: Cell micrographs of ARPE-19 non-cancer cells after 48 hours treatment with SIRT1 inhibitor, EX-527. ....	208
Figure 4.20: mRNA expression of neuronal markers in EX-527 treated ARPE-19 non-cancer cells. ....	209
Figure 4.21: Cell micrographs of CCD 841 CoN non-cancer cells after 48 hours EX-527 treatment. ....	210
Figure 4.22: mRNA expression of neuronal marker MAP1a in CCD 841 CoN cells after treatment with EX-527 for 48 hours. ....	211
Figure 4.23: qPCR analysis of stem cell and pluripotency markers in CCD 841 CoN cells following EX-527 treatment. ....	212
Figure 4.24: Cell micrographs of GBM1 cancer stem like cells after 48 hours EX-527 treatment. ....	213
Figure 4.25: Expression of stem cell markers in EX-527 treated GBM1 cells. ....	214
Figure 4.26: qPCR analysis of neuronal marker expression in GBM1 cells after EX-527 treatment. ....	215
Figure 4.27: Expression of the neuronal marker MAP2 in ARPE-19 cells treated with EX-527. ....	216
Figure 4.28: Cell energy phenotype of non-cancer and cancer cells after 24 hours EX-527 treatment. ....	217
Figure 4.29: Cell energy phenotype of ARPE-19 non-cancer cells after SIRT-FL siRNA transfection. ....	218
Figure 5.1: Schematic of hypothesised model of the effects of LDH-A knock-down/inhibition on histone acetylation. ....	229
Figure 5.2: Schematic summarising the role of LDH-A and MDH1/2 in generation of L-2HG under hypoxia and possible downstream effects of this. ....	230
Figure 5.3: Immunoblot showing changes in key histone modifications in HCT116 p53 <sup>+/+</sup> cancer cells in response to LDH-A silencing by RNAi. ....	232
Figure 5.4: Cell micrographs of HCT116 p53 <sup>+/+</sup> cancer cells after LDH-A knock-down. ....	233
Figure 5.5: Acute metabolic response of HCT116 p53 <sup>+/+</sup> cancer cells to LDH-A inhibitor, NHI-2. ....	235
Figure 5.6: Analysis of 5-hydroxymethylcytosine in HCT116 p53 <sup>+/+</sup> cancer cells treated with '5-aza-'2-deoxycytidine. ....	236
Figure 5.7: Analysis of 5-hydroxymethylcytosine in HCT116 p53 <sup>+/+</sup> cancer cells treated with NHI-2 under different O <sub>2</sub> tensions. ....	237
Figure 5.8: Effects of LDH-A silencing by RNAi on histone modifications in MDA-MB-231 triple negative breast cancer cells. ....	239
Figure 5.9: Effects of LDH-A inhibitor NHI-2 on histone modifications in MDA-MB-231 triple negative breast cancer cells. ....	240
Figure 5.10: qPCR analysis of E-cadherin mRNA expression in MDA-MB-231 cancer cells after EX-527 treatment. ....	242

Figure 5.11: Cell micrographs of MDA-MB-231 after 24 and 48 hours exposure to SIRT1 inhibitor EX-527. ....	243
Figure 5.12: qPCR analysis of E-cadherin under normoxic and hypoxic conditions. ....	244
Figure 5.13: Cell micrographs of MDA-MB-231 after 48 hours EX-527 exposure under normoxic and hypoxia. ....	245
Figure 5.14: qPCR analysis of LDH-A and E-cadherin mRNA expression in MDA-MB-231 cells after RNAi mediated silencing of LDH-A. ....	246
Figure 5.15: Protein expression of E-cadherin after LDH-A knock-down in MDA-MB-231 cancer cells. ....	247
Figure 5.16: Cell micrographs of MDA-MB-231 cells after LDH-A knock-down. ....	248
Figure 5.17: qPCR analysis of E-cadherin mRNA levels in MDA-MB-231 cancer cells after NHI-2 treatment for 48 hours. ....	249
Figure 5.18: Protein expression of E-cadherin in MDA-MB-231 cancer cells after NHI-2 treatment for 48 hours. ....	250
Figure 5.19: qPCR analysis of E-cadherin mRNA expression in MDA-MB-231 cancer cells after EX-527 treatment in the presence or absence of LDH-A knock-down. ....	251
Figure 5.20: qPCR analysis of neuronal markers in MDA-MB-231 cancer cells after EX-527 treatment. ....	252
Figure 5.21: qPCR analysis of neuronal marker mRNA levels after LDH-A knock-down in MDA-MB-231 cancer cells. ....	253
Figure 6.1: Effects of KHS101 treatment in neural progenitor cells. ....	263
Figure 6.2: The glycerol-3-phosphate shuttle. ....	264
Figure 6.3: Cell micrographs of GBM1 cancer cells after treatment with 7.5µM KHS101 for 24 hours. ....	265
Figure 6.4: Cell energy phenotype of NP1 and GBM1 cells after KHS101 treatment. ....	267
Figure 6.5: Quantification of annexin V positive GBM1 cells after treatment with 7.5µM KHS101 in the absence or presence of the autophagy inhibitor bafilomycin for 48 hours. ....	268
Figure 6.6: Decrease in GPD2 activity after KHS101 treatment. ....	270
Figure 6.7: Decrease in NADH levels relative to NAD <sup>+</sup> following 24 hours KHS101 treatment. ....	270
Figure 6.8: Expression of phosphorylated AMPK in GBM11 after KHS101 treatment. ....	271
Figure 6.9: Quantification of annexin V positive cells after 10µM myrtilone treatment. ....	272
Figure 6.10: Summary of KHS101 cytotoxicity towards a panel of non-cancer and cancer cells and lack of cross-resistance with cisplatin. ....	274
Figure 6.11 Preferential cytotoxicity of KHS101 towards cancer cells compared to non-cancer cell models. ....	275
Figure 6.12: Cancer cell selectivity of KHS101 compared to FDA approved platinum based compounds. ....	276
Figure 6.13: The effect of hypoxia on doxorubicin and KHS101 towards HCT116 p53 <sup>+/+</sup> cells. ....	277
Figure 6.14: Percentage cell number and annexin V positive cells after KHS101 treatment in ARPE-19 non-cancer cells and HCT116 p53 <sup>+/+</sup> cancer cells. ....	279

Figure 6.15: Cell micrographs of ARPE-19 and HCT116 p53 <sup>+/+</sup> cancer cells after KHS101 treatment. ....	280
Figure 6.16: Image cytometry analysis of KHS101 and DMSO vehicle control treated cells stained with the autophagic dye CYTO-ID. ....	281
Figure 6.17: Expression of CYTO-ID as a marker of autophagy in HCT116 cancer cells that have been treated with KHS101 for 24 hours. ....	282
Figure 6.18: Expression of CYTO-ID as a marker of autophagy in ARPE-19 non-cancer cells that have been treated with KHS101 for 24 hours.....	283
Figure 6.19: Localisation of CYTO-ID staining to vacuoles in HCT116 p53 <sup>+/+</sup> cancer cells treated with 7.5µM KHS101 or DMSO vehicle control.....	284
Figure 6.20: Quantification of the autophagy marker LC3-II in cells after 5µM KHS101 treatment for 24 hours.....	285
Figure 6.21: Cell energy phenotype of ARPE-19 non-cancer cells and HCT116 p53 <sup>+/+</sup> cancer cells after KHS101 treatment.....	286
Figure 6.22: Mitochondrial stress test response of HCT116 p53 <sup>+/+</sup> cancer cells following direct injection of 2.5µM KHS101 into growth medium.....	288
Figure 6.23: Mitochondrial stress test response of HCT116 p53 <sup>+/+</sup> cancer cells following direct injection of 7.5µM KHS101 into growth medium.....	289
Figure 6.24: Images of media colour change of T25 flasks of cells treated with KHS101. ....	290
Figure 6.25: Effects of KHS101 on total cellular ATP levels. ....	291
Figure 6.26: Protein expression of potential downstream targets of KHS101 in untreated non-cancer and cancer cell lines. ....	292
Figure 6.27: Densitometric quantification of cellular protein expression.....	293
Figure 6.28: Percentage decrease in GPD2 activity after KHS101 treatment. ....	294
Figure 6.29: Decrease in NADH levels relative to NAD <sup>+</sup> following 24 hours KHS101 treatment. ....	295
Figure 6.30: Cell micrographs of ARPE-19 non-cancer cells treated with various KHS101 doses for 24 hours.....	296
Figure 6.31: Cell micrographs of HCT116 p53 <sup>+/+</sup> cancer cells treated with various KHS101 doses for 24 hours.....	297
Figure 6.32: Protein expression of CHOP and other proteins of interest in ARPE-19 non-cancer cells after treatment with various KHS101 doses. ....	298
Figure 6.33: Protein expression of CHOP and other proteins of interest in HCT116 p53 <sup>+/+</sup> cancer cells after treatment with various KHS101 doses. ....	299
Figure 6.34: Densitometric quantification of phosphorylated AMPK.....	300
Figure 6.35: qPCR analysis of neuronal and stem cell markers in ARPE-19 non-cancer cells after KHS1001 treatment.....	301
Figure 6.36: Expression of neuronal marker MAP2 in ARPE-19 non-cancer cells treated with KHS101. ....	302

Figure 9.1: qPCR analysis of SIRT1-FL, SIRT1-Δ8, MAP1a and MAP2 mRNA (data generated by S.J.Allison).....	357
Figure 9.2: Protein expression of p53 in HCT116 p53 <sup>+/+</sup> and HCT116 p53 <sup>-/-</sup> cancer cells.....	358
Figure 9.3: Cell micrographs of non-cancer and cancer cells treated with 10nM FK866 for 24 hours. ....	361
Figure 9.4: Cell micrographs of ARPE-19 non-cancer cells, HCT116 p53 <sup>+/+</sup> cancer cells under normoxic and hypoxic conditions and cancer stem-cell like model GBM1 after EX-527 treatment. ....	363
Figure 9.5: Comparison of IC <sub>50</sub> values of FK866 in HT-29 cancer cells achieved through chemosensitivity assay via SRB or MTT staining. ....	363

# Publications

1. [In preparation]: **H.B.S. Griffiths**, C. Williams, S.J. Allison. Increased dependency of cancer cells on NAMPT to sustain cellular NAD(H) levels – an opportunity for cancer-selective PARP inhibition. [Chapter 4 data].
2. B. da Silva, B.K. Irving, E.S. Polson, A. Droop, **H.B.S. Griffiths**, R.K. Mathew, L.F. Stead, J. Marrison, C. Williams, J. Williams, S.C. Short, M. Scarcia, P.J. O'Toole, S.J. Allison, G. Mavria, and H. Wurdak. Chemically-induced Neurite-like Outgrowth Reveals Multicellular Network Function in Patient-derived Glioblastoma Cells. *Journal of Cell Science*. 228452. (2019).
3. R.J.O. Nichol, A.I. Khalaf, K. Sooda, O. Hussain, **H.B.S. Griffiths**, R. Phillips, F.A. Javid, C.J. Suckling, S.J. Allison, F. Scott. Selective *in vitro* anti-cancer activity of non-alkylating minor groove binders. *MedChemCom*. 10, 1620-1634. (2019). [Chapter 9, Table 9.2]
4. E.S. Polson, V.B. Kuchler, C. Abbosh, E.M. Ross, R.K. Mathew, H.A. Beard, B. da Silva, A.N. Holding, S. Ballereau, E. Chuntharpursat-Bon, J. Williams, **H.B.S. Griffiths**, H. Shao, A. Patel, A.J. Davies, A. Droop, P. Chumas, S.C. Short, M. Lorger, J.E. Gestwicki, L.D. Roberts, R.S. Bon, S.J. Allison, S. Zhu, F. Markowitz and H. Wurdak. KHS101 disrupts energy metabolism in human glioblastoma cells and reduces tumor growth in mice. *Science Translational Medicine*. 10, eaar2718. (2018). [Chapter 6, Figure 6.5, Figure 6.6 & Figure 6.9]
5. S.J. Allison, D. Cooke, F.S. Davidson, P. I. P. Elliott, R.A. Faulkner, **H.B.S. Griffiths**, O.J. Harper, O. Hussain, J. Owen-Lynch, R.M. Phillips, C.R. Rice, S.L. Shepherd, R.T. Wheelhouse. Ruthenium-Containing Linear Helicates and Mesocates with Tuneable p53-Selective Cytotoxicity in Colorectal Cancer Cells. *Angewandte Chemie*. 57, 9799-9804. (2018). [Chapter 9, Table 9.3]

## **Presentations and conferences**

- Poster presentation at Don Whitley Scientific 1st Hypoxia Symposium: The Tumour Microenvironment (Oct. 2019).
- Poster presentation at North of England Cell Biology Forum, Manchester (Sept. 2019).
- Poster presentation at North of England Cell Biology Forum, Hull (Sept. 2017).
- Oral presentation at North of England Cell Biology Forum, Huddersfield (Aug. 2018).
- Attendee of Huddersfield PGR conference (Nov. 2017, Apr. 2019).
- Attendee of York against Cancer 30 Year Anniversary Mini Symposium. (Nov. 2017).

# 1. Introduction

## 1.1 Cancer as a genetic disease and its current treatment

### 1.1.1 Brief definition of cancer

Cancer is an umbrella term for a group of (epi)genetic diseases that result from accumulated mutations in two small subsets of genes, proto-oncogenes and tumour suppressor genes (TSG), leading to loss of normal cell growth control, tumour formation and metastatic spread of cancer cells.

### 1.1.2 Cancer incidence and mortality

In 2015 The World Health Organisation estimated cancer to be the first or second leading cause of death for those aged under 70 years in 91 of 172 countries in the world (Bray *et al.*, 2018). 18.1 million new cases of cancer and 9.6 million cancer related deaths were estimated by GLOBOCAN in 2018 (Bray *et al.*, 2018) and it is currently reported that, in the UK 1 in 2 people will develop cancer within their lifetime (Ahmad *et al.*, 2015).

Cancer can arise from almost any cell or tissue type and there are over 200 types of cancer. Risk factors, symptoms, cancer stages at diagnosis, treatment options and effectiveness of treatments vary depending on the cancer, indicating the complexity of this disease and the challenges it presents. The most common cancers are lung cancer, female breast cancer, colorectal cancer and prostate cancer, with lung cancer (18.4%) and colorectal cancer (9.2%) having the highest mortality rates overall (Bray *et al.*, 2018).

Exposure to certain environmental factors can increase the likelihood of developing particular cancers. These include exposure to cancer-promoting carcinogens, such as those found in cigarette smoke, which can cause DNA mutations (Sankpal *et al.*, 2012). Other risk factors for certain cancers include obesity, high alcohol consumption and exposure to harmful UV radiation from the

sun. Exposure to some of these risk factors may be reduced through lifestyle measures and in the case of cervical cancer, which is causally linked to infection with high-risk human papilloma virus types, a vaccination programme has been introduced.

Whilst most cancers develop from spontaneous mutations in somatic cells, certain individuals may have an increased unavoidable risk of developing a particular cancer due to inheritance of a recessive germline mutation in a particular critical gene (Lu *et al.*, 2014). This will predispose these individuals to developing that cancer with fewer additional mutations required for cancer development.

A major risk factor which is unavoidable and applies for almost all cancers is advancing age. This is consistent with the development of cancer being a multistep process requiring the accumulation of a number of critical mutations in a single cell. With a growing and ageing population, it is perhaps not surprising that the incidence of cancer has been steadily increasing over the past decades, indicating that the 'cancer problem' is not about to go away.

Cancer survival rates in England and Wales have improved in the last 40 years with survival for 10 or more years after diagnosis increasing from 24% to 50% (Quaresma *et al.*, 2015). Although survival as a whole has increased there is considerable variation between different cancer types, for example patients with testicular cancer have a 98.2% chance of survival past 10 years whereas this rate is as low as 1.1% in patients with pancreatic cancer (Quaresma *et al.*, 2015).

Improvements in survival result from increased awareness of symptoms and earlier diagnosis and treatment of cancers, as well as advances in treatments for particular cancers informed by increased knowledge of the cancer. Despite significant improvements for some cancers, for many cancers the treatments currently available only modestly improve survival and many are inherently toxic and lack selectivity towards cancer cells, which limits their effectiveness and can impact on patient quality of life.

There is a clear clinical need for the development of new treatments and therapeutic approaches. This PhD research is focused on the investigation of potential opportunities linked to differences in the metabolism of cancer and non-cancer cells.

### **1.1.3 The genetic basis of cancer**

Cancer is characterised by a loss of normal tissue homeostatic balance between the number of proliferating cells and the number of dying or apoptotic cells, leading to the formation of a tumour mass (Alberts *et al.*, 2014). This is caused by cellular accumulation of genetic mutations in two key types of genes, TSGs and proto-oncogenes, leading to loss of normal cellular regulatory control where cells proliferate abnormally and evade cell death.

In non-cancer cells, TSGs work to prevent tumour development and an inactivating mutation in both alleles will lead to loss of function (May and May, 1999). TSGs can also encounter a mutation in one allele which can lead to suboptimal activity of the protein, a phenomenon known as haploinsufficiency. The normal cellular role of TSGs is as cellular 'brakes', inhibiting cell cycle progression when conditions are inappropriate, for example ensuring repair of damaged DNA and/or death of old/damaged cells to sustain tissue homeostasis and function. Activating mutations in proto-oncogenes result in their constitutive activation, these are dominant gain of function mutations resulting in their being 'on', stimulating proliferation in the absence of an appropriate signal (Hoffman and Liebermann, 1998). The normal physiological role of proto-oncogenes is the stimulation of cell growth and cell survival in response to stimulatory signals from other cells. Inactivation of TSGs and oncogene activation promote the development of cancer and cellular acquisition of the so-called 'hallmarks of cancer'.

### **1.1.4 The hallmarks of cancer**

The hallmarks of cancer are key traits or biological capabilities acquired by cancer cells that are important for cancer development.

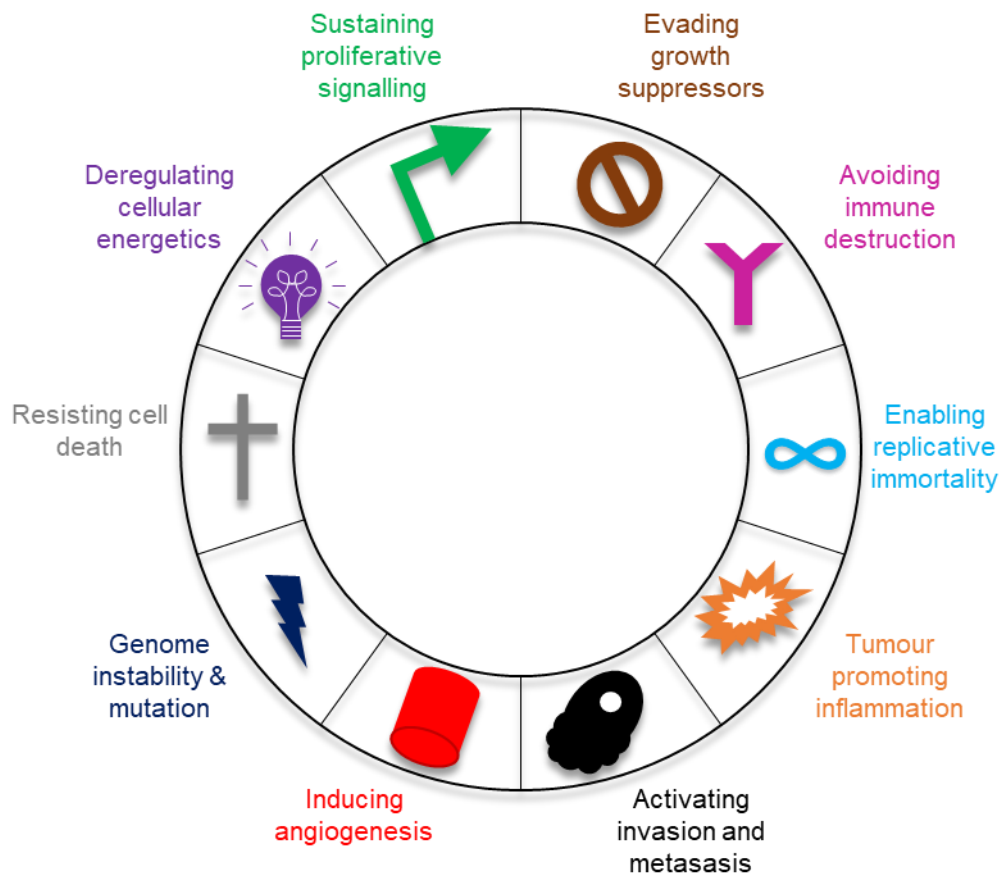


**Figure 1.1: The eight hallmarks and two enabling characteristics of cancer.**

Schematic showing the eight hallmarks and two enabling characteristics of cancer as proposed by Hanahan and Weinberg, figure adapted from Hanahan and Weinberg (2011).

In 2000, Hanahan and Weinberg described six hallmarks that all cancer cells display - sustained proliferative signals, evasion of anti-growth signals, gain of replicative immortality, ability to invade and metastasize, stimulation of angiogenesis and the resistance of cell death (Hanahan and Weinberg, 2000). Subsequently in 2011 two emerging hallmarks, deregulated cellular energetics and avoiding immune destruction, and two enabling characteristics, genome instability and mutation and tumour promoting inflammation, were further proposed by Hanahan and Weinberg (Hanahan and Weinberg, 2011) (Fig. 1.1).

A particular hallmark capability can be acquired by different mechanisms or genetic routes. Mutation of a single TSG or proto-oncogene, depending on its identity and normal function, may partially confer, or it may fully confer, acquisition

of a particular hallmark. The consequence of this genetic heterogeneity is that the molecular bases underpinning acquisition of a particular hallmark can differ for different cancers. This has important implications in the development of targeted anti-cancer therapies as will be discussed in a later section.

The impact of the tumour microenvironment (TME) on each hallmark is also very important. In a patient, cancer cells do not exist in isolation but are in close proximity to other cell types as well as extracellular components. Heterotypic cell interactions in the TME can actively contribute to hallmark acquisition and response to targeting. For solid cancers, chemical gradients of oxygen, nutrients, pH and waste products resulting from poor tumour blood supply exist. These physiochemical aspects of the TME can also contribute to, and help to shape the precise nature of the hallmarks and can profoundly impact on response to therapeutic targeting (Hanahan and Coussens, 2012).

### **1.1.5 Current treatments**

Current cancer treatments include surgery, radiotherapy, immunotherapy and chemotherapy, with choice of treatment or combination of treatments depending on the type of cancer and other factors such as stage and grade.

Surgery is commonly used for the removal of solid tumours that are localised or of low stage and grade and thus can be surgically excised and for localised disease is potentially curative (Sherwood and Brock, 2007). For many cancers however, following surgery some cancer cells may still remain and can lead to tumour recurrence and adjuvant chemotherapy can significantly improve outcome. Surgery may also be used to debulk a tumour to help other treatments work better.

Radiotherapy uses radiation, usually in the form of X-rays, to induce DNA damage in cells, leading to cell death and tumour shrinkage (Baskar *et al.*, 2012). Radiotherapy can be used as a single treatment or can be combined with other forms of treatment. The advantage of radiotherapy is that it can target the specific area where the tumour mass is, but the limitation is that it can also cause DNA damage to some of the normal cells that surround the tumour mass, therefore

leading to on-target side effects in normal tissue (Baskar *et al.*, 2012). Chemotherapy is also commonly used to sensitise tumour cells to the effects of radiation for example by inhibiting repair of radiation-induced DNA damage.

Immunotherapy is a treatment that uses the body's own immune system to fight the cancer, by helping the body recognise and attack the cancer cells. An example of one form of immunotherapy is use of monoclonal antibodies, which recognise and attach to certain proteins on the cell surface of cancer cells making it easier for the immune system to 'find' and attack the cancer cells (Arruebo *et al.*, 2011). The advantage of immunotherapy is that it can cause less side effects than other treatments, although its disadvantage is that the immune system can become over activated and can start attacking non-cancer cells in the body leading to side effects (Arruebo *et al.*, 2011).

Chemotherapy is the use of drugs in the treatment of cancer. A major advantage of chemotherapy compared to surgery and radiotherapy is that it is a systemic therapy and can target cancer cells anywhere in the body. This is extremely important as cancer cells have often spread and disseminated elsewhere in the body at the time of diagnosis but may not be visible and these cells can lead to tumour recurrence and the formation of secondary tumours. The majority of deaths from cancer are due to metastasis of the cancer to vital organs indicating the importance to eliminate cancer cells anywhere in the body rather than simply remove a bulky tumour. The disadvantage of chemotherapy is its side effects, because it is not applied to the part of the body where the tumour mass or cancer cells are located therefore normal cells and tissue are equally exposed to the chemotherapeutic drug (Schirmacher, 2019). There are two major classes of chemotherapeutic drugs, conventional chemotherapeutic drugs and targeted agents which have been developed with the aim of reducing side effects and unwanted toxicity.

#### **1.1.5.1 Traditional chemotherapeutic agents**

Conventional chemotherapeutic drugs work via the principle that cancer cells typically replicate faster than non-cancer cells (Bailón-Moscoso *et al.*, 2014). Their mechanism of action is through induction of cellular DNA damage and its

insufficient repair or interference with DNA/cell replication resulting in the induction of cellular senescence or cell death. However, some cancer cells, for example cancer stem cells (CSC), may not be actively proliferating or are in a quiescent state, and therefore are less susceptible to DNA damage by these drugs and can persist resulting in tumour recurrence (Moore *et al.*, 2012). Another major limitation of these drugs is that they fail to distinguish between proliferating cancer cells and proliferating non-cancer cells; they target any rapidly proliferating cell. Some non-cancer cells, for example blood cells, cells within the hair follicle and the gastrointestinal tract are rapidly proliferative (Schirmacher, 2019). Due to this these drugs can induce dose limiting toxic effects in these cells, leading to side effects in the patients for example being immunocompromised and being prone to infection, anaemia and pancytopenia due to myelosuppression. Other common side effects include hair loss, vomiting and diarrhoea (Schirmacher, 2019).

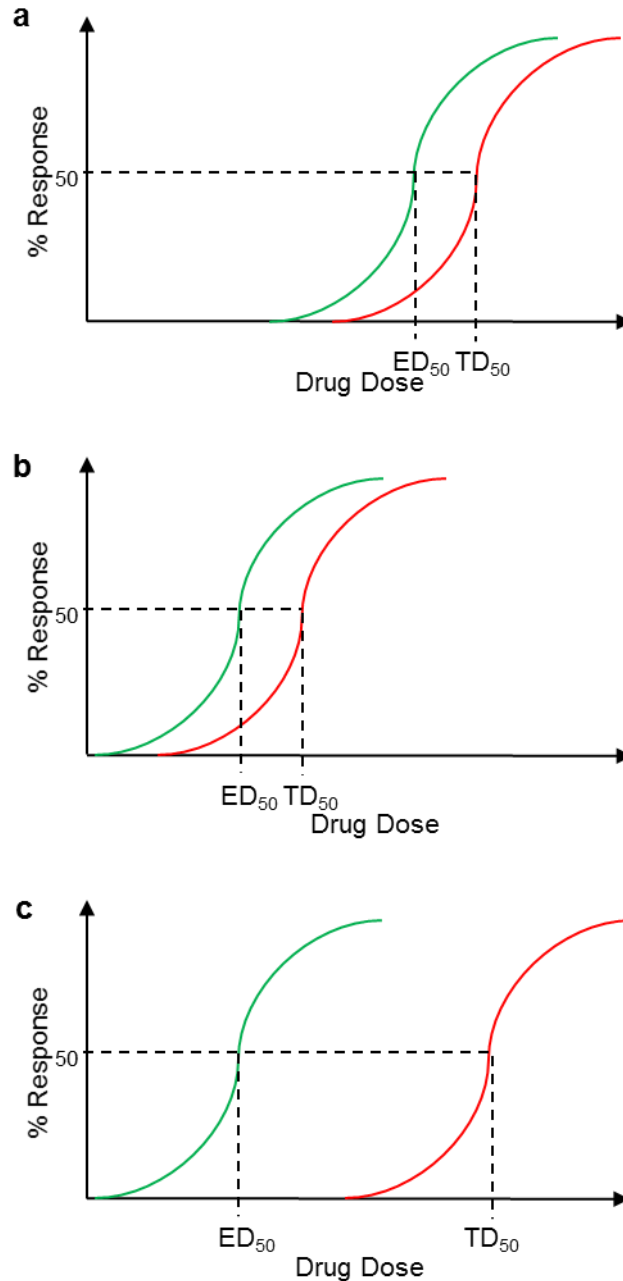


**Figure 1.2: The concept of a small or larger therapeutic index.**

Dose-response curves representing a drug with low potency and a small therapeutic index (or narrow therapeutic index) (a), a drug that is potent but has a similar small therapeutic index (b) and a drug that is potent and has a large therapeutic index (c). ED<sub>50</sub> showing therapeutic effect (green) and TD<sub>50</sub> showing toxic effect (red).

Traditional chemotherapeutic agents have a narrow therapeutic index where the difference in dose between beneficial therapeutic effects and toxic effects is small (Alnaim, 2007) (Fig. 1.2a). This small therapeutic index means that the highest dose that can be used may have limited therapeutic benefit, but higher doses

cannot be used because of toxic effects. This stems from the mechanism of action of conventional agents and their poor selectivity towards cancer cells.

### **1.1.5.2 Targeted approaches/agents in clinical use**

To overcome the problem of poor selectivity of conventional chemotherapeutic agents resulting in dose-limiting toxicities and limited efficacy, there has been more focus on developing drugs that target cancer cells more specifically (Bailón-Moscoso *et al.*, 2014). To achieve this specificity, detailed understanding of differences between cancer and non-cancer cells that could potentially be targeted is required. One major approach is identification of agents that target one or more of the hallmarks of cancer and acquired capabilities of cancer cells but not of non-cancer cells. Our increasing knowledge of cancer cell biology and the molecular alterations that underpin, or are important for sustaining, particular hallmarks are at the core of targeted drug discovery. Figure 1.3 gives some examples of targeted therapies against individual hallmarks of cancer that are in clinical use or in different stages of development towards the clinic.

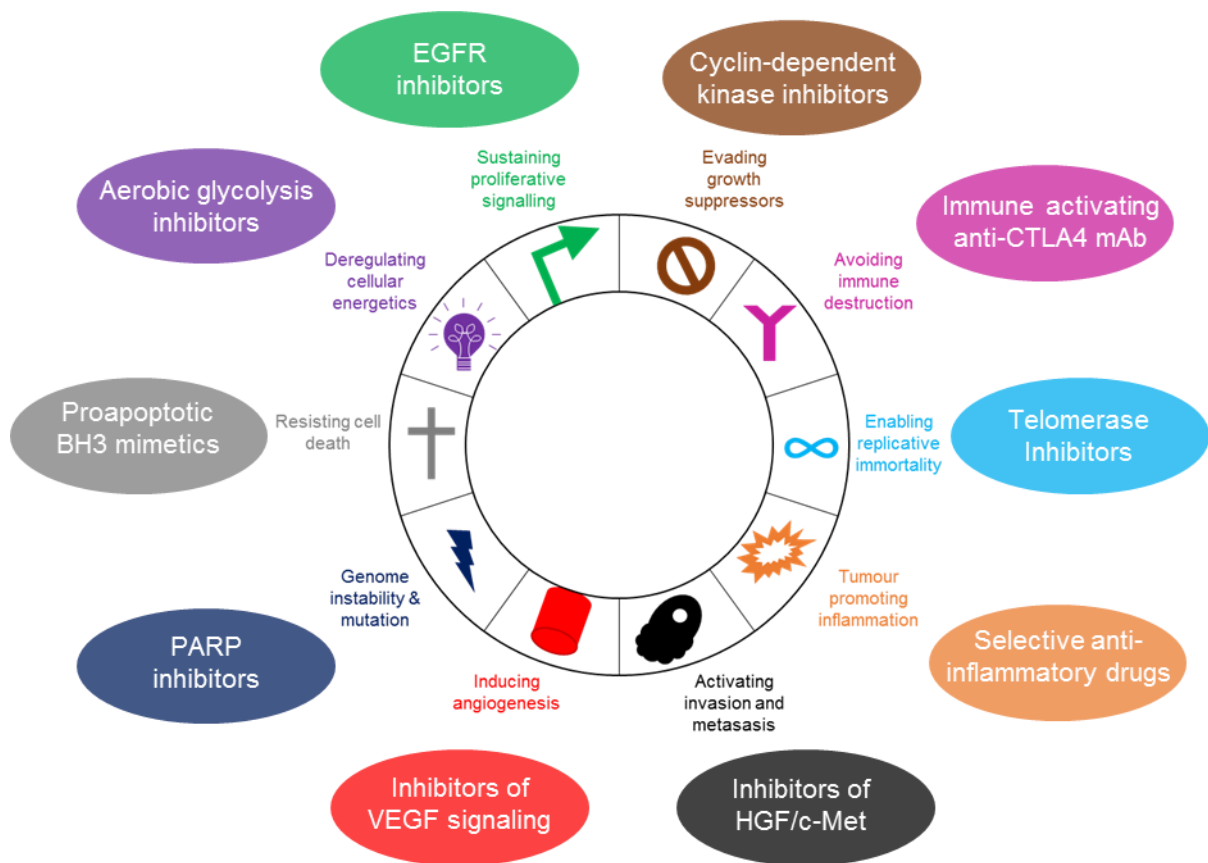


**Figure 1.3: Targeted therapies being developed that target specific hallmarks of cancer.** The hallmarks of cancer with examples of associated targeted therapies, figure adapted from Hanahan and Weinberg (2011).

One of the best known targeted therapies to reach the clinic is the vascular endothelial growth factor A (VEGF-A) inhibitor bevacizumab (Avastin®). Many cancer cells express the pro-angiogenic factor VEGF-A at abnormally high levels resulting in the induction of angiogenesis, one of the hallmarks of cancer (Hanahan and Weinberg, 2011). In contrast, when the adult circulatory system is fully developed most non-cancer cells do not induce angiogenesis with pro-angiogenic signals decreased and anti-angiogenic signals increased (Hanahan and Folkman, 1996). The exceptions of this are cells that are involved in wound healing and the menstrual cycle, where these cells can transiently induce angiogenesis under certain physiological conditions (Hanahan and Folkman, 1996). Cancer cells undergo an ‘angiogenic switch’, where pro-angiogenic signals are increased and anti-angiogenic signals are decreased (Bergers and Benjamin, 2003). To target this hallmark, multiple VEGF inhibitors have been developed and are currently used in the clinic (Jayson *et al.*, 2016). Although this

treatment is targeted towards cancer cells alone, careful consideration must be given with timing of treatment as inhibiting VEGF in non-cancer cells that require it will lead to unwanted on-target side effects. A disadvantage of this treatment is that angiogenesis in some cancers may be induced through other factors and not through VEGFs, therefore VEGF inhibitors would not effectively target these cancers (Arbab, 2012).

Another example of a targeted therapy is poly (ADP-ribose) polymerase (PARP) inhibitors, which exploit the 'enabling characteristic of cancer' that is genome instability and mutation (Hanahan and Weinberg, 2011) to induce synthetic lethality. Synthetic lethality is where the mutation of one gene is non-lethal but it results in dependency upon another, such that their functional inactivation in combination is lethal. For certain breast and ovarian cancers in particular, individuals may have an inherited germline mutation in the TSGs BRCA1 and/or BRCA2. BRCA1 and BRCA2 are essential proteins for the repair of double strand DNA breaks (DSB) by homologous recombination (HR) (Moynahan *et al.*, 1999; Moynahan *et al.*, 2001). For cancers that are deficient in HR, these cells show increased genomic instability and mutation and are more reliant on other pathways of DNA repair (Lord and Ashworth, 2017).

Inhibiting PARP, an enzyme mainly associated with repair of single strand breaks (SSB) (see section 1.4.1), in BRCA mutant cells results in increased unrepaired DSBs and synthetic lethality (Farmer *et al.*, 2005; Bryant *et al.*, 2005). It has also been shown that PARP inhibitors can be effective in cancers that have mutations in other proteins involved in HR (McCabe *et al.*, 2006). Although this treatment is more targeted to cancer cells alone, it is only effective against cancer cells that are deficient in HR.

The main theme that underpins this PhD research is that cancer cells have deregulated cellular energetics, which in 2011 was proposed as an emerging hallmark of cancer cells (Hanahan and Weinberg, 2011). One of the first differences observed between cancer cells and non-cancer cells was by Otto Warburg in the late 1920s, that cancer cells catabolised glucose differently to non-cancer cells. Warburg observed that cancer cells consumed large amounts of glucose and converted it to lactate in the presence of oxygen rather than the

further metabolism of pyruvate by the tricarboxylic acid (TCA) cycle; this is aerobic glycolysis (the Warburg effect) (see section 1.2.2) (Warburg, 1927; Warburg, 1956). Since 2011 growing evidence of different metabolic alterations between cancer and non-cancer cells has confirmed that such alterations are common and widespread, if not universal to cancer cells (Sreedhar and Zhao, 2018). Furthermore, it is now apparent that metabolic differences between cancer cells and non-cancer cells are not simply an effect of increased cancer cell proliferation but are causally linked to cancer development and progression and can impact on multiple hallmarks of cancer.

Similar to other targeted therapies, it has been hypothesised that through targeting metabolic differences between cancer and non-cancer cells, and the proteins responsible, this could lead to more selective ways to eradicate cancer cells with fewer on-target side effects. Here the focus was on investigating proteins/putative targets linked to the nicotinamide adenine dinucleotide (NAD<sup>+</sup>) metabolome and NAD<sup>+</sup>-dependent processes and therapeutic opportunities these may provide for selective targeting of cancer cells. NAD<sup>+</sup> is an essential metabolite for redox reactions which happen during metabolism and is also an essential co-factor or co-substrate of some key cellular enzymes within the cell (for more detail see section 1.4).

## **1.2 Metabolic differences between cancer and non-cancer cells**

### **1.2.1 Glucose metabolism in non-cancer cells and the role of NAD<sup>+</sup>/NADH**

For an individual to survive they require energy to drive biochemical reactions within their cells, this energy can be obtained from the hydrolysis of nucleotide triphosphates, for example adenosine triphosphate (ATP). Cells maintain ATP levels through catabolic reactions, for example by oxidising carbon fuel substrates such as glucose to CO<sub>2</sub> (Bonora *et al.*, 2012).

During glucose catabolism, glucose is transported into the cell by glucose transporters and then undergoes glycolysis in a series of reactions to generate two molecules of pyruvate (Fig. 1.4). Under aerobic conditions, pyruvate is converted to acetyl-CoA which is transferred to the mitochondrial matrix where it is metabolised by the TCA cycle (Fig. 1.5) (Bonora *et al.*, 2012). The electron donors NADH and FADH<sub>2</sub> are formed as a result of various substrate oxidation reactions and are then subsequently oxidised through donating their electrons to the electron transport chain situated in the inner mitochondrial membrane as part of mitochondrial oxidative phosphorylation (Fig. 1.6) (Bonora *et al.*, 2012). This is coupled to the generation of a proton gradient across the mitochondrial inner membrane and production of ATP by ATP synthase (Okuno *et al.*, 2011).

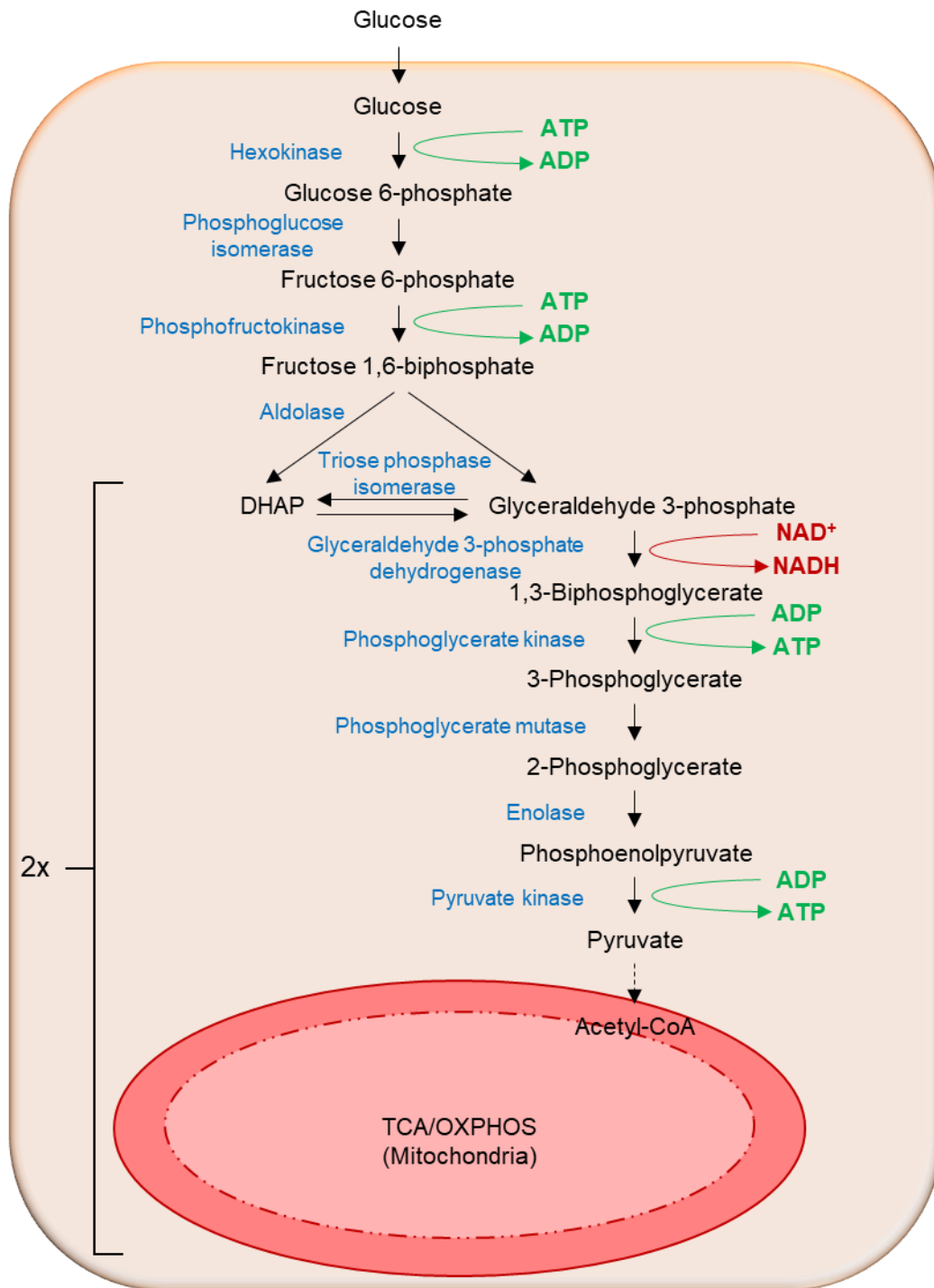


**Figure 1.4: Glycolysis in non-cancer cells.**

The reaction intermediates and enzymes involved in the metabolism of glucose to pyruvate, showing ATP and NADH production.

Glucose is transported into the cell by glucose transporters, for example GLUT1, and is phosphorylated to glucose 6-phosphate by a hexokinase (HK), utilising ATP. This process results in glucose not being able to leave the cell due to the negative charge of the phosphate group. Phosphoglucose isomerase catalyses

the isomerisation of glucose 6-phosphate to fructose 6-phosphate which is then phosphorylated by phosphofructokinase, utilising ATP, resulting in fructose 1,6-biphosphate. The six-carbon sugar is then cleaved by aldolase into glyceraldehyde 3-phosphate and dihydroxyacetone phosphate (DHAP), which both consist of three carbons. DHAP is an isomer of glyceraldehyde 3-phosphate and can readily be converted by triose phosphate isomerase. Glyceraldehyde 3-phosphate is then oxidised by glyceraldehyde 3-phosphate dehydrogenase (GAPDH) using  $\text{NAD}^+$  to 1,3-biophophoglycerate resulting in the release of NADH. Multiple reactions including two transfers of phosphate groups to ADP results in the end formation of pyruvate and release of 2 ATP. The process from glyceraldehyde 3-phosphate to pyruvate happens twice per glucose molecule and therefore in total, 4 ATP and 2 NADH are produced, equating to a net value of 2 ATP per glucose (Berg *et al.*, 2019; Bonora *et al.*, 2012).

The final steps of glucose catabolism require oxygen to be present and under aerobic conditions pyruvate is decarboxylated by the enzyme pyruvate dehydrogenase (PDH), forming acetyl-CoA which is transferred into the mitochondria to drive the TCA cycle (Fig. 1.5). The TCA cycle is a series of oxidation steps of carbon sources where  $\text{NAD}^+$  or FAD is reduced to form NADH or  $\text{FADH}_2$  and  $\text{CO}_2$  is released (Bonora *et al.*, 2012).

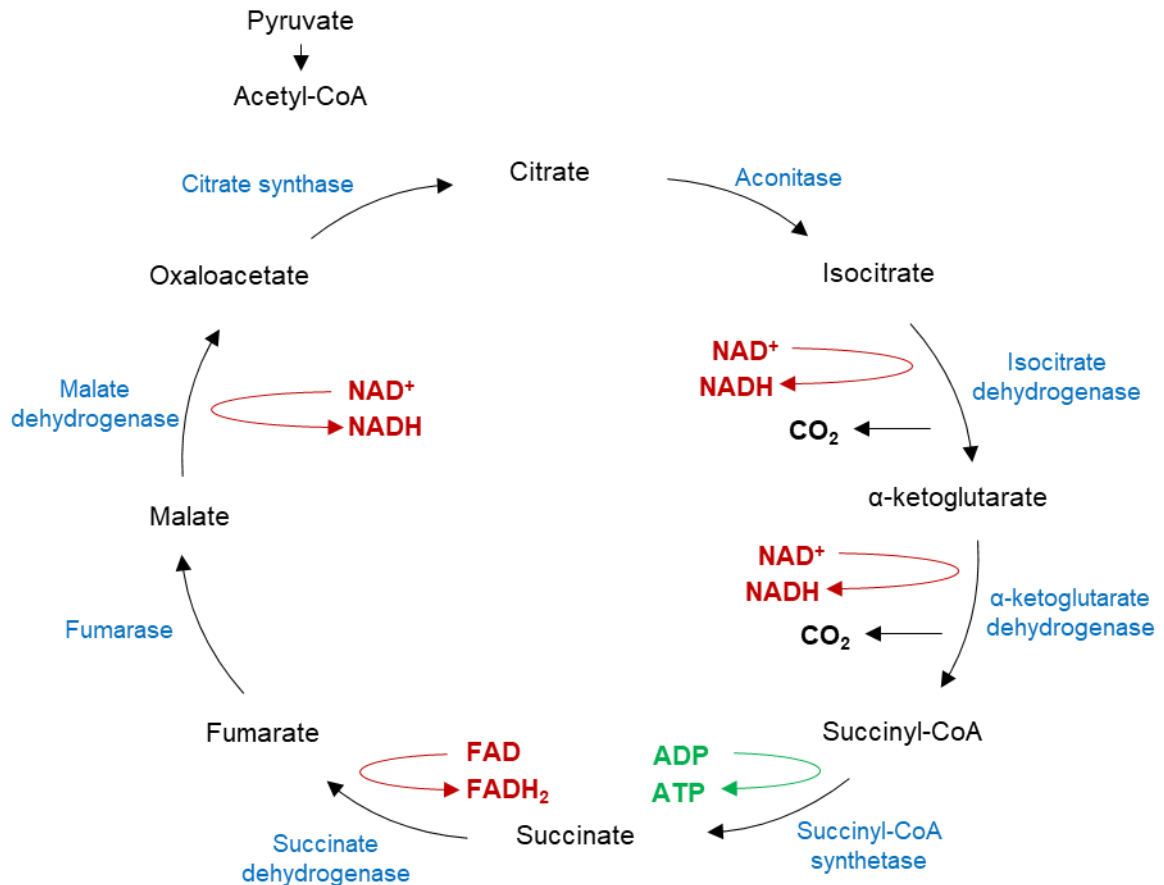


**Figure 1.5: The tricarboxylic acid cycle.**

The multiple enzymatic reactions of the TCA cycle in the mitochondrial matrix resulting in the generation of NADH, FADH<sub>2</sub>, ATP and CO<sub>2</sub>.

Citrate, a 6-unit carbon, is formed from acetyl-CoA and oxaloacetate, catalysed by citrate synthase and is then isomerised to isocitrate by aconitase. Isocitrate is then decarboxylated and oxidised using NAD<sup>+</sup>, first to α-ketoglutarate (α-KG) in a reaction catalysed by isocitrate dehydrogenase (IDH) and then to succinyl-CoA, catalysed by α-ketoglutarate dehydrogenase. During these reactions 2 NADH and 2 CO<sub>2</sub> molecules are generated. Succinyl-CoA is an energy-rich molecule and its cleavage to succinate by succinyl-CoA synthase generates ATP. Succinate is oxidised by FAD forming fumarate which is catalysed by succinate dehydrogenase (SDH) resulting in FADH<sub>2</sub> release. FAD is used here as the oxidising power as the free energy that is released is insufficient to reduce NAD<sup>+</sup>. Hydration of fumarate by fumarase (FH) then forms malate which is oxidised by NAD<sup>+</sup> and catalysed by malate dehydrogenase (MDH), resulting in the reformation of oxaloacetate (Berg *et al.*, 2019; Bonora *et al.*, 2012).

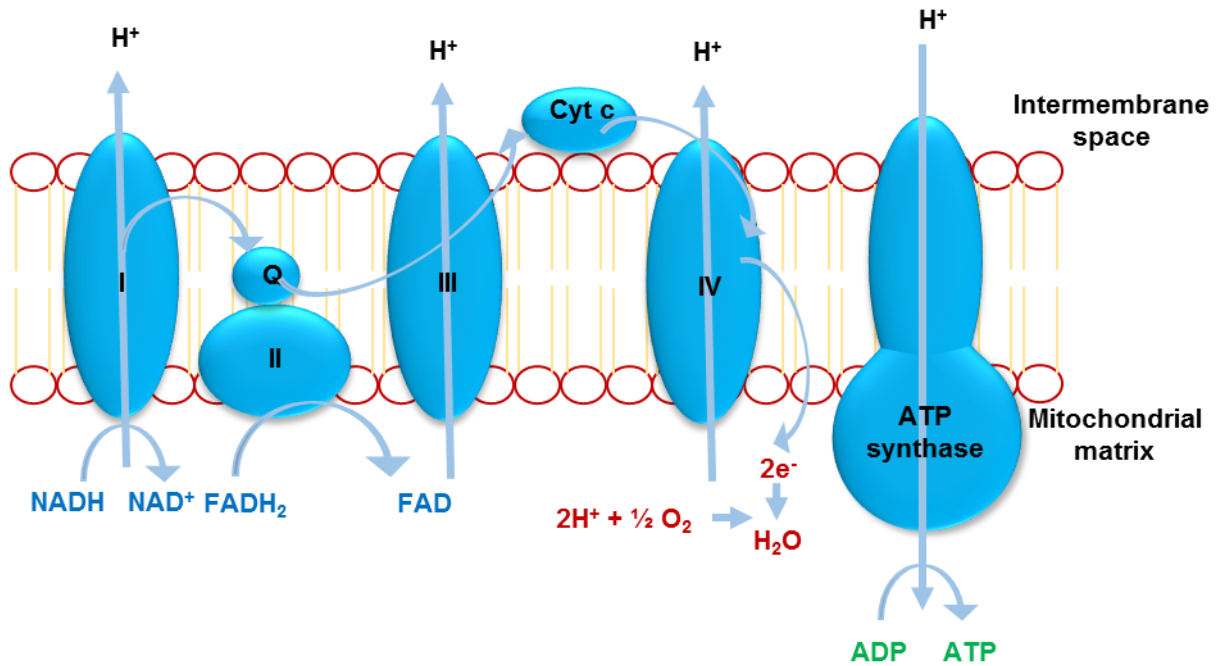


**Figure 1.6: The electron transport chain and oxidative phosphorylation.**

NADH and FADH<sub>2</sub> produced in the mitochondrial matrix during the TCA cycle are oxidised and electrons are transported along the complexes in the electron transport chain while protons are pumped into the intermembrane space. The protons produce a chemiosmotic gradient across the membrane, resulting in the activation of ATP synthase, therefore producing ATP.

Per glucose molecule the TCA cycle results in 6 NADH, 2 FADH<sub>2</sub>, 2 ATP and 4 CO<sub>2</sub> molecules being released into the mitochondrial matrix. The NADH and FADH<sub>2</sub> pass their electrons through a series of electron carrier/acceptor complexes in the electron transport chain (Fig. 1.6) to O<sub>2</sub> as the final electron acceptor resulting in its reduction to water (Bonora *et al.*, 2012). The transfer of electrons down the electron transport chain releases energy which is used to pump protons into the intermembrane space to generate a proton motif force which is used by ATP synthase to drive the synthesis of ATP from ADP and inorganic phosphate (Okuno *et al.*, 2011). On average the whole process produces a net value of 36 ATP per molecule of glucose (Rich, 2003).

As indicated by the above, NAD<sup>+</sup>/NADH play a critical role in cellular redox reactions and in producing ATP as the cell's primary energy source.

## 1.2.2 Glucose metabolism in cancer cells

Cancer cells require high levels of ATP to support their high proliferation rate and need for biomolecule synthesis for cell growth, for example DNA, RNA, proteins and lipids (Hammoudi *et al.*, 2011). In contrast to non-cancer cells which generate most of their ATP by mitochondrial oxidative phosphorylation, paradoxically many cancer cells primarily generate their ATP by aerobic glycolysis rather than through the TCA cycle and oxidative phosphorylation (Hammoudi *et al.*, 2011). Whilst aerobic glycolysis is a less efficient way of generating ATP, giving a net yield of 2 ATP per glucose molecule, it is a quicker way of producing ATP. To generate sufficient ATP, cancer cells have increased expression of glucose transporters on the cell surface and therefore can transport more glucose into the cell to be metabolised (Medina and Owen, 2002). Another alteration is that many of the enzymes involved in glycolysis are upregulated in cancer cells to facilitate the conversion of glucose to pyruvate (Sreedhar and Zhao, 2018). During the reduction of pyruvate to lactate by lactate dehydrogenase-A (LDH-A), NADH is oxidised resulting in NAD<sup>+</sup> (Fig. 1.7). This is important as the NAD<sup>+</sup> can be recycled back into the glycolytic pathway to produce more ATP and sustain a high glycolytic flux whilst maintaining the NAD<sup>+</sup>/NADH ratio.

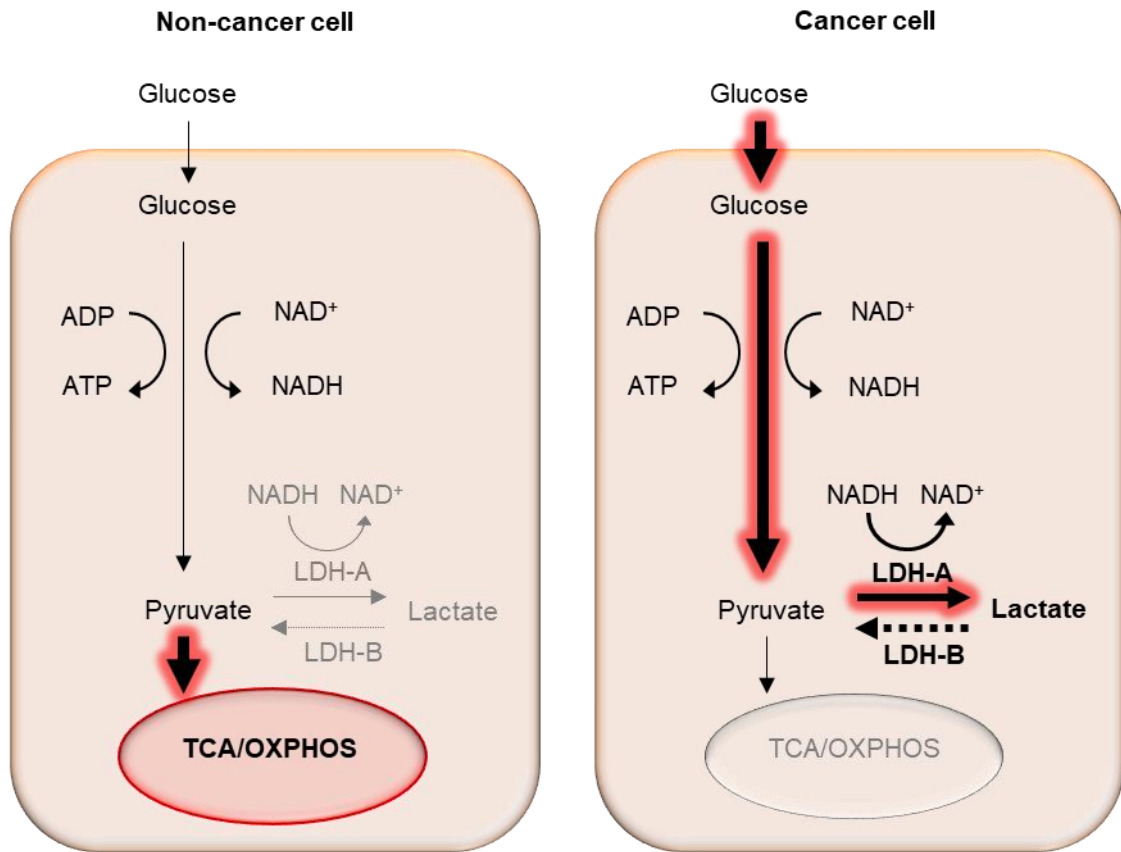


**Figure 1.7: Key events in glucose catabolism in non-cancer and cancer cells.**

Non-cancer cells predominantly produce ATP through oxidative phosphorylation whereas cancer cells predominantly produce ATP through aerobic glycolysis. Cancer cells reduce pyruvate to lactate catalysed by the enzyme lactate dehydrogenase-A (LDH-A) which regenerates NAD<sup>+</sup> necessary to fuel a high glycolytic flux.

It was originally thought that cancer cells relied on aerobic glycolysis to produce ATP due to mutations in enzymes involved in the TCA cycle and mitochondrial dysfunction, or as a way of reducing mitochondrial oxidative stress (Warburg, 1927; Warburg, 1956). More recently, it has been shown that most cancer cells do also utilise oxidative phosphorylation but have a high glycolytic flux which in addition to providing ATP quickly, provides a source of intermediates that can be used for macromolecule biosynthesis (De Berardinis and Chandel, 2016). This alteration in glucose catabolism of cancer cells is one way that they are more reliant upon NAD<sup>+</sup> and why it may be a useful target in terms of selectively targeting cancer cells.

### **1.2.3 Other cancer cell metabolic alterations**

In addition to the Warburg effect, a variety of other metabolic alterations have been observed in many cancer cells compared to their normal counterparts, several examples of which are summarised below.

#### **1.2.3.1 Glutamine addiction**

Although glutamine is a non-essential amino acid, some cancer cells cannot survive in the absence of exogenous glutamine. In addition to the reduced entry of pyruvate into the TCA cycle, cancer cells commonly show a truncated or interrupted TCA cycle with diversion of citrate towards lipid synthesis. However, the TCA cycle is also a major source of other intermediates for anabolic processes to aid growth and division (Choi and Park, 2018). Cancer cells increase the uptake of glutamine and upregulate glutaminolysis providing an alternative source of  $\alpha$ -KG (Vanhove *et al.*, 2019). Glutamine is deaminated to glutamate by the enzyme glutaminase which is then converted to  $\alpha$ -KG by glutamine dehydrogenase. The glutamate or  $\alpha$ -KG can be used as nitrogen or carbon sources in biological molecule synthesis, for example amino acid and nucleotide synthesis, for anaplerosis and as a mitochondrial carbon source (Vanhove *et al.*, 2019). Glutamine addiction is particularly observed in cancer cells showing oncogenic amplification or activation of c-Myc proto-oncogene (Miller *et al.*, 2012).

#### **1.2.3.2 Lipid metabolism**

In non-cancer cells, lipid requirements are maintained by uptake of free fatty acids from the bloodstream and the synthesis of fatty acids is restricted depending on tissue type (liver, adipose). Rapidly proliferating cancer cells require higher levels of lipids in order to support formation of cellular membranes. The reactivation of lipid synthesis through the *de novo* lipid synthesis pathway is observed in many cancer cells (Baenke *et al.*, 2013; Currie *et al.*, 2013).

### **1.2.3.3 Pentose phosphate pathway**

Increased flux into the pentose phosphate pathway (PPP) is commonly observed in cancers (Patra and Hay, 2014). The PPP predominantly produces ribonucleotides and is a major source of nicotinamide adenine dinucleotide phosphate (NADPH). NADPH is important in cancer cells to fuel anabolic metabolism, providing a source of reducing equivalents and sustaining reduced glutathione and other anti-oxidant defence mechanisms (Patra and Hay, 2014; Cosentino *et al.*, 2011).

### **1.2.3.4 Dependency on serine**

It has been observed that some cancer cells have elevated expression of enzymes involved in the *de novo* synthesis of the non-essential amino acid serine. As serine is an amino acid it is required for protein synthesis, but it is also required for other metabolic processes, for synthesis of glycine, glutathione and phospholipids (Luengo *et al.*, 2017). Serine can also contribute to the production of NADPH through one carbon metabolism (folate cycle), therefore helping in maintaining redox homeostasis and for use in anabolic metabolism, including thymidine synthesis and as well as generation of S-adenosylmethionine (SAM), the methyl donor for DNA and histone methylation (Luengo *et al.*, 2017).

## **1.2.4 Regulation of metabolism and its dysregulation in cancer cells**

Whilst differences between cancer and non-cancer cells in metabolism of glucose, glutamine and serine as well as other metabolic pathways have been identified, an understanding of the molecular basis for these differences is needed for therapeutic exploitation.

In normal cells, metabolic pathway utilisation and flux has generally been considered to be largely dependent on substrate availability and consumption, with many metabolic enzymes constitutively expressed (Metallo and Vander Heiden, 2013). Usage of particular metabolic pathways is also dependent on tissue type with tissue-specific expression of certain metabolic enzymes and

endocrine-mediated metabolic regulation ensuring organismal metabolic homeostasis (Metallo and Vander Heiden, 2013). Normal cell metabolism is also subject to additional regulation and modulation in response to both cell-intrinsic and extrinsic stimuli. For example, growth stimuli resulting in temporary activation of proto-oncogenes can lead to increased or decreased metabolic enzyme expression/activation, resulting in alterations in metabolic pathway flux (DeBerardinis, 2008). Stress stimuli such as nutrient deprivation can lead to activation of the tumour suppressor p53 which has multiple reported roles in the regulation of normal cellular metabolism (Ryan and Vousden, 2002; Maddocks *et al.*, 2013). p53 for example can promote mitochondrial oxidative phosphorylation through the upregulation of SCO2 expression (Matoba *et al.*, 2006) and can suppress glycolysis by decreasing expression of enzymes involved in the pathway, for example phosphoglycerate mutase (Puzio-Kuter, 2011).

Dysregulated metabolism in cancer cells appears to be associated with dysregulation of metabolic enzyme expression and/or activity as well as dysregulation of nutrient uptake. There is now a large body of scientific evidence linking the inactivation of specific tumour suppressors and activating mutation of proto-oncogenes to cancer cell metabolic reprogramming and addictions (DeBerardinis *et al.*, 2008; Puzio-Kuter, 2011; Nagarajan *et al.*, 2016).

The oncogenic transcription factor MYC, which is overexpressed or amplified in many cancers (Nagarajan *et al.*, 2016), is known to regulate numerous metabolic enzymes including GLUT1, PFK and enolase, therefore increasing the rate of glycolysis (Shim *et al.*, 1997; Osthus *et al.*, 2000). MYC also promotes glutaminolysis (Wise *et al.*, 2008) for example by increasing glutaminase expression. It also increases nucleotide synthesis and one-carbon metabolism through activating enzymes involved in these processes, for example serine hydroxymethyltransferase (Nikiforov *et al.*, 2002; DeBerardinis *et al.*, 2008). Ras oncogenes (H-Ras, K-Ras, N-Ras) also promote cancer cell metabolic reprogramming in part through stabilisation of MYC. Activated Ras can co-operatively stabilise MYC through both the PI3K and Raf signalling pathways (White, 2013). Ras GTPase proteins work as intracellular relays of extracellular signals and studies have shown that cancer cells which have Ras activated show

increased glucose uptake and higher glycolytic flux, for example GLUT1 expression is correlated with Ras mutated cells (Sasaki *et al.*, 2012). The intermediates of glycolysis in these cells are also known to be shunted to the PPP, which can promote ribonucleotide synthesis (Ying *et al.*, 2012). Ras activated cells are also reprogrammed to rely on glutamine as the primary carbon source of the TCA cycle (Son *et al.*, 2013). Ras activated cancer cells also appear to upregulate autophagy and micropinocytosis to aid their survival through uptake of additional nutrients, for example albumin which can be taken up and be degraded to amino acids which can then be used in the TCA cycle (Bar-Sagi and Feramisco, 1986; Kimmelman, 2015).

In addition to the metabolism of cancer cells being altered through activation of oncogenes such as Ras and MYC and inactivation of TSGs, it is also apparent that several metabolic enzymes in certain cancers are directly mutated which can lead to altered function. A number of cancers are known to have a mutation in the IDH1/2 enzymes, which are primarily involved in the conversion of isocitrate to  $\alpha$ -KG and their mutation is known to promote tumorigenesis (Xiao *et al.*, 2012). When IDH1/2 are mutated they result in the release of D-2hydroxyglutarate (2HG) and not  $\alpha$ -KG. D-2HG is an oncometabolite which can inhibit  $\alpha$ -KG dependent enzymes, which include enzymes that can alter cellular epigenetics such as the Jumonji (JMJD) family of lysine histone demethylases and DNA demethylases (Horbinski, 2013) (section 1.6.2).

The interplay between epigenetics and metabolism is complex and reciprocal. Nutrient/metabolite availability can alter the epigenetic state of the cell with the activity of epigenetic enzymes dependent on metabolic substrate availability, for example histone acetylation requires acetyl CoA and deacetylation by SIRT6 requires NAD<sup>+</sup>. Epigenetic alterations in turn can play an important role in regulation of metabolism where environmental influences can alter the epigenetic state of a cell and lead to increased/decreased expression of proteins/enzymes involved in metabolic pathways (Weaver *et al.*, 2018). An example of this is that HK2 is upregulated in some cancers and is the result of the promoter region being hypomethylated, which leads to increased glycolysis (Goel *et al.*, 2003).

In addition to dysregulation of cancer metabolism driven by genetic or epigenetic changes, the TME can induce similar metabolic alterations, for example through induction of hypoxia-induced HIF-1 $\alpha$  stabilisation leading to increased expression of enzymes involved in the glycolytic pathway (Singh *et al.*, 2017).

### **1.2.5 Therapeutically targeting altered glucose metabolism**

Targeting metabolic differences between cancer and non-cancer cells as a therapeutic approach is appealing as many cancer cells appear to depend on their altered metabolism for survival or growth. In other cases, targeting could impact on other hallmarks of cancer, for example increased extracellular lactate resulting from aerobic glycolysis has been linked to promotion of cancer cell invasiveness and extracellular matrix remodelling (Romero-Garcia *et al.*, 2016).

Antimetabolites are currently used in the clinic which work to target the metabolism of nucleotides. They are small molecules which resemble metabolites involved in nucleotide synthesis and can inhibit the enzymes involved in the pathway, or can be incorporated into the DNA which can result in inhibition of DNA synthesis (Parker, 2009). The use of this type of chemotherapy as treatment is based on the need of cancer cells for increased DNA synthesis as they are usually highly proliferative, although as discussed previously not all cancer cells are highly proliferative and some non-cancer cells have a high proliferation rate, leading to dose limiting toxicities. Cancer cells also have many other metabolic alterations and targeting these may offer a more selective treatment in cancer therapy.

Multiple proteins/enzymes involved in glucose metabolism have been shown to be over expressed in cancer cells (e.g. GLUT1, PDKs, PFKFB3, LDH-A) or different isoforms are preferentially utilised (e.g. HK2).

The glucose transporter GLUT1 is shown to be overexpressed in many cancer types (Kunkel *et al.*, 2003; Younes *et al.*, 1996; Yamamoto *et al.*, 1990) and studies have shown that inhibition of GLUT1 with antibodies reduced glucose uptake and decreased the proliferation rate of cancer cells and led to apoptosis;

it was also seen that it could potentiate the action of DNA damaging agents (Rastogi *et al.*, 2007). Chemical inhibitors of GLUT1 have been developed with cancer cell growth being inhibited *in vitro* and *in vivo* (Zhang *et al.*, 2010). It has also been shown that Phloretin, which inhibits glucose transporters can induce apoptosis and lead to drug resensitisation of hypoxic cancers (Cao *et al.*, 2007). However, a major concern is that GLUT1 is ubiquitously expressed in normal tissues and non-cancer cells also rely on glucose transporters for glucose transport and its targeting may lead to significant on-target side effects.

Pyruvate dehydrogenase kinases (PDK) work by inactivating the enzyme PDH through phosphorylation, therefore can halt the entry of pyruvate into the TCA cycle and oxidative phosphorylation leading to increased glycolytic flux. PDKs are known to be overexpressed in cancer cells and are linked to poor prognosis and inhibition has been shown to shift the metabolism of the cell from glycolysis to oxidative phosphorylation (Cui *et al.*, 2018; Wang *et al.*, 2019). The drug dichloroacetate (DCA), which is a PDK inhibitor, is currently in clinical use against patients that have mitochondrial diseases. *In vitro* and *in vivo* studies have shown that the drug can induce apoptosis in cancer cells and lead to tumour shrinkage (Bonnet *et al.*, 2007). DCA has shown some toxicity through neuropathy which is known to be associated with the age of the patient (Kaufmann *et al.*, 2006). Multiple other drugs that target PDKs have also been developed which are being tested *in vitro* and *in vivo* and have shown promising results, although are yet to be tested in the clinic (Saunier *et al.*, 2016).

One potential issue with targeting glucose metabolism as a targeted anti-cancer approach is that glycolysis is also important for normal cells and most of the glycolytic enzymes used are the same and their inhibition is likely to lead to unwanted toxicity. This indicates the need for careful selection of the glycolytic target. For example, phosphofructose kinase (PFK1) is essential for glycolysis preventing its direct targeting, however, it could be preferentially inhibited in cancer cells by small molecule inhibitors of PFKFB3 which is upregulated in cancer cells and allosterically activates PFK1 (Hay, 2016).

Another potential route of selectively targeting cancer cells is that they utilise different isoforms of the HK enzyme compared to non-cancer cells. HKs catalyse

the first step of glycolysis by phosphorylating glucose to form glucose 6-phosphate (Fig. 1.4). HK1 is expressed across most adult tissues whereas HK2 is expressed in a limited number of tissues (Wilson, 2003). Interestingly cancer cells also show high expression of HK2, indicating a partially selective target for cancer cells (Wu *et al.*, 2017; Peng *et al.*, 2008; Pedersen *et al.*, 2002). Patra *et al.* (2013) show that HK2 silencing in human lung and breast cancer cells reduced their proliferation and in mice that exhibit lung cancer, the growth of the tumour was reduced. Importantly these studies also showed that the systemic deletion of HK2 in mice did not show adverse effects. Multiple drugs have been developed to target HK2 which have shown promising results, where apoptosis has been induced in cancer cells, although some showed no effects *in vivo*, for example 2-deoxyglucose (2-DG) and some had additional targets therefore did not exert their effects primarily through HK2 inhibition, for example lonidamine (Akins *et al.*, 2018). Although many studies show the benefit of targeting HK2, it must be considered that HK2 is also expressed in a small subsection of non-cancer tissues and it must be considered what effects this may have.

The enzyme LDH-A, which converts pyruvate to lactate, is crucial in maintaining cancer cells high glycolytic flux as it regenerates the NAD<sup>+</sup> required for glycolysis and has been shown to be overexpressed in some cancers and is linked to poor prognosis (Feng *et al.*, 2018). Importantly, in non-cancer cells, LDH-A is not required under normal conditions, only being utilised for anaerobic glycolysis, for example by muscle tissue during intense exercise. In support of this, individuals with an identified rare genetic deficiency in LDH-A appear healthy and without symptoms except for myopathy associated with exercising (Kanno *et al.*, 1988). A number of independent studies identify LDH-A as a promising and selective anti-cancer target, both by RNAi-based approaches and through its chemical inhibition, with cancer cell death induced *in vitro* and tumour growth *in vivo* reduced (Fantin *et al.*, 2006; Le *et al.*, 2010; Allison *et al.*, 2014). Multiple LDH-A inhibitors have been developed of varying specificity towards LDH-A compared to LDH-B, LDH-B preferentially catalysing the reverse metabolic reaction. However, to date no LDH-A inhibitor has reached the clinic, with varying issues including off-target toxicity due to poor selectivity and inhibition of other dehydrogenases and poor pharmacokinetics

Allison *et al.* (2014) have shown that LDH-A inhibition/knock-down induces cancer selective cell death *in vitro* independent of p53 status, but also, importantly, that it reduces the ratio of cellular NAD<sup>+</sup> to NADH selectively in p53<sup>+/+</sup> cancer cells. The latter effect resulted in cancer selective activation of the redox sensitive drug EO9 which suggests LDH-A targeting in combination with other drugs could enhance their activity and selectivity to cancer cells (Allison *et al.*, 2014). The ability to modulate the cellular NAD<sup>+</sup>/NADH ratio selectively in cancer cells raises a number of important therapeutic possibilities which are further explored as part of this PhD research.

## 1.3 What is NAD<sup>+</sup> and how is it produced?

### 1.3.1 What is NAD<sup>+</sup>?

NAD is an essential metabolite which exists in a reduced (NADH) (Fig. 1.8a) or oxidised (NAD<sup>+</sup>) (Fig. 1.8b) form and is important for redox reactions within the cell (Cantó *et al.*, 2015). NAD<sup>+</sup> and NADH provide oxidising and reducing power through accepting and donating electrons respectively. As discussed in section 1.2 NAD<sup>+</sup> is essential for both glycolysis and the TCA cycle to proceed whilst NADH generated by the TCA cycle fuels oxidative phosphorylation.

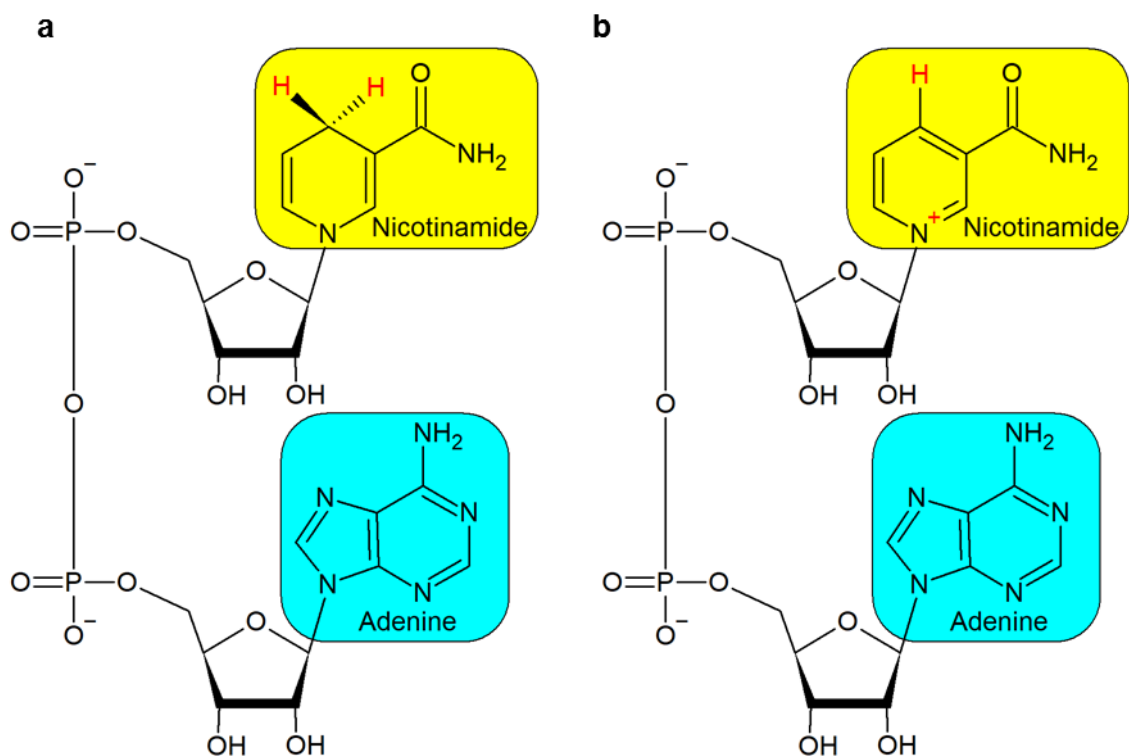


**Figure 1.8: Chemical structure of NAD<sup>+</sup> and NADH.**

Chemical structure of reduced (a) and oxidised (b) form of NAD. Nicotinamide moiety is seen in yellow and the adenine moiety in blue, both linked to individual ribose molecules which are attached to the phosphate backbone. Chemical changes between reduced and oxidised structures can be seen in red.

## 1.3.2 Sources of NAD<sup>+</sup>

### 1.3.2.1 Oxidation of NADH to NAD<sup>+</sup>

NADH and NAD<sup>+</sup> are essential for cellular reduction and oxidation reactions respectively and are converted between each other by these redox reactions without being consumed. Reduction catalysed by NADH results in its oxidation to NAD<sup>+</sup>, and vice-versa for NAD<sup>+</sup>. The ratio of NAD<sup>+</sup> to NADH in the cell or NAD<sup>+</sup>/NADH redox balance is such that there is generally more NAD<sup>+</sup> than NADH therefore favouring oxidative reactions.

### 1.3.2.2 Dephosphorylation of NADP<sup>+</sup> to NAD<sup>+</sup>

NAD<sup>+</sup> can also be phosphorylated to NADP by the enzyme NAD<sup>+</sup> kinase (Agledal *et al.*, 2010). Conversely NADP<sup>+</sup> can be dephosphorylated by NADP<sup>+</sup> phosphatase back to NAD<sup>+</sup> (Kawai and Murata, 2008). NADP<sup>+</sup> can also be reduced to NADPH, these are important cofactors predominantly used in anabolic metabolic pathways, for example amino acid synthesis, consistent with levels of NADPH, providing reducing power, generally being higher than NADP<sup>+</sup>.

### 1.3.2.3 Biosynthesis of NAD<sup>+</sup>

The biosynthesis of NAD<sup>+</sup> in the cell can occur through two pathways, the salvage pathway from either nicotinamide (Nam) or nicotinic acid (NA) where the latter is known as the Preiss-Handler pathway (Preiss and Handler, 1958a; Preiss and Handler, 1958b) and the *de novo* pathway from tryptophan which then leads into the Preiss-Handler pathway (Houtkooper *et al.*, 2010) (Fig. 1.9).

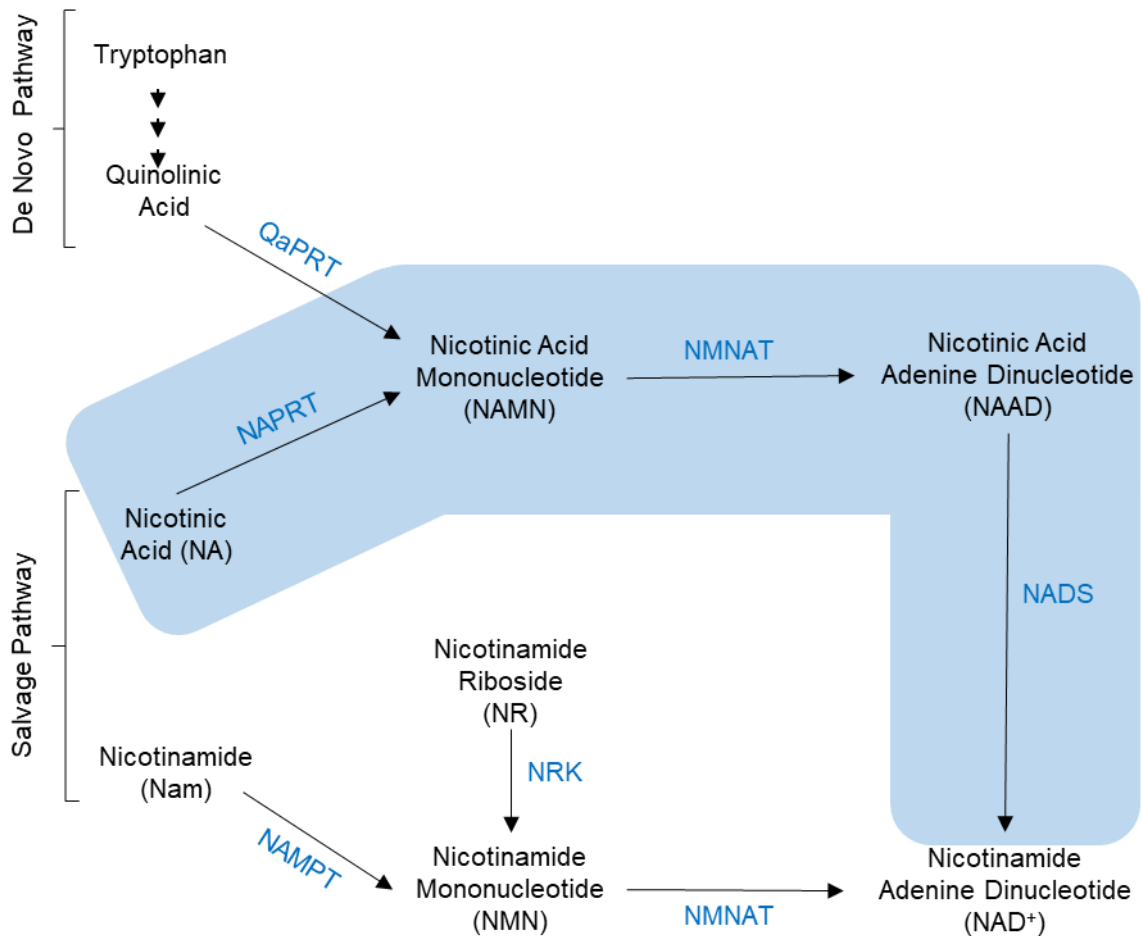


**Figure 1.9: NAD<sup>+</sup> biosynthesis pathways.**

Synthesis of NAD<sup>+</sup> through the *de novo* pathway from tryptophan and through the salvage pathway from nicotinic acid (NA) (Preiss-Handler pathway, shaded in blue) or nicotinamide (Nam).

In the *de novo* pathway tryptophan is taken up from the diet which is converted to quinolinic acid through multiple enzymatic reactions which then forms nicotinic acid mononucleotide (NAMN) and enters the Preiss-Handler pathway (Fig. 1.9). This is then converted to nicotinic acid adenine dinucleotide (NAAD) through nicotinic acid mononucleotide adenylyltransferase (NMNAT) which is then aminated by NAD<sup>+</sup> synthase (NADS), resulting in NAD<sup>+</sup> (Houtkooper *et al.*, 2010).

Although cells can produce NAD<sup>+</sup> through the *de novo* pathway using tryptophan it is only a small contributor to the levels required, therefore NAD<sup>+</sup> is also produced from NAD<sup>+</sup> precursors through the Preiss-Handler and salvage pathways (Fig. 1.9). NAD<sup>+</sup> precursors consist of NA, nicotinamide riboside (NR),

nicotinamide mononucleotide (NMN) and Nam which are all collectively termed niacin/vitamin B3 (Houtkooper *et al.*, 2010).

The conversion of Nam to NMN is catalysed by the rate limiting enzyme nicotinamide phosphoribosyltransferase (NAMPT) (Revollo *et al.*, 2004) and is then converted to NAD<sup>+</sup> by the enzyme NMNAT. NA is the precursor for the Preiss-Handler pathway and begins with the conversion of NA to NAMN through the enzyme nicotinic phosphoribosyltransferase (NAPRT) and is then converted as previously described for the *de novo* pathway. NR enters the pathway through phosphorylation to NMN by the enzyme nicotinamide riboside kinase (NRK) (Fig. 1.9) (Bieganowski and Brenner, 2004). NMN can also efficiently be utilised as a precursor, bypassing the conversion from NR by NRK.

These precursors can be attained by cells through the diet, although importantly Nam is also produced when NAD<sup>+</sup> is consumed by particular cellular NAD<sup>+</sup>-dependent enzymes that use NAD<sup>+</sup> as a substrate and it can be recycled back into the NAD<sup>+</sup> salvage pathway (section 1.4). It is estimated that the amount of NAD<sup>+</sup> consumed by mammalian cells for such reactions equates to gram values of NAD<sup>+</sup> precursors needing to be ingested per day. The daily recommended dose of NAD<sup>+</sup> precursors is in milligram quantities, therefore NAD<sup>+</sup> precursors from the diet must only contribute to a small level of the NAD<sup>+</sup> produced, although insufficient supplementation can lead to the disease pellagra (Goody and Henry, 2018). Due to this it is presumed that in mammals the main source of NAD<sup>+</sup> is through the salvage pathway utilising Nam as its precursor (Houtkooper *et al.*, 2010). The enzyme NAMPT is rate limiting and therefore plays a major role in regulating the levels of cellular NAD<sup>+</sup> (Revollo *et al.*, 2004), which is important in maintaining NAD<sup>+</sup>/NADH levels for redox reactions, other NAD<sup>+</sup>-dependent processes (section 1.4) and for cell survival.

## 1.4 NAD<sup>+</sup> consuming enzymes

Although NAD<sup>+</sup> is mainly associated with its role in providing oxidising power during redox reactions, it is also important for the function of some enzymes in the cell serving as their substrate, for example the PARP and sirtuin family of enzymes (Amé *et al.*, 2004; Landry *et al.*, 2000). The ADP-ribose moiety is cleaved from NAD<sup>+</sup> and the nicotinamide moiety is released and can be recycled into the NAD<sup>+</sup> salvage biosynthetic pathway.

### 1.4.1 Poly (ADP-ribose) polymerase

The PARP family consists of 18 members (Ray Chaudhuri and Nussenzweig, 2017) with diverse functions within the cell (Ko and Ren, 2012). PARPs catalyse the transfer of ADP-ribose from NAD<sup>+</sup> to proteins, therefore utilising NAD<sup>+</sup> as a substrate (Chambon *et al.*, 1963). Depending on the PARP enzyme, multiple ADP-ribose units may be added to a protein resulting in poly (ADP-ribose) (PAR) chains or a single ADP-ribose moiety may be added, both are a type of post translational modification (Fig. 1.10).

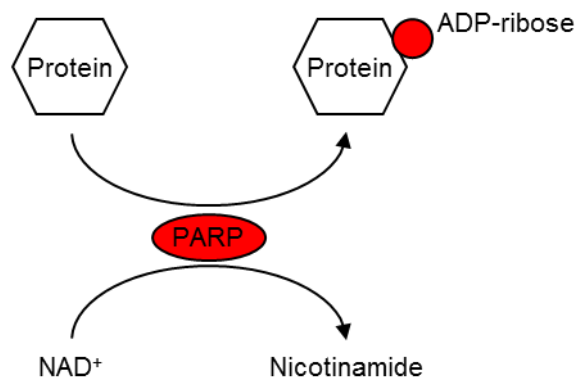


**Figure 1.10: Consumption of NAD<sup>+</sup> by PARP.**

PARP consumes NAD<sup>+</sup> as part of its enzymatic function releasing nicotinamide in the process.

PARP1 and PARP2 enzymes are most commonly known for their roles in DNA repair, although more recently PARP3 has also been reported to have a role in DNA repair (Schreiber *et al.*, 2002; Amé *et al.*, 1999; Boehler *et al.*, 2011).

PARP1, the founding PARP family member, is a 113kDa protein located in the nucleus (Vyas *et al.*, 2013). PARP1 has two zinc finger structures which help in DNA binding, an auto modification domain, a domain with a nuclear localisation signal and a catalytic domain (Amé *et al.*, 2004). PARP1 has an important role in the repair of single strand DNA breaks (Fisher *et al.*, 2007) through base excision repair (BER) although it is also associated with other forms of DNA repair, for example, SSB repair through nucleotide excision repair (NER) and mismatch repair (MMR) and DSB repair through non-homologous end joining (NHEJ) and HR (Yelamos *et al.*, 2011).

During BER, PARP1 is recruited to SSBs where it promotes their repair by recruiting other proteins involved in the repair process, for example X-ray repair cross-complementing protein 1 (XRCC1) (El-Khamisy *et al.*, 2003). It is thought that during BER, PARP1 is recruited to a SSB which has been created by an apurinic/apyrimidinic (AP) endonuclease and PARP auto-PARylates itself. This PARylation causes a negative charge and leads to the DNA being kept in an open state. PARP1 activity helps facilitate the assembly of the BER complex which consists of multiple proteins which include XRCC1 a scaffolding protein, DNA polymerase  $\beta$  which elongates the DNA, and DNA ligase III which repairs the nick in the DNA. While the complex assembles, PARP1 continues to PARylate itself, eventually leading to a high negative charge and disassociation from the DNA, allowing the BER complex to directly access the DNA (Yelamos *et al.*, 2011) (Fig. 1.11).

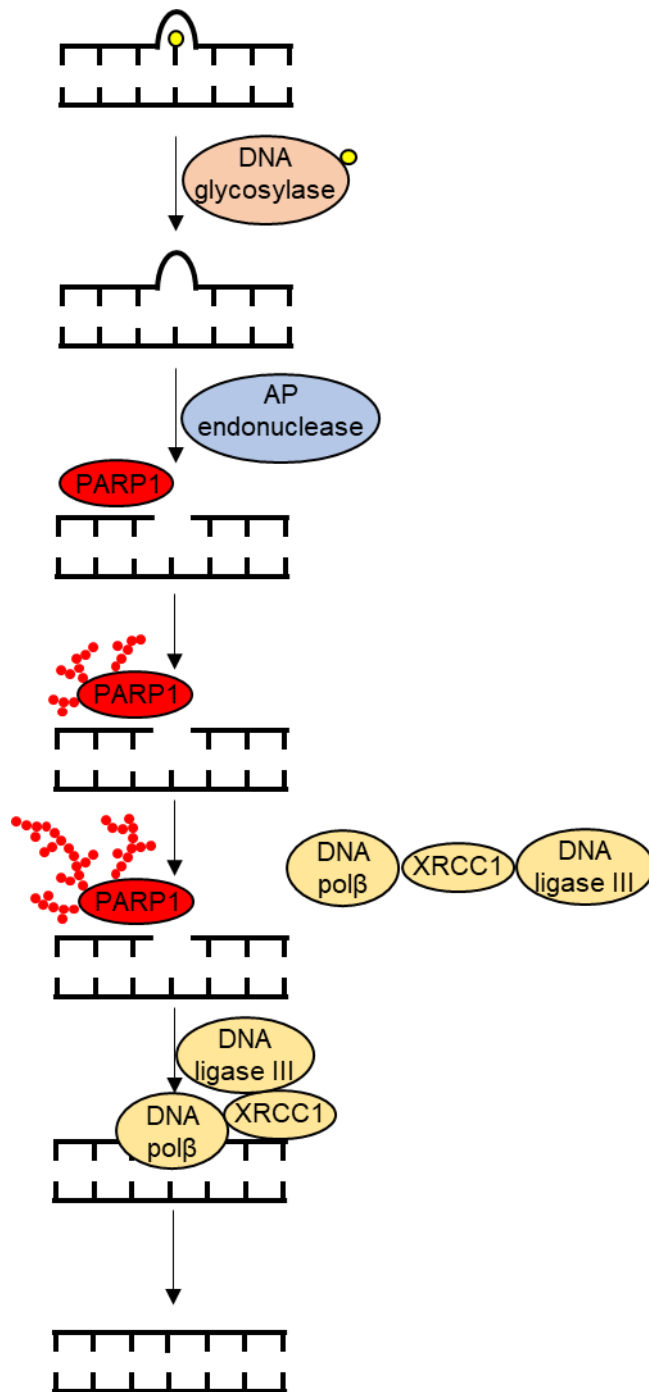


**Figure 1.11: Recruitment of PARP1 during BER.**

During BER, DNA glycosylase detects a mispaired or damaged base in the DNA and removes the base. An apurinic or apyrimidinic (AP) site is then cleaved by AP endonuclease creating a SSB which is detected by PARP1. PARP1 binds to the SSB and PARylates itself, leading to a highly charged structure which keeps DNA in its open structure. During this process the BER complex is recruited which consists of many proteins including XRCC1, DNA polymerase  $\beta$  and DNA ligase III. As the complex is assembled PARP has produced enough charge to disassociate itself from the DNA allowing the BER complex to access the DNA.

#### **1.4.1.1 Clinical use of PARP inhibitors as a single agent – induction of synthetic lethality**

As briefly mentioned in section 1.1.5.2, PARP inhibitors are currently being used in the clinic predominantly to treat patients that have cancer where the cells are deficient in the DNA repair mechanism HR (Jiang *et al.*, 2019; McCann and Hurvitz, 2018). In 2005, Farmer *et al.* and Bryant *et al.* proposed the concept of synthetic lethality, where cells that were deficient in HR due to BRCA mutations and had BER inhibited via PARP inhibition were not viable (Farmer *et al.*, 2005; Bryant *et al.*, 2005). Multiple proteins are involved in the process of HR, including BRCA1 and BRCA2 (Moynahan *et al.*, 2001; Moynahan *et al.*, 1999). Individuals with a germline BRCA1/2 mutation, which is inherited in an autosomal dominant manner, have a higher risk of developing ovarian, breast and prostate cancer (Petruccioli *et al.*, 1993).

If SSB DNA damage occurs in cells that are BRCA mutated, these can be efficiently repaired by BER utilising the enzyme PARP (Yelamos *et al.*, 2011). However, if BER is deficient then the SSBs can develop into DSBs and rely on a different DNA repair mechanism, HR. Although there are other forms of DNA repair these are known to be error-prone and therefore if BER and HR are absent then the cells cannot repair their DNA efficiently which can lead to cell death (Fig. 1.12).

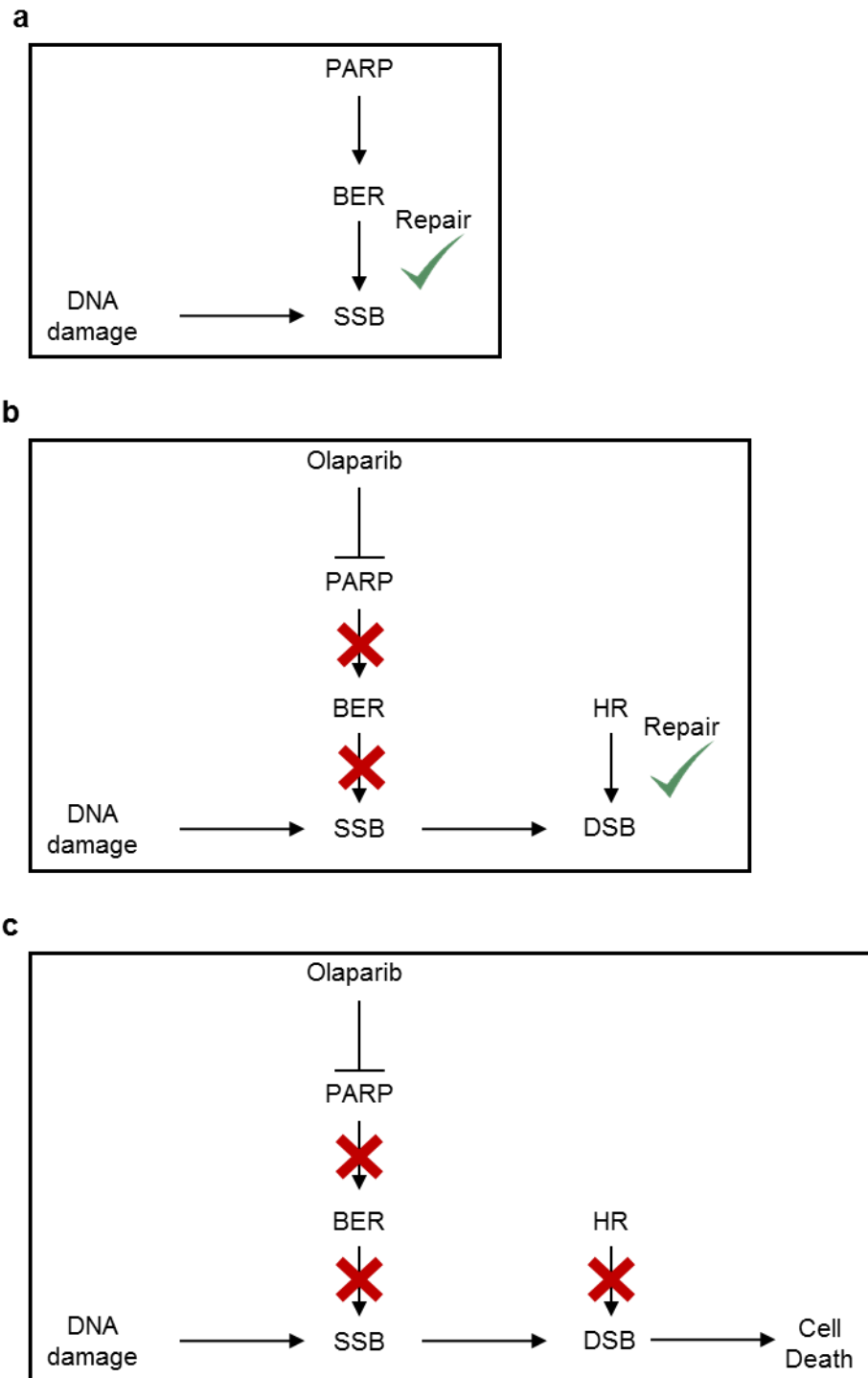


**Figure 1.12: Schematic of synthetic lethality.**

**a.** SSB damage repair by BER through PARP in a 'normal' scenario. **b.** Absence of PARP: SSB developing into DSB and repaired by HR. **c.** Deficient HR and inhibition of PARP, induces synthetic lethality.

In 2014, the first PARP inhibitor, olaparib, was approved by the U.S Food and Drugs Administration (FDA) for use as a monotherapy in patients with germline BRCA mutations who have advanced epithelial ovarian, fallopian tube or primary

peritoneal cancer that have previously had 3 or more chemotherapy treatments (Jiang *et al.*, 2019). At the same time the European Medicines Agency (EMA) approved olaparib as a maintenance therapy in patients with germline or somatic BRCA mutations that had platinum sensitive, relapsed high-grade serous epithelial ovarian, fallopian tube or primary peritoneal cancer, who had complete/partial response to platinum based chemotherapy (Jiang *et al.*, 2019). Since then multiple other PARP inhibitors have been approved by the FDA and EMA for ovarian and breast cancer treatment which are summarised in Table 1.1 (Jiang *et al.*, 2019; McCann and Hurvitz, 2018). More recently clinical trials have focused on the effects of PARP inhibitors on prostate cancer in patients who are HR deficient and also on pancreatic cancer (Kamel *et al.*, 2018).

Drug	Date of approval	Therapy	BRCA status	Indication
Olaparib Capsule	Dec 2014 (EMA)	Maintenance	Germline, Somatic	Platinum sensitive relapsed high-grade serous epithelial ovarian, fallopian tube or primary peritoneal cancer, post complete or partial response to platinum-based chemotherapy
	Dec 2014 (FDA)	Fourth line	Germline	Advanced epithelial ovarian, fallopian tube or primary peritoneal cancer
Olaparib tablets	Aug 2017 (FDA)	Maintenance	-	Recurrent epithelial ovarian, fallopian tube or primary peritoneal cancer, post complete or partial response to platinum-based chemotherapy
		Fourth line	Germline	Advanced epithelial ovarian, fallopian tube or primary peritoneal cancer
	Jan 2018 (FDA)	-	Germline	HER2-negative metastatic breast cancer who have been treated with chemotherapy either in the neoadjuvant, adjuvant, or metastatic setting
	Feb 2018 (EMA)	Maintenance	-	Platinum sensitive relapsed high-grade serous epithelial ovarian, fallopian tube or primary peritoneal cancer, post complete or partial response to platinum-based chemotherapy
	Dec 2018 (FDA)	Maintenance	Germline, Somatic	Advanced epithelial ovarian, fallopian tube or primary peritoneal cancer post complete or partial response to platinum-based chemotherapy
Rucaparib	Dec 2016 (FDA)	Third line	Germline, Somatic	Advanced epithelial ovarian, fallopian tube or primary peritoneal cancer
		Maintenance	-	Recurrent epithelial ovarian, fallopian tube or primary peritoneal cancer, post complete or partial response to platinum-based chemotherapy
	May 2018 (EMA)	Third line	Germline, Somatic	Platinum sensitive relapsed/progressive high-grade epithelial ovarian, fallopian tube or primary peritoneal cancer
Niraparib	Mar 2017 (FDA)	Maintenance	-	Recurrent epithelial ovarian, fallopian tube or primary peritoneal cancer, post complete or partial response to platinum-based chemotherapy
	Nov 2017 (EMA)	Maintenance	-	Platinum sensitive relapsed high-grade serous epithelial ovarian, fallopian tube or primary peritoneal cancer, post complete or partial response to platinum-based chemotherapy
Talazoparib	Oct 2018 (FDA)	-	Germline	HER2-negative locally advanced or metastatic breast cancer

**Table 1.1: Summary of clinically approved PARP inhibitors for single agent use.**

PARP inhibitors which have been approved by the FDA or EMA for use in patients that are BRCA mutant for the treatment of ovarian and breast cancer (Jiang *et al.*, 2019; McCann and Hurvitz, 2018).

Multiple proteins are involved in the process of HR and currently the use of PARP inhibitors has predominantly been focused on patients that are known to have a mutation in BRCA1/2. As many other proteins are involved in the HR pathway,

additional research is ongoing to see whether PARP inhibitors can also be used in patients who have mutations in other proteins that lead to a HR deficient status (McCabe *et al.*, 2006).

#### **1.4.1.2 Combination treatments with PARP inhibitors**

There has also been interested in extending the clinical use of PARP inhibitors to other cancers that are not BRCA or HR deficient as part of a combinatorial treatment. Combinational treatment can be advantageous as a drug that has a high IC<sub>50</sub> and induces unwanted toxic effects due to high drug dose could result in a lower IC<sub>50</sub> when combined with other therapeutics, allowing a lower therapeutic dose to be administered to the patient.

Most current chemotherapy drugs work by inducing DNA damage, therefore it could be advantageous to combine these with drugs that impair DNA repair such as PARP inhibitors, which may allow a lower dose of the DNA damaging agent to be used.

Depending on the PARP inhibitor, these inhibit PARPs by slightly different mechanisms. This includes by direct catalytic inhibition of PARP by competing with NAD<sup>+</sup> for binding to the catalytic site and/or through PARP trapping, where the PARP inhibitor traps PARP onto the damaged DNA and stable PARP-DNA complexes are formed. The PARP inhibitor olaparib has a high PARP trapping capability, in contrast veliparib has only weak trapping capability (Murai *et al.*, 2012). This has important implications in combining PARP inhibitors with different DNA-damaging agents. As different agents cause different types of damage, their repair and dependency on different repair pathways can also vary. Whilst catalytic PARP inhibition induces persistent SSBs and dependency on HR, a number of studies implicate PARPs involvement in other DNA repair mechanisms to SSB repair by BER (Yelamos *et al.*, 2011). Furthermore, studies suggest that repair of PARP trapping is by different mechanisms to HR (Murai *et al.*, 2012).

A number of different DNA-damaging agents that induce different types of damage have been tested in combination with PARP inhibition and are summarised below.

Temozolomide (TMZ) is a monoalkylating agent which is currently used in the clinic primarily for the treatment of glioblastoma multiforme (GBM). TMZ reacts with electron donors on DNA, resulting in the covalent addition of a methyl group. TMZ mainly generates N7-guanine, N3-adenine and O6-guanine methyl adducts with O6-methylguanine being the primary cause of TMZ cytotoxicity. O6-methylguanine is repaired by the enzyme methylguanine-DNA methyltransferase (MGMT) by removal of the methyl group, however, certain cancer cells lack MGMT. If the cells are deficient in MGMT then during DNA replication O6-methylguanine is mispaired with thymine, which activates DNA MMR. As MMR is strand-specific, it recognises the thymine on the daughter strand as the 'wrong' mismatched base and is removed with O6-methylguanine remaining in the parental strand, which leads to futile cycles of MMR, leading to DSBs and eventually cell cycle arrest or apoptosis. Cancer cells that are MGMT-deficient and MMR-positive are thus most sensitive to TMZ (Zhang *et al.*, 2012) (Fig. 1.13).

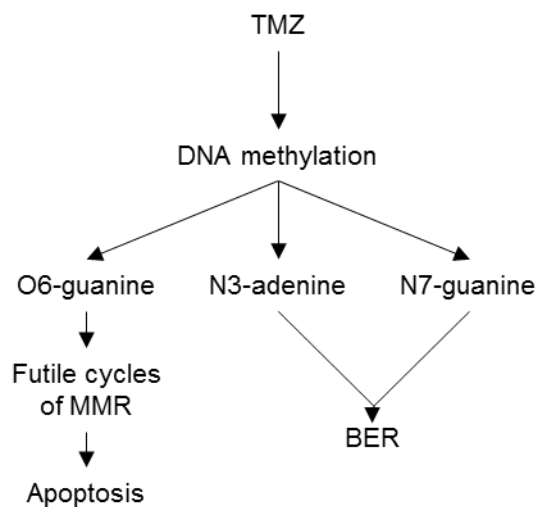


**Figure 1.13: The primary cytotoxic mechanism of action of temozolomide.**

Mechanism of action of the alkylating agent temozolomide (TMZ) in MGMT negative and MMR positive cells.

Although O6-guanine methylation is the principle cause of TMZ cytotoxicity this represents ~6% of TMZ-induced methylation. Most methylation is of N7-guanines (70%) and N3-adenines (9%). Their methylation is repaired efficiently by BER and therefore is not usually cytotoxic. However, as BER is PARP-dependent, PARP inhibitions would prevent their repair. Multiple pre-clinical studies have shown increased activity of TMZ when combined with PARP inhibitors (Daniel *et*

*et al.*, 2009; Palma *et al.*, 2009). Based on the pre-clinical data the first clinical trial of a PARP inhibitor plus TMZ was carried out using rucaparib and showed that the combination was safe (Plummer *et al.*, 2008). A subsequent phase II study against metastatic melanoma showed some myelosuppression in 54% of patients which prompted a 25% reduction in the TMZ dose administered however, encouragingly an increase in progression-free survival was observed (Plummer *et al.*, 2013).

Platinum based chemotherapy, for example cisplatin, causes intra- and inter-strand cross-links within the DNA (Siddik, 2003). Testicular, ovarian, lung, bladder and cervical cancer are some of many cancers where platinum-based chemotherapy is currently used. The DNA adducts caused by cisplatin treatment block DNA replication and their repair is primarily by NER, although NHEJ, HR and MMR are also reported to contribute to repair of platinum/cisplatin-induced lesions (Rocha *et al.*, 2018). During NER a 30nt oligonucleotide is excised where the damage is and is then re-filled by DNA polymerase using the intact DNA strand as a template. PARP1 has been reported to have a role in the repair of DNA damage caused by platinum-based drugs (Guggenheim *et al.*, 2008) and PARP inhibitors are being used in the clinic as a secondary treatment for ovarian cancer that has previously responded to cisplatin (Jiang *et al.*, 2019). Several pre-clinical and clinical studies have shown that PARP inhibition can lead to sensitisation of platinum based compounds (Michels, Vitale, Galluzzi, *et al.*, 2013; Michels, Vitale, Senovilla, *et al.*, 2013; Donawho *et al.*, 2007; McQuade *et al.*, 2018). Effects may be cell context specific (Evers *et al.*, 2008) and more recently Murai *et al.* (2014) have reported that the synergy seen in this combination is minimal compared to the combination of TMZ with PARP inhibitors. Nonetheless, the combination of platinum-based therapy and PARP inhibitors has been reported to provide some protection against neuropathy associated with platinum-based chemotherapy (McQuade *et al.*, 2018).

Topoisomerase 1 (Topo1) poisons such as camptothecin (CPT) trap Topo1 onto the DNA which leads to the DNA 'nicks' caused by Topo1, to enable relief of supercoiling, not being re-ligated, therefore inducing SSBs in the DNA (Hsiangl *et al.*, 1985). One form of repair is through Topo1 excision by tyrosyl-DNA-

phosphodiesterase (Pommier *et al.*, 2006). PARP is crucial in recruiting tyrosyl-DNA-phosphodiesterase and other proteins which are associated with BER, to the DNA damage (Plo *et al.*, 2003; Das *et al.*, 2014). PARP's involvement in the repair of the DNA damage caused by Topo1 poisons rationalises the combination of PARP inhibitors and Topo1 poisons. Pre-clinical studies against neuroblastoma and a phase I study against adult solid tumours and lymphomas indicate that PARP inhibitor treatment can sensitise cells to Topo1 poisons (Bowman *et al.*, 2001; Kummar *et al.*, 2011; Daniel *et al.*, 2009). Murai *et al.* (2014) showed that unlike TMZ where both PARP trapping and catalytic inhibition contributes to effects, the catalytic inhibition of PARP rather than PARP trapping appears responsible for increased sensitivity to CPT.

Topoisomerase 2 (Topo2) poisons such as etoposide and doxorubicin (DOX), by a similar mechanism to Topo1 poisons, trap Topo2 to the DNA leading to the double strand 'nicks' caused by Topo2 not being re-ligated and therefore DSBs are formed (Nitiss, 2009). PARPs are not primarily involved in the repair of DSB damage that is induced by Topo2 poisons. PARP inhibitors in combination with DOX has led to potentiating effects (Park *et al.*, 2018) although other data shows no effect of PARP inhibitors in combination with etoposide (Murai *et al.*, 2014).

Some of the combinations of PARP inhibitors and DNA damaging agents appear promising for particular cancer indications and may be able to give some improvement in survival, enabling use of PARP inhibitors as part of a combinatorial treatment. However, it must also be considered what effects the inhibition of PARP is having on non-cancer cells and tissue when combined with DNA-damaging agents (Chalmers, 2009). As non-cancer cells also rely on the DNA repair machinery, there is a risk that the combinations may lead to increased sensitisation of normal tissue in parallel and increased on-target side effects in non-cancer cells. It has been shown that oral PARP inhibitors have led to unwanted effects in non-cancer cells, for example myelosuppression that is dose limiting has been seen in some patients (Drew and Plummer, 2009). PARP inhibition in both cancer and non-cancer cells in combination with cytotoxic agents may therefore shift the dose response (Fig. 1.2b) whilst the therapeutic index remains as narrow as previously. One aim of this PhD research is to

investigate the possibility of inhibiting PARP selectively in cancer cells alone through its indirect metabolic inhibition as a potential way to widen the therapeutic index of current chemotherapeutic agents in clinical use.

### 1.4.2 Sirtuins

Another  $\text{NAD}^+$ -dependent and  $\text{NAD}^+$ -consuming enzyme of particular cancer relevance is SIRT1. It is one of 7 members of the mammalian sirtuin family and is closely related to the founding member Sir2 in *Saccharomyces cerevisiae* (Frye, 2000). Sir2/SIRT1 is a histone deacetylase (HDAC) (Imai *et al.*, 2000) which is reliant upon  $\text{NAD}^+$  for its function (Landry *et al.*, 2000). The consumption of  $\text{NAD}^+$  during removal of acetyl groups from proteins produces *O*-acetyl-ADP-ribose and nicotinamide, where the latter can be recycled back into the  $\text{NAD}^+$  salvage pathway (Tanner *et al.*, 2000) (Fig. 1.14). SIRT1 not only deacetylates histones which can affect chromatin structure, genomic integrity and gene expression but also deacetylates other proteins, for example the TSG p53 and HIF-1 $\alpha$  as well as other transcription factors such as FOXO4 (Lim *et al.*, 2010; Vaziri *et al.*, 2001; Motta *et al.*, 2004). As such, SIRT1 is a major regulator of gene expression and transcription.

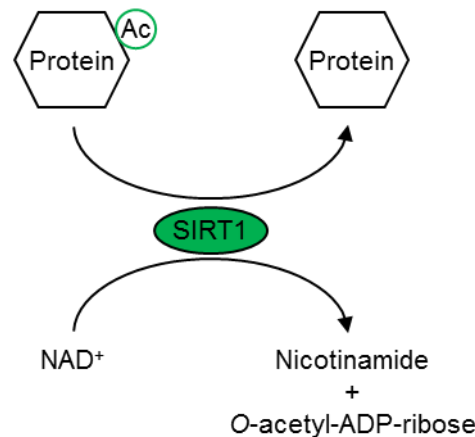


**Figure 1.14: Recycling of  $\text{NAD}^+$  by SIRT1.**

SIRT1 consumes  $\text{NAD}^+$  and recycles it to nicotinamide which can be re-used in the salvage pathway of  $\text{NAD}^+$  biosynthesis, during deacetylation. The process also releases an *O*-acetyl-ADP-ribose molecule.

The sirtuins are involved in many different cellular processes and diseases. Sir2/SIRT1 has previously been shown to promote longevity with its

overexpression increasing the lifespan of multiple organisms including mammals (Kaeberlein *et al.*, 1999; Tissenbaum and Guarente, 2001; Satoh *et al.*, 2013). SIRT1 appears to have a protective role in neurodegeneration; it suppresses  $\beta$ -amyloid production and is protective in Alzheimer's disease models (Kim *et al.*, 2007). SIRT1 is also implicated in many other diseases including type II diabetes (Rahman and Islam, 2011). The focus of this thesis research on SIRT1 is on the therapeutic potential of targeting of SIRT1 in the cancer context, whether there may be a therapeutic window using a small molecule inhibitor or alternative ways it may be targeted.

#### **1.4.2.1 The role of SIRT1 in cancer development**

SIRT1 has a complex role in cancer with some research suggesting that it is tumour promoting (Brunet *et al.*, 2004; Ford *et al.*, 2005; Herranz *et al.*, 2013; Zhang *et al.*, 2016) and other research suggesting it functions as a tumour suppressor (Firestein *et al.*, 2008; Wang *et al.*, 2008). Early evidence that SIRT1 may have tumour promoting properties came from identification of the tumour suppressor protein p53 as a SIRT1 substrate. p53 deacetylation by SIRT1 downregulates p53 transcriptional activity and catalytically inactive SIRT1 potentiated p53-induced apoptosis (Vaziri *et al.*, 2001). Knock-down of SIRT1 by RNAi in multiple cancer cell lines *in vitro* caused cancer cell death (Ford *et al.*, 2005) and *in vivo* SIRT1 has recently been shown to promote thyroid carcinogenesis (Herranz *et al.*, 2013). Increased expression of SIRT1 associated with worse prognosis, is also seen in many cancers, including prostate, colon and lung cancers (Huffman *et al.*, 2007; Stünkel *et al.*, 2007; Chen *et al.*, 2014a; Chen *et al.*, 2012). However, SIRT1 expression has been shown to be reduced in some cancer types, including in glioblastoma, bladder and ovarian cancers (Carafa *et al.*, 2019). In further support of a tumour suppressor function for SIRT1, a key study by Firestein *et al.* (2008) showed that SIRT1 overexpression in mice predisposed to developing cancer showed reduced cancer formation.

Whilst some of these apparently contradictory findings may be explained by differences depending on tissue context and genetic background, additionally a number of SIRT1 splice variants have recently been reported (Deota *et al.*, 2017; Lynch *et al.*, 2010; Shah *et al.*, 2012). Similar to other splice variants, emerging

evidence suggests that these SIRT1 splice variants may function very differently to full-length SIRT1 (SIRT1-FL) (Deota *et al.*, 2017; Lynch *et al.*, 2010; Shah *et al.*, 2012). Due to this a cautious approach must be taken when considering the published literature as research was conducted without knowledge of these variants which, in some cases, but not others, may have inadvertently been targeted.

#### **1.4.2.2 SIRT1 splice variants**

The SIRT1- $\Delta$ 8 splice variant, which lacks exon 8, has a small part of the protein deacetylase domain missing (Fig. 1.15) and has reduced deacetylase activity compared to the full-length variant (SIRT1-FL) (Lynch *et al.*, 2010). Although SIRT1- $\Delta$ 8 appears to be ubiquitously expressed in different tissue types the relative abundance of SIRT1- $\Delta$ 8 and SIRT1-FL varied depending on the tissue with increased SIRT1- $\Delta$ 8 expression in the brain, foetal thymus, testis and heart. In support of differential regulation and interaction partners of SIRT1- $\Delta$ 8 and SIRT1-FL, part of the binding domain for the SIRT1 repressor protein DBC1 is missing in SIRT1- $\Delta$ 8 and no interaction could be detected by immunoprecipitation. Another major difference between SIRT1-FL and SIRT1- $\Delta$ 8 relates to the tumour suppressor p53, with expression of SIRT1- $\Delta$ 8 being stress responsive and negatively regulated by p53 whereas expression of SIRT1-FL is not.

Through further work on SIRT1- $\Delta$ 8 Shah *et al.* (2012) discovered the splice variant SIRT1- $\Delta$ 2/9. This splice variant has a deletion between exons 2 and 9 leading to complete loss of deacetylase function as well as part of the active regulator of SIRT1 (AROS) binding domain and it undergoes a frameshift mutation resulting in a novel C-terminus. mRNA expression of SIRT1- $\Delta$ 2/9 varied across tissue type with it being readily detected in heart, lung and pancreas, whereas it was undetectable in brain, breast, colon. SIRT1- $\Delta$ 2/9 was seen to be over expressed in HCT116 p53<sup>+/+</sup> cancer cells compared to ARPE-19 non-cancer cells and its expression was associated with upregulation of matrix metalloproteinase 2 mRNA, which has a role in metastasis (Shah *et al.*, 2012).

More recently a third splice variant, SIRT1- $\Delta$ E2, that lacks exon 2, was discovered (Deota *et al.*, 2017). This variant has similar deacetylase activity to SIRT1-FL but is a tissue specific splice variant with high levels being found in the brain and testis and no expression in the liver. This differential expression and substrate interaction screening led Deota *et al.* (2017) to propose that the E2 domain has an important role in metabolic homeostasis. SIRT1- $\Delta$ E2 was shown to have less interaction with specific proteins that are needed in the liver whereas proteins that are required in the brain had the same specificity for SIRT1- $\Delta$ E2 as SIRT1-FL. This suggests that the E2 domain is required for protein interaction specificity and the tissue specific role of SIRT1 splice variants (Deota *et al.*, 2017).

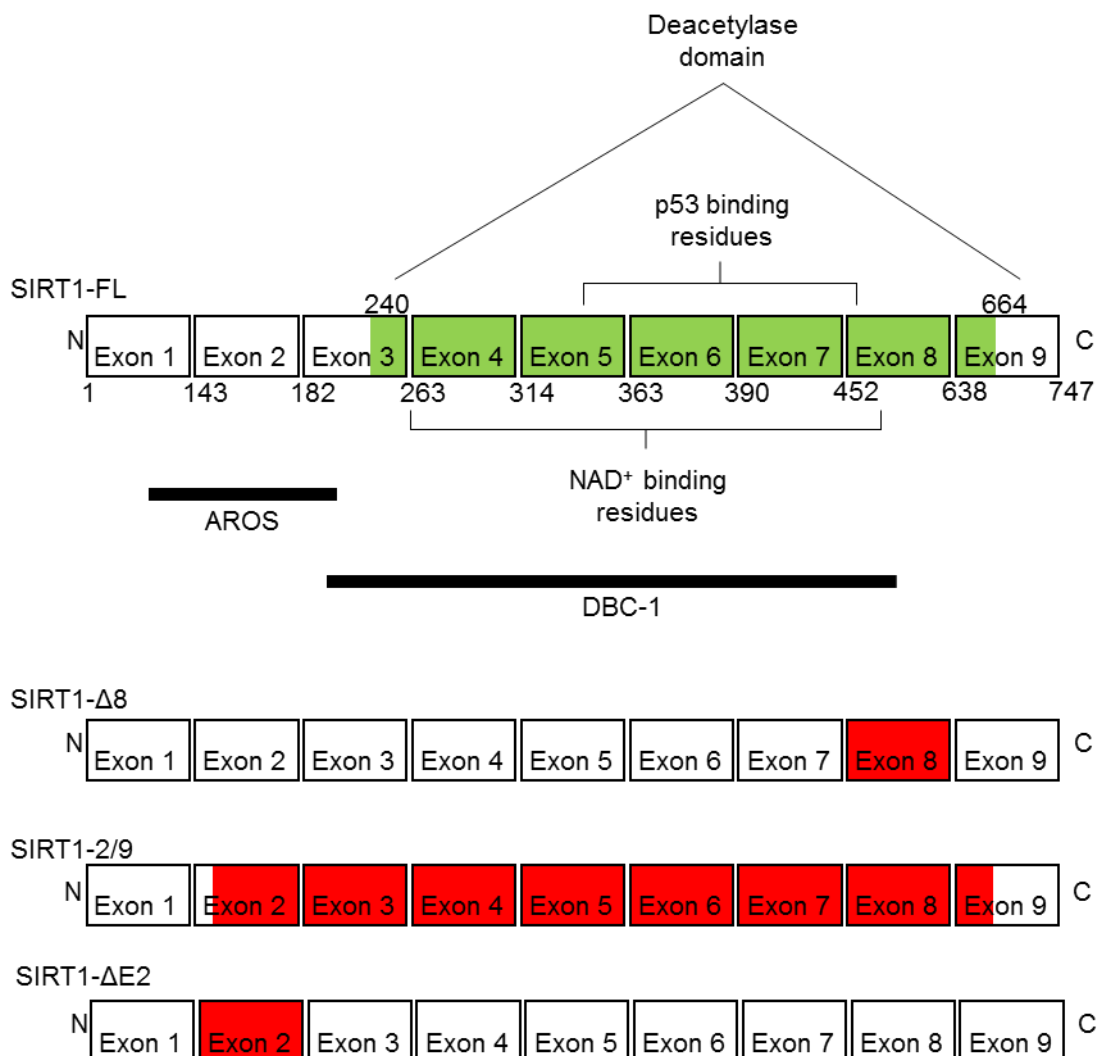


**Figure 1.15: Splice variants of SIRT1.**

Exons of SIRT1-FL with functional deacetylase domain (green). p53 and NAD<sup>+</sup> binding domains and AROS and DBC-1 binding domains also indicated. SIRT1- $\Delta$ 8, SIRT1-2/9 and SIRT1- $\Delta$ E2 with missing regions indicated in red.

The different deacetylase activities, expression and binding domains of these splice variants suggest different protein targets, regulation and functions for the different SIRT1 variant forms, possibly accounting for the complex and varying roles previously described for SIRT1 in different cancers.

Whilst it has previously been noted that SIRT1-FL knock-down induces cell death in cancer cells *in vitro* but not in non-cancer cells, unanswered questions which will be specifically addressed here include, i) whether small molecule SIRT1 inhibition could be a selective approach to killing cancer cells, and ii) based on other preliminary data (see appendix Fig. 9.1), does SIRT1 or its variants have any effect on cell fate/stemness of cancer or non-cancer cells.

## 1.5 NAD<sup>+</sup> as a therapeutic target

### 1.5.1 Targeting NAD<sup>+</sup> via enzymes involved in the NAD<sup>+</sup> salvage pathway

Whilst NAD<sup>+</sup> is an essential metabolite in both non-cancer and cancer cells, NAMPT, which is the rate-limiting enzyme of the NAD<sup>+</sup> salvage pathway, is overexpressed in many cancers (Yaku *et al.*, 2018). It has attracted considerable attention as a potential therapeutic target due to this and suggested increased NAD<sup>+</sup> turnover in cancer cells compared to non-cancer cells.

NAMPT inhibition has been reported to inhibit cancer cell glycolysis due to reduced NAD<sup>+</sup> availability for GAPDH which also reduced carbon flow into the TCA cycle (Tan *et al.*, 2013), providing a mechanistic basis for observed ATP depletion (Hasmann and Schemainda, 2003; Watson *et al.*, 2009). A number of independent studies have shown that targeting of NAMPT induces cancer cell death *in vitro* and inhibits tumour growth *in vivo* (Hjarnaa *et al.*, 1999; Matheny *et al.*, 2013), with effects via the depletion of NAD<sup>+</sup> (Olesen *et al.*, 2008; Hasmann and Schemainda, 2003; Watson *et al.*, 2009).

These encouraging results have led to several phase I clinical trials using the NAMPT inhibitors GMX-1778 and FK866. However, dose-limiting thrombocytopenia and also gastrointestinal and retinal toxicities have been observed (von Heideman *et al.*, 2010; Holen *et al.*, 2008), these effects appear to be on-target. Genetic deletion of NAMPT in photoreceptor cells caused retinal degeneration and blindness in mice with vision loss rescued by administration of the NAD<sup>+</sup> precursor NMN (Lin *et al.*, 2016). Given that NAD<sup>+</sup> is a vital metabolite, these toxicities are perhaps not surprising. Indeed, whole body NAMPT deficiency is embryonically lethal in mice (Revollo *et al.*, 2007). This indicates the importance of dosing regime and duration such that any NAD<sup>+</sup> depletion is not harmful to normal tissue yet is sufficient in cancer cells for therapeutic benefit. One approach has been to administer the NAD<sup>+</sup> precursor NA together with a NAMPT inhibitor. Many cancer cells are known to lack the Preiss-Handler pathway enzyme NAPRT (see section 1.3.2.3) due its epigenetic silencing

whereas non-cancer cells usually express the enzyme (Duarte-Pereira *et al.*, 2016). Non-cancer cells therefore can produce NAD<sup>+</sup> from NA through the Preiss-Handler pathway whereas NAPRT-deficient cancer cells cannot. This suggests NAPRT expression could be used as a biomarker to select for cancers that will be affected by NAMPT inhibition. This combination of NAMPT inhibitor plus NA has been shown to rescue the toxic effects of NAMPT inhibition towards non-cancer cells (Watson *et al.*, 2009; Olesen *et al.*, 2010).

As part of this PhD research a different approach is investigated, namely short term NAMPT inhibition that is non-toxic as a possible way of preferentially depleting NAD<sup>+</sup> in cancer cells analogous to the cancer-selective reduction in NAD<sup>+</sup>/NADH with LDH-A suppression (Allison *et al.*, 2014). It is hypothesised that this could result in reduced activity of NAD<sup>+</sup>-dependent enzymes such as the DNA repair PARP enzymes selectively in cancer cells.

## **1.6 Metabolism, NAD<sup>+</sup> and epigenetics**

NAD<sup>+</sup> biology is also intricately linked to control of gene expression via the NAD<sup>+</sup>-dependent sirtuin family of protein and histone deacetylases (section 1.4.2). The sirtuins provide a link between the metabolic and redox state of the cell and cellular epigenetics.

Epigenetics is the heritable modification of DNA and/or histones which does not affect the nucleotide sequence of DNA but can affect gene expression. Multiple epigenetic alterations are known which include DNA methylation, histone methylation, histone acetylation and histone deacetylation. The different enzymes that catalyse these post-translational modifications are dependent on metabolic substrates or co-factors, therefore linking epigenetics to cellular metabolism. Whilst NAD<sup>+</sup> levels can affect sirtuin activity and therefore histone deacetylation, histone acetylation is dependent on acetyl-CoA as a substrate and methylation of DNA and histones uses SAM as a substrate (section 1.6.1).

Ultimately, cancer is a disease of abnormal gene expression as outlined at the start of the introduction resulting from silencing of TSGs and inappropriate,

constitutive proto-oncogene activation. Whilst these changes commonly occur via gene mutation (genetic alterations), they can also occur via epigenetic effects.

Growing evidence shows that variations in the metabolic state of the cell can influence epigenetic changes within cells (Weyandt *et al.*, 2017; Wong *et al.*, 2017). Many TSGs have been shown to be epigenetically silenced in cancers therefore it is of interest whether these can be selectively re-activated through the targeting of cancer cell metabolic alterations.

### **1.6.1 The rate of one-carbon metabolism alters DNA and histone methylation**

DNA methylation at multiple CpG sites within the promoter of a gene inhibits its transcription resulting in loss of gene expression. The effects of methylation of histones at lysine and arginine residues depends on what residues are methylated, for example methylated K4 of histone H3 is associated with transcriptionally active chromatin, whereas methylation of K9 on histone H3 results in the heterochromatin or euchromatin (Kimura, 2013). It is known that some DNA methyltransferases (DNMT) are overexpressed in cancers (Robertson *et al.*, 1999) and the promoter region of particular TSGs are commonly methylated in certain cancers (e.g. CpG island methylator phenotype of colorectal cancers studied by Ahmed *et al.*, (2013)). Histone and DNA methylation occurs through histone methyltransferases (HMT) and DNMTs respectively, and both achieve methylation of substrates through similar mechanisms. SAM, generated by one-carbon metabolism, is used as the methyl provider for HMTs and DNMTs and results in release of S-adenosylhomocysteine which inhibits their activity. Cancer cells have been shown to have increased one-carbon metabolism and SAM activity (Luengo *et al.*, 2017), which can result in inappropriate methylation and silencing.

## 1.6.2 TCA cycle metabolites affect histone and DNA demethylation

Specific enzymes have been identified that actively demethylate DNA or histones that are methylated at particular amino acids. The activity of these enzymes is affected by levels of the TCA cycle intermediates  $\alpha$ -KG, succinate and fumarate (Fig. 1.5).

DNA demethylation consists of two steps, the oxidation of 5-methylcytosine (5mC) to 5-hydroxymethylcytosine (5hmC) followed by its conversion to cytosine. The Ten-eleven Translocation (TET) family of enzymes which are 5mC hydroxylases catalyse the first step but are dependent on  $\alpha$ -KG as a co-factor for activity (Ito *et al.*, 2010)

Certain lysine demethylases (KDMs) and the Jumonji family of histone demethylases also require  $\alpha$ -KG as a co-factor (Wong *et al.*, 2017). In contrast, succinate and fumarate inhibit the same DNA and histone demethylases by competitive inhibition with  $\alpha$ -KG. Relative levels of TCA cycle intermediates  $\alpha$ -KG, succinate and fumarate can therefore affect both DNA demethylation and the demethylation of specific histone residues. Inactivating mutations in TCA cycle enzymes succinate dehydrogenase (SDH) or fumarase (FH) have been observed in certain cancers resulting in a build-up of succinate or fumarate respectively. SDH and FH are classic TSGs with their mutation promoting tumorigenesis by several different potential mechanisms (Xiao *et al.*, 2012). This build up includes cancer-promoting epigenetic dysregulation due to the disruption of DNA/histone demethylation activities (Wong *et al.*, 2017). In addition, SDH/FH mutation is associated with induction of a pseudo-hypoxic state due to HIF-1 $\alpha$  stabilisation (Selak *et al.*, 2005; Isaacs *et al.*, 2005). HIF-1 $\alpha$  prolyl hydroxylases that promote the oxygen-dependent degradation of HIF-1 $\alpha$  are also  $\alpha$ -KG-dependent and subject to inhibition by succinate and fumarate (Xiao *et al.*, 2012).

In other cancers, in particular gliomas, oncogenic mutation of the isocitrate dehydrogenase isoforms (IDH1/2) occurs. These two isoforms of IDH oxidise isocitrate to  $\alpha$ -KG using NADP<sup>+</sup>. Mutations result in a halt of  $\alpha$ -KG formation from

isocitrate but also lead to a gain of function where  $\alpha$ -KG is converted to the oncometabolite D-2HG, which can competitively inhibit these  $\alpha$ -KG-dependent DNA and histone demethylases resulting in a hypermethylated epigenetic state and epigenetic inactivation of TSGs (Wong *et al.*, 2017).

### **1.6.2.1 Hypoxia induces L-2HG**

L-2HG, an enantiomer D-2HG, can be produced in cells that are wild type for IDH1/2 under hypoxic conditions. L-2HG can also inhibit  $\alpha$ -KG dependent enzymes like D-2HG and the increase in L-2HG under hypoxia can similarly result in increased DNA and histone methylation resulting in gene repression (Intlekofer *et al.*, 2015; Oldham *et al.*, 2015). LDH-A and MDH1/2 catalyse the reduction of  $\alpha$ -KG to L-2HG under hypoxia through promiscuous substrate usage in NADH-dependent reactions resulting in regeneration of  $\text{NAD}^+$ . Intlekofer *et al.* (2015) show that inhibition of MDH has small effects on L-2HG whereas LDH-A inhibition leads to a decrease of the majority of L-2HG produced.

### **1.6.3 Acetyl-CoA and histone acetylation**

Histone acetyltransferases (HATs) acetylate histones at lysine and arginine residues and this is associated with gene activation as it induces a more open chromatin state. Acetyl-CoA which fuels the TCA cycle and is involved in many metabolic pathways is a co-factor for the activity of HATs where CoA is the by-product. The activity of HATs can therefore be influenced by metabolic pathway utilisation and acetyl-CoA availability. For cells to obtain cytoplasmic acetyl-CoA, citrate is diverted from being further metabolised by the TCA cycle and removed from the mitochondria and is cleaved by ATP-citrate lyase (ACL) into acetyl-CoA and oxaloacetate (Wellen *et al.*, 2009). As most citrate is glucose derived, glucose availability and the high glycolytic flux of cancer cells can both potentially impact on acetyl-CoA availability and cellular histone acetylation (Wellen *et al.*, 2009). Knock-down of ACL has been shown to reduce global levels of histone acetylation and expression of genes which regulate glucose metabolism (Wellen *et al.*, 2009). Cancer cells have been shown to overexpress ACL leading to increased acetyl-CoA and histone acetylation (Hatzivassiliou *et al.*, 2005).

## 1.7 Rationale and aims of thesis

Whilst targeted chemotherapeutic agents have substantially improved treatment outcome for some cancers, development of resistance to targeted agents can be a major issue due to their being perhaps 'too targeted' allowing some cells to adapt. For many cancers, conventional DNA-damaging chemotherapeutic agents, despite their toxicity and poor selectivity, remain the mainstay of treatment.

There is an urgent need for new chemotherapeutic approaches that are both more selective towards cancer cells and also sufficiently potent and which act by a different mechanism of action to other agents, with the aim of being able to circumvent any acquired drug resistance.

This thesis investigates therapeutic opportunities that differences in the metabolism of cancer and non-cancer cells may present and related differential dependencies with a focus on NAD<sup>+</sup> metabolism and function. Whilst NAD<sup>+</sup> is a vital metabolite for both non-cancer and cancer cells, based on the available evidence, it was hypothesised that there is opportunity for therapeutic targeting of NAD<sup>+</sup> and key NAD<sup>+</sup>-related functions preferentially in cancer cells.

Specific aims and questions explored in this thesis are as follows: -

1. To determine whether short-term NAMPT inhibition is able to preferentially deplete NAD(H) from cancer cells and not from non-cancer cells and whether this is able to reduce NAD<sup>+</sup>-dependent PARP activity selectively in cancer cells (Chapter 3).
2. To assess whether the activity of current conventional chemotherapeutic agents that induce DNA damage that is repaired by PARPs, can be potentiated selectively in cancer cells by NAMPT inhibition/cancer-selective NAD<sup>+</sup> depletion. i.e. can the cancer cell selectivity (or therapeutic index) of any conventional chemotherapeutic agents in current clinical use be improved? (Chapter 3)

3. To assess whether cancer cell dependency on the full-length variant of the NAD<sup>+</sup>-dependent deacetylase SIRT1 can be recapitulated with a small molecule SIRT1 inhibitor (Chapter 4).
4. To examine what impact SIRT1 knock-down/inhibition has on non-cancer cells beyond it being dispensable for non-cancer cell survival – in particular how does SIRT1/SIRT1 splice variant targeting affect cancer and non-cancer cell fate/stemness/differentiation status? (Chapter 4)
5. To perform preliminary investigations as to whether knock-down/inhibition of the glycolytic enzyme LDH-A can induce cancer cell epigenetic alterations under normoxia and/or hypoxia – and whether this could result in re-expression of epigenetically silenced TSGs (Chapter 5). The rationale here for hypothesising that LDH-A suppression might affect cancer cell epigenetics is based on recent published findings that i) LDH-A inhibition is able to modestly reduce SIRT1 deacetylase activity towards the tumour suppressor p53, and, ii) LDH-A generates L-2HG metabolite under hypoxia which competitively inhibits  $\alpha$ -KG-dependent histone demethylases.
6. To investigate the metabolic effects of the synthetic small molecule KHS101 - and their likely contribution to KHS101-induced death of glioblastoma cancer stem-like cells but not of non-cancerous neural progenitors (Chapter 6). KHS101 was originally identified through a phenotypic chemical screen for compounds that regulate neuronal differentiation. This thesis aim was part of a multidisciplinary collaborative project with the University of Leeds and efforts to 'target deconvolute' KHS101 in the context of its GBM cytotoxicity.
7. To evaluate KHS101 for selective cytotoxic activity against other cancer cell types and its likely mechanism(s) of action in these models (Chapter 6).

## 2. Materials and methods

### 2.1 Cell culture

#### 2.1.1 General cell culture

All cell culture manipulations were performed in a NuAire class II biological safety cabinet using aseptic technique. Cell lines were cultured in antibiotic free complete media (Table 2.1) and kept at 37°C with 5% CO<sub>2</sub> in a humidified NuAire incubator. All cells were used at low passage (passage numbers between 2-14) from stocks that were authenticated and certified to be free of mycoplasma by the supplier (ATCC or ECACC) or other indicated sources (Table 2.1).

Cell Line	Media	Supplements	Source
A2780 - Human ovarian epithelial carcinoma	RPMI-1640 (Sigma-Aldrich #R0883)	10% foetal bovine serum (Gibco), 2mM L-glutamine (Sigma-Aldrich)	ECACC 93112519
A549 - Human lung epithelial carcinoma	RPMI-1640	10% foetal bovine serum, 2mM L-glutamine	ATCC CCL-185
ARPE-19 - Human retinal epithelial non-cancerous	DMEM/F-12 (Gibco #21331020)	10% foetal bovine serum, 2mM L-glutamine	ATCC CRL-2302
CCD 841 CoN - Human colon epithelial non-cancerous	EMEM (ATCC #30-2003)	10% foetal bovine serum, 2mM L-glutamine	ATCC CRL-1790
CP70/A2780cis - Human ovarian carcinoma (resistant to Cisplatin)	RPMI-1640	10% foetal bovine serum, 2mM L-glutamine, maintenance dose of 1µM cisplatin every 2-3 passages	Prof. Roger Phillips, University of Huddersfield
GBM1 - Glioblastoma multiforme - Primary GBM (cancer stem cell model)	Neurobasal media (Gibco #21103049)	40ng/ml hFGF (Invitrogen), 40ng/ml rhEGF (R&D) 0.5x B-27 Supplement (Invitrogen), 0.5x N-2 supplement (Invitrogen)	Dr. Heiko Wurdak, University of Leeds
GBM4 - Glioblastoma multiforme - Primary GBM (cancer stem cell model)			
GBM11 - Glioblastoma multiforme - Gliosarcoma (cancer stem cell model)			
GBM13 - Glioblastoma multiforme - Primary GBM (cancer stem cell model)			

GBM14 - Glioblastoma multiforme - Recurrent Giant Cell GBM (cancer stem cell model)			
GBM20 - Glioblastoma multiforme - Recurrent GBM (cancer stem cell model)			
H460 - Human large cell lung epithelial carcinoma	RPMI-1640	10% foetal bovine serum, 2mM L-glutamine	ATCC HTB-177
HCT116 p53 <sup>+/+</sup> - Human colorectal epithelial carcinoma	DMEM (Gibco #61965026)	10% foetal bovine serum, 2mM L-glutamine	Prof. Bert Vogelstein, John Hopkins University
HCT116 p53 <sup>-/-</sup> - Isogenic clone of HCT116 p53 <sup>+/+</sup> , p53 null	DMEM	10% foetal bovine serum, 2mM L-glutamine	Prof. Bert Vogelstein, John Hopkins University
HT-29 - Human colorectal epithelial adenocarcinoma	DMEM	10% foetal bovine serum, 2mM L-glutamine	ATCC HTB-38
MDA-MB-231 - Human breast epithelial adenocarcinoma	DMEM	10% foetal bovine serum, 2mM L-glutamine	ATCC HTB-26
MDA-MB-436 - Human breast adenocarcinoma	RPMI-1640	10% foetal bovine serum, 2mM L-glutamine	ATCC HTB-130
NP1 – Neural progenitor cells	DMEM/F-12	5% foetal bovine serum, 20ng/ml hFGF, 20ng/ml rhEGF, 0.5x B-27 Supplement, 0.5x N-2 supplement, 1x glutaMAX (Gibco).	Dr. Heiko Wurdak, University of Leeds
PC-3 - Human prostate epithelial adenocarcinoma	RPMI-1640	10% foetal bovine serum, 2mM L-glutamine	ATCC CRL-1435
PNT2 - Human prostate epithelium non-cancerous (immortalised with SV40)	RPMI-1640	10% foetal bovine serum, 2mM L-glutamine	ECACC 95012613

**Table 2.1: Cell line summary.**

Summary of cell lines used with source and appropriate media with supplements.

## 2.1.2 Sub-culturing of cell lines

Maintenance of cell lines were sustained by passaging using standard methodology upon reaching 70-80% confluency. Media was aspirated and the cells were washed with phosphate buffered saline (PBS) (Gibco). To detach the cells, they were incubated with 0.05% or 0.25% Trypsin-EDTA (Gibco), which was then inhibited with the appropriate serum containing media (Table 2.1) and

removed by centrifugation for 3 minutes at 200g. Cells were then resuspended in complete media and passaged according to need.

### **2.1.3 Sub-culturing of GBM and NP1 cells**

For GBM cancer stem cell-like models and NP1 cells, culture vessels were coated with 5µg/ml of Poly-L-Ornithine (Sigma-Aldrich) diluted in cell culture sterile H<sub>2</sub>O (Gibco) for at least 1 hour and 2.4µg/ml Laminin (Invitrogen) diluted in PBS before use. For passaging, media was aspirated from the flask and 1x TrypLE (Gibco) was used to detach the cells from the flask which was diluted in appropriate media or PBS after incubation. The cell suspension was then centrifuged for 5 minutes at 300g and a PBS wash was performed to ensure there was no TrypLE remaining. The cell pellet was then resuspended in fresh media and added to a pre-coated flask and placed in the incubator.

### **2.1.4 Cryopreservation of cells**

In order to preserve and maintain cell line stocks of low passage number, cells were cryopreserved in liquid nitrogen. Cells were resuspended in complete media containing 10% dimethyl sulfoxide (DMSO) (Sigma-Aldrich) and 20% foetal bovine serum (FBS) and a Nalgene® Mr Frosty™ freezing container was used to slowly cool the cells to -80°C before transferring to a dewar containing liquid nitrogen for long term storage.

### **2.1.5 Reviving cells from cryopreservation**

Cells were removed from liquid nitrogen and rapidly thawed in a water bath at 37°C. The stock was then diluted in complete media to reduce the DMSO concentration and centrifuged for 3 minutes at 200g before resuspending in complete media and transferring to a flask.

### **2.1.6 β-galactosidase senescence assay**

To assay cellular senescence, a β-galactosidase assay staining kit (Cell Signalling Technology #9860) was used. Cells in T25 flasks were washed with

PBS and then fixed for 15 minutes using the provided formaldehyde-based 1x fixative solution.  $\beta$ -galactosidase substrate 5-bromo-4-chloro-3-indolyl- $\beta$ -D-galactopyranoside (X-gal), which was buffered to pH 6.0 was added to the cells which were then incubated overnight at 37°C in a non-humidified CO<sub>2</sub> free incubator. Cell cleavage of X-gal generating a blue precipitate was then observed by phase contrast and bright field microscopy.

## 2.2 *In vitro* chemosensitivity analysis of drugs

### 2.2.1 MTT chemosensitivity assay

To assay cytotoxicity of compounds, *in vitro* chemosensitivity assays were performed. 96 well plates were seeded with cells as per Table 2.2 following cell counting using a haemocytometer and 24 hours later treated with a variety of compounds in a range of concentrations (Table 2.3). Within each plate there was a blank lane (media only, no cells), at least one vehicle control lane and 8 replicates of each drug concentration. Cell seeding densities were based on previous determinations to ensure control cells remained in logarithmic growth by the assay endpoint and that a linear relationship between MTT assay end point absorbance and cell number was maintained.

Cell Line	Cells per well (200µl)
A2780	1500
A549	1500
ARPE-19	1500
CCD 841 CoN	3000
CP70/A2780cis	1500
GBM1	3000
H460	1500
HCT116 p53 <sup>+/+</sup>	1500
HCT116 p53 <sup>-/-</sup>	1500
HT-29	1800
MDA-MB-231	1500
MDA-MB-436	3000
NP1	1500
PC-3	2000
PNT2	1500

**Table 2.2: Cell seeding density of a 96 well plate.**

Cell number per well of a 96 well plate for 96 hours drug treatment.

Drug	Dose Range	Supplier	Diluent
Carboplatin	100 $\mu$ M - 0.40 $\mu$ M (2-fold)	Sigma-Aldrich	PBS
Cisplatin	100 $\mu$ M - 0.40 $\mu$ M (2-fold)	Sigma-Aldrich	PBS
EX-527	200 $\mu$ M - 0.78 $\mu$ M (2-fold)	Sigma-Aldrich	DMSO (0.4%)
FK866	20 $\mu$ M - 0.01nM (5-fold)	Sigma-Aldrich	DMSO (0.2%)
KHS101	20, 15, 10, 7.5 5 $\mu$ M - 0.31 $\mu$ M (2-fold)	Sigma-Aldrich	DMSO (0.2%)
Oxaliplatin	50 $\mu$ M - 0.20 $\mu$ M (2-fold)	Tocris	PBS
Temozolomide	800 $\mu$ M - 6.25 $\mu$ M (2-fold)	Sigma-Aldrich	DMSO (0.8%)
Doxorubicin	600nM - 0.03nM (3-fold)	Sigma-Aldrich	PBS

**Table 2.3: Dose range of drugs used for chemosensitivity.**

Dose range and fold dilution of various drugs used in chemosensitivity assays.

96 hours post drug exposure, cell viability was determined using the MTT assay, as previously described (Mosmann, 1983; Phillips *et al.*, 1992). MTT (Fisher Scientific) was added directly to the media in the wells at a final concentration of 0.5mg/ml and 4 hours later any formazan crystals that had formed were dissolved in DMSO (Fisher Scientific). End point absorbance was measured at 540nm using the BMG Labtech FLUOstar® OPTIMA plate reader and used to calculate the IC<sub>50</sub> of the drugs (Allison *et al.*, 2018).

For all chemosensitivity assays, cell confluency and cellular phenotype at the different tested drug concentrations and for the vehicle control cells was assessed by microscopy to check for close agreement of effects on confluency and MTT chemosensitivity 'absorbance readout'. This prevented potential issues of artefacts due to non-toxic decreased metabolism of MTT rather than its intended use as a surrogate readout of cytotoxicity. The sulforhodamine B (SRB) assay was also used for a limited number of experiments using the methodology described by Vichai and Kirtikara (2006) to check that similar results were obtained by both assays.

For hypoxic MTT assays, cells were drug treated under normoxic conditions and then placed at 0.1% O<sub>2</sub> in a Don Whitley H35 hypoxystation for 96 hours as described by Ahmadi *et al.* (2014) before removal of plates to atmospheric oxygen for analysis by microscopy for phenotypic effects, addition of MTT and further incubation for 4h at 21% O<sub>2</sub>. Whilst the efficiency of MTT conversion to formazan crystals may be decreased under hypoxia, it has previously been validated for A549, H460, MDA-MB-231 and other cell lines that the MTT assay

shows a linear relationship between cell number and absorbance under 21% and 0.1% oxygen (Ahmadi *et al.*, 2014).

### **2.2.2 Rescue of FK866 toxicity studies**

In order to observe whether the cytotoxicity of FK866 was due to effects on NAD<sup>+</sup> levels directly, treatment of the compound was combined with the addition of NAD<sup>+</sup> precursors NA (Sigma-Aldrich) or NMN (Sigma-Aldrich). FK866 dose titration was combined with 10 $\mu$ M NA or 100 $\mu$ M NMN for 96 hours before MTT analysis as previously described (Section 2.2.1).

### **2.2.3 Combination studies**

To study the effects of combining the known DNA damaging agent TMZ with FK866, to potentially enhance TMZ cytotoxicity, GBM1 and NP1 cells were seeded at 4500 and 2000 cells/well respectively and incubated for 48 hours before treatment. The cells were then treated with the combination of drugs for 48 hours. FK866 was kept at a constant dose of 1nM and TMZ was diluted 2-fold from 800 $\mu$ M as per Table 2.3. An MTT assay was then completed as per section 2.2.1.

## 2.3 Analysis of cells using the NucleoCounter® NC-3000™ image cytometer

### 2.3.1 Quantification of cell number and viability

Cells were harvested through trypsinisation and resuspended in PBS for determination of cell number and viability as per the manufacturer's protocol (Chemometec; Via1-cassette™ 'viability and cell count assay'). Within the Via1-cassette, acridine orange stains the whole cell population enabling quantification of cell number and DAPI positive staining allows determination of non-viable populations.

### 2.3.2 Quantification of apoptotic cells

Cells were seeded as per Table 2.4 except for KHS101 treated cells where ARPE-19 cells were seeded at  $4 \times 10^5$ /T25. For combination treatments and KHS101, cells were treated 48 hours after seeding and for EX-527, cells were treated 24 hours after. For hypoxic conditions, cells were placed in a Don Whitley H35 hypoxystation at 0.1% O<sub>2</sub> 24 hours post seeding and drug treated 24 hours after exposure to the conditions.

Cell Line	Cell no. per T25
ARPE-19	$1.5 \times 10^5$
A2780	$2.5 \times 10^5$
A549	$2 \times 10^5$
CCD 841 CoN	$3.75 \times 10^5$
CP70/A2780cis	$2.5 \times 10^5$
GBM1	$2.75 \times 10^5$
HCT116 p53 <sup>+/+</sup>	$2.75 \times 10^5$
HCT116 p53 <sup>-/-</sup>	$2.75 \times 10^5$
NP1	$3 \times 10^5$
MDA-MB-231	$1.5 \times 10^5$

Table 2.4: Appropriate seeding density of cell lines for annexin V analysis.

All cells were incubated with the treatments for 48 hours before analysis. Cells were harvested by trypsinisation and cell number was determined for each

treatment as per section 2.3.1. The annexin-V-FLUOS staining kit (Roche #11988549001) was used for cell staining.  $4 \times 10^5$  cells were resuspended in 100  $\mu$ l HEPES incubation buffer containing annexin-V-fluorescein, propidium iodide (PI) and Hoechst 33342 all diluted 1:50, in accordance with the manufacturer's instructions. Cell suspensions were incubated for 15 minutes at 37°C before being mixed and analysed by the NC-3000™, image cytometer. The whole cell population was stained with Hoechst 33342, early apoptotic cells stained with annexin V only and late apoptotic/necrotic cells stained with annexin V and PI.

The HSPD1 inhibitor myrtucommulone was a kind gift from J.Jauch (Saarland University). Cells were treated with 10  $\mu$ M myrtucommulone or DMSO vehicle control for 48 hours before being harvested for annexin V analysis.

### **2.3.3 Quantification of autophagy positive cells by image cytometry**

ARPE-19 and HCT116 p53<sup>+/+</sup> cells were seeded at  $3 \times 10^5$  and  $4 \times 10^5$  cells/T25 respectively and incubated for 48 hours before treatment with 7.5  $\mu$ M KHS101 for 24 hours. To quantify autophagy positive cells the CYTO-ID® autophagy detection kit (Enzo Life Sciences #ENZ-51031-K200) was used. Cell number was determined as per section 2.3.1 and  $1 \times 10^6$  cells were stained with 500  $\mu$ l CYTO-ID® Green dye and Hoechst 33342 diluted 1:2000 in phenol red free media (Gibco) containing 5% FBS, for 30 minutes. Cell suspensions were then analysed using the NC-3000™ image cytometer, with CYTO-ID positive staining detected in fluorescence channel 1 (LED475 light source) with an emission filter wavelength of 560nm (bandwidth  $\pm 35$ nm). Hoechst 33342 staining of all cells was detected in the UV channel (LED365) with an emission filter wavelength of 470nm (bandwidth  $\pm 55$ nm).

### **2.3.4 Cell cycle analysis**

To obtain cell cycle profiles the two-step cell cycle assay (Chemometec) was performed as per the manufacturer's protocol. Single cell suspensions were obtained by trypsinisation and cells were then permeabilised and stained for 5

minutes with 10µg/ml of the fluorescent dye DAPI that binds to DNA stoichiometrically. Cellular DAPI staining was then quantified using a NC-3000™ image cytometer.

## 2.4 Metabolic flux analysis

To assess the effect of compounds on the bioenergetic state of the cells the Seahorse XFp analyser (Agilent) was used. For each cell line the optimal seeding density was determined so that cells were ~80% confluent and in log growth phase. The optimal FCCP concentration was determined (Table 2.5) based on the concentration that induced maximal mitochondrial respiration.

Cell Line	Cells per well (80µl)	Optimal FCCP concentration	Seahorse basal media supplements		
			Glucose	L-Glutamine/ GLUTAMAX	Sodium Pyruvate
ARPE19	2500	0.5µM	10mM	2mM	0.5mM
CCD-841-CoN	5000	0.25µM	5.5mM	2mM	1mM
GBM1	25000	0.5µM	25mM	-	0.5mM
HCT116 p53 <sup>+/+</sup>	7500	0.25µM	10mM	2mM	-
NP1	15000	0.5µM	10mM	1xGLUTAMAX	0.5mM
PNT2	2500	0.125µM	10mM	2mM	-

**Table 2.5: Appropriate conditions for XFp seahorse metabolic analysis**

Optimal seeding density and FCCP concentration for individual cell lines and the appropriate basal media supplements.

### 2.4.1 Cell energy phenotype

XFp cell culture miniplates (Agilent) were seeded with cells (Table 2.5) with the top and bottom wells being left blank with media only and incubated for 24 hours at 37°C in a humidified 5% CO<sub>2</sub> incubator. FK866, EX-527, KHS101 or DMSO vehicle control were added to the cells for 24 hours before analysis. On the day of analysis, the cells were washed twice with Seahorse XFp base media (pH 7.4) (Agilent #102353-100) containing the appropriate supplements (Table 2.5), with fresh media then added to a final volume of 180µl/well before an hour incubation in a humidified non-CO<sub>2</sub> incubator at 37°C. The appropriate concentration of 'stressor mix', containing oligomycin (1µM) and FCCP (Table 2.5), was prepared just before use and loaded into a sensor cartridge (Agilent) that had been previously hydrated with XF calibrant (Agilent) solution overnight. The cartridge was then loaded onto the XFp seahorse analyser to calibrate before addition of the cells. Three readings of oxygen consumption rate (OCR) and extracellular acidification rate (ECAR) were obtained under basal metabolic conditions before

the 'stressor mix' was injected and 5 readings of OCR and ECAR were obtained showing the metabolic stress response of the cells. Data obtained was then analysed using Seahorse Wave software.

## 2.4.2 Rescue studies

As per section 2.2.2 rescue studies were performed in order to see if NAD<sup>+</sup> precursors NA/NMN could rescue the effects of FK866 on cellular energetics. 10µM NA or 100µM NMN was added to the cells 12 hours post seeding and incubated for 12 hours before addition of FK866 for 24 hours. Cells were then analysed as per section 2.4.1.

## 2.4.3 Mitochondria stress test after direct drug injection

XFp cell culture mini plates were seeded with cells and prepared as per section 2.4.1, except that they were left to incubate for 48 hours before the addition of drug by direct injection into the media by the XFp analyser (Fig. 2.1). KHS101 concentrations were prepared alongside vehicle control and were loaded into the sensor cartridge along with 1µM oligomycin, appropriate FCCP concentration (Table 2.5) and 0.5µM Rotenone/Antimycin A.

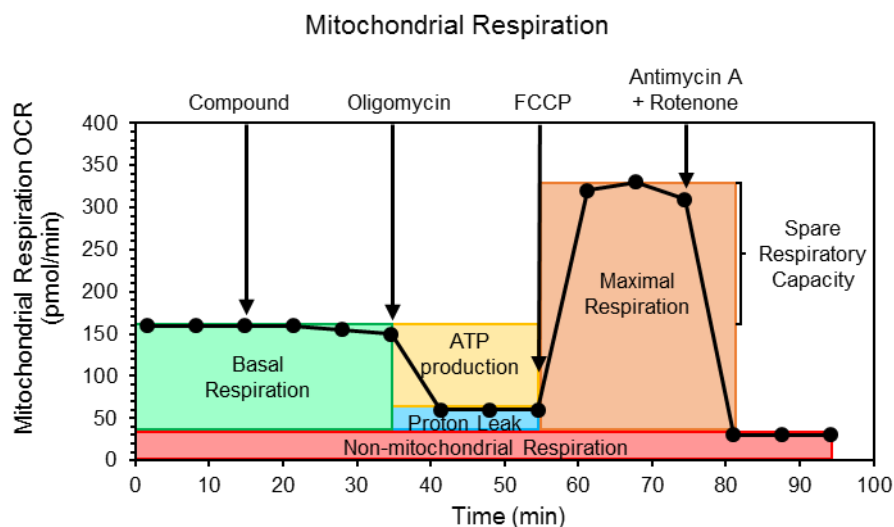


**Figure 2.1: Mitochondrial assay injections.**

Injection timings and parameters of mitochondrial function determined by the Agilent mitochondrial stress test.

#### **2.4.4 Glycolysis stress test after direct drug injection**

HCT116 p53<sup>+/+</sup> cells were seeded as per Table 2.5 and incubated for 48 hours in normal growth media before washing with XFp base media (pH 7.4) supplemented with 2mM glutamine but no glucose. After 1 hour at 37°C in a non-CO<sub>2</sub> humidified incubator the cells were analysed on an XFp Seahorse metabolic analyser by the XFp glycolysis stress test assay (Agilent) modified for test compound injection (1µM NHI-2 final concentration or DMSO vehicle control). Sequential injections of 10mM glucose, 1µM oligomycin and 50mM 2-DG were as described by the assay instructions, enabling determination of glycolytic rate and capacity.

## 2.5 Cellular ATP assay

ARPE-19 and HCT116 p53<sup>+/+</sup> cells were seeded at 7500 cells/well (200µl) in cell culture-treated, white flat bottomed 96 well plates and incubated for 24 hours. The cells were then treated with a range of KHS101 concentrations (0.625-10µM) before determination of total cellular ATP levels using the Glo® Luminescent Cell Viability Assay kit (Promega). Following the removal of 100µl media from wells, 100µl of freshly reconstituted CellTiter-Glo® Reagent was added and the plate was placed on a rocker for 2 minutes to enable cell lysis. The plate was then incubated in the dark at room temperature for 10 minutes before measurement of luminescent signal in each well using a BMG Labtech FLUOstar® OPTIMA plate reader. Automatic plate mode gain adjustment was performed prior to endpoint measurement of luminescent signal that is proportional to ATP content.

## 2.6 siRNA transfection

24 hours prior to transfection, single cell suspensions of low passage number cells in log phase growth were seeded in T25 flasks (Table 2.6), taking care to ensure even cell distribution across the flasks in order to maximise transfection efficiency. siRNAs were diluted in Opti-MEM media (Gibco #51985026) to the desired concentration (100nM final concentration in a T25 as previously described (Ford *et al.*, 2005)) and the Oligofectamine™ (Invitrogen) was diluted 1:5 with Opti-MEM media and incubated at room temperature for 30 minutes. The diluted oligofectamine was then mixed with the diluted siRNA and left at room temperature for 45 minutes for liposomal vesicles to form. To remove serum from the cells, the T25 flasks were washed with Opti-MEM twice before 2ml of Opti-MEM was added to each flask. 500µl of the siRNA/oligofectamine mix was then added to the flasks dropwise before the flasks were gently agitated in all directions for even cell coverage of the siRNA/liposomal mix. 4 hours later, 2.5ml of normal growth media containing twice the standard concentration of supplements and serum was added to flasks. All siRNAs (Table 2.7) used have been previously published and validated for selectivity and efficiency of cellular target knock-down in cell lines. Controls used included liposomes formulated with no siRNA and Silencer™ Select negative control no.1 siRNA (Invitrogen) which was a validated non-targeting control siRNA. 72 hours post transfection cells were harvested for RNA (Section 2.8) or protein (Section 2.11).

Cell Line	Cell no. per T25
ARPE-19	1.5x10 <sup>5</sup>
CCD 841 CoN	2x10 <sup>5</sup>
HCT116 p53 <sup>+/+</sup>	2.75x10 <sup>5</sup>
MDA-MB-231	3x10 <sup>5</sup>

**Table 2.6: Cell number seeding per T25 flask for siRNA transfection.**

Name	Sequence	Reference
LDH-A	5'-CCAGCCGUGAUAUGACCA(dTdT)-3'	Allison <i>et al.</i> , 2014
PARP-1	5'-AAGCCAUGGUGGAGUAUGA(dTdT)-3'	S, Allison. Custom siRNA
SIRT1-FL	5'-ACUUUGCUGUAACCCUGUA(dTdT)-3'	Ford <i>et al.</i> , 2005
SIRT1-Δ8	5'-UAAUCCAAGUAUCAGUA(dTdT)-3'	Lynch <i>et al.</i> , 2010

**Table 2.7: siRNAs used for transfection.**

## **2.7 Metabolic analysis of siRNA transfected cells**

For XFp Seahorse metabolic analysis of siRNA transfected ARPE-19 cells, cells were seeded in XFp cell culture miniplates (Agilent) at 1000 cells/well (80µl) in normal growth media and transfected in the miniplates following the methodology described in section 2.6. 24 hours post-seeding, 60µl of the culture media was removed and the cells were washed twice with 200µl Opti-MEM before addition of 60µl fresh Opti-MEM. 20µl of diluted oligofectamine/siRNA mix was then added dropwise per well with agitation resulting in a final well volume of 100µl. 4 hours post-transfection 50µl of normal growth medium containing three times the standard concentration of supplements and serum was added to wells. 72 hours later, transfected cells were analysed by the Agilent Cell Energy Phenotype as described in section 2.4.1.

## **2.8 Gene expression analysis**

### **2.8.1 RNA extraction from cell pellets**

T25 flasks of treated cells were harvested through trypsinisation, with cell pellets washed twice with PBS to remove any residual serum and culture media before lysis. RNA extraction from cell pellets was performed using the RNeasy mini kit (QIAGEN) with on-column DNase digestion. Cells were lysed in the appropriate volume of RLT buffer containing  $\beta$ -mercaptoethanol and lysates were applied to a QIA shredder column to homogenise the sample, which was then centrifuged at 12,000g for 2 minutes. The 'flow-through' was then mixed with 70% Ethanol at a 1:1 ratio and this was then applied to a RNeasy column and centrifuged at 8000g for 15 seconds. The RW1 buffer was then added to the column as per the protocol and the DNase digestion step was performed with 45 minutes incubation. The samples were then washed with RW1 buffer and RPE buffer twice before the RNA was eluted with RNase free distilled water.

### **2.8.2 Quantification of RNA and reverse transcription**

The concentration of RNA in eluted samples was quantified using the NanoDrop 2000 Spectrophotometer (Thermo Scientific) by measuring absorbance at 260nm and using the extinction coefficient for single stranded RNA. RNA purity was assessed by the 260/280 and 260/230nm absorbance ratios with RNA samples then diluted to 0.2 $\mu$ g/ $\mu$ l with RNase-free water.

Reverse transcription was performed using the High Capacity cDNA Reverse Transcription Kit (Applied Biosystems) to generate cDNA (as per the manufacturers protocol). Per reaction 10 $\mu$ l of RNA at 0.2 $\mu$ g/ $\mu$ l, 3.2 $\mu$ l Nuclease-free H<sub>2</sub>O, 2 $\mu$ l 10x RT buffer, 0.8  $\mu$ l 25x dNTP mix (100mM), 2 $\mu$ l 10x RT random primers, 1 $\mu$ l MultiScribe® Reverse Transcriptase and 1 $\mu$ l RNase inhibitor (Applied Biosystems, #N8080119) were used. One sample contained no MultiScribe® Reverse transcriptase in order to control for any genomic DNA contamination. Samples were loaded onto the DNA Engine Tetrad® 2 Peltier

thermal cycler and the cycling conditions were 10 minutes at 25°C, 120 minutes at 37°C, 5 minutes at 85°C and then a hold step at 4°C.

### 2.8.3 qPCR using TaqMan™ probes

Real-time qPCR was performed on a StepOnePlus™ Real-Time thermal cycler (Applied Biosystems) using Applied Biosystems™ TaqMan™ Universal PCR Master Mix (Applied Biosystems) or PrecisionFAST qPCR Master Mix (Primer Design) and inventorised TaqMan™ probes (Life Technologies) (Table 2.8).

Gene Name	Gene	Code
β-Actin	ACTB	Hs999999903_m1
E-cadherin	CDH1	Hs01023894_m1
c-Myc proto-oncogene	MYC	Hs00153408_m1
Glyceraldehyde 3-phosphate dehydrogenase	GAPDH	Hs999999905_m1
Glucuronidase beta	GUSB	Hs999999908_m1
Kruppel like factor 4	KLF4	Hs00358836_m1
Lamin A/C	LMNA	Hs00153462_m1
Microtubule associated protein 1A	MAP1a	Hs00357973_m1
Nanog homeobox	NANOG	Hs02387400_g1
Nestin	NES	Hs04187831_g1
POU class 5 homeobox 1 (OCT4)	POU5F1	Hs04260367_gH
SRY-box 2	SOX2	Hs01053049_s1

**Table 2.8: TaqMan™ probes for qPCR.**

For both master mixes 40ng of cDNA was used. For the Applied Biosystems master mix a total reaction volume of 25µl was prepared, 11.25µl of cDNA, 1.25µl probe and 12.5µl 2x master mix (2xMM). Thermal cycling conditions were, incubation at 50°C for 2 minutes, activation at 95°C for 10 minutes then 40 cycles of denaturing (95°C for 15 seconds) and annealing/extension (60°C degrees for 1 minute). For the Primer Design protocol, a total reaction volume of 20µl was used with 9µl of cDNA, 1µl of probe and 10µl of 2xMM. Thermal cycling conditions were, hot start activation of Taq polymerase by 95°C for 2 minutes, 40 cycles of denaturation at 95°C for 2 minutes and data collection at 60°C for 20 seconds. cDNA samples were analysed in quadruplicate (1 biological repeat) per qPCR with changes in gene expression of the target mRNA determined by the  $\Delta\Delta C_t$  method (Livak and Schmittgen, 2001).

## 2.8.4 SYBR™ Green qPCR

For SYBR™ Green qPCR, each reaction had 40ng of cDNA in a total volume of 30µl containing 10µl cDNA, 15µl 2x QuantiTect SYBR™ Green PCR master mix (Qiagen), 2.4µl RNase free distilled H<sub>2</sub>O, 1.3µl of 10µM forward primer and 1.3µl of 10µM reverse primer. Primers had been previously designed and verified for specific amplification of the cellular target cDNA (Allison *et al.*, 2014; Ford *et al.*, 2005; Lynch *et al.*, 2010) with primer sequences as described in Table 2.9.

Thermal cycling conditions (StepOnePlus™ Real-Time thermal cycler) were activation at 95°C for 15 minutes, then 40 cycles of 94°C for 15 seconds, an annealing temperature of 53°C for 30 seconds, 72°C for 30 seconds and 75°C for 15 seconds. For melting curve analysis of the PCR products generated, samples were heated from 60°C to 95°C in increments of 0.3°C in order to verify amplification of a specific product and lack of any primer-dimer formation.

Name	Fwd	Rvs
GAPDH	5'-CGGAGTCAACGGATTTGGTCGTAT-3'	5'-AGCCTTCTCCATGGTGGTGAAGAC-3'
MAP2	5'-ATGGCAGATGAACGGAAAGATG-3'	5'-ATCCTTGCAGACACCTCCTC-3'
SIRT1-FL	5'-CTAATTCCAAGTTCCATACCC-3'	5'-CTGAAGAATCTGGTGGTGAAG-3'
SIRT1-Δ8	5'-ACTGTGAAGCTGTACGAGGAG-3'	5'-AACAGATACTGATTACTTGGA-3'
LDH-A	5'-TTGGTCCAGCGTAACGTGAAC-3'	5'-CCAGGATGTGTAGCCTTTGAG-3'

**Table 2.9: Primer sequences for SYBR™ Green qPCR.**

## 2.9 NAD(H) assay

### 2.9.1 Determination of total cellular NAD(H)

Cells were seeded as per Table 2.10 and incubated for 48 hours before being treated with 5 $\mu$ M KHS101 or a range of FK866 doses (0.625-10nM). 24 hours post drug exposure, cells were lysed in NAD(H) extraction buffer (20mM NaHCO<sub>3</sub>, 100mM Na<sub>2</sub>CO<sub>3</sub>, 10mM nicotinamide, 0.05% Triton-X-100) and sonicated on ice using a Sonics Vibra VCX130 probe sonicator at 25% amplitude for 10 seconds on and 1 minute off until the viscosity of the samples was reduced.

Cell Line	Cell no. per T25
ARPE-19	3 x 10 <sup>5</sup>
A2780	3 x 10 <sup>5</sup>
A549	3 x 10 <sup>5</sup>
CCD 841 CoN	3.75 x 10 <sup>5</sup>
CP70/A2780cis	3 x 10 <sup>5</sup>
GBM1	5 x 10 <sup>5</sup>
H460	3 x 10 <sup>5</sup>
HCT116 p53 <sup>-/-</sup>	4 x 10 <sup>5</sup>
HCT116 p53 <sup>+/+</sup>	4 x 10 <sup>5</sup>
MDA-MB-231	3 x 10 <sup>5</sup>
MDA-MB-436	5 x 10 <sup>5</sup>
NP1	3.33 x 10 <sup>5</sup>

**Table 2.10: Appropriate seeding density of cells for cellular NAD(H) determination.**

A NAD(H)-dependent enzymatic cycling reaction assay was performed in order to quantify NAD(H) levels in the cell lysates (Umemura and Kimura, 2005). Each reaction was set up in a well of a 96 well plate and consisted of 168 $\mu$ l of cycling buffer (100mM TrisHCl pH8.0, 5mM EDTA, 0.5mM MTT) containing 0.4mg/ml alcohol dehydrogenase, 2 $\mu$ l of 200mM phenazine ethosulphate and 10 $\mu$ l of lysate with 20 $\mu$ l of 6M ethanol added in order to start the reaction (Umemura and Kimura, 2005). Reaction kinetics were determined by measurement of absorbance at 584nm every 10 seconds for 1 minute using a BMG Labtech FLUOstar® OPTIMA plate reader.

Protein concentration of each sample was obtained as per section 2.11.1. The linear change in absorbance was calculated and based on NAD(H) standard curves the NAD(H) concentration of cell lysates was calculated and normalised to the protein content (Umemura and Kimura, 2005).

## **2.9.2 Nuclear and cytoplasmic quantification of NAD(H)**

$4 \times 10^5$  HCT116 p53<sup>+/+</sup> cells were seeded per T25 (5 per treatment) and incubated for 48 hours before being treated with 5nM FK866 or DMSO vehicle control for 24 hours. Nuclear and cytoplasmic fractions were then prepared using a Pierce NE-PER™ Nuclear and Cytoplasmic Extraction Kit as per the manufacturer's protocol but with minor alterations. Nuclei were lysed directly in NAD(H) extraction buffer and to the cytoplasmic fraction (in CERII) 1/6th volume of NAD(H) buffer was added. Quantification of NAD(H) was performed as described in section 2.9.1.

## 2.10 Mitochondrial GPD2 activity assay

Mitochondrial GPD2 activity was determined as described (Orr *et al.*, 2014) with minor modifications to the method. GBM1, NP1 and HCT116 p53<sup>+/+</sup> cells in logarithmic phase growth (~80% confluent) were treated with 7.5µM KHS101 or DMSO vehicle control for 1 hour before harvesting by standard trypsinisation. Intact mitochondria were isolated from equivalent numbers of cells (2x10<sup>7</sup> cells/treatment) using a mitochondria isolation kit for cultured cells (Thermo Fisher #89874) as per the manufacturers protocol but with minor alterations.

KHS101 or DMSO vehicle control was added to kit reagents A and C throughout the mitochondrial isolation procedure. Mitochondrial pellets were resuspended in 50µl GPD2 assay buffer (50mM KCl, 10mM TrisHCl and 1mM EDTA, pH 7.4) which contained fatty acid free bovine serum albumin (BSA) (1mg/ml). For determination of GPD2 activity each reaction was set up in a 96 well plate with 135µl GPD2 assay buffer with fatty acid free BSA (1mg/ml), 50µl isolated mitochondria and 2µl of 2mM DCPIP with addition of 10µl 300mM glycerol-3-phosphate to start the reaction. The change in absorbance was measured at 600nm using a BMG Labtech FLUOstar® OPTIMA plate reader over a period of 10 minutes.

## **2.11 Quantification of protein expression**

### **2.11.1 Preparation of cell lysates**

Total cell lysates were obtained through addition of RIPA buffer (Sigma-Aldrich) containing protease inhibitor (Sigma-Aldrich #P8340, 25µl per ml RIPA) and phosphatase inhibitor (Sigma-Aldrich #P5726, 10µl per ml RIPA) to cell pellets. Cell lysates were sonicated (30 seconds sonicating, 2 minutes on ice) using a water bath sonicator (Langford Ultrasonics) in order to shear DNA before protein concentration was determined. A bicinchoninic acid (BCA) protein assay (Pierce) was used to determine the protein concentration of samples by using a colorimetric assay where known BSA standards were used to determine sample protein concentration. Samples and 10µl of standards were pipetted into a 96 well plate in quadruplicate and incubated for half hour at room temperature with a 50:1 mixture of buffer A+B as per the manufacturer's protocol. End point absorbance was then measured at 584nm using a BMG Labtech FLUOstar® OPTIMA plate reader. Protein concentrations were calculated using a linear regression standard curve and 4x Laemmli solution containing β-mercaptoethanol was then added to the cell lysates which were then heated at 100°C for 5 minutes.

### **2.11.2 Preparation and running of SDS-PAGE gels**

SDS-PAGE gels were prepared (see appendix Table 9.1) with a 4% stacking and a 15% resolving gel. 40µg of protein was loaded per gel lane and the proteins were then resolved by electrophoresis, in Tris Glycine running buffer (Bio-Rad 10xTGS #161-0772) at 70V for 1 hour. Once samples had entered the resolving gel the voltage was increased to 120V until the dye front reached the bottom of the gel. The protein was then transferred to nitrocellulose membrane in 1x Tris Glycine transfer buffer, containing 20% methanol and 0.1% SDS overnight at 35mAmp.

## 2.11.3 Immunoblotting

Nitrocellulose membranes were left to air-dry for 1 hour at room temperature and then depending on antibody specification (Table 2.11) either washed in PBS-0.1% Tween 20 (PBT-T) or TBS-T for 5 minutes prior to being blocked for 1 hour in either 5% milk PBS-T or 5% milk TBS-T. As standard, all antibodies were diluted in 5% milk PBS-T unless specified on the data sheet where they were diluted in 5% BSA TBS-T. For the antibodies that required BSA as a diluent the nitrocellulose membranes were washed in TBS-T 3 times for 2 minutes after blocking. After addition of antibody the membranes were incubated while being agitated overnight at 4°C.

Primary Antibody	Species	Supplier	Product no	Dilution		Diluent
				ECL	Li-CoR	
Acetylated H3K9	Rabbit	Merck	06-942	1:1000	1:1000	5% milk PBS-T
Actin	Mouse	Merck	mab1501	1:80,000	1:40,000	5% milk PBS-T
AMPK	Rabbit	Cell signalling	2532S	1:1000		5% BSA TBS-T
CHOP	Mouse	Cell signalling	2895S	1:1000		5% BSA TBS-T
E-cadherin	Rabbit	Cell signalling	3195S	1:1000		5% BSA TBS-T
GAPDH	Mouse	ProteinTech	60004-1-ig		1:50,000	5% milk PBS-T
GPDH2	Rabbit	Abcam	ab188585		1:7000	5% milk PBS-T
H3	Rabbit	Abcam	ab1791		1:3500	5% milk PBS-T
H3K9me3	Rabbit	Active Motif	39765	1:2000	1:2000	5% milk PBS-T
HSPD1	Rabbit	Abcam	ab46798	1:20,000	1:20,000	5% milk PBS-T
LC3	Rabbit	Cell signalling	2775S		1:1000	5% BSA TBS-T
LDH	Rabbit	Abcam	ab134187	1:5000	1:5000	5% milk PBS-T
MDH2	Rabbit	Abcam	ab96193		1:1000	5% milk PBS-T
NAMPT	Rabbit	Bethyl	A300-372A	1:5000	1:1000	5% milk PBS-T
NAPRT	Rabbit	Atlas	HPA023739	1:1000	1:500	5% milk PBS-T
p53	Mouse	Santa Cruz	SC-126	1:1000		5% milk PBS-T
PAR	Mouse	Abcam	ab14459	1:500	1:500	5% milk PBS-T
PARP	Mouse	BD Pharmingen	556494	1:1000	1:1000	5% milk PBS-T
Phosphorylated AMPK	Rabbit	Cell signaling	2535S	1:1000		5% BSA TBS-T
SIRT1	Rabbit	Santa Cruz	sc-15404	1:1000	1:1000	5% milk PBS-T

**Table 2.11: Antibody dilutions and conditions for immunoblotting.**

After primary antibody incubation the nitrocellulose membranes were washed three times for 5 minutes in either PBS-T or TBS-T before addition of the appropriate secondary antibody (Table 2.12).

Secondary Antibody	Supplier	Product no	Dilution ECL	Dilution Li-CoR	Diluent
Anti-Rabbit (DyLight 800)	Rockland	039611-145-122		1:10,000	5% milk PBS-T/TBS-T
Anti-Mouse (Alexa Fluor 680)	Invitrogen	A21057		1:10,000	5% milk PBS-T/TBS-T
Anti-Rabbit – HRP	Dako	P0448	1:5000		5% milk PBS-T/TBS-T
Anti-Mouse – HRP	Dako	P0260	1:5000		5% milk PBS-T/TBS-T

**Table 2.12: Secondary antibody conditions for Immunoblotting.**

### 2.11.4 Immunoblotting using the LI-COR system

For analysis of proteins through the Li-COR Odyssey® Near-Infrared Imaging System, fluorescently tagged secondary antibodies (Table 2.12) were used that were diluted in either 5% milk PBS-T or 5% milk TBS-T. The membranes were incubated in the dark for 1 hour at room temperature before being washed three times for 5 minutes with PBS-T or TBS-T.

### 2.11.5 Immunoblotting using enhanced chemiluminescence

For enhanced chemiluminescence (ECL) detection of proteins, horse radish peroxidase (HRP) conjugated secondary antibodies (Table 2.12) were used and diluted in 5% milk PBS-T or 5% milk TBS-T and incubated with membranes for 1 hour before three 5 minute PBS-T/TBS-T washes. In the dark, BM chemiluminescence western blotting substrate (POD) (Roche) was prepared at 1:100 ratio of reagent A and B and the membranes were incubated with this for 1 minute. The membranes were exposed to autoradiography film (GE Healthcare) before being immersed in multigrade developer (Ilford) for 2 minutes, briefly washed in water and then transferred to rapid fixer (Ilford) solution for 2 minutes in a dark room. Densitometric analysis of protein bands was performed using Image Studio Lite.

## 2.12 Quantification of cellular PARP activity

Cells were seeded as per Table 2.13 and incubated for 48 hours before treating with a PARP inhibitor, FK866 or NMN for 24 hours or 48 hours. Cells were lysed in PARP assay extraction buffer (50µl 20xPAR assay buffer, 80µl 5M NaCl, 45µl 20% Triton-x-100, 825µl cell culture grade H<sub>2</sub>O and 10µl HALT protease inhibitor per 1ml) following normalisation to cell number. Cell lysates were centrifuged for 10 minutes at 4°C at 10,000g and the supernatant was used for analysis. A PARP activity ELISA assay was performed using the Trevigen PARP/Apoptosis colorimetric assay kit (#4684-096-K) as per the manufacturer's protocol. Histone coated wells were rehydrated with 1x PAR assay buffer for 30 minutes and a MM without NAD<sup>+</sup> was prepared so that PARP activity was reliant on endogenous NAD<sup>+</sup> alone. Per reaction 21.25µl H<sub>2</sub>O, 1.25µl of 20x PAR assay buffer, 2.5µl 10x activated DNA and 25µl of lysate was pipetted into a histone coated well and incubated at room temperature for 30 minutes to allow for any PARP-catalysed PARylation of histones. Wells were then washed twice with PBS-0.1% Triton-x-100 and twice with PBS before addition of monoclonal PAR primary antibody (1:1000) for 30 minutes. Wells were then washed again as described above and secondary antibody (1:1000) was added for 30 minutes. After incubation, antibody was removed and TACCS sapphire was added to the wells for conversion by the HRP-conjugated secondary antibody, in the dark for 15 minutes. The reaction was then stopped using an equal volume of 0.2M HCl and absorbance at 455nm absorbance was measured using a BMG Labtech FLUOstar® OPTIMA plate reader.

Cell Line	Cell no. per T25
ARPE-19	3 x 10 <sup>5</sup>
GBM1	5 x 10 <sup>5</sup>
HCT116 p53 <sup>+/+</sup>	4 x 10 <sup>5</sup>
NP1	3.33 x 10 <sup>5</sup>

Table 2.13: Seeding densities for PARP ELISA assay.

## 2.13 Quantification of SIRT1 activity

HCT116 p53<sup>+/+</sup> cells were seeded at  $1 \times 10^6$  cells per T75 and incubated for 48 hours before addition of 10nM FK866 or DMSO vehicle control for 24 hours. Cells were harvested and lysed as per the PARP assay extraction method in PARP assay extraction buffer (minus HALT protease inhibitor) (section 2.12). In order to assay cellular SIRT1 activity a fluorometric SIRT1 activity assay (abcam #156065) was used. For each reaction 30 $\mu$ l of lysate or buffer control, 5 $\mu$ l SIRT1 assay buffer, 5 $\mu$ l Fluor-substrate peptide that is specifically deacetylated by SIRT1 leading to a release of a fluorescent signal, 5 $\mu$ l H<sub>2</sub>O and 5 $\mu$ l developer were loaded into a black 96 well plate. A kinetic reading of fluorescence was recorded for 10 minutes to ensure the reaction was linear over its duration with end point fluorescent signal at 10 minutes then used to compare SIRT1 activity between samples.

## 2.14 Immunofluorescent and autophagy staining and imaging

### 2.14.1 Analysis of double strand break DNA damage marker, phosphorylated $\gamma$ H2AX

ARPE-19 and HCT116 p53<sup>+/+</sup> cells were seeded into 8 well chamber slides at  $3.2 \times 10^4$  cells/500 $\mu$ l and  $4.4 \times 10^4$  cells/500  $\mu$ l, respectively. 12 hours after seeding, cells were pre-treated with either 5nM FK866, 500nM rucaparib or DMSO vehicle control for 12 hours before addition of 800 $\mu$ M TMZ in combination with FK866/rucaparib for 4 hours. This was then removed and FK866/rucaparib alone or DMSO vehicle control containing media was replaced on to the cells for 6 hours to allow for DNA damage repair to occur (Fig. 2.2).

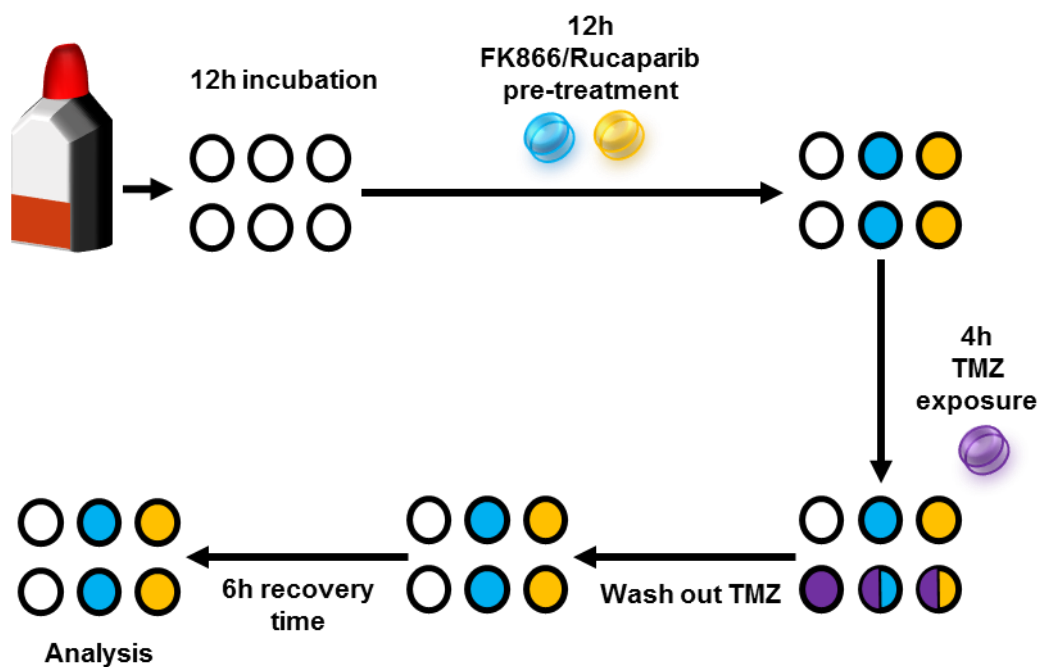


Figure 2.2: Drug treatment set up for DNA damage marker analysis.

To fix the cells, media was removed and ice cold methanol was added and incubated for 20 minutes at  $-20^{\circ}\text{C}$ . The cells were then washed three times with PBS for 5 minutes. Staining was then either performed immediately or the fixed

cells were kept at 4°C with PBS. Cells were permeabilised using 0.1% triton-x-100 in PBS for 10 minutes at room temperature followed by two quick PBS washes and one 5 minute incubation of PBS. 5% BSA in PBS was used to block non-specific antibody binding for 1 hour at 4°C before addition of phosphorylated  $\gamma$ H2AX primary antibody (Millipore #05-636), diluted 1:250 in 3% BSA in PBS overnight at 4°C. After primary antibody incubation, cells were washed three times for 5 minutes with PBS before addition of Alexa Fluor 488 anti-mouse secondary antibody (1:250 dilution; Cell Signalling Technology #4408s) for 1 hour at room temperature. Secondary antibody was removed and three 5 minute PBS washes were performed before 1  $\mu$ g/ml of DAPI was added to the cells for 1 minute before being mounted onto a glass slide using mounting media (Dako). A Zeiss confocal laser scanning microscope LSM880 (Zeiss) was then used to image the fluorescently stained cells.

### **2.14.2 MAP2 cellular staining**

ARPE-19 cells were seeded into 8 well chamber slides at  $8.4 \times 10^3$  cells/500  $\mu$ l. 24 hours after seeding, cells were treated with EX-527 for 48 hours before staining. For KHS101, 48 hours after seeding cells were treated for 24 hours. Cells were fixed with 4% paraformaldehyde in PBS for 10 minutes at room temperature. The cells were permeabilised and blocked before addition of primary antibody MAP2 (abcam #ab5392) diluted 1:2000 in 3% BSA in PBS as per section 2.14.1. Cells were then washed and Alexa Fluor 488 anti-chicken secondary antibody (Invitrogen #A-11039) was used diluted 1:500 in 3% BSA PBS for 1 hour before being stained with DAPI and mounted onto glass slides and imaged as previous (section 2.14.1).

### **2.14.3 Live CYTO-ID® imaging of autophagic cells**

ARPE-19, HCT116 p53<sup>+/+</sup> and HCT116 p53<sup>-/-</sup> cells were seeded into 8 well lumox® chamber slides (Sarstedt) at  $9.6 \times 10^3$  cells/500  $\mu$ l and  $1.28 \times 10^4$  cells/500  $\mu$ l respectively. 48 hours later the cells were treated with KHS101 for 24 hours before being stained with CYTO-ID® green dye (Enzo LifeSciences) diluted 1:500 and Hoechst 33342 diluted 1:1000 in phenol red free media containing 5%

FBS and 2mM L-glutamine for 30 minutes at 37°C using the CYTO-ID® Autophagy detection kit (Enzo LifeSciences) Media was then replaced with fresh phenol red free media before imaging was performed using a Zeiss confocal laser scanning microscope LSM880.

#### **2.14.4 Detection of 5hmC, a marker of demethylation of DNA**

HCT116 p53<sup>+/+</sup> cells were seeded into 8 well chamber slides at a density of  $2.24 \times 10^4$  cells/500µl. Cells were incubated for 48 hours before drug was added. For hypoxic conditions, cells were incubated for 24 hours under normoxic conditions and then 24 hours under hypoxic conditions (0.1% O<sub>2</sub>) in a Don Whitley H35 hypoxystation before drug addition. A dose range of NHI-2 for 48 hours or 10µM '5-aza-'2-deoxycytidine for 24 hours as a positive control were used to treat the cells. Cells were fixed using methanol as per section 2.14.1. To ensure that the DNA was not highly condensed and 5hmC on DNA would be accessible to the primary antibody, the cells were treated with 2N HCl for 15 minutes (Zhong *et al.*, 2017) and then neutralised with 100mM Tris-HCl (pH 8.5) for 10 minutes before blocking as per section 2.14.1. 5hmC primary antibody (Active Motif #39769) was diluted 1:1000 in 3% BSA in PBS and Alexa Fluor 488 anti-rabbit secondary antibody (Cell Signalling Technology #4412s) was diluted 1:250 in 3 % BSA in PBS. Cells were stained with DAPI and mounted onto glass slides and imaged as described in section 2.14.1.

## **2.15 Statistical analysis**

For statistical analysis of significance data was assessed for normal distribution using the Shapiro Wilk test. Following the confirmation of normal distribution an unpaired two tailed t-test or a one-way ANOVA was used to determine variance in samples. A p value of  $<0.05$  was considered statistically significant. All statistical analysis was performed using GraphPad Prism.

# **3. Investigation of NAMPT suppression as a potential strategy to decrease PARP activity selectively in cancer cells**

## **3.1 Introduction**

As previously mentioned (section 1.1.5.1), classic chemotherapeutic drugs which are currently used in the clinic show poor selectivity towards cancer cells alone and result in dose limiting toxicities leading to unpleasant side effects in patients. Current research focuses on improving the treatment of cancer, including producing treatments that have less side effects and by combating treatment resistance.

Classic chemotherapeutic drugs work by causing DNA damage which if extensive, or unrepaired, can lead to induction of cancer cell senescence or cell death, through the cellular DNA damage response. DNA damage can be repaired by different cellular DNA repair enzymes, such as the PARP family of repair enzymes (Amé *et al.*, 2004), promoting cancer cell survival (Fig. 3.1) and upregulation of repair enzymes is one mechanism of chemotherapeutic drug resistance. Recent studies have focused on combining certain DNA damaging agents with PARP inhibitors to suppress DNA repair and potentiate the effects of the DNA damaging agents (section 1.4.1.2). Although this work is promising and extends utilisation of PARP inhibitors beyond synthetic lethality approaches, there have been issues regarding on-target side effects of PARP inhibitors in combination with DNA damaging agents in non-cancer cells, as these also utilise PARP activity to repair damaged DNA (Drew and Plummer, 2009; Chalmers, 2009). There are several clinical trials taking place where PARP inhibitors are being combined with clinically used DNA damaging agents, but it is thought that the therapeutic window is likely to be narrow because of potential parallel sensitisation of normal healthy cells.

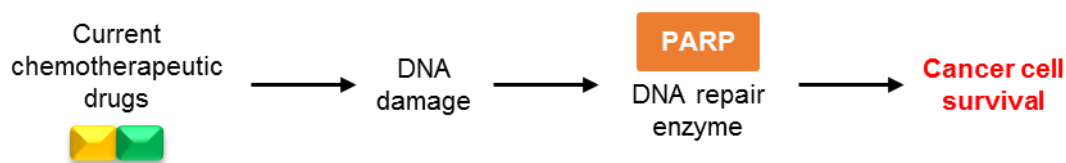


**Figure 3.1: Schematic briefly outlining PARPs involvement in cancer cell survival.** Current chemotherapeutic agents induce DNA damage which can be repaired by DNA repair enzymes, for example PARP, leading to cancer cell survival.

PARP1 and PARP2 are mainly associated with SSB DNA repair and rely on NAD<sup>+</sup> for their activity in repairing the damage (Chambon *et al.*, 1963). Studies indicate that PARP activity is sensitive to physiological changes in cellular NAD<sup>+</sup> levels (Ryu *et al.*, 2018). As such, modulation of NAD<sup>+</sup> levels may provide a potential strategy to indirectly inhibit PARP activity. The principle aim of this chapter was to test the hypothesis that it may be possible to modulate PARP activity in a cancer selective manner through preferential depletion of NAD<sup>+</sup> levels in cancer cells.

As many cancer cells have been shown to have increased glycolytic flux they require increased levels of NAD<sup>+</sup> to fuel this (Hammoudi *et al.*, 2011). Previous research by Allison *et al.* (2014) has shown that NADH/NAD<sup>+</sup> balance can be altered in a cancer selective manner by targeting LDH-A, although this was dependent on p53. The ability to alter NAD(H) levels in a cancer-selective manner offers opportunity, as outlined above, to potentially alter the activity of enzymes that are dependent on NAD<sup>+</sup>, such as the DNA repair PARP enzymes and the sirtuins, selectively in cancer cells. One limitation of LDH-A inhibition, however, is p53 dependency of the observed effects. As NAD<sup>+</sup> is produced through a biosynthetic pathway it is also possible that LDH-A inhibition may not adequately reduce NAD<sup>+</sup> to substantially impact on PARP activity. Due to this, this thesis work focuses on an alternative potential strategy, namely, whether through inhibiting NAMPT, the rate limiting enzyme in the NAD<sup>+</sup> biosynthetic pathway, this can alter NAD(H) levels in cancer cells selectively. As many cancer cells are observed to have increased NAMPT expression (Yaku *et al.*, 2018), potentially due to their increased need for NAD<sup>+</sup>, it was hypothesised that its inhibition may lead to a cancer selective decrease in NAD(H) levels.

To test this, FK866, a small molecule inhibitor of NAMPT, was utilised (Hasmann and Schemainda, 2003). It was hypothesised that should NAMPT inhibition cause a cancer selective decrease in PARP activity this could then lead to decreased repair of damaged DNA , therefore leading to potentiation of DNA damaging agents in a cancer cell selective manner (Fig. 3.2).

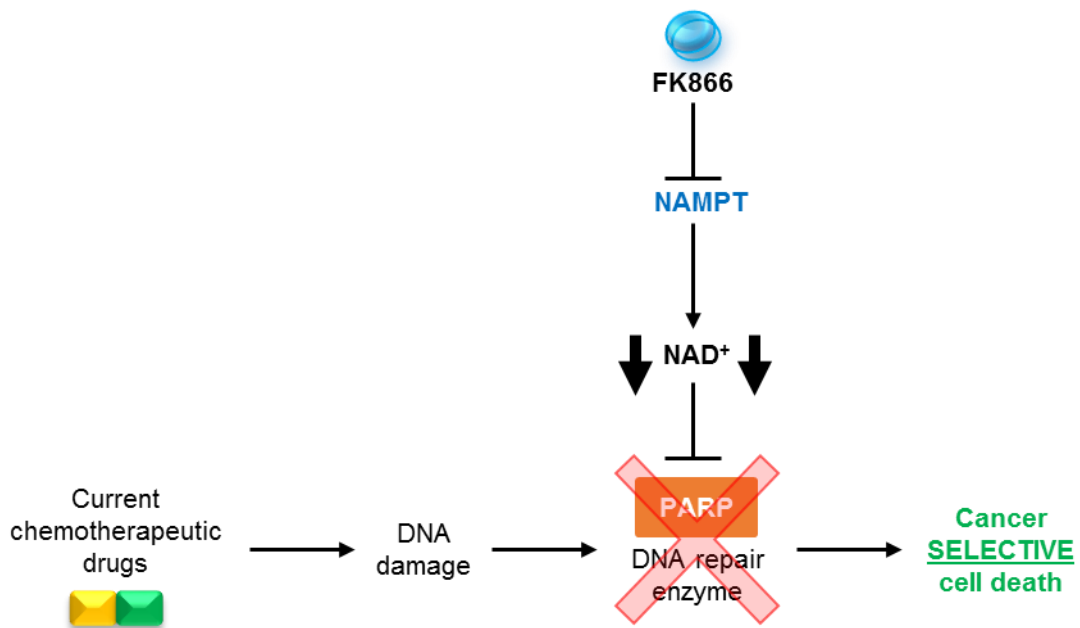


**Figure 3.2: Schematic of potential cancer selective inhibition of PARP.**

Hypothesised approach of potential cancer selective inhibition of PARP leading to potentiation of current chemotherapeutic drugs, to cause cancer selective cell death.

## 3.2 Results

### 3.2.1 Validation of non-cancer cell models

ARPE-19 are human retinal epithelial non-cancer cells and have extensively been used in the literature as a non-cancer cell model, including use in the discovery of cancer selective biological and pharmaceutical agents/targets and for further mechanistic studies as to why this may be (Ford *et al.*, 2005; Allison *et al.*, 2014; Knight *et al.*, 2013; Allison and Milner, 2007). They have also been used in numerous phenotypic drug screens for evaluating cancer cell selectivity of novel compounds showing *in vitro* anti-cancer activity (Allison *et al.*, 2017; Basri *et al.*, 2017; Kaner *et al.*, 2016; Lord *et al.*, 2015). PNT2 are human prostate non-cancer cells that have been immortalised with SV40, which have also been used in the literature as a non-cancer cell model (Scorey *et al.*, 2006). CCD 841 CoN are human colon epithelial non-cancer cells that have also been reported in the literature for studying non-cancer versus cancer effects (Zhu and DePamphilis, 2009). Nevertheless, it was important to independently validate the cell lines to confirm that they were appropriate to be used as non-cancer cell models.

Cellular rates of mitochondrial respiration and glycolysis were determined under normal cell growth conditions in ARPE-19, PNT2 and CCD 841 CoN compared to rates in two cancer cell lines (Fig. 3.3; non-cancer cells ▲; cancer cells ●). Consistent with non-cancer cells generally being less metabolically active than cancer cells (Hammoudi *et al.*, 2011), all three non-cancer cell lines exhibited lower levels of mitochondrial respiration (1.9-fold - 7-fold lower) and glycolysis (1.3-fold - 2.4-fold lower) than in HCT116 p53<sup>+/+</sup> colorectal cancer and GBM1 glioblastoma cell lines.

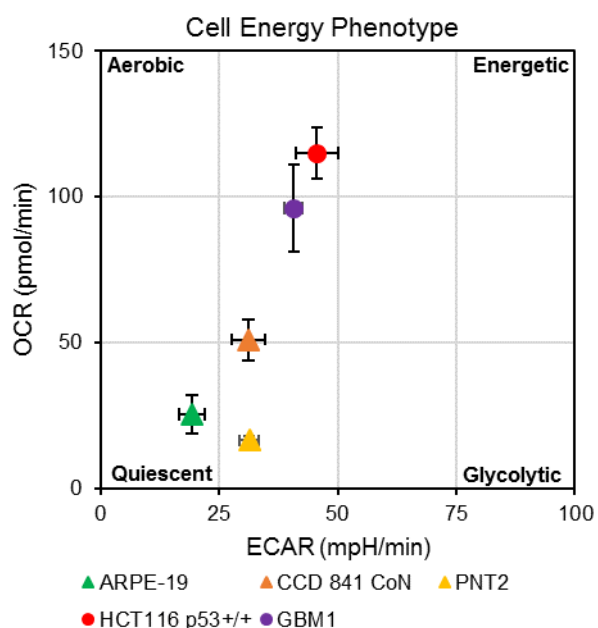


**Figure 3.3: Basal cellular energetics of non-cancer cell models compared to cancer cell lines.**

Cell energy phenotype analysis of ARPE-19, CCD 841 CoN and PNT2 non-cancer cells under basal growth conditions in comparison to HCT116 p53<sup>+/+</sup> cancer cells and GBM1 cancer ‘stem-like’ cells. Error bars show SD from 3 technical repeats, n=1 independent biological repeat.

As the CCD 841 CoN cells were the most metabolically active of the three non-cancer cell line models but have been less widely reported in the literature, they were also analysed for their ability to undergo replicative senescence, a consequence of the Hayflick limit of normal cells (Shay and Wright, 2000; Hayflick and Moorhead, 1961). After 15 passages (p15) CCD 841 CoN cells showed reduced growth following passage or serum stimulation and an enlarged cell size, suggesting that they were starting to senesce. In support of this, CCD 841 CoN cells at p17 showed increased  $\beta$ -galactosidase activity at acidic pH (pH 6) compared to earlier passage cells (Fig. 3.4).

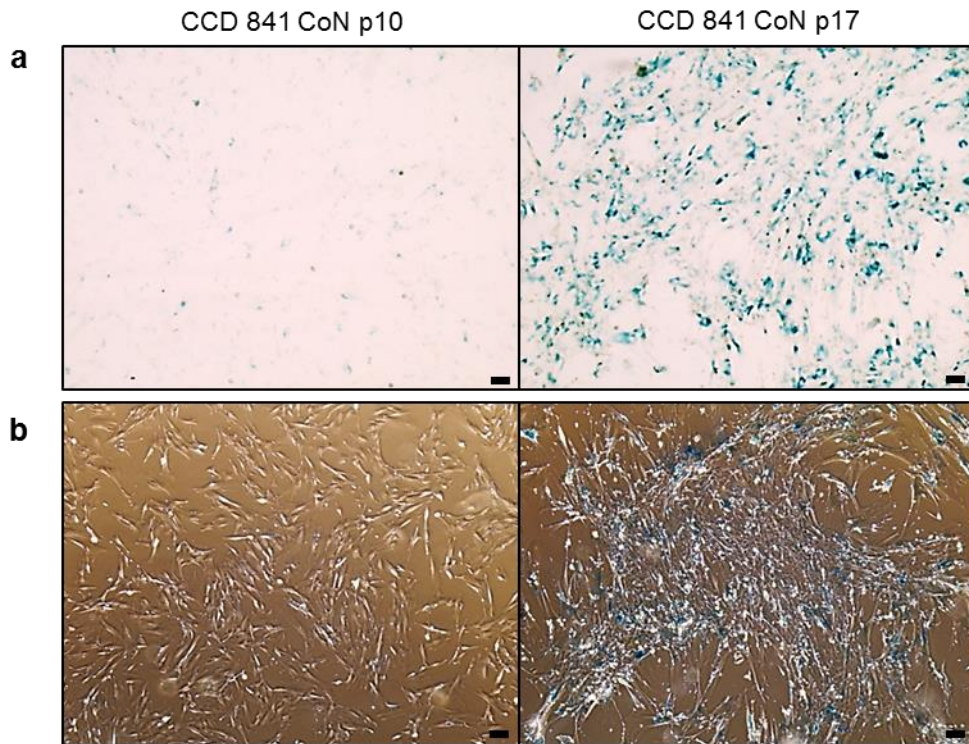


**Figure 3.4: Cell images of CCD 841 CoN cells at different passage numbers following staining for  $\beta$ -galactosidase activity as a marker of cellular senescence.**

Representative cell micrographs of CCD 841 CoN cells showing acidic  $\beta$ -galactosidase activity (blue cellular staining) under bright field (a) and phase contrast conditions (b). Images taken with x4 objective; 100 $\mu$ m scale bar. n=1 biological repeat.

CCD 841 CoN cells phenotypically appeared to contact inhibit upon reaching confluency. Contact inhibition of cell proliferation is a well known feature of non-cancer cells whereas cancer cells lose this characteristic and continue to grow (Hanahan and Weinberg, 2011). In support of CCD 841 CoN contact inhibition, cell cycle analysis of a confluent population showed an increase in the proportion of cells in G1 phase and a decrease in cells in G2/M phase compared to sub-confluent cells (Fig. 3.5).

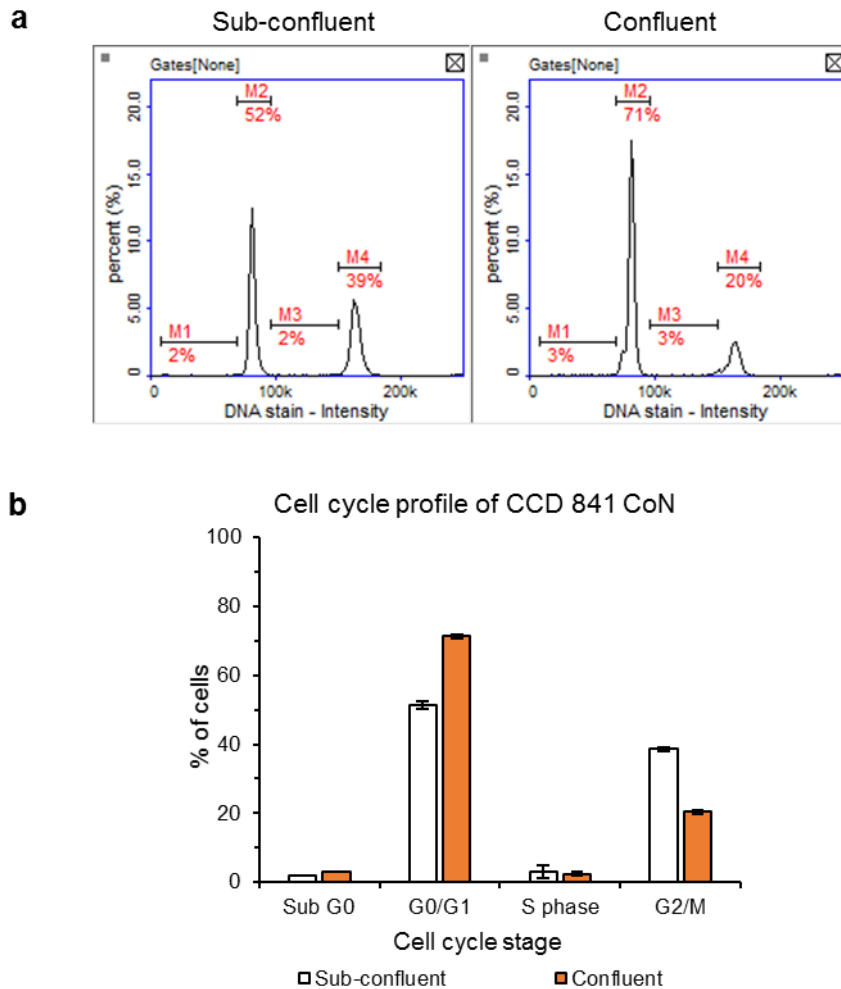


**Figure 3.5: Cell cycle distribution of sub-confluent and confluent CCD 841 CoN cells.** Cell cycle profiles of CCD 841 CoN cells that were allowed to reach confluency and that of control sub-confluent cells. Mean  $\pm$  SD n=1 biological repeat (3 technical replicates).

ARPE-19 cells similarly appeared to contact inhibit on reaching confluency with a decrease in the proportion of cells in the S and G2/M phases and an increase in cells in the G1 phase (Fig. 3.6), consistent with cell cycle arrest and a reduced number of actively proliferating cells.

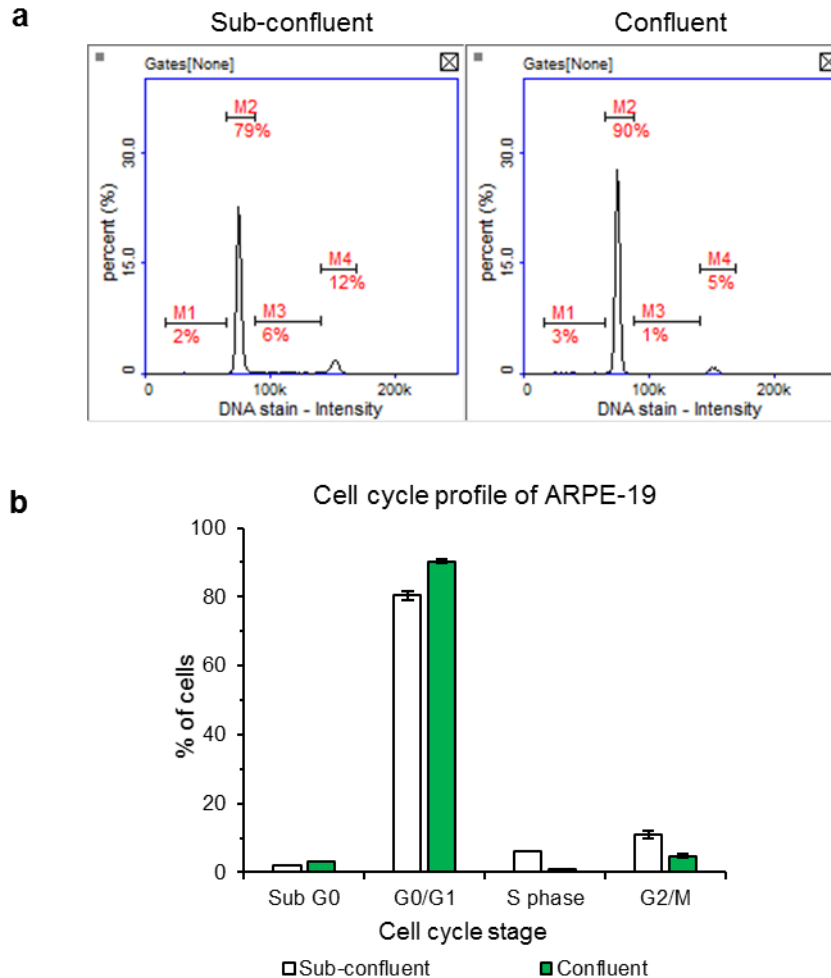


**Figure 3.6: Cell cycle distribution of sub-confluent and confluent ARPE-19 cells.** Representative cell cycle profiles of ARPE-19 cells that were allowed to reach confluency and that of control sub-confluent cells (**a**) and quantification of cell cycle distribution (**b**); mean  $\pm$  SD, n=1 biological repeat (3 technical replicates).

### 3.2.2 Activity and cancer cell selectivity of the NAMPT inhibitor FK866

The *in vitro* activity of the NAMPT inhibitor FK866 (Tan *et al.*, 2013) towards a panel of cancer cell lines derived from tumours of different tissue origins and towards several non-cancer cell models was determined by MTT chemosensitivity assay with quantification of IC<sub>50</sub> values (Table 3.1, Fig. 3.7). Similar IC<sub>50</sub> values were obtained by the SRB assay (e.g. Appendix Fig. 9.5) suggesting that IC<sub>50</sub> values are due to cytotoxicity of the tested agent rather than effects of the agent on the metabolism of MTT. Additionally, for all chemosensitivity assays, cell confluency at the different drug concentrations

relative to control cells was assessed by microscopy to check that 'absorbance readout' and cellular phenotypic effects closely correlated.

FK866	Cell Line	Tissue Origin	Mean IC <sub>50</sub> (nM)	±SEM
Non-Cancer	ARPE-19	Retina	10.49	0.50
	CCD 841 CoN	Colon	8.06	0.74
	PNT2	Prostate	>20,000	N/A
	NP1*	Brain	1.84	0.08
Cancer	A2780	Ovary	0.42	0.03
	CP70/A2780cis	Ovary	0.46	0.01
	HCT116 p53 <sup>+/+</sup> normoxic	Colon	1.74	0.04
	HCT116 p53 <sup>+/+</sup> hypoxic	Colon	1.85	0.14
	HCT116 p53 <sup>-/-</sup>	Colon	0.07	0.00
	HT-29	Colon	1.80	0.24
	PC-3	Prostate	0.40	0.01
	H460	Lung	9.64	0.31
	A549	Lung	1.91	0.21
	MDA-MB-231	Breast	1.91	0.04
	MDA-MB-436	Breast	9.03	0.03
	GBM1**	Brain	0.40	0.01

**Table 3.1: IC<sub>50</sub> values of FK866 towards multiple human cell lines of different tissue origin.** Mean IC<sub>50</sub> values ± SEM, n=3 biological repeats (8 technical replicates per biological repeat) of the NAMPT inhibitor FK866 in multiple non-cancer and cancer cell lines after 96 hours continuous FK866 exposure. NP1\* human neural progenitor cells (oligopotent cells); GBM1\*\* glioblastoma cancer stem cell model.



FK866 showed nM cytotoxicity and preferential activity to all cancer cell lines tested compared to ARPE-19, CCD 841 CoN and PNT2 non-cancer cell models, except for MDA-MB-436 and H460 cancer cells. These two lines displayed similar FK866 sensitivity as sub-confluent ARPE-19 and CCD 841 CoN cells (Table 3.1, Fig. 3.7a & 3.8). PNT2 non-cancer cells appeared to be insensitive to FK866 with no IC<sub>50</sub> being reached with a highest drug concentration tested of 20µM. FK866 also showed promising nM activity towards the patient-derived glioblastoma cancer stem cell-like model GBM1 (Polson *et al.*, 2018), with activity 4.6-fold higher than towards patient-derived neural progenitor cells (non-cancer oligopotent/adult stem cell-like model (Polson *et al.*, 2018)) (Fig. 3.7b). Compared to ARPE-19, CCD 841 CoN and PNT2 non-cancer cell models, FK866 activity towards GBM1 cells was 20-fold - 50,000-fold higher (Fig. 3.8). This selective activity is important given the typical chemo- and radio-resistance of CSCs (LaBarge, 2010) and the cancer stem cell hypothesis for the evolution of tumours (Tan *et al.*, 2006; Zheng *et al.*, 2013).

Interestingly HCT116 p53<sup>-/-</sup> cells (see appendix Fig. 9.2 for p53 immunoblot) appeared ~25-fold more sensitive to FK866 than isogenic HCT116 p53<sup>+/+</sup> cells (Table 3.1) which is important as p53 is known to be mutated or absent in many cancer cells and is often associated with worse outcome (Vogelstein *et al.*, 2000).

A problem associated with many 'classic' chemotherapeutic agents currently in clinical use is that cancer cells resistant to one chemotherapeutic agent also show cross-resistance to other agents (Gillet and Gottesman, 2010). Notably, FK866 appears able to circumvent cisplatin-resistance mechanisms in CP70/A2780cis cells suggesting a different mechanism of action of FK866 to cisplatin (Fig. 3.7c, for IC<sub>50</sub> values of cisplatin see appendix Table 9.2).

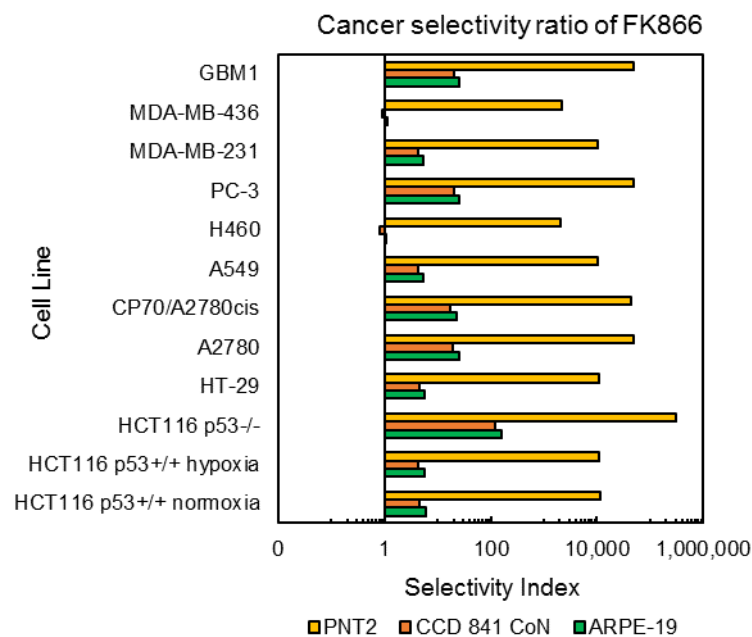


**Figure 3.8: Preferential cytotoxic activity of FK866 towards cancer cells compared to non-cancer cell models.**

Cancer cell versus non-cancer cell selectivity ratios for NAMPT inhibitor FK866 in multiple cancer cell lines compared to ARPE-19, CCD 841 CoN and PNT2 non-cancer cells. The selectivity index was calculated from the  $IC_{50}$  values achieved from 3 biological repeats (8 technical replicates) using the following equation (mean  $IC_{50}$  of non-cancer cells / mean  $IC_{50}$  of cancer cells). A value of 1 indicates equitoxicity of the drug to cancer and non-cancer cells, a value of  $<1$  indicates no preferential cytotoxicity to the cancer cells and a value  $>1$  indicates preferential cytotoxicity to the cancer cells.

The preferential cytotoxicity of FK866 towards cancer cells compared to non-cancer cells *in vitro* was compared to that of FDA-approved platinum-based chemotherapeutic agents cisplatin, carboplatin and oxaliplatin (Fig. 3.9). As oxaliplatin is currently used to treat patients with colorectal cancer (Food and Drug Administration, 2015) activities of the three platينات and FK866 were tested against the HCT116 p53<sup>+/+</sup> colorectal cancer cell line and compared against the human non-cancer colon cell line CCD 841 CoN (Fig. 3.9, selectivity indices (SI); appendix Table 9.3 for  $IC_{50}$  values). As shown in Fig. 3.9, oxaliplatin and cisplatin both resulted in  $SI < 1$ , indicating their preferential cytotoxicity towards the non-cancer cells whereas carboplatin showed a SI of 2.2 which compared to a SI of 4.6 for FK866. Overall, these *in vitro* results indicate that FK866 is both potent and shows good cancer cell selectivity for this panel of cell lines tested.

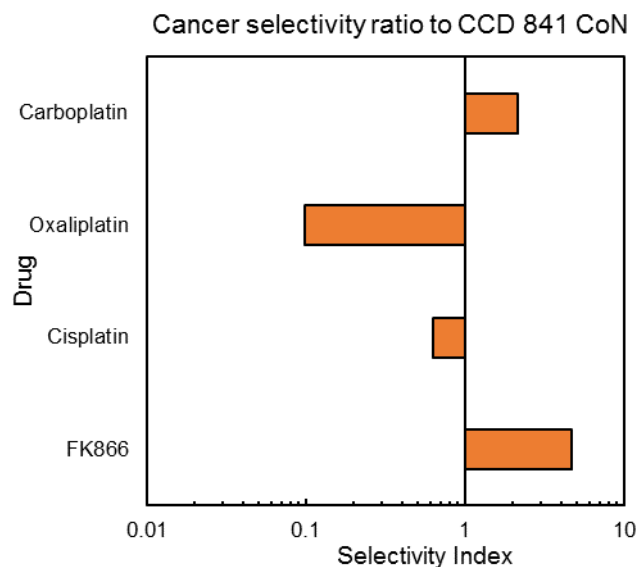


**Figure 3.9: Cancer cell selectivity of FK866 compared to FDA approved platinate based compounds.**

Cancer cell selectivity ratios were calculated from the  $IC_{50}$  values achieved from 3 biological repeats (8 technical replicates) which compared the activity of FK866 and clinically used platinates (cisplatin, oxaliplatin, carboplatin) in HCT116 p53<sup>+/+</sup> cancer cells and CCD 841 CoN non-cancer cells after 96 hours drug exposure. SI = mean  $IC_{50}$  of non-cancer cells / mean  $IC_{50}$  of cancer cells.

The activity of FK866 against hypoxic cancer cells compared to the same cell line grown under normoxic conditions was also tested as hypoxic regions of tumours are usually less responsive to chemotherapeutic agents and are a major cause of tumour recurrence and poor outcome (Phillips, 2016). FK866 cytotoxicity towards HCT116 p53<sup>+/+</sup> cancer cells grown under 0.1% and 21% O<sub>2</sub> conditions was compared to that of the clinically used chemotherapeutic DOX, a Topo2 poison (appendix Table 9.4 for  $IC_{50}$  values). Whilst DOX was 1.6-fold less active against hypoxic cells which is consistent with reduced cancer cell proliferation under hypoxia that was evident by microscopy, interestingly FK866 showed similar activity (equitoxicity) against both normoxic and hypoxic cancer cells (Fig. 3.10).

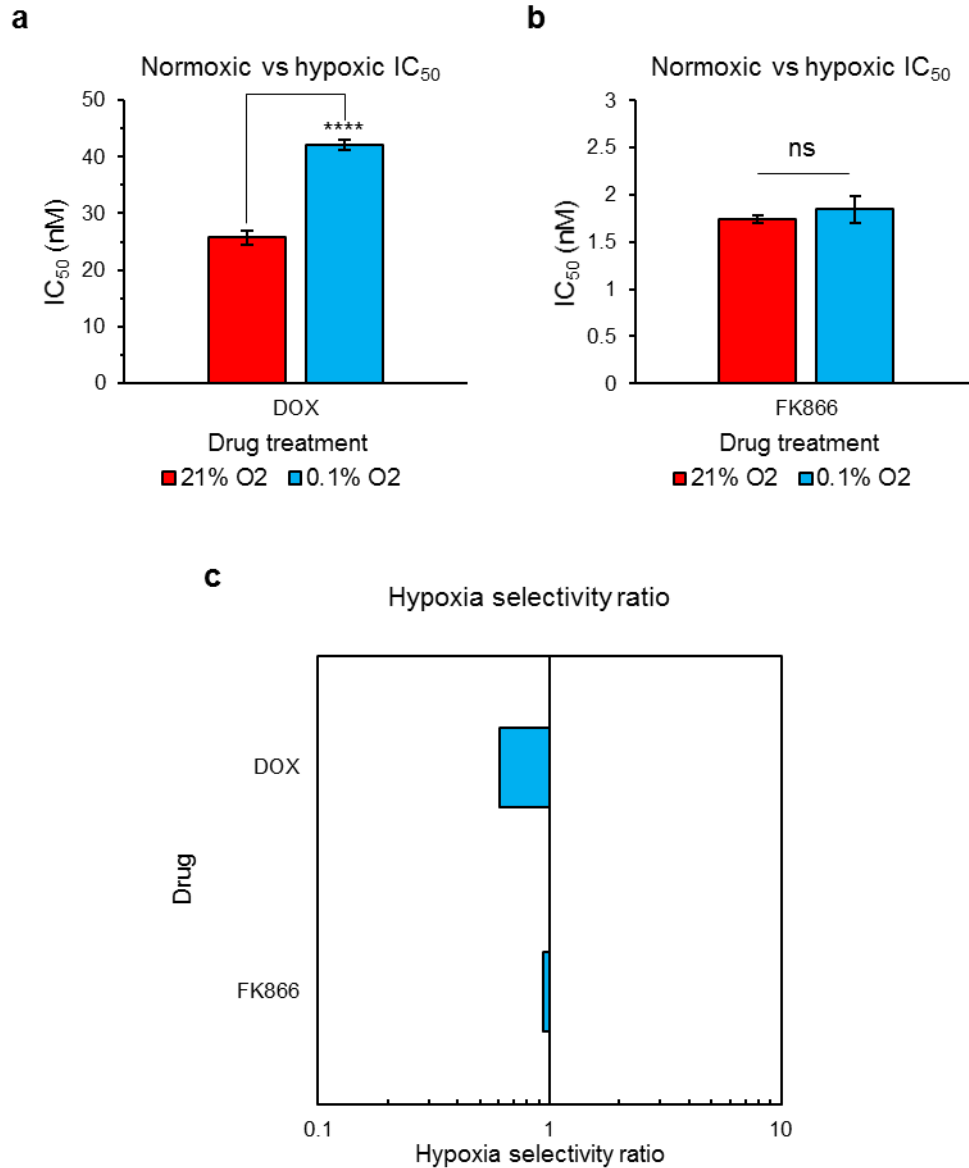


**Figure 3.10: The effect of hypoxia on doxorubicin and FK866 cytotoxicity towards HCT116 p53<sup>+/+</sup> cells.**

Mean  $IC_{50}$  values  $\pm$ SEM, n=3 biological repeats (8 technical repeats), of doxorubicin (DOX) (**a**) and FK866 (**b**) under normoxic and hypoxic (0.1% O<sub>2</sub>) conditions in HCT116 p53<sup>+/+</sup> cancer cells after 96 hours continuous drug exposure. A two-tailed t-test was performed where \*\*\*\*p<0.0001, ns=not significant. **c**. Hypoxia selectivity ratio ( $IC_{50}$  normoxic cells /  $IC_{50}$  hypoxic cells) for DOX and FK866. A value of 1 indicates equitoxicity of the drug under normoxic and hypoxic conditions, a value of <1 indicates preferential cytotoxicity to normoxic cells and a value of >1 indicates preferential cytotoxicity to hypoxic cells. Values were achieved using  $IC_{50}$  values from 3 biological repeats (8 technical replicates).

### 3.2.3 Relationship between chemosensitivity to FK866 and cellular NAMPT expression

To investigate whether there was any correlation between chemosensitivity to FK866 and cellular NAMPT protein expression, immunoblots were performed (Fig. 3.11) and quantified by densitometry (Fig. 3.12).

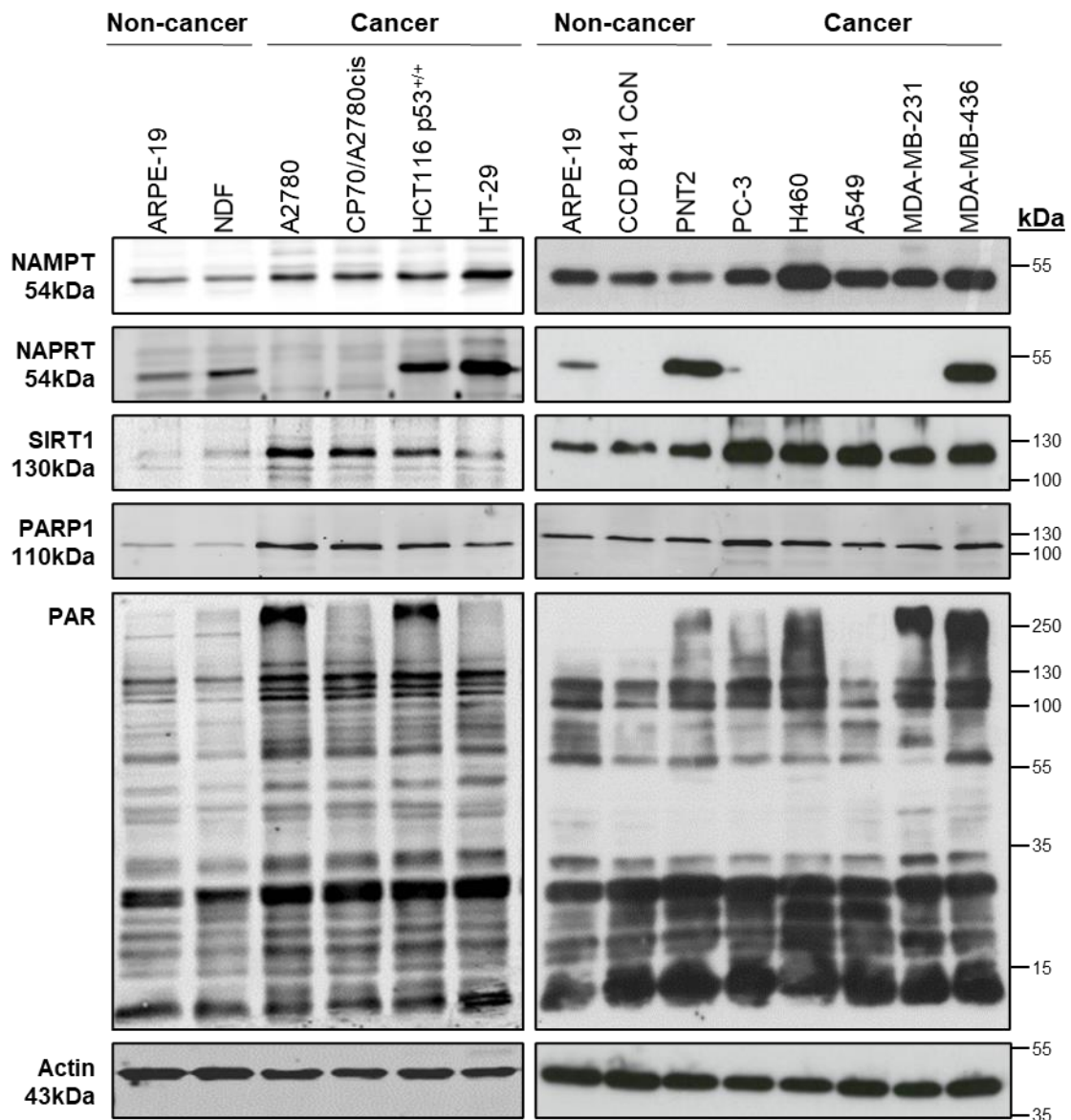


**Figure 3.11: Protein expression of NAMPT and associated proteins in human non-cancer and cancer cell lines.**

Immunoblots showing protein expression levels of NAMPT, NAPRT, SIRT1, PARP1 and PARylated proteins (PAR) in whole cell lysates of the indicated cell lines; actin was used as an endogenous loading control. n=1 biological repeat.

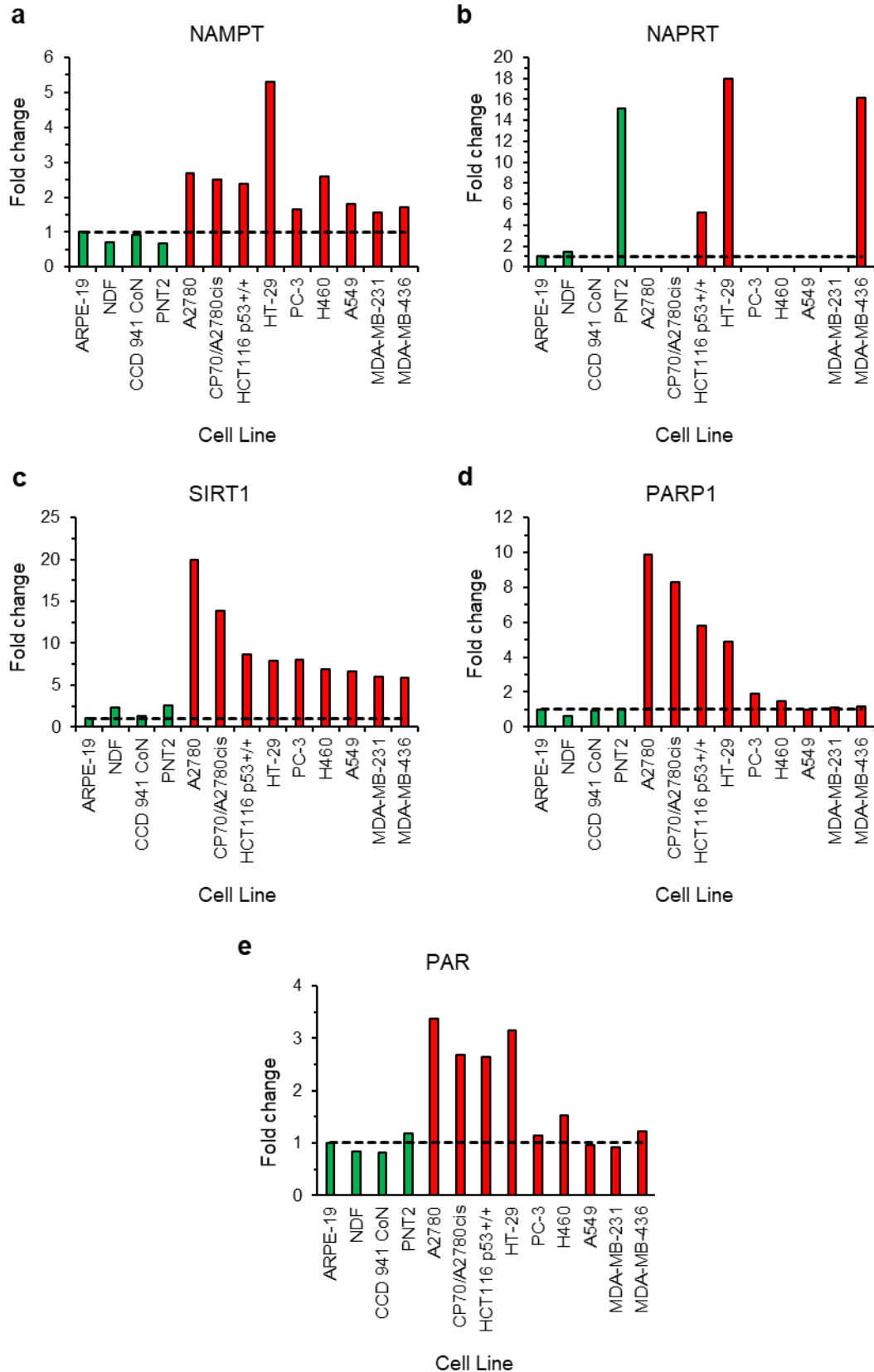


**Figure 3.12: Densitometric quantification of cellular protein expression.**

Fold change in protein expression of NAMPT, NAPRT, SIRT1, PARP1 and total PARylated protein (PAR) normalised to loading control actin and expressed relative to actin-normalised expression in ARPE-19 non-cancer cells (set as 1) of blots presented in Fig. 3.11 (n=1 biological repeat).

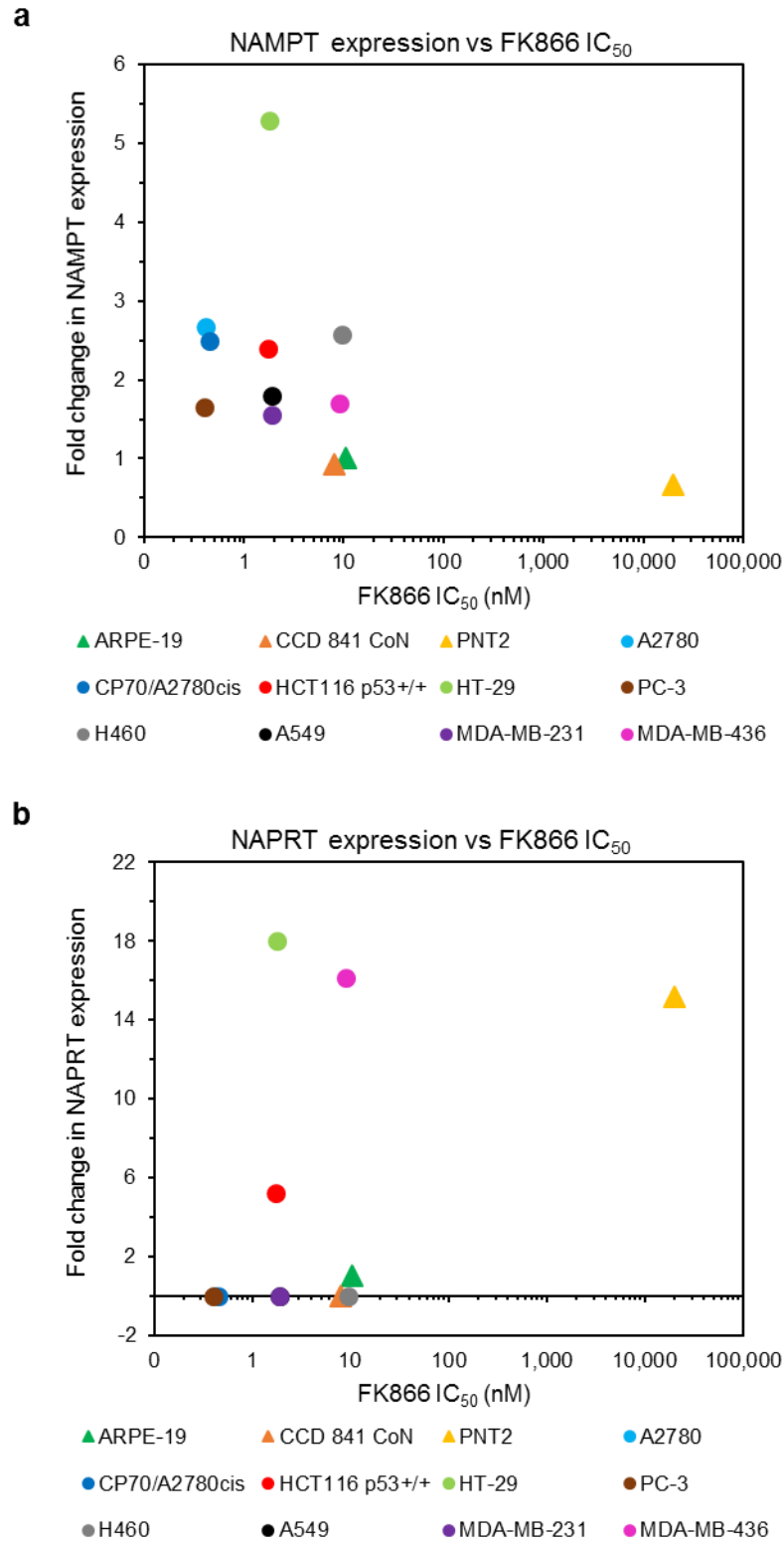


**Figure 3.13: Protein expression of NAMPT and NAPRT compared to cellular FK866 chemosensitivity (IC<sub>50</sub>).**

Fold change in NAMPT (a) and NAPRT (b) expression compared to FK866 mean IC<sub>50</sub> values. Triangles represent non-cancer cells and circles represent individual cancer cell lines. Fold change in protein expression is relative to expression level in ARPE-19 non-cancer cells (set at 1). Black horizontal line in (b) represents no detectable NAPRT expression. IC<sub>50</sub> values are based on n=3 biological repeats (Table 3.1) and changes in protein expression on n=1 biological repeat.

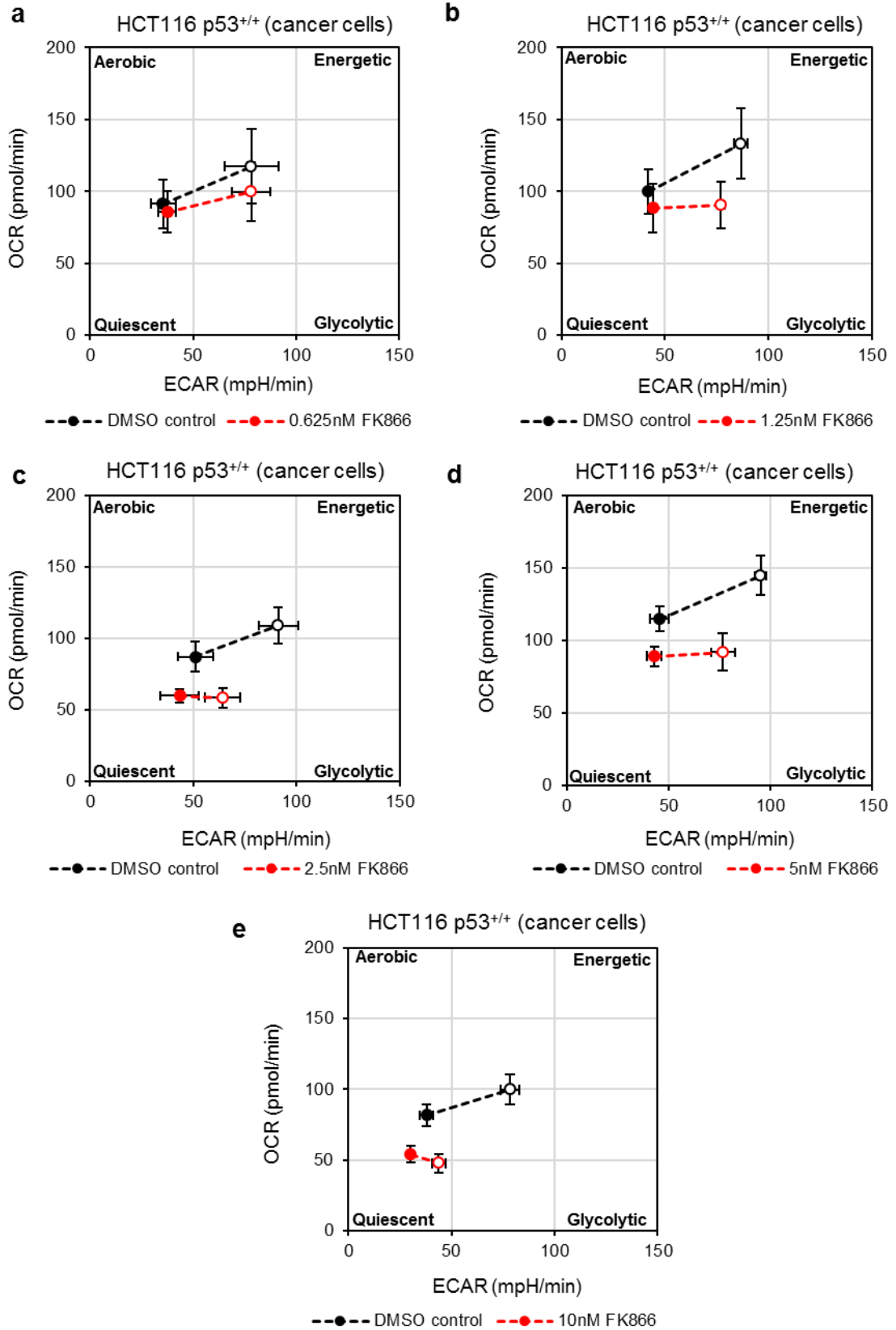
All the cancer cell lines analysed showed increased protein expression of NAMPT compared to non-cancer cells (Fig. 3.11 & Fig. 3.12), suggesting that cancer cells may be more reliant on the NAMPT enzyme to sustain the levels of cellular NAD<sup>+</sup> that they require. This was consistent with the increased chemosensitivity of most of the cancer cell lines to the NAMPT inhibitor FK866 (Fig. 3.7 & Fig. 3.8) compared to the non-cancer cell models. However, as shown in Figure 3.13 within the panel of different cancer cell lines there is no clear correlation between levels of NAMPT expression and FK866 IC<sub>50</sub>. This likely reflects the influence of other factors, such as differential expression and activity of NAD<sup>+</sup> consuming enzymes such as PARP1 and SIRT1, and NAPRT enzymatic activity that may enable compensatory restoration of NAD<sup>+</sup> levels in response to NAMPT inhibition. For example, HT-29 showed the highest normalised expression of NAMPT (5.3-fold higher than ARPE-19 cells) but its chemosensitivity to FK866 was lower (higher IC<sub>50</sub>) than a number of other cancer cell lines. This is possibly due to the fact that HT-29 express NAPRT at high levels (18-fold higher than ARPE-19 cells) (Fig. 3.11-3.13) and therefore may be able to compensate and restore NAD<sup>+</sup> levels through the NAPRT pathway. Unexpectedly H460 and MDA-MB-436 cancer cells showed similar chemosensitivity to ARPE-19 and CCD 841 CoN non-cancer cells despite higher protein expression of NAMPT and SIRT1 (Fig. 3.11 & Fig. 3.12). In the case of H460 cells, it has previously been reported that NAMPT is mutated at S165Y which is further away from the active site than other mutations which can lead to NAMPT inhibitor resistance, although it does lead to the unwinding of a helix in the active site, which can lead to reduced binding of NAMPT inhibitors. Previous research has shown that H460 S165Y mutant cells have a 10-fold higher FK866 IC<sub>50</sub> compared to the parental cell line (Wang *et al.*, 2014).

It was hypothesised that MDA-MB-436 may be the most sensitive to FK866 of the cancer cell lines tested as these cells are BRCA1 mutated (Elstrodt *et al.*, 2006) and that NAMPT inhibition may be synthetically lethal with BRCA mutation. However, they were surprisingly less sensitive than other cancer cells with 96 hours continuous drug exposure which may be due to very high NAPRT expression (Fig. 3.11 - 3.13, 16.1-fold higher NAPRT expression than ARPE-19 cells) enabling them to compensate for NAMPT inhibition and restore cellular

NAD<sup>+</sup> levels. The non-cancer prostate cells PNT2 were the least sensitive to FK866 with an IC<sub>50</sub> value of >20µM which correlated with both low NAMPT expression, suggestive of reduced dependency, and also very high expression of NAPRT (15.2-fold higher compared to ARPE-19 non-cancer cells) (Fig. 3.11-3.13), which would facilitate compensatory restoration of NAD<sup>+</sup> levels via the NAPRT pathway. A2780 and CP70/A2780cis ovarian cancer cells were amongst the most sensitive to FK866 consistent with high expression of NAD<sup>+</sup> consuming enzymes PARP1 and SIRT1 (Fig. 3.12).

### **3.2.4 Cancer selective metabolic effects of NAMPT inhibition**

It was hypothesised that NAMPT inhibition, if this were to cause a decrease in total cellular NAD(H) levels, could negatively impact upon cellular glycolytic and mitochondrial respiration rates as both these processes are dependent on NAD(H) for redox electron transfer. Rates of glycolysis and mitochondrial respiration and reserve capacities ('Seahorse XFp Cell Energy Phenotype') were compared under normal growth conditions and after 24 hours exposure to non-toxic FK866 doses in HCT116 p53<sup>+/+</sup> cancer cells and ARPE-19 non-cancer cells (Fig. 3.14 & 3.15). Whilst HCT116 p53<sup>+/+</sup> and ARPE-19 are both epithelial, CCD 841 CoN cells were additionally treated with 10nM FK866 so that tissue type could be compared directly between cancer and non-cancer cells (colon epithelial) (Fig. 3.16). Reserve capacities were determined through addition of a metabolic stress 'mix' consisting of the mitochondrial uncoupler FCCP and ATP synthase inhibitor oligomycin.

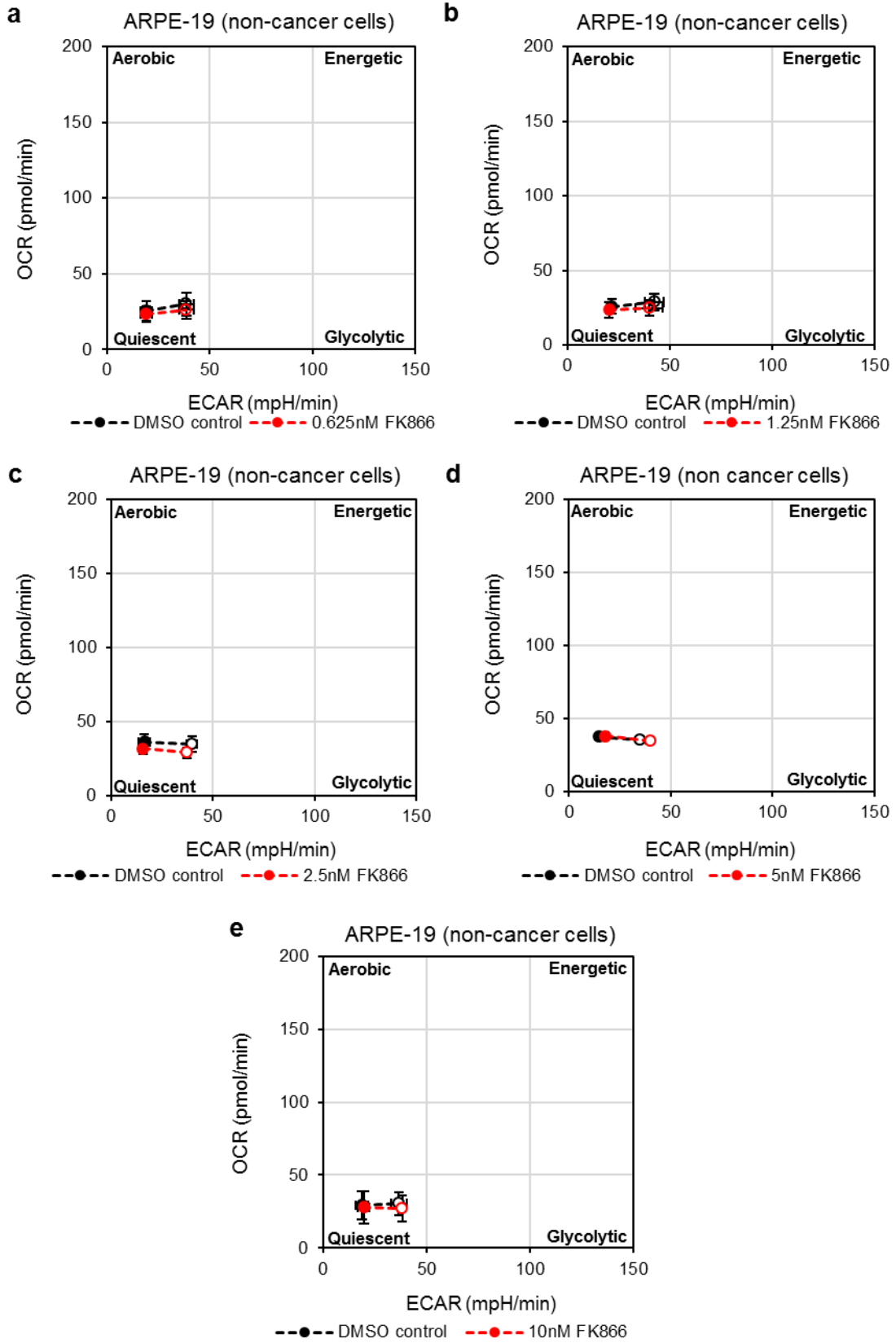


f

	0.625nM FK866	1.25nM FK866	2.5nM FK866	5nM FK866	10nM FK866
<b>Baseline OCR DMSO control</b>	ns	ns	ns	ns	ns
<b>Stressed OCR DMSO control</b>	ns	ns	*	*	*
<b>Baseline ECAR DMSO control</b>	ns	ns	ns	ns	ns
<b>Stressed ECAR DMSO control</b>	ns	ns	ns	ns	**

**Figure 3.14: Cell energy phenotype of HCT116 p53<sup>+/+</sup> cancer cells treated with NAMPT inhibitor FK866.**

HCT116 p53<sup>+/+</sup> cancer cells were treated with the indicated FK866 doses (**a-e**), or solvent (DMSO) control, for 24 hours prior to analysis. Mean cell energy phenotypes  $\pm$  SEM, n=3 biological repeats (3 technical replicates per repeat) are shown; basal metabolic phenotype is indicated by closed circles; metabolic stress response/capacity is indicated by open circles. **f**. Statistical analysis comparing baseline oxygen consumption rate (OCR), stressed OCR, baseline extracellular acidification rate (ECAR) and stressed ECAR of DMSO control cells to FK866 treated cells. A two-tailed t-test was performed where \*p<0.05, \*\*p<0.01, ns=not significant.



f

	0.625nM FK866	1.25nM FK866	2.5nM FK866	5nM FK866	10nM FK866
<b>Baseline OCR DMSO control</b>	ns	ns	ns	ns	ns
<b>Stressed OCR DMSO control</b>	ns	ns	ns	ns	ns
<b>Baseline ECAR DMSO control</b>	ns	ns	ns	ns	ns
<b>Stressed ECAR DMSO control</b>	ns	ns	ns	*	ns

**Figure 3.15: Cell energy phenotype of ARPE-19 non-cancer cells treated with NAMPT inhibitor FK866.**

ARPE-19 non-cancer cells were treated with the indicated FK866 doses (a-e), for 24 hours prior to analysis. Mean cell energy phenotypes  $\pm$  SEM, n=3 biological repeats (3 technical replicates per repeat), are shown compared to DMSO control cells; basal metabolic phenotype is indicated by closed circles; metabolic stress response/capacity is indicated by open circles. f. Statistical analysis comparing base line OCR, stressed OCR, baseline ECAR and stressed ECAR of DMSO control cells to FK866 treated cells. A two-tailed t-test was performed where \*p<0.05, ns=not significant.

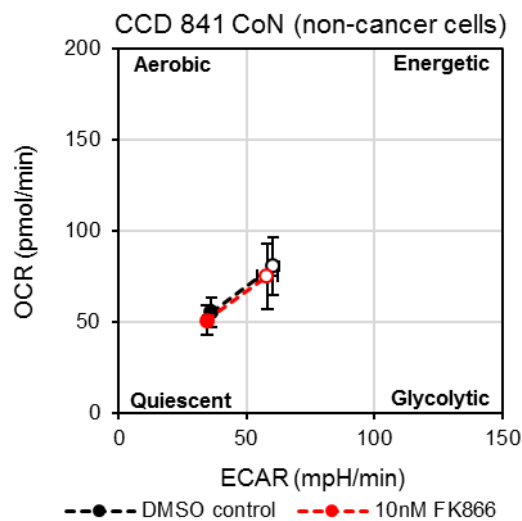


**Figure 3.16: Cell energy phenotype of CCD 841 CoN non-cancer cells treated with 10nM FK866.**

CCD 841 CoN non-cancer cells were treated with 10nM FK866 for 24 hours prior to analysis. Mean cell energy phenotypes  $\pm$  SEM, n=2 biological repeats (3 technical replicates per repeat), are shown compared to DMSO control cells; basal metabolic phenotype is indicated by closed circles; metabolic stress response/capacity is indicated by open circles.

In the HCT116 p53<sup>+/+</sup> cancer cells, reduced mitochondrial respiratory capacity (metabolic stress response) was observed at FK866 concentrations of 1.25nM

and above with a reduction in basal respiratory rate at  $\geq 2.5$ nM FK866 (Fig. 3.14). A dose-dependent reduction in glycolytic capacity was also observed in the HCT116 p53<sup>+/+</sup> cancer cells (Fig. 3.14). In contrast, in the ARPE-19 and CCD 841 CoN non-cancer cells, rates of mitochondrial respiration and glycolysis as well as respiratory and glycolytic capacities appeared unaffected by 24 hours FK866 treatment (up to 10nM FK866; Fig. 3.15 & Fig. 3.16).

### 3.2.5 Ability of NAD<sup>+</sup> precursors to rescue the effects of FK866

It was important to verify that the effects of FK866 on cell survival (Fig. 3.7) were due to NAMPT inhibition and were not caused by off-target effects. To assess this, FK866 chemosensitivity assays were performed with the exogenous addition of NAD<sup>+</sup> precursors NA or NMN which were hypothesised to enable rescue of NAD<sup>+</sup> levels (see intro Fig. 1.9) and FK866-induced cell death. As shown in Figure 3.17, both NA and NMN addition were able to rescue the cytotoxic effects of FK866 towards HCT116 p53<sup>+/+</sup> cancer cells.

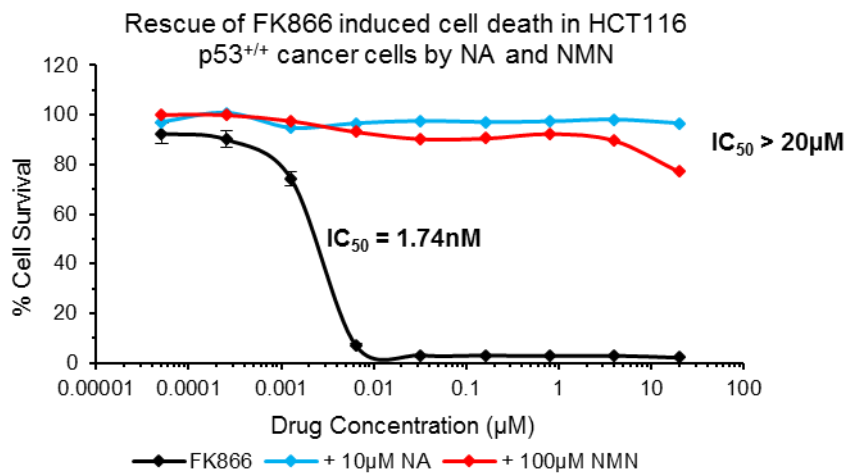


**Figure 3.17: Chemosensitivity dose response for FK866 in HCT116 p53<sup>+/+</sup> cancer cells in the presence or absence of NA and NMN.**

Dose response curve of HCT116 p53<sup>+/+</sup> cancer cells after 96 hours exposure to FK866 alone (n=3 biological repeats, 8 technical replicates) or in combination with 10µM NA or 100µM NMN (n=1 biological repeat, 8 technical replicates).

Similarly, exogenous NA and to a lesser extent NMN, were able to rescue the effects of FK866 on cellular metabolism (Fig. 3.18), further supporting the notion that the observed effects of FK866 are caused by on-target inhibition of NAMPT.

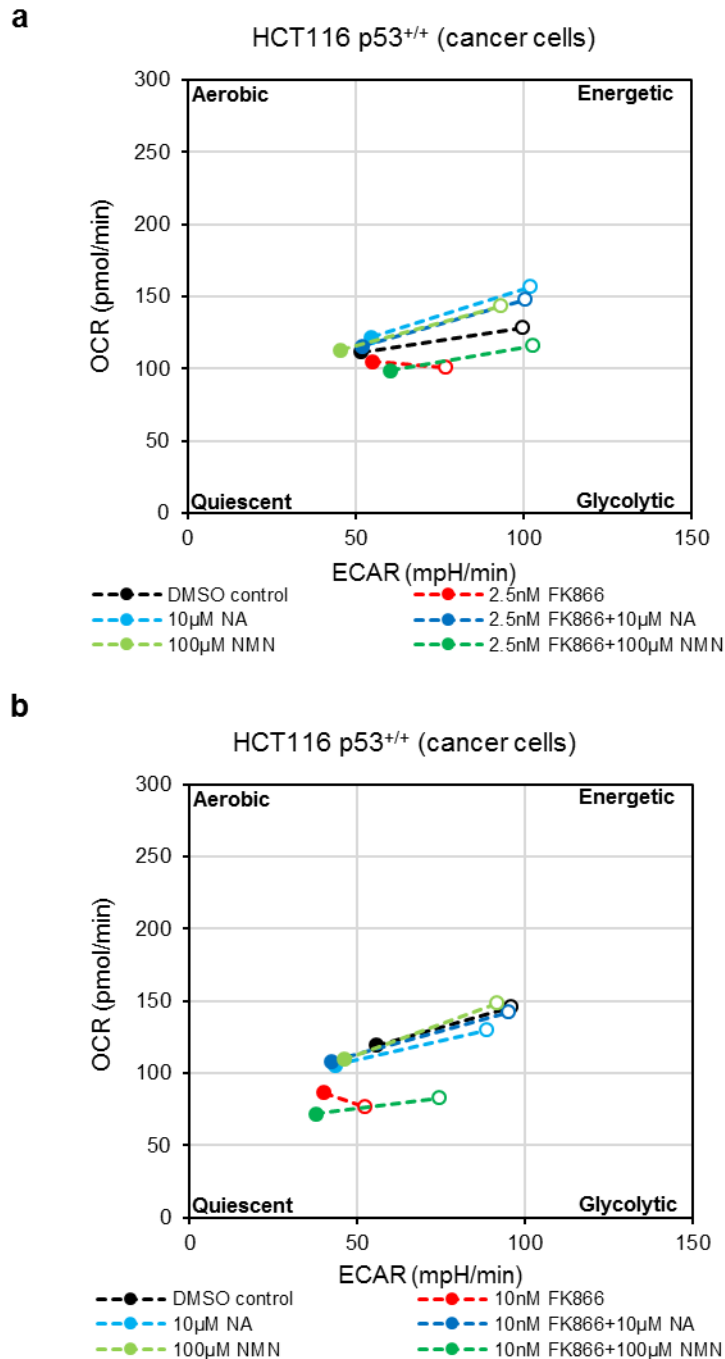


**Figure 3.18: Cell energy phenotype of HCT116 p53<sup>+/+</sup> cancer cells after FK866 treatment ± NA/NMN.**

HCT116 p53<sup>+/+</sup> cancer cells were pre-treated with 10µM NA or 100µM NMN for 12 hours before 2.5nM FK866 (a), 10nM FK866 (b) or DMSO solvent control was added for 24 hours prior to analysis. Cell energy phenotypes can be seen for each drug treatment, basal metabolic phenotype: closed circle; metabolic stress response/capacity: open circles. n=1 biological repeat,

### 3.2.6 Effects of FK866 on cellular NAD(H)

To directly examine the effects of inhibiting NAMPT on cancer and non-cancer cellular NAD(H) levels, NAD(H) assays were performed following 24 hours treatment of cells with non-toxic doses of FK866 (see appendix Fig. 9.3 for cell images at 24 hours). Data is presented as a fold-change in levels of NAD(H) which represents total levels of NAD<sup>+</sup> and NADH. In contrast to LDH-A targeting which alters the ratio between NAD<sup>+</sup> and NADH (Allison *et al.*, 2014), FK866 was found to reduce levels of both NAD<sup>+</sup> and NADH and by the same extent resulting in no change in balance or ratio between the oxidised and reduced forms.

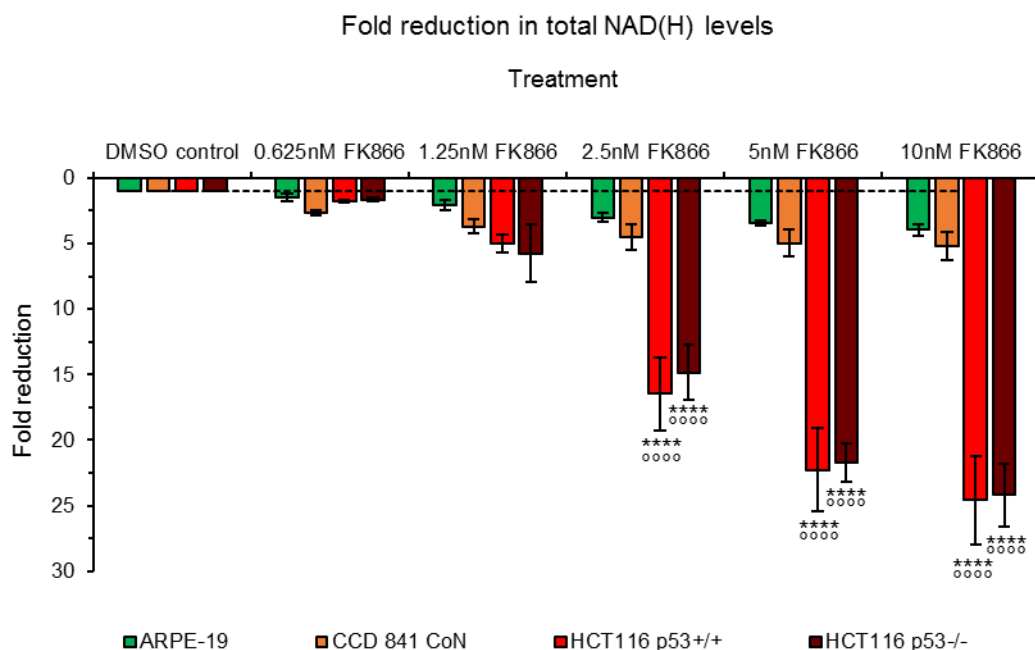


**Figure 3.19: Total cellular NAD(H) reduction in cells treated with FK866.**

Average fold decrease in total cellular NAD(H) levels  $\pm$  SEM, n=3 biological repeats (2 technical replicates per repeat), after indicated FK866 treatments for 24 hours. Fold change is relative to DMSO control for indicated cell line. A one way ANOVA was performed where \*\*\*\* p<0.0001 compared to ARPE-19 non-cancer cells and 0000 p<0.0001 compared to CCD 841 CoN non-cancer cells.

As shown in Figure 3.19, total cellular NAD(H) levels were preferentially reduced in HCT116 p53<sup>+/+</sup> and p53<sup>-/-</sup> cancer cells compared to ARPE-19 and CCD 841 CoN non-cancer cells following 24 hours treatment with a range of different FK866 doses. A statistically significant greater fold decrease in NAD(H) was seen in HCT116 p53<sup>+/+</sup> and HCT116 p53<sup>-/-</sup> cancer cells compared to ARPE-19 and

CCD 841 CoN non-cancer cells at 2.5nM, 5nM and 10nM FK866 ( $p < 0.0001$ ). In the non-cancer cells, at a dose of 10nM FK866, levels of total NAD(H) were reduced by 4-fold - 5.2-fold compared to 24-fold in the HCT116 cancer cells. There appeared to be similar reduction of NAD(H) in  $p53^{+/+}$  and  $p53^{-/-}$  cancer cells which is important as previous research to modulate NAD(H) via targeting of LDH-A reduced the ratio of  $NAD^+$  relative to NADH in  $p53$ -wild type cancer cells but did not have any effects in  $p53^{-/-}$  cells (Allison *et al.*, 2014). The ability to reduce NAD(H) in cancer cells of different  $p53$  status is important as  $p53$  is known to mutated or null in many cancers (Vogelstein *et al.*, 2000).

The effects of FK866 in additional cancer cell lines were also analysed at a single non-toxic dose of FK866 (10nM, see appendix Fig. 9.3 for cell images at 24 hours). Results indicated that 10nM FK866 caused a greater decrease in NAD(H) in all cancer cell lines tested compared to ARPE-19 and CCD 841 CoN non-cancer cells apart from for H460 cells which correlates with their mutated NAMPT status and relative insensitivity to FK866 (Fig. 3.20).

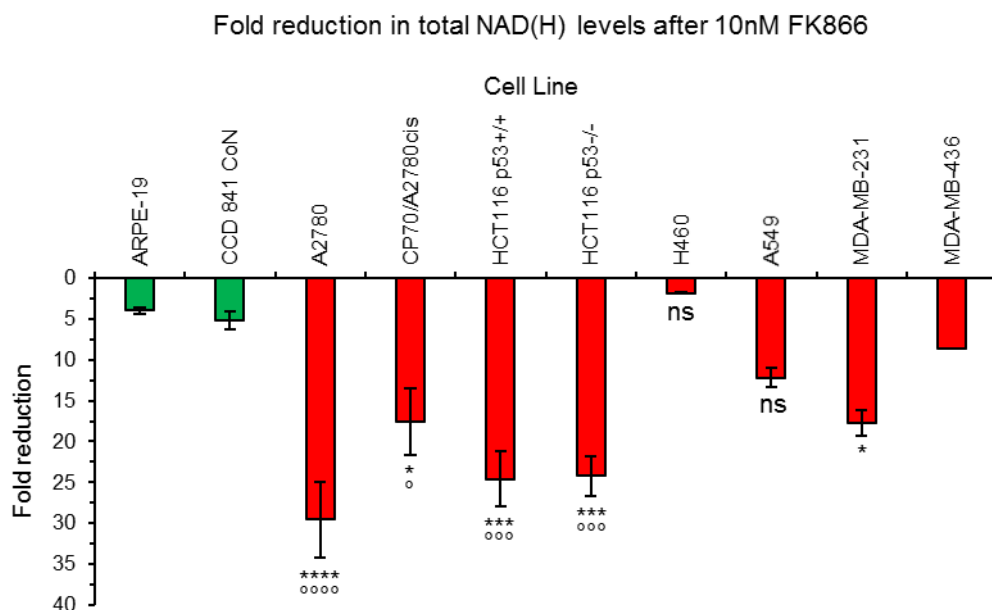


**Figure 3.20: Fold reduction in NAD(H) levels in multiple non-cancer and cancer cell lines after 10nM FK866 treatment.**

Mean fold reduction  $\pm$  SEM of total cellular NAD(H) levels relative to DMSO control cells for multiple cell lines after 10nM FK866 treatment for 24 hours.  $n=3$  biological repeats (2 technical replicates per repeat) except for MDA-MB-436 ( $n=1$  biological repeat). A one way ANOVA was performed where \* $p < 0.05$ , \*\*\* $p < 0.001$ , \*\*\*\* $p < 0.0001$  compared to ARPE-19 non-cancer cells and ° $p < 0.05$  °° $p < 0.001$  °°° $p < 0.0001$  compared to CCD 841 CoN non-cancer cells.

### 3.2.7 Effects of FK866 on NAD(H) in the nucleus

As PARP DNA repair activity takes place in the nucleus (Vyas *et al.*, 2013) it was important to investigate whether FK866 was able to reduce nuclear NAD(H) or whether the decrease in total cellular NAD(H) was due to selective depletion of the cytoplasmic NAD(H) pool. A nuclear and cytoplasmic fractionation after 24 hours treatment of HCT116 p53<sup>+/+</sup> cells with 5nM FK866 followed by a NAD(H) assay revealed that nuclear and cytoplasmic NAD(H) pools were similarly reduced by FK866 (Fig. 3.21).

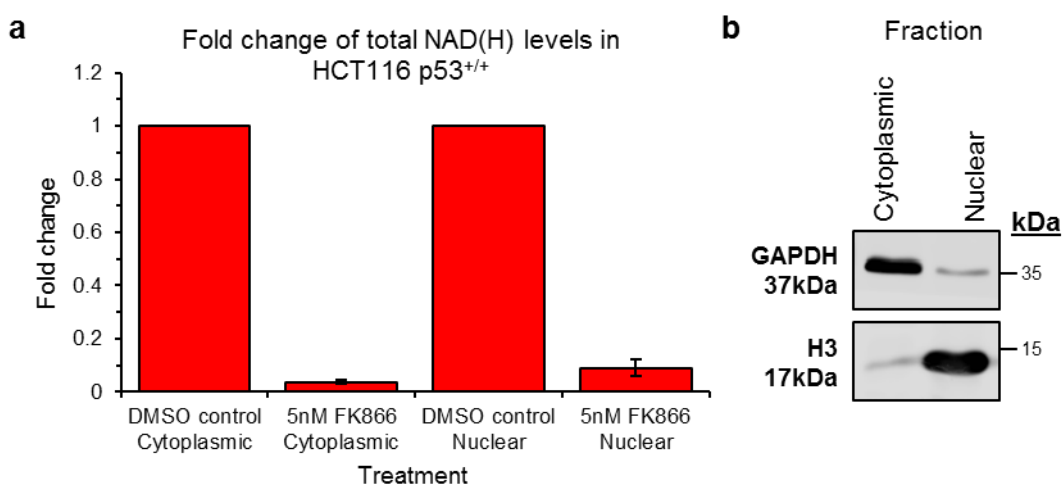


**Figure 3.21: Reduction of nuclear and cytoplasmic NAD(H) pools by FK866.**

**a.** Fold change  $\pm$  SD of NAD(H) levels in cytoplasmic and nuclear fractions of HCT116 p53<sup>+/+</sup> cells after 5nM treatment of FK866 for 24 hours compared to DMSO control treated cells, n=3 technical replicates, n=1 biological repeat. **b.** Protein expression of cytoplasmic marker GAPDH and nuclear marker Histone H3 in both cell fractions.

### 3.2.8 Assessment of effects of FK866 on PARP activity

As both cytoplasmic and nuclear NAD(H) pools were reduced by FK866 treatment (Fig. 3.21) and cellular NAD(H) decrease was greater in cancer cells compared to non-cancer cells (Fig. 3.19 & Fig. 3.20), it was hypothesised that FK866 treatment could selectively or preferentially decrease PARP activity in cancer cells compared to non-cancer cells.

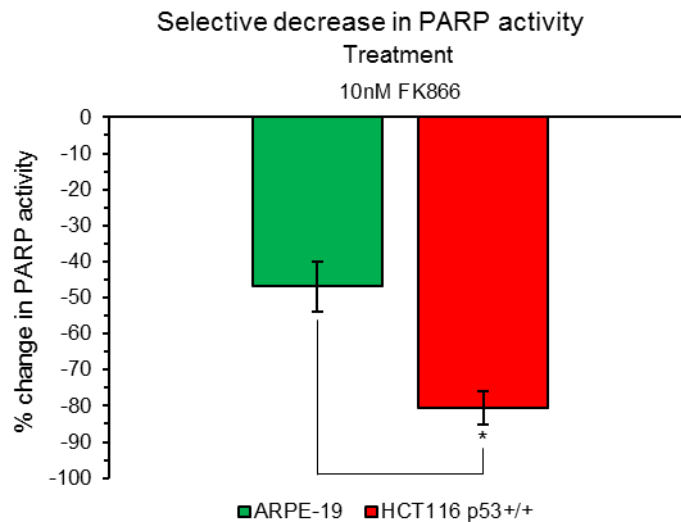


**Figure 3.22: Quantification of PARP activity after cellular FK866 treatment.**

Average percentage decrease  $\pm$  SEM,  $n=3$  biological repeats (4 technical replicates per repeat), of PARP activity in ARPE-19 non-cancer cells and HCT116 p53<sup>+/+</sup> cancer cells after treatment with 10nM FK866 for 24 hours. A two-tailed t-test was performed where  $*p<0.05$ .

As shown in Figure 3.22 24 hours 10nM FK866 treatment reduced PARP activity in the HCT116 p53<sup>+/+</sup> cancer cells by 80% compared to a 47% decrease in the ARPE-19 non-cancer cells ( $p<0.05$ ).

To further confirm the effects of FK866 on PARP activity, western blots were performed to investigate if there was any decrease in cellular protein PARylation levels after FK866 treatment. MDA-MB-436 cancer cells were treated with a dose range of FK866 for 24 hours and immunoblots were performed and quantified (Fig. 3.23 & Fig. 3.24).

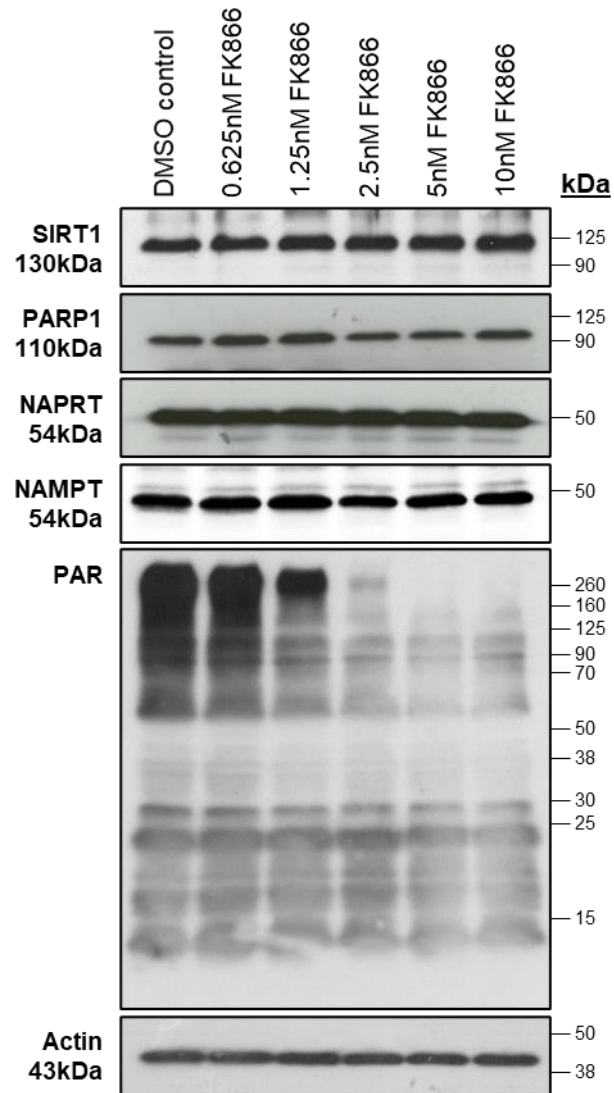


**Figure 3.23: Decreased protein PARylation in MDA-MB-436 cancer cells following 24 hours FK866 treatment.**

Western blot analysis of SIRT1, PARP1, NAPRT, NAMPT and PAR protein expression with actin used as a loading control, in MDA-MB-436 cancer cells treated with the indicated FK866 doses for 24 hours. n=1 biological repeat.

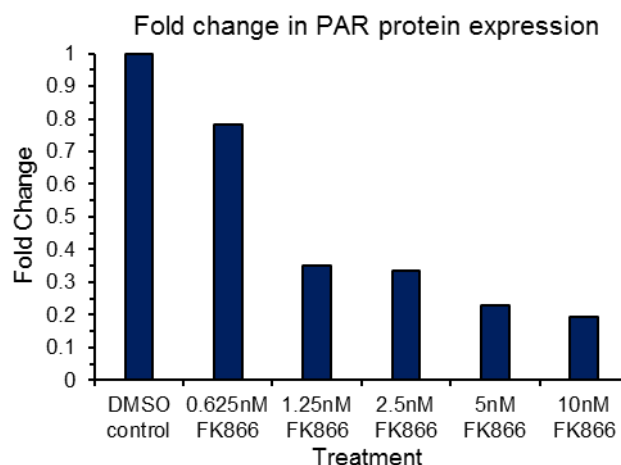


**Figure 3.24: Densitometric quantification of protein PARylation levels in MDA-MB-436 cells after 24 hours FK866 treatment.**

Fold change in PAR levels in MDA-MB-436 cancer cells after 24 hours treatment with the indicated FK866 doses. Levels normalised to total PARP expression and then to loading control actin, fold change expressed compared to DMSO control.

NAMPT and NAPRT protein levels were unaffected by FK866 treatment whereas PAR levels decreased in a dose-dependent manner by up to 5.2-fold (Fig. 3.23 & Fig. 3.24), indicative of a dose-dependent reduction in PARP activity. PARP1 protein expression and SIRT1 levels were largely unaffected by FK866.

To ensure that the decrease in PARP activity in Figure 3.22 was directly due to NAD<sup>+</sup> depletion, a rescue study was performed using a NAD<sup>+</sup> precursor, NMN. Figure 3.25 shows that the combination of FK866 plus NMN was able to rescue some of the effects of FK866 on PARP activity.

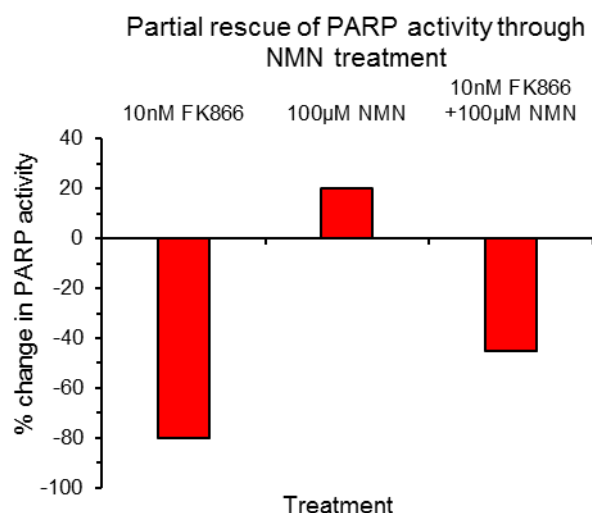


**Figure 3.25: Partial rescue of decreased PARP activity, caused by FK866 treatment, by co-treatment with NAD<sup>+</sup> precursor NMN.**

Percentage decrease in PARP activity in HCT116 p53<sup>+/+</sup> cells treated with 10nM FK866 alone or in combination with 100µM NMN for 48 hours (n=1 biological repeat, n=4 technical replicates).

### 3.2.9 Can FK866 potentiate current chemotherapeutic drugs?

As NAD(H) levels (Fig. 3.20) and PARP activity (Fig. 3.22) were preferentially depleted in cancer cells compared to non-cancer cells tested, it was hypothesised that combined treatment of certain DNA damaging chemotherapeutic agents and FK866 could potentiate chemotherapeutic agent cytotoxicity selectively in cancer cells through cancer-selective reduction of PARP-mediated DNA repair. This was tested using several DNA damaging chemotherapeutic agents that are in clinical use which have previously been reported to be potentiated by PARP inhibition (see section 1.4.1.2). These included the Topo1 poison CPT (Bowman *et al.*, 2001; Murai *et al.*, 2014), Topo2 poison DOX (Park *et al.*, 2018) and the alkylating agent TMZ (Plummer *et al.*, 2008; Plummer *et al.*, 2013; Murai *et al.*, 2014).

Effects were compared to those obtained with combining the chemotherapeutic agent directly with a known FDA approved PARP inhibitor. Based on concentrations reported in the literature PARP inhibitors rucaparib and olaparib were first compared for their ability to effectively inhibit cellular PARP activity (García-Parra *et al.*, 2014; Prasad *et al.*, 2017) (Fig. 3.26).

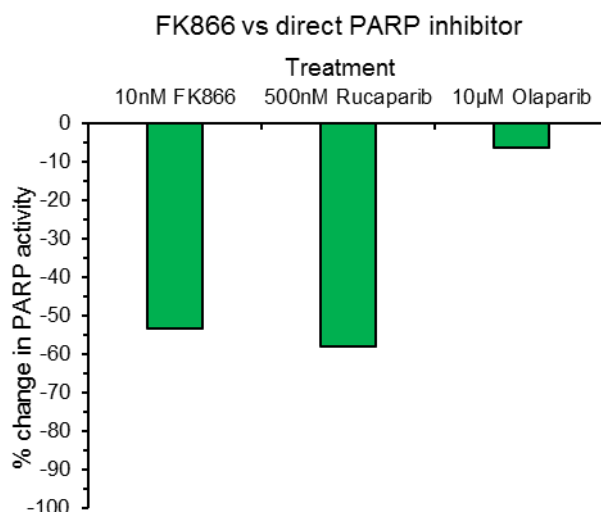


**Figure 3.26: Quantification of PARP activity after PARP inhibitor or FK866 treatment.** Percentage decrease in PARP activity in ARPE-19 non-cancer cells after FK866, rucaparib or olaparib treatment at the indicated doses for 24 hours (n=1 biological repeat, 4 technical replicates).

The results indicated that rucaparib reduced PARP activity greater than olaparib and to a similar level as FK866 at the indicated tested doses (Fig. 3.26) and of the two PARP inhibitors it was therefore selected for subsequent combination studies. Higher doses of rucaparib were not used due to reported off-target kinase inhibition at sub- to low micromolar concentrations (Antolín and Mestres, 2014; Antolin *et al.*, 2019).

Effects of CPT on cancer and non-cancer cell number and viability when cells were treated alone, or in combination with FK866 or rucaparib, are shown in Figure 3.27. CPT treatment alone (40nM, 48 hours) caused a significant reduction in cell number in both the ARPE-19 non-cancer cells and HCT116 p53<sup>+/+</sup> cancer cells but when combined with FK866 or rucaparib there was no significant further reduction. Combination treatments had no significant effect on total cell viability (as assayed by the immediate cellular uptake of DAPI) compared to CPT alone. Interestingly however, apoptotic quantification by annexin V/propidium iodide (PI) staining revealed a small but statistically significant increase in the proportion of late apoptotic/necrotic cells in the HCT116 p53<sup>+/+</sup> cancer cells with combined treatment of CPT and FK866 compared to either treatment alone (Fig. 3.28). Importantly, this potentiation was not observed in either of the non-cancer cell models or with rucaparib in combination with CPT.

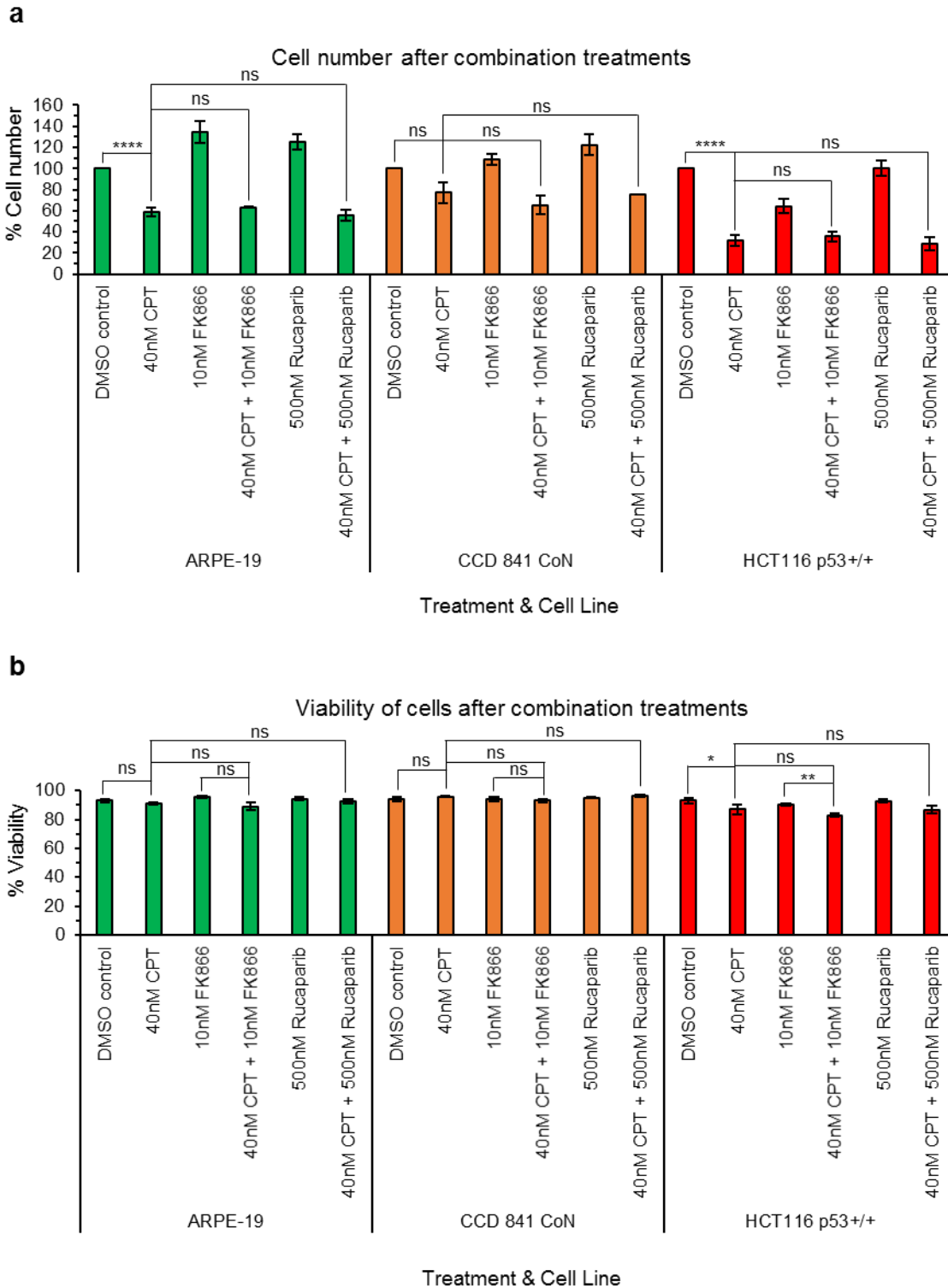


**Figure 3.27: Total cell number and viability after 48 hours camptothecin treatment of non-cancer and cancer cell lines in the presence or absence of FK866 or PARP inhibitor rucaparib.**

Average total cell number relative to DMSO vehicle control treatment (a) and % viability (b)  $\pm$  SEM of ARPE-19 and CCD 841 CoN non-cancer cells and HCT116 p53<sup>+/+</sup> cancer cells after 48 hours treatment with 10nM FK866 or 500nM rucaparib  $\pm$  40nM camptothecin (CPT). A one way ANOVA was performed where \* $p < 0.05$ , \*\* $p < 0.01$ , \*\*\*\* $p < 0.0001$ , ns=not significant,  $n=3$  biological repeats (2 technical replicates). Values determined by acridine orange (cell count) and DAPI (viability) staining (see Methods 2.3.1).

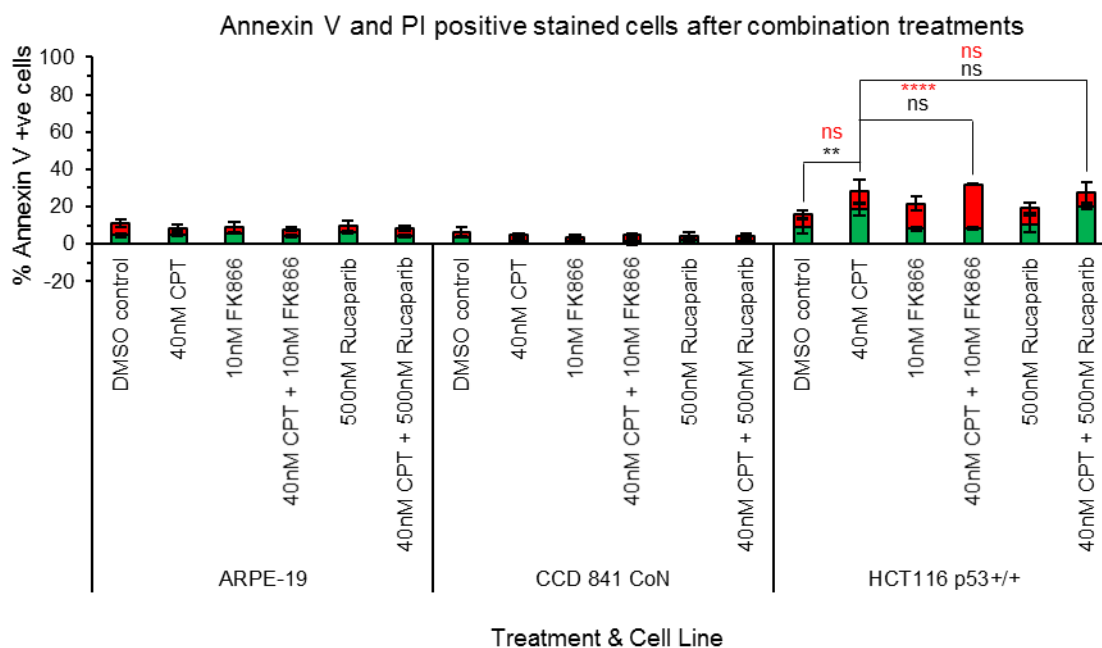


**Figure 3.28: Quantification of annexin V positive cells after treatment with camptothecin in the presence or absence of FK866 or PARP inhibitor rucaparib.**

Mean percentage ( $\pm$  SEM) of annexin V positive/PI negative and annexin V positive/PI positive ARPE-19 and CCD 841 CoN non-cancer cells and HCT116 p53<sup>+/+</sup> cancer cells after 48 hours treatment with 40nM camptothecin (CPT) in the presence or absence of 10nM FK866 or 500nM rucaparib as indicated. Green bars represent early apoptotic cells (annexin V positive only); red bars indicate late apoptotic/necrotic cells (annexin V positive, propidium iodide (PI) positive). A one way ANOVA was performed where \*\* $p < 0.01$ , \*\*\*\* $p < 0.0001$ , ns=not significant. Statistical significance in total % apoptosis indicated in black and in red for the % of late apoptotic/necrotic cells.  $n = 3$  biological repeats (2 technical replicates).

For DOX combination studies, DOX alone caused a similar reduction in cell number and viability in ARPE-19 non-cancer cells and HCT116 p53<sup>+/+</sup> cancer cells (Fig. 3.29) indicating poor cancer cell selectivity as a single agent. Similarly to CPT, DOX in combination with FK866 or rucaparib resulted in no additive or synergistic reduction in total cell number and had little further effect on cell viability (reduced from 82.4% to 76.6% in ARPE-19 cells and from 78.4% to 66% in HCT116 p53<sup>+/+</sup> for DOX in combination with FK866). Importantly, however, DOX in combination with FK866 resulted in a small but statistically significant increase in the proportion of apoptotic HCT116 p53<sup>+/+</sup> cancer cells (increased from 46.4% to 67.8%) whereas in the ARPE-19 or CCD 841 CoN non-cancer cells there was no significant change (Fig. 3.30). This indicates cancer cell selectivity of the potentiation effect. In contrast, the percentage of apoptotic HCT116 p53<sup>+/+</sup> cells following DOX and rucaparib co-treatment were similar to those with DOX alone.

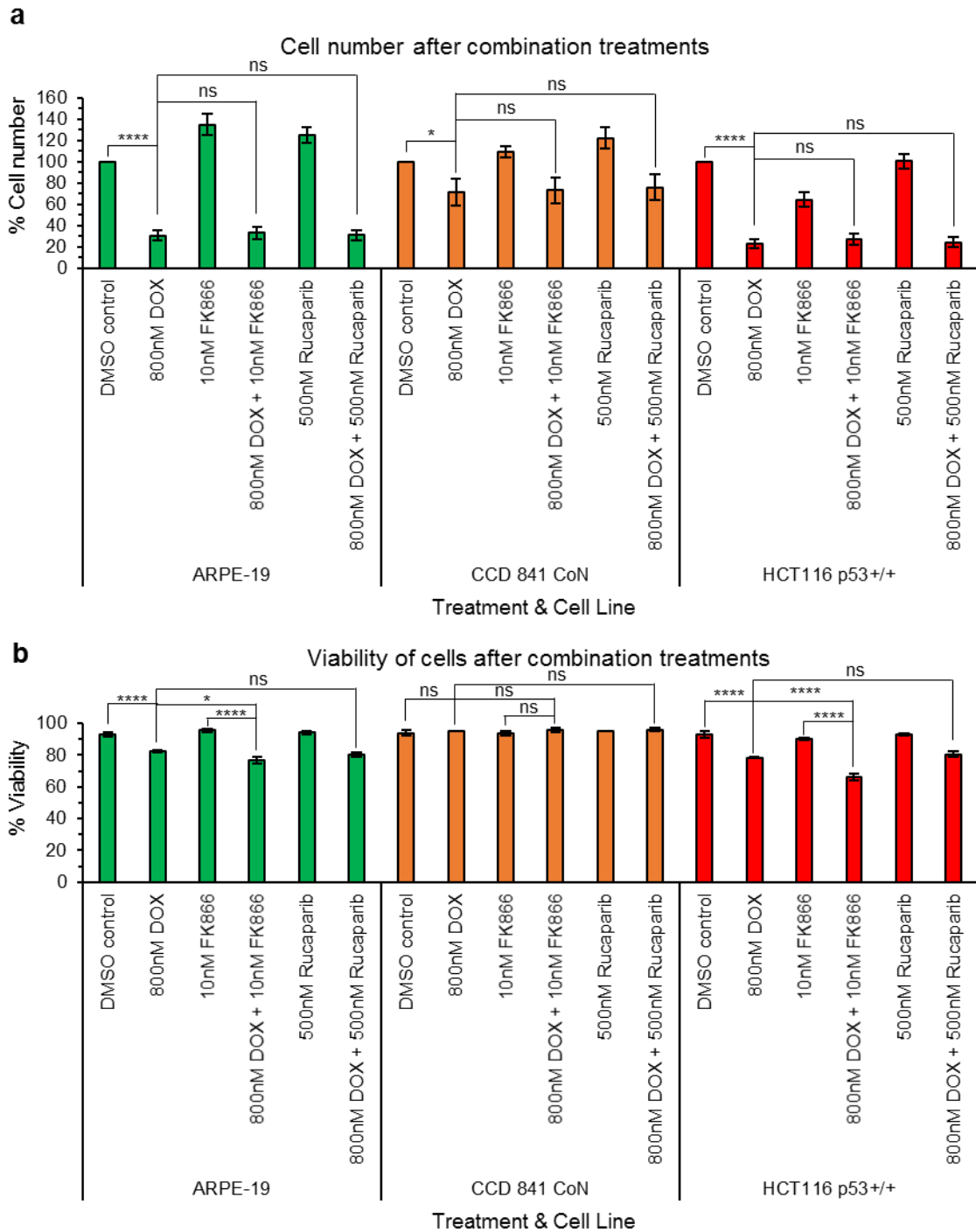


**Figure 3.29: Total cell number and viability after non-cancer and cancer cell line treatment with doxorubicin in the presence or absence of FK866 or PARP inhibitor rucaparib.**

Mean total cell number relative to DMSO vehicle control treatment (**a**) and % viability (**b**)  $\pm$  SEM of ARPE-19 and CCD 841 CoN non-cancer cells and HCT116 p53<sup>+/+</sup> cancer cells after 48 hours treatment with 10nM FK866 or 500nM rucaparib  $\pm$  800nM doxorubicin (DOX). A one way ANOVA was performed where \* $p < 0.05$ , \*\*\*\* $p < 0.0001$ , ns=not significant, n=3 biological repeats (2 technical replicates). Values determined by acridine orange (cell count) and DAPI (viability) staining (see Methods 2.3.1).

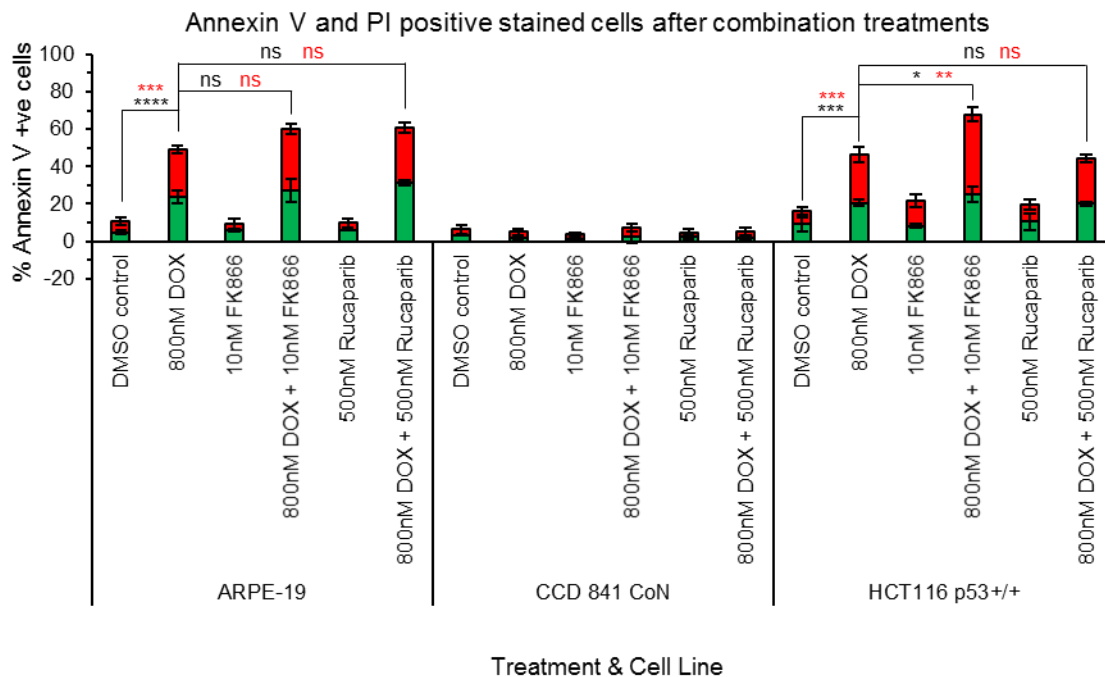


**Figure 3.30: Quantification of annexin V positive cells after treatment with doxorubicin in the presence or absence of FK866 or PARP inhibitor rucaparib.**

Mean percentage ( $\pm$  SEM) of annexin V positive/PI negative and annexin V positive/PI positive ARPE-19 and CCD 841 CoN non-cancer cells and HCT116 p53<sup>+/+</sup> cancer cells after 48 hours treatment with 800nM doxorubicin (DOX) in the presence or absence of 10nM FK866 or 500nM rucaparib. Green bars represent early apoptotic cells (annexin V positive only); red bars indicate late apoptotic/necrotic cells (annexin V positive, PI positive). A one way ANOVA was performed where \*\* $p < 0.01$ , \*\*\* $p < 0.001$ , \*\*\*\* $p < 0.0001$ , ns=not significant. Statistical significance in total % apoptosis indicated in black and in red for the % of late apoptotic/necrotic cells.  $n = 3$  biological repeats (2 technical replicates).

The most pronounced and cancer cell selective effects on cell number and viability were observed when FK866 was combined with the DNA alkylating agent TMZ (Fig. 3.31 & Fig. 3.32). TMZ treatment alone had little or no effect on cell viability in the cancer and non-cancer cells tested and caused similar small but non-significant decreases in cell number (Fig. 3.32). In contrast, TMZ in combination with FK866 caused a 74.8% decrease in cell number (cf. a 23.8% decrease with TMZ alone) and an 80% decrease in viability (cf. a 7% decrease with TMZ alone) in the HCT116 p53<sup>+/+</sup> cancer cells (Fig. 3.32;  $p < 0.001$  and  $p < 0.0001$ , respectively cf. TMZ alone). Whereas TMZ and FK866 co-treatment had no synergistic or additive effects in the ARPE-19 and CDD 841 CoN non-cancer cells, rucaparib in combination with TMZ reduced cell number in both HCT116 cancer cells and ARPE-19 non-cancer cells. TMZ and rucaparib had no significant effect on cell viability suggesting that this combination was both less

potent and less selective than the combination of FK866 and TMZ. Potentiation of TMZ by FK866 in the HCT116 cancer cells but not in the ARPE-19 or CCD 841 CoN non-cancer cells was also evident in apoptotic assays (Fig. 3.33) whereas no potentiation was observed combining rucaparib with TMZ.

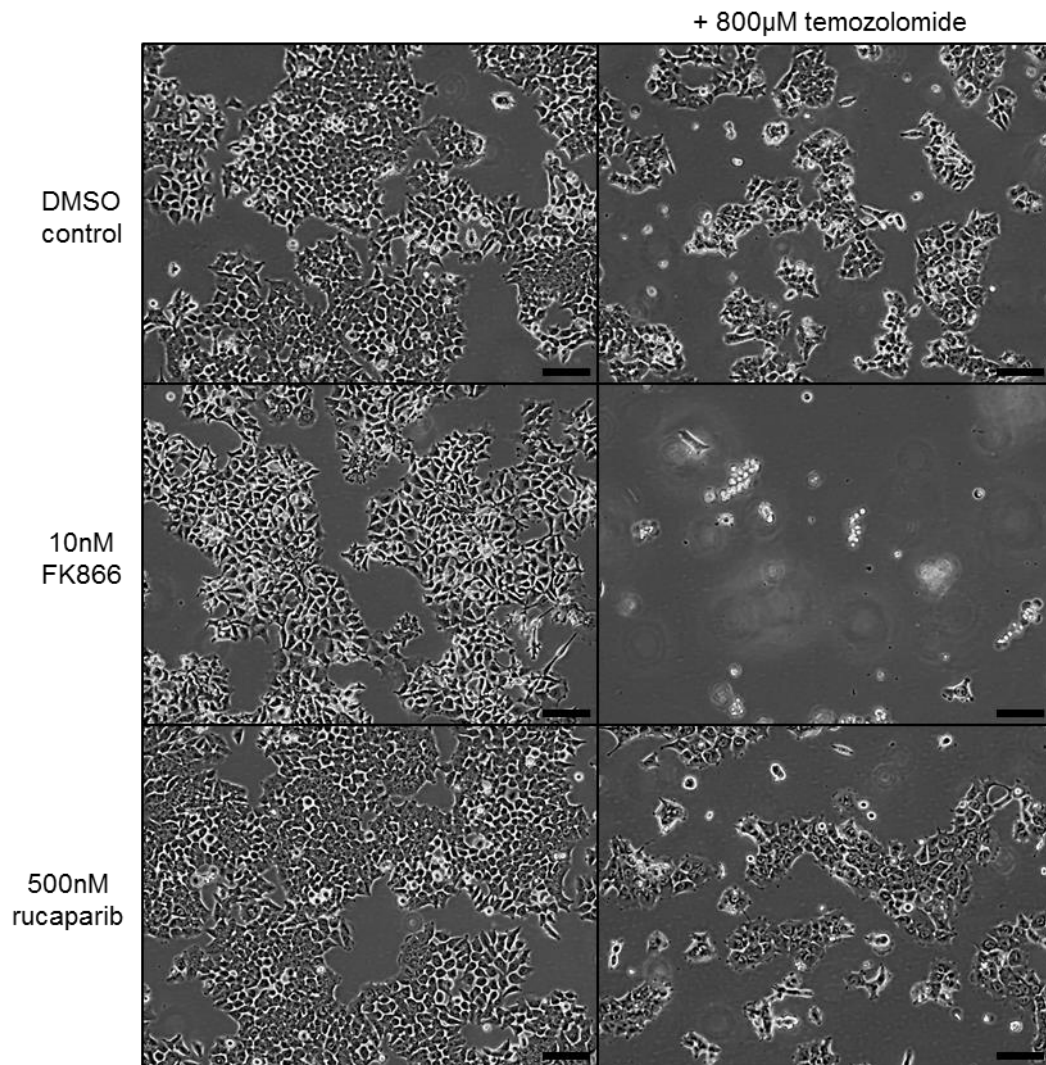


**Figure 3.31: Cell micrographs of HCT116 p53<sup>+/+</sup> cancer cells after 48 hours treatment of temozolomide in the absence or presence of FK866 or PARP inhibitor rucaparib.** Representative cell micrographs of HCT116 p53<sup>+/+</sup> cancer cells treated with 10nM FK866 or 500nM rucaparib ± 800µM temozolomide (TMZ) for 48 hours. Images taken with x10 objective; scale bar represents 100µm. n=3 biological repeats.

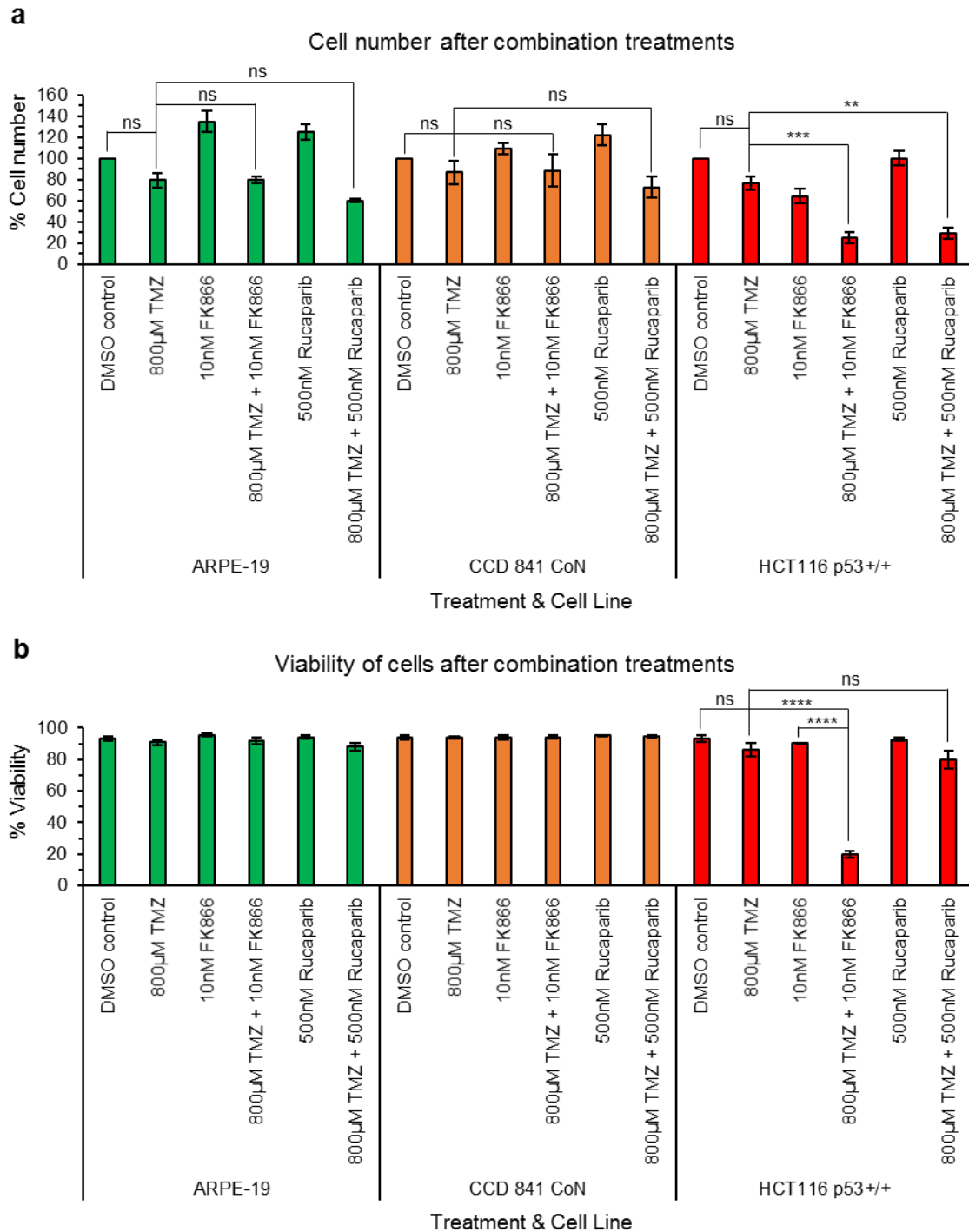


**Figure 3.32: Total cell number and viability after 48 hours temozolomide treatment of non-cancer and cancer cell lines in the presence or absence of FK866 or PARP inhibitor rucaparib.**

Average total cell number relative to DMSO vehicle control treatment (a) and % viability (b)  $\pm$ SEM of ARPE-19 and CCD 841 CoN non-cancer cells and HCT116 p53<sup>+/+</sup> cancer cells after 48 hours treatment with 10nM FK866 or 500nM rucaparib  $\pm$  800µM temozolomide (TMZ). A one way ANOVA was performed where \*\*p<0.01, \*\*\*\*p<0.0001, ns=not significant, n=3 biological repeats (2 technical replicates). Values determined by acridine orange (cell count) and DAPI (viability) staining (see Methods 2.3.1).

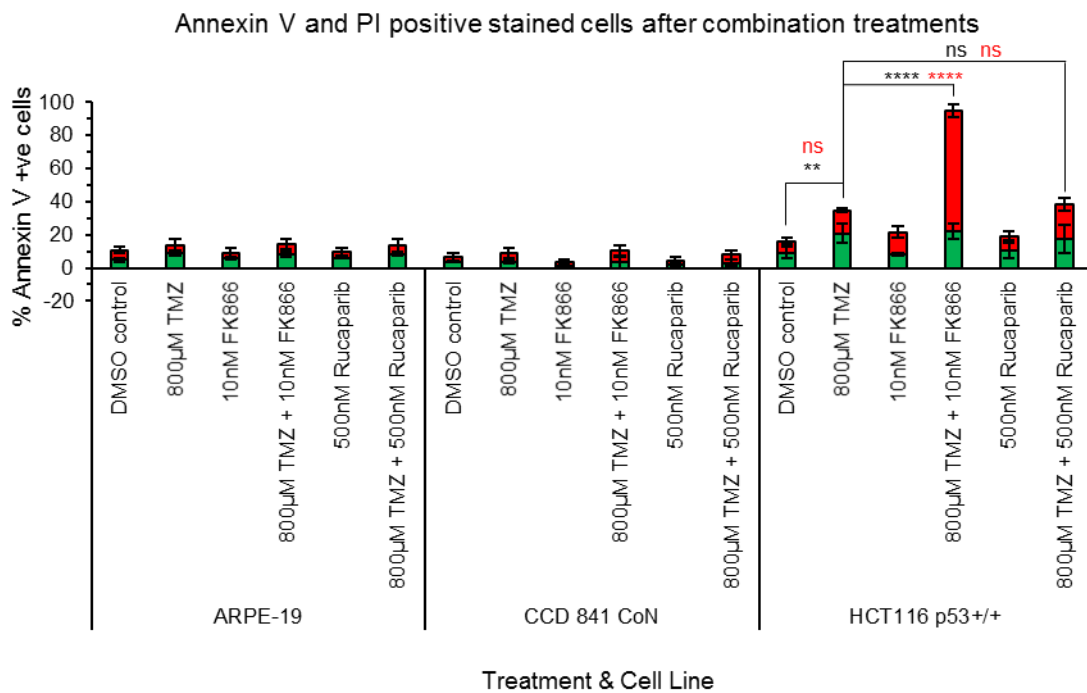


**Figure 3.33: Quantification of annexin V positive cells after treatment with temozolomide in the presence or absence of FK866 or PARP inhibitor rucaparib.**

Mean percentage ( $\pm$  SEM) of annexin V positive/PI negative and annexin V positive/PI positive ARPE-19 and CCD 841 CoN non-cancer cells and HCT116 p53<sup>+/+</sup> cancer cells after 48 hours treatment with 800µM temozolomide (TMZ) in the presence or absence of 10nM FK866 or 500nM rucaparib as indicated. Green bars represent early apoptotic cells (annexin V positive only); red bars indicate late apoptotic/necrotic cells (annexin V positive, PI positive). A one way ANOVA was performed where \*\* $p < 0.01$ , \*\*\*\* $p < 0.0001$ , ns=not significant. Statistical significance in total % apoptosis indicated in black and in red for the % of late apoptotic/necrotic cells.  $n = 3$  biological repeats (2 technical replicates).

Similar potentiation of TMZ by FK866 was also observed in isogenic p53-null HCT116 cancer cells (Fig. 3.34 & Fig. 3.35) indicating that potentiation effects are independent of p53 status.

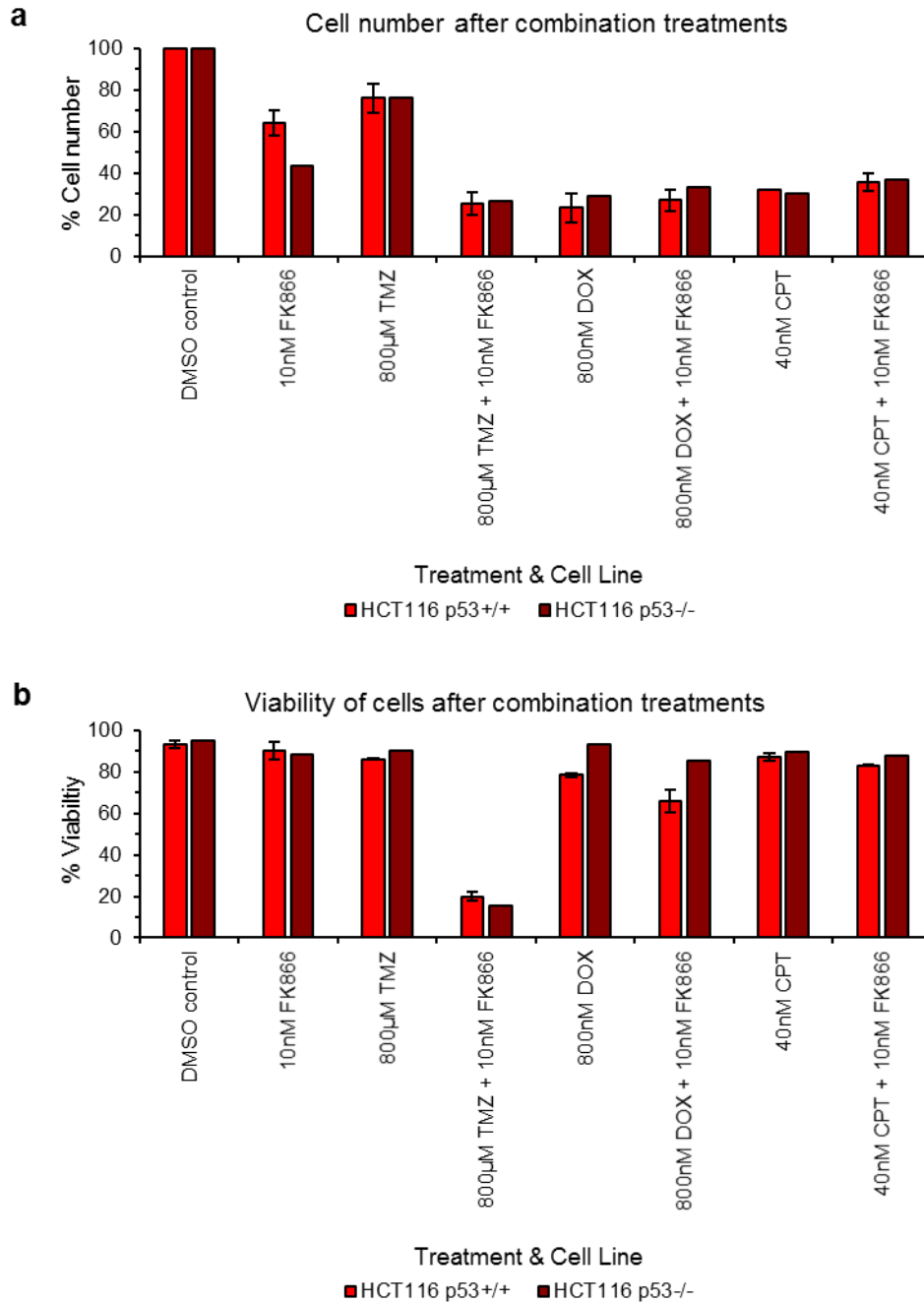


**Figure 3.34: Total cell number and viability of isogenic HCT116 p53<sup>+/+</sup> and HCT116 p53<sup>-/-</sup> cancer cells after combination treatments of DNA-damaging chemotherapeutic agents with FK866.**

Total cell number relative to DMSO control treated cells (a) and cell viability (b) after 48 hours treatment with the indicated combination treatments in HCT116 p53<sup>+/+</sup> and HCT116 p53<sup>-/-</sup> cancer cells, n=3 biological repeats (2 technical replicates per repeat) for HCT116 p53<sup>+/+</sup> and n=1 biological repeat (2 technical replicates) for HCT116 p53<sup>-/-</sup>. Values determined by acridine orange (cell count) and DAPI (viability) staining (see Methods 2.3.1).

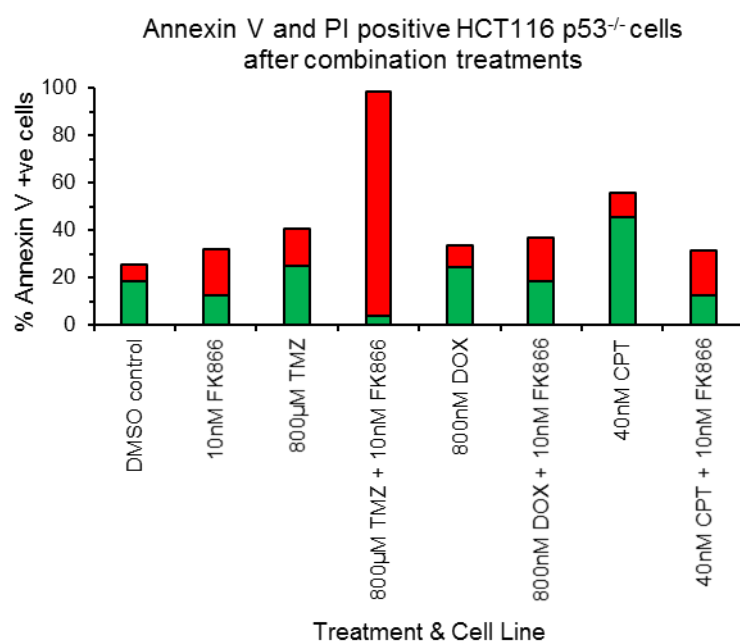


**Figure 3.35: Quantification of annexin V positive cells after combination treatments of DNA-damaging chemotherapeutic agents with FK866 in HCT116 p53<sup>-/-</sup> cancer cells.**

Percentage of annexin V positive/PI negative and annexin V positive/PI positive HCT116 p53<sup>-/-</sup> cancer cells after 48 hours treatment with the indicated combination treatments. Green bars represent early apoptotic cells (annexin V positive only); red bars indicate late apoptotic/necrotic cells (annexin V positive, PI positive), n=1 biological repeat (2 technical replicates).

As chemotherapeutic drug potentiation by FK866 was most pronounced using the DNA-alkylating agent TMZ, it was assessed whether similar potentiation of TMZ by FK866 occurs in other cancer cells of different tissue origin (Fig. 3.36 & Fig. 3.37). In both A2780 and CP70/A2780cis cisplatin-resistant human ovarian cancer cells, FK866 in combination with TMZ caused a notable reduction in both cell number and viability (Fig. 3.36). Interestingly, rucaparib in combination with TMZ similarly reduced ovarian cancer cell number but had little effect on cell viability. Potentiation of TMZ by FK866 resulting in loss of cell viability was also observed in MDA-MB-231 triple negative breast cancer cells, whereas in A549 lung cancer cells, FK866 and rucaparib in combination in TMZ both resulted in reduced cell number suggestive of effects on cell proliferation. Consistent with potentiation effects on cell viability observed by DAPI uptake (Fig. 3.36), FK866 in combination with TMZ led to an increase in annexin V and PI positive (late apoptotic/necrotic) cells in A2780, CP70/A2780cis and MDA-MB-231 cancer cells but not in A549 lung cancer cells (Fig. 3.37).

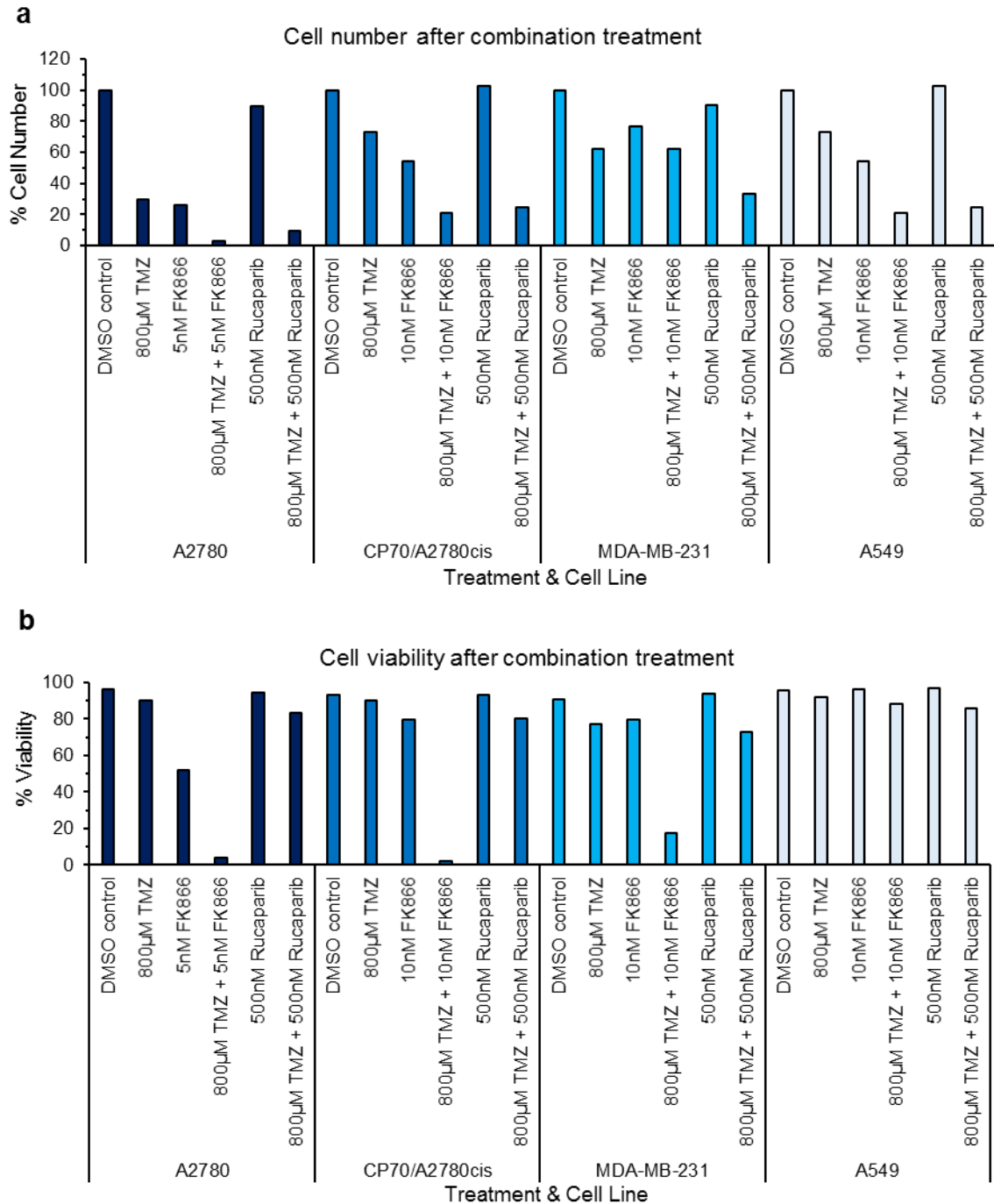


**Figure 3.36: Total cell number and viability in other cancer cells after 48 hours treatment with temozolomide in the presence or absence of FK866 or rucaparib.**

Total cell number relative to DMSO vehicle control treatment (**a**) and % viability (**b**) after 48 hours treatment with 5nM/10nM FK866 or 500nM rucaparib ± 800µM temozolomide (TMZ) in A2780, CP70/A2780cis, MDA-MB-231 and A549 cancer cells. n=1 biological repeat (2 technical replicates). Values determined by acridine orange (cell count) and DAPI (viability) staining (see Methods 2.3.1).

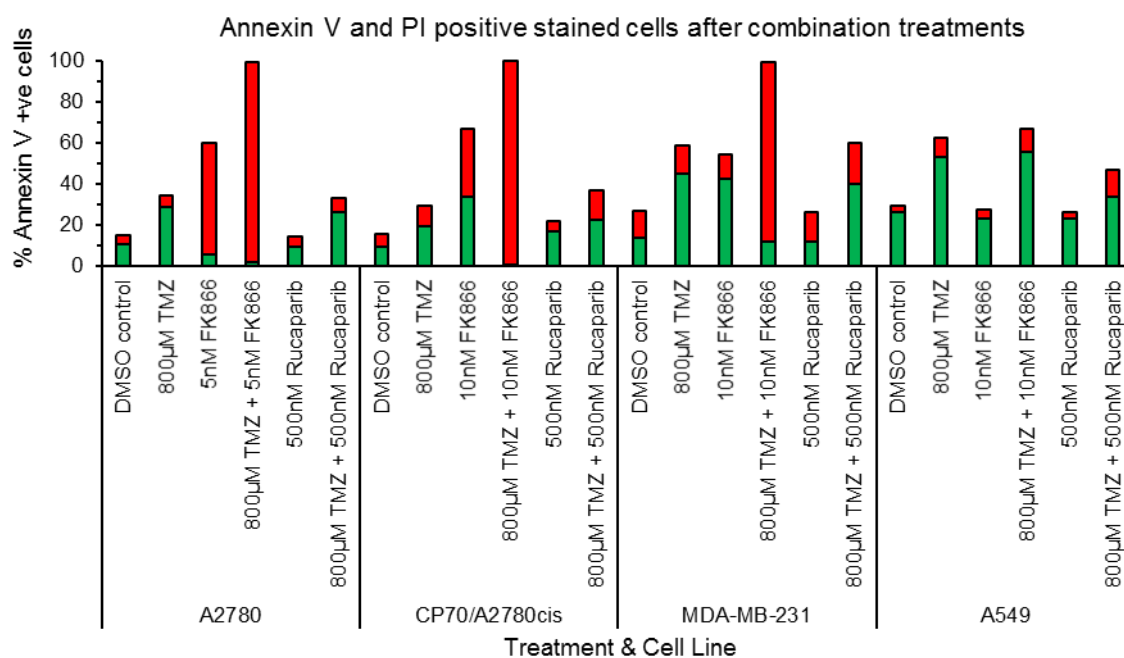


**Figure 3.37: Quantification of annexin V positive cells after 48 hours treatment with temozolomide in the presence or absence of FK866 or PARP inhibitor rucaparib.** Percentage of annexin V positive/PI negative and annexin V positive/PI positive A2780, CP70/A2780cis MDA-MB-231 and A549 cancer cells after 48 hours of 5nM/10nM FK866 or 500nM rucaparib ± 800µM temozolomide (TMZ). Green bars represent early apoptotic cells (annexin V positive only); red bars indicate late apoptotic/necrotic cells (annexin V positive, PI positive), n=1 biological repeat (2 technical replicates).

### 3.2.10 Effect of FK866 in combination with microtubule targeting chemotherapeutic agent paclitaxel

It was hypothesised that FK866 potentiates TMZ and certain other DNA-damaging agents, due to a reduction of DNA repair via reduced PARP activity (Fig. 3.22) or by other NAD(H)-associated mechanisms resulting in enhanced DNA damage. On this basis, it was further hypothesised that FK866 would not potentiate chemotherapeutic agents acting via a different mechanism of action that is independent of DNA damage. As an initial assessment of this, the microtubule targeting agent paclitaxel, which binds to microtubule polymers preventing their disassembly and progression of mitosis, was tested (Weaver, 2014). No additive or synergistic effects on cell number, apoptosis or total cell viability were seen when paclitaxel was combined with FK866 (Fig. 3.38 & Fig. 3.39).

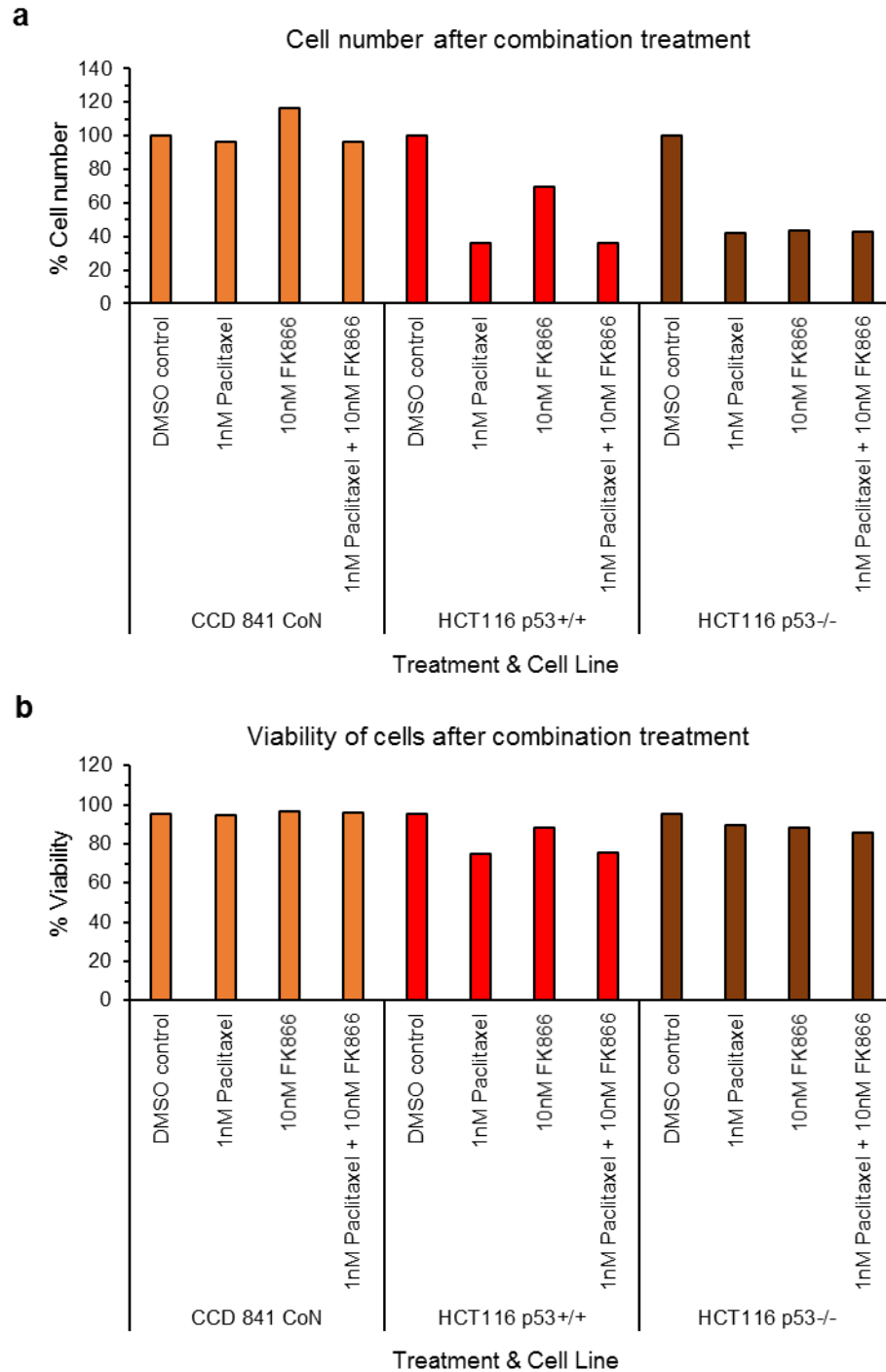


**Figure 3.38: Cell number and viability after 48 hours treatment of cancer and non-cancer cells with paclitaxel in the presence or absence of FK866.**

Total cell number relative to DMSO vehicle control treatment (a) and % cell viability (b) after 48 hours treatment with 10nM FK866 ± 1nM paclitaxel in CCD 841 CoN non-cancer cells and HCT116 p53<sup>+/+</sup> and HCT116 p53<sup>-/-</sup> cancer cells, n=1 biological repeat (2 technical replicates). Values determined by acridine orange (cell count) and DAPI (viability) staining (see Methods 2.3.1).

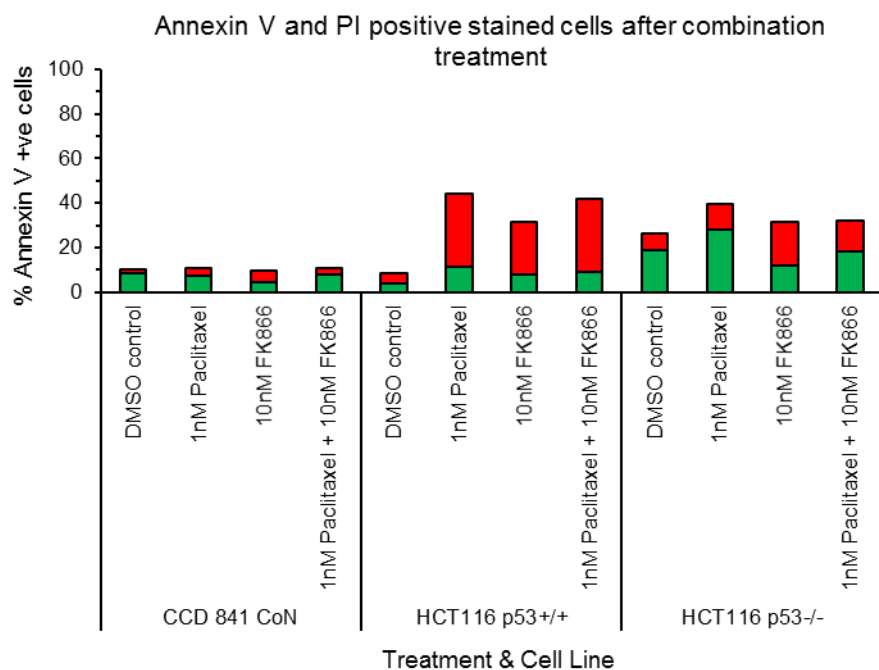


**Figure 3.39: Quantification of annexin V positive cells after treatment with paclitaxel in the presence or absence of FK866.**

Percentage of annexin V positive/PI negative and annexin V positive/PI positive CCD 841 CoN non-cancer cells and HCT116 p53<sup>+/+</sup> and HCT116 p53<sup>-/-</sup> cancer cells after 48 hours of 10nM FK866 ± 1nM paclitaxel. Green bars represent early apoptotic cells (annexin V positive only); red bars indicate late apoptotic/necrotic cells (annexin V positive, PI positive), n=1 biological repeat (2 technical replicates).

### 3.2.11 Potentiation of temozolomide by PARP1 knock-down is not selective to cancer cells

The cancer cell selective effects of TMZ in combination with FK866 on cell number and viability were compared with the effects of PARP1 knock-down by RNAi and TMZ treatment. Figure 3.40 shows the reduction in levels of PARP1 protein by PARP1 siRNA in the HCT116 p53<sup>+/+</sup> cancer cells 72 hours following siRNA transfection.

ARPE-19 non-cancer cells and HCT116 p53<sup>+/+</sup> cancer cells were transfected with PARP1 siRNA and 24 hours later were treated with TMZ for 48 hours.

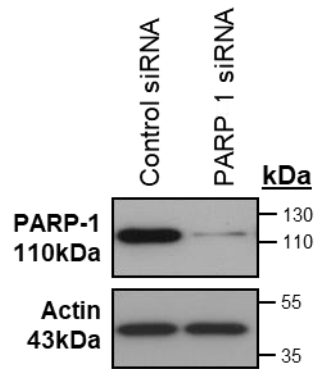


**Figure 3.40: RNAi mediated PARP1 silencing in HCT116 p53<sup>+/+</sup> cancer cells.**

Western blot analysis of PARP1 protein in HCT116 p53<sup>+/+</sup> cancer cells after PARP1 or control siRNA transfection for 72 hours, actin used as loading control. n=1 biological repeat.

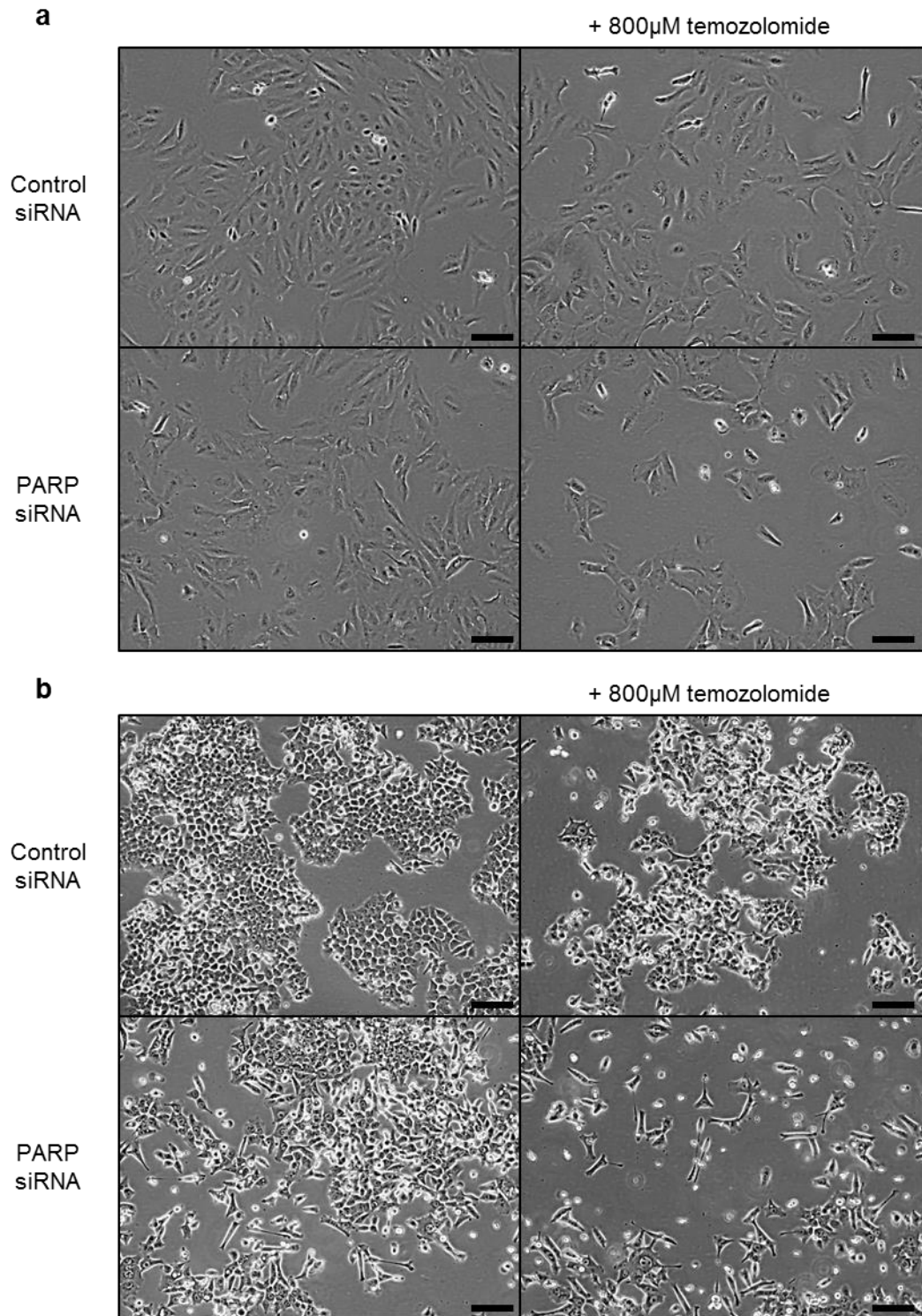


**Figure 3.41: Cell micrographs after 48 hours temozolomide treatment following transfection with control or PARP1 siRNA.** Representative cell images of ARPE-19 non-cancer cells (**a**) and HCT116 p53<sup>+/+</sup> cancer cells (**b**) after 48 hours treatment with 800 $\mu$ M temozolomide (TMZ) following transfection with control or PARP1 siRNA. Images taken with x20 objective and scale bar represents 100 $\mu$ m.

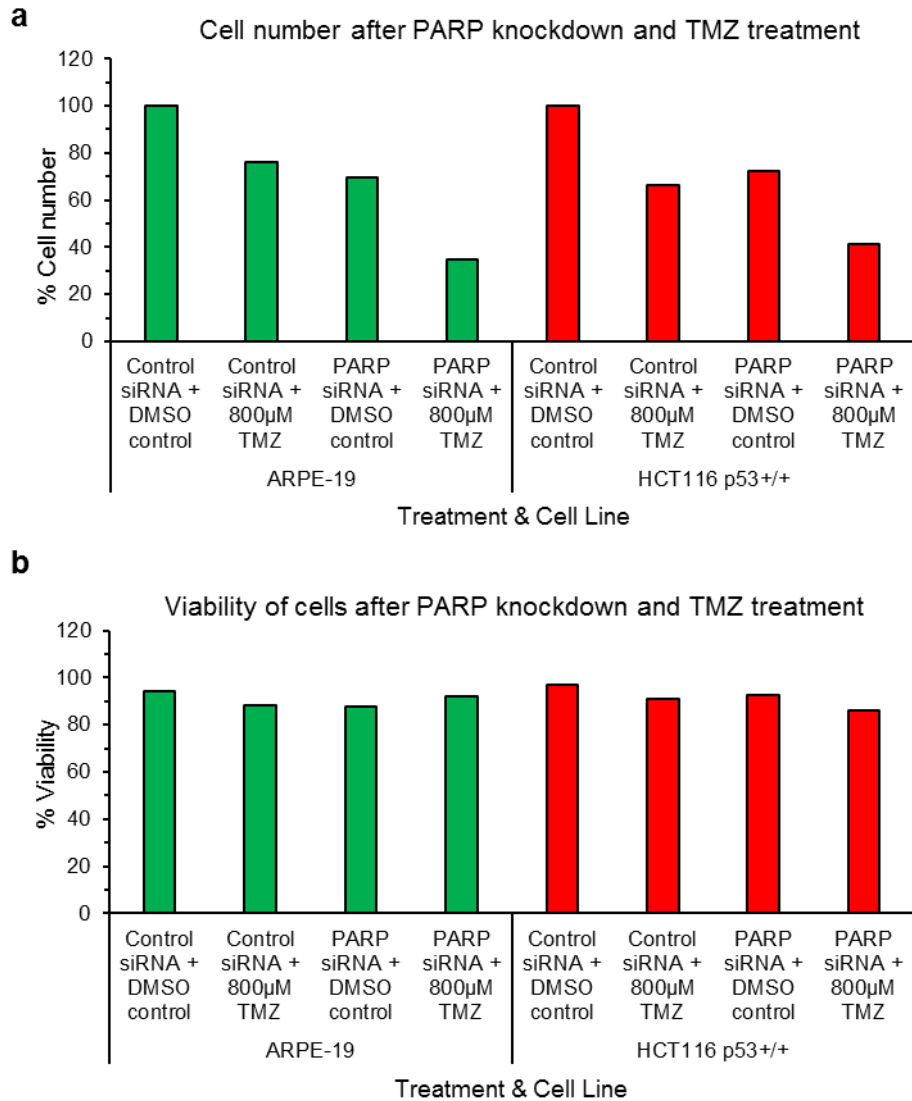


**Figure 3.42: Cell number and viability after RNAi-mediated PARP1 knock-down and temozolomide treatment.**

Average total cell number relative to control knock-down/treatment (a) and % cell viability (b) of ARPE-19 non-cancer cells and HCT116 p53<sup>+/+</sup> cancer cells after 72 hours following PARP1 siRNA transfection ± 800µM temozolomide (TMZ) treatment for 48 hours. n=1 biological repeat (2 technical replicates). Values determined by acridine orange (cell count) and DAPI (viability) staining (see Methods 2.3.1).

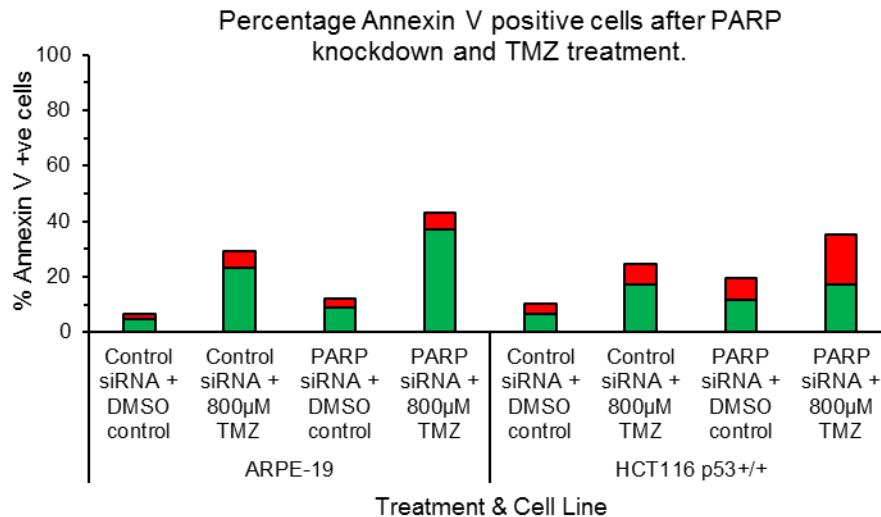


**Figure 3.43: Quantification of annexin V positive cells after RNAi-mediated PARP1 knockdown and temozolomide treatment.**

Average percentage of annexin V positive/PI negative and annexin V positive/PI positive ARPE-19 non-cancer cells and HCT116 p53<sup>+/+</sup> cancer cells 72 hours following PARP1 or control siRNA transfection ± 48 hours 800µM temozolomide (TMZ) treatment. Green bars represent early apoptotic cells (annexin V positive only); red bars indicate late apoptotic/necrotic cells (annexin V positive, PI positive), n=1 biological repeat (2 technical replicates).

The combination of PARP knock-down (Fig. 3.40) and TMZ had little or no effect on cell viability (Fig. 3.42b). In contrast, total cell number was reduced from 69.4% (TMZ + control siRNA) to 34.8% (TMZ + PARP siRNA) in the ARPE-19 non-cancer cells and from 66.1% (TMZ + control siRNA) to 41.1% (TMZ + PARP siRNA) in HCT116 p53<sup>+/+</sup> cancer cells. This indicates no selectivity in any potentiation of TMZ through targeting of PARP directly. This was also supported by an annexin V assay which showed a small increase in total apoptotic cells in both non-cancer and cancer cells in PARP1 siRNA transfected cells in combination with TMZ (Fig. 3.43).

### 3.2.12 Reduction in NAD(H) and PARP activity and temozolomide potentiation in GBM1 cancer stem cell-like cells

As there was a clear difference in FK866 IC<sub>50</sub> between the human cancer stem cell-like GBM1 model and NP1 non-cancer neural progenitor cells (oligopotent, ‘stem-like’) cells (Table 3.1, Fig. 3.7) it was hypothesised that FK866 may be able

to induce similar selective effects in these models. Whether FK866 is able to potentiate TMZ in this context was also a very important question as TMZ is part of standard clinical treatment for glioblastomas.

Similar to the cancer-selective metabolic effects of FK866 on glycolysis and mitochondrial respiration observed in HCT116 p53<sup>+/+</sup> cancer cells, GBM1 cells that had been treated with FK866 (2.5nM) were less able to increase respiration and glycolysis in response to metabolic stress (Fig. 3.44b). Effects were less pronounced in the non-cancer NP1 cells (Fig. 3.44a).

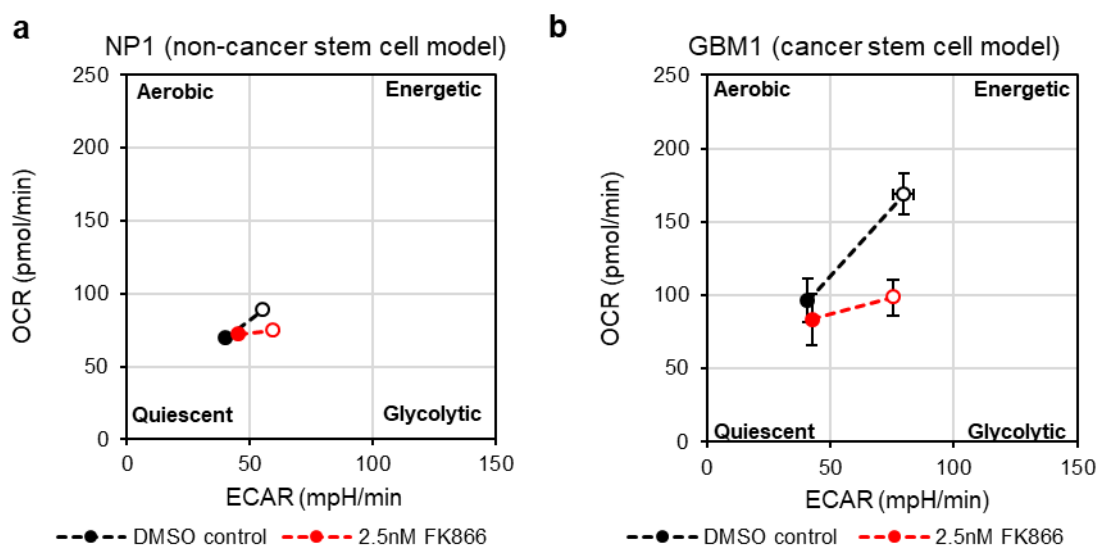


**Figure 3.44: Cell energy phenotype of NP1 and GBM1 cells following 24 hours 2.5nM FK866 treatment.**

NP1 neural progenitor cells (a) and the GBM1 cancer stem cell-like cell model (b) were treated with 2.5nM FK866 or DMSO vehicle control for 24 hours prior to analysis. The cell energy phenotypes are shown compared to DMSO control cells; basal metabolic phenotype is indicated by closed circles; metabolic stress response/capacity is indicated by open circles. NP1, n=1 biological repeat (3 technical replicates). GBM1, n=2 biological repeats (3 technical replicates) with SEM indicated.

Cancer selective effects on metabolism suggested that FK866 may induce differential effects on NAD(H) levels in NP1 and GBM1 cells. After treatment of the cells with a non-toxic dose of FK866 (1.25nM) for 24 hours there was a significant difference in NAD(H) depletion between the treated NP1 and GBM1 cell lines (Fig. 3.45), showing selectivity of FK866.

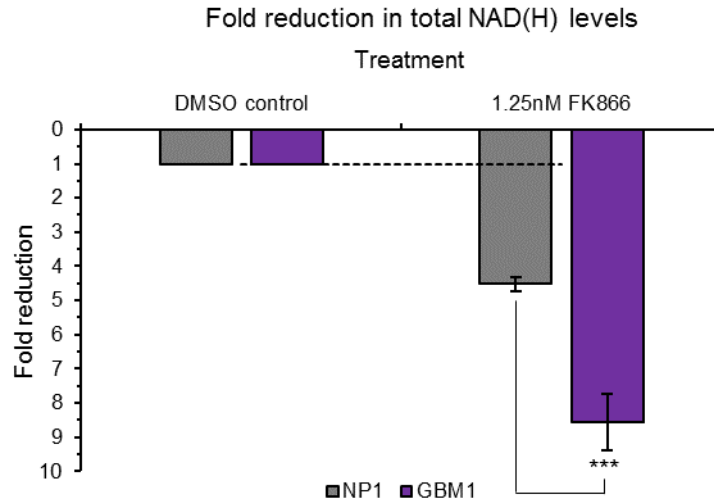


**Figure 3.45: Fold reduction in NP1 and GBM1 total cellular NAD(H) levels with 24 hours FK866 treatment.**

Mean fold reduction in total cellular NAD(H)  $\pm$  SEM, n=3 biological repeats (2 technical replicates), for GBM1 cells and NP1 neural progenitor cells after 24 hours treatment with 1.25nM FK866. Fold reduction is relative to DMSO control. A two-tailed t-test was performed where \*\*\* p<0.001.

As with ARPE-19 non-cancer cells and HCT116 p53<sup>+/+</sup> cancer cells (Fig. 3.20) it was important to see if the differential effects in NAD(H) levels could affect PARP activity selectively.

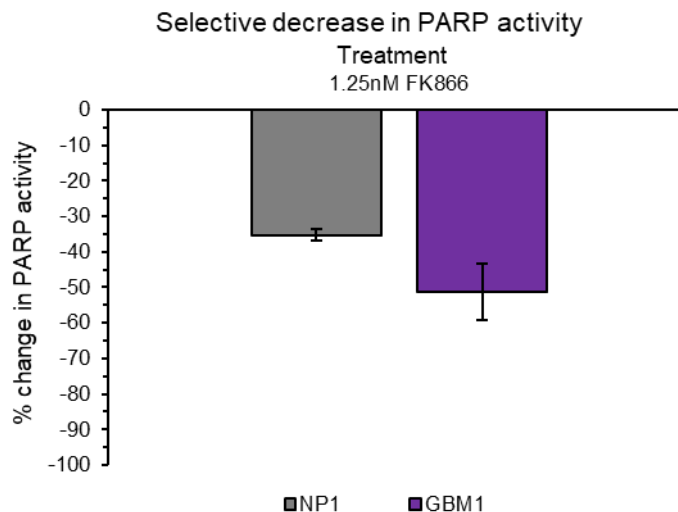


**Figure 3.46: Quantification of PARP activity after 24 hours FK866 treatment.**

Mean percentage decrease  $\pm$  SEM, n=2 biological repeats (3 technical replicates per repeat), of PARP activity in the GBM1 cancer stem cell-like cell model and NP1 neural progenitor cells after 24 hours treatment with 1.25nM FK866.

FK866 at the tested dose did preferentially decrease PARP activity in the GBM1 cancer stem cell-like cells compared to non-cancer NP1 progenitor cells (Fig. 3.46; 51.2% reduction in GBM1 cf. 35.3% in NP1). This suggested that the addition of FK866 to DNA damaging agents could potentially result in selective potentiation in the GBM1 cells.

To preliminarily examine the effects of combining the DNA damaging agent TMZ with either the direct PARP inhibitor rucaparib or with FK866, 48 hours combination chemosensitivity assays were performed (Fig. 3.47). This indicated promising potentiation of TMZ by FK866 selectively in the GBM1 cancer stem cell-like cells enabling an  $IC_{50}$  value to be reached for TMZ (349 $\mu$ M cf. >800 $\mu$ M with TMZ alone).

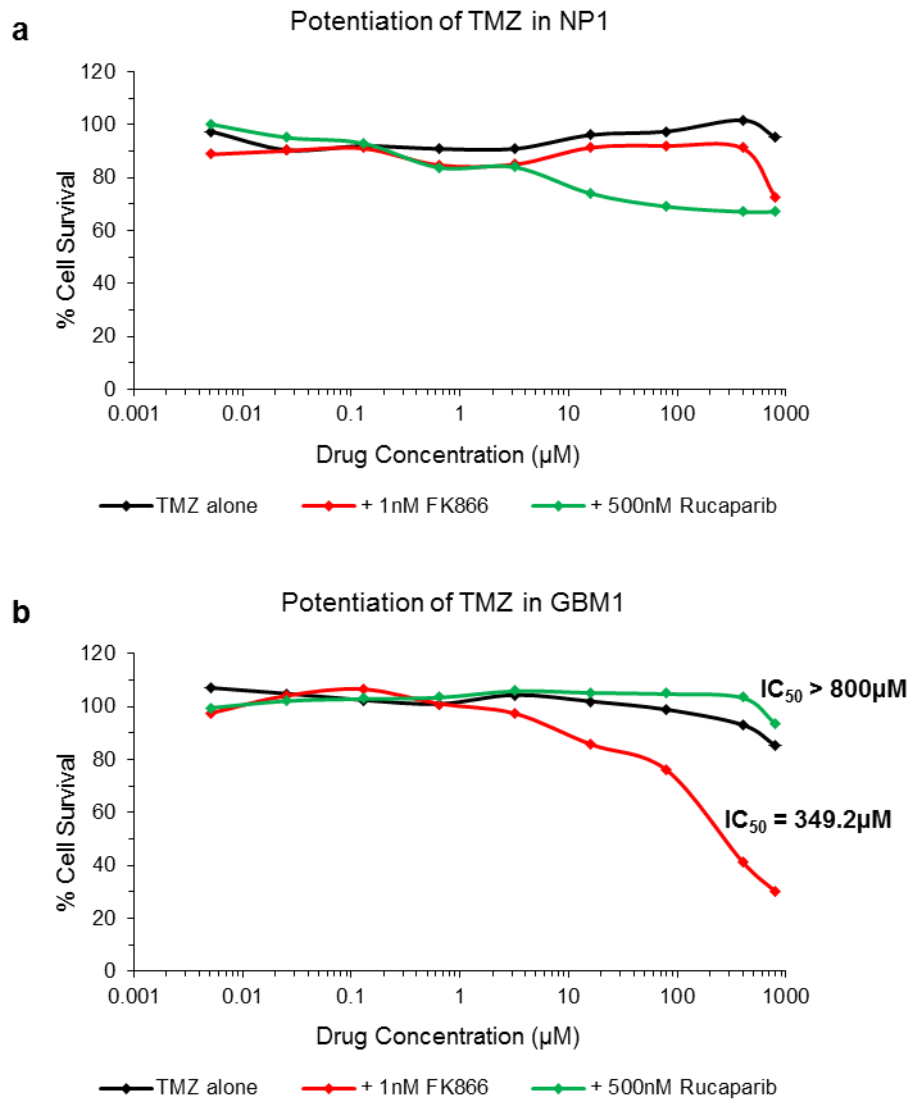


**Figure 3.47: Chemosensitivity dose response to temozolomide in the presence or absence of FK866 or rucaparib in NP1 and GBM1 cells.**

Dose response curve of NP1 neural progenitor/oligopotent cells (**a**) and the cancer stem cell-like cell model GBM1 (**b**) after 48 hours exposure to dose range of temozolomide (TMZ) alone or in combination with 1nM FK866 or 500nM rucaparib. n=1 biological repeat, (8 technical replicates).

In an independent set of experiments, T25 flasks of GBM1 cells were treated with a single dose of TMZ alone or in combination with FK866 for 48 hours with effects on total cell number, cell viability and percentage of apoptotic cells analysed (Fig. 3.48 & Fig. 3.49). Preliminary data (1 biological repeat) indicated enhanced reduction in GBM1 cell number and viability and increased levels of apoptosis with combined TMZ and FK866 treatment.

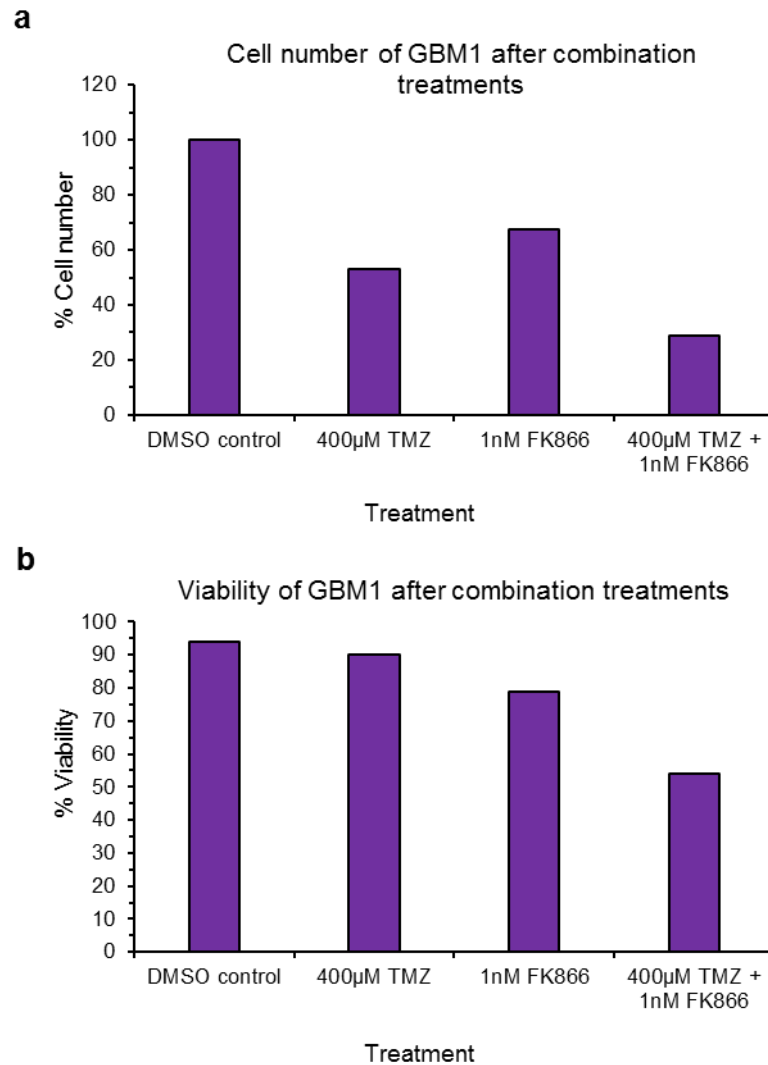


**Figure 3.48: Total cell number and viability after 48 hours temozolomide treatment in GBM1 cells in the presence or absence of FK866.**

Total cell number relative to DMSO vehicle control treatment (**a**) and % viability (**b**) of GBM1 cells after 48 hours treatment with 1nM FK866 ± 400µM temozolomide (TMZ), n=1 biological repeat (2 technical replicates). Values determined by acridine orange (cell count) and DAPI (viability) staining (see Methods 2.3.1).

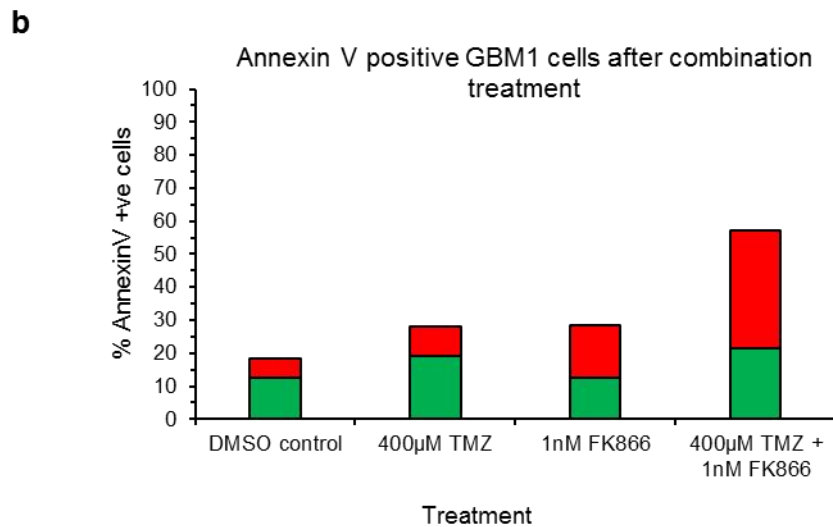
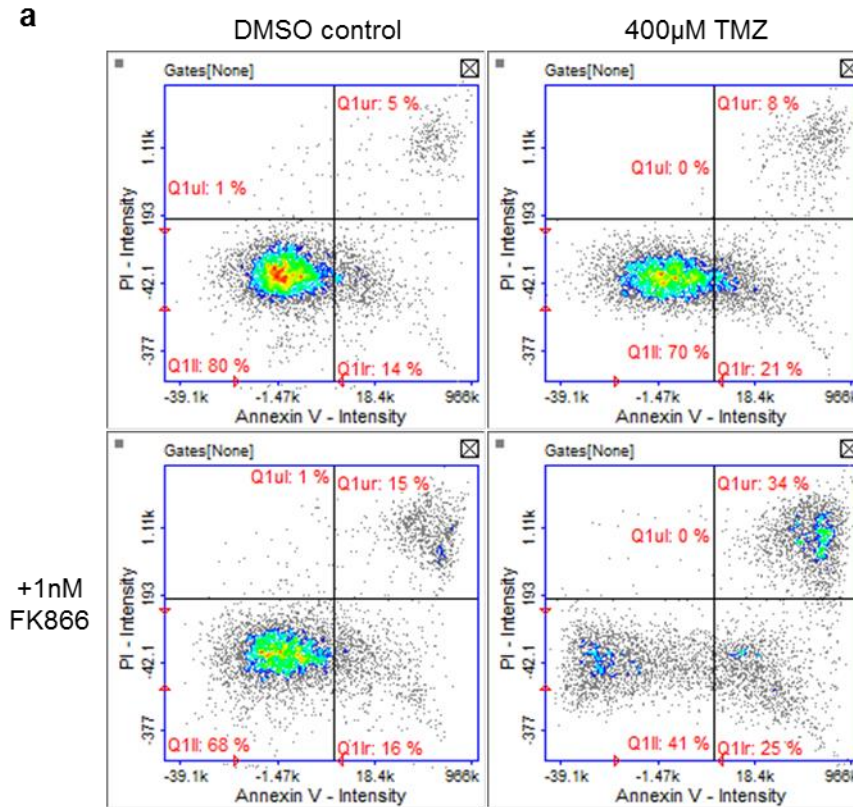


**Figure 3.49: Quantification of annexin V positive GBM1 cells after treatment with 400µM temozolomide in the absence or presence of 1nM FK866 for 48 hours.**

**a.** Annexin V assay dot plots quantifying the proportion of early apoptotic and late apoptotic/necrotic cells through differential annexin V/PI staining after treatment with 400µM temozolomide (TMZ) in the presence or absence of 1nM FK866. Lower left quadrant indicates alive cells, lower right quadrant indicates early apoptotic cells (annexin V positive, PI negative) and upper right quadrant indicates late apoptotic/necrotic cells (annexin V positive, PI positive). **b.** Bar chart summary of annexin V positive and Annexin V and PI positive cells. Green bars represent early apoptotic cells (annexin V positive only); red bars indicate late apoptotic/necrotic cells (annexin V positive, propidium iodide (PI) positive), n=1 biological repeat (2 technical replicates).

The same experiments were performed in parallel in the NP1 neural progenitor cells to assess cancer cell selectivity of effects. As Figure 3.50 shows, FK866 in combination with TMZ had no discernible adverse effect on cell growth/confluency whereas the combination of rucaparib and TMZ clearly resulted in reduced cell confluency. To further investigate this, cell number and viability assays were performed (Fig. 3.51) which indicated that effects of TMZ plus rucaparib on confluency were likely to be due to reduced cell proliferation/growth rather than induction of cell death. Cell cycle analyses showed that TMZ in combination with rucaparib resulted in loss of G1 and G2/M subpopulations and accumulation of cells in S phase, suggesting S phase cell cycle arrest (Fig. 3.52). Importantly the combination of FK866 and TMZ did not cause these effects in NP1 cells suggesting a cancer selective effect of the combination compared to direct inhibition of PARP.

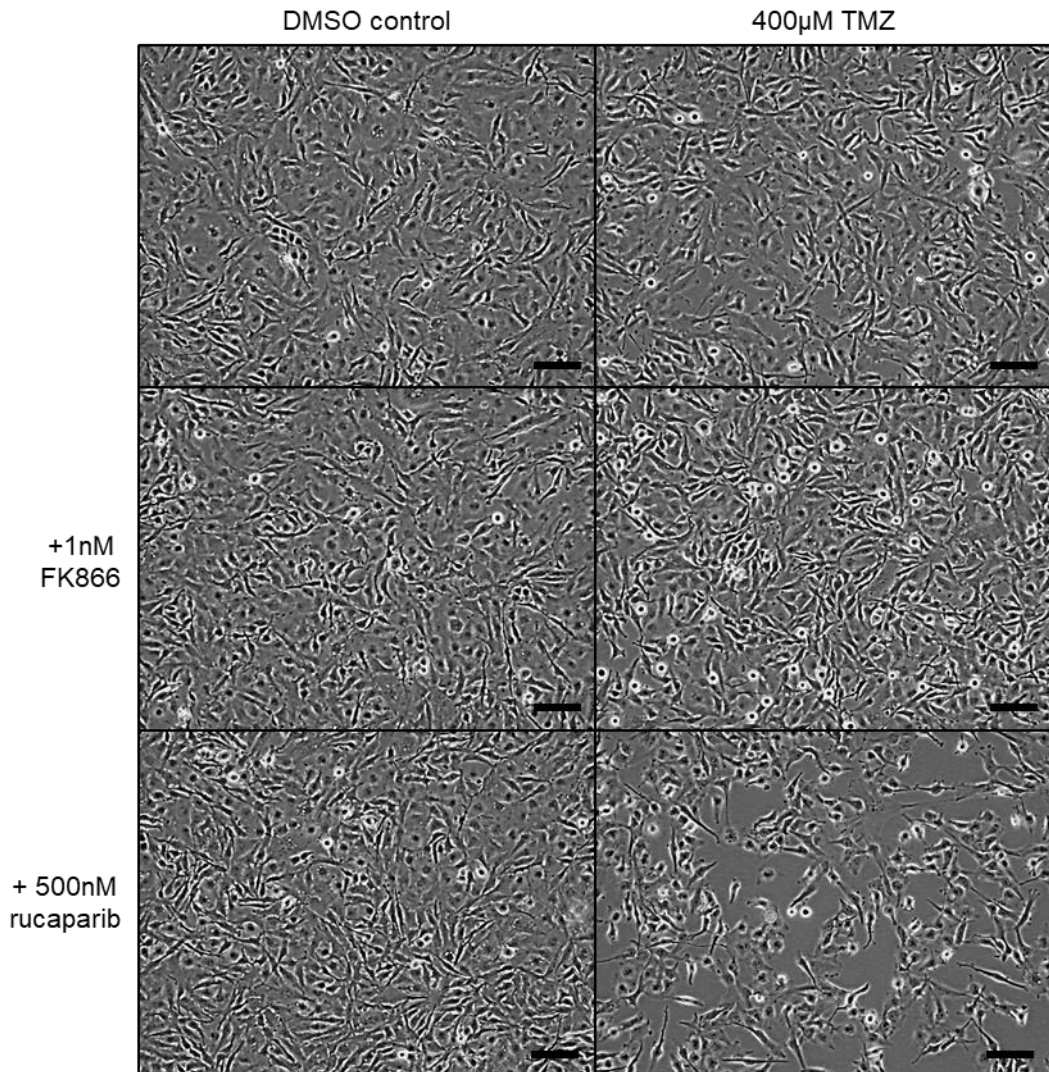


**Figure 3.50: Cell micrographs of NP1 cells after 48 hours treatment with temozolomide in the absence or presence of FK866 or PARP inhibitor rucaparib.** Cell images of NP1 neural progenitor cells after 48 hours treatment with 1nM FK866 or 500nM rucaparib  $\pm$  400µM temozolomide (TMZ). Images taken with x10 objective and scale bar represents 100µm. n=3 biological repeats.

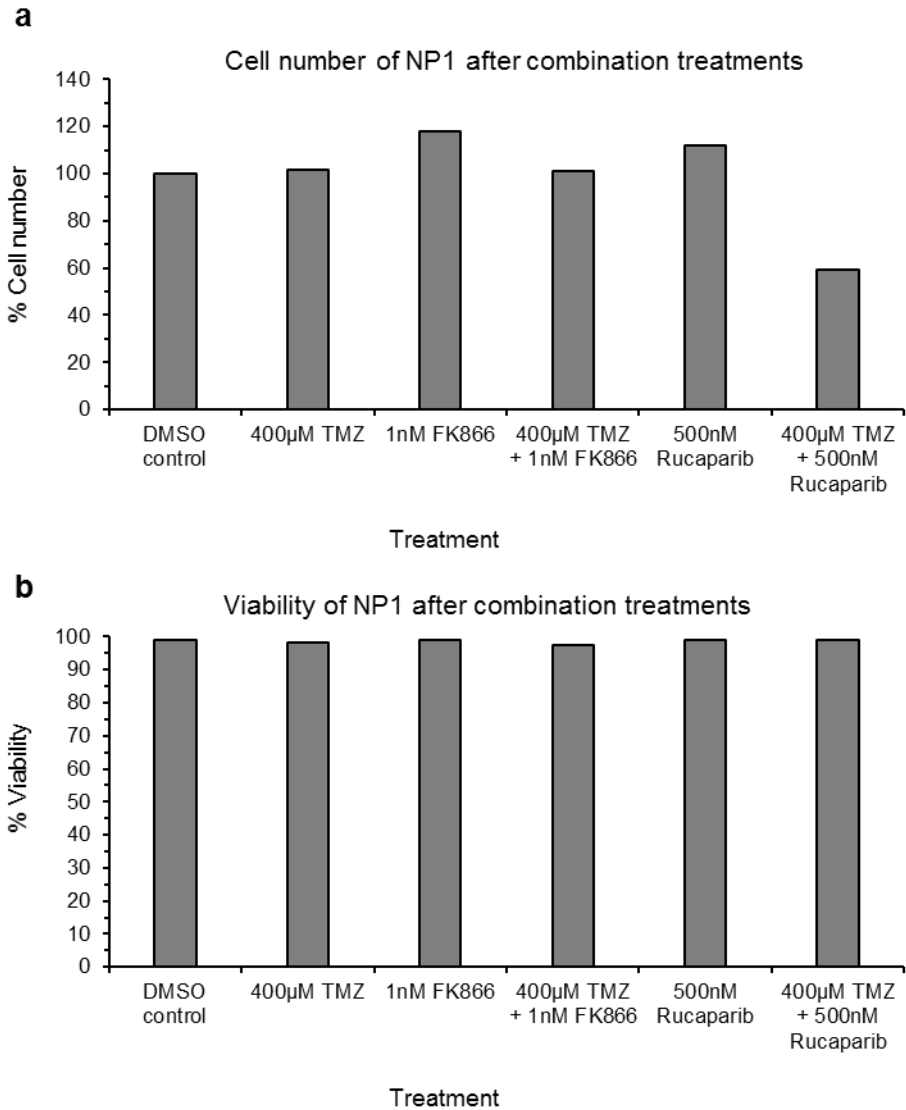


**Figure 3.51: Total cell number and viability after 48 hours temozolomide treatment in NP1 cells in the presence or absence of FK866 or rucaparib.**

Total cell number relative to DMSO vehicle control treatment (a) and % viability (b) of NP1 neural progenitor cells after 48 hours treatment with 1nM FK866 or 500nM rucaparib ± 400µM temozolomide (TMZ), n=1 biological repeat (2 technical replicates). Values determined by acridine orange (cell count) and DAPI (viability) staining (see Methods 2.3.1).

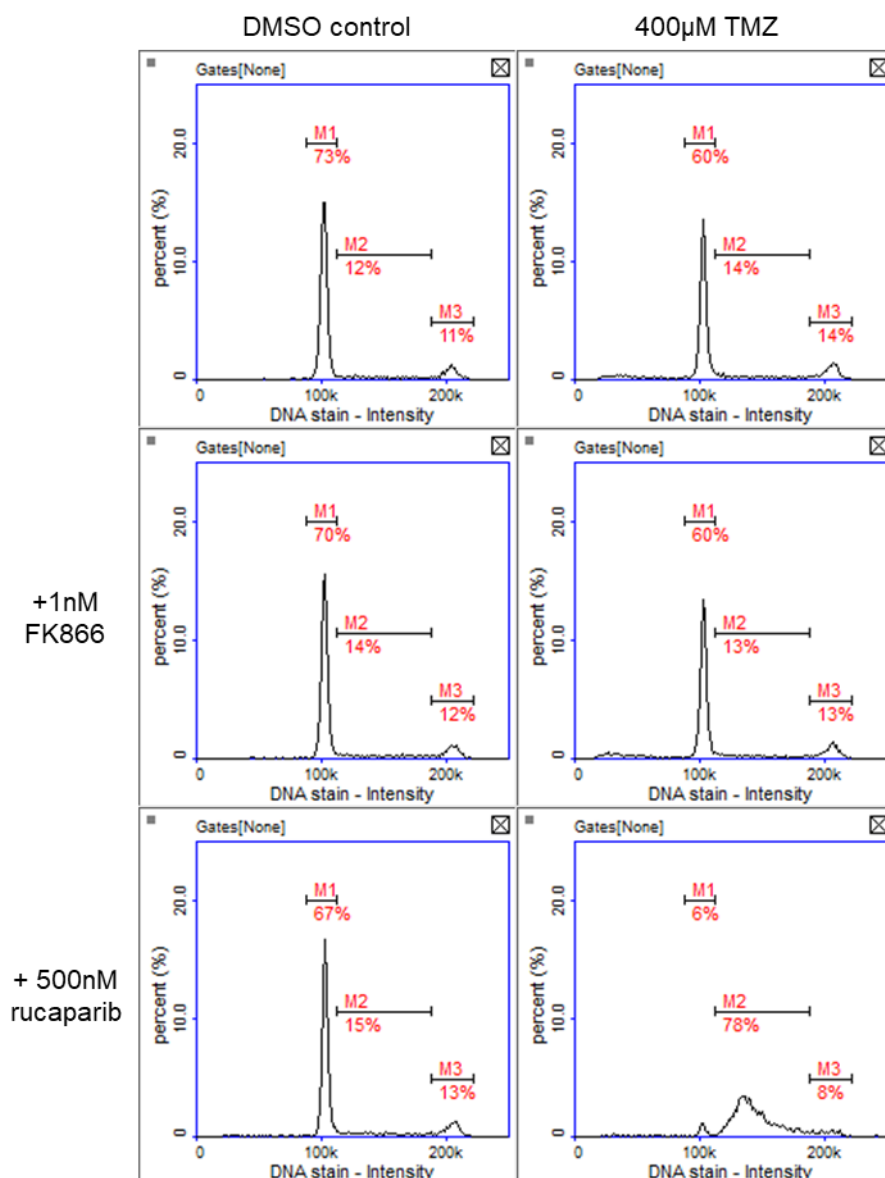


**Figure 3.52: Cell cycle analysis after combination treatment.**

Cell cycle profiles of NP1 non-cancer stem cell model treated with 1nM FK866 or 500nM rucaparib  $\pm$  400µM temozolomide (TMZ) for 48 hours. n=1 biological repeat (2 technical replicates).

### 3.2.13 Does FK866 treatment lead to an impairment in DNA repair?

Given the inhibition of PARP activity by FK866 (Fig. 3.22 & Fig. 3.46), a potential mechanism of action for the observed potentiation of DNA-damaging agents such as TMZ by FK866 is cancer cell selective reduction of PARP-mediated DNA repair. To assess this possibility further, an indirect assay of DNA repair was utilised (Allison *et al.*, 2017) based on the detection of  $\gamma$ H2AX phosphorylation as

a surrogate endpoint marker of persistent, unrepaired DNA damage. As indicated in Figure 2.2, cells were first pre-treated with FK866 to reduce cellular NAD(H) levels and then exposed to TMZ to induce SSB DNA damage which is normally efficiently repaired by PARP-mediated BER. TMZ was then ‘washed-out’ and the cells were further incubated for 6 hours to enable DNA repair followed by cell staining for phosphorylated  $\gamma$ H2AX.

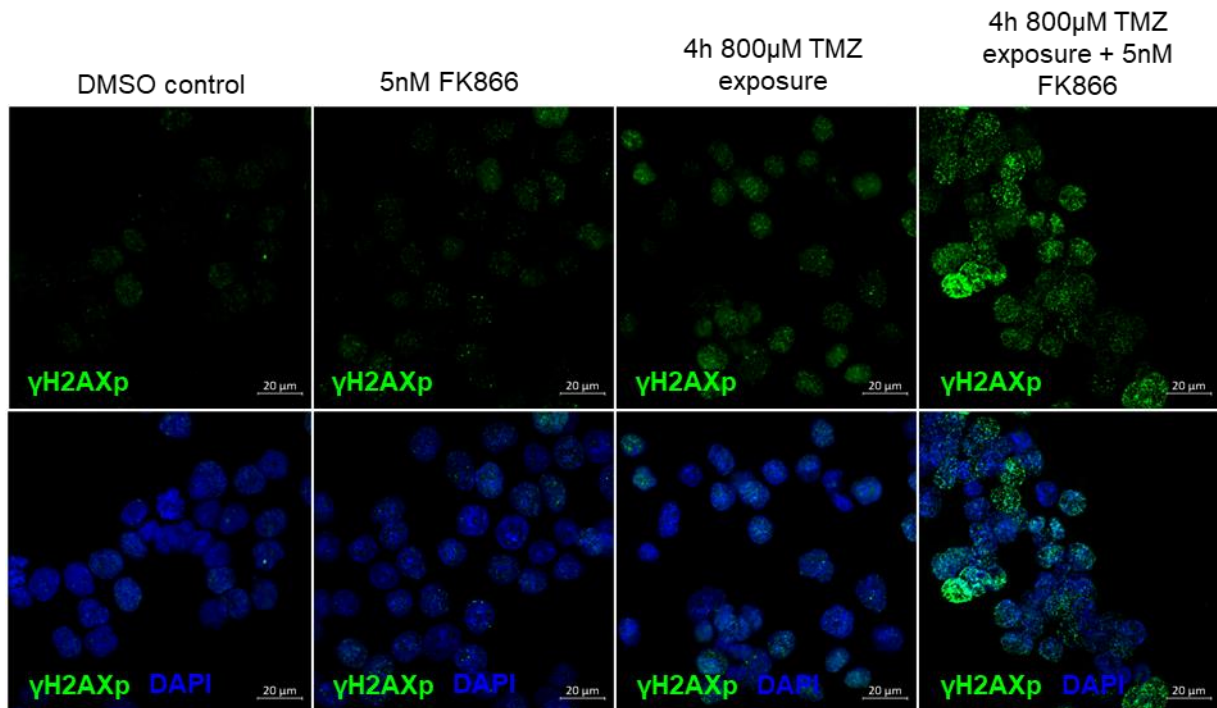


**Figure 3.53: Expression of phosphorylated gamma H2AX as a marker of DSB DNA damage in HCT116 p53<sup>+/+</sup> cancer cells after FK866 pre-treatment and temozolomide exposure.** Representative immunofluorescent images of HCT116 p53<sup>+/+</sup> cancer cells showing phosphorylated gamma H2AX (green) as a marker of DSB DNA damage and nuclear localisation marker DAPI (blue). Pre-treatment of 5nM FK866 was performed for 12 hours before addition of 800µM temozolomide (TMZ) for 4 hours, where this was then removed, and the cells were given 6 hours ‘repair-time’ before staining. Images taken with x63 objective and scale bar represents 20µm, n=1 biological repeat.

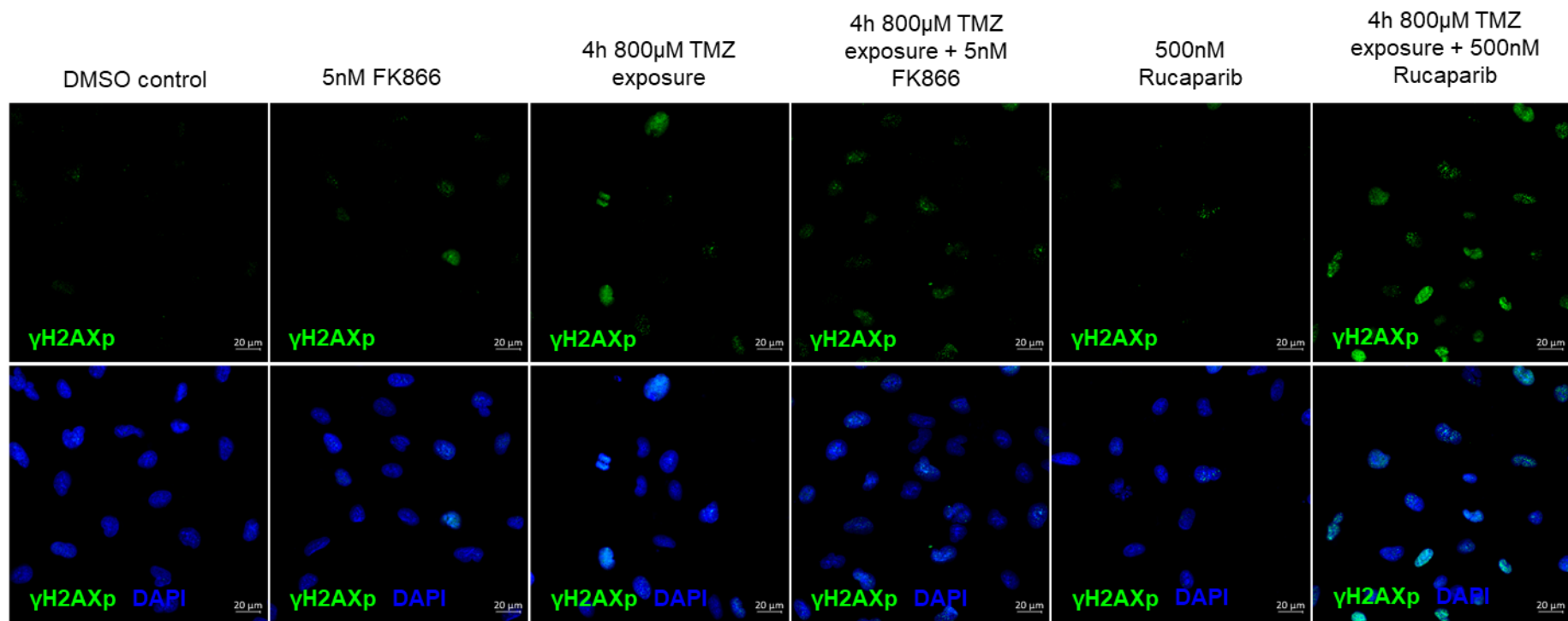


**Figure 3.54: Expression of phosphorylated gamma H2AX as a marker of DSB DNA damage in ARPE-19 non-cancer cells after FK866 or rucaparib pre-treatment and temozolomide exposure.**

Representative immunofluorescent images of ARPE-19 non-cancer cells showing phosphorylated gamma H2AX (green) as a marker of DSB DNA damage and nuclear localisation marker DAPI (blue). Pre-treatment of 5nM FK866 or 500nM rucaparib was performed for 12 hours before addition of 800µM temozolomide (TMZ) for 4 hours, where this was then removed and the cells were given 6 hours 'repair-time' before staining. Images taken with x40 objective and scale bar represents 20µm, n=1 biological repeat.

FK866 in combination with TMZ resulted in increased phosphorylated  $\gamma$ H2AX in HCT116 p53<sup>+/+</sup> cells (Fig. 3.53) whereas this was less so for ARPE-19 non-cancer cells (Fig. 3.54), suggesting that the cancer cells were less able to repair DNA damage. This indicates the cancer cell selectivity of impaired DNA repair resulting from FK866 treatment. The PARP inhibitor, rucaparib, combined with TMZ resulted in elevated phosphorylated  $\gamma$ H2AX in non-cancer ARPE-19 cells, further supporting the proposed notion that combining DNA-damaging agents with PARP inhibitors may lack selectivity.

### 3.2.14 Effects of FK866 on SIRT1 activity

Whilst FK866 appears able to reduce PARP-mediated DNA repair in cancer cells (Fig. 3.53), it was noteworthy that potentiation of TMZ cytotoxicity in cancer cells by rucaparib or by PARP1 knock-down was less pronounced than with FK866 (Fig. 3.32, Fig. 3.33, Fig. 3.42 & Fig. 3.43). This raises the possibility that other enzymes that utilise NAD<sup>+</sup> may contribute to the potentiation of TMZ by FK866. The NAD<sup>+</sup> dependent protein deacetylase SIRT1 has previously been reported to affect genome stability and DNA repair and to promote cancer cell survival in certain contexts (Mei *et al.*, 2016) and effects on its activity were therefore investigated.

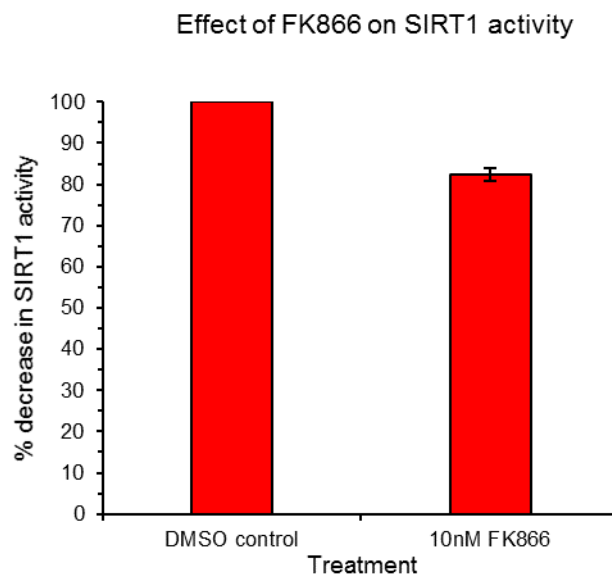


**Figure 3.55: Effect of FK866 on SIRT1 activity in HCT116 p53<sup>+/+</sup> cancer cells**  
Mean percentage decrease in SIRT1 activity ( $\pm$  SEM) in HCT116 p53<sup>+/+</sup> cancer cells after 10nM FK866 treatment for 24 hours, n=2 biological repeats (3 technical replicates).

As shown in Figure 3.55, 10nM FK866 modestly reduced SIRT1 activity in HCT116 p53<sup>+/+</sup> cancer cells (17.5% decrease). In preliminary experiments using the SIRT1 inhibitor, EX-527 (Peck *et al.*, 2010), in combination with TMZ, the combination modestly reduced cell number (Fig. 3.56a) although there was little effect on cell viability or percentage of apoptotic cells (Fig. 3.56b & Fig. 3.57). However, it is noted that 100µM EX-527 alone caused an increase in annexin V positive cells, which is interesting as it is known that SIRT1 knock-down causes HCT116 p53<sup>+/+</sup> cancer cell death (Ford *et al.*, 2005).

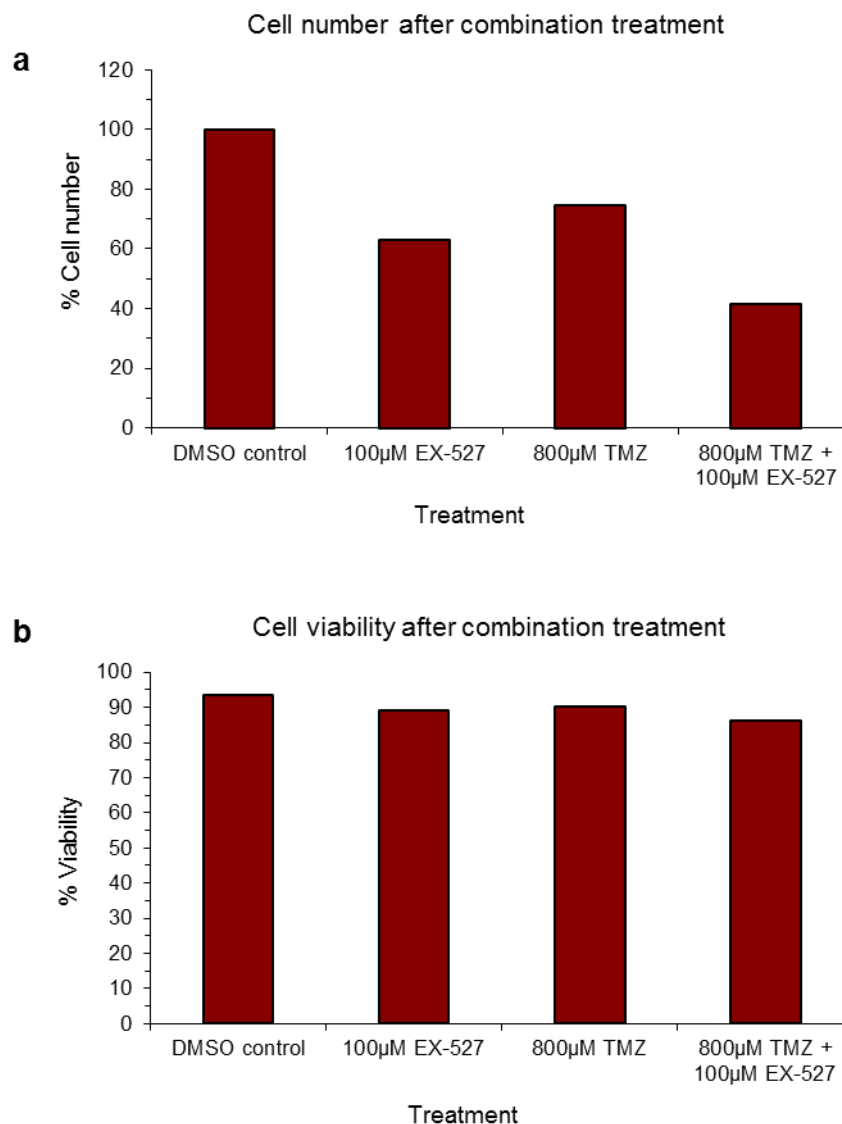


**Figure 3.56: Total cell number and viability of HCT116 p53<sup>-/-</sup> cells after 48 hours treatment with temozolomide in the absence of presence of SIRT1 inhibitor EX-527.**

Total cell number relative to DMSO vehicle control treatment (a) and % viability (b) of HCT116 p53<sup>-/-</sup> cells after treatment with 800µM temozolomide (TMZ) ± 100µM EX-527 and DNA damaging agent TMZ for 48 hours, n=1 biological repeat (n=2 technical replicates).

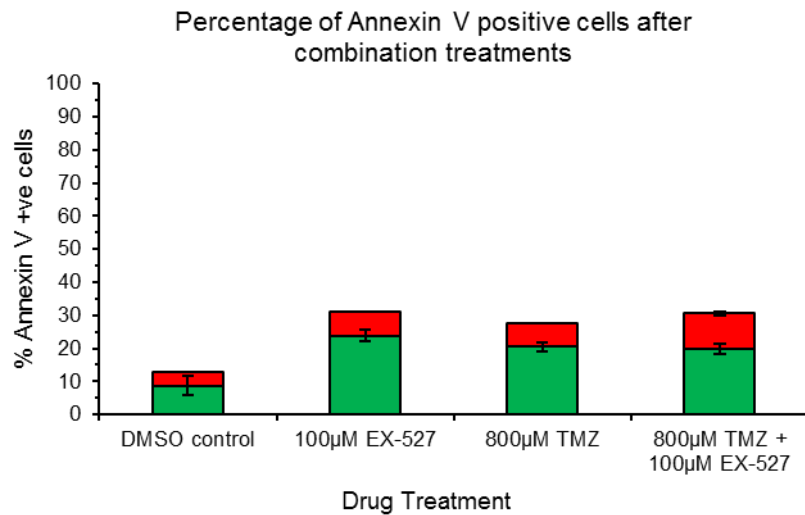


**Figure 3.57: Quantification of apoptosis in HCT116 p53<sup>-/-</sup> cancer cells after treatment of temozolomide in the presence and absence of SIRT1 inhibitor EX-527.**

Percentage of annexin V positive/PI negative and annexin V positive/PI positive HCT116 p53<sup>+/+</sup> cancer cells after 48 hours treatment with 800µM temozolomide (TMZ) ± 100µM EX-527. Green bars represent early apoptotic cells (annexin V positive only); red bars indicate late apoptotic/necrotic cells (annexin V positive, PI positive), n=1 biological repeat (n=2 technical replicates).

## 3.3 Discussion and Conclusions

### 3.3.1 Chemosensitivity to FK866 and correlation with NAMPT/NAPRT expression and cellular NAD<sup>+</sup>-consuming activity

NAMPT inhibitor FK866 showed potent (nM) activity against the panel of cancer cell lines screened. Whilst FK866 activity against two of the non-cancer cell models used was also in the nM range with 96 hours continuous exposure, it was significantly less active (by >4-fold) than towards all, but two, of the eleven cancer cell lines analysed (Fig. 3.7 & Fig. 3.8, n=3 independent biological repeats). FK866 on-target toxicity, including retinal toxicity, has been reported in the literature in phase I clinical trials (von Heideman *et al.*, 2010; Holen *et al.*, 2008; Lin *et al.*, 2016). However, interestingly, against a retinal epithelial non-cancer cell model (ARPE-19) used here, FK866 showed only modest activity compared to cancer cell models. Comparison of FK866 with clinically used platinates indicated more favourable selectivity of FK866 towards cancer cells (Fig. 3.9, n=3 independent biological repeats).

There has been renewed interest in the clinical use of NAMPT inhibitors as a single agent. The discovery that many tumours lack NAPRT while most normal cells express NAPRT and that administration of NA can restore NAD<sup>+</sup> to these cells, but not to NAPRT-deficient tumours, suggests a favourable therapeutic index could be achievable at least for a subset of tumours (Duarte-Pereira *et al.*, 2016; Watson *et al.*, 2009; Olesen *et al.*, 2010). The cell line panel used here was analysed for NAMPT and NAPRT protein expression to see if there were any clear correlations with sensitivity to FK866 that might assist in selection of tumours most likely to be sensitive to FK866. The cancer cells all expressed higher levels of NAMPT than the non-cancer cell models consistent with IC<sub>50</sub>s and supportive of increased cancer cell dependency on NAMPT. However, within the cancer cell line panel further definitive correlations with differential FK866 sensitivity were more difficult to draw although differences in NAPRT expression appeared to be affecting sensitivity, with high NAMPT expressing and low/no

NAPRT expressing cells generally being the most sensitive (Fig. 3.13). A recent study by Chowdhry *et al.* (2019) describes tumour sensitivity as largely being dictated by NAPRT expression, with cancers expressing high NAPRT due to gene amplification being highly NAPRT dependent and those with low or no NAPRT expression being NAMPT-dependent. Our limited cell line panel analysis is in broad agreement with these findings but also indicates the limitations of reliance of analyses of a single parameter or two (e.g. NAPRT, NAMPT expression). Expression levels do not always correlate strongly with activity or dependency, and here expression of NAD<sup>+</sup>-consuming enzymes SIRT1 and PARP1 and PAR levels as a surrogate measure of PARP activity were also analysed (Fig. 3.12 n=1 biological repeat). Interestingly, A2780 ovarian cancer cells, which were amongst the most sensitive lines to FK866, expressed similar NAMPT levels to other lines but expressed higher levels of SIRT1, PARP1 and PAR.

Activity of FK866 towards the hypoxic fraction of tumours has not been previously reported; here preliminary *in vitro* results indicate equitoxic activity although analyses are required in other cancer cell lines and at different oxygen tensions as well as in other models of the TME. Against the GBM1 cancer stem cell-like cell model, FK866 was very active, 4.6-fold more active than against neural progenitors indicating potential activity against aggressive brain tumours and CSCs. Interestingly, Thakur *et al.* (2012) previously report that leukemic cells that were p53 mutant or non-functional were less sensitive to FK866. In contrast, here it is shown that HCT116 p53<sup>-/-</sup> cells were more sensitive to FK866 than the isogenic parental p53<sup>+/+</sup> cells. These results suggest possible differences depending on tissue type and/or genetic background of the cells but this requires further investigation, for example p53 knock-down/overexpression studies in individual cell lines. From these results it would also be interesting to observe if there were any differences in sensitivity of cancer cells which have other common cancer mutations, for example Ras.

### **3.3.2 NAMPT inhibition preferentially depletes cellular NAD<sup>+</sup> and NADH from cancer cells independent of cancer cell p53 status and is able to deplete the nuclear NAD(H) pool**

24 hours FK866 treatment reduced total cellular NAD<sup>+</sup> and NADH levels preferentially in cancer cell lines in a range of different tissue types (e.g. ovarian, colorectal, breast) compared to non-cancer cell models (Fig. 3.19 & Fig. 3.20, n=3 independent biological repeats). More studies are required to extend this analysis to a wider range of cell lines covering more tissue types to see whether some tissues are more sensitive than others and to see if there is heterogeneity in response. Importantly isogenic HCT116 cancer cells showed decreased NAD(H) levels independently of their p53 status, indicating a clear advantage of targeting NAMPT compared to LDH-A to reduce NAD<sup>+</sup> levels (Allison *et al.*, 2014) (Fig. 3.19, n=3 independent biological repeats). These cancer selective effects of FK866 on cellular NAD(H) levels were supported by metabolic phenotyping which revealed a cancer selective reduction in oxygen consumption and metabolic capacity (Fig. 3.14 - Fig. 3.16 n=3 independent biological repeats), which could be rescued by NAD<sup>+</sup> precursors NA/NMN (Fig. 3.18, n=1 biological repeat).

PARP DNA repair activity localises to the cell nucleus (Vyas *et al.*, 2013) and it could be possible that FK866 caused a reduction in total cellular NAD(H) levels but without a substantial effect on NAD<sup>+</sup> levels in the nucleus, as it is known that NAD<sup>+</sup> is not free to move within the cell but is compartmentalised in pools (Nikiforov *et al.*, 2015). Importantly, 5nM FK866, a dose which showed significant cancer-selective reduction in NAD(H), was also able to reduce the nuclear pool of NAD(H) by ~90% (Fig. 3.21, n=1 biological repeat).

Previous research on NAD<sup>+</sup> depletion has stated that a way of overcoming on target side effects in non-cancer cells is to supplement patients with NA, as many cancer cells do not express NAPRT (Duarte-Pereira *et al.*, 2016; Yaku *et al.*, 2018). Interestingly here it is shown that CCD 841 CoN non-cancer cells do not show expression of NAPRT (Fig. 3.11, n=1 biological repeat), which was

unexpected, although these cells did not appear any more sensitive to NAD(H) depletion compared to ARPE-19 non-cancer cells which do express NAPRT.

### **3.3.3 Reduction of PARP DNA repair activity selectively in cancer cells and improving the selectivity of current chemotherapeutic agents**

Having observed a preferential decrease in NAD<sup>+</sup> the next question was whether this was sufficient to cause a decrease in NAD<sup>+</sup>-dependent PARP activity. This was likely to depend on the binding affinity or K<sub>m</sub> of PARPs for NAD<sup>+</sup> and whether levels of free NAD<sup>+</sup> were reduced below this by FK866 treatment. There are differing reports of the K<sub>m</sub> of PARPs for NAD<sup>+</sup> reported in the literature and also of how much 'free' NAD(H) compared to unavailable/sequestered NAD<sup>+</sup> there is in the nucleus (Houtkooper *et al.*, 2010; Cantó *et al.*, 2013). Nevertheless, studies suggest that PARP activity is sensitive to physiological changes in NAD<sup>+</sup> concentration (Ryu *et al.*, 2018). Here, several lines of evidence are provided that show that the decrease in NAD<sup>+</sup> is sufficient to reduce PARP activity:

- 1) FK866 reduced PARP activity of HCT116 p53<sup>+/+</sup> cancer cells in a PARP ELISA assay based on PARylation of histones and to a significantly greater extent than in ARPE-19 non-cancer cells (Fig. 3.22).
- 2) Reduction in PARP activity was partially rescued by treatment with NAD<sup>+</sup> precursor NMN (Fig. 3.25).
- 3) Reduced levels of total cellular protein PARylation were observed in a FK866 dose-dependent manner whilst total PARP1 protein levels were unchanged. (Fig. 3.23 & Fig. 3.24).

This is the first time it has been shown that it is possible to reduce PARP activity preferentially in cancer cells. Previous studies have shown that PARP inhibition or knock-down can potentiate the effects of some DNA damaging agents, however, the problem with this is likely parallel sensitisation of non-cancer cells and tissue (see section 1.4.1.2). The inhibition of PARP activity preferentially in

cancer cells has the potential to potentiate some DNA damaging agents in cancer cells alone.

Here the PARP inhibitor, rucaparib, or PARP knock-down by siRNA was used as a positive control, where the assumption was that PARP knock-down or PARP inhibition may potentiate the DNA damaging agents, but in both non-cancer and cancer cells hence the need for potential cancer-selective PARP inhibiting approaches such as via NAMPT inhibition. When rucaparib was combined with the DNA alkylating agent TMZ a reduction in cell number was seen in both non-cancer and cancer cells (Fig. 3.27 & Fig. 3.28, n=3 independent biological repeats), and in neural progenitor cells TMZ in combination with rucaparib led to S-phase arrest (Fig. 3.52, n=1 biological repeat). Knock-down of PARP1 in combination with TMZ reduced cell number and modestly increased the number of apoptotic cells in both HCT116 p53<sup>+/+</sup> cancer cells and ARPE-19 non-cancer cells (Fig. 3.42 & Fig. 3.43), indicating the lack of cancer selectivity in targeting PARP directly. For future studies, it would also be useful to assess the reduction in PARP1 mRNA and protein at the point of TMZ addition (time course of expression levels) as it is possible that levels of PARP1 are higher at this time point which may account for the modest induction of apoptosis observed. Another possible approach would be use of PARP1 CRISPR knock-out cells compared to wild-type cells which would overcome any issues of reduced levels of PARP enzyme being able to sufficiently sustain PARP1 DNA repair activity.

These results partially follow what has been reported in the literature, although the literature indicates more pronounced effects on cell death of PARP inhibition with chemotherapeutic agents (Daniel *et al.*, 2009), which may relate to dose of rucaparib used and differences in treatment duration and perhaps drug dose/timing alterations need to be considered. Differential effects have also been seen in potentiation of DNA damaging agents depending on which PARP inhibitor, as some PARP inhibitors not only catalytically inhibit PARP but also result in PARP trapping, which when combined with some DNA damaging agents has shown increased potentiation (Murai *et al.*, 2012; Murai *et al.*, 2014).

Annexin V apoptotic assays revealed that FK866 was able to potentiate CPT and DOX in HCT116 p53<sup>+/+</sup> cancer cells compared to ARPE-19 and CCD 841 CoN

non-cancer cells but to a much lesser extent than observed with TMZ (Fig. 3.28, Fig. 3.30 & Fig. 3.33, n=3 independent biological repeats). CPT is a Topo1 inhibitor, inducing SSB which require the repair activity of PARP (see section 1.4.1.2), and inhibition may mean that breaks are likely to remain ultimately leading to cell death. DOX is a Topo2 poison and induces DSB, which are less associated with the repair activity of PARP, although previous studies have also shown that PARP inhibition has led to the potentiation of Topo2 poisons (Park *et al.*, 2018). Other studies indicated that this is not the case (Murai *et al.*, 2014) and it is presently unclear why potentiation was less with CPT and DOX than TMZ, requiring further investigation. It is possible that more pronounced apoptotic induction or cell death would be observed with longer incubation with these agents, for example due to persistent DNA damage. For future studies, it would be beneficial to quantify apoptotic levels as part of a time course and beyond 72 hours as well as the investigation of different concentrations of CPT and DOX. For apoptotic assays in the non-cancer cells where apoptosis induced remained relatively low following drug treatment, inclusion of a positive control (e.g. UV irradiation or higher concentration of cytotoxic agent) for induction of significant levels of apoptosis would also be beneficial.

It has previously been reported that due to TMZ treatment inducing PARP activity and therefore utilising NAD<sup>+</sup> its treatment leads to a reduction in NAD<sup>+</sup> levels (Boulton *et al.*, 1995). This may be a reason why there is greater potentiation of TMZ by FK866 than other DNA damaging agents. It would be interesting to observe whether other DNA damaging agents decrease NAD<sup>+</sup> levels.

The potentiation of the alkylating agent TMZ was initially tested in HCT116 p53<sup>+/+</sup> cancer cells which are MGMT negative and MMR deficient (Bocangel *et al.*, 2009; Perez *et al.*, 2016). Due to MMR deficiency the cells are resistant to TMZ and therefore PARP is also involved in the repair of DNA damage through BER. All other cancer cells tested differed in MGMT and MMR status but overall their status resulted in the cells mainly being resistant to TMZ. It would be interesting to observe if TMZ can also be potentiated by FK866 in cancer cells which are sensitive to TMZ and have a MGMT negative and MMR proficient status (Fig. 3.36 & Fig. 3.37).

In contrast to the observed potentiation of DNA damaging agents via FK866, paclitaxel, a mitotic spindle inhibitor, would not be expected to be potentiated by PARP inhibition and was assessed to see if FK866 was able to potentiate its activity. This showed no potentiation in the cell lines with addition of FK866 (Fig. 3.38 & Fig. 3.39, n=1 biological repeat). This and the effects of FK866 on the potentiation of DNA damaging agents that cause DNA damage that requires PARP activity for its repair and the direct decrease in PARP activity seen with FK866 treatment (Fig. 3.22, n=3 independent biological repeats), highly suggests that the mechanism of potentiation is via inhibition of PARP DNA repair activity.

It was hypothesised that this potentiation of TMZ in HCT116 p53<sup>+/+</sup> cancer cells through FK866 was due to decreased PARP activity and therefore cells were unable to repair SSB damage which then led to DSB damage which ultimately resulted in cell death. In support of this hypothesis that the effects on viability were due to an inability of the treated cells to repair damaged DNA, phosphorylated  $\gamma$ H2AX levels (a marker of DSB) of the cells were increased where cells had been pre-treated with FK866 and then exposed to TMZ compared to single drug treatments. Following 6 hours 'repair time', after TMZ removal, the HCT116 p53<sup>+/+</sup> cancer cells showed enhanced levels of  $\gamma$ H2AX compared to ARPE-19 non cancer cells (Fig. 3.53 & Fig. 3.54, n=1 biological repeat). However, additional biological repeats are required to confirm this and quantification of the number of phosphorylated  $\gamma$ H2AX foci would then enable analysis of statistical significance of any effects. For future work, inclusion of a known DSB inducer (e.g. doxorubicin) alongside as a positive control would provide a useful comparison. The analysis of phosphorylated  $\gamma$ H2AX over time after drug wash-out as a 'surrogate' marker of DNA repair followed published methodology as described in Allison *et al.* (2017).

Time course assessment of single strand DNA breaks (SSBs, from t=0) via increased intranuclear foci of the single stranded DNA binding protein Replication Protein A (RPA) would enable analysis of initial basal SSB damage, induction by TMZ and temporal reduction following washout, or potential persistence and conversion to DSBs. Such analyses or the use of the alkaline and neutral comet assay (with drug washout) would add weight to these novel results suggesting

that FK866 can potentiate TMZ via decreased NAD<sup>+</sup>-dependent PARP-mediated DNA repair.

TMZ is currently used for the treatment of glioblastoma in the clinic and importantly, potentiation of TMZ by FK866 was also observed in the GBM1 cancer stem cell model (67% methylated at the MGMT promoter; (Polson *et al.*, 2018)) (Fig. 3.48 & Fig. 3.49) and not in the NP1 non-cancer cell model (Fig. 3.51). Mechanism of action studies, including NAD(H) assay and PARP activity assay showed cancer selective effects and had similar outcomes as other cancer versus non-cancer cells. This is important as many types of glioblastoma are known to be resistant to TMZ and preliminary results suggest that FK866 could resensitise the cells to the drug. These results warrant further investigation to see whether the potentiation of TMZ can be observed through FK866 in other GBM subtypes, and to see what effect the NAMPT/NAPRT status of the cells has on its success.

Importantly, here it is shown that FK866 has only a small effect on activity of the NAD<sup>+</sup> dependent SIRT1 enzyme (Fig. 3.55) and that when using a SIRT1 inhibitor in combination with TMZ, little or no potentiation effect on cell viability is seen in contrast to FK866 in combination with TMZ (Fig. 3.56). Whilst this suggests effects of FK866 are likely to be principally due to reduced PARP activity it is possible that other NAD<sup>+</sup> dependent enzymes may be contributing to this effect.

Previous studies have shown that a combination of the PARP inhibitor olaparib (and the DNA damaging agent CPT) can lead to radiosensitisation of a tumour (Miura *et al.*, 2012). As radiotherapy can induce damage which can lead to the activation of the DNA repair enzyme PARP, it would be interesting to observe whether FK866 treatment can enhance toxicity of radiotherapy towards cancer cells selectively.

### **3.3.4 Conclusion**

To conclude, short term treatment with the NAMPT inhibitor, FK866, was able to deplete NAD(H) levels selectively in cancer cells *in vitro* (e.g. Fig. 3.19, n=3 independent biological repeats), which was sufficient to cause a decrease in

PARP activity preferentially in cancer cells (Fig. 3.22, n=3 independent biological repeats & Fig. 3.23, n=1 biological repeat), indicating a cancer selective approach to deplete PARP activity. This selective decrease in PARP activity through FK866 correlated with potentiation of DNA damaging agents in cancer cells selectively (e.g Fig.3.32 & Fig. 3.33, n=3 independent biological repeats). This potentiation is proposed to be due to the cancer cells being unable to repair DNA damage efficiently (Fig. 3.53 & Fig. 3.54, n=1 biological repeat), although the possibility of other contributing mechanisms cannot be excluded.

For some of the cancer cell lines and experiments, additional biological replicates are required for confirmation of these conclusions as is evident from individual figure legends. However, in some such cases there are also different experimental approaches or 'readouts' lending support to particular conclusions (e.g. Fig. 3.36 cell number and viability measurement & Fig. 3.37 Annexin V apoptotic quantification which independently support the conclusion of potentiation of TMZ by FK866 in A2780, CP70/A2780cis and MDA-MB-231 cancer cells).

## **4. NAD<sup>+</sup>-dependent protein deacetylase SIRT1 as a potential anti-cancer therapeutic target and constitutive repressor of a neuronal-like phenotype switch in non-cancer and cancer cells**

### **4.1 Introduction**

As previously discussed in section 1.4.2 SIRT1 is a histone and protein deacetylase that is dependent on NAD<sup>+</sup> for its activity (Landry *et al.*, 2000). There are conflicting results around targeting SIRT1 therapeutically as reports of its role in cancer differ. For example there are some reports of SIRT1 suppressing tumorigenesis (Firestein *et al.*, 2008) and others reporting it as tumour promoting or critical for cancer survival (Vaziri *et al.*, 2001; Ford *et al.*, 2005; Zhao *et al.*, 2011; Herranz *et al.*, 2013). Additionally, several splice variants of SIRT1 have been identified (Lynch *et al.*, 2010; Shah *et al.*, 2012; Deota *et al.*, 2017) which likely contribute to the complexity of SIRT1 functions and its (dys)regulation in cancers. The existence of these splice variants could explain some of the apparently conflicting results in the literature depending on which experimental tools were used, the expression of different variants in different cells/tissues and which forms of SIRT1 were targeted in different studies.

Several independent studies suggest that for some cancers at least, cancer cells rely on SIRT1 for their survival, with knock-down of SIRT1 full-length protein resulting in cancer cell death with non-cancer cell viability unaffected (Ford *et al.*, 2005; Zhao *et al.*, 2011). This cancer cell SIRT1 dependency suggests it as a potential novel target for inducing cancer selective cell death. Further work is needed to understand which cancers are addicted to SIRT1, how these are identified as well as rationalising of its pleiotropic functions (tumour suppressing vs. tumour promoting). To date demonstration of the role of full-length SIRT1 (SIRT-FL) as a cancer survival factor has been using RNAi or other genetic

approaches. A key aim of this chapter, particularly in light of the identification of multiple SIRT1 splice variants which could impact on cellular response, is whether similar selective cancer cell death can be recapitulated with a small molecule inhibitor. This is important for further validation of SIRT1 as a target and also because of current challenges associated with successful translation of RNAi-based therapeutic approaches into the clinic. There is only one FDA-approved siRNA therapeutic to date (Kim *et al.*, 2019). Challenges include loss of efficacy due to siRNA susceptibility to degradation by serum nucleases, inefficient payload release from carriers, cost, accessibility, safety concerns with viral vectors and possible disruption of endogenous RISC/RNAi (Kim *et al.*, 2019; Castanotto and Rossi, 2009; Burnett *et al.*, 2011).

For this study, the small molecule SIRT1 inhibitor, EX-527, was used as it is ~100-fold more selective towards SIRT1 compared to other sirtuins. Previous sirtuin inhibitors have been designed to target the yeast homolog Sir2 and therefore are not specific towards SIRT1 (Gertz *et al.*, 2013).

The second major aim of this chapter was further investigation of the effects of SIRT1 knock-down/inhibition in both non-cancer and cancer cells beyond the simple 'readout' of SIRT1 being essential for cancer cell survival and dispensable in non-cancer cells. Studies from the Allison group and Jo Milner's group (University of York, unpublished observations) show that SIRT1-FL knock-down can induce a neuronal like morphology in ARPE-19 non-cancer cells suggesting that they undergo neuronal transdifferentiation. This is further investigated here using both a RNAi knock-down approach and the small molecule SIRT1 inhibitor EX-527. This is very relevant in a non-cancer context as a number of studies report SIRT1 or SIRT1 activators to have a neuroprotective role with beneficial effects in a number of neurodegenerative disease models (Donmez and Outeiro, 2013). It is hypothesised that this neuronal-like phenotype/cell fate change induced by SIRT1-FL knock-down requires some de- and re-differentiation and changes in somatic reprogramming factors and/or pluripotent/stem cell factors. This would be important as it would support literature evidence for a role of SIRT1 in regulation of stemness/differentiation in different contexts, for example the regulation of lineage differentiation of mesenchymal stem cells (Simic *et al.*,

2013). In the context of the multistep progression of cancer, the cancer stem cell theory and the known chemoresistance of CSCs (LaBarge, 2010), therapeutic targets that reduce cancer stemness are sought. Here, it is tested whether SIRT1 targeting/inhibition may induce a more differentiated state of the GBM1 cancer stem cell-like model.

## 4.2 Results

### 4.2.1 SIRT1 knock-down induces cancer cell death *in vitro*

SIRT-FL knock-down by siRNA induced apoptotic cell death in HCT116 p53<sup>+/+</sup> cancer cells (Fig. 4.1), consistent with previous published findings (Ford *et al.*, 2005; Allison and Milner, 2014). Having confirmed this, it was next assessed whether the small molecule SIRT1 Inhibitor EX-527 was able to induce similar effects.

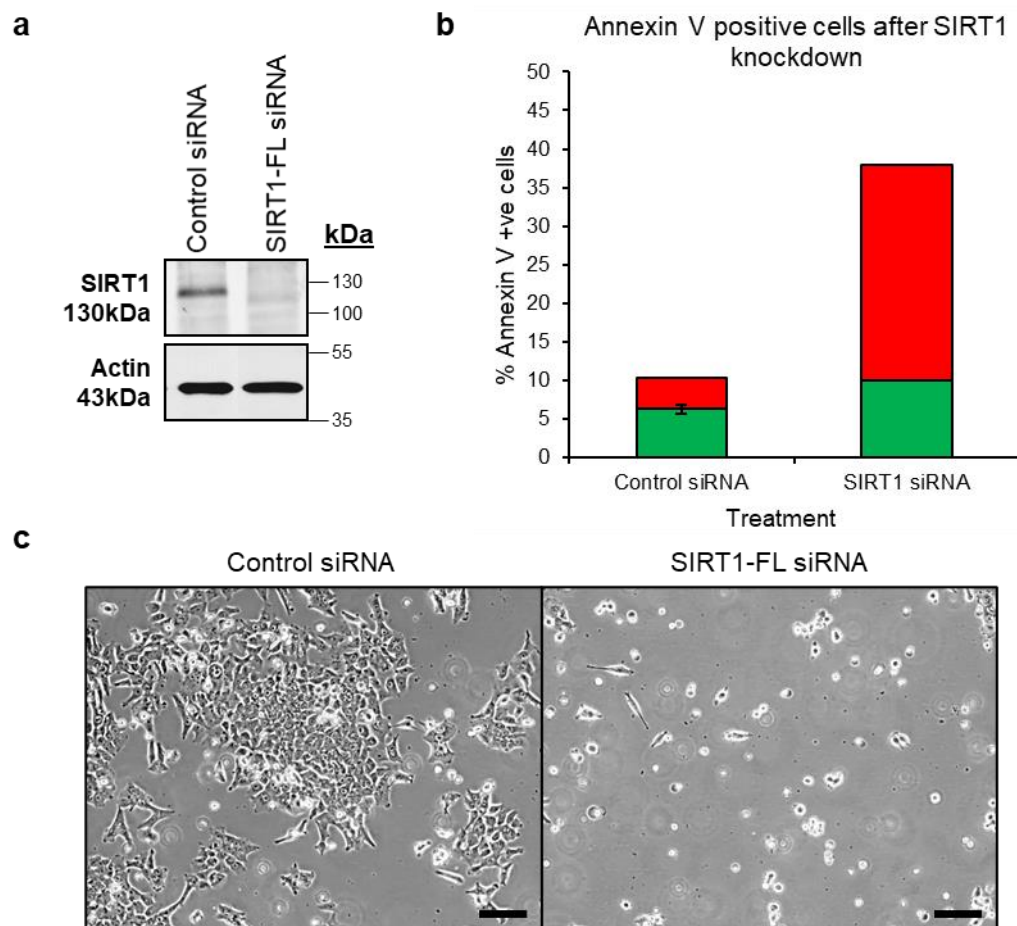


**Figure 4.1: RNAi mediated SIRT1 silencing and phenotypic effects in HCT116 p53<sup>+/+</sup> cancer cells.**

**a.** Immunoblots showing SIRT1 knock-down at the protein level in HCT116 p53<sup>+/+</sup> cells, actin used as loading control. **b.** Quantification of annexin V positive HCT116 p53<sup>+/+</sup> cancer cells after transfection with SIRT1 siRNA for 72 hours. Green bars represent early apoptotic cells (annexin V positive only); red bars indicate late apoptotic/necrotic cells (annexin V positive, PI positive), n=1 biological repeat (3 technical repeats). **c.** Cell micrographs of HCT116 p53<sup>+/+</sup> cancer cells 72 hours post SIRT1 siRNA transfection, images taken with x10 objective and scale bar indicates 100µm.

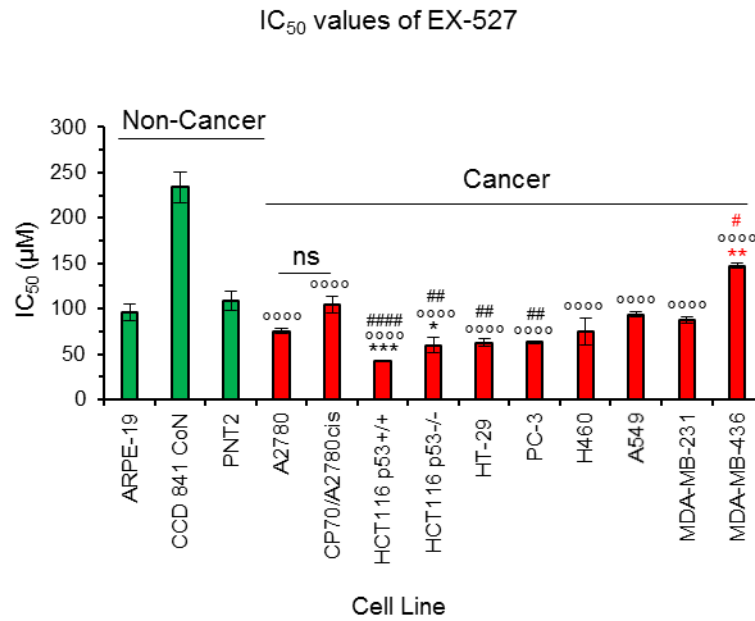
## 4.2.2 Selectivity and activity of the small molecule inhibitor EX-527

The activity of EX-527 and its selectivity towards cancer cells was initially tested by chemosensitivity assay (Table 4.1, Fig. 4.2 & Fig. 4.3).

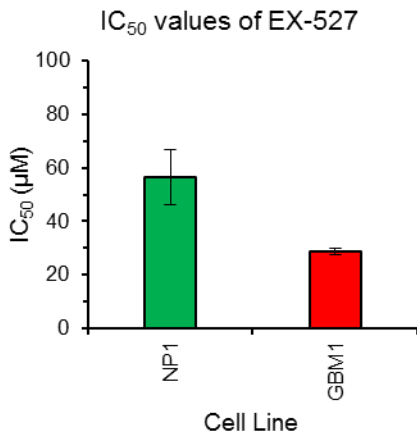
EX-527	Cell Line	Tissue Origin	Average IC <sub>50</sub> (μM)	±SEM
Non-Cancer	ARPE-19	Retina	95.46	9.04
	CCD 841 CoN	Colon	233.71	17.11
	PNT2	Prostate	108.69	10.55
	NP1*	Brain	56.52	10.37
Cancer	A2780	Ovary	75.37	3.32
	CP70/A2780cis	Ovary	104.81	9.15
	HCT116 p53 <sup>+/+</sup> normoxic	Colon	41.92	0.70
	HCT116 p53 <sup>+/+</sup> hypoxic	Colon	42.59	0.89
	HCT116 p53 <sup>-/-</sup>	Colon	59.63	8.47
	HT-29	Colon	62.53	4.13
	PC-3	Prostate	63.09	1.32
	H460	Lung	75.03	14.40
	A549	Lung	93.41	2.62
	MDA-MB-231	Breast	88.03	3.50
	MDA-MB-436	Breast	147.31	2.74
	GBM1**	Brain	28.74	0.99

**Table 4.1: IC<sub>50</sub> values of EX-527 towards multiple human cell lines of different tissue origin.** Mean IC<sub>50</sub> values ± SEM, n=3, biological repeats (8 technical replicates), of the SIRT1 inhibitor EX-527 in multiple non-cancer and cancer cell lines after 96 hours continuous EX-527 exposure. NP1\* human neural progenitor cells (oligopotent cells); GBM1\*\* glioblastoma cancer stem cell model.

**a**



**b**



**c**

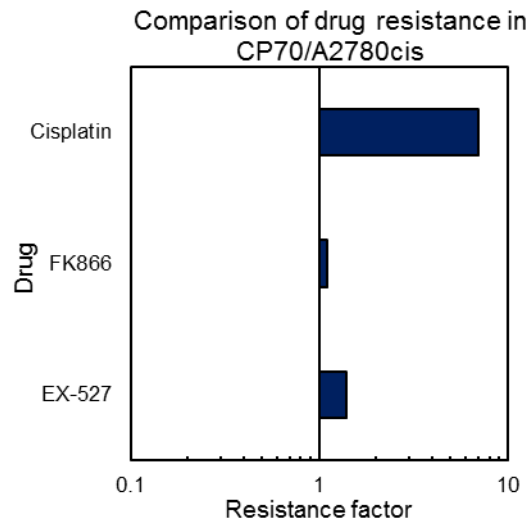


**Figure 4.2: Summary of EX-527 cytotoxicity towards a panel of non-cancer and cancer cells and determination of a lack of cross-resistance with cisplatin.**

**a.** Mean IC<sub>50</sub> values ± SEM, n=3 biological repeats (8 technical replicates), of the SIRT1 inhibitor EX-527 in multiple cancer and non-cancer cell lines as determined by MTT chemosensitivity assay. A one way ANOVA was performed where \*p<0.05 \*\*p<0.01 compared to ARPE-19, \*\*\*\*p<0.0001 compared to CCD 841 CoN and ##p<0.01, ###p<0.001 compared to PNT2 ns=not significant (red indicates significantly higher). **b.** Average IC<sub>50</sub> values ± SEM, n=3 biological repeats (8 technical replicates), of EX-527 in non-cancer progenitor/stem cell-like model NP1 and cancer stem cell model GBM1. **c.** Comparison of resistance factor of A2780 and CP70/A2780cis cancer cells to cisplatin and EX-527 (IC<sub>50</sub> in CP70/A2780cis cells divided by IC<sub>50</sub> in A2780 cells; resistance factor >1 indicates less activity towards CP70/A2780cis cells than parental A2780 cells) (FK866 shown for comparison purpose).

EX-527 had  $\mu\text{M}$  activity towards cell lines with 96 hours continuous drug exposure. CCD 841 CoN non-cancer colon epithelial cells appeared to be the least sensitive to EX-527 with its  $\text{IC}_{50}$  significantly higher than that for all cancer cells tested (Fig. 4.2 & Fig. 4.3). Preferential activity of EX-527 towards the cancer cells was much less apparent when compared against the ARPE-19 and PNT2 non-cancer cells however, with EX-527 cancer selectivity ratios being 2.6 or less for many of the cancer cells (Fig. 4.3). A statistically significant lower  $\text{IC}_{50}$  for EX-527 was observed in the isogenic  $\text{p53}^{+/+}$  and  $\text{p53}^{-/-}$  HCT116 colorectal cancer cells, the HT-29  $\text{p53}$  mutant colorectal cancer cells and the PC-3 prostate cancer cells (Muller *et al.*, 2013) when compared against PNT2 and CCD 841 CoN non-cancer cells (Fig. 4.2). NP1 neural progenitors appeared quite sensitive to EX-527, however, importantly were  $\sim 2$ -fold less sensitive than the GBM1 cancer stem cell-like model (Fig. 4.2b). EX-527 showed comparable activity (1.4-fold less active) towards cis-resistant A2780cis ovarian cancer cells and the parental cis-sensitive cells (Fig. 4.2c), indicative that EX-527 is largely able to circumvent acquired cisplatin resistance.

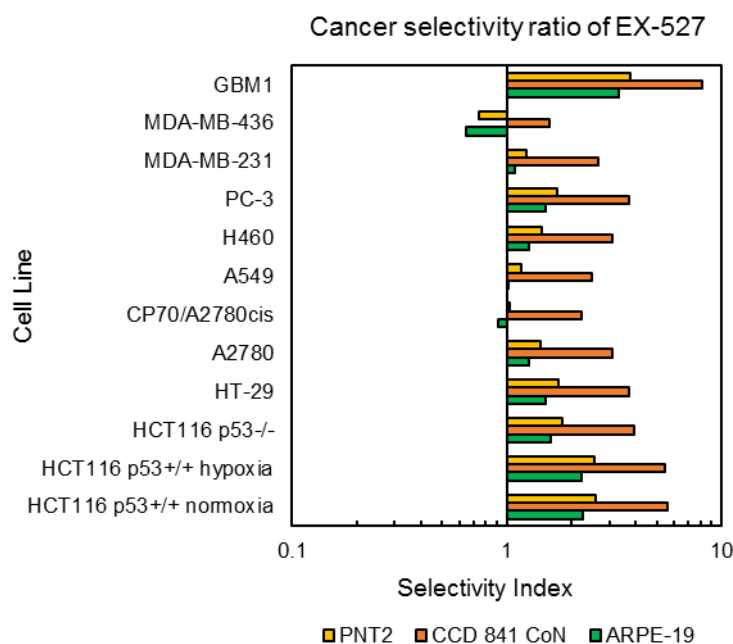


**Figure 4.3: Preferential cytotoxicity activity of EX-527 towards cancer cells compared to non-cancer cell models.**

Cancer cell versus non-cancer cell selectivity ratios for SIRT1 inhibitor EX-527 in multiple cancer cell lines compared to ARPE-19, CCD 841 CoN and PNT2 non-cancer cells. The selectivity index was calculated from the  $\text{IC}_{50}$  values achieved from 3 biological repeats (8 technical replicates) using the following equation (mean  $\text{IC}_{50}$  of non-cancer cells / mean  $\text{IC}_{50}$  of cancer cells). A value of 1 indicates equitoxicity of the drug to cancer and non-cancer cells, a value of  $<1$  indicates no preferential cytotoxicity to the cancer cells and a value  $>1$  indicates preferential cytotoxicity to the cancer cells.

Selectivity of EX-527 towards HCT116 p53<sup>+/+</sup> colon cells compared to CCD 841 CoN non-cancer colon cells was similar to that observed with FK866 with improved selectivity compared to clinically used platينات cisplatin, oxaliplatin and carboplatin (Fig. 4.4).

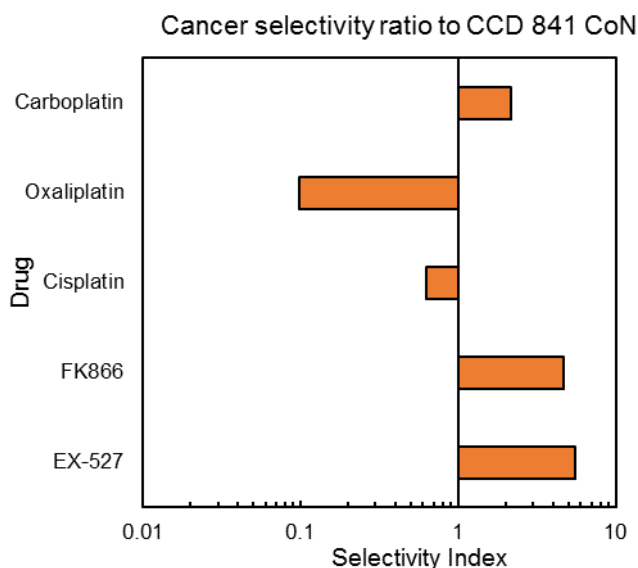


**Figure 4.4: Cancer selectivity of EX-527 compared to FDA approved platinate based compounds.**

Cancer cell selectivity ratios were calculated from the IC<sub>50</sub> values achieved from 3 biological repeats (8 technical replicates) which compared the activity of EX-527 and clinically used platينات (cisplatin, oxaliplatin, carboplatin) in HCT116 p53<sup>+/+</sup> cancer cells and CCD 941 CoN non-cancer cells after 96 hours drug exposure. SI = mean IC<sub>50</sub> of non-cancer cells / mean IC<sub>50</sub> of cancer cells (FK866 shown for comparison).

Compared to FK866 and Topo2 inhibitor DOX, EX-527 was much less active towards HCT116 p53<sup>+/+</sup> cancer cells with activity in the micromolar range rather than nM activity under normoxic conditions. Importantly, however, in contrast to DOX, activity of EX-527 appeared to be similar towards HCT116 p53<sup>+/+</sup> cancer cells grown under 21% or 0.1% oxygen conditions (Fig. 4.5) although this has not been tested against other cancer cell lines.

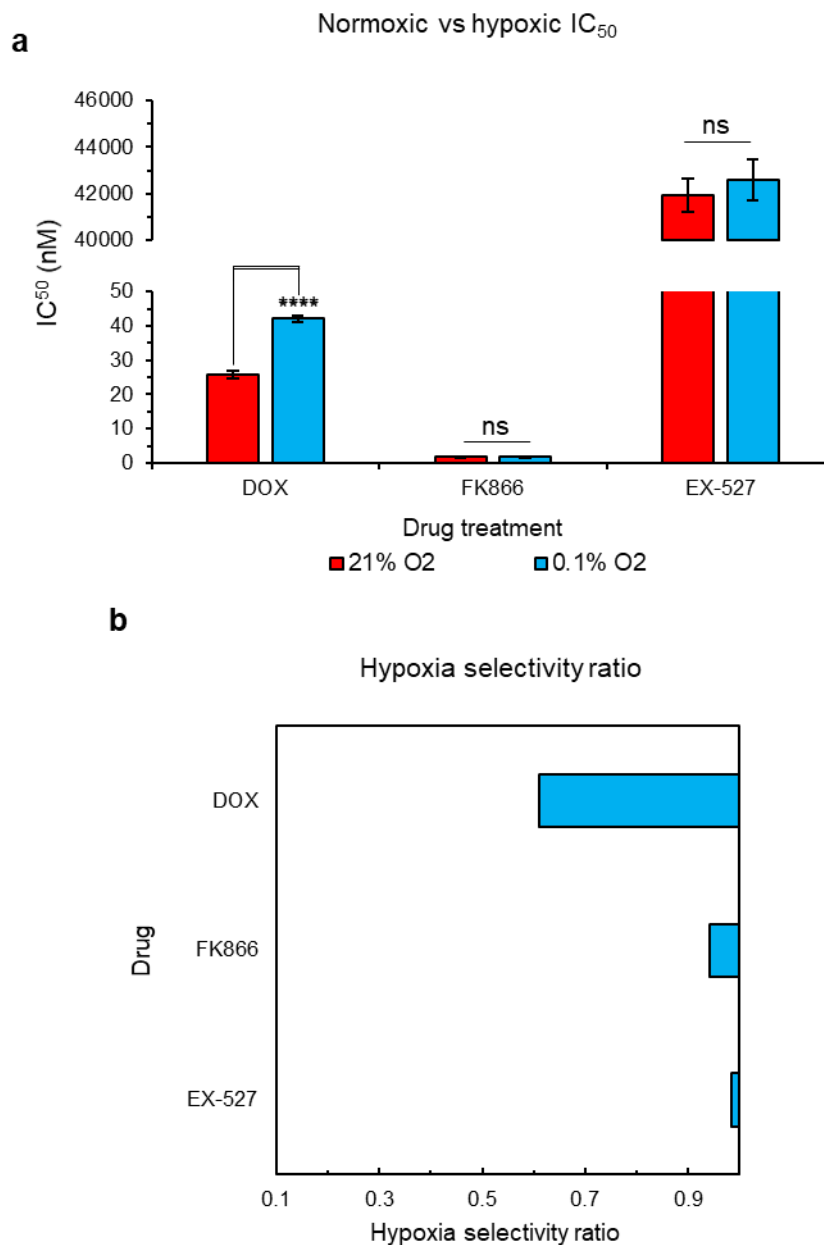


**Figure 4.5: The effect of hypoxia on doxorubicin and EX-527 cytotoxicity towards HCT116 p53<sup>+/+</sup> cells.**

Mean IC<sub>50</sub> values, n=3 biological repeats (8 technical replicates) of doxorubicin (DOX), FK866 and EX-527 (**a**) under normoxic and hypoxic conditions in HCT116 p53<sup>+/+</sup> cancer cells after 96 hours continuous drug exposure. A two-tailed t-test was performed where \*\*\*\*p<0.0001, ns=not significant. **b**. Hypoxia selectivity ratio (IC<sub>50</sub> normoxic cells / IC<sub>50</sub> hypoxic cells) for DOX, FK866 (shown for comparison purpose) and EX-527. A value of 1 indicates equitoxicity of the drug under normoxic and hypoxic conditions, a value of <1 indicates preferential cytotoxicity to normoxic cells and a value of >1 indicates preferential cytotoxicity to hypoxic cells. Values were achieved using IC<sub>50</sub> values from 3 biological repeats (8 technical replicates).

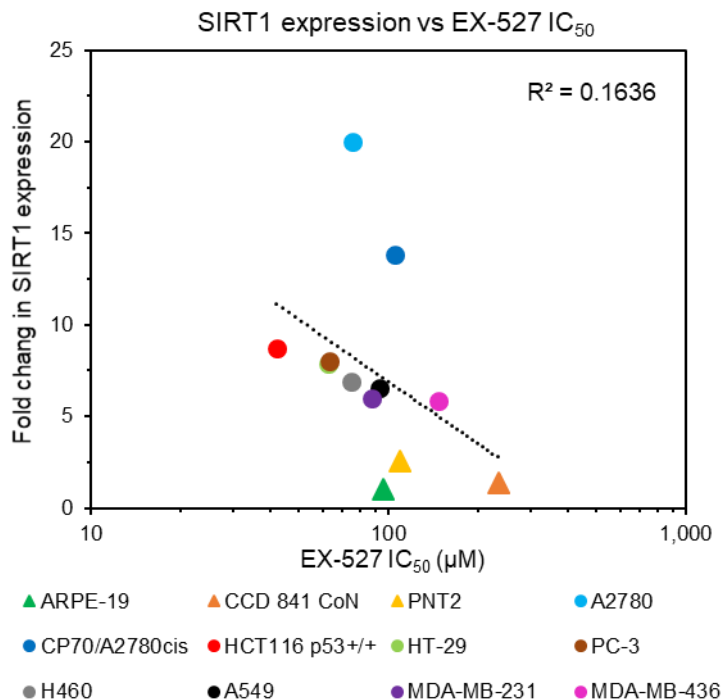


**Figure 4.6: Protein expression of SIRT1 compared to cellular EX-527 chemosensitivity (IC<sub>50</sub>).**

Fold change in SIRT1 expression compared to EX-527 mean IC<sub>50</sub> values. Triangles represent non-cancer cells and circles represent individual cancer cell lines. Fold change in protein expression relative to expression levels in ARPE-19 non-cancer cells (set at 1). Black dotted line is line of best fit where R<sup>2</sup> value = 0.1636. IC<sub>50</sub> values based on n=3 biological repeats (Table 4.1) and protein expression on n=1.

Figure 4.6 compared cell line EX-527 IC<sub>50</sub> values relative to SIRT1 protein expression. As this indicates, there is some ‘loose’ inverse correlation (for a cluster of the cancer cell lines) but no strict relationship and there are a large number of outliers (R<sup>2</sup> = 0.1636).

Given the excellent selective cytotoxicity of SIRT1 silencing previously reported (Ford *et al.*, 2005), it was decided to analyse further the effects of EX-527 on a limited number of cell lines at defined doses with a shorter drug exposure time of 48 hours. Against HCT116 p53<sup>+/+</sup> cancer cells reduced confluency was apparent under the microscope at 50 and 100µM EX-527 doses (see appendix Fig. 9.4), whereas EX-527 appeared to have little effect against the ARPE-19 non-cancer cells. As Figure 4.7 shows, at 200µM EX-527 the ARPE-19 non-cancer cells showed some reduction in confluency compared to controls with some cells showing a more elongated, or ‘fibroblast-like’ morphology. In contrast, most of the HCT116 p53<sup>+/+</sup> cancer cells (normoxic and hypoxic) were rounded up and floating

suggestive they may be undergoing cell death and for the GBM1 cancer cells cell confluency was substantially reduced. Effects of EX-527 on cell viability and number were quantified by image cytometry (Fig. 4.8).

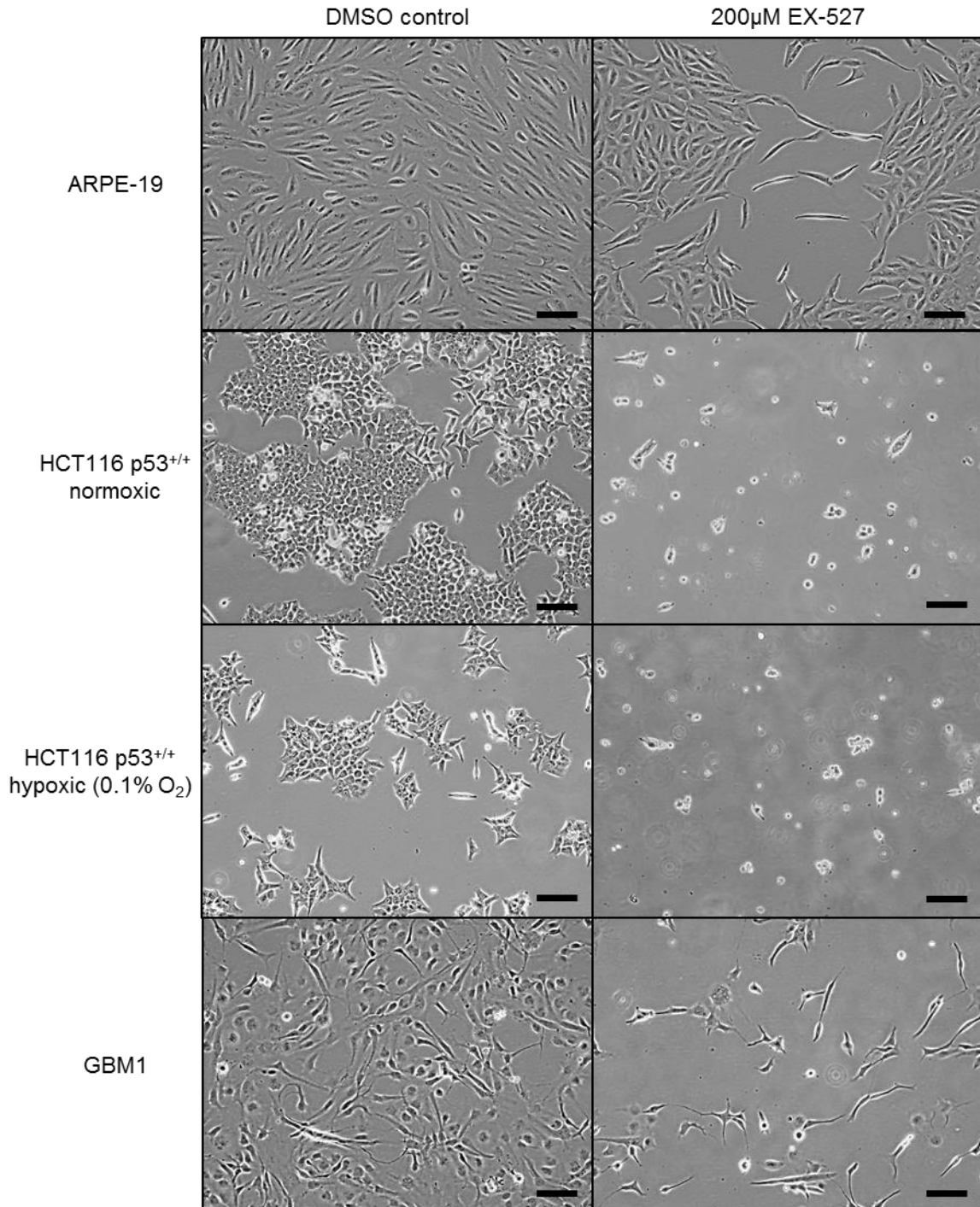


**Figure 4.7: Cell micrographs of ARPE-19 non-cancer cells, HCT116 p53<sup>+/+</sup> cancer cells under normoxic and hypoxic conditions and cancer stem cell-like model GBM1 after EX-527 treatment.**

Representative cell micrographs of ARPE-19, HCT116 p53<sup>+/+</sup> and GBM1 cells after 48 hours treatment with 200 $\mu$ M EX-527 or DMSO vehicle control. Images taken with x10 objective and scale bar indicates 100 $\mu$ m (see appendix Fig. 9.4 for other doses). n=3 biological repeats.

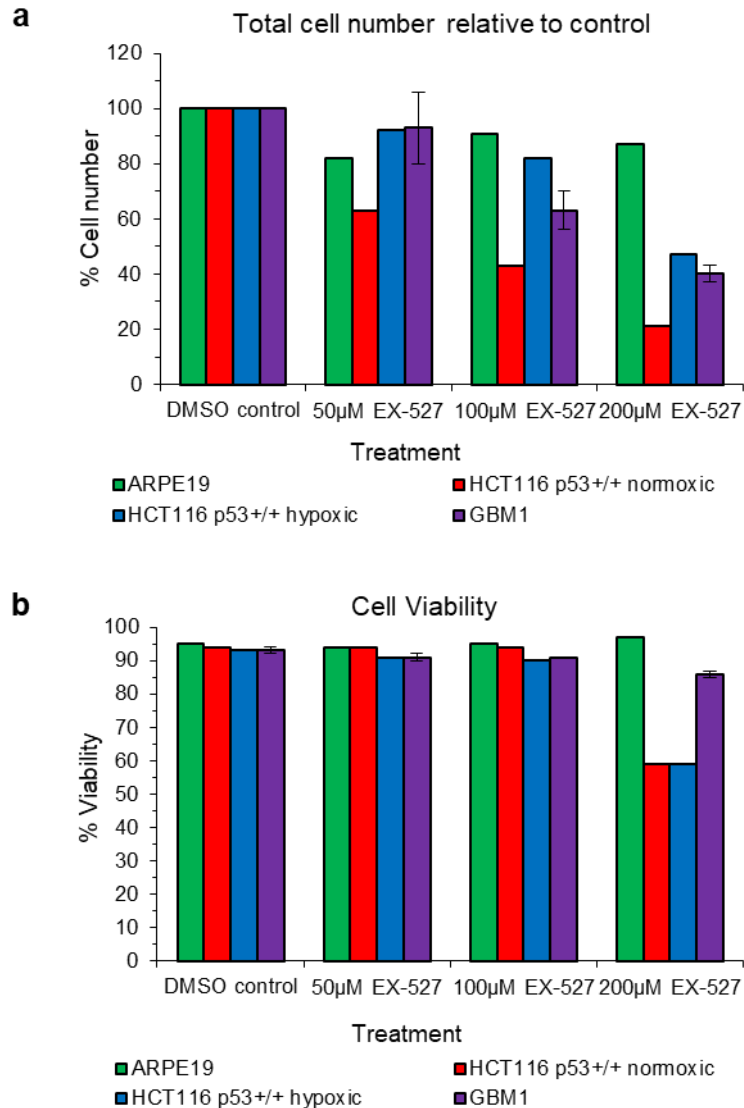


**Figure 4.8: Total cell number and viability after 48 hours EX-527 treatment.**

Total cell number relative to DMSO vehicle control treatment (a) and % viability (b) of ARPE-19 non-cancer cells, HCT116 p53<sup>+/+</sup> (normoxic and hypoxic) cancer cells and GBM1 cancer stem cell-like model after 48 hours EX-527 treatment. n=1, biological repeat except GBM1, n=2 biological repeats (2 technical replicates) (showing ± SEM). Values determined by acridine orange (cell count) and DAPI (viability) staining (see Methods 2.3.1).

EX-527 at the tested doses had no effect on cell viability of ARPE-19 non-cancer cells. In contrast, 200µM EX-527 was cytotoxic towards the HCT116 p53<sup>+/+</sup> cancer cells and both HCT116 p53<sup>+/+</sup> and GBM1 cancer cells showed a dose-dependent reduction in cell number (Fig. 4.8). A similar reduction in cell viability was observed for the hypoxic and normoxic HCT116 p53<sup>+/+</sup> cancer cells (Fig. 4.8) which was consistent with EX-527 equitoxicity in chemosensitivity assays (Fig.

4.2), although some difference in reduction of cell number was evident which may reflect the lower proliferation rate of the cells under hypoxic conditions.

### **4.2.3 EX-527 induces cell death by apoptosis**

Whilst reduced cell viability indicated induction of cell death by EX-527, there are multiple mechanisms by which cell death can occur. One hallmark of cancers is evasion of apoptosis; annexin V assays were performed to investigate whether EX-527 cytotoxicity was via apoptosis, as has previously been reported for SIRT1 knock-down (Fig. 4.1). Additionally, a number of the floating cells morphologically appeared to resemble apoptotic cells under the microscope.

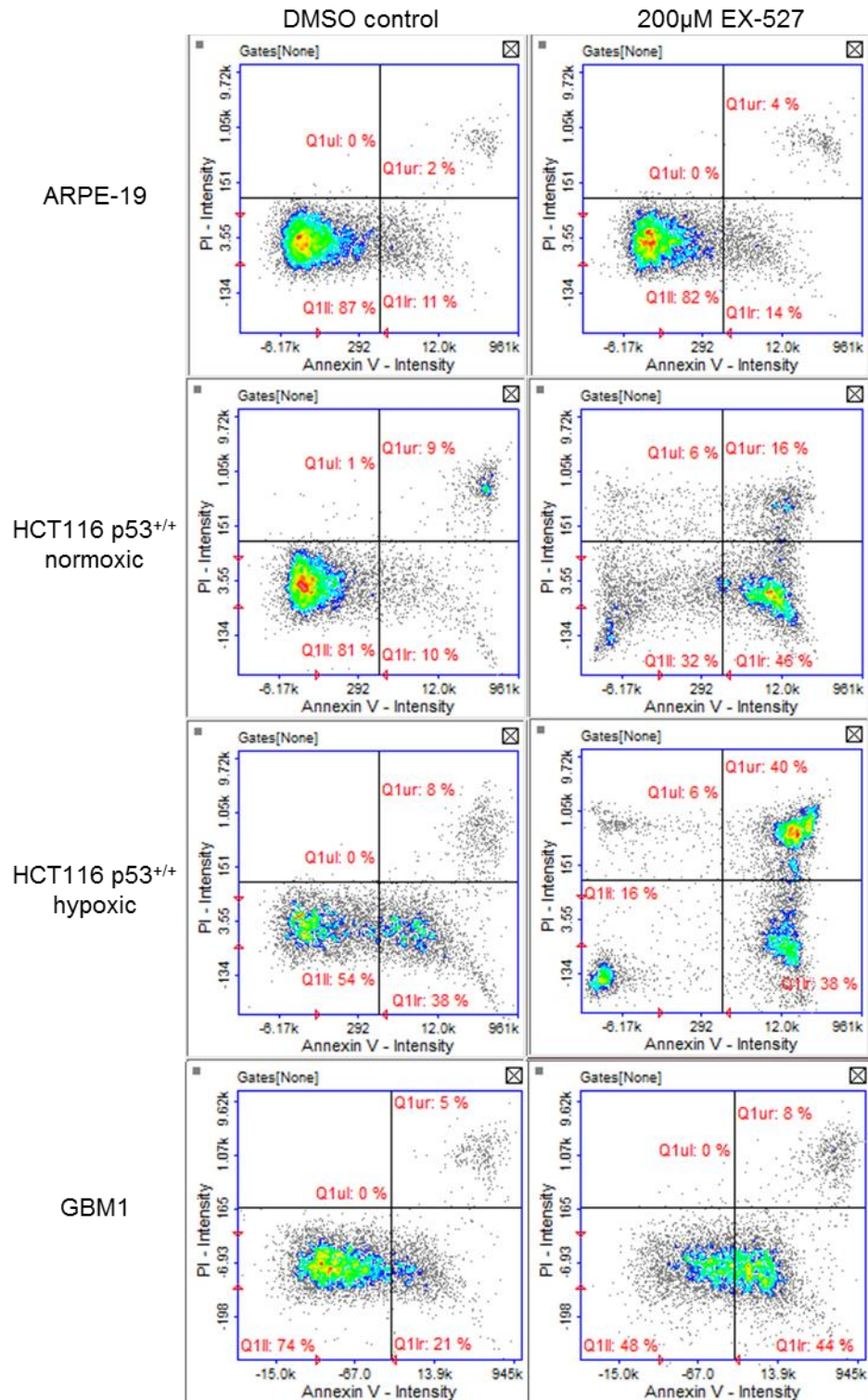


**Figure 4.9: Annexin V assay dot plots showing induction of apoptosis by SIRT1 inhibitor EX-527 in cancer cells and not in ARPE-19 non-cancer cells.**

Quantification of the proportion of early apoptotic and late apoptotic/necrotic cells through differential annexin V/PI staining after treatment with 200µM EX-527 for 48 hours in ARPE-19 non-cancer cells, HCT116 p53<sup>+/+</sup> cancer cells (normoxic and hypoxic) and GBM1 cancer stem-like cell model. Lower left quadrant indicates alive cells, lower right quadrant indicates early apoptotic cells (annexin V positive, PI negative) and upper right quadrant indicates late apoptotic/necrotic cells (annexin V positive, PI positive). n=1 or n=2 (GBM1) biological repeats (2 technical replicates).

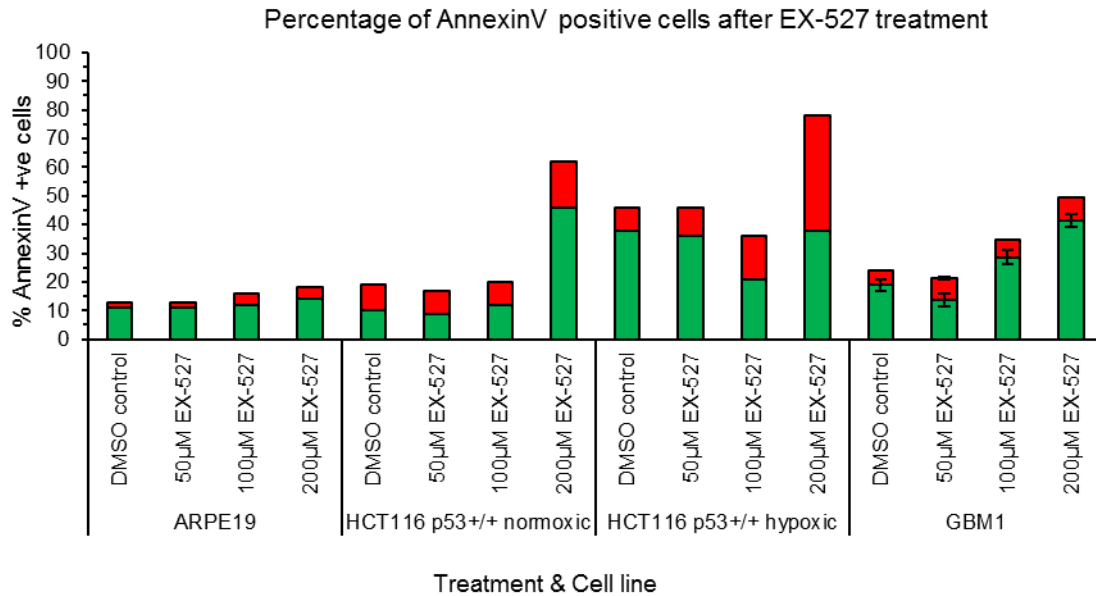


**Figure 4.10: Quantification of annexin V positive cells in response to treatment with SIRT1 inhibitor EX-527.**

Bar chart summarising percentage of early apoptotic and late apoptotic/necrotic cells after 48 hours EX-527 treatment in the indicated cell lines and conditions. Green bars represent early apoptotic cells (annexin V positive only); red bars indicate late apoptotic/necrotic cells (annexin V positive, PI positive.) n=1 biological repeat, except GBM1 n=2 biological repeats (2 technical replicates) (showing ± SEM).

As indicated by the raw annexin V data plots (Fig. 4.9), 200 μM EX-527 selectively induced cancer cell apoptosis with little or no induction of apoptosis evident in ARPE-19 non-cancer cells. In the GBM1 cancer stem cell-like model, consistent with the lower 96 hours IC<sub>50</sub> (Table 4.1), increased levels of apoptosis were also detected after 100 μM (Fig. 4.10).

Overall, these results indicate that the SIRT1 inhibitor EX-527 can partially recapitulate some of the cancer cell selective effects on survival previously reported with SIRT1-FL silencing. However, depending on cell/tissue context and with 96 hours exposure, these results suggest that selectivity with EX-527 may be less than with an RNAi-based approach.

#### 4.2.4 SIRT1-FL knock-down by siRNA and effects on neural stem cell and pluripotency markers

Whilst SIRT1-FL silencing does not induce cell death of ARPE-19 cells (Ford *et al.*, 2005), unpublished investigations (Allison *et al.* in preparation) indicate that it

can induce neuronal trans-differentiation of these retinal epithelial non-cancer cells. This seems to be dependent on expression of the SIRT1 splice variant SIRT1- $\Delta$ 8 as summarised in the schematic shown in Figure 4.11. To investigate this and potential effects of targeting SIRT1/SIRT1- $\Delta$ 8 on cell potency/stemness, ARPE-19 cells were transfected with SIRT1-FL and/or SIRT1- $\Delta$ 8 splice variant-specific siRNA. SIRT1-FL siRNA induced a neuronal-like morphology indicating successful siRNA transfection (Fig. 4.12). SIRT1- $\Delta$ 8 siRNA transfection did not induce a similar phenotype and appeared to rescue the effects of SIRT1-FL siRNA when co-transfected, consistent with SIRT1- $\Delta$ 8 being required for neuronal differentiation.

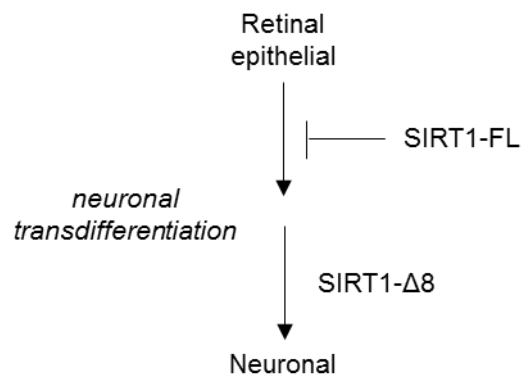


**Figure 4.11: Schematic summarising the current model for the proposed roles of SIRT1-FL and SIRT1- $\Delta$ 8 in ARPE-19 neuronal differentiation.**

ARPE-19 human retinal epithelial non-cancer cells transdifferentiate to neuronal like cells when SIRT1-FL is selectively depleted and SIRT1- $\Delta$ 8 remains. This suggests that SIRT1-FL represses the differentiation of the cells whilst SIRT1- $\Delta$ 8 is required. Based on unpublished findings (Allison *et al.* in preparation).

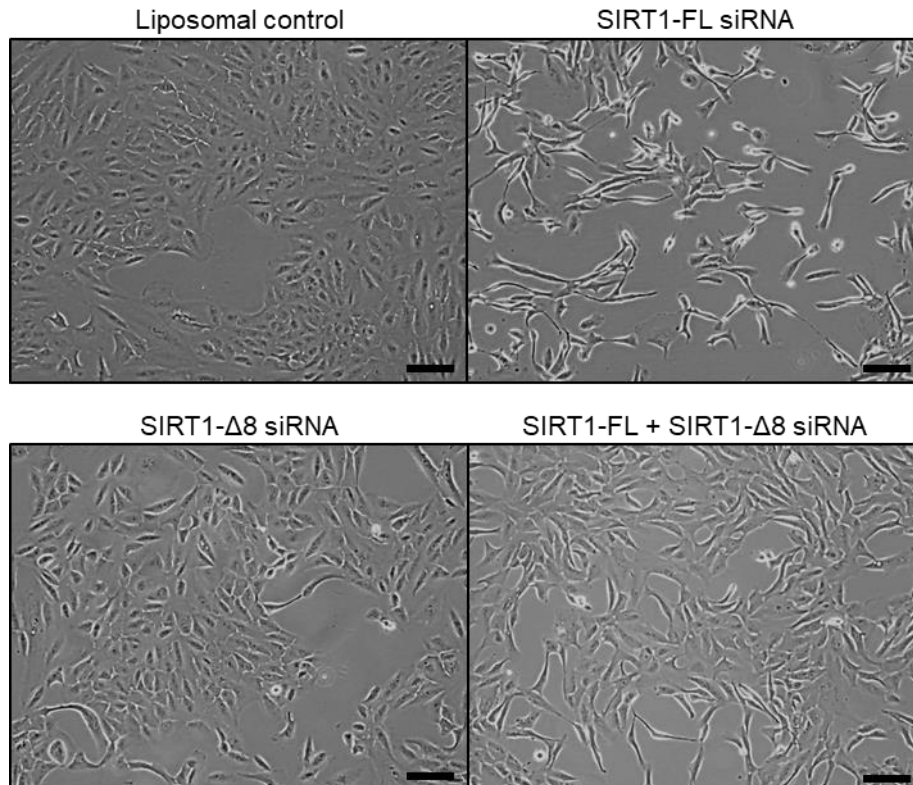


**Figure 4.12: Cell micrographs of ARPE-19 non-cancer cells after siRNA transfections to selectively deplete SIRT1-FL and/or SIRT1- $\Delta$ 8 mRNA.**

Cell images of ARPE-19 non-cancer cells 72 hours post transfection with the indicated siRNAs. Images taken with x10 objective and scale bar shows 100 $\mu$ m. n=3 biological repeats.

To verify that the siRNAs used successfully resulted in target mRNA knock-down, qPCR was performed to quantify the fold change in SIRT1-FL and SIRT1- $\Delta$ 8 mRNAs. SIRT1-FL mRNA was reduced by 84% by SIRT1-FL siRNA compared to control cells whereas SIRT1- $\Delta$ 8 mRNA levels increased. In response to SIRT1- $\Delta$ 8 siRNA, SIRT1- $\Delta$ 8 mRNA was reduced by 53%, and by 67% in co transfected cells (Fig. 4.13).

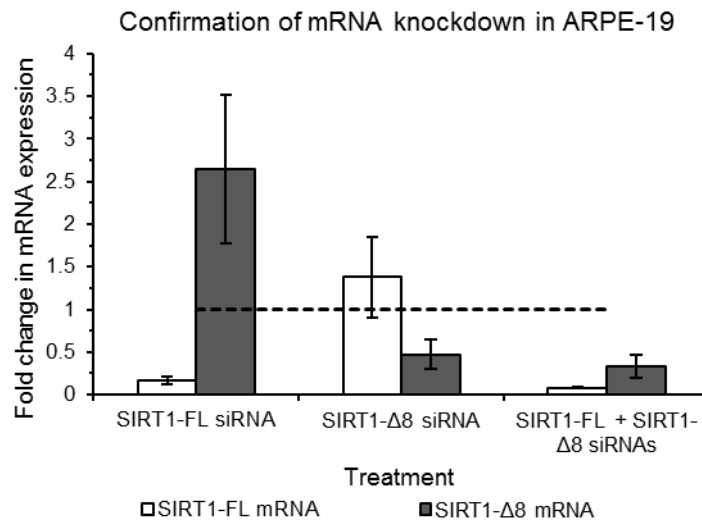


**Figure 4.13: qPCR analysis of SIRT1-FL and SIRT1-Δ8 mRNA after siRNA transfection in ARPE-19 non-cancer cells.**

Fold change of SIRT1-FL and SIRT1-Δ8 mRNA expression in ARPE-19 non-cancer cells after 72 hours SIRT1-FL or SIRT1-Δ8 siRNA transfection, alone or in combination. n=4 technical repeats ± SD from 1 biological repeat. Levels relative to liposomal control (black dotted line).

Given the transdifferentiation and apparently opposite effects of SIRT1-FL and SIRT1-Δ8 on the phenotype, it was hypothesised that SIRT1-FL/SIRT1-Δ8 knock-down may differentially affect the expression of different stem cell/reprogramming factors and pluripotency markers, furthermore terminal cellular differentiation involves loss of cell potency/stemness.

Having verified selective SIRT1-FL and SIRT1-Δ8 mRNA knock-down, their effects on expression of a number of stem cell factors/pluripotent markers were analysed.

SIRT1-FL and SIRT1-Δ8 mRNA knock-down decreased OCT4 mRNA levels by 35% and 48% respectively whilst Nanog expression was unchanged. In contrast, mRNA levels of the neural stem cell markers Nestin (Mangiola *et al.*, 2007) and KLF4 (Qin and Zhang, 2012) were both increased by ~10-fold and ~4-fold respectively in response to SIRT1-FL knock-down (Fig. 4.14). The increase in Nestin expression was specific to SIRT1-FL knock-down, consistent with its selective induction of a neuronal phenotype.

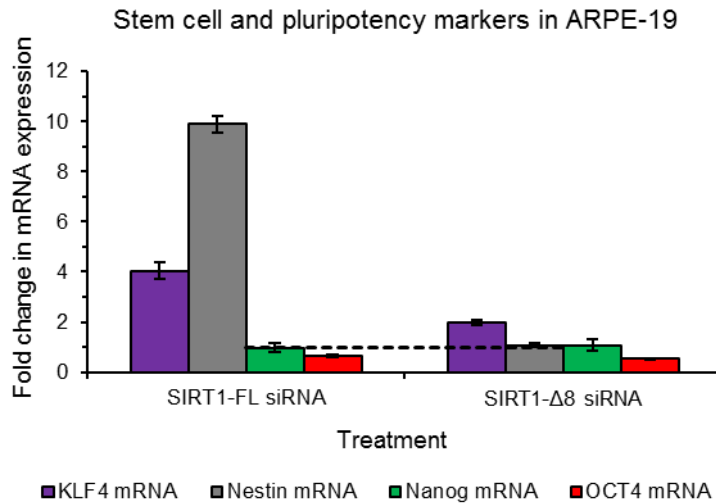


**Figure 4.14: mRNA expression of stem cell and pluripotency markers following splice variant specific siRNA mediated silencing of SIRT1 in ARPE-19 cells.**

Fold change of KLF4, Nestin, Nanog and OCT4 mRNA expression in ARPE-19 non-cancer cells after 72 hours SIRT1-FL or SIRT1-Δ8 siRNA transfection. n=4 technical repeats ± SD from 1 biological repeat. Levels relative to liposomal control (black dotted line).

To see if this effect was specific to the ARPE-19 cells or whether SIRT1-FL/SIRT1-Δ8 targeting has similar effects in a different cell context, non-cancerous colon cells CCD 841 CoN were similarly transfected. This was also performed to determine whether the CCD 841 CoN cells could be successfully siRNA-transfected as this has not been reported elsewhere.

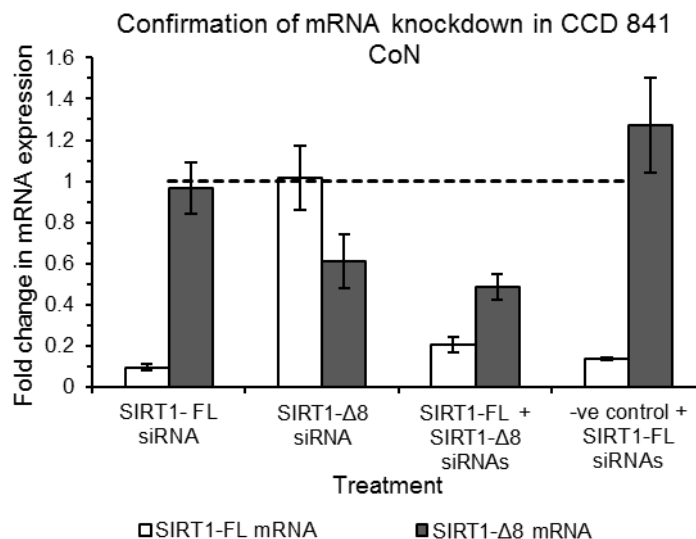


**Figure 4.15: qPCR analysis of SIRT1-FL and SIRT1-Δ8 mRNA after siRNA transfection in CCD 841 CoN non-cancer cells.**

Fold change of SIRT1-FL and SIRT1-Δ8 mRNA expression in CCD 841 CoN non-cancer cells after 72 hours SIRT1-FL or SIRT1-Δ8 siRNA transfection, alone or in combination. n=4 technical repeats ± SD from 1 biological repeat. Levels relative to negative control siRNA (black dotted line).

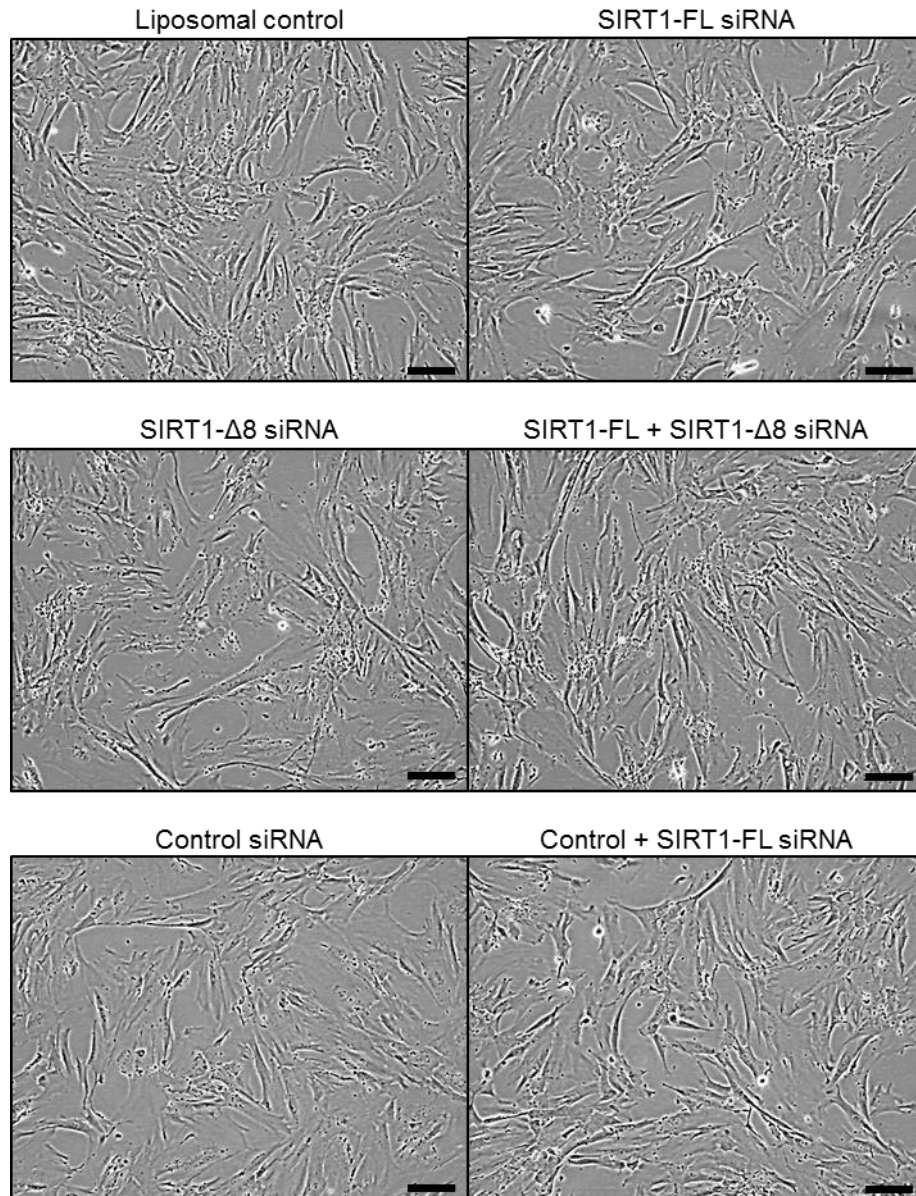


**Figure 4.16: Cell micrographs of CCD 841 CoN non-cancer cells after siRNA transfection to selectively deplete SIRT1-FL and/or SIRT1-Δ8 mRNA.**

Cell images of CCD 841 CoN non-cancer cells taken 72 hours post transfection with the indicated siRNAs. Images taken with x10 objective and scale bar indicates 100μm. n=2 biological repeats.

Selective mRNA knock-down in the CCD 841 CoN cells was confirmed by qPCR (Fig. 4.15). Although levels of SIRT1-FL mRNA knock-down were similar in the ARPE-19 and CCD 841 CoN cells (84% reduction and 91% reduction respectively), CCD 841 CoN cells showed little or no change in cell morphology (Fig. 4.16). However, the ‘normal’ morphology of CCD 841 CoN cells is not classically epithelial and is more ‘fibroblast-like’ which could make any switch towards a more neuronal-like state less phenotypically apparent. To investigate

this further, qPCRs were performed to determine expression of the stem cell/pluripotent factors that were previously analysed in the ARPE-19 cells (Fig. 4.14) as well as that of the established neuronal marker MAP1a (Nakayama *et al.*, 2003).

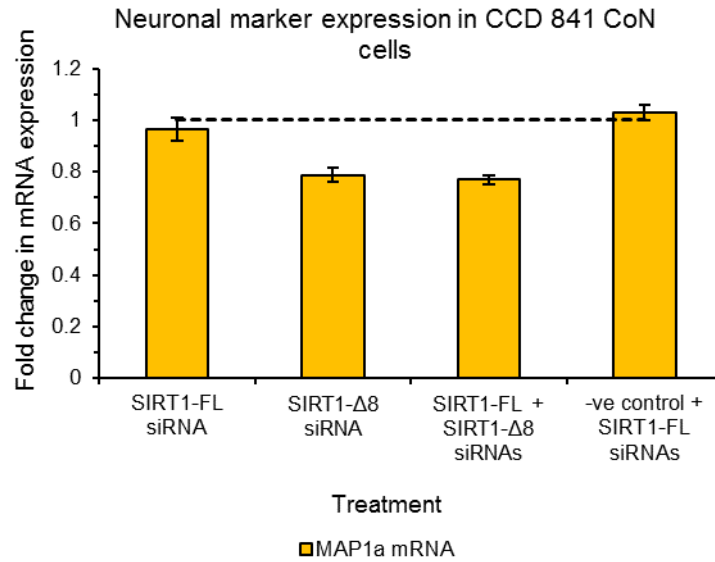


**Figure 4.17: mRNA expression of neuronal marker MAP1a following splice variant specific siRNA mediated silencing of SIRT1 in CCD 841 CoN.**

Fold change of MAP1a mRNA expression in CCD 841 CoN non-cancer cells after 72 hours SIRT1-FL or SIRT1-Δ8 siRNA transfection, alone or in combination. n=4 technical repeats ± SD from 1 biological repeat. Levels relative to negative control siRNA (black dotted line).

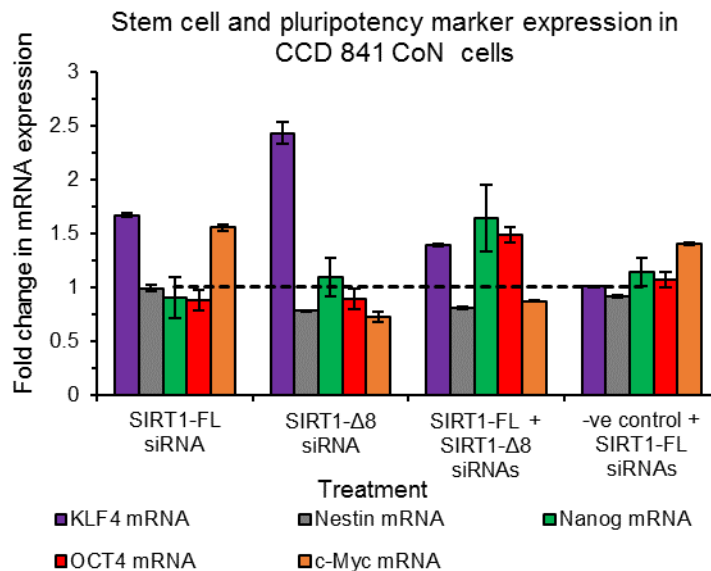


**Figure 4.18: qPCR analysis of stem cell and pluripotency markers following splice variant specific siRNA mediated silencing of SIRT1 in CCD 841 CoN.**

Fold change of KLF4, Nestin, Nanog, OCT4 and c-Myc mRNA expression in CCD 841 CoN non-cancer cells after 72 hours SIRT1-FL or SIRT1-Δ8 siRNA transfection, alone or in combination. n=4 technical repeats ± SD from 1 biological repeat. Levels relative to negative control siRNA (black dotted line).

SIRT1-FL knock-down in the ARPE-19 cells led to increased expression of the neuronal markers MAP1a and MAP2 (Allison *et al.* in preparation). Consistent with lack of morphological change of CCD 841 CoN cells after SIRT1-FL knock-down (Fig. 4.16) there was no MAP1a induction (Fig. 4.17). Although there was no apparent neuronal differentiation as seen in ARPE-19 cells it was important to assess whether SIRT1 knock-down had any similar effects on markers of cell potency/somatic reprogramming. No major effects were seen on OCT4 and Nanog mRNA levels and neural stem cell marker Nestin was not increased after SIRT1-FL knock-down as seen in ARPE-19, consistent with lack of neuronal differentiation. The most notable change was in increase in KLF4 mRNA with SIRT1- $\Delta$ 8 siRNA, which was increased by a similar level by SIRT1- $\Delta$ 8 siRNA in ARPE-19 cells. However, in contrast to ARPE-19, KLF4 mRNA showed little or no change in expression in response to SIRT1-FL siRNA. Overall, changes in gene expression observed were quite small in magnitude with some unexpected variation (e.g. small increase in KLF4 with SIRT1-FL siRNA but not with control siRNA + SIRT1-FL siRNA).

Although the effects of SIRT1 knock-down in CCD 841 CoN cells were different to ARPE-19 and it did not appear to induce neuronal differentiation, importantly SIRT1 knock-down did not induce cell death as seen in HCT116 p53<sup>+/+</sup> cancer cells (Fig. 4.1). This is consistent with the reported cancer cell selectivity of SIRT1-FL knock-down and relative insensitivity of CCD 841 CoN non-cancer cells to EX-527 (Table 4.1).

#### **4.2.5 Small molecule chemical inhibition of SIRT1 via EX-527 induces neuronal trans-differentiation of ARPE-19 and CCD 841 CoN non-cancer cells**

Having observed that EX-527 was able to partially recapitulate the effects of SIRT1-FL knock-down on cancer versus non-cancer cell survival (Fig. 4.8 & Fig. 4.10) the question was whether it could similarly induce neuronal transdifferentiation of non-cancer cells. ARPE-19 cell micrographs indicated that EX-527 induced a similar 'neuronal-like' or fibroblast-like morphology at higher doses suggestive of possible transdifferentiation (Fig. 4.19).

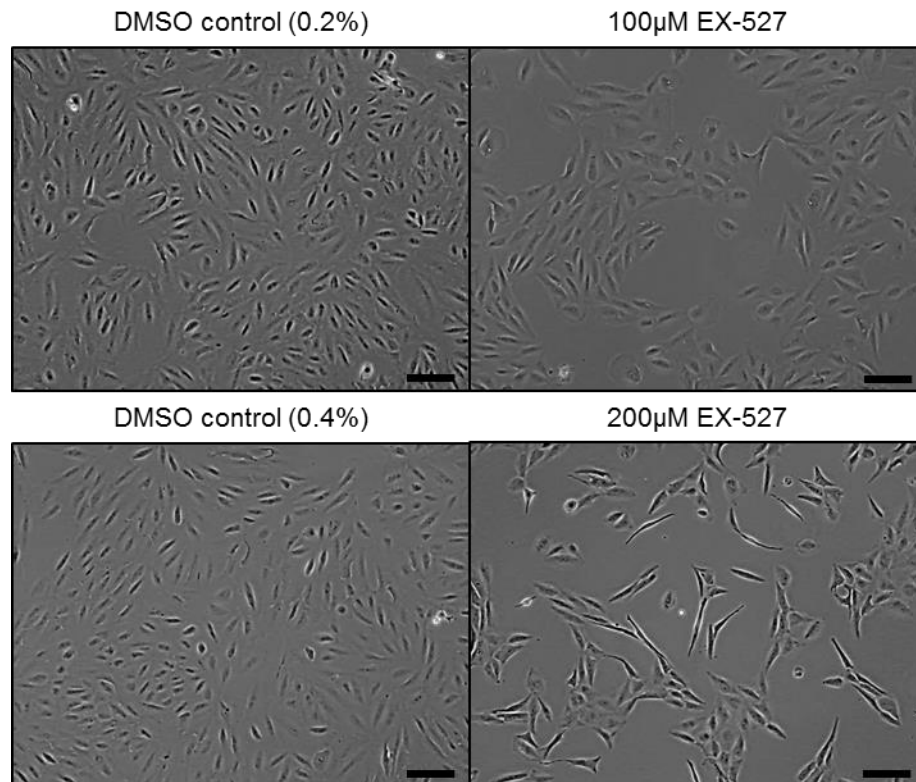


**Figure 4.19: Cell micrographs of ARPE-19 non-cancer cells after 48 hours treatment with SIRT1 inhibitor, EX-527.**

Cell images of ARPE-19 non-cancer cells 48 hours post exposure to the indicated EX-527 doses compared to their corresponding DMSO controls. Images taken with x10 objective and scale bar indicates 100µm. n=3 biological repeats.

To assess whether or not the cells had neuronally transdifferentiated or had undergone transdifferentiation to another cell type with a mesenchymal morphology, mRNA expression of two key neuronal markers MAP1a and MAP2 (Soltani *et al.*, 2005; Nakayama *et al.*, 2003) were determined. Similar to effects induced by SIRT1-FL knock-down (appendix Fig. 9.1), 200µM EX-527 increased MAP1a and MAP2 mRNA expression by ~4.5-fold and ~12-fold respectively (Fig. 4.20).

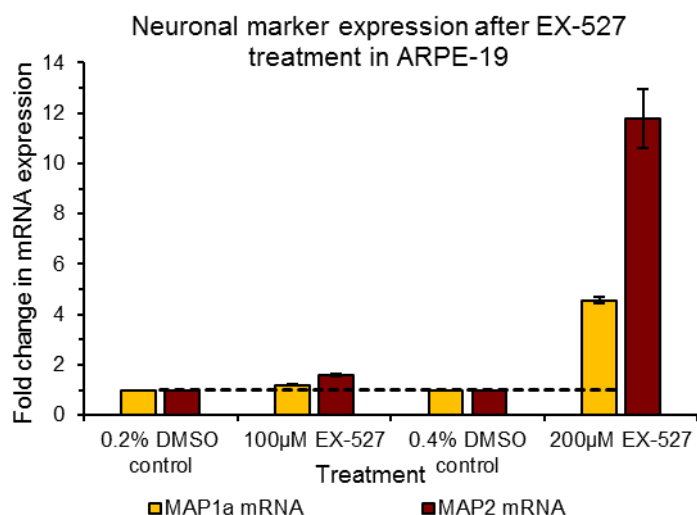


**Figure 4.20: mRNA expression of neuronal markers in EX-527 treated ARPE-19 non-cancer cells.**

Fold change in mRNA expression of neuronal markers MAP1a and MAP2 in ARPE-19 non-cancer cells after 48 hours exposure to the indicated EX-527 doses, n=4 technical repeats  $\pm$  SD from 1 biological repeat. Levels relative to individual DMSO vehicle controls (black dotted line).

Interestingly and in contrast to the lack of morphological change with SIRT1-FL knock-down in the CCD 841 CoN cells, EX-527 treatment of these cells induced a clear change in cell morphology with cells becoming more elongated and starting to resemble neuronal cells (Fig. 4.21). It was also noted that at higher doses of EX-527 fewer cells were evident consistent with terminal differentiation and cell cycle exit.

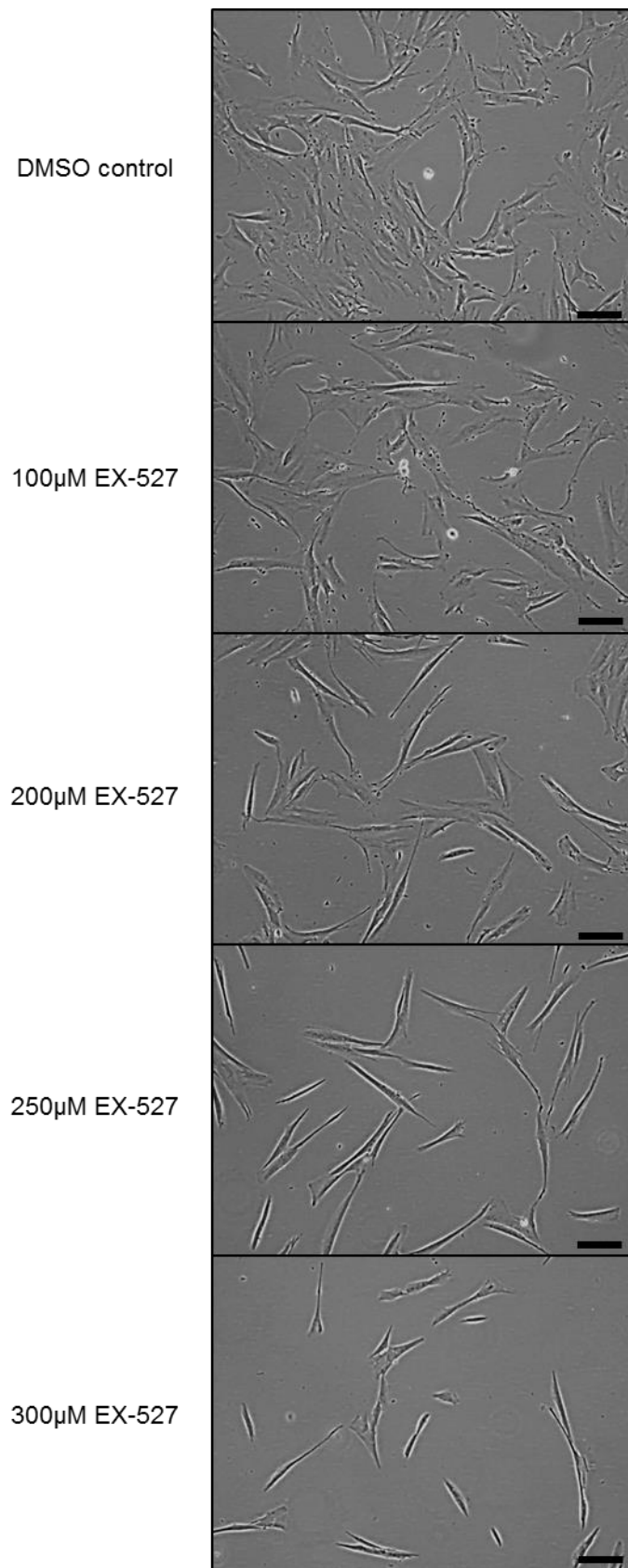


**Figure 4.21: Cell micrographs of CCD 841 CoN non-cancer cells after 48 hours EX-527 treatment.**

Cell images of CCD 841 CoN non-cancer cells 48 hours after treatment with EX-527 at the indicated doses or DMSO vehicle control. Images taken with x10 objective and scale bar indicates 100µm. n=3 biological replicates.

qPCR analysis revealed a 2.5-fold increase in expression of the neuronal marker MAP1a (Fig. 4.22), suggesting that SIRT1 also promotes neuronal transdifferentiation of these non-cancer cells. In further support of this, mRNA expression of the neural stem cell marker Nestin was increased ~5.5-fold (Fig. 4.23). Expression of somatic reprogramming/stem cell factors KFL4 and Nanog both increased in a dose dependent manner consistent with transdifferentiation of these cells whilst OCT4 expression showed a small decrease (Fig. 4.23).

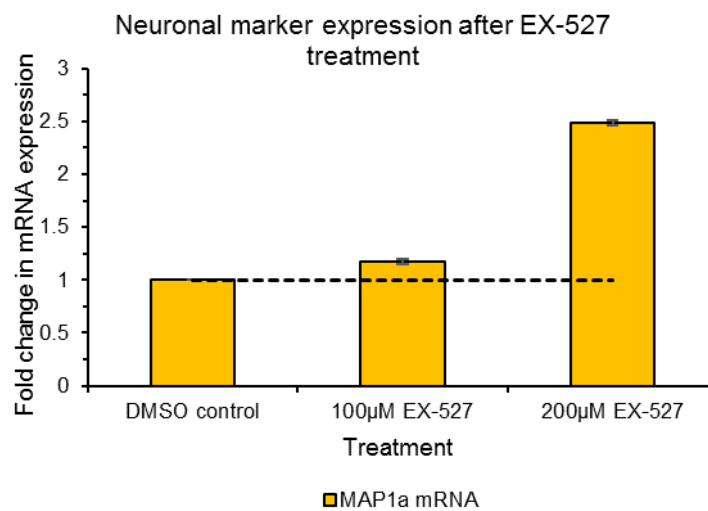


**Figure 4.22: mRNA expression of neuronal marker MAP1a in CCD 841 CoN cells after treatment with EX-527 for 48 hours.**

Fold change in mRNA expression of the neuronal marker MAP1a in CCD 841 CoN non-cancer cells after treatment with the indicated doses of EX-527 or DMSO vehicle control for 48 hours. n=4 technical repeats  $\pm$  SD from 1 biological repeat. Levels relative to DMSO vehicle controls (black dotted line).

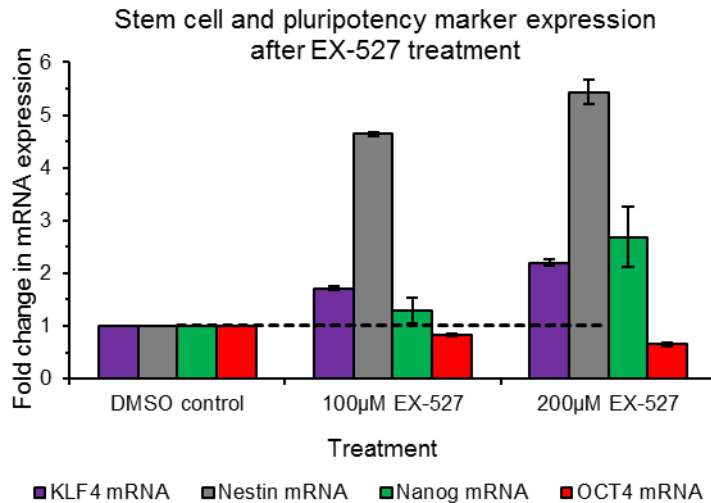


**Figure 4.23: qPCR analysis of stem cell and pluripotency markers in CCD 841 CoN cells following EX-527 treatment.**

Fold change of KLF4, Nestin Nanog and OCT4 mRNA expression in CCD 841 CoN non-cancer cells after 48 hours treatment with the indicated EX-527 doses and DMSO vehicle control. n=4 technical repeats  $\pm$  SD from 1 biological repeat. Levels relative to DMSO vehicle controls (black dotted line).

#### **4.2.6 Effects of EX-527 treatment on cancer cell ‘stemness’ in the GBM1 cancer stem cell model.**

GBM1 cells have been extensively characterised and are considered to be cancer stem cell-like (Wurdak *et al.*, 2010b). Importantly whilst EX-527 was able to reduce viability of the GBM1 cells (Fig. 4.10) it was also noted that cell morphology changed with cells phenotypically showing neurite-like projections (Fig. 4.24). It was therefore investigated whether EX-527 was able to alter the cancer stem cell-ness/differentiated state of GBM1 cells.

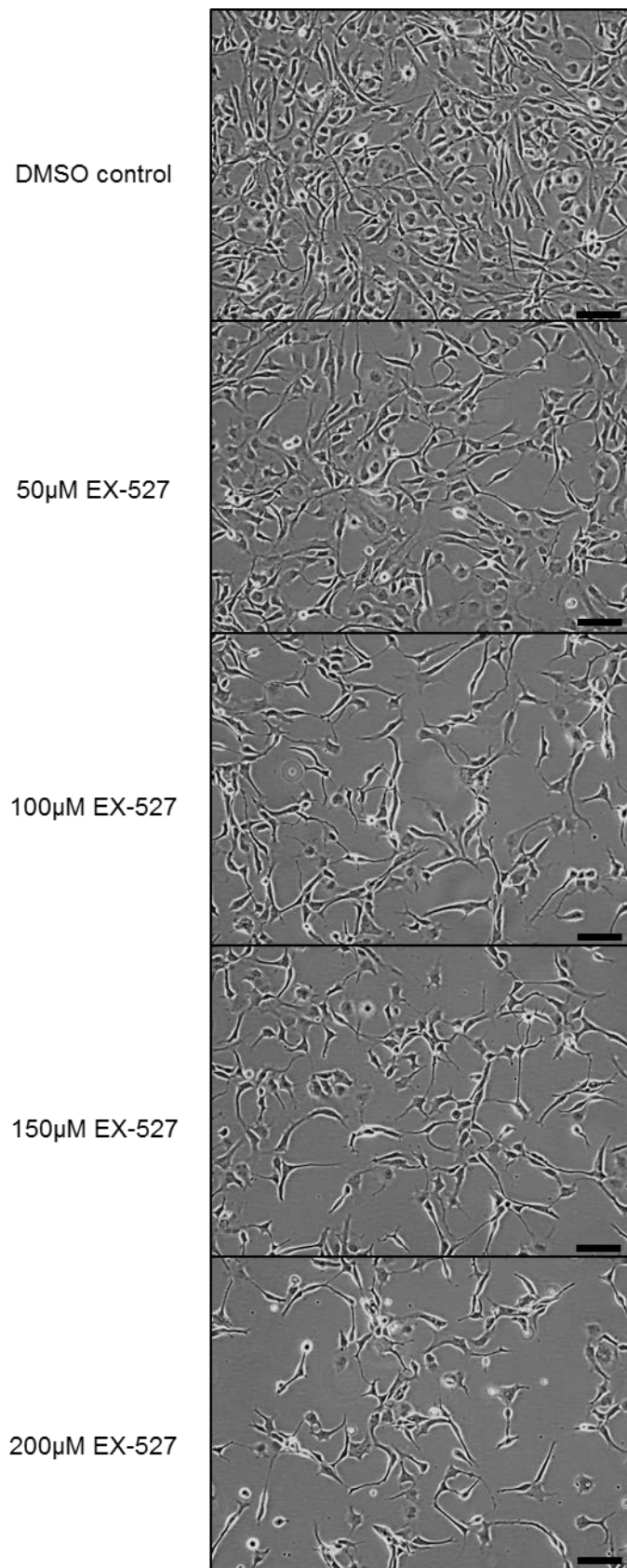


**Figure 4.24: Cell micrographs of GBM1 cancer stem like cells after 48 hours EX-527 treatment.**

Cell images of GBM1 cancer stem cell like cells 48 hours after treatment with EX-527 at the indicated doses or DMSO vehicle control. Images taken with x10 objective and scale bar indicates 100µm. n=2 biological repeats.

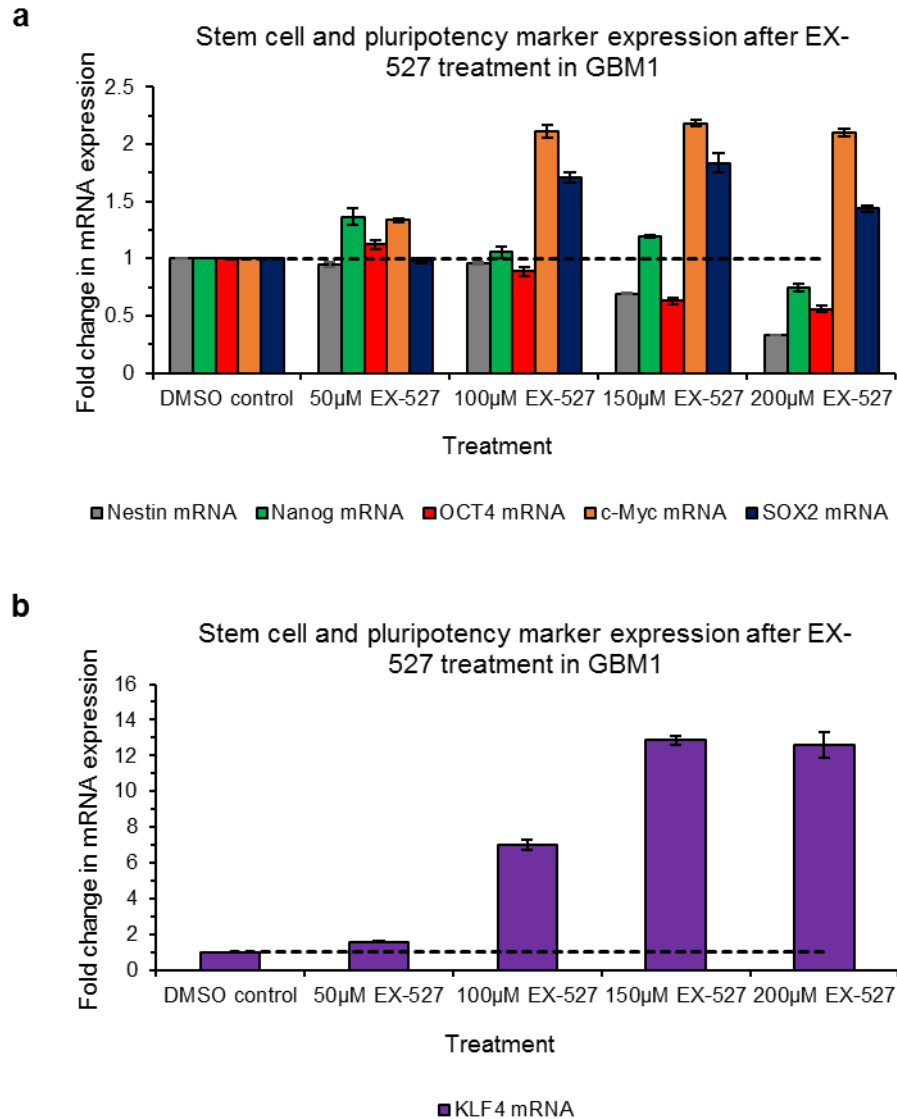


**Figure 4.25: Expression of stem cell markers in EX-527 treated GBM1 cells.**

Fold change in mRNA expression of stem cell markers in GBM1 cells after 48 hours exposure to the indicated EX-527 doses, n=4 technical repeats  $\pm$  SD from 1 biological repeat.

mRNA expression of the neural stem cell factor Nestin, which is highly expressed in GBM1 cells under normal growth conditions (Wurdak *et al.*, 2010b) was reduced by 3-fold by 200μM EX-527, consistent with progression towards a more differentiated state. Levels of OCT4 mRNA decreased whilst expression of the neuronal marker MAP1a increased modestly (Fig. 4.26).

KLF4 mRNA expression was induced by ~12.6-fold with 150 and 200μM EX-527 treatment (Fig. 4.25), consistent with KLF4 induction in CCD 841 CoN treated with EX-527 and ARPE-19 with SIRT1-FL knock-down, which both showed

neuronal transdifferentiation. SOX2 and c-Myc mRNA expression showed a small increase by up to 1.5-fold and 2-fold respectively with EX-527 treatment.

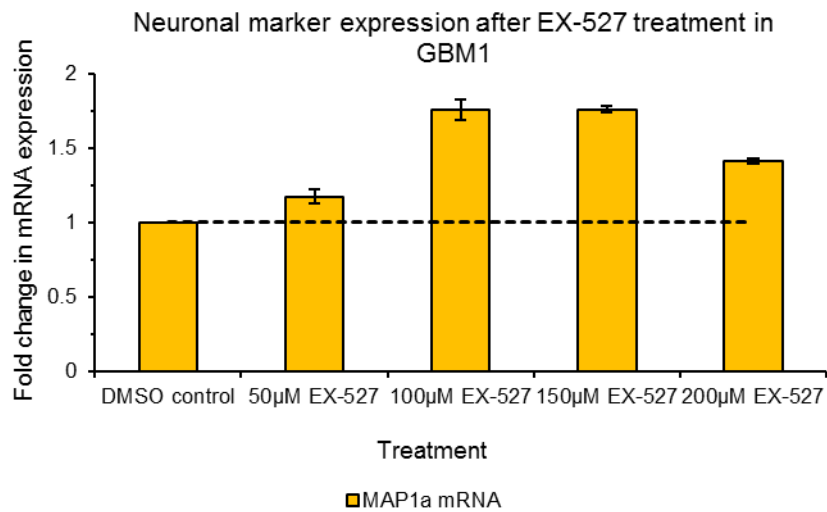


**Figure 4.26: qPCR analysis of neuronal marker expression in GBM1 cells after EX-527 treatment.**

Fold change in MAP1a mRNA levels in GBM1 cancer stem like cells after 48 hours exposure to the indicated EX-527 doses, n=4 technical repeats  $\pm$  SD from 1 biological repeat.

#### **4.2.7 Increase in MAP2 protein expression with EX-527 treatment**

As mRNA levels of the neuronal markers MAP1a and MAP2 were increased after EX-527 treatment it was important to see whether this resulted in their increased protein expression. ARPE-19 cells were treated with EX-527 at the indicated doses for the same time course (48 hours) and were then fixed.

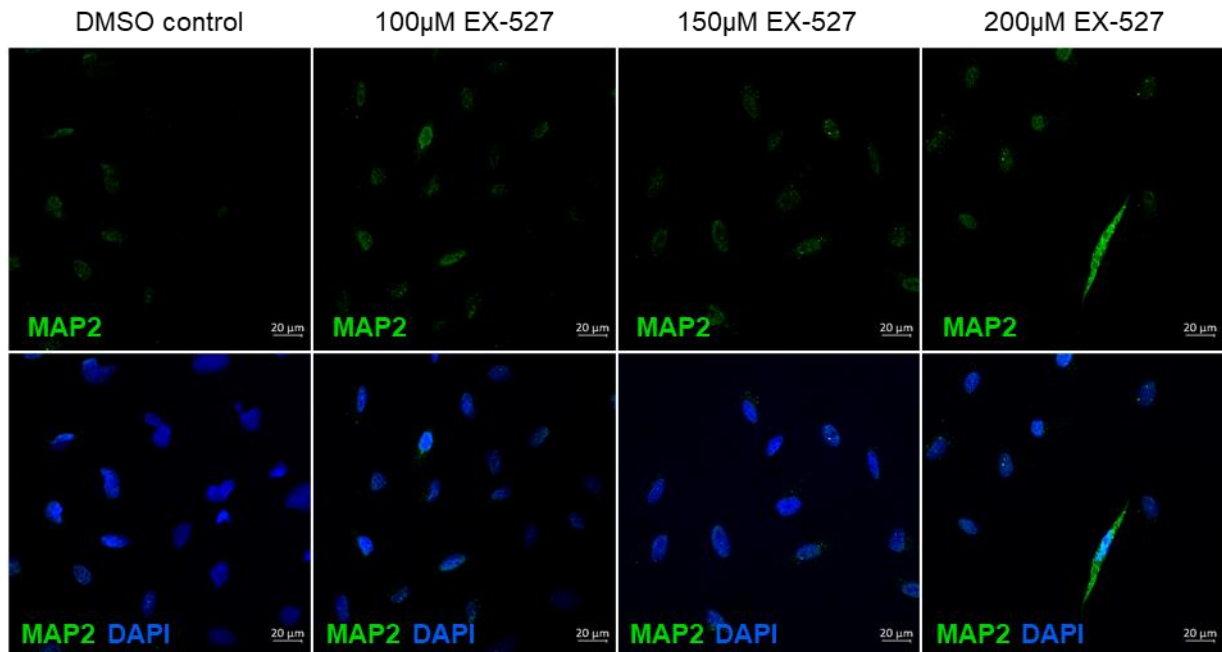


**Figure 4.27: Expression of the neuronal marker MAP2 in ARPE-19 cells treated with EX-527.**

Representative immunofluorescent cell micrographs of ARPE-19 cells treated with the indicated EX-527 doses and DMSO control, showing the neuronal marker MAP2 (green) and nuclear marker DAPI (blue). Images taken with x40 objective and scale bar indicates 20µm. n=1 biological repeat.

Preliminary immunofluorescence analysis indicated an increase in MAP2 expression with EX-527 treatment, with highest levels in cells with an elongated neuronal morphology (Fig. 4.27).

#### 4.2.8 Metabolic effects of SIRT1 knock-down/inhibition

It has previously been shown that cellular differentiation can affect cell metabolism but also that the opposite is true, that the metabolic status of the cell can affect cell fate (Zheng *et al.*, 2016; Ryu *et al.*, 2018). As it was observed that SIRT1 knock-down or inhibition induced neuronal transdifferentiation it was assessed whether targeting SIRT1 resulted in any changes in the metabolic state of the cells.

ARPE-19 and CCD 841 CoN non-cancer cells and HCT116 p53<sup>+/+</sup> cancer cells were treated with EX-527 for 24 hours and their metabolic response was investigated using the Seahorse XFP metabolic analyser.

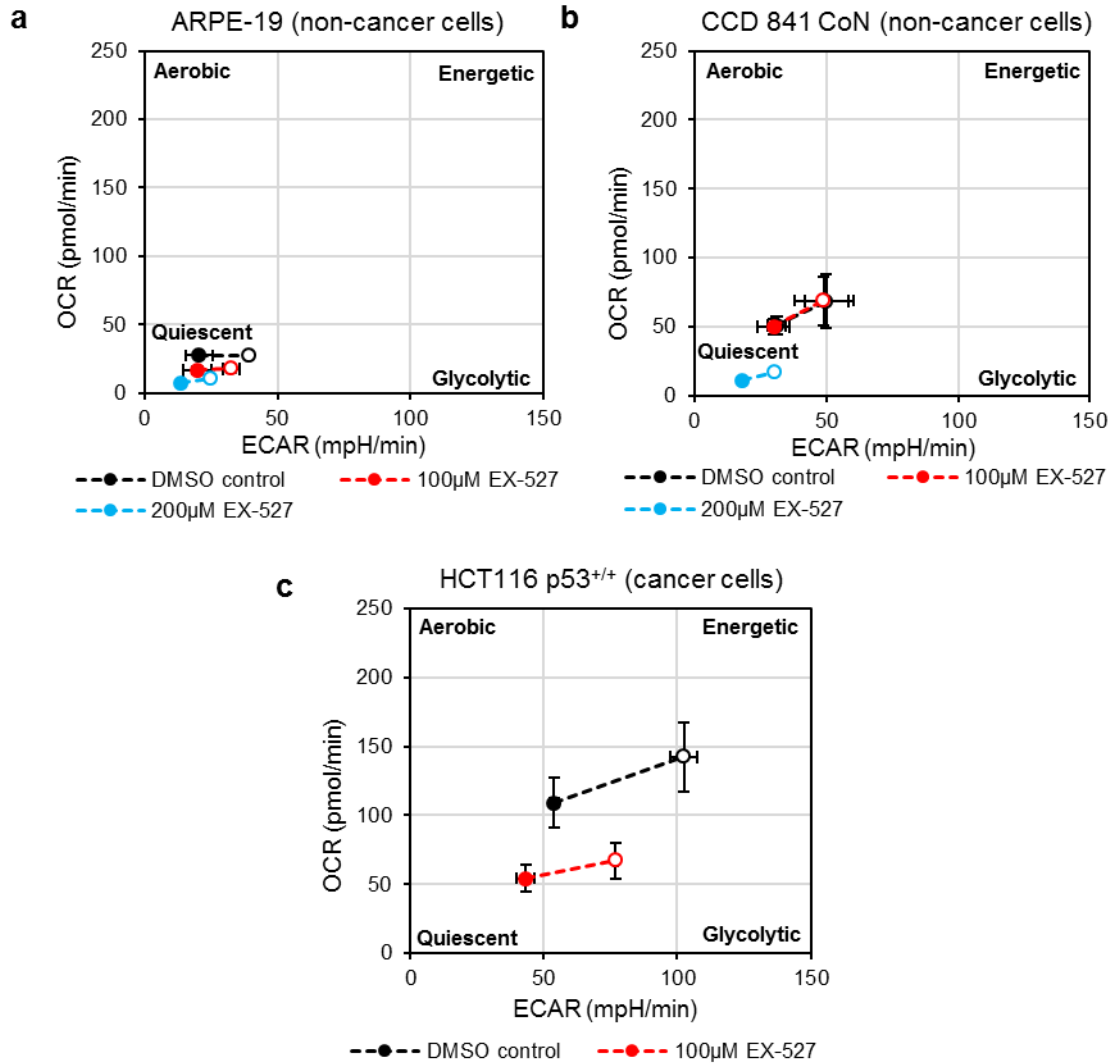


**Figure 4.28: Cell energy phenotype of non-cancer and cancer cells after 24 hours EX-527 treatment.**

ARPE-19 (a) CCD 841 CoN (b) non-cancer cells and HCT116 p53<sup>+/+</sup> cancer cells (c) were treated with the indicated EX-526 doses for 24 hours prior to analysis. Cell energy phenotypes are shown compared to DMSO control cells; basal metabolic phenotype is indicated by closed circles; metabolic stress response/capacity is indicated by open circles. n=3 biological repeats (3 technical replicates) ± SEM.

ARPE-19 and CCD 841 CoN non-cancer cells appeared to be largely unaffected by 100µM EX-527 treatment (Fig. 4.28a & b), whereas 200µM EX-527 resulted in a more quiescent metabolic phenotype (glycolysis and oxidative phosphorylation were both reduced) which is consistent with their differentiated neuronal phenotype. As 200µM EX-527 induced toxic effects in HCT116 p53<sup>+/+</sup> cancer cells which would lead to effects on metabolism, they were only analysed after 100µM EX-527. This dose of EX-527 led to an impairment in mitochondrial

respiration and during metabolic stress their ability to upregulate mitochondrial respiration or glycolysis was reduced compared to the DMSO control (Fig. 4.28c).

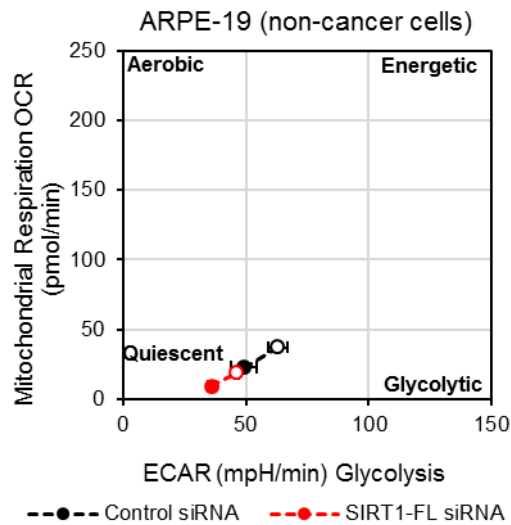


**Figure 4.29: Cell energy phenotype of ARPE-19 non-cancer cells after SIRT-FL siRNA transfection.**

ARPE-19 non-cancer cells were transfected with SIRT1-FL siRNA for 72 hours prior to analysis. Cell energy phenotype is shown compared to negative control siRNA transfected cells; basal metabolic phenotype is indicated by closed circles; metabolic stress response/capacity is indicated by open circles. n=3 technical repeats  $\pm$  SD from 1 biological replicate.

Where ARPE-19 non-cancer cells had been transfected with SIRT1-FL siRNA, the rate of oxidative phosphorylation and glycolysis was decreased compared to the cells that had been transfected with control siRNA, showing that similarly to 200 $\mu$ M EX-527 that the cells were more quiescent.

## 4.3 Discussion and Conclusions

### 4.3.1 Preferential cytotoxic activity of the SIRT1 inhibitor EX-527 towards cancer cells *in vitro*, partially mimicking the effects of SIRT1-full length knock-down by RNAi

The SIRT1 inhibitor EX-527 is reported to be ~100 fold more selective towards SIRT1 than SIRT2 or SIRT3. However, based on available mechanism of action data (Gertz *et al.*, 2013), it might also be predicted to inhibit SIRT1- $\Delta$ E2 and SIRT1- $\Delta$ 8 although this has not been demonstrated. Nevertheless, in 96 hours continuous drug exposure chemosensitivity assays EX-527 was significantly more active towards all ten cancer cell lines analysed compared to CCD 841 CoN non-cancer cells ( $p < 0.0001$ ) (Fig. 4.2 & Fig. 4.3,  $n=3$  independent biological repeats). This included activity against seven cancer cell lines not previously analysed by SIRT1-FL knock-down (ovarian A2780 & CP70, prostate PC-3, lung H460 & A549, breast MDA-MB-231 & MDA-MB-436).

Compared against ARPE-19 and PNT2 non-cancer cells, EX-527 showed small significant preferential cancer cell cytotoxicity but only towards a modest subset of the cancer cells tested, namely HCT116 p53<sup>+/+</sup>, HCT116 p53<sup>-/-</sup>, HT-29 and PC3 (Fig. 4.2,  $n=3$  independent biological repeats). In comparison with FDA-approved platinates (although this was restricted to HCT116 p53<sup>+/+</sup> vs CCD 841 CoN), EX-527 showed improved cancer cell selectivity on a par with that of FK866 (Fig. 4.4) indicating perhaps that it may have some therapeutic potential as a single agent towards certain cancers. It is presently unclear whether differences in activity towards different cell lines, including non-cancer cells, reflect EX-527 on-target effects (towards SIRT1-FL) and differential dependencies or off-target EX-527 effects (e.g. towards SIRT1- $\Delta$ E2, SIRT1- $\Delta$ 8, other sirtuins or other proteins). Different tissues have been reported to express different relative levels of the different splice variants (Shah *et al.*, 2012; Lynch *et al.*, 2010) with SIRT1- $\Delta$ E2 identified as a tissue-restrictive isoform (Deota *et al.*, 2017) (section 1.4.2.2). The functional interrelationships and roles of the different variants are also not fully

understood with respect to redundancy or overlap of functions (adaptive response), opposing functions and distinct/unique functions.

Preferential cytotoxicity of EX-527 was also observed with a shorter exposure of 48 hours, with EX-527 inducing cancer cell apoptotic death (Fig. 4.9 & Fig. 4.10 n=1 or n=2 biological repeats), as has previously been reported with SIRT1-FL knock-down (Ford *et al.*, 2005). This was confirmed here, with SIRT1-FL knock-down in the HCT116 p53<sup>+/+</sup> cancer cells inducing a ~3.5 fold increase in the proportion of apoptotic cells (Fig. 4.1, n=1 biological repeat) which was similar to previously reported (Ford *et al.*, 2005). Importantly, 48 hours 200µM EX-527 treatment induced a comparable ~3-3.5-fold increase in apoptosis compared to DMSO vehicle controls in the HCT116 p53<sup>+/+</sup> cancer cells but had little effects in ARPE-19 non-cancer cells (Fig. 4.9 & Fig. 4.10) suggesting improved cancer cell selectivity of EX-527 over a shorter exposure period. Importantly, selective activity was also observed against hypoxic HCT116 p53<sup>+/+</sup> cancer cells, both by chemosensitivity assay (96 hours; Table 4.1 & Fig. 4.5, n=3 independent biological repeats) and 48 hours analyses (cell micrographs, cell counts, apoptotic assays; Fig. 4.7 – Fig. 4.10, n=2 biological repeats). Further investigations in other hypoxic cancer cells are required and at other oxygen tensions; interestingly, EX-527 also showed promising activity towards the GBM1 cancer stem cell-like model (Fig. 4.7 – Fig. 4.10).

Overall, EX-527 was able to partially recapitulate the effects of SIRT1-FL knock-down and these results provide some validation of SIRT1-FL as a potential target for a subset of cancers. However, cancer cell selectivity appeared less than with an RNAi-based approach raising the possibility of off-target effects. With the advent of new genome editing technology, a CRISPR-based approach provides another therapeutic possibility for the future. It would be interesting to test whether EX-527 cancer cell cytotoxicity observed here could be rescued with knock-down of the transcription factor FOXO4. Previously, cancer cell apoptotic death induced by SIRT-FL knock-down was shown to be dependent on FOXO4 (Ford *et al.*, 2005; Allison *et al.*, 2014) so this would provide an indication of what proportion of EX-527 cancer cell toxicity is due to on-target SIRT1-FL inhibition.

SIRT1 protein expression analyses indicated that the three non-cancer cell models all expressed lower SIRT1 levels than the cancer cell lines and there was some very weak inverse correlation between expression and IC<sub>50</sub> in the cancer cells (Fig. 4.6). However, expression of splice variants was not analysed due to antibody availability and further work is required to understand which cancers are most dependent on SIRT1 for survival and in which contexts a sufficient therapeutic window may exist. Based on these findings as well as tumour suppressing/normal functions of SIRT1 reported in the literature (section 1.4.2), it may be a systemic approach to targeting SIRT1 is challenging and a loco-regional approach or perhaps a SIRT1-based prodrug may be more appropriate. Thus, whilst the hypothesis that inhibition of SIRT1 is preferentially cytotoxic towards cancer cells is partially supported, the data suggests that this depends on the particular cancer cells. Additional work is required to fully understand which cancers may be most sensitive to SIRT1 and why.

### **4.3.2 SIRT1 inhibitor EX-527 induces neuronal trans-differentiation of ARPE-19 and CCD 841 CoN non-cancer cells**

SIRT1-FL knock-down by RNAi in the ARPE-19 retinal epithelial non-cancer cells induced a neuronal-like morphology that was rescued by SIRT1- $\Delta$ 8 co-silencing (Fig. 4.12 & Fig. 4.13, n=1 or n=2 biological repeats), consistent with earlier findings (Allison *et al.* in preparation). These results support the model proposed in Figure 4.11 which suggest that SIRT1-FL constitutively suppresses neuronal transdifferentiation of these cells whereas SIRT1- $\Delta$ 8 has an opposing function, being required for neuronal transdifferentiation. Importantly, EX-527 was able to induce similar neuronal-like morphology in the ARPE-19 cells and also in colon epithelial CCD 841 CoN non-cancer cells (Fig. 4.19 & Fig. 4.21, n=3 biological repeats) demonstrating that SIRT1-mediated regulation of cell fate or differentiation state was not restricted to the ARPE-19 cells. This also suggests that any inhibition of SIRT1- $\Delta$ 8 by EX-527 is small at the tested doses as gene silencing experiments indicate that SIRT1- $\Delta$ 8 is required for the neuronal phenotypic switch (Fig. 4.12). It would be interesting to further test this by

silencing SIRT1- $\Delta$ 8 in EX-527 treated cells to see whether this prevents the EX-527-induced neuronal phenotype.

Importantly, further analyses showed that EX-527 induced mRNA expression of the commonly used neuronal markers MAP1a and MAP2 (Halpain and Dehmelt, 2006; Dehmelt and Halpain, 2005) in the ARPE-19 and CCD 841 CoN cells (Fig. 4.20 & Fig. 4.22, n=1 biological repeat) mimicking the effects of SIRT1-FL silencing in the ARPE-19 cells (appendix Fig. 9.1). This indicates that EX-527 induces neuronal transdifferentiation and the neuronal-like/mesenchymal morphology is not induced epithelial-mesenchymal transition (EMT) or transdifferentiation to a mesenchymal cell type. Increased expression of MAP2 protein was also evident in ARPE-19 non-cancer cells after 200 $\mu$ M EX-527 exposure in more phenotypically elongated cells (Fig. 4.27). Further work is required to determine whether EX-527 treated cells permanently exit the cell cycle and terminally differentiate, or whether with EX-527 removal the differentiation phenotype is lost. Another key question is whether mature, functional neurons can be generated. This has important therapeutic implications with neurodegeneration being a major societal health problem. Previous research shows that SIRT1 has a role in neuroprotection, for example Kim *et al.* (2007) report that upregulation of SIRT1 or its activation by resveratrol, promotes neuronal survival and slows neurodegeneration. Here it is shown that 2 splice variants of SIRT1, SIRT1-FL and SIRT1- $\Delta$ 8 have opposing effects on inducing the neuronal phenotype, with SIRT1-FL having a role in repressing the phenotype and SIRT1- $\Delta$ 8 being required for it. Levels of SIRT1- $\Delta$ 8 have previously been reported to be high in the brain (Lynch *et al.*, 2010) which is interesting and consideration must be taken in terms of what splice variants have been targeted during previous studies which show that SIRT1 has a protective role in neurogenesis.

### **4.3.3 Effects of SIRT1-FL and SIRT1-Δ8 targeting on expression of stem cell and pluripotent/somatic reprogramming factors**

It was hypothesised that the neuronal transdifferentiation induced by SIRT1-FL silencing, or EX-527, may involve changes in somatic reprogramming factors or pluripotent/stem cell factors as it depends on some degree of de- and re-differentiation. In 2006, Yamanaka and colleagues showed that it was possible to reprogram adult somatic cells (fibroblasts) to a pluripotent stem cell state (iPSCs) by the exogenous addition of four transcription factors OCT4, SOX2, KLF4 and c-Myc (Takahashi and Yamanaka, 2006). Here, the effects of SIRT1-FL and SIRT1-Δ8 silencing and EX-527 on expression of somatic reprogramming factors and stem cell factors was assessed.

SIRT1-FL silencing in the ARPE-19 cells caused a 10-fold increase in expression of the neural stem cell marker Nestin (Mangiola *et al.*, 2007) whereas SIRT1-Δ8 silencing had no effects (Fig. 4.14) consistent with their differential effects on ARPE-19 neuronal transdifferentiation. Similarly, EX-527 caused a 5.5-fold increase in Nestin expression in the CCD 841 CoN cells (Fig. 4.23). The effects of EX-527 on Nestin (and other stem cell factors) in the ARPE-19 cells is yet to be investigated. SIRT1-FL silencing in the ARPE-19 cells and EX-527 treatment in the CCD 841 CoN cells both also caused an increase in mRNA expression of the somatic reprogramming factor KLF4 but a small decrease in OCT4 (Fig. 4.14 & Fig. 4.23). A ~2.5-fold increase in Nanog expression was also observed with 200μM EX-527 treatment in the CCD 841 CoN cells (Fig. 4.23). Overall, these results indicate changes in stem cell/somatic reprogramming factors which are consistent with transition to a different neuronal differentiation state via a more progenitor state. It is currently unclear how SIRT1-FL silencing/inhibition results in these changes in expression, but it is hypothesised that they may be caused by epigenetic changes at the gene promoters given SIRT-FL function as a histone and protein deacetylase.

In the case of retinal pigment epithelia (RPE), RPE cellular senescence and cell loss is a major cause of age-related macular degeneration (AMD) which can lead

to blindness (Kozlowski, 2012). There is interest as to whether differentiated RPE or other retinal cells could be reprogrammed to iPSC. Following de-differentiation, the ability to promote neuronal differentiation, for example by inhibiting SIRT1 (these results), rather than mesenchymal differentiation to adipocytes or chondrocytes (Salero *et al.*, 2012) could potentially be used to facilitate restoration of the retina in AMD or after injury.

#### **4.3.4 Inhibition of SIRT1 reduces ‘stemness’ of GBM1 cancer stem cell-like cells**

ARPE-19 retinal epithelial non-cancer cells and CCD 841 CoN colon epithelial non-cancer cells actively proliferate *in vitro*. SIRT1 inhibitor EX-527 appears to induce their transdifferentiation to a non-proliferative neuronal-like phenotype (Fig. 4.19 & Fig. 4.21), raising the possibility that SIRT1 inhibition might affect cancer cell ‘stemness’. Targeting of CSCs is a major research priority due to growing evidence of their contribution to poor outcome (LaBarge, 2010). Previous research has shown that colon CSCs show high levels of SIRT1 and that its knock-down can result in a decrease in OCT4 and Nanog cancer stem cell markers, on the other hand SOX2 for example did not show a decrease (Chen *et al.*, 2014b). GBM1s are characterised in the literature as being a cancer stem cell-like model due to their high expression of the neural markers Nestin and SOX2 and also they have the ability to self-renew and undertake multilineage differentiation (Wurdak *et al.*, 2010b; Mangiola *et al.*, 2007; Gangemi *et al.*, 2009; Pollard *et al.*, 2009). Interestingly, EX-527 treatment of the GBM1 cells resulted in substantially reduced confluency and cell number compared to controls (Fig. 4.7, Fig. 4.8a, n=2 biological repeats) and some apoptosis (Fig. 4.9 & Fig. 4.10, n=2 biological repeats). However, there was also evidence of a change in morphology of adhered cells with some increased neurite-like projections suggestive of neuronal-like differentiation (Fig. 4.7 & Fig. 4.24). Consistent with progression to a more differentiated state, expression of somatic reprogramming factor KLF4 was increased by ~12-13 fold by 150 and 200µM EX-527 (Fig. 4.25b). The functional consequences of this are unclear as KLF4 has been reported to promote glial/astrocyte differentiation (Qin and Zhang, 2012). c-Myc

expression was also increased by up to 2-fold (Fig. 4.25) and a modest increase in neuronal marker MAP1a was also observed (Fig. 4.26). Further work is warranted to determine whether cells fully differentiate and to which neuronal lineage and to assess effects of EX-527 as well as SIRT1-FL and SIRT1- $\Delta$ 8 knock-down on the differentiation and stemness of the other GBM cancer stem cell-like models. Nevertheless, these results suggest the potential of EX-527 as a differentiation-inducing therapeutic agent.

### **4.3.5 Metabolic effects of suppressing SIRT1**

In the more metabolically active HCT116 p53<sup>+/+</sup> cancer cells 100 $\mu$ M EX-527 reduced cellular mitochondrial respiration and glycolysis and cellular capacity to respond to metabolic stress (Fig. 4.28, n=3 biological repeats). SIRT1 is reported in the literature to have complex roles in metabolism through its cellular substrates and depending on tissue context (Li, 2013). It deacetylates both HIF-1 $\alpha$  and HIF-2 $\alpha$ , p53, and also the transcriptional co-activator PGC1 $\alpha$  with which it co-localises to mitochondria implicating a role in regulation of mitochondrial biogenesis (Knight and Milner, 2012). Under fasting conditions SIRT1 can decrease the activity of phosphoglycerate mutase, leading to inhibition of glycolysis (Hallows *et al.*, 2012).

Metabolic flux analysis of ARPE-19 and CCD 841 CoN non-cancer cells under normal growth conditions indicated a 'quiescent' energy phenotype consistent with their non-cancer status (Fig. 4.28, n=3 biological repeats). 200 $\mu$ M EX-527 treatment further promoted this 'quiescent' phenotype which is consistent with cell cycle exit/terminal differentiation (Fig. 4.28) and SIRT1-FL knock-down in ARPE-19 non-cancer cells similarly resulted in more quiescent metabolic state (Fig. 4.29, n=1 biological repeat). It will be interesting to observe whether SIRT1- $\Delta$ 8 knock-down or co-silencing with SIRT1-FL results in similar or different metabolic effects and whether these might be causally linked to the differentiation phenotype observed or a consequence of the differentiation phenotype or simply of SIRT1 targeting. Recently Ryu *et al.* (2018) showed that increased cytosolic NAD<sup>+</sup> and reduced nuclear NAD<sup>+</sup> resulted in adipocyte differentiation, whilst

increased nuclear NAD<sup>+</sup> sustained a preadipocyte state because of ADP-ribosylation and inactivation of an adipogenic transcription factor.

### **4.3.6 Conclusions**

The SIRT1 small molecule inhibitor EX-527 induced cancer selective cell death by apoptosis in a subset of cancer cell lines validating SIRT1-FL knock-down studies and feasibility with a small molecule inhibitor (Fig. 4.2, n=3 biological repeats & Fig. 4.7 - 4.10, n=2 biological repeats). In a non-cancer cell context, the data obtained suggests that EX-527 induces neuronal transdifferentiation of both ARPE-19 retinal epithelial and CCD 841 CoN colon epithelial cells extending previous SIRT1-FL ARPE-19 studies (Fig. 4.19-4.23). This was associated with induction of the neural stem cell marker Nestin and expression of neuronal markers MAP1a and MAP2. Preliminary data suggests that EX-527 is able to reduce stemness of GBM1 cancer stem cell-like cells with decreased expression of Nestin evident. However, additional work such as analysis of protein levels of neuronal and stem cell markers is required as well as further biological replicates for some experiments.

# **5. Epigenetic effects of suppressing LDH-A and the therapeutic potential to re-express epigenetically silenced tumour suppressor genes**

## **5.1 Introduction**

It is well known that in cancer cells many genes are epigenetically silenced or activated differentially to their non-cancer equivalents. There is therefore focus on developing drugs that can alter the epigenetic status of cancer cells which may lead to re-activation of silenced TSGs or silencing of activated oncogenes.

Epigenetic therapy currently consists of DNA methylation inhibitors and/or histone deacetylation inhibitors. These result in hypomethylated DNA and histone acetylation respectively leading to a more open chromatin structure and therefore more active genes. 5'azacytidine and 5'aza-2'-deoxycytidine which are DNMT inhibitors and suberoylanilidehydroxamic acid and romidepsin (a depsipeptide) which are HDAC inhibitors are currently approved by the FDA for use as single treatments for some forms of cancer (Ahuja *et al.*, 2016). There are also multiple ongoing clinical trials which are investigating the effects of combining HDAC inhibitors with DNMT inhibitors and also the use of them alongside clinically available cancer therapies (Ahuja *et al.*, 2016). Although these drugs have been approved by the FDA for use in the clinic, as with many other approved chemotherapeutic drugs they lack specificity towards cancer cells leading to dose limiting side effects. A key consideration is what these drugs are doing to the epigenetic state of non-cancer cells.

Identifying treatments that selectively alter the epigenetic state of cancer cells and not non-cancer cells to cause re-expression of epigenetically silenced TSGs or silence activated oncogenes, may lead to better patient outcome. Therefore, the aim of this chapter was to preliminary investigate possible approaches to

target/reverse cancer cell epigenetic alterations specifically without affecting the epigenetics of non-cancer cells.

SIRT1 is an NAD<sup>+</sup>-dependent histone and protein deacetylase (section 1.4.2) and an established epigenetic regulator of cellular transcriptional activity both through the direct deacetylation of histones and of chromatin-modifying enzymes (e.g. p300 HAT) (Bouras *et al.*, 2005). One of the primary substrates of SIRT1 is acetylated K9 of histone H3 which is an active chromatin mark and associated with transcriptional activation (Vaquero *et al.*, 2004). When the residue is deacetylated it is available for methyl addition which promotes a more condensed chromatin structure and is associated with transcriptional silencing. SIRT1 has also been reported to deacetylate H3K14 and H4K16 (Zhang and Kraus, 2010).

Whilst there have been a number of 'epigenetic therapy' studies on the class I, II and IV HDACs, which are not dependent on NAD<sup>+</sup> for deacetylase activity, there have been few studies on targeting SIRT1 as a potential way of altering the epigenetics of cancer cells. An important study by Pruitt *et al.* (2006) report that shRNA-mediated knock-down of SIRT1 or inhibition using the *S. cerevisiae* Sir2 inhibitor splitomicin leads to the reactivation of several epigenetically silenced TSGs. Used in combination with DNMT inhibitors or the class I/II HDAC inhibitor TSA, this led to a synergistic increase in gene expression. The SIRT1 inhibitor used in this study was splitomicin which is not specific towards the mammalian SIRT1 orthologue alone. Nevertheless, the findings are very promising and suggest SIRT1 as a potential target to re-activate TSGs, however, possible unwanted effects of SIRT1 silencing or inhibition on non-cancer gene expression were not analysed. In chapter 4 it is shown that the activity and cancer cell vs. non-cancer cell selectivity of selective SIRT1 inhibitor EX-527 varies depending on the non-cancer/cancer cell line, which may be due to differences in the epigenetics of the different cell lines. Inhibition of SIRT1 in a cancer selective manner would be useful in terms of potentially altering cancer cell epigenetics without on-target side effects in non-cancer cells.

LDH-A knock-down/inhibition, through cancer selective NADH increase and NAD<sup>+</sup> decrease, can modestly decrease SIRT1 activity in a cancer selective manner, although as previously mentioned is dependent on the p53 status of the

cell (Allison *et al.*, 2014). It was hypothesised that suppressing LDH-A may therefore, via its effects on SIRT1 activity, provide a way for cancer selective alteration of histone acetylation/epigenetic state (Fig. 5.1).

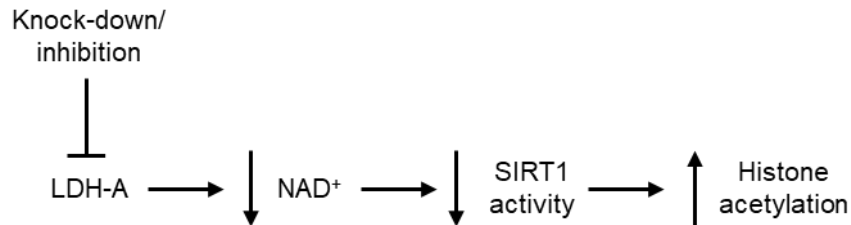


**Figure 5.1: Schematic of hypothesised model of the effects of LDH-A knock-down/inhibition on histone acetylation.**

Inhibition or knock-down of LDH-A results in a cancer selective reduction in NADH/NAD<sup>+</sup> ratio which modestly decreases SIRT1 activity (Allison *et al.*, 2014), leading to the possibility that LDH-A targeting can alter acetylation status of histones and gene expression.

In addition, another potential mechanism by which LDH-A could impact on epigenetics has emerged. It has been reported that under hypoxic conditions LDH-A and MDH1/2 through promiscuous substrate use, catalyse the reduction of  $\alpha$ -KG to L-2HG (Intlekofer *et al.*, 2015; Oldham *et al.*, 2015). L-2HG is an oncometabolite which is known to competitively antagonise and inhibit  $\alpha$ -KG dependent TET enzymes involved in the demethylation of DNA and also the  $\alpha$ -KG dependent Jumonji family of lysine histone demethylases (see section 1.6.2). Due to this, methylation of DNA and specific histones regulated by the Jumonji family of demethylases could increase, which may result in a more condensed chromatin structure and gene repression (Fig. 5.2).

As mentioned in section 1.6.2 the TET enzymes catalyse the first step of the demethylation of 5-methylcytosine (5mC) to 5-hydroxymethylcytosine (5hmC) and this process relies on  $\alpha$ -KG for its action (Ito *et al.*, 2010). Different members of the  $\alpha$ -KG dependent Jumonji family of histone demethylases have specificity for different methylated lysines. This includes KDM4C which specifically demethylates the repressive histone mark tri-methylated H3K9 and has been shown to be inhibited by L-2HG (Intlekofer *et al.*, 2015).

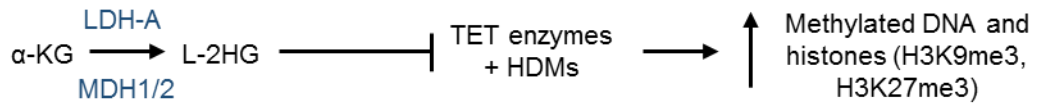


**Figure 5.2: Schematic summarising the role of LDH-A and MDH1/2 in generation of L-2HG under hypoxia and possible downstream effects of this.**

LDH-A and MDH1/2 are reported to catalyse  $\alpha$ -KG reduction to L-2HG under hypoxic conditions. L-2HG inhibits  $\alpha$ -KG-dependent TET enzymes involved in DNA demethylation and  $\alpha$ -KG-dependent histone demethylases (KDMs), leading to increased DNA and histone methylation.

Based on these findings it was hypothesised that there are two potential mechanisms by which LDH-A knock-down/inhibition might selectively affect the epigenetic state of cancer cells i) via cancer selective SIRT1 inhibition under normoxia/hypoxia and ii) specifically under hypoxia via inhibition of L-2HG oncometabolite production.

## **5.2 Results**

### **5.2.1 LDH-A knock-down in HCT116 p53<sup>+/+</sup> cancer cells leads to alterations in histone modifications**

HCT116 p53<sup>+/+</sup> cancer cells were initially chosen to assess whether LDH-A targeting has any epigenetic effects as it has previously been shown that LDH-A silencing in these cells can modestly reduce SIRT1 activity (Allison *et al.*, 2014).

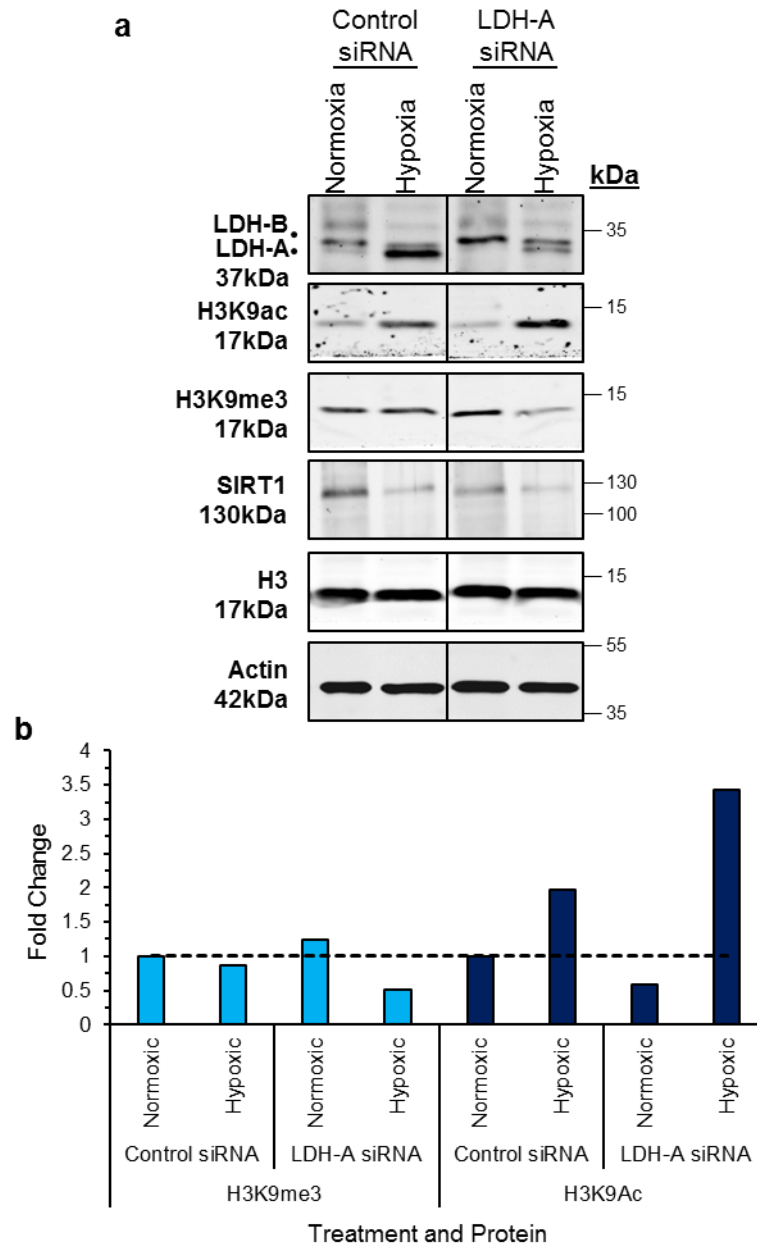


**Figure 5.3: Immunoblots showing changes in key histone modifications in HCT116 p53<sup>+/+</sup> cancer cells in response to LDH-A silencing by RNAi.**

**a.** Western blot analysis of the effects of LDH-A silencing on histone modifications H3K9me3 and H3K9ac in HCT116 p53<sup>+/+</sup> cells under normoxic and hypoxic conditions 72 hours post transfection with LDH-A siRNA. Histone H3 and actin shown as loading controls. n=1 biological repeat. **b.** Densitometric quantification of H3K9ac and H3K9me3 protein levels after transfection of HCT116 p53<sup>+/+</sup> cells with LDH-A siRNA under normoxic and hypoxic conditions. Levels are normalised to total H3 and expressed as a fold change relative to levels in control siRNA transfected cells under normoxic conditions.

Immunoblots (Fig. 5.3) showed that LDH-A protein expression was decreased after LDH-A siRNA transfection by 58% under normoxic conditions and 62% under hypoxic conditions. Interestingly under hypoxic conditions, LDH-A knock-

down in HCT116 p53<sup>+/+</sup> cancer cells resulted in a decrease in total levels of the repressive histone mark trimethylated lysine 9 (K9) of histone H3 (H3K9me3) (1.7-fold decrease) and an increase in levels of the active histone mark acetylated H3K9 (H3K9ac) (by 1.7-fold) compared to control cells (Fig. 5.3). This is consistent with reduced L-2HG levels under hypoxia and reduced inhibition of  $\alpha$ -KG dependent demethylases as a result of LDH-A depletion. However, it has not been experimentally tested whether LDH-A knock-down does indeed cause a decrease in L-2HG. Some modest effects were also observed under normoxic conditions with total levels of trimethylated H3K9 increasing slightly in response to LDH-A siRNA and levels of acetylated H3K9 showing a concomitant small decrease (Fig. 5.3).

The other notable and unexpected change was an increase in total acetylated H3K9 under hypoxic conditions compared to normoxia. Interestingly, protein levels of the deacetylase SIRT1, which is known to deacetylate this specific lysine on H3 (Vaquero *et al.*, 2004) were also reduced under hypoxia possibly accounting for the increased acetylated K9 levels observed.

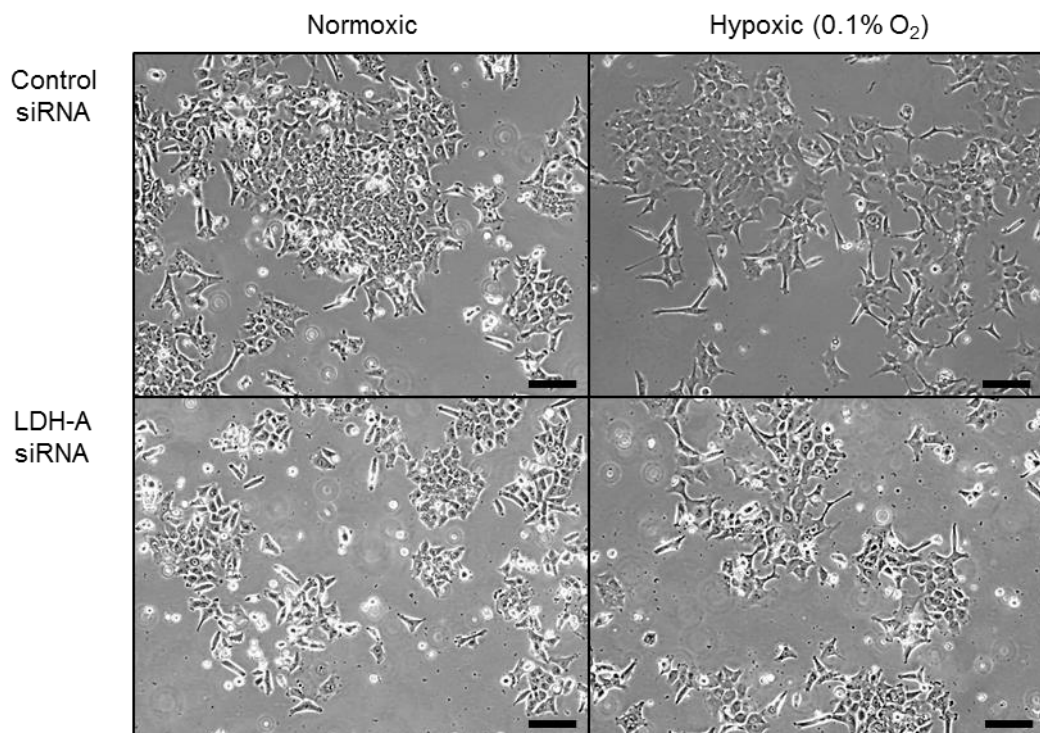


**Figure 5.4: Cell micrographs of HCT116 p53<sup>+/+</sup> cancer cells after LDH-A knock-down.** Cell images taken 72 hours post LDH-A or control siRNA transfection under normoxic (21% O<sub>2</sub>) and hypoxic (0.1% O<sub>2</sub>) conditions in HCT116 p53<sup>+/+</sup> cancer cells. Images taken with x10 objective and scale bar indicates 100 $\mu$ m. n=2 biological repeats.

Phenotypically partial LDH-A depletion by RNAi resulted in reduced cell number and an increase in the number of floating birefringent cells (Fig. 5.4) suggestive of reduced cell growth and increased death. This is consistent with previous studies (Ford *et al.*, 2005). At present it is unclear whether the observed epigenetic effects of LDH-A knock-down and potential effects on epigenetically regulated TSG and oncogenes are causally related to the reduced cell number/death observed.

### **5.2.2 Effects of LDH-A inhibition on levels of 5-hydroxymethylcytosine (5hmC), a marker of DNA demethylation**

The effects of LDH-A knock-down on methylated and acetylated K9 of H3 under hypoxia are consistent with an L-2HG/ $\alpha$ -KG-related mechanism (Fig. 5.2) and increased activity of KDMs and TET enzymes, raising the possibility of effects of LDH-A knock-down/inhibition on DNA methylation. To assess this further, effects of the LDH-A small molecule inhibitor NHI-2 (Granchi *et al.*, 2013) on levels of 5hmC were assessed.

NHI-2 has previously been shown to selectively inhibit LDH-A (5-fold preferential activity towards LDH-A cf. LDH-B in cell-free assays) (Granchi *et al.*, 2013) and to reduce the cancer cell NAD<sup>+</sup>:NADH ratio in p53 wild-type cancer cells consistent with LDH-A inhibition. To further test the cellular selectivity of NHI-2 towards LDH-A, the effects of acute cellular exposure to NHI-2 on glycolysis and oxygen consumption were determined using the Seahorse XFp metabolic analyser (Fig. 5.5). Acute cellular exposure to 1 $\mu$ M NHI-2 modestly reduced glycolytic rate in HCT116 p53<sup>+/+</sup> cancer cells (Fig. 5.5a) and glycolytic capacity (Fig. 5.5b) consistent with inhibition of LDH-A glycolytic activity whereas no effects on mitochondrial respiration (OCR) (Fig. 5.5c) were observed.

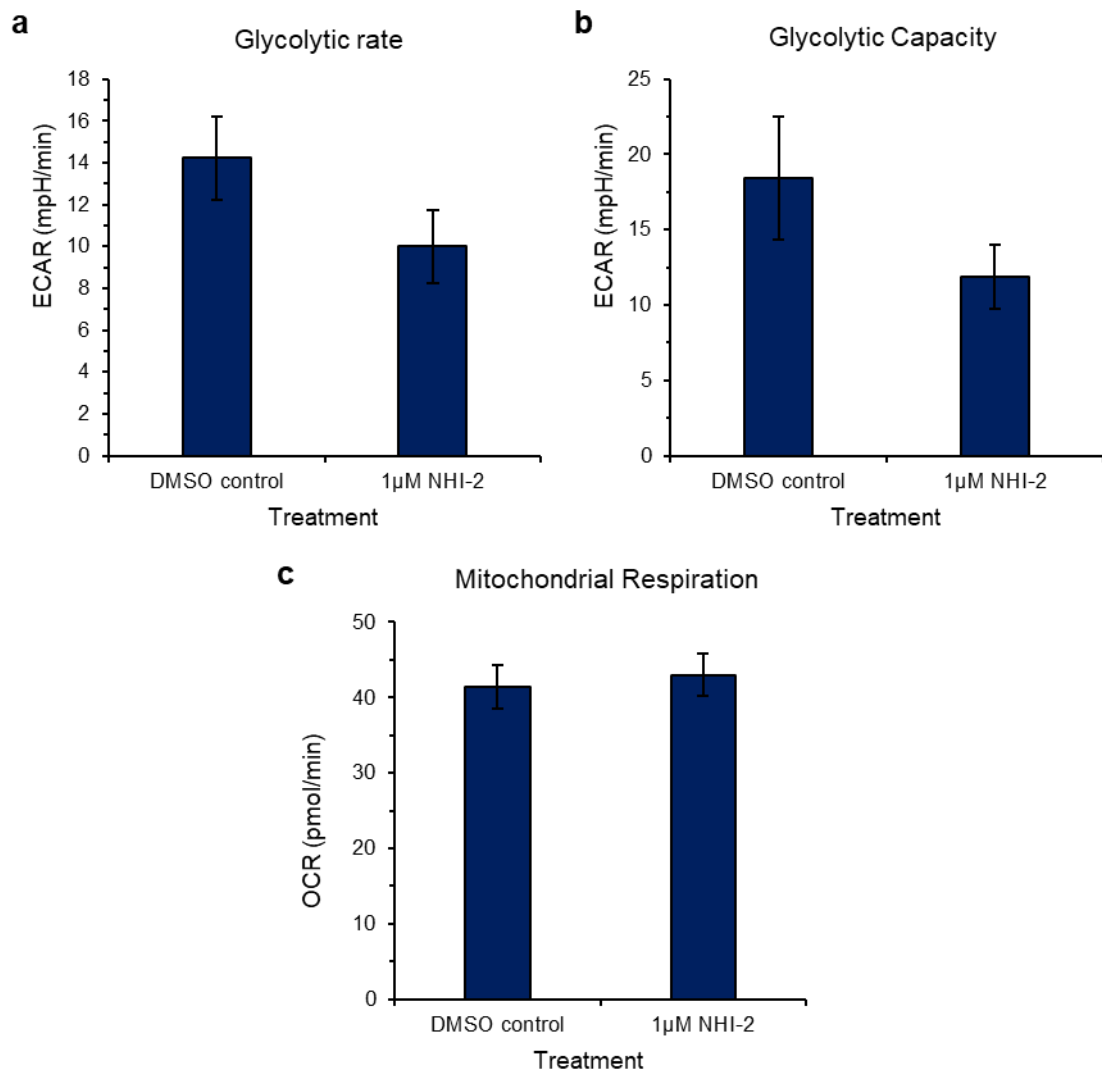


**Figure 5.5: Acute metabolic response of HCT116 p53<sup>+/+</sup> cancer cells to LDH-A inhibitor, NHI-2.**

HCT116 p53<sup>+/+</sup> cancer cells were analysed for immediate metabolic effects of 1µM NHI-2 exposure compared with DMSO vehicle control, as determined using the XFp glycolytic stress test. Mean glycolytic rate (a), capacity (b) and oxygen consumption rate (OCR) (c) were recorded. n=3 technical repeats ± SD from 1 biological repeat.

As a positive control for increased levels of 5hmC, cells were treated with the DNA demethylating agent 5'-aza-2'deoxyctidine (decitabine). Whilst 5'-aza-2'deoxyctidine results in DNA demethylation principally through sequestering and inhibition of DNMTs, studies have shown that 5'-aza-2'deoxyctidine increases 5hmC levels, although this can be cell-context specific (Vetö *et al.*, 2018; Sajadian *et al.*, 2015).

In the HCT116 p53<sup>+/+</sup> cells, 24 hours treatment with 5'-aza-2'deoxyctidine increased 5hmC nuclear staining with punctate foci apparent in nuclear regions

that stained less intensely with nuclear dye DAPI (DAPI binding preference for AT-rich dsDNA) (Fig. 5.6). However, some positive staining was also evident outside the nucleus in both treated and control cells, suggesting some non-specific binding and that immunofluorescence conditions could be further optimised.

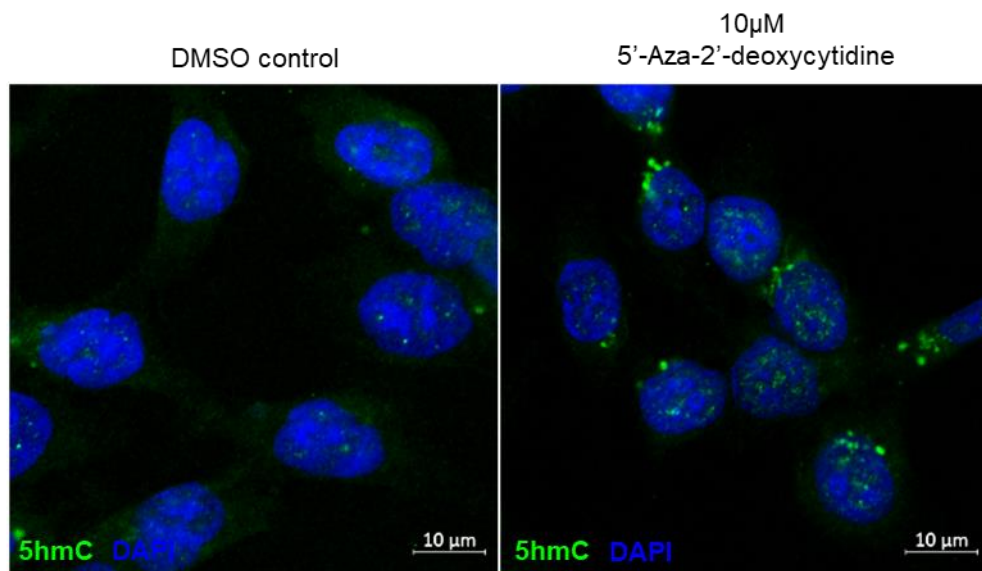


**Figure 5.6: Analysis of 5-hydroxymethylcytosine in HCT116 p53<sup>+/+</sup> cancer cells treated with 5-aza-2-deoxycytidine.**

Representative immunofluorescent images of HCT116 p53<sup>+/+</sup> cancer cells showing expression of 5-hydroxymethylcytosine (5hmC) (green) after treatment with 10μM 5-aza-2-deoxycytidine for 24 hours, fixed cells counterstained with DAPI (blue). x63 objective; scale bar indicates 10μm. n=1 biological repeat.

HCT116 p53<sup>+/+</sup> cells were treated with several different concentrations of LDH-A inhibitor NHI-2 for 48 hours and effects on 5hmC levels were similarly assessed for possible effects of LDH-A inhibition on DNA demethylation (Fig. 5.7). In contrast to the increase in 5hmC with 5-aza-2-deoxycytidine treatment, there was no discernible induction of 5hmC in response to any of the tested NHI-2 concentrations. This was the case both for cells treated under normoxia and also under hypoxic conditions (Fig. 5.7) where effects on histone demethylation were earlier observed (Fig. 5.3).

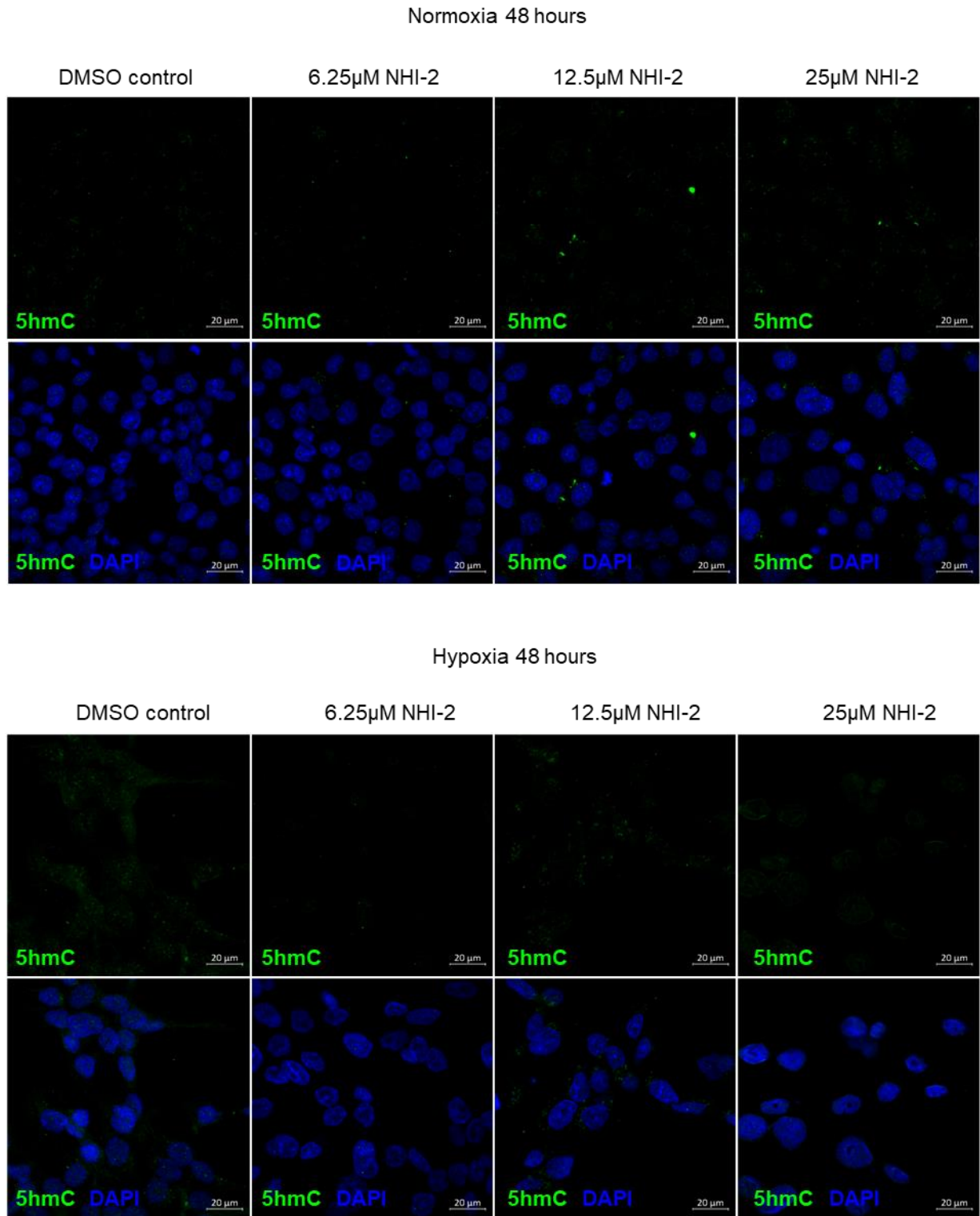


**Figure 5.7: Analysis of 5-hydroxymethylcytosine in HCT116 p53<sup>+/+</sup> cancer cells treated with NHI-2 under different O<sub>2</sub> tensions.**

Representative immunofluorescent images of HCT116 p53<sup>+/+</sup> cancer cells showing expression of 5-hydroxymethylcytosine (5hmC) (green) after treatment with LDH inhibitor NHI-2 at the indicated doses for 48 hours under normoxic (21% O<sub>2</sub>) and hypoxic conditions (0.1% O<sub>2</sub>), fixed cells counterstained with DAPI (blue). x63 objective and scale bar represents 20 $\mu$ m. n=1 biological repeat.

### 5.2.3 Epigenetic effects of targeting LDH-A in other cancer cell lines

The epigenetic effects of LDH-A knock-down were next examined in MDA-MB-231 triple negative breast cancer cells, to assess whether there are similar effects on histone modifications as observed in the HCT116 p53<sup>+/+</sup> colorectal cancer cells. In addition, it has previously been reported that the cell-cell adhesion molecule E-cadherin, a TSG, is epigenetically silenced in MDA-MB-231 cells (Chao *et al.*, 2010). Furthermore, work by Pruitt *et al.* (2006) have shown that E-cadherin mRNA expression can be re-activated following knock-down of deacetylase SIRT1. It was hypothesised that modifications of histones via LDH-A knock-down may also lead to the re-expression of E-cadherin.

As Figure 5.8 shows, in the absence of any knock-down, comparing histone modification levels under normoxic and hypoxic conditions, as in the HCT116 p53<sup>+/+</sup> cells, basal total levels of acetylated H3K9 increased. In contrast to the HCT116 p53<sup>+/+</sup> cells, however, levels of trimethylated H3K9 also increased. In response to LDH-A silencing, under normoxic conditions levels of trimethylated H3K9 decreased (1.4-fold) whereas levels of acetylated H3K9 increased modestly. These effects are broadly consistent with what one might expect with a reduction in SIRT1 deacetylase activity as a result of LDH-A silencing (Allison *et al.*, 2014) although this has not been investigated further and other mechanisms may be at play. Under hypoxia, a reduction in trimethylated H3K9 was also observed but this was also the case for acetylated H3K9 levels.

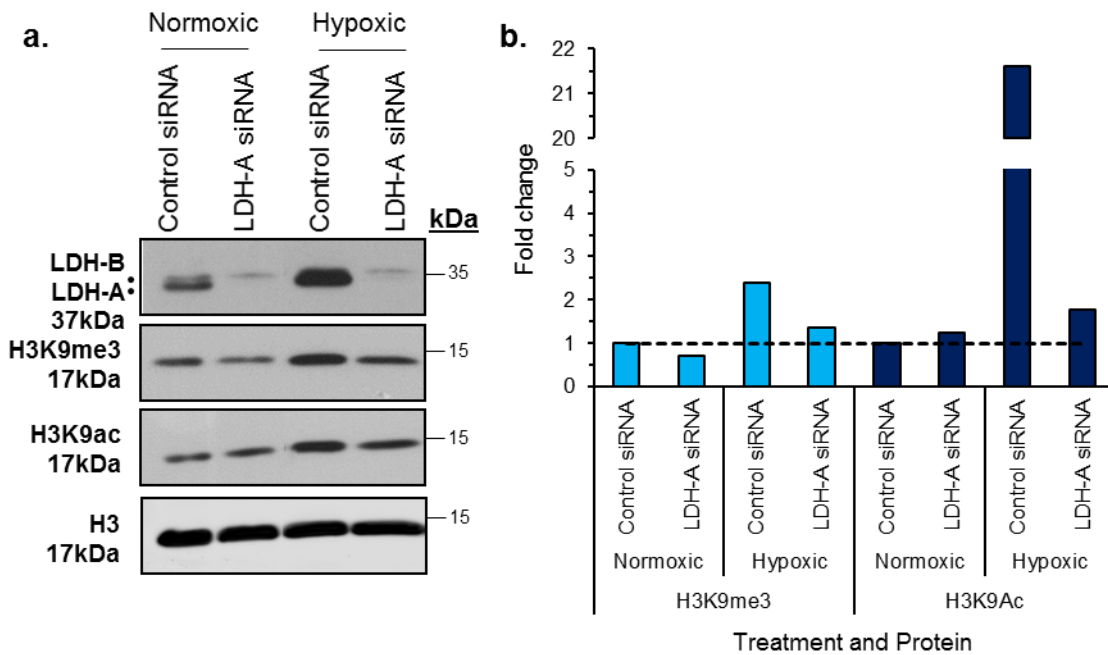


**Figure 5.8: Effects of LDH-A silencing by RNAi on histone modifications in MDA-MB-231 triple negative breast cancer cells.**

**a.** Western blot analysis of LDH-A/B protein levels, and histone modifications H3K9me3 and H3K9ac in MDA-MB-231 cancer cells after LDH-A silencing by RNAi for 72 hours; histone H3 as loading control. n=1 biological repeat. **b.** Densitometric quantification of H3K9me3 and H3K9ac protein expression after LDH-A RNAi treatment under normoxic and hypoxic conditions. Levels normalised to total H3 and fold change expressed compared to normoxic siRNA negative control.

To see if the LDH-A inhibitor, NHI-2, induces similar effects to LDH-A knock-down in the MDA-MB-231 cells under normoxic conditions, the cells were treated with NHI-2 for 48 hours and then harvested for analysis of histone modifications by immunoblotting (Fig. 5.9).

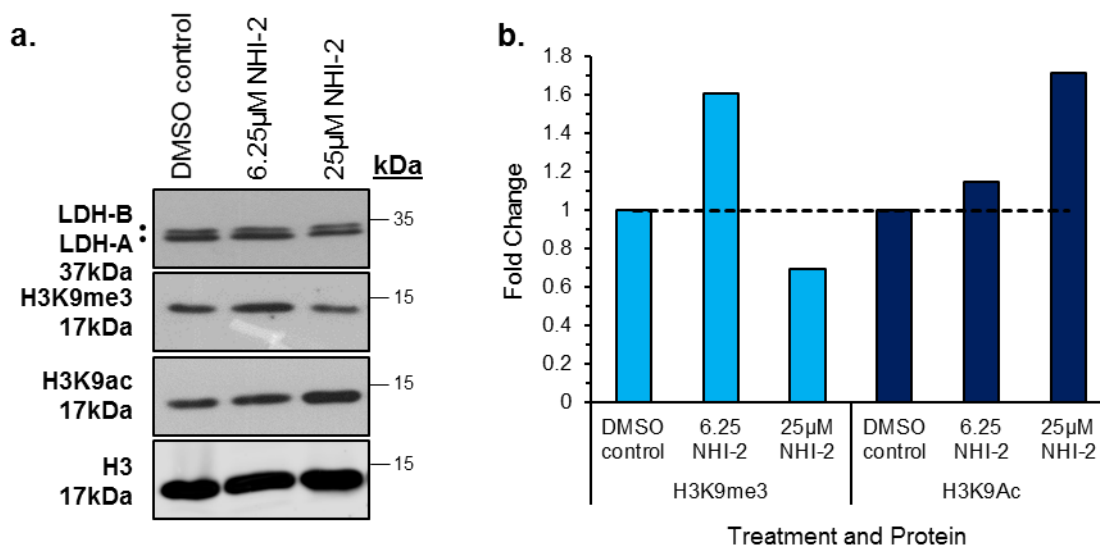


**Figure 5.9: Effects of LDH-A inhibitor NHI-2 on histone modifications in MDA-MB-231 triple negative breast cancer cells.**

**a.** Western blot analysis of LDH-A/B protein levels, and histone modifications H3K9me3 and H3K9ac in MDA-MB-231 cancer cells treated with NHI-2 at the indicated doses for 48 hours; histone H3 as loading control. n=1 biological repeat. **b.** Densitometric quantification of H3K9me3 and H3K9ac protein expression after NHI-2 treatment under normoxic (21% O<sub>2</sub>) conditions. Levels normalised to total H3 and fold change expressed compared to DMSO control.

Effects were dose-dependent and modest, however, similar to the effects observed with LDH-A knock-down under normoxic conditions (Fig. 5.8), 25µM NHI-2 resulted in a small reduction in total levels of trimethylated H3K9 and an increase in acetylated H3K9 (Fig. 5.9).

These results in the MDA-MB-231 cancer cells, whilst reporting total levels of two key histone H3 modifications rather than epigenetic modifications at specific gene promoters, suggest that targeting LDH-A may result in a less repressive epigenetic state (total levels of H3K9me3 decrease (repressive histone mark), levels of H3K9ac increase (active histone mark)). Whilst requiring further investigation, this in turn increases the likelihood that LDH-A targeting could potentially provide a means to re-activate epigenetically silenced TSGs such as E-cadherin in certain cell contexts.

#### **5.2.4 SIRT1 inhibitor EX-527 induces re-expression of epigenetically silenced E-cadherin in MDA-MB-231 cancer cells**

Prior to investigation of effects of targeting LDH-A on epigenetically silenced E-cadherin in the MDA-MB-231 cells, it was determined whether the SIRT1 inhibitor, EX-527, was able to re-activate expression of E-cadherin. Previously, Pruitt *et al.* (2006) reported that SIRT1 shRNAs and the yeast Sir2 inhibitor splitomicin induce expression of E-cadherin mRNA in MDA-MB-231 cancer cells (Pruitt *et al.*, 2006). As seen in Figure 5.10 qPCR analysis shows that the SIRT1 small molecule inhibitor EX-527 was also able to induce gene expression of epigenetically silenced TSG E-cadherin in a dose- and time- dependent manner. mRNA levels increased by >50-fold with 200 $\mu$ M EX-527 treatment for 48 hours.

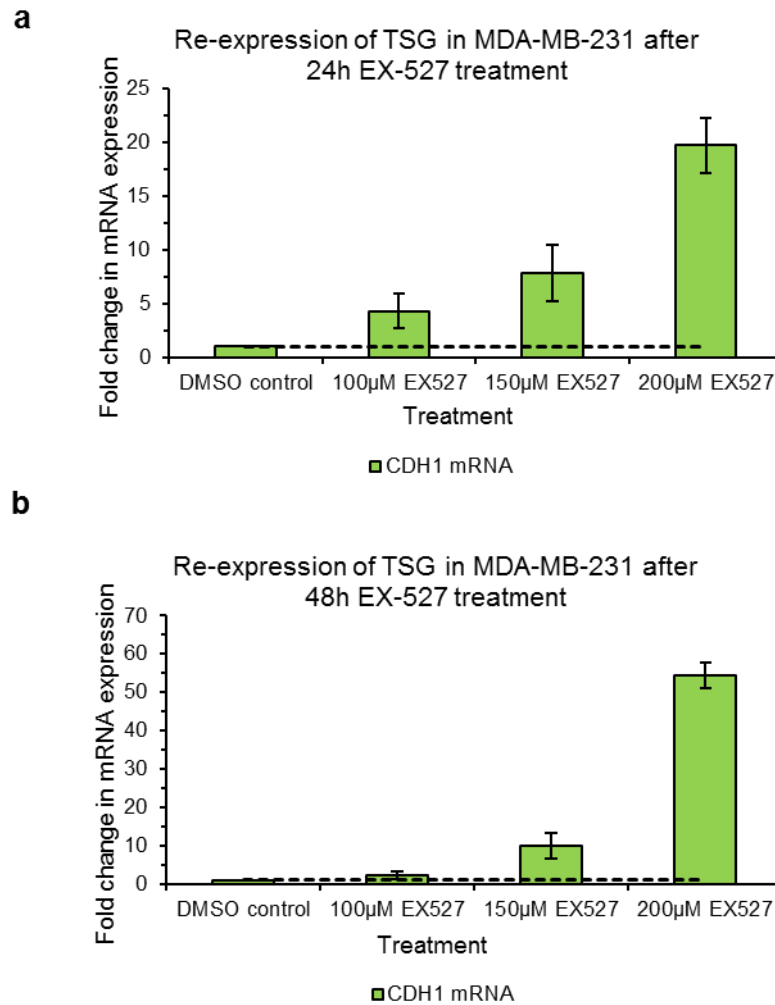


**Figure 5.10: qPCR analysis of E-cadherin mRNA expression in MDA-MB-231 cancer cells after EX-527 treatment.**

Fold change in E-cadherin (CDH1) mRNA expression in MDA-MB-231 cells after exposure to the indicated EX-527 doses for 24 (a) and 48 hours (b). n=4 technical repeats  $\pm$  SD from 1 biological replicate.

Phenotypically, the MDA-MB-231 cells became more elongated with EX-527 treatment, with a notable reduction in cell number following 48 hours treatment also evident compared to vehicle control cells (Fig. 5.11). EX-527 did not appear to induce cell death as it does in the HCT116 p53<sup>+/+</sup> cancer cells (Fig. 4.8 & Fig. 4.10) consistent with its higher 96 hours IC<sub>50</sub> towards MDA-MB-231 cells (Fig. 4.2), although viability was not directly assayed. This suggested that the reduced cell number may be due to inhibition of cell growth or cell cycle effects. Unexpectedly, the observed morphological change was not to a more classically epithelial-like state suggesting other effects of EX-527 beyond re-expression of E-cadherin, although the migratory potential of the cells was not assessed.

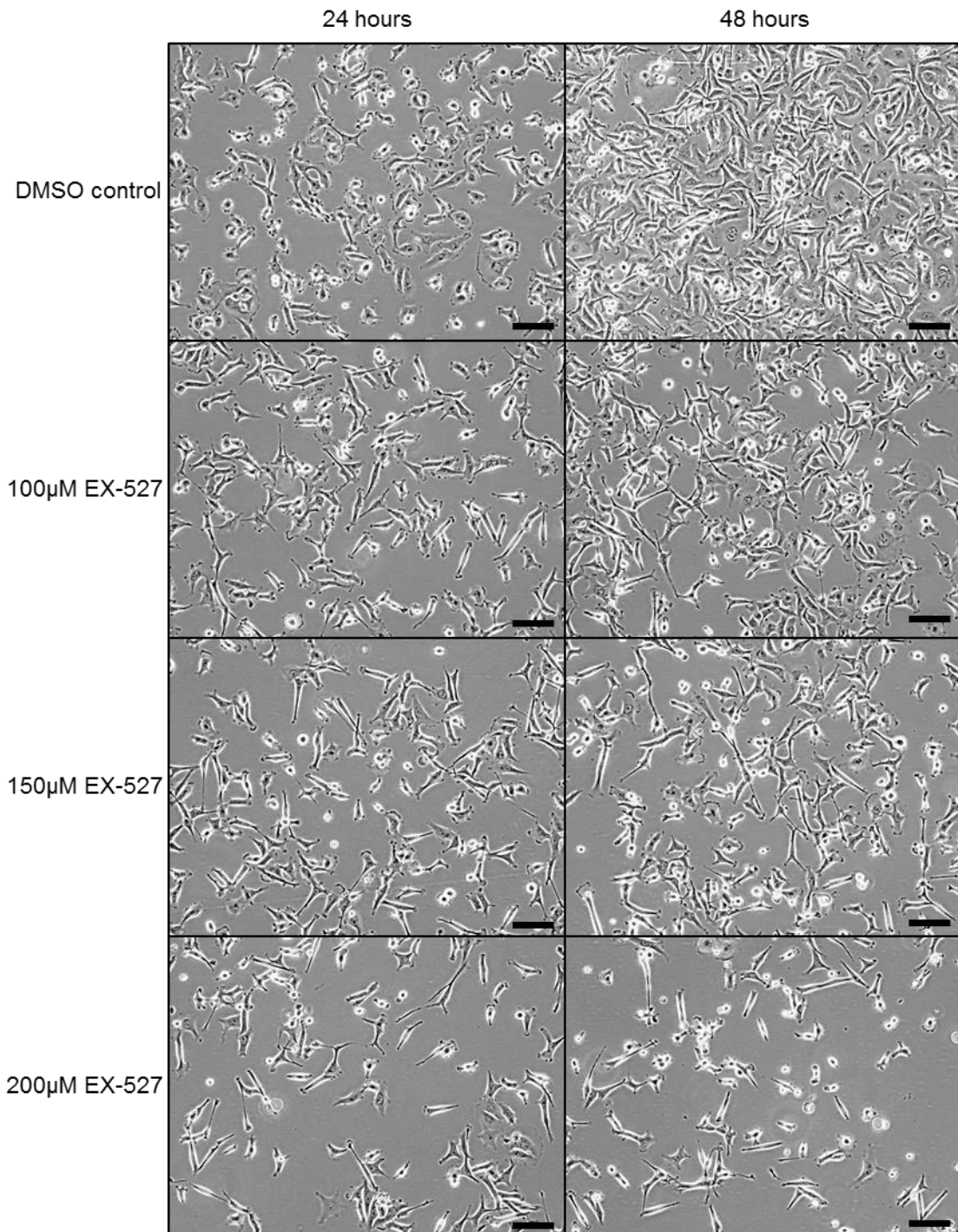


**Figure 5.11: Cell micrographs of MDA-MB-231 after 24 and 48 hours exposure to SIRT1 inhibitor EX-527.**

Cell images of MDA-MB-231 cells treated with EX-527 at the indicated doses for 24 and 48 hours. Images taken with x10 objective and scale bar indicates 100µm. n=2 biological repeats

## 5.2.5 E-cadherin re-expression with EX-527 treatment in hypoxic MDA-MB-231 cancer cells

The ability of SIRT1 inhibition or knock-down to re-activate epigenetically silenced genes under hypoxic conditions has not previously been reported in the literature. Given the typical chemo- and radio-resistance of hypoxic cancer cells and also commonly an increased migratory phenotype (Muz *et al.*, 2015), the question was whether EX-527 could induce expression of epigenetically silenced E-cadherin under hypoxic conditions. As Figure 5.12 shows, 100 $\mu$ M EX-527 treatment for 48 hours induced E-cadherin mRNA levels in hypoxic MDA-MB-231 cells by 2.3-fold whereas at this concentration little induction was observed under normoxic conditions.

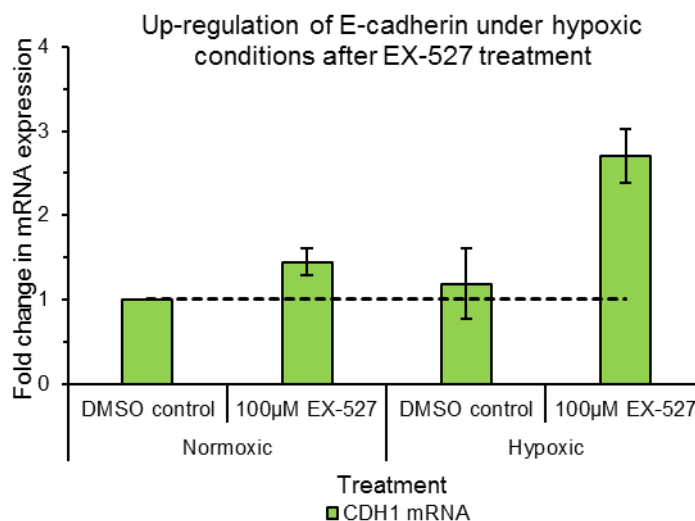


**Figure 5.12: qPCR analysis of E-cadherin under normoxic and hypoxic conditions.**

Fold change in E-cadherin (CDH1) mRNA expression in MDA-MB-231 cancer cells after 48 hours exposure to 100 $\mu$ M EX-527 under normoxic and hypoxic conditions, n=4 technical repeats  $\pm$  SD from 1 biological replicate.

MDA-MB-231 cells cultured under hypoxic conditions appeared to grow more slowly than a parallel culture grown under normoxic conditions (Fig. 5.13) and were more elongated/mesenchymal in morphology. Morphology appeared similar or more pronounced with EX-527 treatment.

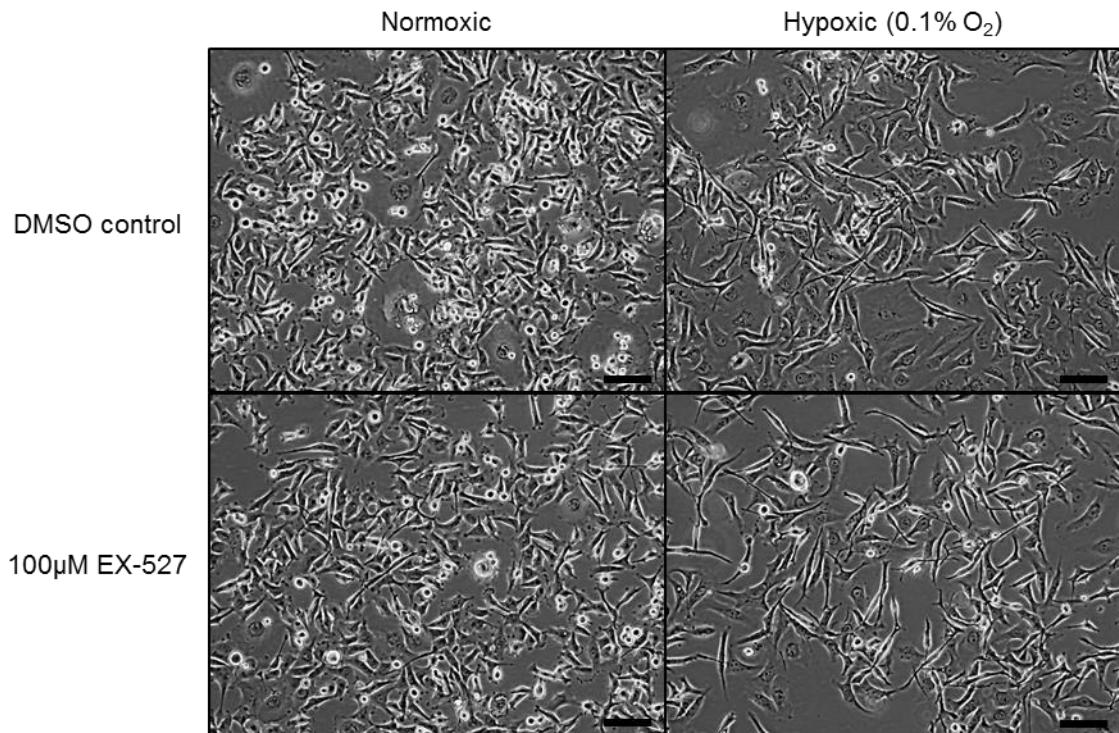


**Figure 5.13: Cell micrographs of MDA-MB-231 after 48 hours EX-527 exposure under normoxic and hypoxia.**

Cell images of MDA-MB-231 cancer cells after 48 hours treatment with 100µM EX-527 under normoxic (21% O<sub>2</sub>) and hypoxic (0.1% O<sub>2</sub>) conditions. Images taken with x10 objective and scale bar indicates 100µm. n=2 biological repeat.

## 5.2.6 Effects of targeting LDH-A on E-cadherin expression

Having observed re-activation of epigenetically silenced E-cadherin by SIRT1 inhibition (Fig. 5.10) and induction of active histone markers by LDH-A knock-down/inhibition (Fig. 5.8 + Fig. 5.9), effects of targeting LDH-A on E-cadherin expression was assessed. As Figure 5.14 shows, LDH-A siRNA reduced LDH-A mRNA levels by 64% compared to control siRNA under normoxic conditions. Under hypoxia, LDH-A mRNA levels were increased consistent with upregulation of LDH-A by HIF-1α but with mRNA levels reduced by LDH-A siRNA to similar levels as silencing under normoxia. Importantly expression of E-cadherin mRNA increased by 2.3-fold in MDA-MB-231 cells in response to LDH-A silencing under normoxic conditions. No increase was seen under hypoxic conditions consistent with complex effects seen on histone modifications under hypoxia (decreased H3K9me3 and decreased H3K9ac). Although LDH-A silenced MDA-MB-231 cells

under normoxia showed increased E-cadherin at the mRNA level, immunoblot analysis failed to detect E-cadherin at the protein level (Fig. 5.15).

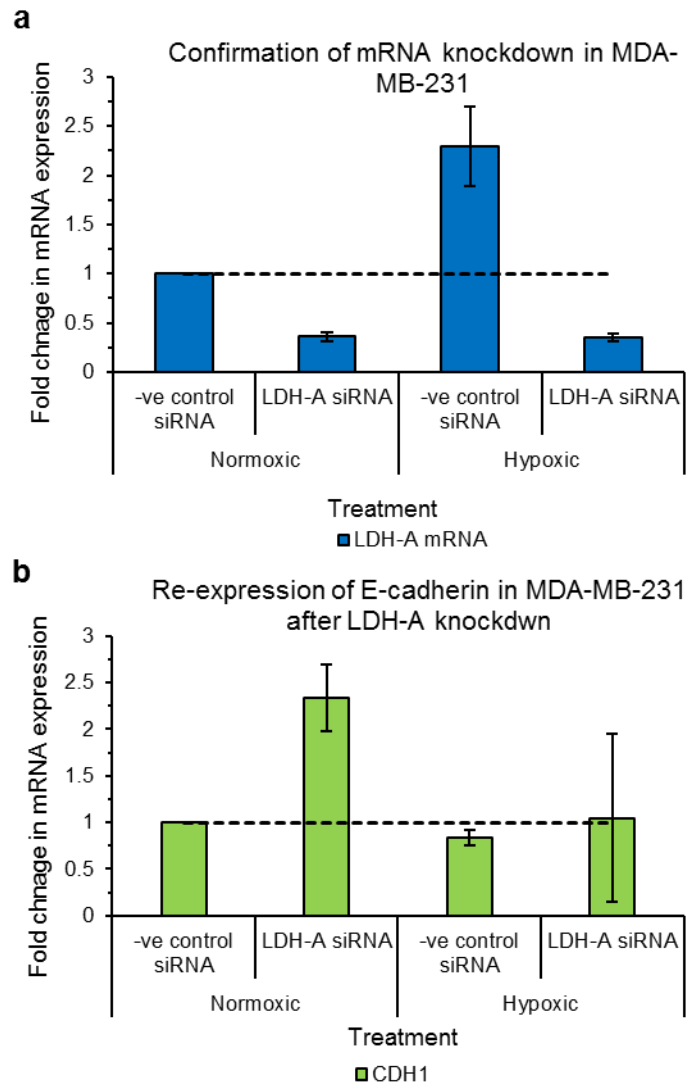


**Figure 5.14: qPCR analysis of LDH-A and E-cadherin mRNA expression in MDA-MB-231 cells after RNAi mediated silencing of LDH-A.** Fold change in LDH-A (a) and E-cadherin (CDH1) (b) mRNA expression in MDA-MB-231 after transfection with LDH-A or control siRNA for 72 hours under normoxic (21% O<sub>2</sub>) and hypoxic (0.1% O<sub>2</sub>) conditions. n=4 technical repeats ± SD from 1 biological replicate.

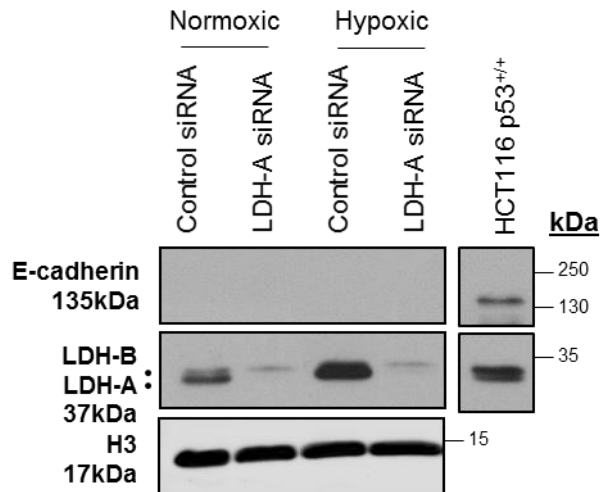


**Figure 5.15: Protein expression of E-cadherin after LDH-A knock-down in MDA-MB-231 cancer cells.**

Immunoblots showing any potential re-expression of E-cadherin protein in MDA-MB-231 cancer cells after LDH-A or control siRNA transfection for 72 hours under normoxic (21% O<sub>2</sub>) and hypoxic (0.1% O<sub>2</sub>) conditions. HCT116 p53<sup>+/+</sup> epithelial cancer cells shown as a positive control for cells that express E-cadherin. Histone H3 shown as loading control and LDH-A shown to confirm reduction in LDH-A protein by LDH-A siRNA. n=1 biological repeat.

Phenotypically the number of MDA-MB-231 cells appeared reduced following LDH-A silencing compared to siRNA control and cell morphology was altered but notably differently to that with EX-527 (Fig. 5.16).

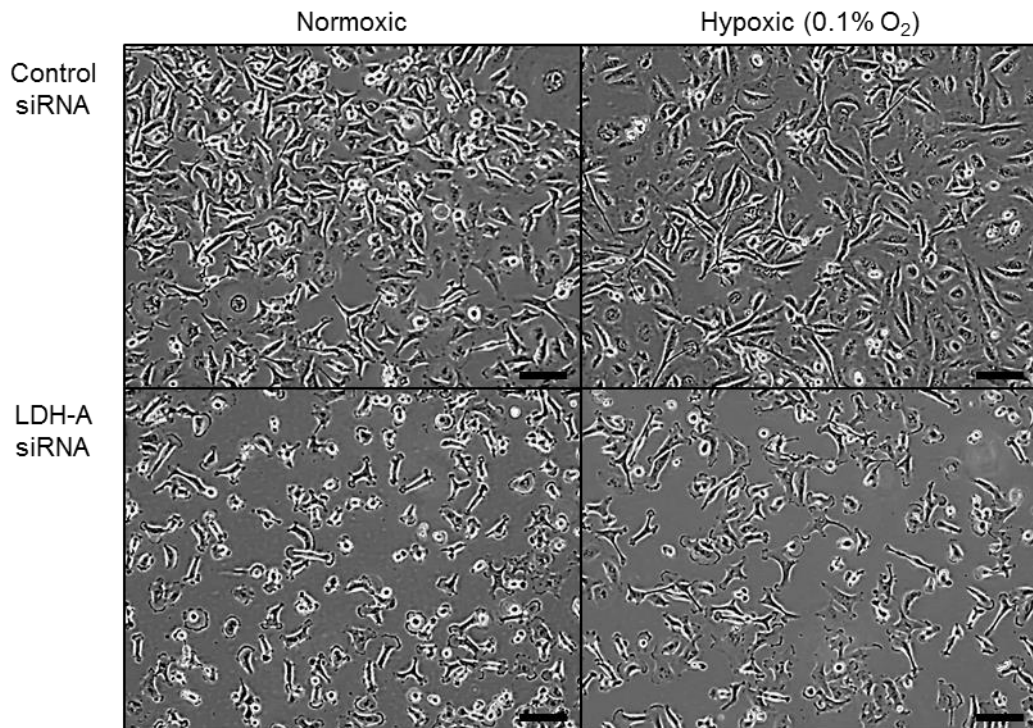


**Figure 5.16: Cell micrographs of MDA-MB-231 cells after LDH-A knock-down.**

Cell images of MDA-MB-231 cancer cells 72 hours post LDH-A or control siRNA transfection under normoxic (21% O<sub>2</sub>) and hypoxic (0.1% O<sub>2</sub>) conditions. Images taken with x10 objective and scale bar indicates 100µm. n=2 biological repeat.

Effects on E-cadherin expression were also analysed following treatment of MDA-MB-231 cells with NHI-2 given its effects on total levels of trimethylated H3K9 (Fig. 5.9). No major effects on E-cadherin expression at the mRNA levels were seen after NHI-2 treatment (Fig. 5.17) or at the protein level (Fig. 5.18).

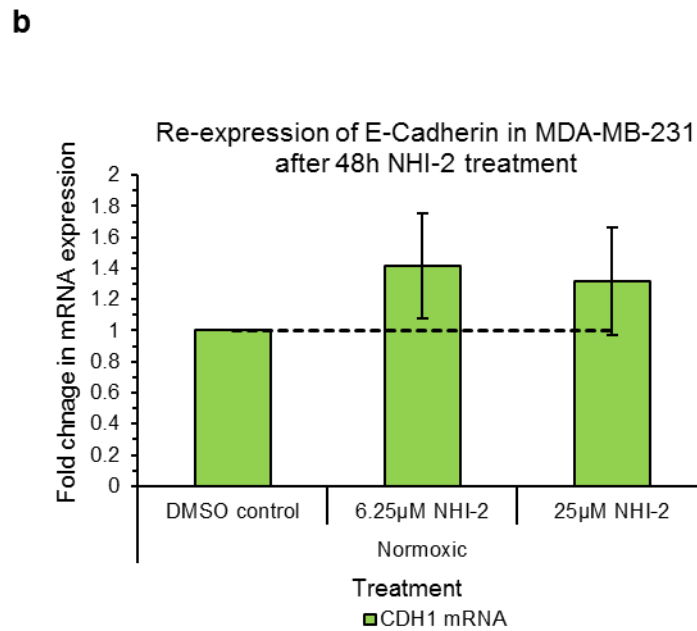
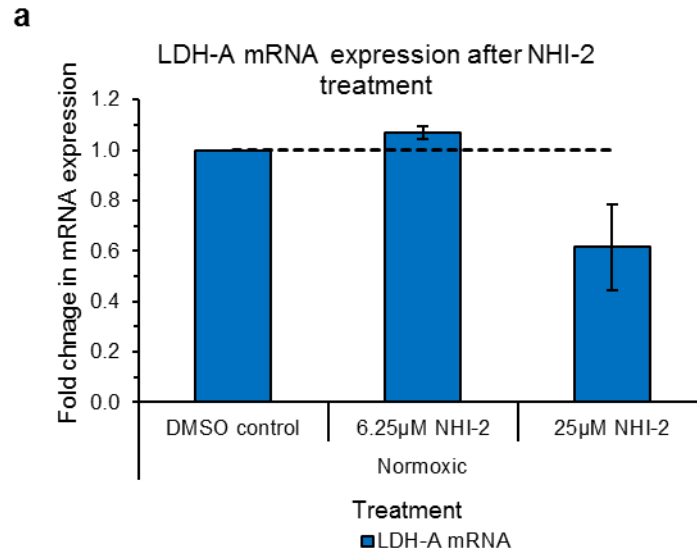


**Figure 5.17: qPCR analysis of E-cadherin mRNA levels in MDA-MB-231 cancer cells after NHI-2 treatment for 48 hours.**

Fold change in LDH-A (**a**) and E-cadherin (CDH1) (**b**) mRNA expression in MDA-MB-231 cancer cells after treatment with NHI-2 or DMSO vehicle control at the indicated doses for 48 hours. n=4 technical repeats  $\pm$  SD from 1 biological replicate.

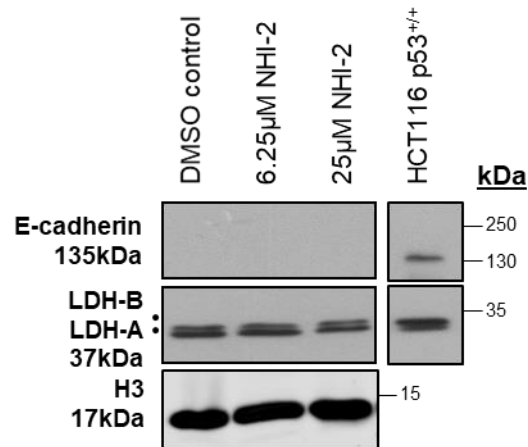


**Figure 5.18: Protein expression of E-cadherin in MDA-MB-231 cancer cells after NHI-2 treatment for 48 hours.**

Immunoblot analysis of potential E-cadherin protein re-expression in MDA-MB-231 cancer cells after treatment with NHI-2 or DMSO vehicle control at the indicated doses for 48 hours. HCT116 p53<sup>+/+</sup> cells shown as a positive control of E-cadherin expression. Histone H3 shown as loading control. n=1 biological repeat.

### **5.2.7 Effect of EX-527 treatment combined with LDH-A knock-down on E-cadherin expression under hypoxic conditions**

Under hypoxia, EX-527 induced E-cadherin mRNA expression (Fig. 5.12) whereas LDH-A silencing had little or no effect (Fig. 5.14). It was hypothesised that epigenetic effects of targeting LDH-A may not be sufficient to induce expression but that combination with EX-527 enhanced expression could be observed.

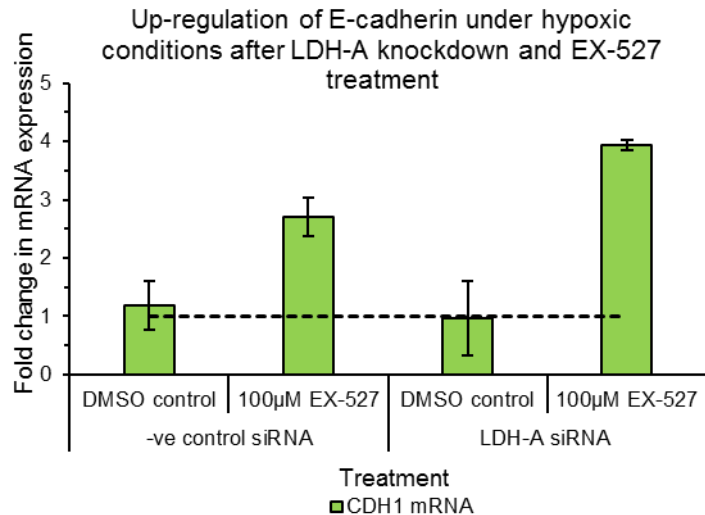


**Figure 5.19: qPCR analysis of E-cadherin mRNA expression in MDA-MB-231 cancer cells after EX-527 treatment in the presence or absence of LDH-A knock-down.**

Fold change in E-cadherin (CDH1) mRNA levels in MDA-MB-231 cancer cells after 48 hours treatment with 100µM EX-527 in the absence or presence of LDH-A knock-down for 72 hours under normoxic (21% O<sub>2</sub>) and hypoxic (0.1% O<sub>2</sub>) conditions. n=4 technical repeats ± SD from 1 biological replicate.

As shown in Figure 5.19 the combination of LDH-A knock-down and inhibition of SIRT1 with EX-527 under hypoxia did lead to a modest increase in E-cadherin mRNA expression compared to EX-527 treatment or LDH-A knock-down alone.

### **5.2.8 EX-527 treatment of MDA-MB-231 cancer cells induces expression of neuronal markers- an effect that is partially mirrored by LDH-A knock-down**

Whilst EX-527 treatment of MDA-MB-231 cancer cells and LDH-A knock-down induced mRNA expression of epigenetically silenced E-cadherin, no E-cadherin protein was detectable and there was no evidence of increased cell-cell contacts or development of a more epithelial-like morphology. Indeed, in response to EX-527 it was noted that the cells became more elongated, mesenchymal like or more neuronal like cells (Fig. 5.11), which corresponded with what was seen when ARPE-19 and CCD 841 CoN non-cancer cells were treated with EX-527 (Fig. 4.19 & Fig. 4.21).

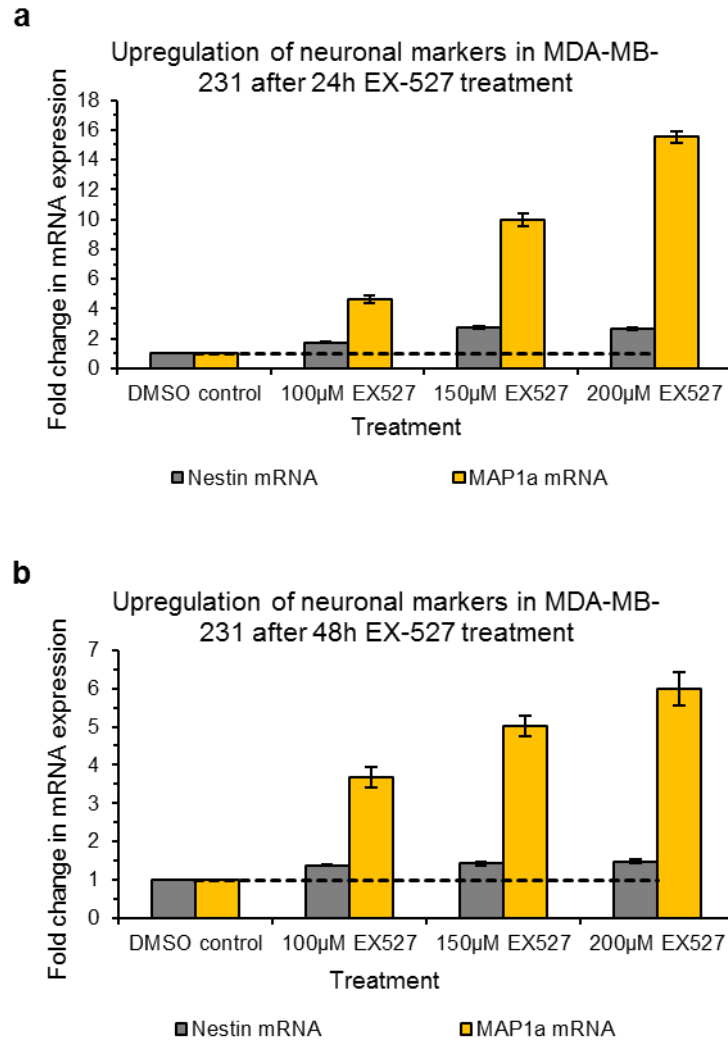


**Figure 5.20: qPCR analysis of neuronal markers in MDA-MB-231 cancer cells after EX-527 treatment.**

Fold change in MAP1a and Nestin mRNA levels in MDA-MB 231 cancer cells after treatment with indicated EX-527 doses or DMSO vehicle control for 24 (a) and 48 hours (b), n=4 technical repeats  $\pm$  SD from 1 biological replicate.

To see whether this change in morphology might be due to neuronal transdifferentiation as seen in ARPE-19 and CCD 841 CoN non-cancer cells, qPCR analysis was performed to examine the mRNA levels of the neuronal markers MAP1a and neural stem cell marker Nestin. MAP1a mRNA levels were increased up to 16-fold and 6-fold in MDA-MB-231 cancer cells after 24 and 48 hours exposure to 200µM EX-527 respectively. Nestin mRNA levels were also increased after 24 hours EX-527 but as with MAP1a at 48 hours the increase was less (Fig. 5.20).

A change in morphology was also noted when LDH-A knock-down was performed in the MDA-MB-231 cells (Fig. 5.16), although less resembling a neuronal morphology compared to that with EX-527 treatment. qPCR analysis in Figure 5.21 showed that MAP1a and Nestin mRNA levels were both increased by 2.6 and 2.2-fold and 1.5 and 5.5-fold after LDH-A knock-down under normoxic and hypoxic conditions, respectively.

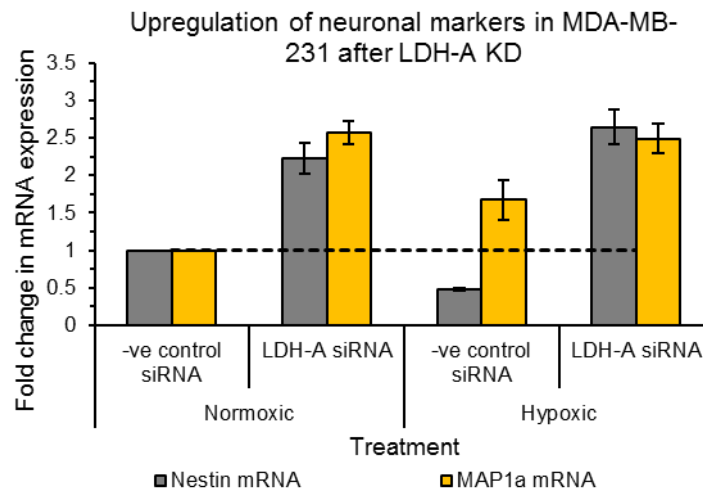


**Figure 5.21: qPCR analysis of neuronal marker mRNA levels after LDH-A knock-down in MDA-MB-231 cancer cells.**

Fold change in MAP1a and Nestin mRNA levels in MDA-MB-231 cancer cells after LDH-A or control siRNA transfection for 72 hours under normoxic (21% O<sub>2</sub>) and hypoxic (0.1% O<sub>2</sub>) conditions. n=4 technical repeats ± SD from 1 biological replicate.

## 5.3 Discussion and conclusions

### 5.3.1 Suppressing LDH-A increases global levels of acetylated K9 of histone H3 and reduces global levels of trimethylated H3K9 but with cancer cell heterogeneity

It was hypothesised that targeting of the glycolytic enzyme LDH-A, could provide a potential way of reversing cancer cell epigenetic modifications, such as epigenetic silencing of TSGs without the epigenetics of non-cancer cells also being affected. Whilst initial investigations here were restricted to two cancer cell line models and non-cancer cells have not been analysed for lack of any effects, preliminary proof-of-principle is provided that targeting LDH-A can impact on cellular histone modifications (via use of a validated LDH-A siRNA and small molecule inhibitor (Allison *et al.*, 2014)). However, additional biological replicates are required to confirm this and whilst the data is broadly supportive of the hypothesis that LDH-A can affect cancer cell epigenetics, more work is required to investigate the mechanisms responsible as discussed below.

In HCT116 p53<sup>+/+</sup> colorectal cancer cells, LDH-A knock-down by RNAi under hypoxic conditions (0.1% O<sub>2</sub>) resulted in a decrease in trimethylated K9 of H3, which is known to be a repressive transcriptional mark and an increase in acetylated H3K9, which is associated with active gene transcription and a more open chromatin structure (Kimura, 2013) (Fig. 5.3). These results are consistent with the model proposed in Figure 5.2, that LDH-A knock-down under hypoxic conditions reduces levels of the oncometabolite L-2HG being produced leading to reduced inhibition of the  $\alpha$ -KG dependent Jumonji family of lysine histone demethylases. Whilst this would account for the global decrease in trimethylated H3K9 and enable acetylation of demethylated K9 residues, L-2HG levels have not been measured and it is possible that other mechanisms may be responsible.

In the triple negative breast cancer cell line MDA-MB-231, LDH-A knock-down in hypoxic cells also reduced trimethylated H3K9 levels but acetylated K9 levels also decreased (Fig. 5.8). Further experiments are required to confirm the

reproducibility of these findings in both HCT116 p53<sup>+/+</sup> and MDA-MB-231 cells and also to examine effects of LDH-A targeting under hypoxia on trimethylated H3K9/acetylated H3K9 in a range of other cancer cell lines. Direct measurement of L-2HG levels, for example by GC-MS (Oldham *et al.*, 2015) would allow correlation of any histone methylation effects with changes in L-2HG levels.

To further dissect the mechanism(s) involved, and the proposed role of changes in L-2HG levels, it would be interesting to assess whether artificial restoration of L-2HG levels, for example using a cell-permeable L-2HG derivative (Oldham *et al.*, 2015) was able to reverse the global reduction in trimethylated H3K9 levels. The enzyme L-2HG dehydrogenase catalyses the oxidation of L-2HG to  $\alpha$ -KG and similarly it could be overexpressed in cells to see if this can recapitulate the effects of LDH-A knock-down.

Effects of targeting LDH-A on acetylated/methylated K9 were also examined under normoxic conditions (Fig. 5.3, Fig. 5.8 & Fig. 5.9). In the HCT116 p53<sup>+/+</sup> cells, there was little effect of LDH-A knock-down with a very small decrease in acetylated H3K9 and a small increase in trimethylated H3K9 observed, however, this is not consistent with the model proposed in Figure. 5.1. In contrast, in MDA-MB-231 cells a small increase in global levels of acetylated H3K9 with a concomitant decrease in trimethylated H3K9 was observed both with LDH-A silencing and with NHI-2 treatment (Fig. 5.8 & Fig. 5.9), which would be consistent with a reduction in SIRT1 activity due to reduced NAD<sup>+</sup> levels (Fig. 5.1). Previously, however, it has been reported that reduced NAD<sup>+</sup> relative to NADH caused by LDH-A targeting is dependent on wild-type p53 and is not observed in p53-null cells (Allison *et al.*, 2014). Interestingly, though, possible effects on NADH/NAD<sup>+</sup> have not been examined in p53 mutant cells. MDA-MB-231 cells have a missense mutation resulting in an amino acid substitution (R280K) (Bae *et al.*, 2014). Importantly, some p53 mutations are reported to confer novel, gain of function including R280K substitution (Bae *et al.*, 2014). It would be worthwhile to assess what effect LDH-A targeting has on NADH/NAD<sup>+</sup>, nuclear NAD<sup>+</sup> and SIRT1 activity in these cells. Although LDH-A knock-down did not globally increase acetylated H3K9 levels in the HCT116 p53<sup>+/+</sup> cells, previously reported effects on SIRT1 activity were modest and focused on p53 as a substrate (Allison

*et al.*, 2014). Nevertheless, it is possible that LDH-A silencing and decreased SIRT1 activity results in localised increases in acetylated H3K9 at individual gene promoters that are not discernible with analysis of total/global acetylated H3K9 levels.

The other notable observation from analysis of global acetylated/methylated H3K9 was increased total levels of acetylated H3K9 under hypoxia compared to normoxia in both the HCT116 p53<sup>+/+</sup> and MDA-MB-231 cells (Fig. 5.3 & Fig. 5.8). This correlates with reduced total levels of SIRT1 protein under hypoxia (0.1% O<sub>2</sub>) in the HCT116 p53<sup>+/+</sup> cells (Fig. 5.3) and it will be interesting to assess whether this is a general phenomenon and/or is also observed in the MDA-MB-231 cells.

Effects of the LDH-A inhibitor NHI-2 on global levels of 5hmC in the HCT116 p53<sup>+/+</sup> cells under normoxic and hypoxic conditions were also examined by immunofluorescence. In line with the model presented in Figure 5.2 and LDH-A catalysed generation of L-2HG under hypoxia, it was hypothesised that with LDH-A suppression, activity of  $\alpha$ -KG-dependent TET enzymes would increase leading to increased levels of 5hmC. However, no increase in nuclear 5hmC staining was evident under hypoxia in response to increasing doses of NHI-2 (Fig. 5.7). Whilst this might suggest that L-2HG levels were perhaps not sufficiently decreased by NHI-2 treatment for significant release of TET enzyme from inhibition to detectably increase global 5hmC, 5hmC generally proved difficult to detect, including under normoxia (Fig. 5.6 & 5.7). TET enzymes are often downregulated in cancer cells compared to normal cells (Rasmussen and Helin, 2016) and immunofluorescence conditions appeared suboptimal with high background staining also observed. As a positive control, 5'aza-2'-deoxycytidine was used, however, here strong non-nuclear staining was also observed which may relate to use of hydrochloric acid to denature the DNA and increase epitope accessibility of the 5hmC antibody (Zhong *et al.*, 2017). These results are thus considered inconclusive. For future studies, it is proposed that cells engineered to overexpress TET enzymes could be used as a positive control for 5hmC with the first question then being whether hypoxic conditions could detectably reduce 5hmC levels before analysis of effects of LDH-A targeting. It would also be

beneficial to stain for 5mC to assess changes in DNA methylation. Other methodological approaches for analysis of changes in global levels of 5hmC/5mC that could be used include dot blots and TET-assisted bisulfide sequencing (TAB-seq) (Yu *et al.*, 2012).

### **5.3.2 Re-expression of epigenetically silenced E-cadherin is induced by SIRT1 inhibitor EX-527 under normoxic and hypoxic conditions and by LDH-A silencing under normoxic conditions**

Previously Pruitt *et al.* (2006) have reported that SIRT1 shRNA and Sir2 inhibitor splitomicin can induce re-expression of epigenetically silenced TSGs, for example E-cadherin and SFRP1, in MDA-MB-231 cancer cells. Given the decrease in global levels of the repressive chromatin mark H3K9me3 and increase in active mark H3K9Ac in response to LDH-A suppression in the MDA-MB-231 cells (Fig. 5.8 & 5.9), it was hypothesised that LDH-A knock-down might similarly induce silenced TSGs.

Using the SIRT1 inhibitor EX-527 as a positive control, effects of siRNA-mediated LDH-A knock-down on expression of silenced E-cadherin was analysed in the MDA-MB-231 cells. In support of previous findings of Pruitt *et al.* (2006), the more selective SIRT1 inhibitor EX-527 increased E-cadherin mRNA expression by >50-fold with 48 hours treatment (Fig. 5.10). E-cadherin is an essential cell-cell adhesion molecule in epithelial tissue and is an integral component of adhesive cell-cell junctions (adherens and desmosomes) (Pećina-Šlaus, 2003). Loss, or reduction, of E-cadherin expression in epithelial cancers is associated with associated with reduction in cell-cell contacts, EMT, and increased migratory and metastatic potential (Pećina-Šlaus, 2003). The ability to induce re-expression of silenced E-cadherin with a specific SIRT1 inhibitor is therefore important given that most cancer deaths are caused by metastases.

Effects of EX-527 on E-cadherin mRNA expression were also analysed in hypoxic MDA-MB-231 cells (Fig. 5.12) as hypoxic cancer cells are commonly more migratory and metastatic (Araos *et al.*, 2018). Importantly, here it is shown for the

first time that SIRT1 targeting is able to induce re-expression of E-cadherin in hypoxic cancer cells. Further studies are required, however, to assess whether E-cadherin protein is expressed and what effect SIRT1 targeting has on cell migration.

However, as outlined in the introduction (section 5.1), cancer cell selectivity of the SIRT1 inhibitor EX-527 is variable and relatively modest (Fig. 4.3) and more selective ways to induce changes in the cancer epigenome and re-express TSGs would be advantageous. Importantly, LDH-A knock-down in normoxic MDA-MB-231 cells increased E-cadherin mRNA expression by ~2.3 fold (Fig. 5.14). Whilst this induction is very small compared to that observed with EX-527, proof-of-principle is provided that LDH-A targeting is able to induce re-expression of an epigenetically silenced TSG. Although LDH-A siRNA treatment modestly increased E-cadherin mRNA levels, E-cadherin protein expression could not be detected by immunoblotting (Fig. 5.15). Further work is required to assess effects of LDH-A *versus* SIRT1 targeting on histone modifications, DNA methylation and recruitment of the transcriptional apparatus (e.g. pol II) at the E-cadherin promoter by ChIP. It might be that LDH-A targeting has more pronounced effects on E-cadherin expression in other cancer cell types/lines or it maybe it could be used as part of a combinatorial strategy to improve the cancer cell selectivity of other epigenetic modifiers. Indeed, LDH-A siRNA used in combination with low dose EX-527 treatment was able to increase expression of E-cadherin mRNA in hypoxic MDA-MB-231 cells (Fig. 5.12). LDH-A silencing alone was insufficient to induce silenced E-cadherin in hypoxic MDA-MB-231 cells (Fig. 5.14) and it would be interesting to compare epigenetic modifications at the E-cadherin promoter under normoxic and hypoxic conditions. Given the model proposed in Figure 5.2, it may be that MDH1/2 is able to partially compensate for LDH-A suppression in the generation of L-2HG and more pronounced epigenetics effects (e.g. increased 5hmC) may be observed with co-silencing of LDH-A and MDH1/2.

### **5.3.3 LDH-A knock-down induces expression of neural stem cell factor Nestin and neuronal marker MAP1a in MDA-MB-231 breast cancer cells**

MDA-MB-231 breast cancer cells are classified as a mesenchymal stem-like triple negative breast cancer (TNBC) subtype (Lehmann *et al.*, 2011). Whilst the SIRT1 inhibitor EX-527 caused a >50-fold increase in E-cadherin mRNA expression, morphologically cells appeared more mesenchymal- or neuronal-like rather than more epithelial (Fig. 5.11), with a reduction in cell number also evident. EX-527 induces ARPE-19 retinal epithelial and CCD 841 CoN colon epithelial non-cancer cells to undergo neuronal transdifferentiation (Chapter 4). It was hypothesised that SIRT1 inhibition may be promoting progression of poorly differentiated MDA-MB-231 cancer cells towards a neuronal/neural differentiation state. In support of this, mRNA expression of the neural stem cell marker Nestin was increased by up to ~2.5-fold (Fig. 5.20a) and neuronal marker MAP1a by up to 16-fold (Fig. 5.20b). Similarly, but to a lesser extent, Nestin mRNA and MAP1a mRNA were also induced by LDH-A knock-down (by ~2-2.5-fold, Fig. 5.21) in both normoxia and hypoxia suggesting that LDH-A silencing may reduce SIRT1 activity in these cells. It would be interesting to determine what effect SIRT1 inhibition and LDH-A targeting has on epigenetic modifications at the Nestin and MAP1a promoters in the MDA-MB-231 cells and also in the non-cancer cell models. Whilst Nestin and MAP1a are not TSGs, the ability to potentially selectively alter their expression to promote a more differentiated (neuronal) phenotype may be therapeutically advantageous or if cancer cell stemness is reduced.

### **5.3.4 Future work**

For future investigations, more in-depth epigenetic analyses would be beneficial as measurement of total/global levels of particular histone modifications or 5hmC/5mC does not provide information as to the epigenetic state at individual gene promoters. There is also the possibility of SIRT1/LDH-A targeting impacting on other DNA-related processes such as DNA damage/repair if promoting a more open chromatin structure. RNAseq would enable identification of epigenetically

silenced TSGs in different cell contexts and any effect of SIRT1 and/or LDH-A targeting on their expression, with ChIPseq or TABseq enabling epigenetic modifications at individual TSG promoters to be analysed on a genome-wide scale. Another limitation of this work was that analyses of histone modifications were restricted to acetylated H3K9 and trimethylated H3K9 and other activating and repressive histone modifications should also be analysed.

Whilst the effects of LDH-A targeting on expression of the epigenetically silenced TSG E-cadherin were much less than with SIRT1 inhibitor EX-527, it may be that effects of suppressing LDH-A are more pronounced at other silenced TSGs. Indeed, it is possible that cancer cell selective death induced by prolonged LDH-A knock-down in different cancer cell contexts (Allison *et al.*, 2014) could be partly linked to re-expression of pro-apoptotic silenced TSGs.

It would also be beneficial to assess whether NAMPT suppression, which can deplete NAD<sup>+</sup> preferentially in cancer cells independent of p53 status (Chapter 3), in combination with LDH-A suppression can result in enhanced cancer-selective reduction of SIRT1 activity than LDH-A targeting alone.

### **5.3.5 Conclusions**

Preliminary evidence is presented which suggests that targeting of the glycolytic enzyme LDH-A can affect the cancer cell epigenome and could potentially, either alone or in combination with other approaches, provide a mechanism to re-activate epigenetically silenced TSGs selectively in cancer cells. In two cancer cell lines *in vitro*, LDH-A silencing by RNAi resulted in reduced global levels of trimethylated H3K9 and increased acetylated H3K9 that are associated with more transcriptionally active chromatin (Fig. 5.3, n=1 biological repeat & Fig. 5.8, n=1 biological repeat). The mechanisms of action are likely to be via those proposed, through decreased SIRT1 activity or decreased L-2HG or a combination of both, however, this has yet to be experimentally verified. LDH-A silencing modestly increased mRNA expression of epigenetically silenced TSG E-cadherin under normoxic conditions and under hypoxic conditions in combination with a low dose of SIRT1 inhibitor EX-527 (Fig. 5.14, n=1 biological repeat & Fig. 5.19, n=1 biological repeat). It was also able to induce expression of neuronal lineage

markers in MDA-MB-231 breast cancer cells, partially mimicking effects of SIRT1 inhibition and indicating a likely SIRT1-dependent mechanism (Fig. 5.20, n=1 biological repeat & Fig. 5.21, n=1 biological repeat).

As indicated, the data presented in this chapter, whilst highly novel, is preliminary and 'pump-priming' in nature and conclusions made are subject to confirmation by additional biological repeats. Due to the different themes linked to the NAD(H) metabolome being investigated as part of this thesis and running concurrently, due to lack of time, most of the results from this chapter have been conducted only once.

## **6. Effects of small molecule KHS101 on glioblastoma cells *in vitro* and its therapeutic potential for selective targeting of other cancer types**

### **6.1 Introduction**

Previous chapters have focused on the use of targeted approaches with the aim of inhibiting or depleting a particular intracellular protein target linked to NAD<sup>+</sup> functions and hypothesised to result in cancer cell selective effects. This chapter investigates a synthetic small molecule, KHS101, that was identified through a chemical phenotypic screen for molecules that can induce neuronal differentiation of rat hippocampal neural progenitor cells (Warashina *et al.*, 2006; Wurdak *et al.*, 2010a). Here, KHS101 is investigated for its effects on cellular metabolism and anti-cancer therapeutic potential.

KHS101 can cross the blood brain barrier and is reported to have neurogenic properties in the adult rat brain (Wurdak *et al.*, 2010a). Treatment of rat hippocampal neural progenitor cells with KHS101 *in vitro* and *in vivo* specifically leads to their neuronal differentiation and not astrocytes or oligodendrocytes (Fig. 6.1). Target deconvolution studies by Wurdak *et al.* (2010a) indicate that KHS101 induces neuronal differentiation of rat neural progenitor cells by KHS101 binding to transforming acidic coiled coil containing protein (TACC3). TACC3 is important in mitotic spindle formation and cell cycle progression and its knock-down was able to recapitulate the neuronal KHS101 phenotype (Wurdak *et al.*, 2010a).

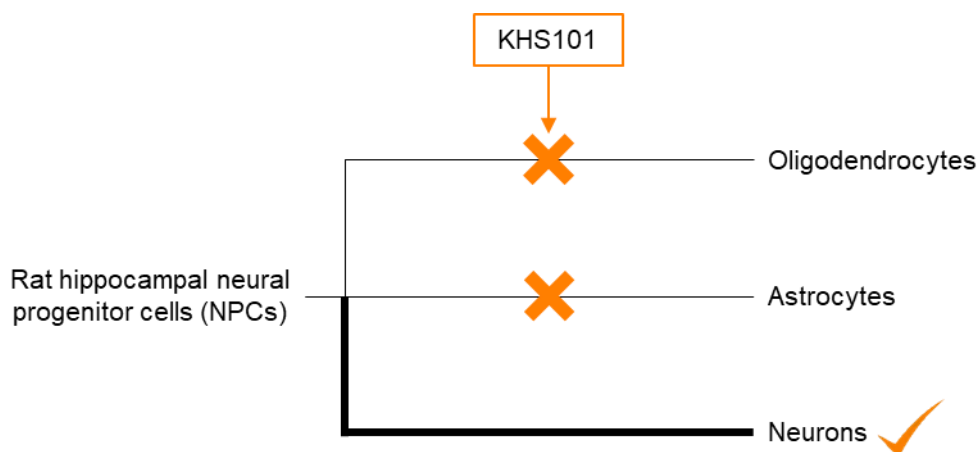


**Figure 6.1: Effects of KHS101 treatment in neural progenitor cells.**

KHS101 treatment of rat neural progenitor cells promotes their neuronal differentiation whereas differentiation to astrocytes or oligodendrocytes is inhibited (Wurdak *et al.*, 2010a).

More recent work by the Wurdak group, in part through collaboration with ourselves, shows that KHS101 induces autophagy and cell death in multiple glioblastoma (GBM) subtypes and not in non-cancer adult neural progenitor cells (Polson *et al.*, 2018). Here, it is investigated how the GBM cells die and whether the autophagy is likely to be the cause of death or a pro-survival stress response. Affinity-based target ID and mechanism of action studies by Leeds suggest that the phenotypic effects of KHS101 in GBM cells are not via TACC3 but through inhibition of the mitochondrial heat shock protein 1 (HSPD1(Hsp60)) (Polson *et al.*, 2018). HSPD1 is a molecular chaperone important for the correct folding of mitochondrial proteins (Bross and Fernandez-Guerra, 2016). Amongst effects observed by the Wurdak group, metabolomics analyses revealed reduced levels of DHAP and increased levels of glycerol-3-phosphate (G3P) (Polson *et al.*, 2018). Based upon this, it was hypothesised that KHS101, via HSPD1, may perturb the mitochondrial G3P shuttle (Fig. 6.2), which is important in selective tissues (Mráček *et al.*, 2013) for the re-oxidisation of cytosolic NADH without lactate accumulation. Investigations have begun here at Huddersfield into this, and the potential inhibition of mitochondrial G3P dehydrogenase (GPD2) by KHS101 and perturbation of cellular NAD<sup>+</sup>/NADH and ATP generation. In addition, it is investigated whether the effects of KHS101 can be recapitulated with a recently reported inhibitor of HSPD1 of different chemical structure to KHS101 as part of the target validation of HSPD1 (Wiechmann *et al.*, 2017).

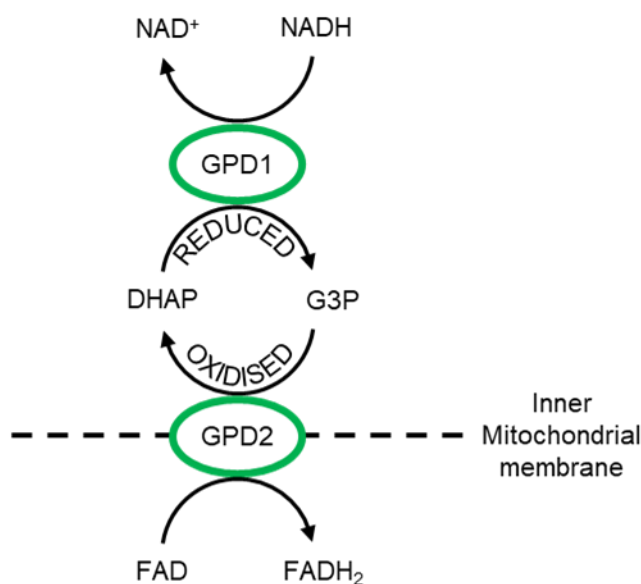


**Figure 6.2: The glycerol-3-phosphate shuttle.**

Mitochondrial glycerol-3-phosphate dehydrogenase (GPD2) is located on the outer surface of the inner mitochondrial membrane and catalyses the oxidation of G3P to dihydroxyacetone phosphate (DHAP) using FAD as an electron acceptor. This is coupled to the reduction of DHAP to G3P by cytoplasmic GPD1 using NADH as an electron donor which results in regeneration of NAD<sup>+</sup> from NADH. In this way reducing equivalents are transferred from the cytoplasm to the mitochondria and into mitochondrial oxidative phosphorylation.

Another important and unexplored question investigated here was whether KHS101 might have selective cytotoxic activity against other cancer cell types and, if so, whether the mechanistic bases for this are similar to or different from those in the GBM context. It was hypothesised that KHS101 may induce similar selective death in other cancer cell types which would indicate a potential strategy to extend the therapeutic application of KHS101, or a similar molecule, beyond glioblastoma to a broader range of cancer types.

## 6.2 Results

### 6.2.1 Vacuolisation induction and metabolic effects of KHS101

Treatment of patient derived GBM1 glioblastoma cells with KHS101 resulted in the appearance of intracellular vacuoles (Fig. 6.3), in agreement with studies at the University of Leeds (Wurdak group). Further investigation revealed these to be autophagic vacuoles that are induced by KHS101 in GBM cell models but not in non-cancerous human neural progenitor cells (NP1) (Polson *et al.*, 2018).

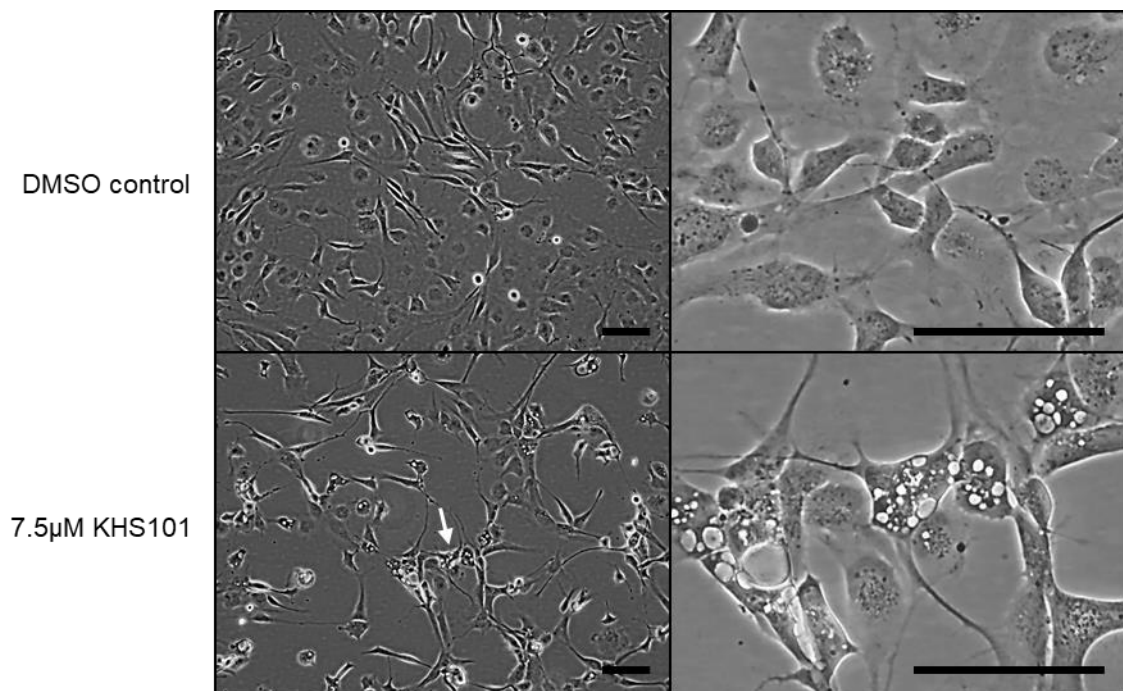


**Figure 6.3: Cell micrographs of GBM1 cancer cells after treatment with 7.5µM KHS101 for 24 hours.**

Cell images of the GBM1 cancer stem cell-like model after 7.5µM KHS101 treatment for 48 hours. White arrow indicating vacuoles. Images taken with x10 and x40 objectives, scale bar indicates 100µm. n=3 biological repeats.

Whilst autophagy is commonly regarded as a mechanism of cell death, it can be induced by cellular stress such as starvation, hypoxia and low ATP levels and in such circumstances may promote cell survival (Das *et al.*, 2018). It was hypothesised that the autophagy observed might be a survival or metabolic stress response. As part of the process of ‘target deconvolution’ of KHS101 it was

therefore investigated whether KHS101 had any effects on GBM1 or NP1 cellular bioenergetics. The rates of glycolysis and mitochondrial respiration and reserve capacities were compared under normal growth conditions and after 24 hours exposure to 7.5 $\mu$ M KHS101. 24 hours KHS101 treatment diminished the basal OCR (mitochondrial respiration) of GBM1 cells by 5-fold whereas basal glycolytic rates (ECAR) were unchanged (Fig. 6.4). The non-cancer NP1 cells also had decreased basal oxygen consumption but to a lesser extent than in the GBM1 cells (reduced by 1.8-fold in the NP1 cells). Importantly, the NP1 cells showed upregulated glycolysis in response to KHS101 and their decreased oxygen consumption, with the glycolytic rate increased to its maximum capacity (Fig. 6.4a). This was presumed to be a compensatory metabolic response in the NP1 cells to partially impaired mitochondrial respiration in order to try and sustain cellular energy levels. In contrast, in the GBM1 cells there was no compensatory increase in glycolysis and following KHS101 treatment both glycolytic and mitochondrial respiratory capacity appeared to be severely impaired (Fig. 6.4b). Overall, these results are consistent with a selective autophagic response in the GBM1 cancer cells correlating with impaired ability to metabolically compensate to decreased mitochondrial respiration by increasing glycolysis and the preferential toxicity of KHS101 (Polson *et al.*, 2018).

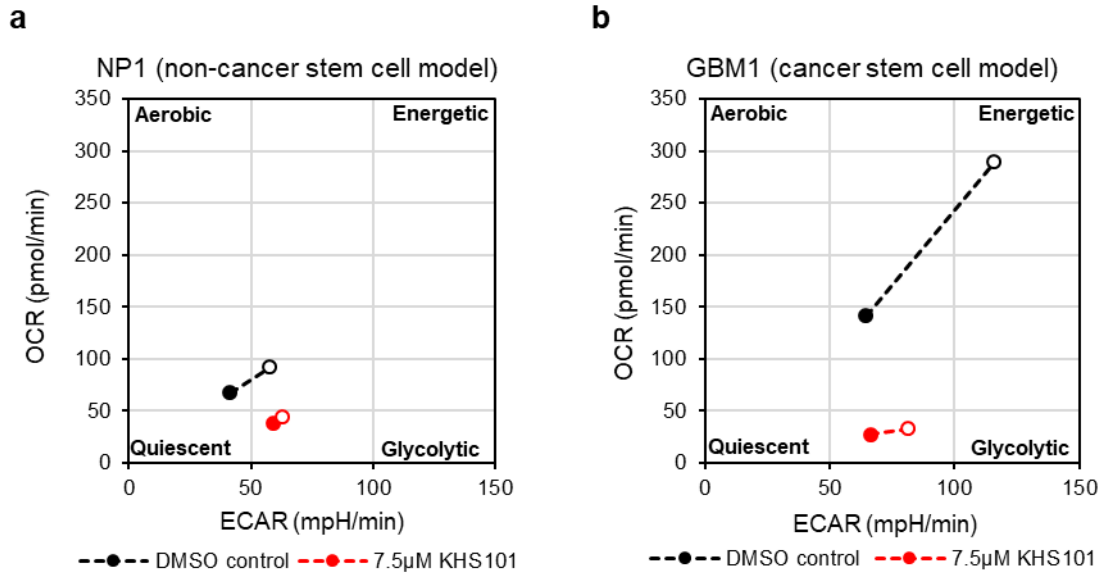


**Figure 6.4: Cell energy phenotype of NP1 and GBM1 cells after KHS101 treatment.** NP1 neural progenitor (oligopotent) non-cancer cells (a) and GBM1 cancer stem-like cells (b) treated with 7.5µM KHS101 for 24 hours prior to analysis. Mean cell energy phenotypes are shown compared to DMSO vehicle control cells; basal metabolic phenotype is indicated by closed circles; metabolic stress response/capacity is indicated by open circles, n=1 biological repeat (3 technical replicates per repeat).

## 6.2.2 KHS101 induces GBM1 cancer cell death by apoptosis

Given the respiratory dysfunction induced by KHS101 in GBM1 cells and lack of glycolytic compensatory response, this led to the assumption that the autophagy phenotype was a pro-survival catabolic response to sustain cellular bioenergetics. At a later time-point of 48 hours, under the microscope a number of the KHS101 treated cells morphologically resembled apoptotic cells with some membrane blebbing and apoptotic-like bodies visible. Indeed, staining of cells with annexin V and PI and cytometric analysis showed a significant increase in the number of apoptotic GBM1 cells following KHS101 treatment (Fig. 6.5), indicating that KHS101 induces GBM1 apoptotic cell death.

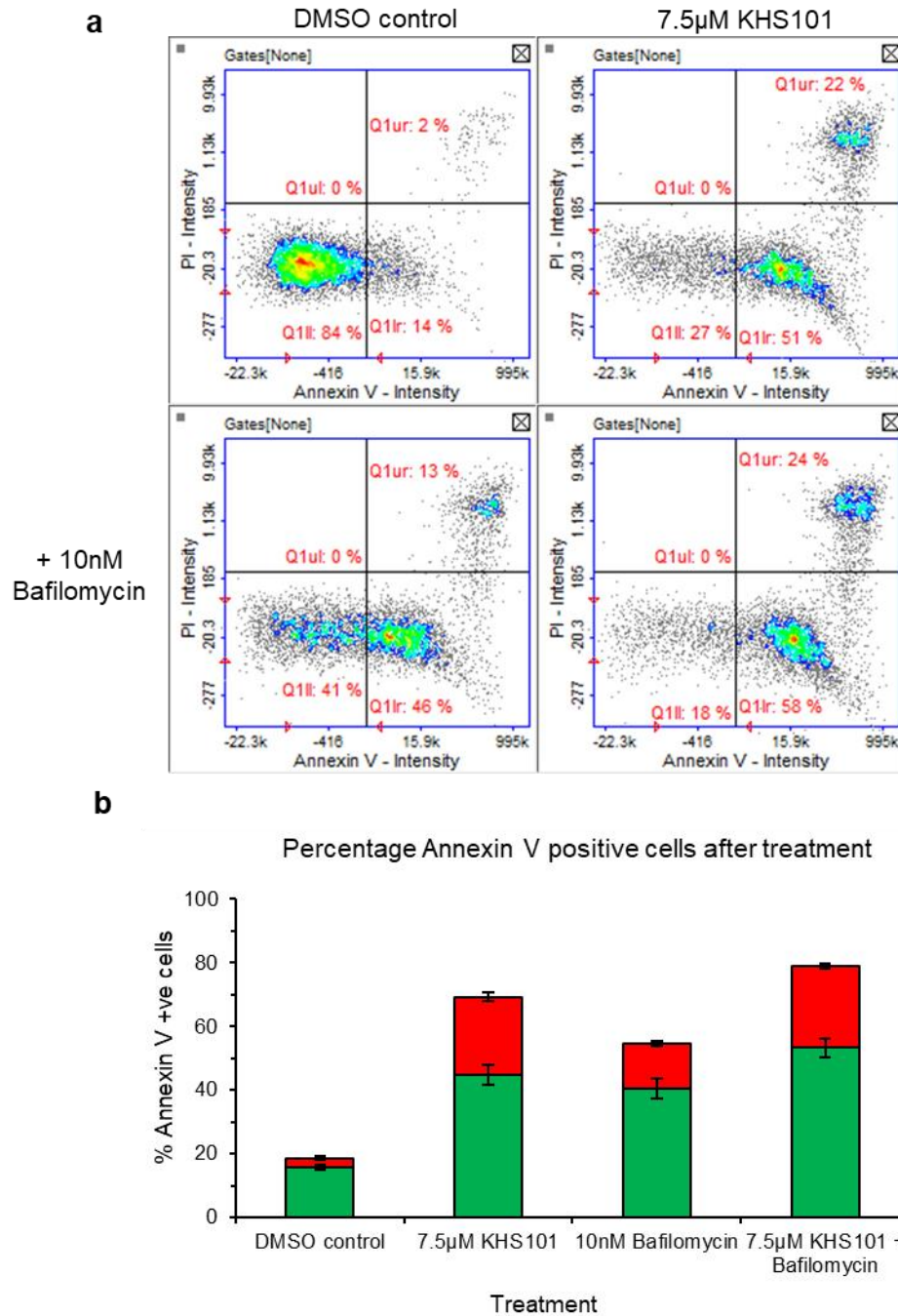


**Figure 6.5: Quantification of annexin V positive GBM1 cells after treatment with 7.5 $\mu$ M KHS101 in the absence or presence of the autophagy inhibitor bafilomycin for 48 hours.**

**a.** Annexin V assay dot plots quantifying the proportion of early apoptotic and late apoptotic/necrotic cells through differential annexin V/PI staining after treatment with 7.5 $\mu$ M KHS101 in the absence or presence of 10nM bafilomycin for 48 hours. Lower left quadrant indicates alive cells, lower right quadrant indicates early apoptotic cells (annexin V positive, PI negative) and upper right quadrant indicates late apoptotic/necrotic cells (annexin V positive, PI positive). **b.** Bar chart showing mean percentage of annexin V positive GBM1 cells  $\pm$  SEM, n=3 biological repeats (2 technical replicates), in response to 7.5 $\mu$ M KHS101 in the absence or presence of 10nM bafilomycin for 48 hours compared to DMSO control treated cells. Green bars represent early apoptotic cells (annexin V positive only); red bars indicate late apoptotic/necrotic cells (annexin V positive, PI positive).

To further dissect the role of autophagy, GBM1 cells were treated with KHS101 and the late stage autophagy inhibitor bafilomycin. The basis for doing this was that if autophagy is promoting cell death its inhibition would increase cell survival. As Figure 6.5 shows, KHS101-induced apoptosis is modestly increased in the presence of autophagy inhibitor bafilomycin indicating that apoptosis is not autophagy-dependent and suggesting that autophagy has a pro-survival role.

### **6.2.3 Mechanism of action of KHS101 in glioblastoma cells**

Commercial analysis (Human Metabolome Technologies Inc.) of intracellular metabolites using capillary electrophoresis mass spectrometry (Wurdak group) provided further insight into KHS101-induced metabolic perturbation. Analyses of metabolite levels after 30 minutes 7.5 $\mu$ M KHS101 treatment in NP1 and GBM1 cells revealed a dramatic reduction in levels of G3P shuttle metabolite DHAP and increased G3P selectively in the GBM1 cells. Given the inability of KHS101-treated GBM1 cells to metabolically compensate for reduced mitochondrial respiration by upregulating glycolysis (Fig. 6.4) and reduced levels of G3P shuttle metabolite DHAP (Polson *et al.*, 2018), this led us to speculate that KHS101 may be affecting the activity of the mitochondrial G3P shuttle enzyme GPD2. GPD2 coupled with cytosolic GPD1 activity can regenerate cytosolic NAD<sup>+</sup> which is important for high glycolytic flux (Mráček *et al.*, 2013) and the shuttle transfers reducing equivalents from the cytosol to the mitochondria (from cytosolic NADH to mitochondrial FADH<sub>2</sub>; Fig. 6.2). A GPD2 activity assay revealed that acute KHS101 treatment for 1 hour significantly reduced GPD2 activity of GBM1 cells (63% decrease) and had little or no effect on non-cancer NP1 cells (Fig. 6.6).

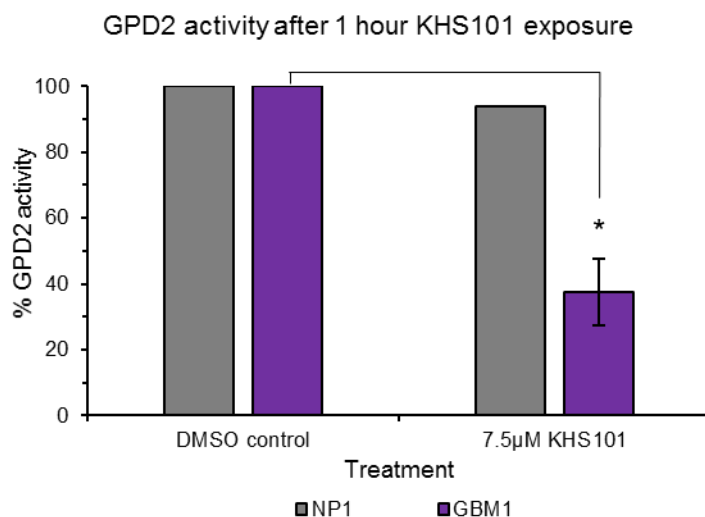


**Figure 6.6: Decrease in GPD2 activity after KHS101 treatment.**

Percentage decrease in GPD2 activity in GBM1 cancer stem like cells and NP1 non-cancer oligopotent cells after 1 hour treatment with 7.5µM KHS101. n=3 biological repeats (1 technical repeat) for GBM1 ( $\pm$ SEM) and n=1 biological repeat (1 technical repeat) for NP1. A two-tailed t-test was performed where \* $p < 0.05$ .

Given the functions of the G3P shuttle, it was hypothesised that KHS101-induced inhibition of GPD2 may perturb cellular NADH:NAD<sup>+</sup> balance. 5µM KHS101 treatment for 24 hours did not affect total NAD(H) levels but reduced the NADH levels relative to NAD<sup>+</sup> by 68% in the GBM1 cells and by 37% in the NP1 cells.

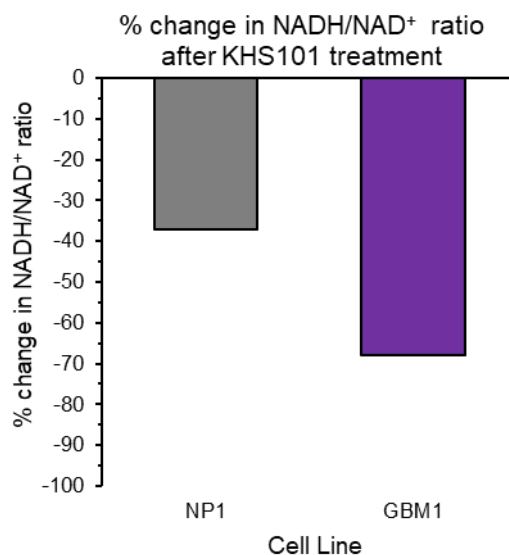


**Figure 6.7: Decrease in NADH levels relative to NAD<sup>+</sup> following 24 hours KHS101 treatment.** Percentage decrease in NADH/NAD<sup>+</sup> ratio in GBM1 cancer stem like cells and NP1 non-cancer stem like cells treated with 5µM KHS101 for 24 hours, n=1 biological repeat, (2 technical replicates).

Dysregulated NADH:NAD<sup>+</sup> balance (Fig. 6.7) and attenuated mitochondrial respiration and glycolysis (Fig. 6.4) in the GBM1 cells led us to further speculate that they are unable to sustain cellular ATP levels hence the autophagic phenotype. In support of this, KHS101 treatment resulted in a time-dependent increase in levels of phosphorylated AMP-activated protein kinase (AMPK) in the GBM11 glioblastoma model (Fig. 6.8). AMPK is phosphorylated and activated in response to low energy (high cellular AMP and ADP relative to ATP) and can also stimulate autophagy (Hardie, 2011).

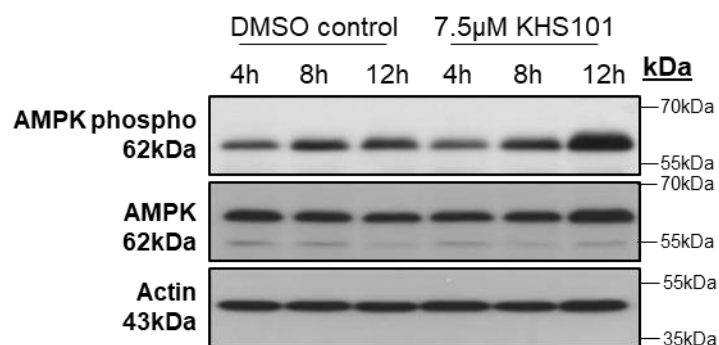


**Figure 6.8: Expression of phosphorylated AMPK in GBM11 after KHS101 treatment.** Immunoblot analysis of phosphorylated AMPK and total AMPK in GBM11 cancer stem-like cell model 4, 8 and 12 hours post exposure to 7.5μM KHS101 or DMSO vehicle control, actin shown as loading control. n=1 biological repeat.

## 6.2.4 HSPD1 inhibitor myrtucommulone recapitulates the GBM-selective lethal effects of KHS101

Further studies by the Wurdak group using an affinity-based pull-down assay and proteomics identified that the mitochondrial chaperone HSPD1 specifically interacts with KHS101 (Polson *et al.*, 2018). Additional investigations suggested that KHS101 binds to HSPD1 disrupting its function resulting in selective mis-aggregation of mitochondrial and glycolytic enzymes (Polson *et al.*, 2018).

Whilst studies suggested that the selective toxicity of KHS101 towards GBM models was due to inactivation of HSPD1, it was important to independently validate this. It was possible that other unidentified cellular target(s)/interaction partner(s) of KHS101 were required or responsible for the lethal phenotype. The effects of the natural product myrtucommulone (MC) that has been recently

identified as a selective HSPD1 inhibitor (Wiechmann *et al.*, 2017), and is of different chemical structure to KHS101, was tested to see if it could recapitulate the effects of KHS101. As Figure 6.9 shows, 48 hours 10 $\mu$ M MC treatment induced apoptotic cell death in each of six different patient-derived GBM models tested that are representative of different GBM subtypes but it had little effect towards non-cancerous neural progenitors.

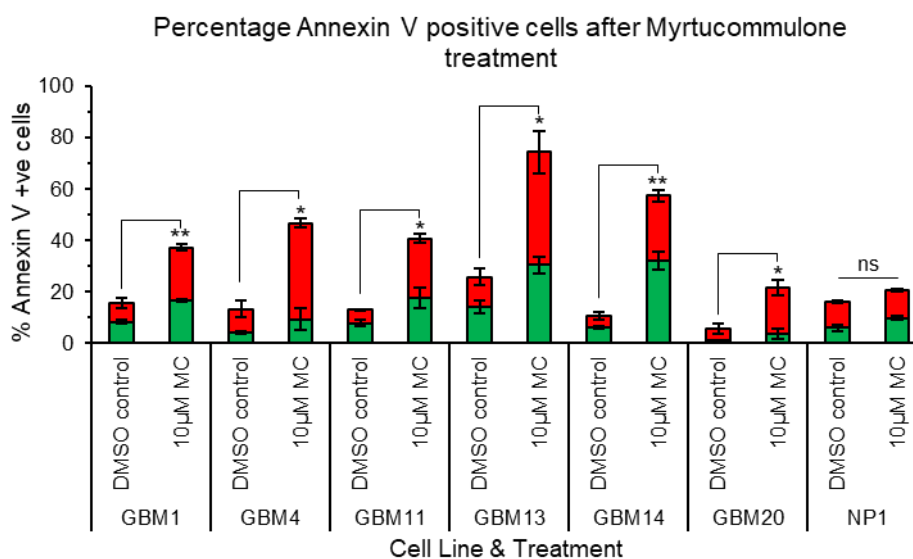


**Figure 6.9: Quantification of annexin V positive cells after 10 $\mu$ M myrtucommulone treatment.**

Mean percentage  $\pm$  SEM, of annexin V and PI positive patient derived GBM cancer cell models and NP1 neural progenitor non-cancer cells after treatment with 10 $\mu$ M myrtucommulone (MC) for 48 hours. Green bars represent early apoptotic cells (annexin V positive only); red bars indicate late apoptotic/necrotic cells (annexin V positive, PI positive). Two-tailed t-tests were performed where \* $p$ <0.05, \*\* $p$ <0.01, ns=not significant,  $n$ =3 biological repeats (2 technical replicates).

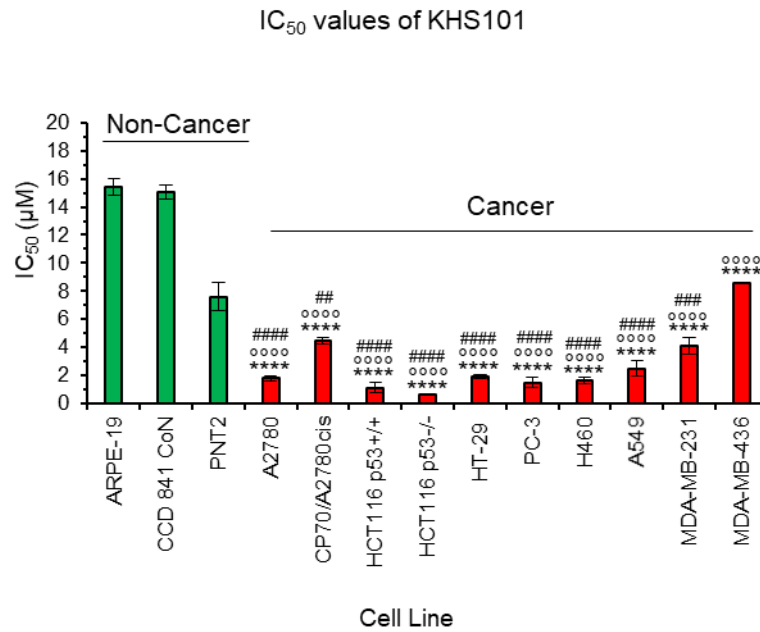
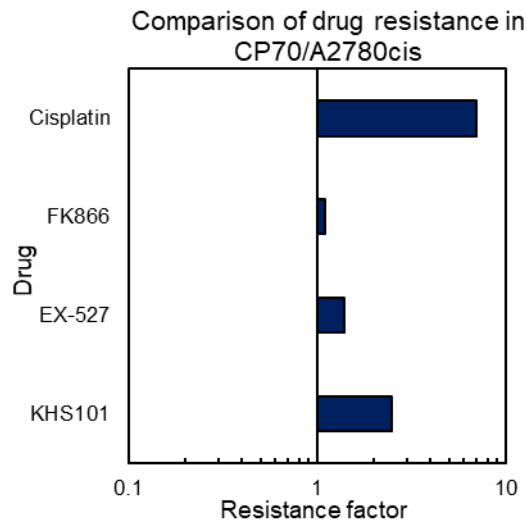
## 6.2.5 Investigation of KHS101 activity against other cancer cell types

Whilst KHS101 appears to be a very promising small molecule for selective targeting of glioblastoma cells without adverse effects on non-cancerous brain cells (Polson *et al.*, 2018), it has not been tested against other cancer types. KHS101 was therefore tested in chemosensitivity assays against a panel of different cancer cell lines of different tissue type for any preferential activity compared to non-cancer cell models (Table 6.1).

KHS101	Cell Line	Tissue Origin	Average IC <sub>50</sub> (μM)	±SEM
Non-Cancer	ARPE-19	Retina	15.47	0.59
	CCD 841 CoN	Colon	15.06	0.47
	PNT2	Prostate	7.61	0.97
Cancer	A2780	Ovary	1.78	0.20
	CP70/A2780cis	Ovary	4.45	0.22
	HCT116 p53 <sup>+/+</sup> normoxic	Colon	1.11	0.36
	HCT116 p53 <sup>+/+</sup> hypoxic	Colon	4.30	0.70
	HCT116 p53 <sup>-/-</sup>	Colon	0.62	0.03
	HT-29	Colon	1.91	0.10
	PC-3	Prostate	1.49	0.36
	H460	Lung	1.59	0.22
	A549	Lung	2.50	0.57
	MDA-MB-231	Breast	4.08	0.57
	MDA-MB-436	Breast	8.60	0.05

**Table 6.1: IC<sub>50</sub> values of KHS101 towards multiple human cell lines of different tissue origin.**

Mean IC<sub>50</sub> values ± SEM, n=3 biological repeats (8 technical replicates per repeat), of the small molecule KHS101 in multiple non-cancer and cancer cell lines after 96 hours continuous exposure to KHS101.

**a****b**

**Figure 6.10: Summary of KHS101 cytotoxicity towards a panel of non-cancer and cancer cells and lack of cross-resistance with cisplatin.**

**a.** Mean IC<sub>50</sub> values ± SEM, n=3 biological repeats (8 technical replicates per repeat), of the small molecule KHS101 in multiple cancer and non-cancer cell lines as determined by MTT chemosensitivity assay. A one way ANOVA was performed where \*\*\*\*p<0.0001 compared to ARPE-19, °°°°p<0.0001 compared to CCD 841 CoN and ##p<0.01, ###p<0.001, ####p<0.0001 compared to PNT2 non cancer cells. **b.** Comparison of resistance factor of A2780 and CP70/A2780cis cancer cells to cisplatin and KHS101 (FK866 and EX-527 shown for comparison) (IC<sub>50</sub> in CP70/A2780cis cells divided by IC<sub>50</sub> in A2780 cells; resistance factor >1 indicates less activity towards CP70/A2780cis cells than parental A2780 cells).

As summarised in Figure 6.10, KHS101 was significantly more active against all the cancer cells tested compared to ARPE-19, CCD 841 CoN and PNT-2 non-cancer cell models (except for MDA-MB-436 versus PNT2). Interestingly KHS101

appeared to be 1.8-fold more active towards HCT116 p53<sup>-/-</sup> cells compared to isogenic HCT116 p53<sup>+/+</sup> cells. Although KHS101 was less toxic towards the cisplatin resistant CP70/A2780cis cancer cell line than the cisplatin-sensitive parental line (A2780) it is important to note that the resistance factor was ~4-fold lower than that with Cisplatin (Fig. 6.10a & appendix Table 9.2) (resistance factor of 2.5 compared to 10).

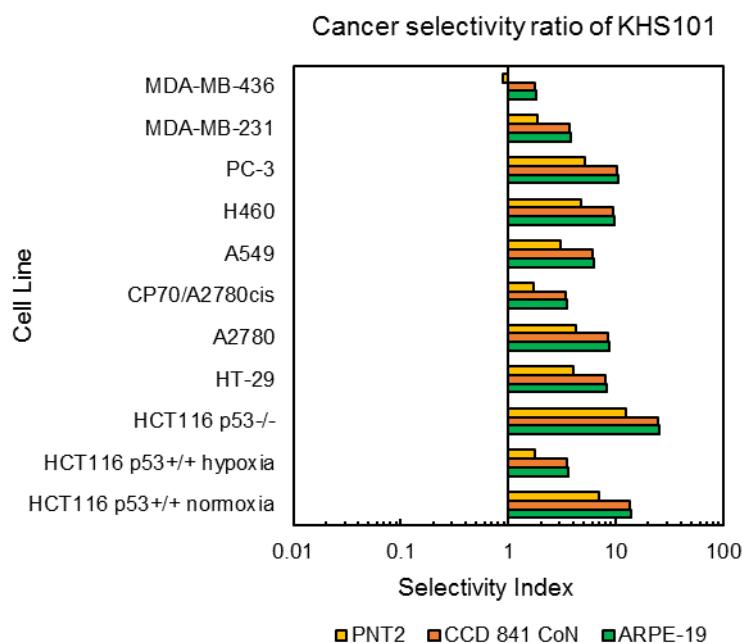


**Figure 6.11 Preferential cytotoxicity of KHS101 towards cancer cells compared to non-cancer cell models.**

Cancer cell versus non-cancer cell selectivity ratios for KHS101 in multiple cancer cell lines compared to ARPE-19, CCD 841 CoN and PNT-2 non-cancer cells. The selectivity index was calculated from the IC<sub>50</sub> values achieved from 3 biological repeats (8 technical replicates) using the following equation (mean IC<sub>50</sub> of non-cancer cells / mean IC<sub>50</sub> of cancer cells). A value of 1 indicates equitoxicity of the drug to cancer and non-cancer cells, a value of <1 indicates no preferential cytotoxicity to the cancer cells and a value >1 indicates preferential cytotoxicity to the cancer cells.

Importantly, KHS101 activity (Table 6.1) and *in vitro* cancer cell selectivity (Fig. 6.11) was broadly comparable to that of KHS101 towards the GBM models and NP non-cancerous neural progenitors (GBM1 IC<sub>50</sub> 2.23µM; NP1 >20µM, NP2 18.24µM; (Polson *et al.*, 2018)). As with FK866 and EX-527, the cancer cell selectivity of KHS101 was compared to FDA-approved platinate based chemotherapeutic agents cisplatin, carboplatin and oxaliplatin (Fig. 6.12).

KHS101 was 13.6-fold more selective towards the HCT116 p53<sup>+/+</sup> colorectal cancer cells compared to CCD 841 CoN non cancer colon cells.

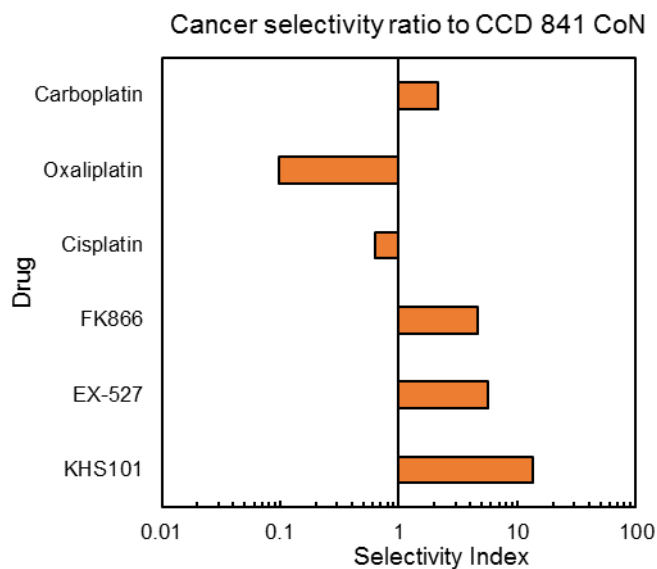


**Figure 6.12: Cancer cell selectivity of KHS101 compared to FDA approved platinate based compounds.**

Cancer cell selectivity ratios were calculated from the IC<sub>50</sub> values achieved from 3 biological repeats (8 technical replicates) which compared the activity of KHS101 and clinically used platينات (cisplatin, oxaliplatin, carboplatin) in HCT116 p53<sup>+/+</sup> cancer cells and CCD 841 CoN non-cancer cells after 96 hours exposure. SI = mean IC<sub>50</sub> of non-cancer cells / mean IC<sub>50</sub> of cancer cells (FK866 and EX-527 shown for comparison purposes).

Polson *et al.* (2018) had previously reported that KHS101 had equitoxic activity to GBM1 cells under 5% O<sub>2</sub> tension. Interestingly, in the HCT116 p53<sup>+/+</sup> cancer cell model, KHS101 was 3.9-fold less active under hypoxic conditions of 0.1% O<sub>2</sub> compared to atmospheric 21% O<sub>2</sub> (Fig. 6.13).

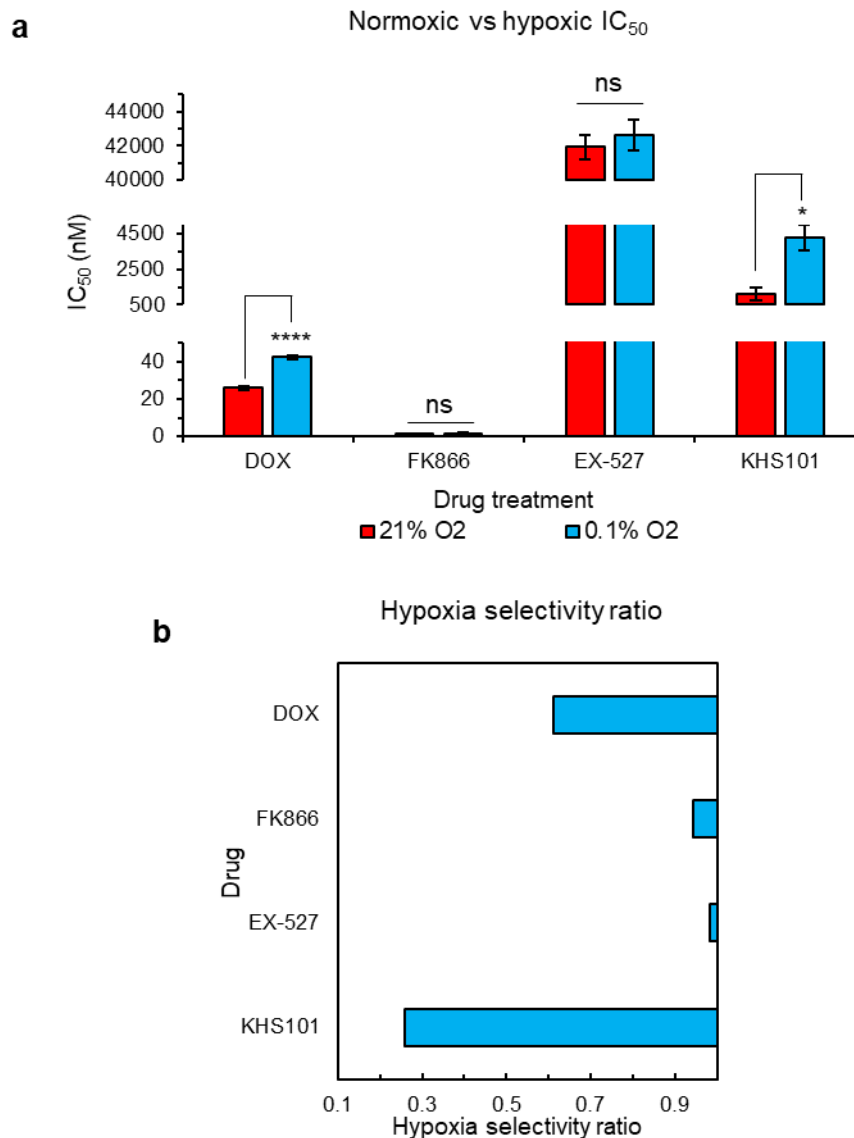


**Figure 6.13: The effect of hypoxia on doxorubicin and KHS101 towards HCT116 p53<sup>+/+</sup> cells.** Mean IC<sub>50</sub> values, n=3 biological repeats (8 technical replicates) of doxorubicin (DOX), FK866, EX-527 and KHS101 (**a**) under normoxic (21% O<sub>2</sub>) and hypoxic (0.1% O<sub>2</sub>) conditions in HCT116 p53<sup>+/+</sup> cancer cells after 96 hours continuous drug exposure. Two-tailed t-tests were performed where \*p<0.05, \*\*\*\*p<0.0001. **b.** Hypoxia selectivity ratio (IC<sub>50</sub> normoxic cells / IC<sub>50</sub> hypoxic cells) for DOX, FK866, EX-527 (shown for comparison purpose) and KHS101. A value of 1 indicates equitoxicity of the drug under normoxic and hypoxic conditions, a value of <1 indicates preferential cytotoxicity to normoxic cells and a value of >1 indicates preferential cytotoxicity to hypoxic cells. Values were achieved using IC<sub>50</sub> values from 3 biological repeats (8 technical replicates).

## 6.2.6 Mechanism(s) of action of KHS101 towards other cancer cell types

Although KHS101 showed promising preferential activity towards other cancer cell types *in vitro*, this could be by similar or different mechanisms to those in glioblastomas. Here, effects of KHS101 towards the HCT116 p53<sup>+/+</sup> colorectal cancer cell line and the experimentally amenable ARPE-19 non-cancer cell model were further investigated.

Over 96 hours, KHS101 was 13.6-fold more active towards the HCT116 cells (Table 6.1) which displayed a similar IC<sub>50</sub> to the GBM1 cells (Polson *et al.*, 2018). 48 hours exposure to 7.5µM KHS101 induced pronounced apoptosis in the GBM1 cells (Fig. 6.5) with 70% of cells staining annexin V-positive. Interestingly, however, in a preliminary experiment in the HCT116 p53<sup>+/+</sup> cells whilst there was some induction of apoptosis, <50% of cells stained positive for annexin V with background levels of apoptosis in control cells also being quite high (Fig. 6.14b). 31% of the KHS101 treated HCT116 p53<sup>+/+</sup> cells appeared early apoptotic suggesting that there may be time-dependent differences compared to GBM1 cells in any apoptotic response to KHS101. At this time point, any differential apoptotic response between ARPE-19 and HCT116 p53<sup>+/+</sup> cells was also quite modest, however, further biological repeats and evaluation at later time points is warranted. A more notable difference between the ARPE-19 and HCT116 cells following 48 hours KHS101 treatment was observed in cell number with a 27% decrease in the ARPE-19 non-cancer cells and a 67% decrease in the HCT116 p53<sup>+/+</sup> cancer cells (Fig. 6.14a) suggesting differential impairment of cell growth.

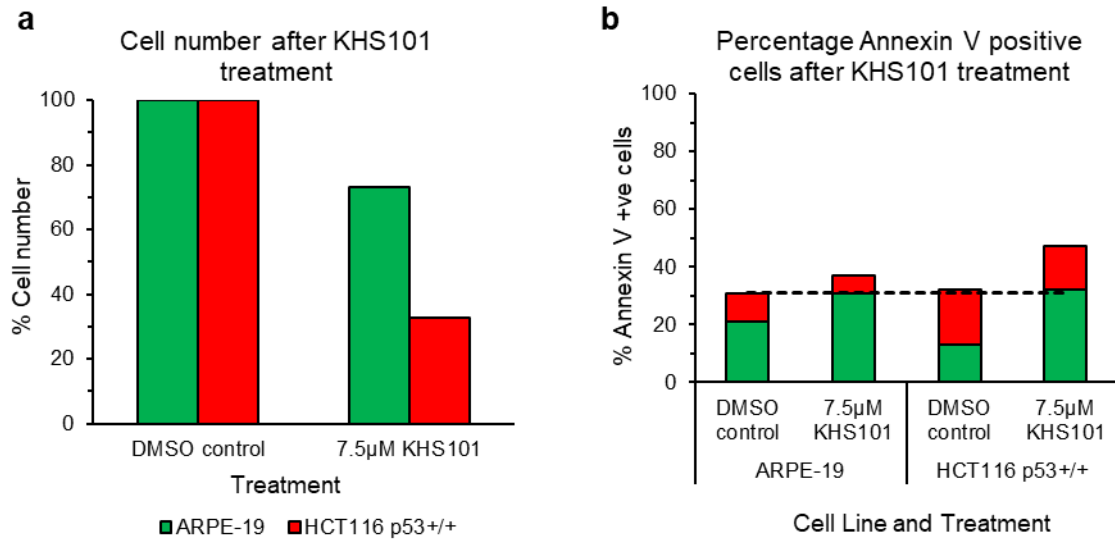


**Figure 6.14: Percentage cell number and annexin V positive cells after KHS101 treatment in ARPE-19 non-cancer cells and HCT116 p53<sup>+/+</sup> cancer cells.**

Percentage total cell number relative to DMSO vehicle control (a) after 48 hours exposure to 7.5μM KHS101 or DMSO vehicle control. b. Percentage of annexin V positive/PI negative and annexin V positive/PI positive ARPE-19 non-cancer cells and HCT116 p53<sup>+/+</sup> cancer cells after 48 hours exposure to 7.5μM KHS101. Green bars represent early apoptotic cells (annexin V positive only); red bars indicate late apoptotic/necrotic cells (annexin V positive, propidium iodide (PI) positive). n=1 biological repeat, (2 technical replicates).

Another key question was whether KHS101 induces autophagy. Interestingly, whilst not visible at low magnification, at higher magnification small cytosolic vacuoles, that could be autophagic, were visible in KHS101-treated HCT116 p53<sup>+/+</sup> cancer cells at 24 hours (Fig. 6.15). Unexpectedly, dark ‘particulates’ or ‘speckles’ were also evident in the cytosol of both ARPE-19 and HCT116 p53<sup>+/+</sup> cells.

To directly assess whether autophagy was induced in HCT116 p53<sup>+/+</sup> and ARPE-19 cells, cells were stained with the fluorescent dye ‘CYTO-ID’ (Enzo LifeSciences). CYTO-ID is a cationic amphiphilic tracer dye and is reported to specifically label autophagic compartments with minimal staining of lysosomes (Chan *et al.*, 2012). Both ARPE-19 and HCT116 p53<sup>+/+</sup> cells showed increased CYTO-ID staining following KHS101 treatment (Fig. 6.16a) with 54% and 61% of cells respectively staining positively for CYTO-ID (Fig.6.16b).

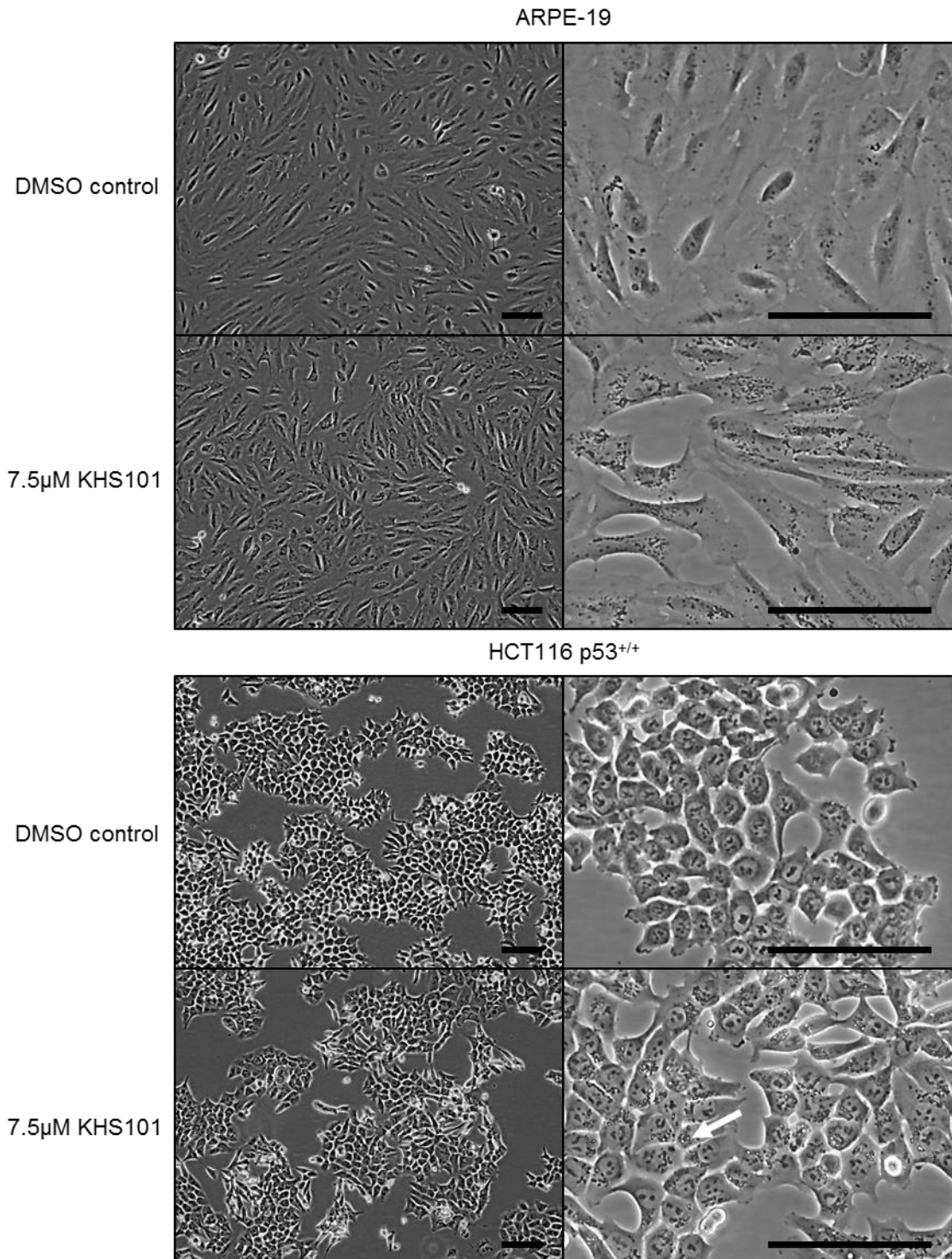


**Figure 6.15: Cell micrographs of ARPE-19 and HCT116 p53<sup>+/+</sup> cancer cells after KHS101 treatment.**

Cell images of ARPE-19 non-cancer cells and HCT116 p53<sup>+/+</sup> cancer cells after 24 hours treatment with 7.5μM KHS101. Images taken with x10 and x40 objectives and scale bars indicates 100μm. White arrow indicating vacuoles in HCT116 p53<sup>+/+</sup> cancer cells. n=3 biological repeats.

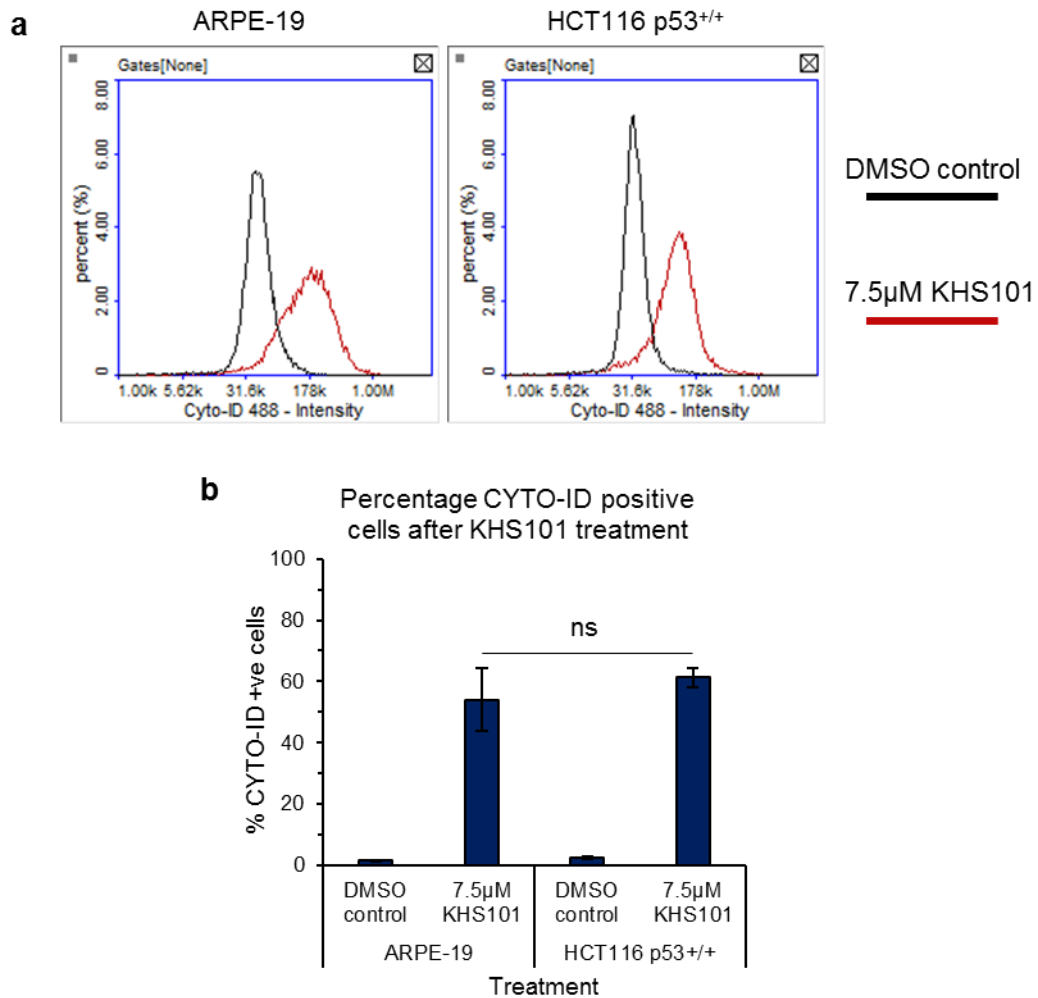


**Figure 6.16: Image cytometry analysis of KHS101 and DMSO vehicle control treated cells stained with the autophagic dye CYTO-ID.**

**a.** Histogram of ARPE-19 non-cancer cells and HCT116 p53<sup>+/+</sup> cancer cells treated with 7.5µM KHS101 (red) or DMSO vehicle control (black) for 24 hours that were then analysed for CYTO-ID positive labelling. **b.** Bar chart quantifying mean percentage of ARPE-19 non-cancer cells and HCT116 p53<sup>+/+</sup> cancer cells that are staining positively for CYTO-ID having been treated with 7.5µM KHS101 or DMSO vehicle control for 24 hours. Average determined following quadrant gating of CYTO-ID positive cells. n=3 biological repeats (2 technical replicates) ±SEM, a two tailed t-test was performed where ns=not significant.

In addition to image cytometry analysis, the effects of a range of different KHS101 concentrations on CYTO-ID staining was analysed by fluorescent microscopy (Fig. 6.17 & Fig. 6.18). CYTO-ID staining was cytoplasmic and punctate and increased with KHS101 treatment in ARPE-19 non-cancer and isogenic p53<sup>+/+</sup> and p53 null HCT116 cancer cells in a dose dependent manner. Overlay images of fluorescent CYTO-ID staining with bright-field cell images indicated co-localisation of the green fluorescent CYTO-ID staining to vacuoles (Fig. 6.19).

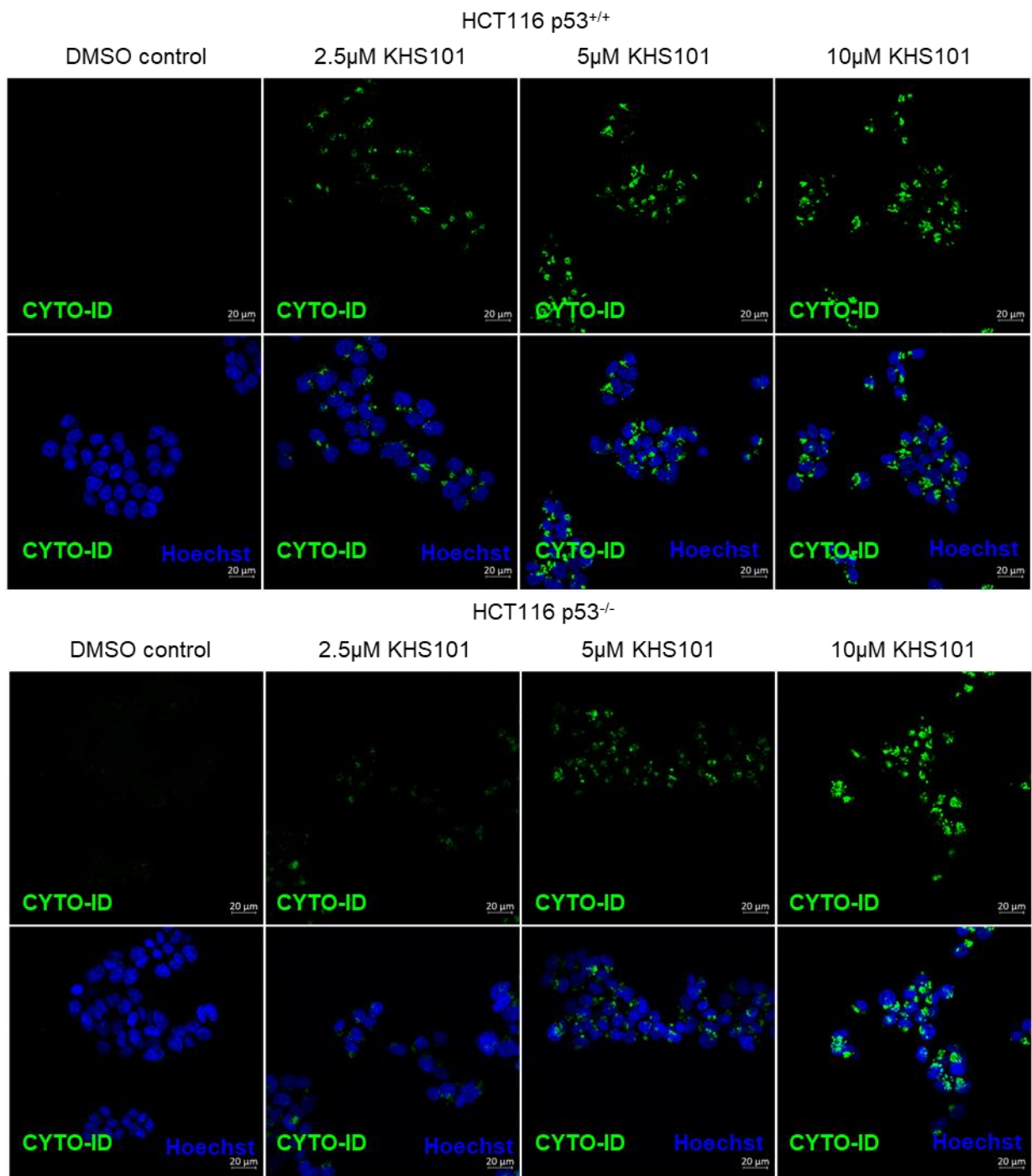


**Figure 6.17: Expression of CYTO-ID as a marker of autophagy in HCT116 cancer cells that have been treated with KHS101 for 24 hours.**

Representative fluorescent cell images of HCT116 p53<sup>+/+</sup> and HCT116 p53<sup>-/-</sup> cancer cells that have stained positive for CYTO-ID (green) and nuclear marker Hoechst (blue) after treatment with indicated KHS101 doses or DMSO vehicle control for 24 hours. Images taken with x40 objective and scale bar indicates 20μm. n=1 biological repeat.

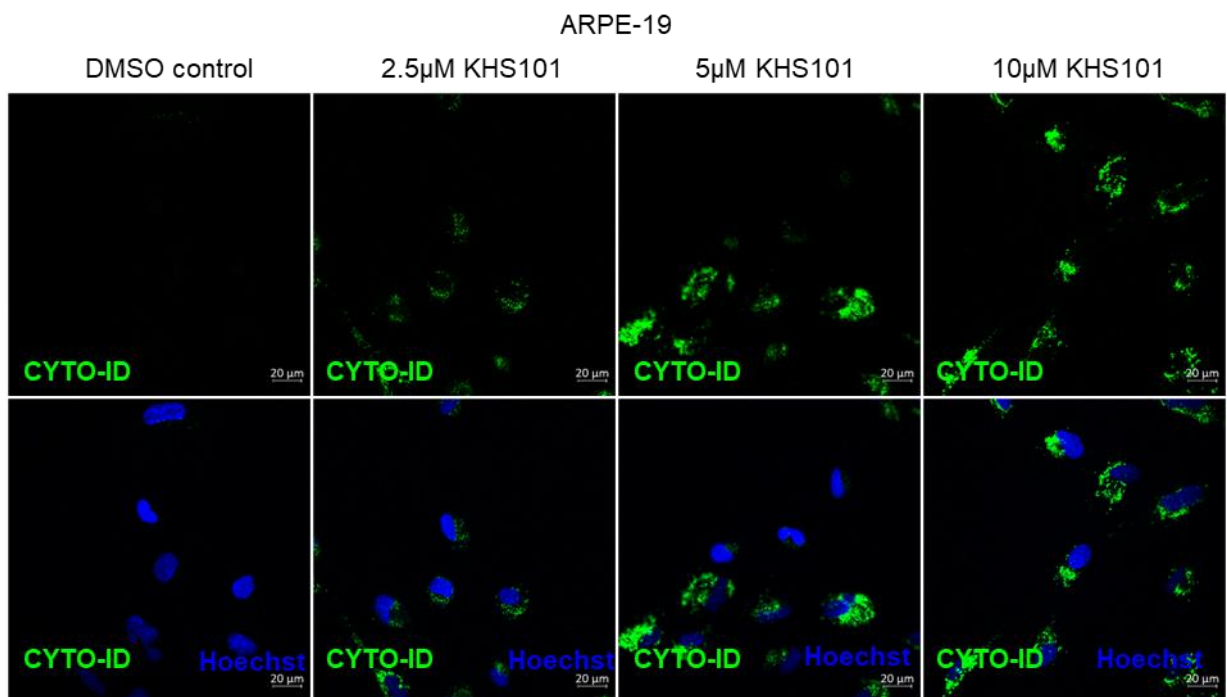


**Figure 6.18: Expression of CYTO-ID as a marker of autophagy in ARPE-19 non-cancer cells that have been treated with KHS101 for 24 hours.**

Representative fluorescent cell images of ARPE-19 non-cancer cells that have stained positive for CYTO-ID (green) and nuclear marker Hoechst (blue) after treatment with indicated KHS101 doses or DMSO vehicle control for 24 hours. Images taken with x40 objective and scale bar indicates 20 $\mu$ m. n=1 biological repeat.

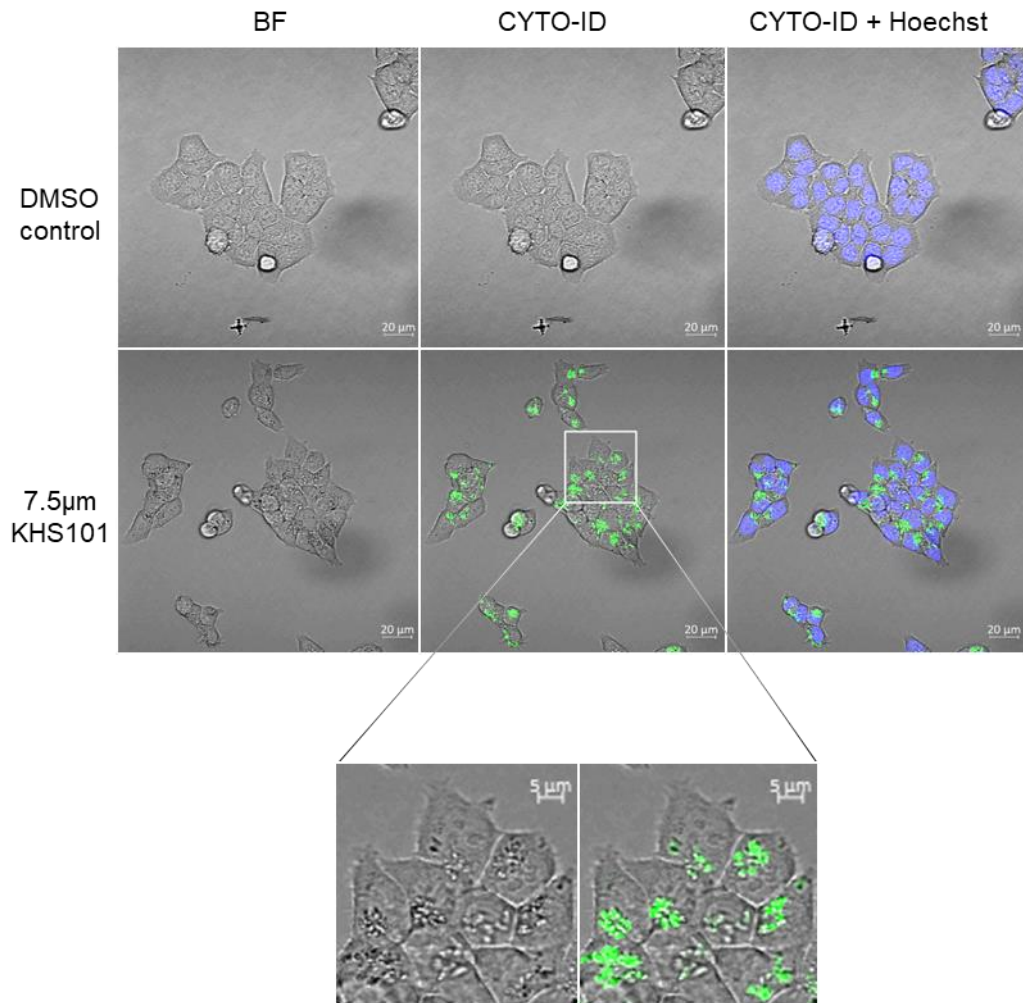


**Figure 6.19: Localisation of CYTO-ID staining to vacuoles in HCT116 p53<sup>+/+</sup> cancer cells treated with 7.5µM KHS101 or DMSO vehicle control.**

Representative fluorescent and bright field (BF) cell images of HCT116 p53<sup>+/+</sup> cells after KHS101 treatment for 24 hours showing localisation of CYTO-ID staining (green) to the vacuoles seen in the cells. Nuclear Hoechst staining (blue). Images taken with x40 objective and scale bar indicates 20µm or 5µm. n=1 biological repeat.

To further confirm the induction of autophagy by KHS101 in these cells, whole cell lysates were prepared and the levels of the autophagic marker LC3-II (Tanida *et al.*, 2008) were analysed by immunoblotting (Fig. 6.20). For comparison, levels of LC3-I (non-lipidated LC3) and LC3-II (lipidated LC3) were also determined in the NP1 and GBM1 cells. The GBM1 cells treated with KHS101 showed increased levels of LC3-II relative to control cells and to treated NP1 cells (Fig. 6.20), consistent with preferential autophagy induction by KHS101 in the GBM1 cells (Polson *et al.*, 2018). KHS101 preferentially induced LC3-II expression in

the HCT116 p53<sup>+/+</sup> cancer cells by 9.8-fold compared to ARPE-19 non-cancer cells (Fig. 6.20).

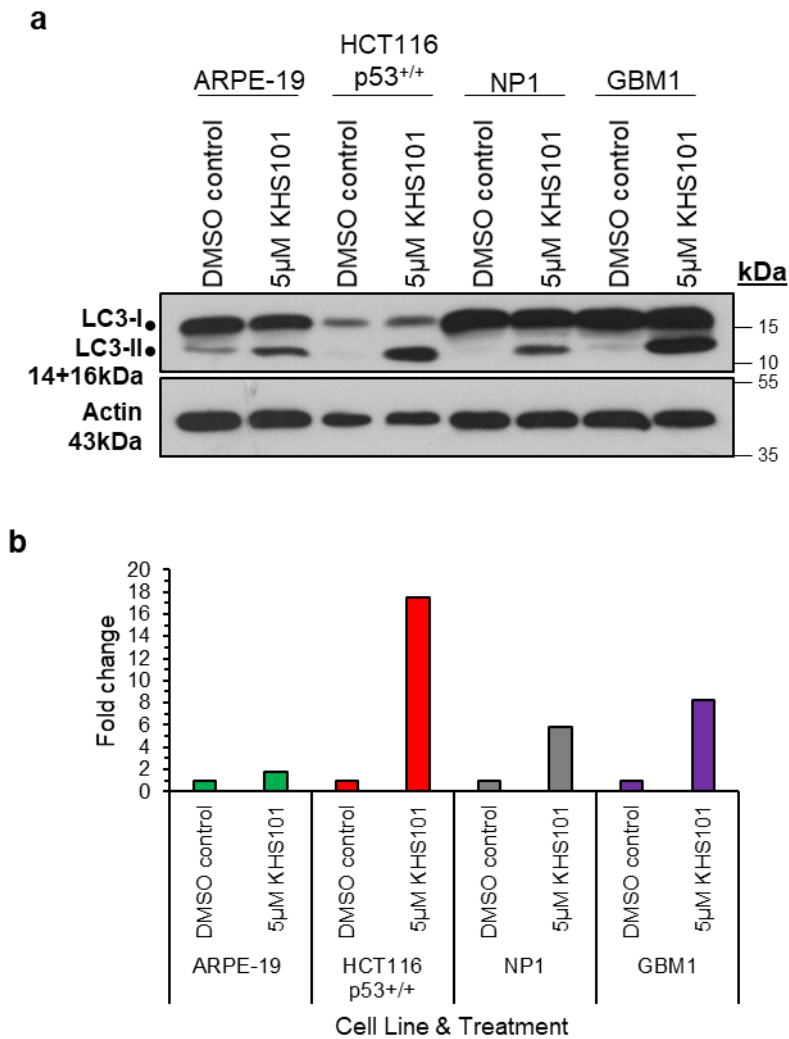


**Figure 6.20: Quantification of the autophagy marker LC3-II in cells after 5µM KHS101 treatment for 24 hours.**

**a.** Immunoblot analysis of LC3-I and LC3-II protein expression in ARPE-19 non-cancer cells, HCT116 p53<sup>+/+</sup> cancer cells, NP1 neural progenitor non-cancer cells and GBM1 cancer stem like cells after 24 hours exposure to 5µM KHS101, actin shown as loading control. **b.** Densitometric analysis quantifying the expression of LC3-II. Levels normalised to actin, fold change expressed compared to each DMSO vehicle control. n=1 biological repeat.

## 6.2.7 Does KHS101 produce differential effects on cellular metabolism in other cancer and non-cancer cells?

KHS101 treatment of the GBM1 cancer stem cell-like model and NP1 neural progenitor non-cancer cells showed that NP1 cells could compensate for the

effects of KHS101 on oxidative phosphorylation by upregulating glycolysis, whereas GBM1 cells could not (Fig. 6.4). It was hypothesised that this may also be true for ARPE-19 non-cancer cells and HCT116 p53<sup>+/+</sup> cancer cells.

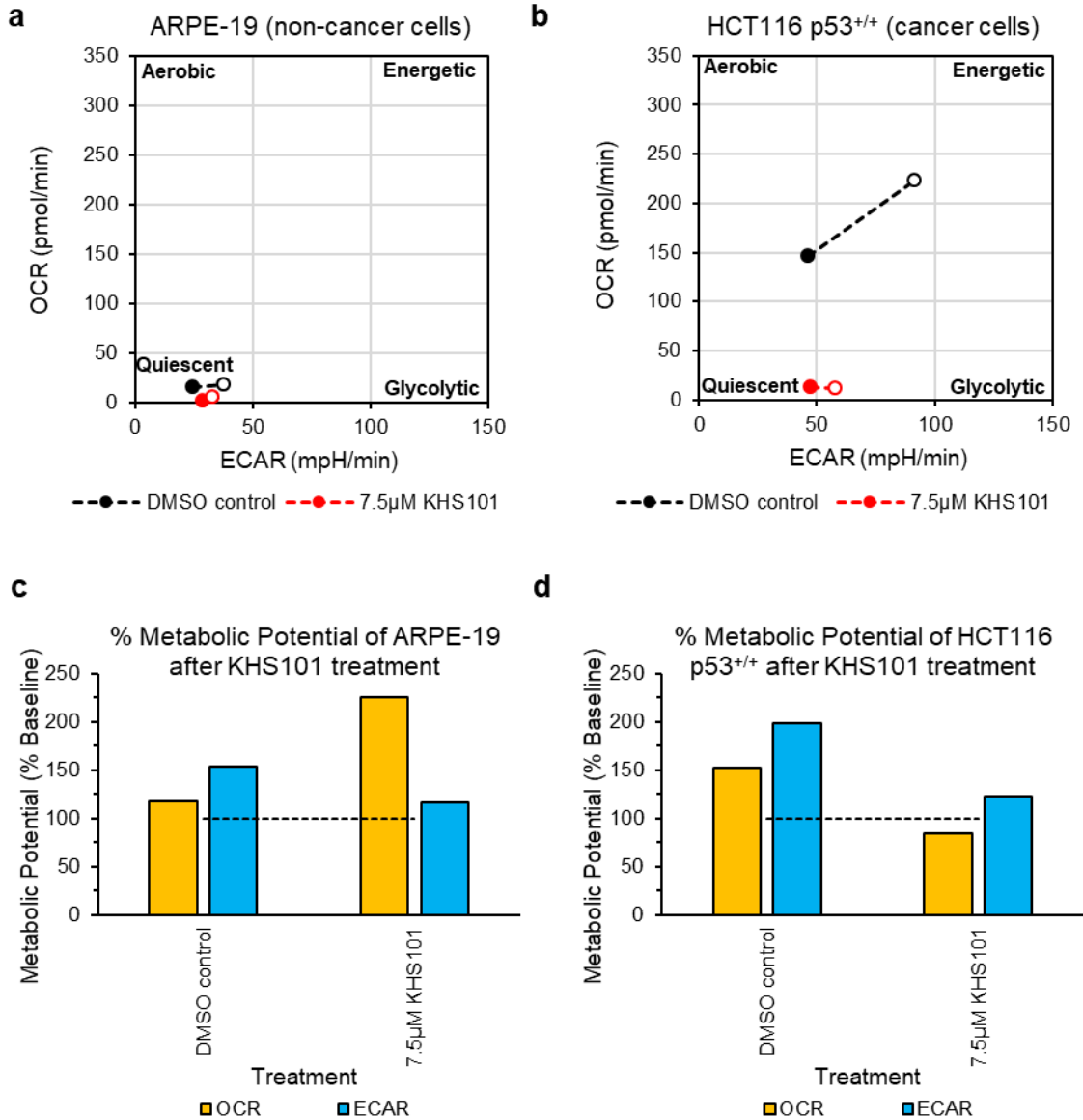


**Figure 6.21: Cell energy phenotype of ARPE-19 non-cancer cells and HCT116 p53<sup>+/+</sup> cancer cells after KHS101 treatment.**

ARPE-19 non-cancer cells and HCT116 p53<sup>+/+</sup> cancer cells were treated with 7.5 μM KHS101 24 hours prior to analysis. Cell energy phenotypes are shown compared to DMSO vehicle control treated cells (a) (b), basal metabolic phenotype is indicated by closed circles; metabolic stress response/capacity is indicated by open circles. Percentage metabolic potential of KHS101 treated ARPE-19 (c) and HCT116 p53<sup>+/+</sup> (d) cells compared to DMSO control treated cells, showing % change in ECAR and OCR compared to baseline (black dotted line). n=1 biological repeat, (3 technical replicates).

7.5 $\mu$ M KHS101 treatment for 24 hours led to major effects on basal oxygen consumption in the HCT116 p53<sup>+/+</sup> cancer cells (decreased by 11-fold compared to 7-fold in the ARPE-19 non-cancer cells) (Fig. 6.21). Furthermore, the HCT116 p53<sup>+/+</sup> cancer cells showed complete loss of respiratory capacity whereas ARPE-19 cells retained some respiratory capacity and were able to increase mitochondrial respiration in response to FCCP and oligomycin mix (Fig. 6.21). The basal rate of glycolysis appeared modestly increased in ARPE-19 non-cancer cells but not in HCT116 p53<sup>+/+</sup> cancer cells.

Metabolic effects of KHS101 were also determined following immediate cell exposure (XFp metabolic analyser, direct injection). The OCR of HCT116 p53<sup>+/+</sup> cancer cells after direct injection of both KHS101 doses (2.5 $\mu$ M and 7.5 $\mu$ M) was reduced compared to DMSO control, with greater effects being seen for the higher KHS101 dose (Fig. 6.22a & Fig. 6.23a). Alongside this the ECAR was increased after KHS101 treatment indicating that the cells were compensating from decreased mitochondrial respiration by upregulating glycolysis (Fig. 6.22b & Fig. 6.23b). For HCT116 p53<sup>+/+</sup> cells treated with 2.5 $\mu$ M KHS101, injection of ATP synthase inhibitor oligomycin indicated some ATP production from mitochondrial respiration (37% of control cells) whereas 7.5 $\mu$ M KHS101 treated cells (direct injection) showed no mitochondrial ATP production.

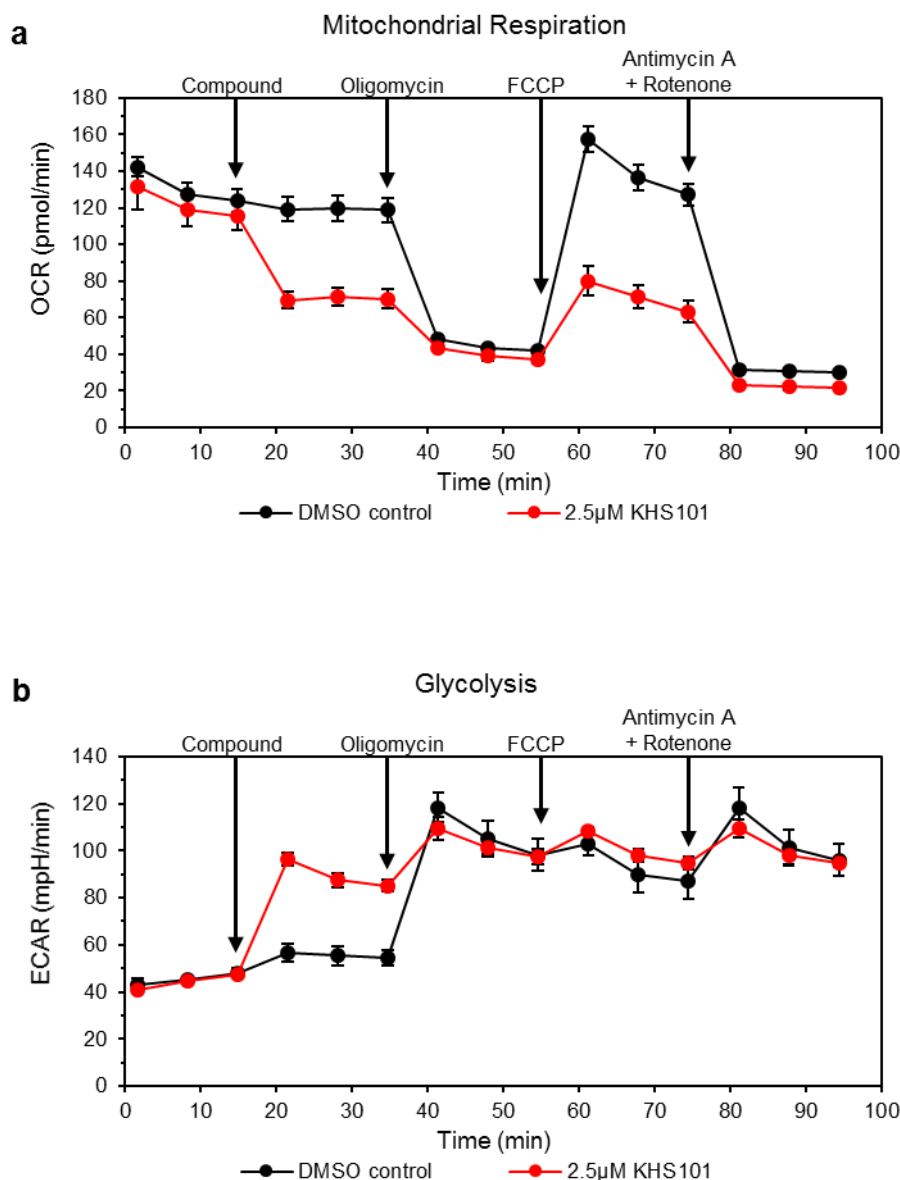


**Figure 6.22: Mitochondrial stress test response of HCT116 p53<sup>+/+</sup> cancer cells following direct injection of 2.5µM KHS101 into growth medium.**

HCT116 p53<sup>+/+</sup> cells were injected with 2.5µM KHS101 or DMSO control. Oxygen consumption rate (OCR) (a) and extracellular acidification rate (ECAR) (b) is shown in response to various injections, ATP synthase inhibitor; oligomycin, uncoupling agent; FCCP, and mix of complex I inhibitor; rotenone and complex III inhibitor; antimycin A. n=3 technical repeats (showing ± SD) from 1 biological repeat.

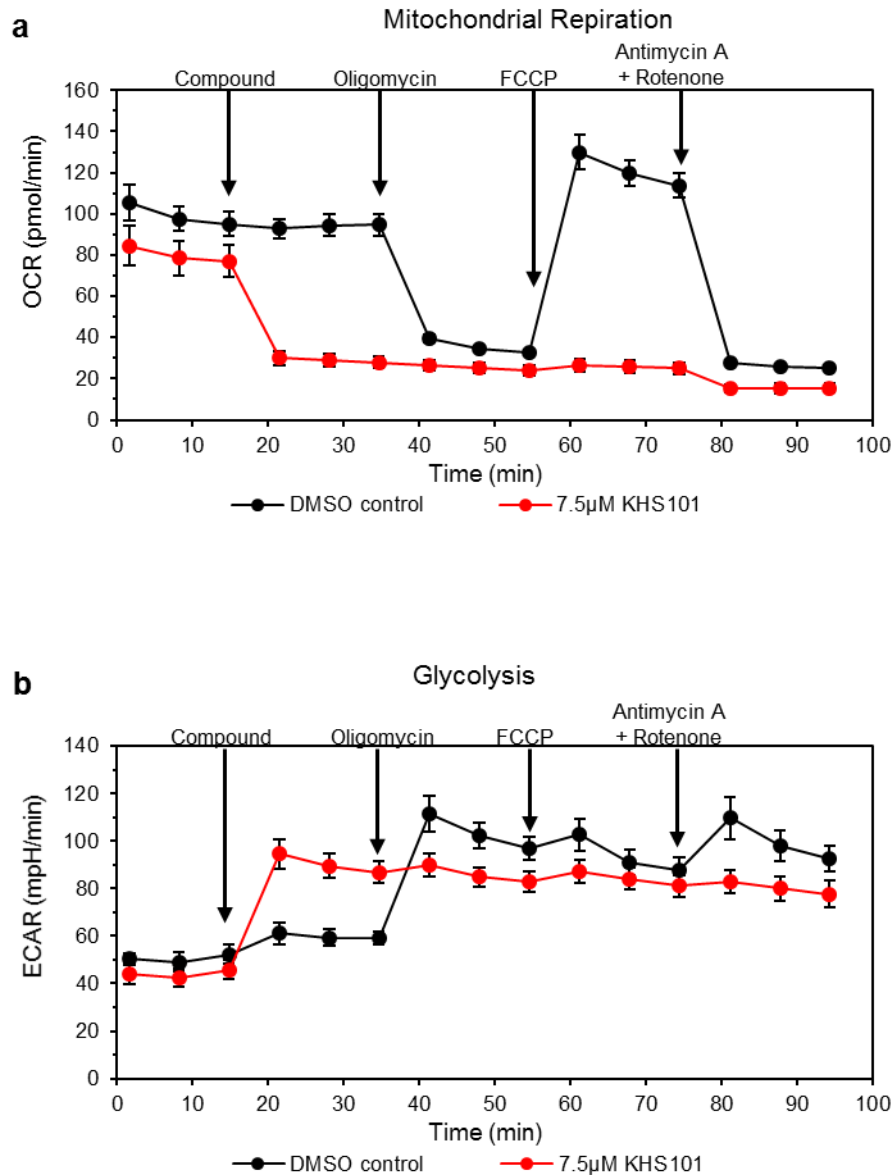


**Figure 6.23: Mitochondrial stress test response of HCT116 p53<sup>+/+</sup> cancer cells following direct injection of 7.5µM KHS101 into growth medium.**

HCT116 p53<sup>+/+</sup> cells were injected with 7.5µM KHS101 or DMSO control. Oxygen consumption rate (OCR) (a) and extracellular acidification rate (ECAR) (b) is shown in response to various injections, ATP synthase inhibitor; oligomycin, uncoupling agent; FCCP, and mix of complex I inhibitor; rotenone and complex III inhibitor; antimycin A. n=3 technical repeats (showing ± SD) from 1 biological repeat.

## 6.2.8 Differential effects linked to aerobic glycolysis of KHS101 treatment of HCT116 and GBM1 cancer cells

The HCT116 p53<sup>+/+</sup> cancer cells, following the injection of KHS101 (2.5 or 7.5µM) into the growth media, showed a ~2-fold increase in ECAR indicative of increased aerobic glycolysis (Fig. 6.22b & Fig. 6.23b). This increased rate appeared to be

largely maintained over the short duration of these assays and after 24 hours KHS101 treatment ECAR was at the level of control cells although glycolytic capacity was decreased (Fig. 6.21). Overall, these observations are consistent with the HCT116 p53<sup>+/+</sup> cancer cells being able to partially compensate for decreased oxidative phosphorylation by increasing glycolysis, but that this cannot be sustained longer-term at high levels.

In further support of a KHS101-induced glycolytic compensatory response in the HCT116 p53<sup>+/+</sup> cancer cells, 48 hours post KHS101 treatment, interesting differences in media colour between KHS101 treated and DMSO control cells was observed. The media of KHS101 treated HCT116 p53<sup>+/+</sup> cells had become notably more yellow compared to DMSO control cells and compared to KHS101 treated ARPE-19 and GBM1 cells (Fig. 6.24). The change in media colour suggesting a lowering of media pH is consistent with increased aerobic glycolysis and lactate release.

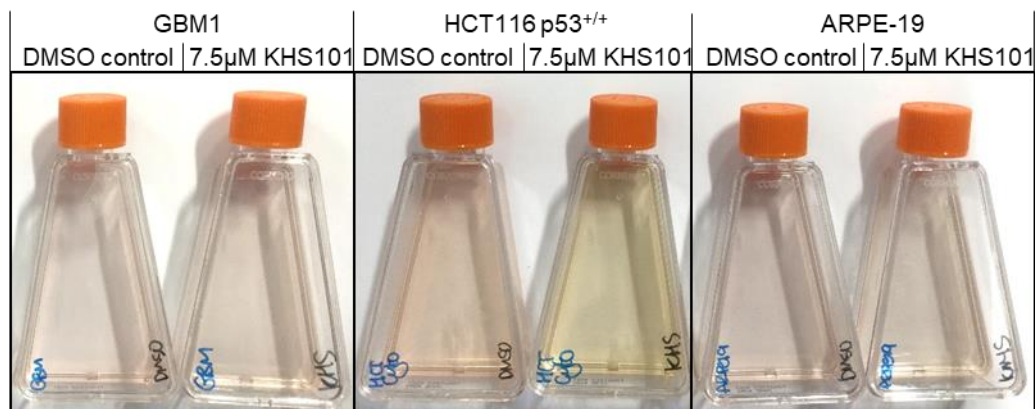


**Figure 6.24: Images of media colour change of T25 flasks of cells treated with KHS101.** Representative differential colour in media of T25 flasks of GBM1 cancer stem like cells, HCT116 p53<sup>+/+</sup> cancer cells and ARPE-19 non-cancer cells treated with 7.5µM KHS101 for 48 hours (n=2 biological repeats).

## 6.2.9 KHS101 treatment differentially affects ATP levels in cancer and non-cancer cells

Given the dramatic reduction in oxidative phosphorylation and impaired glycolytic capacity in HCT116 p53<sup>+/+</sup> cancer cells following 24 hours KHS101 treatment

(Fig. 6.21), it was hypothesised that they may be unable to sustain cellular ATP levels.

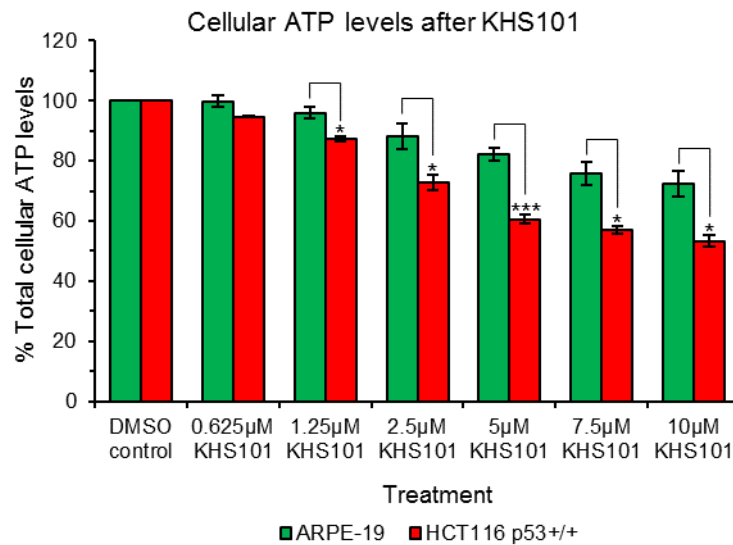


**Figure 6.25: Effects of KHS101 on total cellular ATP levels.**

Average percentage of total cellular ATP levels  $\pm$  SEM,  $n=4$  biological repeats (8 technical replicates per repeat), of ARPE-19 non-cancer and HCT116 p53<sup>+/+</sup> cancer cells after treatment with the indicated doses of KHS101 for 20 hours. Two-tailed t-tests were performed where \* $p<0.05$ , \*\*\* $p<0.001$ .

Analysis of total cellular ATP levels showed that at all doses of KHS101 tested (except 0.625µM) there was a significant decrease in total cellular levels of ATP in the HCT116 p53<sup>+/+</sup> cancer cells compared to the ARPE-19 non-cancer cells (Fig. 6.25). This indicates that the HCT116 p53<sup>+/+</sup> cancer cells are less able to sustain cellular bioenergetics and energy production than the ARPE-19 non-cancer cells which is consistent with the increased cytotoxicity of KHS101 towards the cancer cells (Table 6.1, Fig. 6.10 & Fig. 6.11).

## 6.2.10 Expression of potential downstream targets of KHS101 in a cell line screen

As it had previously been noted that KHS101 reduced GPD2 activity and worked through interacting and inhibiting HSPD1 function in GBM1 cells it was important to compare levels of these proteins in other non-cancer and cancer cells. The levels of MDH2 were also analysed as this is part of the malate-aspartate shuttle which like the G3P shuttle can transfer NAD<sup>+</sup>/NADH.

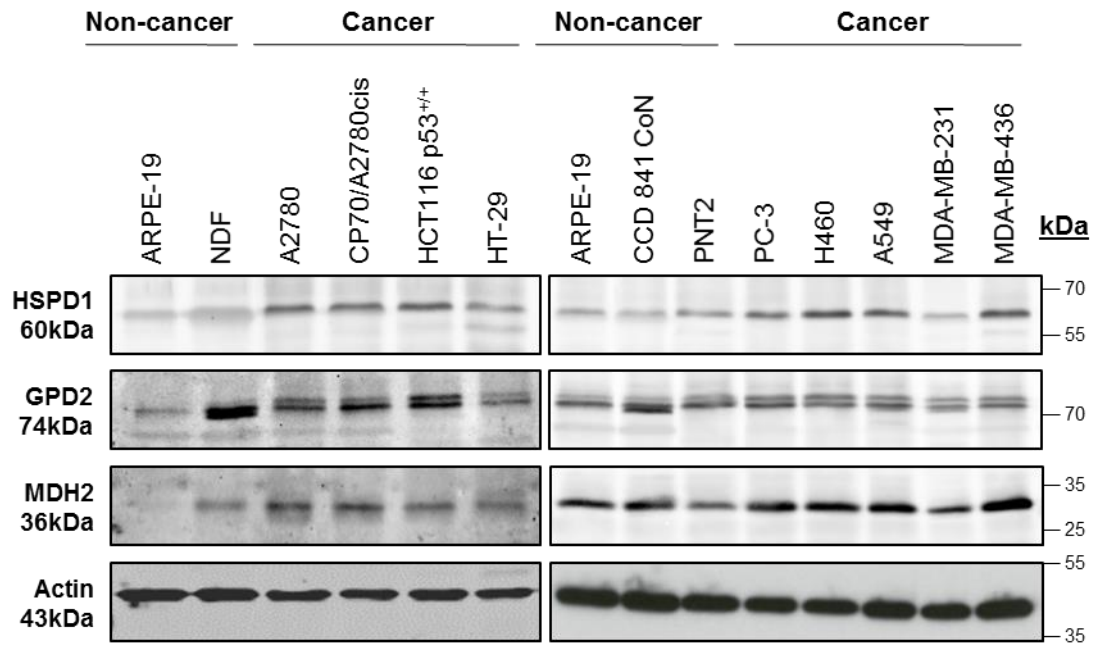


**Figure 6.26: Protein expression of potential downstream targets of KHS101 in untreated non-cancer and cancer cell lines.**

Immunoblots showing protein expression of HSPD1, GPD2, and MDH2 in whole cell lysates of the indicated cell lines, actin was used as an endogenous loading control. n=1 biological repeat.

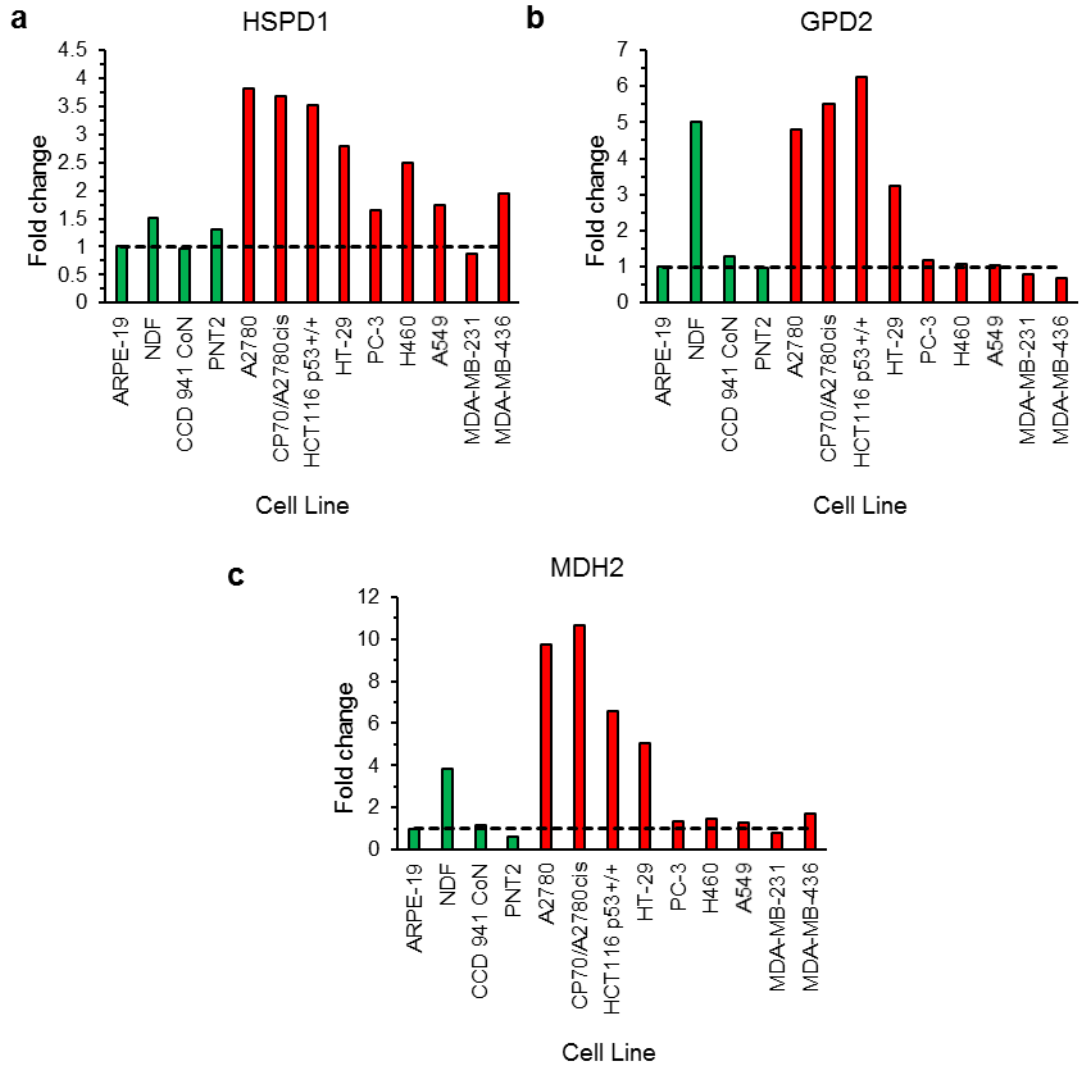


**Figure 6.27: Densitometric quantification of cellular protein expression.**

Fold change in protein expression of HSPD1, GPD2 and MDH1 normalised to loading control actin and expressed relative to actin-normalised expression in ARPE-19 non-cancer cells (set as 1) data from Fig. 6.26, n=1 biological repeat.

Immunoblots and densitometric quantification revealed that HSPD1 expression was higher in all cancer cells compared to non-cancer cells except for MDA-MB-231 (Fig. 6.26 & Fig. 6.27), suggestive of potential increased dependency. GPD2 (multiple bands) and MDH2 were detected in cell lines but varied in expression across cancer and non-cancer cells.

### 6.2.11 Action of KHS101 on GPD2 activity and NAD(H) in HCT116 p53<sup>+/+</sup> cancer cells.

Given the increased expression of GPD2 in the HCT116 p53<sup>+/+</sup> cells compared to ARPE-19 non-cancer cells, a GPD2 assay was performed to see if, as in GBM1 cells, KHS101 inhibited GPD2 activity. As shown in Figure 6.28, a preliminary experiment indicated that GPD2 activity was decreased by 57% in HCT116 p53<sup>+/+</sup> cancer cells after 1 hour exposure to 7.5 $\mu$ M KHS101.

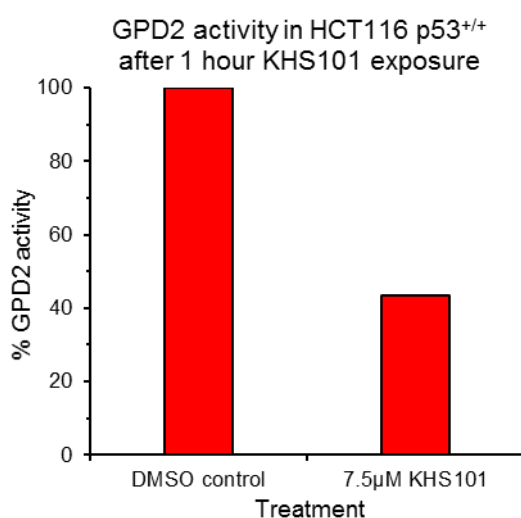


**Figure 6.28: Percentage decrease in GPD2 activity after KHS101 treatment.**

Percentage decrease in GPD2 activity in HCT116 p53<sup>+/+</sup> cancer cells after 1 hour treatment with 7.5 $\mu$ M KHS101. n=1 biological repeat, (1 technical replicate)

Effects on NAD(H) were also analysed as previously performed for NP1 and GBM1 cells (Fig. 6.7). HCT116 p53<sup>+/+</sup> cells were treated with 5 $\mu$ M KHS101 for 24 hours alongside CCD 841 CoN non-cancer cells and an NAD(H) assay was performed. Analysis showed that in the HCT116 p53<sup>+/+</sup> cancer cells NADH/NAD<sup>+</sup> ratio was reduced by 75% indicating perturbation of the NAD<sup>+</sup>/NADH redox balance, whereas in the CCD 841 CoN non-cancer cells it was modestly increased by 35% (Fig. 6.29).

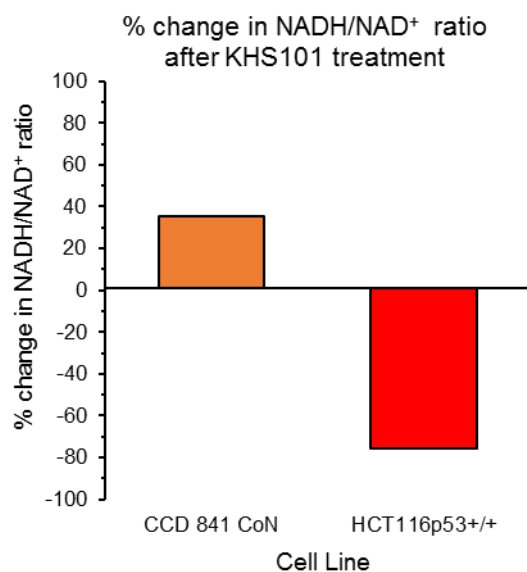


**Figure 6.29: Decrease in NADH levels relative to NAD<sup>+</sup> following 24 hours KHS101 treatment.**

Percentage decrease in NADH/NAD<sup>+</sup> ratio in CCD 841 CoN non-cancer cells and HCT116 p53<sup>+/+</sup> cancer cells after treatment with 5 $\mu$ M KHS101 for 24 hours, n=1 biological repeat (2 technical replicates).

## 6.2.12 Cytoplasmic ‘speckles’/particulates induced by KHS101

In GBM1 cancer cells, KHS101 causes selective protein aggregation linked with the inhibition of HSPD1 chaperone function (Polson *et al.*, 2018). In ARPE-19 non-cancer and HCT116 p53<sup>+/+</sup> cancer cells treated with KHS101 for 24 hours, dark ‘speckles/putative aggregates’ were visible in the cytoplasm of cells at high magnification (Fig. 6.30 & Fig. 6.31). Whilst it is currently unknown what these dark ‘speckles’ are, it was hypothesised that these may relate to KHS101 induced protein aggregation.

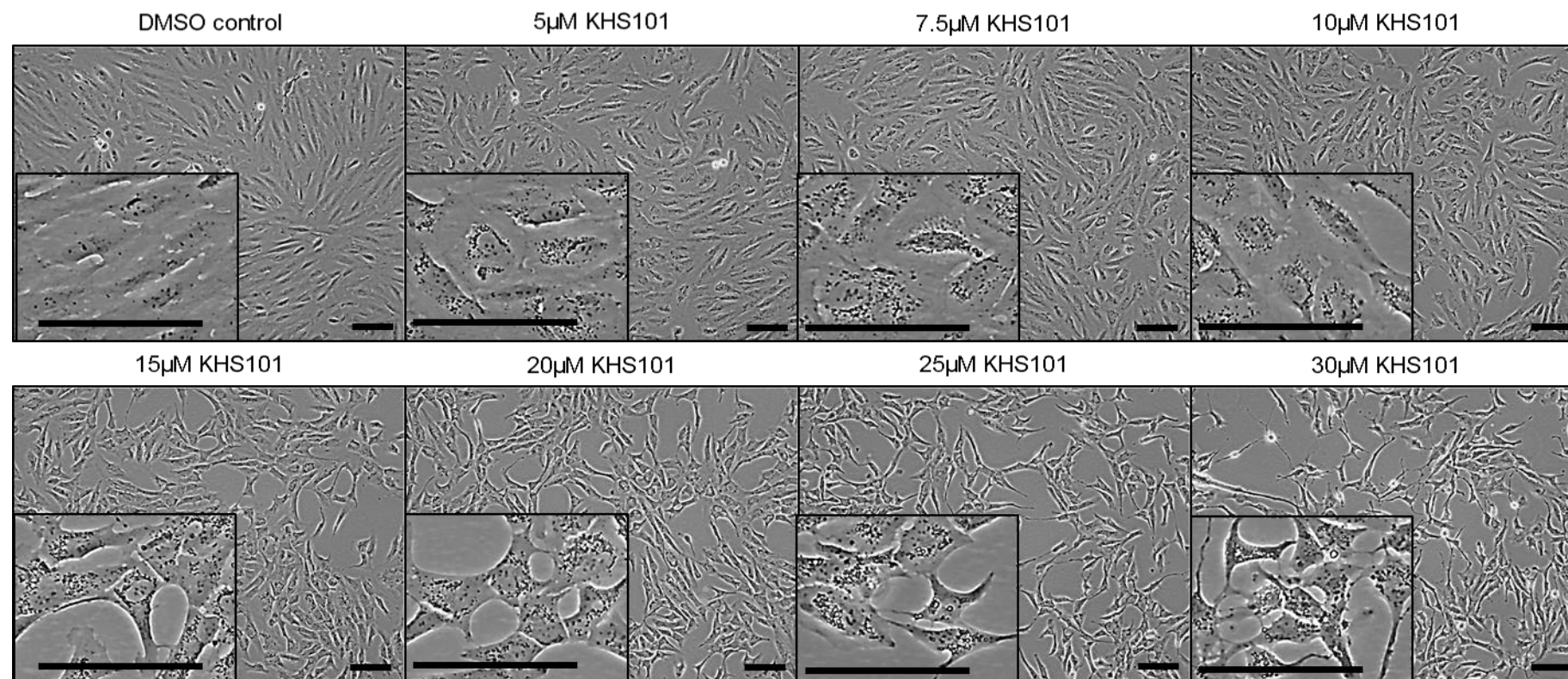


**Figure 6.30: Cell micrographs of ARPE-19 non-cancer cells treated with various KHS101 doses for 24 hours.** Cell images of ARPE-19 non-cancer cells treated with the indicated KHS101 doses for 24 hours. Images taken with x10 and x40 objectives, scale bar indicates 100µm. n=3 biological repeats.

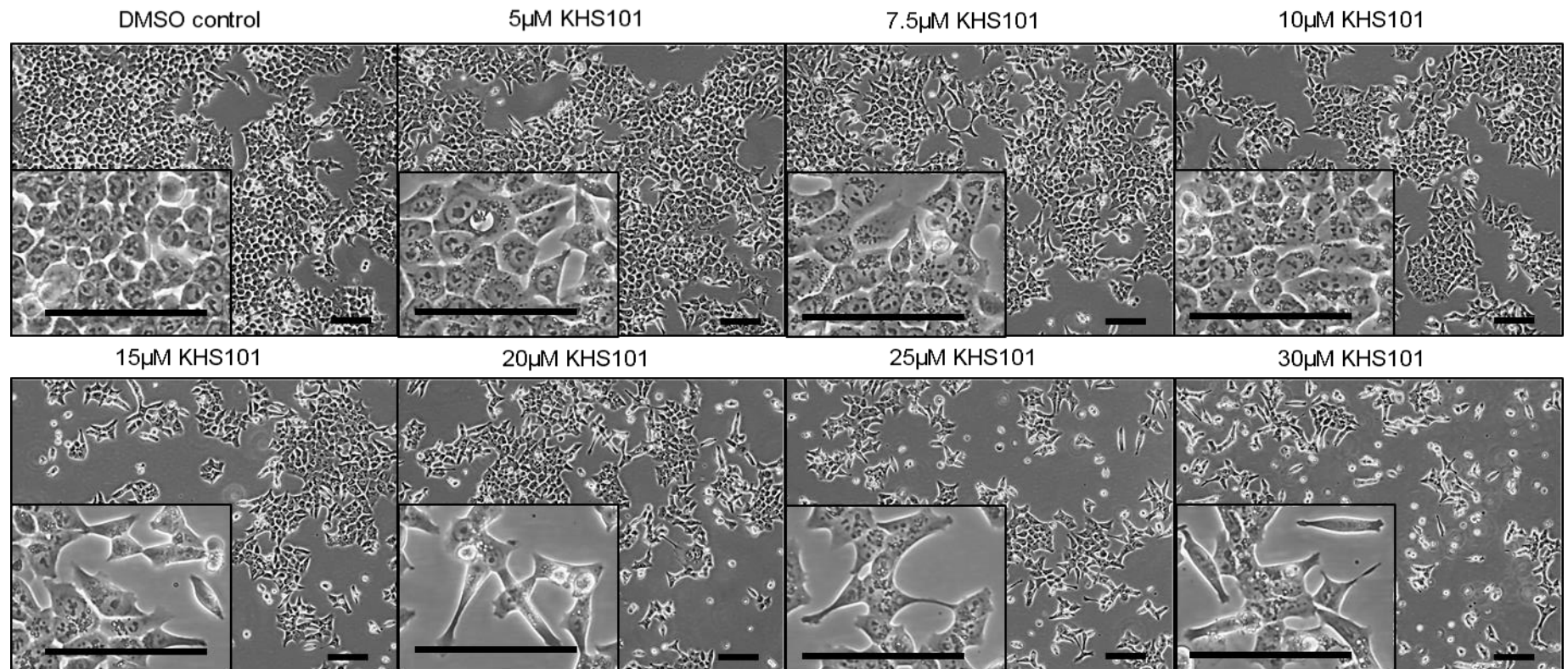


**Figure 6.31: Cell micrographs of HCT116 p53<sup>+/+</sup> cancer cells treated with various KHS101 doses for 24 hours.** Cell images of HCT116 p53<sup>+/+</sup> cancer cells treated with the indicated KHS101 doses for 24 hours. Images taken with x10 and x40 objectives, scale bar indicates 100µm. n=3 biological repeats.

To investigate further whether protein aggregation might occur after KHS101 treatment in other cells as per GBM1 cells, expression of C/EBP homologous protein (CHOP), a marker of the unfolded protein response (Nishitoh, 2012) was analysed by western blot alongside other proteins of interest. CHOP levels varied in both ARPE-19 non-cancer cells and HCT116 p53<sup>+/+</sup> cancer cells depending on KHS101 dose, but there was induction in both cell lines at higher doses (Fig. 6.32 & Fig. 6.33).

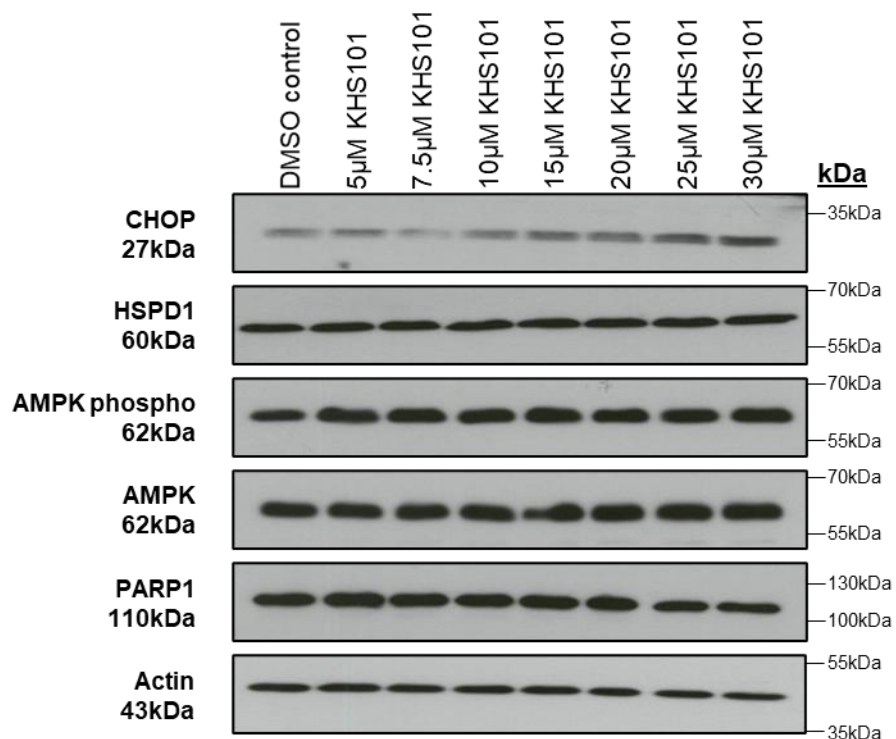


**Figure 6.32: Protein expression of CHOP and other proteins of interest in ARPE-19 non-cancer cells after treatment with various KHS101 doses.** Immunoblots showing protein expression of CHOP, HSPD1, phosphorylated AMPK, total AMPK and PARP1 in ARPE-19 non-cancer cells treated with indicated KHS101 doses for 24 hours. Actin was used as an endogenous loading control. n=1 biological repeat.

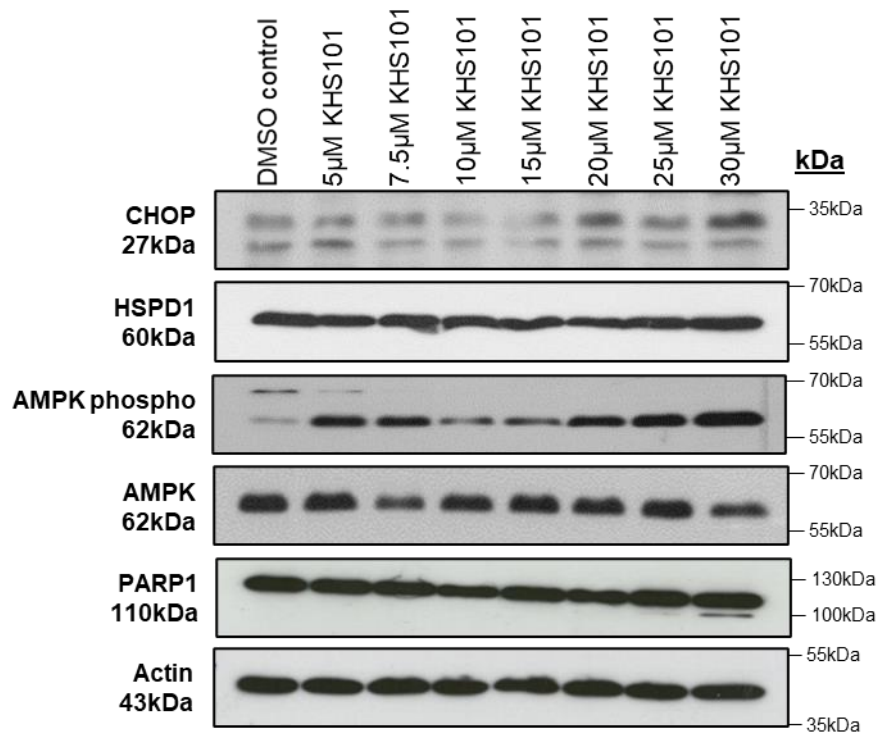


**Figure 6.33: Protein expression of CHOP and other proteins of interest in HCT116 p53<sup>+/+</sup> cancer cells after treatment with various KHS101 doses.**

Immunoblots showing protein expression of CHOP, HSPD1, phosphorylated AMPK, total AMPK and PARP1 in HCT116 p53<sup>+/+</sup> cancer cells treated with indicated KHS101 doses for 24 hours. Actin was used as an endogenous loading control. n=1 biological repeat.

Expression of the proposed target, HSPD1 appeared unaffected in both cell lines along with total PARP1 levels. PARP1 cleavage to an 89kDa fragment by caspases (Gobeil *et al.*, 2001) is commonly used to assess apoptosis and it can clearly be seen that at 30µM of KHS101 in HCT116 p53<sup>+/+</sup> cancer cells that there is a 90-100kDa band (Fig. 6.33), suggesting cells are undergoing apoptosis but not in the ARPE-19 cells (Fig. 6.32). Phosphorylated AMPK levels were increased in HCT116 p53<sup>+/+</sup> cells at all KHS101 doses compared to ARPE-19 non-cancer cells (Fig. 6.32), this is consistent with selective ATP deficiency in the HCT116 p53<sup>+/+</sup> cancer cells (Fig. 6.25).

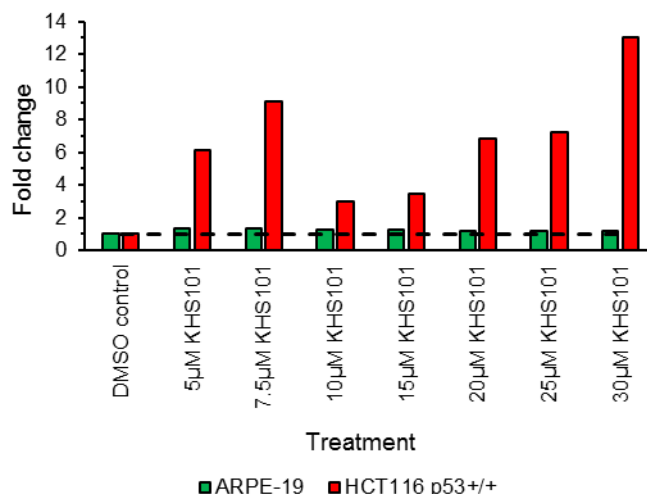


**Figure 6.34: Densitometric quantification of phosphorylated AMPK.**

Comparison of phosphorylated AMPK protein levels in ARPE-19 non-cancer cells and HCT116 p53<sup>+/+</sup> cancer cells treated with the indicated doses of KHS101 for 24 hours. Levels normalised to total AMPK and then to actin loading control. Levels expressed compared to DMSO control.

### 6.2.13 KHS101 induces neuronal differentiation of ARPE-19 non-cancer cells

KHS101 has previously been reported to have neurogenic properties and can induce neuronal differentiation of rat neural progenitor cells (Wurdak *et al.*, 2010a). It was hypothesised that KHS101 may have similar effects in human ARPE-19 non-cancer cells which could partly account for reduced cytotoxicity compared to cancer cells. As seen in Figure 6.30 increasing doses of KHS101 induces a neuronal-like change in morphology in the ARPE-19 cells after 24 hours treatment. To confirm that the phenotype was of neuronal type, mRNA levels of MAP1a were examined with expression levels found to increase as the dose of KHS101 increased (Fig. 6.35a). The mRNA expression of Nestin, KLF4 and OCT4 were also examined which were all decreased after KHS101 treatment consistent with a more differentiated phenotype (Fig. 6.35b).

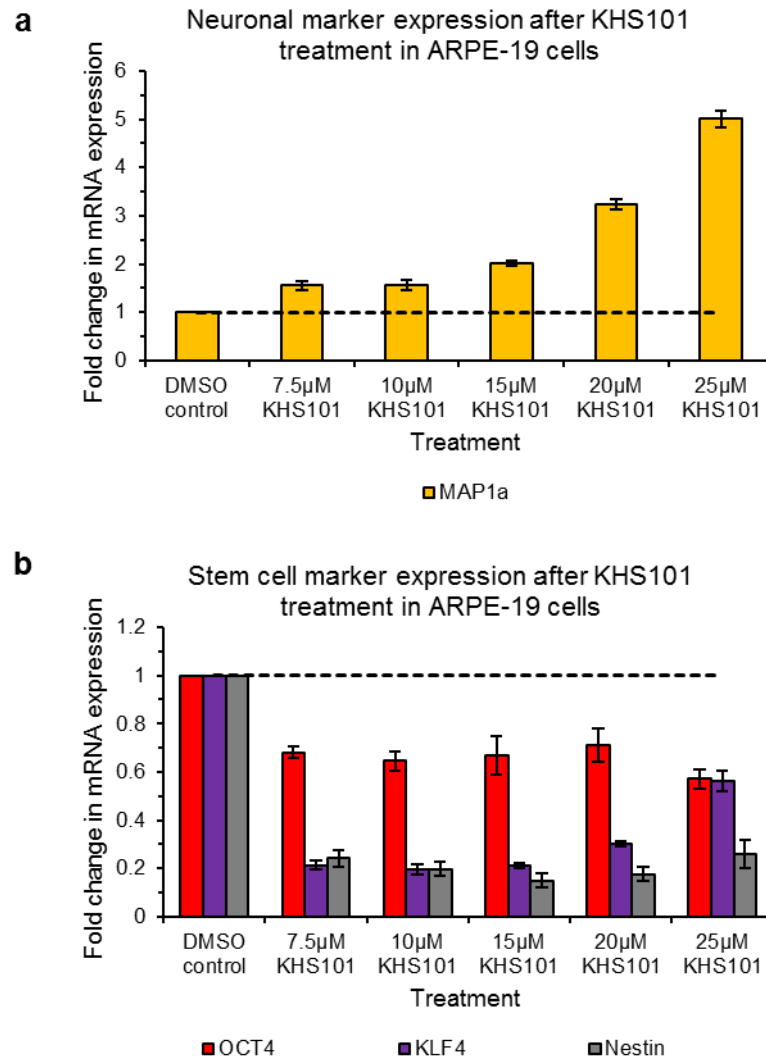


**Figure 6.35: qPCR analysis of neuronal and stem cell markers in ARPE-19 non-cancer cells after KHS1001 treatment.**

Fold change in neuronal marker MAP1a (a) stem cell markers (OCT4, KLF4, Nestin) (b) in ARPE-19 non-cancer cells after treatment with various KHS101 doses or DMSO vehicle control for 24 hours. n=4 technical repeats  $\pm$  SD from 1 biological repeat.

Protein expression of another neuronal marker MAP2 was also investigated. Preliminary analysis by immunofluorescence indicated an increase in expression with KHS101 treatment (Fig. 6.36).

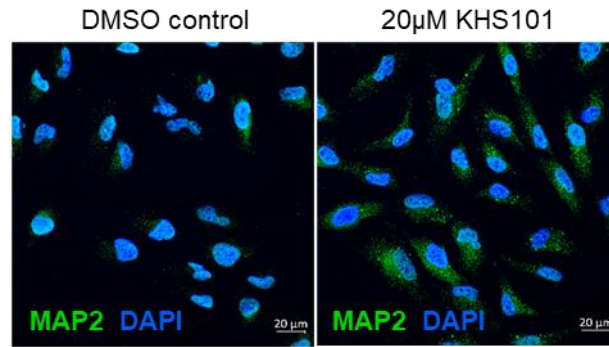


**Figure 6.36: Expression of neuronal marker MAP2 in ARPE-19 non-cancer cells treated with KHS101.**

Representative immunofluorescent cell images of ARPE-19 non-cancer cells showing MAP2 protein expression (green) and nuclear marker DAPI (blue) after treatment with 20µM KHS101 for 24 hours. Images taken with x40 objective and scale bar indicates 20µm. n=1 biological repeat.

## 6.3 Discussion and conclusions

### 6.3.1 Induction of apoptotic cell death by KHS101 and HSPD1 inhibitor myrtoCommulone in GBM cell models

Glioblastomas (GBM) are one of the deadliest types of brain cancer. They are highly aggressive and infiltrative with a particularly poor response to treatments and a poor survival rate (<5% survival 5 years after diagnosis) (Carlsson *et al.*, 2014). Development of new and more effective therapeutic approaches is an urgent priority. GBM tumours also show considerable inter- and intra-tumoral heterogeneity which contributes to the therapeutic challenges. This has led to the classification of different GBM molecular subtypes based on (epi)genetic features and gene expression signatures (Verhaak *et al.*, 2010).

It is also apparent that glioblastomas contain a subpopulation of CSCs or cancer stem cell-like cells that share similarities with neural stem cells, which are highly tumorigenic and are a likely cause of intratumoral heterogeneity (Lee *et al.*, 2018; Dirks, 2010). Previous work by Heiko Wurdak and colleagues identified the small molecule KHS101 as being able to induce neuronal differentiation of rat neural progenitor cells (Wurdak *et al.*, 2010a). This led to their asking whether KHS101 might have similar effects on GBM cancer stem-like cells and be able to induce their neuronal differentiation and half GBM growth (Wurdak *et al.*, 2010a). Unexpectedly, KHS101 appeared cytotoxic rather than cytostatic towards multiple GBM cancer stem cell-like models and, instead, across the diverse models representing different subtypes, a pronounced vacuolisation phenotype was observed (Polson *et al.*, 2018).

The vacuoles induced which were found to be autophagic, were not induced in non-cancerous human neural progenitor cells and KHS101 showed selective activity in chemosensitivity assays towards GBM cells (Polson *et al.*, 2018). The GBM vacuolisation phenotype was readily reproducible in our hands (Fig. 4.3). A key question, however, was why KHS101 induced autophagy and whether this was the cause of GBM cell death (autophagic cell death) or whether it might be a pro-survival response. Autophagy (literally meaning 'self eating') is a catabolic

process and can be induced by metabolic stress such as starvation enabling energy generation through breakdown of macromolecules (Glick *et al.*, 2010). Cellular bioenergetics analyses revealed that 24 hours KHS101 treatment severely reduced oxygen consumption (mitochondrial respiration) of GBM1 cells (Fig. 6.4). In non-cancer NP1 cells, oxygen consumption was also reduced by KHS101, however, glycolytic rate was increased. In contrast, GBM1 cells showed no increase in glycolysis and reduced glycolytic capacity (Fig. 6.4b). The lack of compensatory glycolytic response in the GBM1 cells and activation of 'low ATP sensing' AMPK (Fig. 6.8) and reduced cellular ATP levels (Fig. 6.25, n=4 biological repeats) lent support to the hypothesis that autophagy may be part of a pro-survival response to rescue the bioenergetics of the cell. Further analyses showed that by 48 hours, KHS101 induced significant apoptotic cell death with inhibition of autophagy using bafilomycin unable to rescue apoptosis (Fig. 6.5). Further experiments would be beneficial, for example with different timings or use of other, early stage autophagy inhibitors, however, overall the results suggest a pro-survival rather than a pro-death role of autophagy.

Target pull-down by the Wurdak group and further functional studies suggested that KHS101-mediated disruption of mitochondrial chaperone HSPD1 function was responsible for the autophagic phenotype (Polson *et al.*, 2018). Importantly, myrtucommulone, a selective HSPD1 inhibitor recently reported in the literature, was able to provide independent chemical validation, with induction of autophagy (Polson *et al.*, 2018) and apoptosis in all 6 GBM cell models (representing different GBM subtypes) but not in NP1 cells (Fig. 6.9).

### **6.3.2 Decrease in GPD2 activity with acute KHS101 exposure and perturbation of cellular NADH/NAD<sup>+</sup> balance**

Whilst HSPD1 functional inhibition provided a logical mechanistic explanation for inhibited mitochondrial respiration, it was initially less clear why glycolysis may also be impaired. However, with 30 minutes KHS101 exposure, substantially elevated G3P levels and decreased DHAP levels were observed suggesting disruption of the G3P shuttle which connects glycolysis and mitochondrial

respiration. One function in different tissue contexts of the G3P shuttle is re-oxidation of cytosolic NADH (Fig. 6.2) which generates NAD<sup>+</sup> that is required to fuel glycolysis (Mráček *et al.*, 2013). Here, 1 hour KHS101 treatment of NP1 and GBM1 cells reduced activity of the G3P shuttle enzyme GPD2 in the GBM1 cancer cells by 63% whereas no inhibition was seen in the NP1 non-cancer cells (Fig. 6.6, n=3 biological repeats GBM1; n=1 biological repeats NP1). Due to the reduction in GPD2 activity it was hypothesised that cellular NADH/NAD<sup>+</sup> balance may be disturbed. Interestingly, examination of total cellular NADH and NAD<sup>+</sup> levels revealed that NADH levels were decreased by 68% compared to NAD<sup>+</sup> in the GBM1 cells and to a lesser extent of 37% in the NP1 non-cancer cells (Fig. 6.7). This was the opposite of what was predicted based on GPD2 inhibition, however, it is also worth noting that it was total cellular levels of NADH and NAD<sup>+</sup> that were examined. In future experiments, cytosolic NADH/NAD<sup>+</sup> and mitochondrial NADH/NAD<sup>+</sup> ratios should be compared either following subcellular fractionation or through use of genetically encoded fluorescent NADH/NAD<sup>+</sup> sensors (Zhao and Yang, 2016). Nevertheless, the data indicates perturbation of NADH/NAD<sup>+</sup> and the increase in NAD<sup>+</sup> is consistent with it not being consumed by glycolysis. In addition to KHS101 inducing mis-aggregation of mitochondrial enzymes through its effects on the mitochondrial HSPD1 chaperone, proteomics analysis identified several glycolytic enzymes in KHS101-induced aggregates which might account for the impairment of glycolysis (Polson *et al.*, 2018) There is growing evidence of substrate channelling in metabolic regulation. Formation of transient multi-enzyme assemblies to facilitate substrate channelling might explain how a mitochondrial chaperone could result in glycolytic enzyme aggregation (Sweetlove and Fernie, 2018).

### **6.3.3 Cancer selective activity of KHS101 towards other cancer cell types**

Against the 6 GBM cancer cell models, 96 hours exposure to KHS101 resulted in IC<sub>50</sub> values ranging from 0.97-5.05µM compared to >20µM in the non-cancer NP1 cell line (Polson *et al.*, 2018). Consistent with lack of evident normal tissue toxicity *in vivo* (Polson *et al.*, 2018), here KHS101 also showed relative inactivity towards three other non-cancer cell models (Table 6.1, n=3 biological repeats). ARPE-19

retinal epithelial and CCD 841 CoN colon epithelial non-cancer cells showed similar  $IC_{50}$  values  $\sim 15\text{-}16\mu\text{M}$  although PNT2 prostate cells appeared more sensitive ( $7.6\mu\text{M}$ ). All 10 cancer cell lines tested were more sensitive to KHS101 than ARPE-19 or CCD 841 CoN cells ( $IC_{50}$ s ranging from  $0.62\text{-}8.6\mu\text{M}$ ) (Fig. 6.10 & Fig. 6.11) indicating potential for therapeutic use of KHS101 towards other cancer types. Interestingly KHS101 appeared more cytotoxic to HCT116  $p53^{-/-}$  cancer cells compared to the isogenic HCT116  $p53^{+/+}$  cells, this was similarly observed with FK866 (Fig. 3.7) and requires further investigation as to why, with use of  $p53$  knockdown or re-expression studies. There was a 2.5-fold difference in  $IC_{50}$  between the cisplatin resistant CP70/A2780cis cancer cells and the cisplatin sensitive A2780 cancer cells (Fig. 6.10b) compared to a 10-fold difference seen with cisplatin, indicating potential of KHS101 for treating tumours resistant to cisplatin.

### **6.3.4 Induction of autophagy by KHS101 in HCT116 cancer cells and ARPE-19 non-cancer cells**

In support of a similar mechanism of action of KHS101 in other cancer cell types, HCT116  $p53^{+/+}$  cancer cells that had been treated with KHS101 for 24 hours contained small vacuoles visible by phase contrast microscopy (Fig. 6.15). To verify that these vacuoles were autophagic, several different techniques were used including analysis of CYTO-ID positive staining (Chan *et al.*, 2012) by both image cytometer and fluorescence microscopy and quantification of LC3-II levels.

Consistent with the induction of autophagy by KHS101, levels of staining with autophagic dye CYTO-ID (Chan *et al.*, 2012) were notably increased in response to 24 hours KHS101 treatment although unexpectedly this was the case in both HCT116  $p53^{+/+}$  cancer cells and ARPE-19 non-cancer cells (Fig. 6.16a). Quantification of 'CYTO-ID positive' cells after quadrant gating indicated similar levels in HCT116  $p53^{+/+}$  cancer cells and ARPE-19 non-cancer cells following KHS101 treatment (Fig. 6.16b,  $n=3$  biological repeats). Analyses by confocal microscopy showed dose-dependent increases in CYTO-ID fluorescent staining in HCT116  $p53^{+/+}$  and  $p53^{-/-}$  cells and ARPE-19 non-cancer cells in response to KHS101 treatment although these were not formally quantified. Staining was

cytoplasmic, punctuate and co-localised with vacuoles indicating staining specificity (Fig. 6.17-Fig. 6.19). The increase in CYTO-ID fluorescence in the HCT116 p53<sup>-/-</sup> cells suggests that KHS101-induced autophagy is not p53-dependent which is important as p53 is widely reported to activate autophagy (White, 2016). This also suggests that the increased sensitivity of the HCT116 p53<sup>-/-</sup> cells to KHS101 compared to their isogenic p53<sup>+/+</sup> cells (Table 1.1) is not due to lack of pro-survival autophagy induction although it is possible there are differences in absolute levels.

Quantification of LC3-II levels by immunoblotting showed increased levels in the HCT116 p53<sup>+/+</sup> cancer cells compared to the ARPE-19 non-cancer cells after 24 hours 5µM KHS101 treatment (Fig. 6.20, n=1 biological repeat). These findings differed to the similar levels of staining seen by CYTO-ID analysis instead suggesting increased levels of autophagy in the HCT116 p53<sup>+/+</sup> cancer cells than in the ARPE-19 non-cancer cells. Indeed, increased KHS101-induced LC3-II levels in the HCT116 p53<sup>+/+</sup> cancer cells compared with the ARPE-19 cells were similar to, or more pronounced than, the LC3-II difference between GBM1 and NP1 cells which were assayed in parallel (Fig. 6.20).

It should be noted that differences in intensity among cells classed as CYTO-ID 'positive' were not analysed. For future quantitative autophagy studies, it would also be beneficial to perform kinetic measurements to determine autophagic flux. As the gold standard for autophagy detection, it would also be useful to carry out transmission electron microscopy to see whether intracellular double-membraned autophagosomes containing electron dense material are visible. These differences obtained with CYTO-ID staining compared with LC3-II indicate the need for further experiments and quantitative analyses to determine whether there is preferential autophagy induction in the cancer cells or not. To determine whether autophagy in these cells is actually pro-survival, future work including use of an autophagy inhibitor for example bafilomycin or 3-MA should also be performed as done in the GBM1 cells (Fig. 6.5).

### **6.3.5 Glycolytic compensation and differential effects on cellular ATP levels of KHS101 treatment in HCT116 p53<sup>+/+</sup> and ARPE-19 cells**

24 hours KHS101 treatment induced similar effects on core cellular metabolism in the HCT116 p53<sup>+/+</sup> cancer cells and ARPE-19 non-cancer cells (Fig. 6.21) as was seen in the GBM1 cancer cells and NP1 non-cancer cells (Fig. 6.4). In the HCT116 p53<sup>+/+</sup> cancer cells the basal rate of mitochondrial respiration was severely diminished (11-fold) with no compensatory increase in glycolysis. In the much less metabolically active ARPE-19 cells, basal respiration was also decreased (7-fold) but a very modest increase in basal glycolysis was also evident. Interestingly, however, immediately following KHS101 cellular exposure, HCT116 p53<sup>+/+</sup> cancer cells increased glycolysis (>2-fold) indicating a glycolytic compensatory response (Fig. 6.22 & Fig. 6.23). In further support of this, where HCT116 p53<sup>+/+</sup> cancer cells had been treated with KHS101 for 48 hours the colour of the culture media was visibly more yellow in colour than control cells (Fig. 6.24) despite reduced cell number (Fig. 6.14). This colour change suggests acidification of the media which could be caused by increased lactate release into the media due to increased glycolysis to compensate for decreased mitochondrial respiration. Further studies are required to analyse lactate levels in the media after KHS101 treatment; interestingly, KHS101-treated GBM1 cells did not show a similar change in media colour (Fig. 6.24). These results also suggest that combining KHS101 with LDH-A inhibition could be more cytotoxic towards the HCT116 cancer cells and this would be worthy of investigation although there is a risk of increased cytotoxicity to non-cancerous cells also.

A significant decrease in cellular ATP levels was observed in the HCT116 p53<sup>+/+</sup> cancer cells compared to ARPE-19 non-cancer cells with 20 hours KHS101 treatment over a range of different KHS101 concentrations (Fig. 6.25, n=4 biological repeats). Levels of phosphorylated AMPK were also elevated with KHS101 treatment to a greater extent in the HCT116 p53<sup>+/+</sup> cancer cells compared to ARPE-19 non-cancer cells (Fig. 6.32-Fig. 6.34). These results suggest that the HCT116 p53<sup>+/+</sup> cancer cells were less able to metabolically

compensate for attenuated mitochondrial respiration than ARPE-19 non-cancer cells; this may also relate to their very different basal metabolic activity.

### **6.3.6 Decreased GPD2 activity in HCT116 cells and differential HSPD1 expression**

It was hypothesised that if KHS101 was working through a similar mechanism of action then GPD2 activity may be decreased in other cancer cells upon treatment. 1 hour cellular KHS101 exposure induced a decrease in GPD2 activity in the HCT116 p53<sup>+/+</sup> cancer cells (Fig. 6.28, n=1 biological repeat) which was similar to what was observed in the GBM1 cells (Fig. 6.6). Further analyses in additional cancer cells are required as well as in other non-cancer cells to see if any reduction in activity is cancer selective. Analysis of GPD2 protein levels indicated its expression in all cell lines tested however levels appeared variable with multiple bands detected on SDS-PAGE of similar molecular weight of different intensity in different cell line lysates (Fig. 6.26). Further work is needed to investigate whether all these bands are specific and whether they correspond to different GPD2 isoforms or different post-translationally modified GPD2. Interestingly, NADH:NAD<sup>+</sup> levels were decreased with 24 hours KHS101 treatment in the HCT116 p53<sup>+/+</sup> cancer cells (Fig. 6.29) similar to what was observed in the GBM1 cells (Fig. 6.7), consistent with perturbed metabolism and inability to sustain ATP levels (Fig. 6.25).

Analysis of HSPD1 indicated modestly increased protein expression (by ~2-fold) in most of the cancer cell lines in the cell line panel compared to expression in the non-cancer cell models, except for MDA-MB-231 (Fig. 6.26, n=1 biological repeat). While this may be suggestive of increased HSPD1 dependency of the cancer cells, future studies are required where HSPD1 is directly targeted, for example using myrtucommulone or through HSPD1 silencing by RNAi, to see if this recapitulates effects and cancer cell selectivity of KHS101.

Overall, the results are supportive of the hypothesis that KHS101 has selective cytotoxic activity towards cancer cells via metabolic effects (evidence presented of induction of autophagy, inhibition of mitochondrial respiration and depleted

ATP). However, further repeats are required to confirm involvement of the GPD2 shuttle and perturbed total cellular balance of NADH/NAD<sup>+</sup>.

### **6.3.7 Cytoplasmic protein aggregates induced by KHS101**

In both HCT116 p53<sup>+/+</sup> cancer cells and ARPE-19 non-cancer cells a striking consequence of KHS101 treatment was the appearance of numerous cytoplasmic 'speckles/aggregates' visible by phase contrast microscopy at high magnification (Fig. 6.15, Fig. 6.30 & Fig. 6.31, n=3 biological repeats). It was hypothesised that these 'speckles' may be protein aggregates resulting from inhibition of HSPD1 chaperone function by KHS101. Western blot analysis of the unfolded protein response marker (UPR), CHOP (Nishitoh, 2012) showed a small increase in levels at higher KHS101 doses in both the HCT116 p53<sup>+/+</sup> cancer cells and ARPE-19 non-cancer cells (Fig. 6.32 & 6.33). More detailed investigation of effects of KHS101 on both the mitochondrial UPR and endoplasmic reticulum UPR would be informative. To further elucidate whether the 'speckles' are protein aggregates and their subcellular localisation, specific fluorescent stains for different organelles could be used together with thioflavin T which has been used as a fluorescent label for protein aggregates such as amyloid fibrils (Xue *et al.*, 2017). Proteomics-based ID of (mis)aggregated proteins resulting from KHS101 treatment and differences between cancer and non-cancer cells, or in total levels of protein aggregation would further facilitate understanding of KHS101 cancer selectivity. There may also be important differences in aggregation kinetics or rates of clearance (e.g. by autophagy or UPR).

### **6.3.8 Induction of neuronal differentiation by KHS101 in ARPE-19 retinal epithelial non-cancer cells**

In addition to the appearance of cytoplasmic 'aggregates', ARPE-19 non-cancer cells treated with higher doses of KHS101 ( $\geq 20\mu\text{M}$ ) for 24 hours showed a clear change in morphology (Fig. 6.30) that was similar to that observed in response to the SIRT1 inhibitor EX-527 (Fig. 4.19). Cell number was reduced suggestive of possible cell cycle exit and cells were more elongated in morphology. Since

KHS101 has previously been shown to induce neuronal differentiation of rat hippocampal neural progenitor cells (Wurdak *et al.*, 2010a) it was hypothesised that KHS101 may be inducing neuronal transdifferentiation of human ARPE-19 cells. In support of this, mRNA of neuronal marker MAP1a was increased > 5-fold by 25µM KHS101 (Fig. 6.35) and MAP2 protein expression was increased (Fig. 6.36). As Wurdak *et al.* (2010a) show that KHS101-induced neuronal differentiation in the rat is due to its binding to TACC3, it will be interesting to determine whether knock-down of TACC3 in ARPE-19 cells induces a similar neuronal phenotype and increase in MAP1a and MAP2.

### 6.3.9 Conclusions

Here it shown that KHS101 induces apoptotic cell death of GBM1 cells (Fig. 6.5, n=3 biological repeats) with HSPD1 inhibitor myrtocommulone able to recapitulate this in all 6 GBM cancer stem cell-like models (Fig. 6.9, n=3 biological repeats). Evidence is presented suggesting that KHS101-induced autophagy (Fig. 6.16, n=3 biological repeats, Fig. 6.17, 6.18, 6.20, n=1 biological repeat) is a pro-survival metabolic stress response to diminished respiration and energy deficiency (e.g. Fig. 6.25, n=4 biological repeats, Fig. 6.4, 6.8, 6.21 - 6.23, n=1 biological repeat). Specific effects of KHS101 in GBM1 and HCT116 cancer cells include reduced activity of G3P shuttle enzyme GPD2 and perturbed NADH:NAD<sup>+</sup> balance (Fig. 6.6, n=3 biological repeats, Fig. 6.7, 6.28, 6.29, n=1 biological repeat). Importantly, selective cytotoxic activity of KHS101 is also observed towards a range of cancer cell lines of different tissue type (Fig. 6.10, n=3 biological repeats) raising the possibility of therapeutic potential of KHS101 against multiple cancer types and not just glioblastomas. Mechanism of action studies suggest a similar mechanism of action in other cancer cells to that in GBM cells with attenuation of mitochondrial function and autophagy induction (Fig. 6.16, 6.17, 6.21-6.23, n=1 biological repeat) which preliminary data suggests is independent of p53 status (Fig. 6.17, n=1 biological repeat). Cytoplasmic 'speckles' detected (Fig. 6.15, 6.30, 6.31, n=3 biological repeats) are hypothesised to be due to disruption of HSPD1 chaperone function and be protein aggregates. A notable difference in the metabolic response of HCT116 cancer cells to KHS101 treatment compared to GBM cells is short-term elevated

glycolysis (Fig. 6.22 - Fig. 6.24 n=1 or n=2 biological repeats) as a likely compensatory response suggesting that its co-targeting could be therapeutically beneficial. Preliminary data suggests that KHS101, akin to its neurogenic effects towards rat neural progenitor cells, can promote neuronal transdifferentiation of human ARPE-19 non-cancer cells (Fig. 6.30, n=3 biological repeats, Fig. 6.35, 6.36, n=1 biological repeat) which has important implications for potential KHS101 therapeutic application outside of cancer treatment.

For some of the experiments, additional biological replicates are required for confirmation of these conclusions and to enable testing for statistical significance as is evident from individual figure legends. However, as indicated above, it should also be noted for some of these findings, use of independent experimental approaches or 'readouts' (whilst lacking in n=3 biological replicates) lend support and confidence to some of the findings and avoid potential issues of reproducible false negative or false positive results that can sometimes be obtained through reliance on a particular experimental methodology.

## 7. Summary and perspectives

The focus of this research was to investigate potential cancer cell molecular vulnerabilities, or differential dependencies of cancer versus non-cancer cells, linked to NAD<sup>+</sup> biology. The underlying hypothesis was that fundamental differences in NAD<sup>+</sup> biology/function exist between cancer and non-cancer cells and that these could potentially be exploited for improved and/or novel chemotherapeutic approaches. As outlined in the introduction of this thesis, chemotherapy remains an essential part of cancer treatments today but is also a major cause of treatment failure. The development of chemotherapeutic approaches that are sufficiently selective towards cancer cells and sufficiently potent are major ongoing challenges. There is also a continued debate as to the 'best' approach for current anti-cancer drug discovery and development. Whilst classic chemotherapeutic drugs are potent but lack good selectivity to cancer cells, targeted therapies are selective but can lack the potency that classic chemotherapeutics display and for both approaches development of drug resistance is problematic.

Here, several novel therapeutic approaches have been identified or explored linked to NAD<sup>+</sup> biology and experimentally dissected to differing extents in an *in vitro* context, which are outlined and further assessed below.

1. Most classic chemotherapeutic drugs have a small therapeutic index and are not selective to cancer cells alone. Previous research has shown that the use of PARP inhibitors alongside DNA damaging agents can increase their potency. The issue with this is that non-cancer cells also require PARPs for efficient repair of certain types of DNA damage and increased toxicity to non-cancer cells is likely with combining PARP inhibitors with DNA damaging agents. Here data is presented suggesting that PARP activity can be selectively decreased in cancer cells compared to non-cancer cells through modulation of NAD<sup>+</sup> levels through use of the NAMPT inhibitor, FK866. Importantly, the combination of FK866 with selective DNA damaging agents resulted in drug potentiation and enhanced cytotoxicity towards cancer cells whereas there was no potentiation of

effect towards non-cancer cells. Longer term assays (e.g. clonogenic assays) would be useful to determine whether cancer cell selectivity and potency is sustained following drug treatment and washout. *In vivo* studies are also required, however, these findings suggest a possible way of improving the cancer selectivity and therapeutic index of current chemotherapeutic drugs enabling the use of a more effective dose and/or fewer side effects. More extensive preclinical studies are also required to understand why some chemotherapeutic agents that induce DNA damage that is repaired by PARP are potentiated (e.g. TMZ) but others are not or much less so. This may be due to repair by other compensatory DNA repair pathways. It is also possible that potentiation by FK866 of TMZ and other DNA damaging agents is via other or additional mechanisms to decreased PARP activity. An 'omics' based approach may provide unbiased insight here or combination effects could be analysed in a PARP-null background.

2. RNAi-mediated knock-down of NAD<sup>+</sup>-dependent deacetylase SIRT1 has previously been reported to induce apoptosis in multiple cancer cell lines whilst non-cancer cell viability is unaffected. However, the impact of the existence of a number of SIRT1 splice variants on this and targeting SIRT1 via a small molecule has not previously been investigated. Here it is shown that the small molecule inhibitor of SIRT1, EX-527, can recapitulate effects of full-length SIRT1 knock-down although cancer selective activity with 96 hours EX-527 exposure depended on cell line and was less than expected. This may relate to duration of exposure and testing of other dose durations would be worthwhile and whether these effects are on- or off-target.

Importantly, SIRT1 suppression also appeared to affect non-cancer and cancer cell differentiation status. Inhibition of SIRT1 in two different non-cancer cell models induced a neuronal-like phenotype and gene expression changes consistent with neuronal transdifferentiation. Further studies are required to determine whether functional neurons can be formed and the reversibility of any cell fate change as well as the mechanistic bases for these effects. mRNA changes suggestive of

reduced stemness/potency and progression towards a neuronal fate were also observed in GBM cancer stem cell-like cells. Further verification of this is required including a direct stem cell assay and inhibition of SIRT1 for longer duration to see whether more pronounced mRNA changes as well as changes in protein expression indicative of neuronal differentiation are observed. Nevertheless, these preliminary results suggest SIRT1 inhibition may have therapeutic potential of for targeting the cancer stem cell fraction of tumours.

3. Many TSGs are epigenetically silenced in cancer cells and one potential approach to treating cancer is to induce their re-expression. However, current epigenetic agents lack selectivity towards cancer cells which raises issues of likely toxicity or adverse gene expression changes in non-cancer cells as targeting may alter their epigenetic status also. Here suppression of glycolytic enzyme LDH-A is shown to induce global alterations in histone H3 modifications that are associated with a more transcriptionally active state. It was also able to cause a modest increase in mRNA expression of epigenetically silenced TSG E-cadherin although effects at the E-cadherin promoter were not analysed. This research identifies LDH-A as a potential novel target for selective modification of the cancer cell epigenome. Future work will investigate whether its targeting is sufficient to promote re-expression of epigenetically silenced tumour suppressors without adverse epigenetic effects on non-cancer cells or whether through a combinatorial approach it can improve selectivity of other epigenetic modifiers.
4. Small molecule KHS101 is selectively cytotoxic towards multiple patient-derived glioblastoma (GBM) cell models *in vitro* with the viability of non-cancerous neural progenitor cell lines unaffected (Polson *et al.*, 2018). KHS101 also reduced tumour growth in mouse xenograft models (Polson *et al.*, 2018). Here, it was shown that KHS101 induces apoptotic cancer cell death with induction of autophagy a likely pro-survival metabolic response to diminished respiration. Mechanism of action studies here indicated cancer cell selective inhibition of G3P shuttle enzyme GPD2 consistent with mitochondrial chaperone HSPD1 as the identified target of

KHS101. KHS101 also perturbed NAD<sup>+</sup>/NADH balance and cancer cells were unable to sustain cellular ATP levels. KHS101 also showed promising *in vitro* cancer selective activity towards other cancer cell lines of different tissue type suggesting therapeutic potential of KHS101, or another HSPD1-targeting small molecule, against other cancer types in addition to GBM. KHS101 mechanism of action seemed similar in other cancer cell lines but further experiments are required to validate HSPD1 as the relevant target.

Further research is required to build on these *in vitro* proof-of-principle studies, and in particular whether the key findings observed here 'stand up' or can translate into an *in vivo* setting or, the ultimate aim, into a clinical setting.

For these *in vitro* studies, the cancer cell line panel screened was composed of established lines derived from epithelial tumours of different tissue origin, in some cases with several cell lines derived from the same tissue. Whilst this provided some indication of the likely relevance of the different putative cancer cell targets in different contexts and broad *versus* restricted (e.g. tissue type-specific) anti-cancer activity of the small molecule inhibitors, the panel was quite small. Evaluation of a larger panel of cancer cell lines would be beneficial to assess heterogeneity of response. p53 null and p53 wild-type isogenic cancer clones (HCT116) were utilised, however, including additional paired isogenic lines would enable analyses of the impact of other common genetic lesions on response together with RNAi-based knock-down or CRISPR knock-out/in approaches. Non-cancer cell models used were also epithelial but were not necessarily of matched tissue type, however, given the systemic nature of chemotherapy this was still informative as an initial assessment of toxicity towards normal cells.

Whilst cancer cell lines are highly amenable to experimental manipulation and dissection of the consequences of any targeting, expression of putative targets in cell lines and in clinical cancer and healthy tissue can vary. It would therefore be beneficial in future studies to analyse the expression of proposed targets, and of any emerging factors that may influence response to targeting, in tissue microarrays or clinical specimens.

Another limitation of the 'reductionist' approach used here is that the impact of the tumour microenvironment (TME) on cellular response to targeting has yet to be considered. Prior to assessing some of the proposed cancer cell vulnerabilities/targeting strategies in an *in vivo* setting, a better and more ethical strategy (3Rs) perhaps would be to first examine for efficacy in different *in vitro* models of the TME. It is well documented that both physico-chemical aspects of the TME and also heterotypic cell interactions can profoundly affect cancer cell metabolism and potentially response to targeting (Hanahan and Coussens, 2012). The use of *in vitro* models which mimic different aspects of the TME will enable analysis of how these different aspects can affect the target(s) and response.

Future investigation of hypoxia and varying oxygen tension is one element that may be explored. EX-527 and FK866 were equitoxic at 21% and 0.1% O<sub>2</sub> however within the TME different oxygen tensions exist depending on the distance of the cancer cells from a blood vessel. For our cells cultured in 'normoxic' conditions atmospheric O<sub>2</sub> tension (21% O<sub>2</sub>) was used for convenience, although it is known that within the body normoxic tissue O<sub>2</sub> tension is usually well below this (Carreau *et al.*, 2011). Polson *et al.* (2018) showed that KHS101 had equitoxic activity when comparing cells grown under 21% O<sub>2</sub> and 5% O<sub>2</sub>. Here, activity of KHS101 in cells cultured at 21% O<sub>2</sub> and 0.1% O<sub>2</sub> were compared and the cells cultured at 0.1% O<sub>2</sub> were found to be less sensitive to KHS101. This indicates the importance of testing multiple O<sub>2</sub> tensions on response and to compare this to a more physiologically normal O<sub>2</sub> tension. However, it should also be noted that in the pathophysiological TME, cancer cells are also prone to fluctuating oxygen tensions as the leaky and poorly formed blood vessels can commonly become temporarily blocked and then re-open. The effects of fluctuating oxygen tension on chemosensitivity to the different small molecule inhibitors tested here would be interesting to evaluate as well as oxygen tensions where there is likely to be less of an effect on cell proliferation than at 0.1% O<sub>2</sub>.

Another important component of the TME is the presence of other cell types. For example, work by Michael Lisanti and colleagues suggests that for certain breast

cancers, stromal fibroblast cells in the TME are metabolically subverted by the breast cancer cells (Pavlidis *et al.*, 2009). This indicates the potential need for analyses and comparison of targeting efficacy in co-cultures *versus* individual cultures. Another important cell type found in the TME is cancer stem cells (CSCs) and these are often found in hypoxic regions of tumours. CSCs are a major therapeutic challenge and are typically resistant to both traditional chemotherapy and radiotherapy. Non-cancer adult stem cells are cells that have the capability to self-renew and develop into differentiated cells of a tissue type, which is important for homeostatic control in tissues that undergo high cell turnover. CSCs are hypothesised to originate from adult stem cells or from the progenitors of stem cells where either have acquired additional genetic mutations. CSCs also have the capability to self-renew and therefore lead to additional CSCs and progeny which differentiate into different cell types within a tumour. Therapies must ensure that the whole CSC population is eliminated to guarantee effective treatment. Patients could show an initial good response to treatment and almost all cancer cells may be eliminated but if CSCs remain it can lead to tumour recurrence (Tan *et al.*, 2006). As current traditional cancer therapies usually work to target the rapid proliferation of the cells, they are not successful against targeting the slower proliferative CSCs, which raises issues in terms of treatment effectiveness (Zheng *et al.*, 2013). Although the GBM stem cell-like models have been utilised here, there is a need for evaluation of the proposed therapeutic approaches against other CSC models.

A general concept that is emerging from multiple independent studies of the TME is that it increases cancer cell plasticity (Hanahan and Coussens, 2012). Recent collaborative studies that I was lucky to be involved in that are not reported in this thesis have shown that GBM cells can be chemically induced to form connections that enable intercellular transfer of organelles. When GBM cells were treated with a chemical inhibitor of RHO-associated serine/threonine kinase proteins (ROCK), a connecting network between the cells through neurite-like projections was induced. GBM cells were able to traffic lysosomes and mitochondria between cells through these projections (da Silva *et al.*, 2019). Whilst this was artificially induced, it is possible that similar 'networks' may form in the context of the TME. Given that KHS101 impairs mitochondrial function, formation or induction of such

a 'network' in the TME might enable cancer cell survival if 'healthy' mitochondria could traffic to these cells, which could potentially lead to KHS101 resistance. It would be interesting to see if inhibition of ROCK can induce similar networking in other cancer cells.

Another consideration is the possibility of transfer or 'sharing' of NAD<sup>+</sup> or other metabolites between cells in such a 'connected network' if levels are depleted in some cells but not in others. It has also been reported that NAMPT can be secreted from cells and found extracellularly in the bloodstream (eNAMPT) and be taken up by other cells through extracellular vesicles increasing NAD<sup>+</sup> synthesis in cells it is transferred to (Yoshida *et al.*, 2019). With the more efficient vasculature of normal tissues compared to tumours this may help to circumvent any toxicity of NAMPT inhibition in normal cells through restoration of NAMPT function, but it could also reduce efficacy of NAMPT inhibitors towards cancer cells.

This research also indicates several different cellular targets and small molecule inhibitors that induce or influence neuronal (trans)differentiation. The results presented in Chapter 4 show that SIRT1 inhibition and/or SIRT1-FL knock-down promotes neuronal transdifferentiation of two non-cancer cell models whereas SIRT1- $\Delta$ 8 knock-down prevented neuronal transdifferentiation induced by SIRT1-FL knock-down. In Chapter 6, KHS101 was shown to have a similar effect to SIRT1 inhibition inducing a neuronal-like phenotype and increasing expression of neuronal markers MAP1a and MAP2. Previously, KHS101 has been shown to induce neuronal differentiation of rat NPCs due to binding of TACC3 (Wurdak *et al.*, 2010a) although the role of TACC3 in this context (human retinal epithelial cells) has not been determined. A key question for future investigations is whether these are independent pathways to neuronal differentiation or whether they are interlinked - whether SIRT1 inhibition affects TACC3 function and whether SIRT1 inhibition or SIRT1- $\Delta$ 8 expression is required for KHS101-induced neuronal differentiation. This is also relevant in the context of SIRT1 inhibition (EX-527) also promoting a neuronal-like morphology/differentiation phenotype and expression of neuronal markers in MDA-MB-231 breast cancer cells and in GBM1 cells. It will be interesting to see whether TACC3 knock-down recapitulates this

or whether in combination with EX-527 a more pronounced phenotype is observed suggesting potential as a part of an anti-cancer differentiation therapy.

To summarise, this PhD research identifies a number of potential opportunities linked to the NAD<sup>+</sup> metabolome for selective therapeutic targeting of cancer cells or improving the effectiveness or selectivity of existing approaches. Whilst *in vitro* proof-of-principle is mostly provided, these targets/approaches now require investigation in more physiologically relevant models in particular taking into account the impact of different aspects of the TME before possible *in vivo* studies.

## 8. References

- Agledal, L., Niere, M., Ziegler, M. (2010). The phosphate makes a difference: cellular functions of NADP. *Redox report: communications in free radical research*. **15**(1), 2–10.
- Ahmad, A.S., Ormiston-Smith, N., Sasieni, P.D. (2015). Trends in the lifetime risk of developing cancer in Great Britain: Comparison of risk for those born from 1930 to 1960. *British Journal of Cancer*. **112**(5), 943–947.
- Ahmadi, M., Ahmadihosseini, Z., Allison, S.J., Begum, S., Rockley, K., Sadiq, M., Chintamaneni, S., Lokwani, R., Hughes, N., Phillips, R.M. (2014). Hypoxia modulates the activity of a series of clinically approved tyrosine kinase inhibitors. *British Journal of Pharmacology*. **171**(1), 224–236.
- Ahmed, D., Eide, P.W., Eilertsen, I.A., Danielsen, S.A., Eknæs, M., Hektoen, M., Lind, G.E., Lothe, R.A. (2013). Epigenetic and genetic features of 24 colon cancer cell lines. *Oncogenesis*. **2**.
- Ahuja, N., Sharma, A.R., Baylin, S.B. (2016). Epigenetic Therapeutics: A New Weapon in the War Against Cancer. *Annual Review of Medicine*. **67**(1), 73–89.
- Akins, N.S., Nielson, T.C., Le, H. V. (2018). Inhibition of Glycolysis and Glutaminolysis: An Emerging Drug Discovery Approach to Combat Cancer. *Current Topics in Medicinal Chemistry*. **18**(6), 494–504.
- Alberts, B., Johnson, A., Lewis, J., Morgan, D., Raff, M., Roberts, K., Walter, P. (2014). *Molecular Biology of the Cell*. 6th ed. Garland Science.
- Allison, S.J., Cooke, D., Davidson, F.S., Elliott, P.I.P., Faulkner, R.A., Griffiths, H.B.S., Harper, O.J., Hussain, O., Owen-Lynch, P.J., Phillips, R.M., Rice, C.R., Shepherd, S.L., Wheelhouse, R.T. (2018). Ruthenium-Containing Linear Helicates and Mesocates with Tuneable p53-Selective Cytotoxicity in Colorectal Cancer Cells. *Angewandte Chemie - International Edition*. **57**(31), 9799–9804.
- Allison, S.J., Knight, J.R.P., Granchi, C., Rani, R., Minutolo, F., Milner, J., Phillips, R.M. (2014). Identification of LDH-A as a therapeutic target for cancer cell killing

via (i) p53/NAD(H)-dependent and (ii) p53-independent pathways. *Oncogenesis*. **3**, e102.

Allison, S.J., Milner, J. (2014). RNA Interference by Single- and Double-stranded siRNA With a DNA Extension Containing a 3' Nuclease-resistant Mini-hairpin Structure. *Molecular Therapy - Nucleic Acids*, e141.

Allison, S.J., Milner, J. (2007). SIRT3 is pro-apoptotic and participates in distinct basal apoptotic pathways. *Cell Cycle*. **6**(21), 2669–2677.

Allison, S.J., Sadiq, M., Baronou, E., Cooper, P.A., Dunnill, C., Georgopoulos, N.T., Latif, A., Shepherd, S., Shnyder, S.D., Stratford, I.J., Wheelhouse, R.T., Willans, C.E., Phillips, R.M. (2017). Preclinical anti-cancer activity and multiple mechanisms of action of a cationic silver complex bearing N-heterocyclic carbene ligands. *Cancer letters*. **403**, 98–107.

Alnaim, L. (2007). Therapeutic drug monitoring of cancer chemotherapy. *Journal of Oncology Pharmacy Practice*. **13**(4), 207–221.

Amé, J.C., Rolli, V., Schreiber, V., Niedergang, C., Apiou, F., Decker, P., Muller, S., Höger, T., Ménissier-de Murcia, J., De Murcia, G. (1999). PARP-2, a novel mammalian DNA damage-dependent poly(ADP-ribose) polymerase. *Journal of Biological Chemistry*. **274**(25), 17860–17868.

Amé, J.C., Spenlehauer, C., De Murcia, G. (2004). The PARP superfamily. *BioEssays*. **26**(8), 882–893.

Antolin, A.A., Ameratunga, M., Banerji, U., Clarke, P.A., Workman, P., Al-Lazikani, B. (2019). The off-target kinase landscape of clinical PARP inhibitors. *bioRxiv*, 520023.

Antolín, A.A., Mestres, J. (2014). Linking off-target kinase pharmacology to the differential cellular effects observed among PARP inhibitors. *Oncotarget*. **5**(10), 3023–3028.

Araos, J., Sleeman, J.P., Garvalov, B.K. (2018). The role of hypoxic signalling in metastasis: towards translating knowledge of basic biology into novel anti-tumour

strategies. *Clinical and Experimental Metastasis*. **35**(7), 563–599.

Arbab, A.S. (2012). Activation of alternative pathways of angiogenesis and involvement of stem cells following anti-angiogenesis treatment in glioma. *Histology and Histopathology*. **27**(5), 549.

Arruebo, M., Vilaboa, N., Sáez-Gutierrez, B., Lambea, J., Tres, A., Valladares, M., González-Fernández, Á. (2011). Assessment of the evolution of cancer treatment therapies. *Cancers*. **3**(3), 3279–3330.

Bae, Y.H., Shin, J.M., Park, H.J., Jang, H.O., Bae, M.K., Bae, S.K. (2014). Gain-of-function mutant p53-R280K mediates survival of breast cancer cells. *Genes and Genomics*. **36**(2), 171–178.

Baenke, F., Peck, B., Miess, H., Schulze, A. (2013). Hooked on fat: The role of lipid synthesis in cancer metabolism and tumour development. *DMM Disease Models and Mechanisms*. **6**(6), 1353–1363.

Bailón-Moscoso, N., Romero-Benavides, J.C., Ostrosky-Wegman, P. (2014). Development of anticancer drugs based on the hallmarks of tumor cells. *Tumor Biology*. **35**(5), 3981–3995.

Bar-Sagi, D., Feramisco, J.R. (1986). Induction of membrane ruffling and fluid-phase pinocytosis in quiescent fibroblasts by ras proteins. *Science*. **233**(4768), 1061–1068.

Baskar, R., Lee, K.A., Yeo, R., Yeoh, K.W. (2012). Cancer and radiation therapy: Current advances and future directions. *International Journal of Medical Sciences*. **9**(3), 193–199.

Basri, A.M., Lord, R.M., Allison, S.J., Rodríguez-Bárzano, A., Lucas, S.J., Janeway, F.D., Shepherd, H.J., Pask, C.M., Phillips, R.M., McGowan, P.C. (2017). Bis-picolinamide Ruthenium(III) Dihalide Complexes: Dichloride-to-Diiodide Exchange Generates Single *trans* Isomers with High Potency and Cancer Cell Selectivity. *Chemistry - A European Journal*. **23**(26), 6341–6356.

De Berardinis, R.J., Chandel, N.S. (2016). Fundamentals of cancer metabolism.

*Science Advances*. **2**(5).

Berg, J.M., Tymoczko, J.L., Gregory, G.J., Stryer, L. (2019). *Biochemistry*. 9th ed. WH Freeman.

Bergers, G., Benjamin, L.E. (2003). Tumorigenesis and the angiogenic switch. *Nature Reviews Cancer*. **3**(6), 401–410.

Bieganowski, P., Brenner, C. (2004). Discoveries of nicotinamide riboside as a nutrient and conserved NRK genes establish a Preiss-Handler independent route to NAD<sup>+</sup> in fungi and humans. *Cell*. **117**(4), 495–502.

Bocangel, D., Sengupta, S., Mitra, S., Bhakat, K.K. (2009). p53-mediated down-regulation of the human DNA repair gene O<sup>6</sup>-methylguanine-DNA methyltransferase (MGMT) via interaction with Sp1 transcription factor. *Anticancer Research*. **29**(10), 3741–3750.

Boehler, C., Gauthier, L.R., Mortusewicz, O., Biard, D.S., Saliou, J.M., Bresson, A., Sanglier-Cianferani, S., Smith, S., Schreiber, V., Boussin, F., Dantzer, F. (2011). Poly(ADP-ribose) polymerase 3 (PARP3), a newcomer in cellular response to DNA damage and mitotic progression. *Proceedings of the National Academy of Sciences of the United States of America*. **108**(7), 2783–2788.

Bonnet, Sébastien, Archer, S.L., Allalunis-Turner, J., Haromy, A., Beaulieu, C., Thompson, R., Lee, C.T., Lopaschuk, G.D., Puttagunta, L., Bonnet, Sandra, Harry, G., Hashimoto, K., Porter, C.J., Andrade, M.A., Thebaud, B., Michelakis, E.D. (2007). A Mitochondria-K<sup>+</sup> Channel Axis Is Suppressed in Cancer and Its Normalization Promotes Apoptosis and Inhibits Cancer Growth. *Cancer Cell*. **11**(1), 37–51.

Bonora, M., Patergnani, S., Rimessi, A., de Marchi, E., Suski, J.M., Bononi, A., Giorgi, C., Marchi, S., Missiroli, S., Poletti, F., Wieckowski, M.R., Pinton, P. (2012). ATP synthesis and storage. *Purinergic Signalling*. **8**(3), 343–357.

Boulton, S., Pemberton, L.C., Porteous, J.K., Curtin, N.J., Griffin, R.J., Golding, B.T., Durkacz, B.W. (1995). Potentiation of temozolomide-induced cytotoxicity: A comparative study of the biological effects of poly(ADP-ribose) polymerase

inhibitors. *British Journal of Cancer*. **72**(4), 849–856.

Bouras, T., Fu, M., Sauve, A.A., Wang, F., Quong, A.A., Perkins, N.D., Hay, R.T., Gu, W., Pestell, R.G. (2005). SIRT1 deacetylation and repression of p300 involves lysine residues 1020/1024 within the cell cycle regulatory domain 1. *Journal of Biological Chemistry*. **280**(11), 10264–10276.

Bowman, K.J., Newell, D.R., Calvert, A.H., Curtin, N.J. (2001). Differential effects of the poly (ADP-ribose) polymerase (PARP) inhibitor NU1025 on topoisomerase I and II inhibitor cytotoxicity in L1210 cells in vitro. *British Journal of Cancer*. **84**(1), 106–112.

Bray, F., Ferlay, J., Soerjomataram, I., Siegel, R.L., Torre, L.A., Jemal, A. (2018). Global cancer statistics 2018: GLOBOCAN estimates of incidence and mortality worldwide for 36 cancers in 185 countries. *CA: A Cancer Journal for Clinicians*. **68**(6), 394–424.

Bross, P., Fernandez-Guerra, P. (2016). Disease-associated mutations in the HSPD1 gene encoding the large subunit of the mitochondrial HSP60/HSP10 chaperonin complex. *Frontiers in Molecular Biosciences*. **3**(AUG).

Brunet, A., Sweeney, L.B., Sturgill, J.F., Chua, K.F., Greer, P.L., Lin, Y., Tran, H., Ross, S.E., Mostoslavsky, R., Cohen, H.Y., Hu, L.S., Cheng, H.L., Jedrychowski, M.P., Gygi, S.P., Sinclair, D.A., Alt, F.W., Greenberg, M.E. (2004). Stress-Dependent Regulation of FOXO Transcription Factors by the SIRT1 Deacetylase. *Science*. **303**(5666), 2011–2015.

Bryant, H.E., Schultz, N., Thomas, H.D., Parker, K.M., Flower, D., Lopez, E., Kyle, S., Meuth, M., Curtin, N.J., Helleday, T. (2005). Specific killing of BRCA2-deficient tumours with inhibitors of poly(ADP-ribose) polymerase. *Nature*. **434**(7035), 913–917.

Burnett, J.C., Rossi, J.J., Tiemann, K. (2011). Current progress of siRNA/shRNA therapeutics in clinical trials. *Biotechnology Journal*. **6**(9), 1130–1146.

Cantó, C., Menzies, K.J., Auwerx, J. (2015). NAD<sup>+</sup> Metabolism and the Control of Energy Homeostasis: A Balancing Act between Mitochondria and the Nucleus.

*Cell Metabolism*. **22**(1), 31–53.

Cantó, C., Sauve, A.A., Bai, P. (2013). Crosstalk between poly(ADP-ribose) polymerase and sirtuin enzymes. *Molecular Aspects of Medicine*. **34**(6), 1168–1201.

Cao, X., Fang, L., Gibbs, S., Huang, Y., Dai, Z., Wen, P., Zheng, X., Sadee, W., Sun, D. (2007). Glucose uptake inhibitor sensitizes cancer cells to daunorubicin and overcomes drug resistance in hypoxia. *Cancer chemotherapy and pharmacology*. **59**(4), 495–505.

Carafa, V., Altucci, L., Nebbioso, A. (2019). Dual tumor suppressor and tumor promoter action of sirtuins in determining malignant phenotype. *Frontiers in Pharmacology*. **9**(JAN).

Carlsson, S.K., Brothers, S.P., Wahlestedt, C. (2014). Emerging treatment strategies for glioblastoma multiforme. *EMBO Molecular Medicine*. **6**(11), 1359–1370.

Carreau, A., Hafny-Rahbi, B. El, Matejuk, A., Grillon, C., Kieda, C. (2011). Why is the partial oxygen pressure of human tissues a crucial parameter? Small molecules and hypoxia. *Journal of Cellular and Molecular Medicine*. **15**(6), 1239–1253.

Castanotto, D., Rossi, J.J. (2009). The promises and pitfalls of RNA-interference-based therapeutics. *Nature*. **457**(7228), 426–433.

Chalmers, A.J. (2009). The potential role and application of PARP inhibitors in cancer treatment. *British Medical Bulletin*. **89**(1), 23–40.

Chambon, P., Weill, J.D., Mandel, P. (1963). Nicotinamide mononucleotide activation of a new DNA-dependent polyadenylic acid synthesizing nuclear enzyme. *Biochemical and Biophysical Research Communications*. **11**(1), 39–43.

Chan, L.L.-Y., Shen, D., Wilkinson, A.R., Patton, W., Lai, N., Chan, E., Kuksin, D., Lin, B., Qiu, J. (2012). A novel image-based cytometry method for autophagy detection in living cells. *Autophagy*. **8**(9), 1371–82.

Chao, Y.L., Shepard, C.R., Wells, A. (2010). Breast carcinoma cells re-express E-cadherin during mesenchymal to epithelial reverting transition. *Molecular Cancer*. **9**.

Chen, H.C., Jeng, Y.M., Yuan, R.H., Hsu, H.C., Chen, Y.L. (2012). SIRT1 promotes tumorigenesis and resistance to chemotherapy in hepatocellular carcinoma and its expression predicts poor prognosis. *Annals of Surgical Oncology*. **19**(6), 2011–2019.

Chen, X., Hokka, D., Maniwa, Y., Ohbayashi, C., Itoh, T., Hayashi, Y. (2014). Sirt1 is a tumor promoter in lung adenocarcinoma. *Oncology Letters*. **8**(1), 387–393.

Chen, X., Sun, K., Jiao, S., Cai, N., Zhao, X., Zou, H., Xie, Y., Wang, Z., Zhong, M., Wei, L. (2014). High levels of SIRT1 expression enhance tumorigenesis and associate with a poor prognosis of colorectal carcinoma patients. *Scientific Reports*. **4**.

Choi, Y.K., Park, K.G. (2018). Targeting glutamine metabolism for cancer treatment. *Biomolecules and Therapeutics*. **26**(1), 19–28.

Chowdhry, S., Zanca, C., Rajkumar, U., Koga, T., Diao, Y., Raviram, R., Liu, F., Turner, K., Yang, H., Brunk, E., Bi, J., Furnari, F., Bafna, V., Ren, B., Mischel, P.S. (2019). NAD metabolic dependency in cancer is shaped by gene amplification and enhancer remodelling. *Nature*. **569**(7757), 570–575.

Cosentino, C., Grieco, D., Costanzo, V. (2011). ATM activates the pentose phosphate pathway promoting anti-oxidant defence and DNA repair. *EMBO Journal*. **30**(3), 546–555.

Cui, L., Cheng, Z., Liu, Y., Dai, Y., Pang, Y., Jiao, Y., Ke, X., Cui, W., Zhang, Q., Shi, J., Fu, L. (2018). Overexpression of PDK2 and PDK3 reflects poor prognosis in acute myeloid leukemia. *Cancer Gene Therapy*.

Currie, E., Schulze, A., Zechner, R., Walther, T.C., Farese, R. V (2013). Cell Metabolism Perspective Cellular Fatty Acid Metabolism and Cancer. *Cell Metabolism*. **18**(2), 153–161.

Daniel, R.A., Rozanska, A.L., Thomas, H.D., Mulligan, E.A., Drew, Y., Castelbuono, D.J., Hostomsky, Z., Plummer, E.R., Boddy, A. V., Tweddie, D.A., Curtin, N.J., Clifford, S.C. (2009). Inhibition of poly(ADP-Ribose) polymerase-1 enhances temozolomide and topotecan activity against childhood Neuroblastoma. *Clinical Cancer Research*. **15**(4), 1241–1249.

Das, B.B., Huang, S.N., Murai, J., Rehman, I., Amé, J.C., Sengupta, S., Das, S.K., Majumdar, P., Zhang, H., Biard, D., Majumder, H.K., Schreiber, V., Pommier, Y. (2014). PARP1-TDP1 coupling for the repair of topoisomerase I-induced DNA damage. *Nucleic Acids Research*. **42**(7), 4435–4449.

Das, C.K., Mandal, M., Kögel, D. (2018). Pro-survival autophagy and cancer cell resistance to therapy. *Cancer and Metastasis Reviews*. **37**(4), 749–766.

DeBerardinis, R.J. (2008). Is cancer a disease of abnormal cellular metabolism? New angles on an old idea. *Genetics in Medicine*. **10**(11), 767–777.

DeBerardinis, R.J., Lum, J.J., Hatzivassiliou, G., Thompson, C.B. (2008). The Biology of Cancer: Metabolic Reprogramming Fuels Cell Growth and Proliferation. *Cell Metabolism*. **7**(1), 11–20.

Dehmelt, L., Halpain, S. (2005). The MAP2/Tau family of microtubule-associated proteins. *Genome Biology*. **6**(1).

Deota, S., Chattopadhyay, T., Ramachandran, D., Armstrong, E., Camacho, B., Maniyadath, B., Fulzele, A., Gonzalez-de-Peredo, A., Denu, J.M., Kolthur-Seetharam, U. (2017). Identification of a Tissue-Restricted Isoform of SIRT1 Defines a Regulatory Domain that Encodes Specificity. *Cell Reports*. **18**(13), 3069–3077.

Dirks, P.B. (2010). Brain tumor stem cells: The cancer stem cell hypothesis writ large. *Molecular Oncology*. **4**(5), 420–430.

Donawho, C.K., Luo, Yan, Luo, Yanping, Penning, T.D., Bauch, J.L., Bouska, J.J., Bontcheva-Diaz, V.D., Cox, B.F., DeWeese, T.L., Dillehay, L.E., Ferguson, D.C., Ghoreishi-Haack, N.S., Grimm, D.R., Guan, R., Han, E.K., Holley-Shanks, R.R., Hristov, B., Idler, K.B., Jarvis, K., Johnson, E.F., Kleinberg, L.R., Klinghofer,

V., Lasko, L.M., Liu, X., Marsh, K.C., McGonigal, T.P., Meulbroek, J.A., Olson, A.M., Palma, J.P., Rodriguez, L.E., Shi, Y., Stavropoulos, J.A., Tsurutani, A.C., Zhu, G.D., Rosenberg, S.H., Giranda, V.L., Frost, D.J. (2007). ABT-888, an orally active poly(ADP-ribose) polymerase inhibitor that potentiates DNA-damaging agents in preclinical tumor models. *Clinical Cancer Research*. **13**(9), 2728–2737.

Donmez, G., Outeiro, T.F. (2013). SIRT1 and SIRT2: Emerging targets in neurodegeneration. *EMBO Molecular Medicine*. **5**(3), 344–352.

Drew, Y., Plummer, R. (2009). PARP inhibitors in cancer therapy: Two modes of attack on the cancer cell widening the clinical applications. *Drug Resistance Updates*. **12**(6), 153–156.

Duarte-Pereira, S., Pereira-Castro, I., Silva, S.S., Correia, M.G., Neto, C., da Costa, L.T., Amorim, A., Silva, R.M. (2016). Extensive regulation of nicotinate phosphoribosyltransferase (NAPRT) expression in human tissues and tumors. *Oncotarget*. **7**(2), 1973–1983.

El-Khamisy, S.F., Masutani, M., Suzuki, H., Caldecott, K.W. (2003). A requirement for PARP-1 for the assembly or stability of XRCC1 nuclear foci at sites of oxidative DNA damage. *Nucleic Acids Research*. **31**(19), 5526–5533.

Elstrodt, F., Hollestelle, A., Nagel, J.H.A., Gorin, M., Wasielewski, M., van den Ouweland, A., Merajver, S.D., Ethier, S.P., Schutte, M. (2006). BRCA1 mutation analysis of 41 human breast cancer cell lines reveals three new deleterious mutants. *Cancer research*. **66**(1), 41–5.

Evers, B., Drost, R., Schut, E., De Bruin, M., Van Burg, E. Der, Derksen, P.W.B., Holstege, H., Liu, X., Van Drunen, E., Beverloo, H.B., Smith, G.C.M., Martin, N.M.B., Lau, A., O'Connor, M.J., Jonkers, J. (2008). Selective inhibition of BRCA2-deficient mammary tumor cell growth by AZD2281 and cisplatin. *Clinical Cancer Research*. **14**(12), 3916–3925.

Fantin, V.R., St-Pierre, J., Leder, P. (2006). Attenuation of LDH-A expression uncovers a link between glycolysis, mitochondrial physiology, and tumor maintenance. *Cancer Cell*. **9**(6), 425–434.

Farmer, H., McCabe, H., Lord, C.J., Tutt, A.H.J., Johnson, D.A., Richardson, T.B., Santarosa, M., Dillon, K.J., Hickson, I., Knights, C., Martin, N.M.B., Jackson, S.P., Smith, G.C.M., Ashworth, A. (2005). Targeting the DNA repair defect in BRCA mutant cells as a therapeutic strategy. *Nature*. **434**(7035), 917–921.

Feng, Y., Xiong, Y., Qiao, T., Li, X., Jia, L., Han, Y. (2018). Lactate dehydrogenase A: A key player in carcinogenesis and potential target in cancer therapy. *Cancer Medicine*. **7**(12), 6124–6136.

Firestein, R., Blander, G., Michan, S., Oberdoerffer, P., Ogino, S., Campbell, J., Bhimavarapu, A., Luikenhuis, S., de Cabo, R., Fuchs, C., Hahn, W.C., Guarente, L.P., Sinclair, D.A. (2008). The SIRT1 deacetylase suppresses intestinal tumorigenesis and colon cancer growth. *PLoS ONE*. **3**(4).

Fisher, A.E.O., Hochegger, H., Takeda, S., Caldecott, K.W. (2007). Poly(ADP-Ribose) Polymerase 1 Accelerates Single-Strand Break Repair in Concert with Poly(ADP-Ribose) Glycohydrolase. *Molecular and Cellular Biology*. **27**(15), 5597–5605.

Food and Drug Administration (2015). Eloxatin Information. [online]. Available from: <https://www.fda.gov/drugs/postmarket-drug-safety-information-patients-and-providers/eloxatin-information> [Accessed November 28, 2019].

Ford, J., Jiang, M., Milner, J. (2005). Cancer-specific functions of SIRT1 enable human epithelial cancer cell growth and survival. *Cancer Research*. **65**(22), 10457–10463.

Frye, R.A. (2000). Phylogenetic classification of prokaryotic and eukaryotic Sir2-like proteins. *Biochemical and Biophysical Research Communications*. **273**(2), 793–798.

Gangemi, R.M.R., Griffero, F., Marubbi, D., Perera, M., Capra, M.C., Malatesta, P., Ravetti, G.L., Zona, G.L., Daga, A., Corte, G. (2009). SOX2 Silencing in Glioblastoma Tumor-Initiating Cells Causes Stop of Proliferation and Loss of Tumorigenicity. *Stem Cells*. **27**(1), 40–48.

García-Parra, J., Dalmases, A., Morancho, B., Arpí, O., Menendez, S., Sabbaghi,

M., Zazo, S., Chamizo, C., Madoz, J., Eroles, P., Servitja, S., Tusquets, I., Yelamos, J., Lluch, A., Arribas, J., Rojo, F., Rovira, A., Albanell, J. (2014). Poly (ADP-ribose) polymerase inhibition enhances trastuzumab antitumour activity in HER2 overexpressing breast cancer. *European Journal of Cancer*. **50**(15), 2725–2734.

Gertz, M., Fischer, F., Nguyen, G.T.T., Lakshminarasimhan, M., Schutkowski, M., Weyand, M., Steegborn, C. (2013). Ex-527 inhibits Sirtuins by exploiting their unique NAD<sup>+</sup>-dependent deacetylation mechanism. *Proceedings of the National Academy of Sciences of the United States of America*. **110**(30).

Gillet, J.P., Gottesman, M.M. (2010). Mechanisms of multidrug resistance in cancer. *Methods in molecular biology (Clifton, N.J.)*. **596**, 47–76.

Glick, D., Barth, S., Macleod, K.F. (2010). Autophagy: cellular and molecular mechanisms.

Gobeil, S., Boucher, C.C., Nadeau, D., Poirier, G.G. (2001). Characterization of the necrotic cleavage of poly (ADP-ribose) polymerase (PARP-1): Implication of lysosomal proteases. *Cell Death and Differentiation*. **8**(6), 588–594.

Goel, A., Mathupala, S.P., Pedersen, P.L. (2003). Glucose metabolism in cancer: Evidence that demethylation events play a role in activating type II hexokinase gene expression. *Journal of Biological Chemistry*. **278**(17), 15333–15340.

Goody, M.F., Henry, C.A. (2018). A need for NAD<sup>+</sup> in muscle development, homeostasis, and aging. *Skeletal Muscle*. **8**(1).

Granchi, C., Calvaresi, E.C., Tuccinardi, T., Paterni, I., Macchia, M., Martinelli, A., Hergenrother, P.J., Minutolo, F. (2013). Assessing the differential action on cancer cells of LDH-A inhibitors based on the N-hydroxyindole-2-carboxylate (NHI) and malonic (Mal) scaffolds. *Organic and Biomolecular Chemistry*. **11**(38), 6588–6596.

Guggenheim, E.R., Ondrus, A.E., Movassaghi, M., Lippard, S.J. (2008). Poly(ADP-ribose) polymerase-1 activity facilitates the dissociation of nuclear proteins from platinum-modified DNA. *Bioorganic and Medicinal Chemistry*.

16(23), 10121–10128.

Hallows, W.C., Yu, W., Denu, J.M. (2012). Regulation of glycolytic enzyme phosphoglycerate mutase-1 by Sirt1 protein-mediated deacetylation. *Journal of Biological Chemistry*. **287**(6), 3850–3858.

Halpain, S., Dehmelt, L. (2006). The MAP1 family of microtubule-associated proteins. *Genome Biology*. **7**(6), 224.

Hammoudi, N., Ahmed, K.B.R., Garcia-Prieto, C., Huang, P. (2011). Metabolic alterations in cancer cells and therapeutic implications. *Chinese Journal of Cancer*. **30**(8), 508–525.

Hanahan, D., Coussens, L.M. (2012). Accessories to the Crime: Functions of Cells Recruited to the Tumor Microenvironment. *Cancer Cell*. **21**(3), 309–322.

Hanahan, D., Folkman, J. (1996). Patterns and Emerging Mechanisms Review of the Angiogenic Switch during Tumorigenesis. *Cell*. **86**, 353–364.

Hanahan, D., Weinberg, R.A. (2011). Hallmarks of cancer: The next generation. *Cell*. **144**(5), 646–674.

Hanahan, D., Weinberg, R.A. (2000). The hallmarks of cancer. *Cell*. **100**(1), 57–70.

Hardie, D.G. (2011). AMP-activated protein kinase-an energy sensor that regulates all aspects of cell function. *Genes and Development*. **25**(18), 1895–1908.

Hasmann, M., Schemainda, I. (2003). FK866, a Highly Specific Noncompetitive Inhibitor of Nicotinamide Phosphoribosyltransferase, Represents a Novel Mechanism for Induction of Tumor Cell Apoptosis. *Cancer Research*. **63**(21), 7436–7442.

Hatzivassiliou, G., Zhao, F., Bauer, D.E., Andreadis, C., Shaw, A.N., Dhanak, D., Hingorani, S.R., Tuveson, D.A., Thompson, C.B. (2005). ATP citrate lyase inhibition can suppress tumor cell growth. *Cancer Cell*. **8**(4), 311–321.

Hay, N. (2016). Reprogramming glucose metabolism in cancer: Can it be exploited for cancer therapy? *Nature Reviews Cancer*. **16**(10), 635–649.

Hayflick, L., Moorhead, P.S. (1961). The serial cultivation of human diploid cell strains. *Experimental Cell Research*. **25**(3), 585–621.

von Heideman, A., Berglund, A., Larsson, R., Nygren, P. (2010). Safety and efficacy of NAD depleting cancer drugs: results of a phase I clinical trial of CHS 828 and overview of published data. *Cancer chemotherapy and pharmacology*. **65**(6), 1165–72.

Herranz, D., Maraver, A., Cañamero, M., Gómez-López, G., Inglada-Pérez, L., Robledo, M., Castelblanco, E., Matias-Guiu, X., Serrano, M. (2013). SIRT1 promotes thyroid carcinogenesis driven by PTEN deficiency. *Oncogene*. **32**(34), 4052–4056.

Hjarnaa, P.J., Jonsson, E., Latini, S., Dhar, S., Larsson, R., Bramm, E., Skov, T., Binderup, L. (1999). CHS 828, a novel pyridyl cyanoguanidine with potent antitumor activity in vitro and in vivo. *Cancer research*. **59**(22), 5751–7.

Hoffman, B., Liebermann, D.A. (1998). The proto-oncogene c-myc and apoptosis. *Oncogene*. **17**(25), 3351–3357.

Holen, K., Saltz, L.B., Hollywood, E., Burk, K., Hanauske, A.R. (2008). The pharmacokinetics, toxicities, and biologic effects of FK866, a nicotinamide adenine dinucleotide biosynthesis inhibitor. *Investigational New Drugs*. **26**(1), 45–51.

Horbinski, C. (2013). What do we know about IDH1/2 mutations so far, and how do we use it? *Acta Neuropathologica*. **125**(5), 621–636.

Houtkooper, R.H., Cantó, C., Wanders, R.J., Auwerx, J. (2010). The secret life of NAD<sup>+</sup>: An old metabolite controlling new metabolic signaling pathways. *Endocrine Reviews*. **31**(2), 194–223.

Hsiangl, Y.-H., Hertzbergj, R., Hechtj, S., Lius, L.F. (1985). Camptothecin Induces Protein-linked DNA Breaks via Mammalian DNA Topoisomerase I\*. *The*

*Journal of biological chemistry.* **260**(27), 14873–14878.

Huffman, D.M., Grizzle, W.E., Bamman, M.M., Kim, J.S., Eltoum, I.A., Elgavish, A., Nagy, T.R. (2007). SIRT1 is significantly elevated in mouse and human prostate cancer. *Cancer Research.* **67**(14), 6612–6618.

Imai, S.I., Armstrong, C.M., Kaeberlein, M., Guarente, L. (2000). Transcriptional silencing and longevity protein Sir2 is an NAD-dependent histone deacetylase. *Nature.* **403**(6771), 795–800.

Intlekofer, A.M., DeMatteo, R.G., Venneti, S., Finley, L.W.S., Lu, C., Judkins, A.R., Rustenburg, A.S., Grinaway, P.B., Chodera, J.D., Cross, J.R., Thompson, C.B. (2015). Hypoxia Induces Production of L-2-Hydroxyglutarate. *Cell Metabolism.* **22**(2), 304–311.

Isaacs, J.S., Yun, J.J., Mole, D.R., Lee, S., Torres-Cabala, C., Chung, Y.L., Merino, M., Trepel, J., Zbar, B., Toro, J., Ratcliffe, P.J., Linehan, W.M., Neckers, L. (2005). HIF overexpression correlates with biallelic loss of fumarate hydratase in renal cancer: Novel role of fumarate in regulation of HIF stability. *Cancer Cell.* **8**(2), 143–153.

Ito, S., Dalessio, A.C., Taranova, O. V., Hong, K., Sowers, L.C., Zhang, Y. (2010). Role of tet proteins in 5mC to 5hmC conversion, ES-cell self-renewal and inner cell mass specification. *Nature.* **466**(7310), 1129–1133.

Jayson, G.C., Kerbel, R., Ellis, L.M., Harris, A.L. (2016). Antiangiogenic therapy in oncology: current status and future directions. *The Lancet.* **388**(10043), 518–529.

Jiang, X., Li, W., Li, X., Bai, H., Zhang, Z. (2019). Current status and future prospects of PARP inhibitor clinical trials in ovarian cancer. *Cancer Management and Research.* **Volume 11**, 4371–4390.

Kaeberlein, M., McVey, M., Guarente, L. (1999). The SIR2/3/4 complex and SIR2 alone promote longevity in *Saccharomyces cerevisiae* by two different mechanisms. *Genes & development.* **13**(19), 2570–80.

Kamel, D., Gray, C., Walia, J.S., Kumar, V. (2018). PARP Inhibitor Drugs in the Treatment of Breast, Ovarian, Prostate and Pancreatic Cancers: An Update of Clinical Trials. *Current Drug Targets*. **19**(1).

Kaner, R.A., Allison, S.J., Faulkner, A.D., Phillips, R.M., Roper, D.I., Shepherd, S.L., Simpson, D.H., Waterfield, N.R., Scott, P. (2016). Anticancer metallohelices: Nanomolar potency and high selectivity. *Chemical Science*. **7**(2), 951–958.

Kanno, T., Sudo, K., Maekawa, M., Nishimura, Y., Ukita, M., Fukutake, K. (1988). Lactate dehydrogenase M-subunit deficiency: a new type of hereditary exertional myopathy. *Clinica Chimica Acta*. **173**(1), 89–98.

Kaufmann, P., Engelstad, K., Wei, Y., Jhung, S., Sano, M.C., Shungu, D.C., Millar, W.S., Hong, X., Gooch, C.L., Mao, X., Pascual, J.M., Hirano, M., Stacpoole, P.W., DiMauro, S., De Vivo, D.C. (2006). Dichloroacetate causes toxic neuropathy in MELAS: A randomized, controlled clinical trial. *Neurology*. **66**(3), 324–330.

Kawai, S., Murata, K. (2008). Structure and function of NAD kinase and NADP phosphatase: key enzymes that regulate the intracellular balance of NAD(H) and NADP(H). *Bioscience, biotechnology, and biochemistry*. **72**(4), 919–30.

Kim, B., Park, J., Sailor, M.J. (2019). Rekindling RNAi Therapy: Materials Design Requirements for In Vivo siRNA Delivery. *Advanced Materials*. **31**(49), 1903637.

Kim, D., Dang Nguyen, M., Dobbin, M.M., Fischer, A., Sananbenesi, F., Rodgers, J.T., Delalle, I., Baur, J.A., Sui, G., Armour, S.M., Puigserver, P., Sinclair, D.A., Tsai, L.-H. (2007). SIRT1 deacetylase protects against neurodegeneration in models for Alzheimer's disease and amyotrophic lateral sclerosis. *The EMBO Journal*. **26**, 3169–3179.

Kimmelman, A.C. (2015). Metabolic dependencies in RAS-driven cancers. *Clinical Cancer Research*. **21**(8), 1828–1834.

Kimura, H. (2013). Histone modifications for human epigenome analysis. *Journal of Human Genetics*. **58**(7), 439–445.

Knight, J.R.P., Milner, J. (2012). SIRT1, metabolism and cancer. *Current opinion in oncology*. **24**(1), 68–75.

Knight, J.R.P., Willis, A.E., Milner, J. (2013). Active regulator of SIRT1 is required for ribosome biogenesis and function. *Nucleic Acids Research*. **41**(7), 4185–4197.

Ko, H.L., Ren, E.C. (2012). Functional aspects of PARP1 in DNA repair and transcription. *Biomolecules*. **2**(4), 524–548.

Kozlowski, M.R. (2012). RPE cell senescence: A key contributor to age-related macular degeneration. *Medical Hypotheses*. **78**(4), 505–510.

Kummar, S., Chen, A., Ji, J., Zhang, Y., Reid, J.M., Ames, M., Jia, L., Weil, M., Speranza, G., Murgo, A.J., Kinders, R., Wang, L., Parchment, R.E., Carter, J., Stotler, H., Rubinstein, L., Hollingshead, M., Melillo, G., Pommier, Y., Bonner, W., Tomaszewski, J.E., Doroshow, J.H. (2011). Phase I study of PARP inhibitor ABT-888 in combination with topotecan iKummar, S., Chen, A., Ji, J., Zhang, Y., Reid, J. M., Ames, M., ... Doroshow, J. H. (2011). Phase I study of PARP inhibitor ABT-888 in combination with topotecan in adults with refractor. *Cancer Res*. **71**(17), 5626–34.

Kunkel, M., Reichert, T.E., Benz, P., Lehr, H.-A., Jeong, J.-H., Wieand, S., Bartenstein, P., Wagner, W., Whiteside, T.L. (2003). Overexpression of Glut-1 and increased glucose metabolism in tumors are associated with a poor prognosis in patients with oral squamous cell carcinoma. *Cancer*. **97**(4), 1015–1024.

LaBarge, M.A. (2010). The difficulty of targeting cancer stem cell niches. *Clinical cancer research: an official journal of the American Association for Cancer Research*. **16**(12), 3121–9.

Landry, J., Sutton, A., Tafrov, S.T., Heller, R.C., Stebbins, J., Pillus, L., Sternglanz, R. (2000). The silencing protein SIR2 and its homologs are NAD-dependent protein deacetylases. *Proceedings of the National Academy of Sciences of the United States of America*. **97**(11), 5807–5811.

Le, A., Cooper, C.R., Gouw, A.M., Dinavahi, R., Maitra, A., Deck, L.M., Royer, R.E., Vander Jagt, D.L., Semenza, G.L., Dang, C. V. (2010). Inhibition of lactate dehydrogenase A induces oxidative stress and inhibits tumor progression. *Proceedings of the National Academy of Sciences of the United States of America*. **107**(5), 2037–2042.

Lee, E., Yong, R.L., Paddison, P., Zhu, J. (2018). Comparison of glioblastoma (GBM) molecular classification methods. *Seminars in Cancer Biology*. **53**, 201–211.

Lehmann, B.D., Bauer, J.A., Chen, X., Sanders, M.E., Chakravarthy, A.B., Shyr, Y., Pietsenpol, J.A. (2011). Identification of human triple-negative breast cancer subtypes and preclinical models for selection of targeted therapies. *Journal of Clinical Investigation*. **121**(7), 2750–2767.

Li, X. (2013). SIRT1 and energy metabolism. *Acta Biochimica et Biophysica Sinica*. **45**(1), 51–60.

Lim, J.H., Lee, Y.M., Chun, Y.S., Chen, J., Kim, J.E., Park, J.W. (2010). Sirtuin 1 modulates cellular responses to hypoxia by deacetylating hypoxia-inducible factor 1alpha. *Molecular cell*. **38**(6), 864–878.

Lin, J.B., Kubota, S., Ban, N., Yoshida, M., Santeford, A., Sene, A., Nakamura, R., Zapata, N., Kubota, M., Tsubota, K., Yoshino, J., Imai, S. ichiro, Apte, R.S. (2016). NAMPT-Mediated NAD + Biosynthesis Is Essential for Vision In Mice. *Cell Reports*. **17**(1), 69–85.

Livak, K.J., Schmittgen, T.D. (2001). Analysis of relative gene expression data using real-time quantitative PCR and the 2- $\Delta\Delta$ CT method. *Methods*. **25**(4), 402–408.

Lord, C.J., Ashworth, A. (2017). PARP Inhibitors: The First Synthetic Lethal Targeted Therapy Europe PMC Funders Group. *Science*. **355**(6330), 1152–1158.

Lord, R.M., Hebden, A.J., Pask, C.M., Henderson, I.R., Allison, S.J., Shepherd, S.L., Phillips, R.M., McGowan, P.C. (2015). Hypoxia-Sensitive Metal  $\beta$ -

Ketoiminato Complexes Showing Induced Single-Strand DNA Breaks and Cancer Cell Death by Apoptosis. *Journal of Medicinal Chemistry*. **58**(12), 4940–4953.

Lu, K.H., Wood, M.E., Daniels, M., Burke, C., Ford, J., Kauff, N.D., Kohlmann, W., Lindor, N.M., Mulvey, T.M., Robinson, L., Rubinstein, W.S., Stoffel, E.M., Snyder, C., Syngal, S., Merrill, J.K., Wollins, D.S., Hughes, K.S. (2014). American society of clinical oncology expert statement: Collection and use of a cancer family history for oncology providers. *Journal of Clinical Oncology*. **32**(8), 833–840.

Luengo, A., Gui, D.Y., Vander Heiden, M.G. (2017). Review Targeting Metabolism for Cancer Therapy. *Cell Chemical Biology*. **24**, 1161–1180.

Lynch, C.J., Shah, Z.H., Allison, S.J., Ahmed, S.U., Ford, J., Warnock, L.J., Li, H., Serrano, M., Milner, J. (2010). SIRT1 undergoes alternative splicing in a novel auto-regulatory loop with p53. *PLoS ONE*. **5**(10).

Maddocks, O.D.K., Berkers, C.R., Mason, S.M., Zheng, L., Blyth, K., Gottlieb, E., Vousden, K.H. (2013). Serine starvation induces stress and p53 dependent metabolic remodeling in cancer cells Europe PMC Funders Group. *Nature*. **493**(7433), 542–546.

Mangiola, A., Lama, G., Giannitelli, C., De Bonis, P., Anile, C., Lauriola, L., La Torre, G., Sabatino, G., Maira, G., Jhanwar-Uniyal, M., Sica, G. (2007). Stem cell marker nestin and c-Jun NH2-terminal kinases in tumor and peritumor areas of glioblastoma multiforme: Possible prognostic implications. *Clinical Cancer Research*. **13**(23), 6970–6977.

Matheny, C.J., Wei, M.C., Bassik, M.C., Donnelly, A.J., Kampmann, M., Iwasaki, M., Piloto, O., Solow-Cordero, D.E., Bouley, D.M., Rau, R., Brown, P., McManus, M.T., Weissman, J.S., Cleary, M.L. (2013). Next-generation NAMPT inhibitors identified by sequential high-throughput phenotypic chemical and functional genomic screens. *Chemistry and Biology*. **20**(11), 1352–1363.

Matoba, S., Kang, J.G., Patino, W.D., Wragg, A., Boehm, M., Gavrilova, O.,

Hurley, P.J., Bunz, F., Hwang, P.M. (2006). p53 regulates mitochondrial respiration. *Science*. **312**(5780), 1650–1653.

May, P., May, E. (1999). Twenty years of p53 research: Structural and functional aspects of the p53 protein. *Oncogene*. **18**(53), 7621–7636.

McCabe, N., Turner, N.C., Lord, C.J., Kluzek, K., Białkowska, A., Swift, S., Giavara, S., O'Connor, M.J., Tutt, A.N., Zdzienicka, M.Z., Smith, G.C.M., Ashworth, A. (2006). Deficiency in the repair of DNA damage by homologous recombination and sensitivity to poly(ADP-ribose) polymerase inhibition. *Cancer Research*. **66**(16), 8109–8115.

McCann, K.E., Hurvitz, S.A. (2018). Advances in the use of PARP inhibitor therapy for breast cancer. *Drugs in Context*. **7**.

McQuade, R.M., Stojanovska, V., Bornstein, J.C., Nurgali, K. (2018). PARP inhibition in platinum-based chemotherapy: Chemopotentiation and neuroprotection. *Pharmacological Research*. **137**, 104–113.

Medina, R.A., Owen, G.I. (2002). Glucose transporters: Expression, regulation and cancer. *Biological Research*. **35**(1), 9–26.

Mei, Z., Zhang, X., Yi, J., Huang, J., He, J., Tao, Y. (2016). Sirtuins in metabolism, DNA repair and cancer. *Journal of Experimental and Clinical Cancer Research*. **35**(1).

Metallo, C.M., Vander Heiden, M.G. (2013). Understanding metabolic regulation and its influence on cell physiology. *Mol Cell*. **49**(3), 388–398.

Michels, J., Vitale, I., Galluzzi, L., Adam, J., Olaussen, K.A., Kepp, O., Senovilla, L., Talhaoui, I., Guegan, J., Enot, D.P., Talbot, M., Robin, A., Girard, P., Orear, C., Lissa, D., Sukkurwala, A.Q., Garcia, P., Behnam-Motlagh, P., Kohno, K., Wu, G.S., Brenner, C., Dessen, P., Saporbaev, M., Soria, J.C., Castedo, M., Kroemer, G. (2013). Cisplatin resistance associated with PARP hyperactivation. *Cancer Research*. **73**(7), 2271–2280.

Michels, J., Vitale, I., Senovilla, L., Enot, D.P., Garcia, P., Lissa, D., Olaussen,

- K.A., Brenner, C., Soria, J.C., Castedo, M., Kroemer, G. (2013). Synergistic interaction between cisplatin and PARP inhibitors in non-small cell lung cancer. *Cell Cycle*. **12**(6), 877–883.
- Miller, D.M., Thomas, S.D., Islam, A., Muench, D., Sedoris, K. (2012). c-Myc and cancer metabolism. *Clinical Cancer Research*. **18**(20), 5546–5553.
- Miura, K., Sakata, K. ichi, Someya, M., Matsumoto, Y., Matsumoto, H., Takahashi, A., Hareyama, M. (2012). The combination of olaparib and camptothecin for effective radiosensitization. *Radiation Oncology*. **7**(1).
- Moore, N., Houghton, J., Lyle, S. (2012). Slow-cycling therapy-resistant cancer cells. *Stem Cells and Development*. **21**(10), 1822–1830.
- Mosmann, T. (1983). Rapid colorimetric assay for cellular growth and survival: Application to proliferation and cytotoxicity assays. *Journal of Immunological Methods*. **65**(1–2), 55–63.
- Motta, M.C., Divecha, N., Lemieux, M., Kamel, C., Chen, D., Gu, W., Bultsma, Y., McBurney, M., Guarente, L. (2004). Mammalian SIRT1 Represses Forkhead Transcription Factors. *Cell*. **116**(4), 551–563.
- Moynahan, M.E., Chiu, J.W., Koller, B.H., Jasint, M. (1999). Brca1 controls homology-directed DNA repair. *Molecular Cell*. **4**(4), 511–518.
- Moynahan, M.E., Pierce, A.J., Jasin, M. (2001). BRCA2 is required for homology-directed repair of chromosomal breaks. *Molecular Cell*. **7**(2), 263–272.
- Mráček, T., Drahota, Z., Houštěk, J. (2013). The function and the role of the mitochondrial glycerol-3-phosphate dehydrogenase in mammalian tissues.
- Muller, P.A.J., Trinidad, A.G., Timpson, P., Morton, J.P., Zanivan, S., Van Den Berghe, P.V.E., Nixon, C., Karim, S.A., Caswell, P.T., Noll, J.E., Coffill, C.R., Lane, D.P., Sansom, O.J., Neilsen, P.M., Norman, J.C., Vousden, K.H. (2013). Mutant p53 enhances MET trafficking and signalling to drive cell scattering and invasion. *Oncogene*. **32**(10), 1252–1265.
- Murai, J., Huang, S.Y.N., Das, B.B., Renaud, A., Zhang, Y., Doroshow, J.H., Ji,

J., Takeda, S., Pommier, Y. (2012). Trapping of PARP1 and PARP2 by clinical PARP inhibitors. *Cancer Research*. **72**(21), 5588–5599.

Murai, J., Zhang, Y., Morris, J., Ji, J., Takeda, S., Doroshow, J.H., Pommier, Y. (2014). Rationale for poly(ADP-ribose) polymerase (PARP) inhibitors in combination therapy with camptothecins or temozolomide based on PARP trapping versus catalytic inhibition. *Journal of Pharmacology and Experimental Therapeutics*. **349**(3), 408–416.

Muz, B., de la Puente, P., Azab, F., Azab, A.K. (2015). The role of hypoxia in cancer progression, angiogenesis, metastasis, and resistance to therapy. *Hypoxia*, 83.

Nagarajan, A., Malvi, P., Wajapeyee, N. (2016). Oncogene-directed alterations in cancer cell metabolism. *Trends in cancer*. **2**(7), 365–377.

Nakayama, A., Murakami, H., Maeyama, N., Yamashiro, N., Sakakibara, A., Mori, N., Takahashi, M. (2003). Role for RFX transcription factors in non-neuronal cell-specific inactivation of the microtubule-associated protein MAP1A promoter. *Journal of Biological Chemistry*. **278**(1), 233–240.

Nikiforov, A., Kulikova, V., Ziegler, M. (2015). The human NAD metabolome: Functions, metabolism and compartmentalization. *Critical Reviews in Biochemistry and Molecular Biology*. **50**(4), 284–297.

Nikiforov, M.A., Chandriani, S., O'Connell, B., Petrenko, O., Kotenko, I., Beavis, A., Sedivy, J.M., Cole, M.D. (2002). A Functional Screen for Myc-Responsive Genes Reveals Serine Hydroxymethyltransferase, a Major Source of the One-Carbon Unit for Cell Metabolism. *Molecular and Cellular Biology*. **22**(16), 5793–5800.

Nishitoh, H. (2012). CHOP is a multifunctional transcription factor in the ER stress response. *Journal of Biochemistry*. **151**(3), 217–219.

Nitiss, J.L. (2009). Targeting DNA topoisomerase II in cancer chemotherapy. *Nature Reviews Cancer*. **9**(5), 338–350.

Okuno, D., Iino, R., Noji, H. (2011). Rotation and structure of FoF1-ATP synthase. *Journal of Biochemistry*. **149**(6), 655–664.

Oldham, W.M., Clish, C.B., Yang, Y., Loscalzo, J. (2015). Hypoxia-Mediated Increases in l-2-hydroxyglutarate Coordinate the Metabolic Response to Reductive Stress. *Cell Metabolism*. **22**(2), 291–303.

Olesen, U.H., Christensen, M.K., Björkling, F., Jäättelä, M., Jensen, P.B., Sehested, M., Nielsen, S.J. (2008). Anticancer agent CHS-828 inhibits cellular synthesis of NAD. *Biochemical and Biophysical Research Communications*. **367**(4), 799–804.

Olesen, U.H., Thougard, A. V, Jensen, P.B., Sehested, M. (2010). A preclinical study on the rescue of normal tissue by nicotinic acid in high-dose treatment with APO866, a specific nicotinamide phosphoribosyltransferase inhibitor. *Molecular cancer therapeutics*. **9**(6), 1609–17.

Orr, A.L., Ashok, D., Sarantos, M.R., Ng, R., Shi, T., Gerencser, A.A., Hughes, R.E., Brand, M.D. (2014). Novel inhibitors of mitochondrial sn-glycerol 3-phosphate dehydrogenase. *PLoS ONE*. **9**(2).

Osthus, R.C., Shim, H., Kim, S., Li, Q., Reddy, R., Mukherjee, M., Xu, Y., Wonsey, D., Lee, L.A., Dang, C. V. (2000). Deregulation of glucose transporter 1 and glycolytic gene expression by c-Myc. *Journal of Biological Chemistry*. **275**(29), 21797–21800.

Palma, J.P., Wang, Y.-C., Rodriguez, L.E., Montgomery, D., Ellis, P.A., Bukofzer, G., Niquette, A., Liu, X., Shi, Y., Lasko, L., Zhu, G.-D., Penning, T.D., Giranda, V.L., Rosenberg, S.H., Frost, D.J., Donawho, C.K. (2009). ABT-888 confers broad in vivo activity in combination with temozolomide in diverse tumors. *Clinical cancer research: an official journal of the American Association for Cancer Research*. **15**(23), 7277–90.

Park, H.J., Bae, J.S., Kim, K.M., Moon, Y.J., Park, S.H., Ha, S.H., Hussein, U.K., Zhang, Z., Park, H.S., Park, B.H., Moon, W.S., Kim, J.R., Jang, K.Y. (2018). The PARP inhibitor olaparib potentiates the effect of the DNA damaging agent

doxorubicin in osteosarcoma. *Journal of Experimental and Clinical Cancer Research*. **37**(1).

Parker, W.B. (2009). Enzymology of purine and pyrimidine antimetabolites used in the treatment of cancer. *Chemical Reviews*. **109**(7), 2880–2893.

Patra, K.C., Hay, N. (2014). The pentose phosphate pathway and cancer. *Trends in Biochemical Sciences*. **39**(8), 347–354.

Patra, K.C., Wang, Q., Bhaskar, P.T., Miller, L., Wang, Z., Wheaton, W., Chandel, N., Laakso, M., Muller, W.J., Allen, E.L., Jha, A.K., Smolen, G.A., Clasquin, M.F., Robey, R.B., Hay, N. (2013). Hexokinase 2 is required for tumor initiation and maintenance and its systemic deletion is therapeutic in mouse models of cancer. *Cancer Cell*. **24**(2), 213–228.

Pavlidis, S., Whitaker-Menezes, D., Castello-Cros, R., Flomenberg, N., Witkiewicz, A.K., Frank, P.G., Casimiro, M.C., Wang, C., Fortina, P., Addya, S., Pestell, R.G., Martinez-Outschoorn, U.E., Sotgia, F., Lisanti, M.P. (2009). The reverse Warburg effect: Aerobic glycolysis in cancer associated fibroblasts and the tumor stroma. *Cell Cycle*. **8**(23), 3984–4001.

Pećina-Šlaus, N. (2003). Tumor suppressor gene E-cadherin and its role in normal and malignant cells. *Cancer Cell International*. **3**.

Peck, B., Chen, C.Y., Ho, K.K., Di Fruscia, P., Myatt, S.S., Charles Coombes, R., Fuchter, M.J., Hsiao, C.D., Lam, E.W.F. (2010). SIRT inhibitors induce cell death and p53 acetylation through targeting both SIRT1 and SIRT2. *Molecular Cancer Therapeutics*. **9**(4), 844–855.

Pedersen, P.L., Mathupala, S., Rempel, A., Geschwind, J.F., Ko, Y.H. (2002). Mitochondrial bound type II hexokinase: A key player in the growth and survival of many cancers and an ideal prospect for therapeutic intervention. *Biochimica et Biophysica Acta - Bioenergetics*. **1555**(1–3), 14–20.

Peng, S.Y., Lai, P.L., Pan, H.W., Hsiao, L.P., Hsu, H.C. (2008). Aberrant expression of the glycolytic enzymes aldolase B and type II hexokinase in hepatocellular carcinoma are predictive markers for advanced stage, early

recurrence and poor prognosis. *Oncology Reports*. **19**(4), 1045–1053.

Perez, R.E., Shen, H., Duan, L., Kim, R.H., Kim, T., Park, N.H., Maki, C.G. (2016). Modeling the etiology of p53-mutated cancer cells. *Journal of Biological Chemistry*. **291**(19), 10131–10147.

Petrucci, N., Daly, M.B., Pal, T. (1993). BRCA1- and BRCA2-Associated Hereditary Breast and Ovarian Cancer. *GeneReviews®*.

Phillips, R.M. (2016). Targeting the hypoxic fraction of tumours using hypoxia-activated prodrugs Cytotoxic Reviews Godefridus J. Peters and Eric Raymond. *Cancer Chemotherapy and Pharmacology*. **77**(3), 441–457.

Phillips, R.M., Hulbert, P.B., Bibby, M.C., Sleight, N.R., Double, J.A. (1992). In vitro activity of the novel indoloquinone EO-9 and the influence of pH on cytotoxicity. *British journal of cancer*. **65**(3), 359–64.

Plo, I., Liao, Z.Y., Barceló, J.M., Kohlhagen, G., Caldecott, K.W., Weinfeld, M., Pommier, Y. (2003). Association of XRCC1 and tyrosyl DNA phosphodiesterase (Tdp1) for the repair of topoisomerase I-mediated DNA lesions. *DNA repair*. **2**(10), 1087–100.

Plummer, R., Jones, C., Middleton, M., Wilson, R., Evans, J., Olsen, A., Curtin, N., Boddy, A., McHugh, P., Newell, D., Harris, A., Johnson, P., Steinfeldt, H., Dewji, R., Wang, D., Robson, L., Calvert, H. (2008). Phase I study of the poly(ADP-ribose) polymerase inhibitor, AG014699, in combination with temozolomide in patients with advanced solid tumors. *Clinical cancer research : an official journal of the American Association for Cancer Research*. **14**(23), 7917–23.

Plummer, R., Lorigan, P., Steven, N., Scott, L., Middleton, M.R., Wilson, R.H., Mulligan, E., Curtin, N., Wang, D., Dewji, R., Abbattista, A., Gallo, J., Calvert, H. (2013). A phase II study of the potent PARP inhibitor, Rucaparib (PF-01367338, AG014699), with temozolomide in patients with metastatic melanoma demonstrating evidence of chemopotential. *Cancer Chemotherapy and Pharmacology*. **71**(5), 1191–1199.

Pollard, S.M., Yoshikawa, K., Clarke, I.D., Danovi, D., Stricker, S., Russell, R., Bayani, J., Head, R., Lee, M., Bernstein, M., Squire, J.A., Smith, A., Dirks, P. (2009). Glioma Stem Cell Lines Expanded in Adherent Culture Have Tumor-Specific Phenotypes and Are Suitable for Chemical and Genetic Screens. *Cell Stem Cell*. **4**(6), 568–580.

Polson, E.S., Kuchler, V.B., Abbosh, C., Ross, E.M., Mathew, R.K., Beard, H.A., Silva, B. Da, Holding, A.N., Ballereau, S., Chuntharpursat-Bon, E., Williams, J., Griffiths, H.B., Shao, H., Patel, A., Davies, A.J., Droop, A., Chumas, P., Short, S.C., Lorgier, M., Gestwicki, J.E., Roberts, L.D., Bon, R.S., Allison, S.J., Zhu, S., Markowitz, F., Wurdak, H. (2018). KHS101 disrupts energy metabolism in human glioblastoma cells and reduces tumor growth in mice. *Science Translational Medicine*. **10**(454).

Pommier, Y., Barcelo, J.M., Rao, V.A., Sordet, O., Jobson, A.G., Thibaut, L., Miao, Z.H., Seiler, J.A., Zhang, H., Marchand, C., Agama, K., Nitiss, J.L., Redon, C. (2006). Repair of Topoisomerase I-Mediated DNA Damage. *Progress in Nucleic Acid Research and Molecular Biology*. **81**, 179–229.

Prasad, C.B., Prasad, S.B., Yadav, S.S., Pandey, L.K., Singh, S., Pradhan, S., Narayan, G. (2017). Olaparib modulates DNA repair efficiency, sensitizes cervical cancer cells to cisplatin and exhibits anti-metastatic property. *Scientific Reports*. **7**(1).

Preiss, J., Handler, P. (1958a). Biosynthesis of diphosphopyridine nucleotide. I. Identification of intermediates. *The Journal of biological chemistry*. **233**(2), 488–92.

Preiss, J., Handler, P. (1958b). Biosynthesis of diphosphopyridine nucleotide. II. Enzymatic aspects. *The Journal of biological chemistry*. **233**(2), 493–500.

Pruitt, K., Zinn, R.L., Ohm, J.E., McGarvey, K.M., Kang, S.H.L., Watkins, D.N., Herman, J.G., Baylin, S.B. (2006). Inhibition of SIRT1 reactivates silenced cancer genes without loss of promoter DNA hypermethylation. *PLoS Genetics*. **2**(3), 0344–0352.

- Puzio-Kuter, A.M. (2011). The role of p53 in metabolic regulation. *Genes and Cancer*. **2**(4), 385–391.
- Qin, S., Zhang, C.-L. (2012). Role of Kruppel-Like Factor 4 in Neurogenesis and Radial Neuronal Migration in the Developing Cerebral Cortex. *Molecular and Cellular Biology*. **32**(21), 4297–4305.
- Quaresma, M., Coleman, M.P., Rachet, B. (2015). 40-year trends in an index of survival for all cancers combined and survival adjusted for age and sex for each cancer in England and Wales, 1971-2011: A population-based study. *The Lancet*. **385**(9974), 1206–1218.
- Rahman, S., Islam, R. (2011). Mammalian Sirt1: Insights on its biological functions. *Cell Communication and Signaling*. **9**.
- Rasmussen, K.D., Helin, K. (2016). Role of TET enzymes in DNA methylation, development, and cancer. *Genes and Development*. **30**(7), 733–750.
- Rastogi, S., Banerjee, S., Chellappan, S., Simon, G.R. (2007). Glut-1 antibodies induce growth arrest and apoptosis in human cancer cell lines. *Cancer Letters*. **257**(2), 244–251.
- Ray Chaudhuri, A., Nussenzweig, A. (2017). The multifaceted roles of PARP1 in DNA repair and chromatin remodelling. *Nature Reviews Molecular Cell Biology*. **18**(10), 610–621.
- Revollo, J.R., Grimm, A.A., Imai, S.I. (2004). The NAD biosynthesis pathway mediated by nicotinamide phosphoribosyltransferase regulates Sir2 activity in mammalian cells. *Journal of Biological Chemistry*. **279**(49), 50754–50763.
- Revollo, J.R., Körner, A., Mills, K.F., Satoh, A., Wang, T., Garten, A., Dasgupta, B., Sasaki, Y., Wolberger, C., Townsend, R.R., Milbrandt, J., Kiess, W., Imai, S. ichiro (2007). Nampt/PBEF/Visfatin Regulates Insulin Secretion in  $\beta$  Cells as a Systemic NAD Biosynthetic Enzyme. *Cell Metabolism*. **6**(5), 363–375.
- Rich, P.R. (2003). The molecular machinery of Keilin's respiratory chain. *Biochemical Society Transactions*. **31**(6), 1095–1105.

Robertson, K.D., Uzvolgyi, E., Liang, G., Talmadge, C., Sumegi, J., Gonzales, F.A., Jones, P.A. (1999). The human DNA methyltransferases (DNMTs) 1, 3a and 3b: Coordinate mRNA expression in normal tissues and overexpression in tumors. *Nucleic Acids Research*. **27**(11), 2291–2298.

Rocha, C.R.R., Silva, M.M., Quinet, A., Cabral-Neto, J.B., Menck, C.F.M. (2018). DNA repair pathways and cisplatin resistance: An intimate relationship. *Clinics*. **73**.

Romero-Garcia, S., Moreno-Altaminaro, M.M.B., Prado-Garcia, H., Sanchez-Garcia, F.J. (2016). Lactate Contribution to the Tumor Microenvironment: Mechanisms, effects on immune Cells and Therapeutic Relevance. . **7**, 1.

Ryan, K.M., Vousden, K.H. (2002). Cancer: Pinning a change on p53. *Nature*. **419**(6909), 795–797.

Ryu, K.W., Nandu, T., Kim, J., Challa, S., DeBerardinis, R.J., Lee Kraus, W. (2018). Metabolic regulation of transcription through compartmentalized NAD + biosynthesis. *Science*. **360**(6389).

Sajadian, S.O., Ehnert, S., Vakilian, H., Koutsouraki, E., Damm, G., Seehofer, D., Thasler, W., Dooley, S., Baharvand, H., Sipos, B., Nussler, A.K. (2015). Induction of active demethylation and 5hmC formation by 5-azacytidine is TET2 dependent and suggests new treatment strategies against hepatocellular carcinoma. *Clinical Epigenetics*. **7**(1).

Salero, E., Blenkinsop, T.A., Corneo, B., Harris, A., Rabin, D., Stern, J.H., Temple, S. (2012). Adult human RPE can be activated into a multipotent stem cell that produces mesenchymal derivatives. *Cell Stem Cell*. **10**(1), 88–95.

Sankpal, U.T., Pius, H., Khan, M., Shukoor, M.I., Maliakal, P., Lee, C.M., Abdelrahim, M., Connelly, S.F., Basha, R. (2012). Environmental factors in causing human cancers: Emphasis on tumorigenesis. *Tumor Biology*. **33**(5), 1265–1274.

Sasaki, H., Shitara, M., Yokota, K., Hikosaka, Y., Moriyama, S., Yano, M., Fujii, Y. (2012). Overexpression of GLUT1 correlates with Kras mutations in lung

carcinomas. *Molecular Medicine Reports*. **5**(3), 599–602.

Satoh, A., Brace, C.S., Rensing, N., Clifton, P., Wozniak, D.F., Herzog, E.D., Yamada, K.A., Imai, S.-I. (2013). Sirt1 extends life span and delays aging in mice through the regulation of Nk2 homeobox 1 in the DMH and LH.

Saunier, E., Benelli, C., Bortoli, S. (2016). The pyruvate dehydrogenase complex in cancer: An old metabolic gatekeeper regulated by new pathways and pharmacological agents. *International Journal of Cancer*. **138**(4), 809–817.

Schirrmacher, V. (2019). From chemotherapy to biological therapy: A review of novel concepts to reduce the side effects of systemic cancer treatment (Review). *International Journal of Oncology*. **54**(2), 407–419.

Schreiber, V., Amé, J.C., Dollé, P., Schultz, I., Rinaldi, B., Fraulob, V., Ménissier-de Murcia, J., De Murcia, G. (2002). Poly(ADP-ribose) polymerase-2 (PARP-2) is required for efficient base excision DNA repair in association with PARP-1 and XRCC1. *Journal of Biological Chemistry*. **277**(25), 23028–23036.

Scorey, N., Fraser, S.P., Patel, P., Pridgeon, C., Dallman, M.J., Djamgoz, M.B.A. (2006). Notch signalling and voltage-gated Na<sup>+</sup> channel activity in human prostate cancer cells: Independent modulation of in vitro motility. *Prostate Cancer and Prostatic Diseases*. **9**(4), 399–406.

Selak, M.A., Armour, S.M., MacKenzie, E.D., Boulahbel, H., Watson, D.G., Mansfield, K.D., Pan, Y., Simon, M.C., Thompson, C.B., Gottlieb, E. (2005). Succinate links TCA cycle dysfunction to oncogenesis by inhibiting HIF- $\alpha$  prolyl hydroxylase. *Cancer Cell*. **7**(1), 77–85.

Shah, Z.H., Ahmed, S.U., Ford, J.R., Allison, S.J., Knight, J.R.P., Milner, J. (2012). A Deacetylase-Deficient SIRT1 Variant Opposes Full-Length SIRT1 in Regulating Tumor Suppressor p53 and Governs Expression of Cancer-Related Genes. *Molecular and Cellular Biology*. **32**(3), 704–716.

Shay, J.W., Wright, W.E. (2000). Hayflick, his limit, and cellular ageing. *Nature Reviews Molecular Cell Biology*. **1**(1), 72–76.

Sherwood, J.T., Brock, M. V (2007). Lung cancer: new surgical approaches. *Respirology (Carlton, Vic.)*. **12**(3), 326–32.

Shim, H., Dolde, C., Lewis, B.C., Wu, C.S., Dang, G., Jungmann, R.A., Dalla-Favera, R., Dang, C. V. (1997). c-Myc transactivation of LDH-A: Implications for tumor metabolism and growth. *Proceedings of the National Academy of Sciences of the United States of America*. **94**(13), 6658–6663.

Siddik, Z.H. (2003). Cisplatin: Mode of cytotoxic action and molecular basis of resistance. *Oncogene*. **22**(47 REV. ISS. 6), 7265–7279.

da Silva, B., Irving, B.K., Polson, E.S., Droop, A., Griffiths, H.B.S., Mathew, R.K., Stead, L.F., Marrison, J., Williams, C., Williams, J., Short, S.C., Scarcia, M., O'Toole, P.J., Allison, S.J., Mavria, G., Wurdak, H. (2019). Chemically induced neurite-like outgrowth reveals a multicellular network function in patient-derived glioblastoma cells. *Journal of cell science*. **132**(19).

Simic, P., Zainabadi, K., Bell, E., Sykes, D.B., Saez, B., Lotinun, S., Baron, R., Scadden, D., Schipani, E., Guarente, L. (2013). SIRT1 regulates differentiation of mesenchymal stem cells by deacetylating  $\beta$ -catenin. *EMBO Molecular Medicine*. **5**(3), 430–440.

Singh, D., Arora, R., Kaur, P., Singh, B., Mannan, R., Arora, S. (2017). Overexpression of hypoxia-inducible factor and metabolic pathways: possible targets of cancer. *Cell & Bioscience*. **7**(1), 62.

Soltani, M.H., Pichardo, R., Song, Z., Sangha, N., Camacho, F., Satyamoorthy, K., Sanguenza, O.P., Setaluri, V. (2005). Microtubule-associated protein 2, a marker of neuronal differentiation, induces mitotic defects, inhibits growth of melanoma cells, and predicts metastatic potential of cutaneous melanoma. *The American journal of pathology*. **166**(6), 1841–50.

Son, J., Lyssiotis, C.A., Ying, H., Wang, X., Hua, S., Ligorio, M., Perera, R.M., Ferrone, C.R., Mullarky, E., Shyh-Chang, N., Kang, Y., Fleming, J.B., Bardeesy, N., Asara, J.M., Haigis, M.C., Depinho, R.A., Cantley, L.C., Kimmelman, A.C. (2013). Glutamine supports pancreatic cancer growth through a KRAS-regulated

metabolic pathway. *Nature*. **496**(7443), 101–105.

Sreedhar, A., Zhao, Y. (2018). Dysregulated metabolic enzymes and metabolic reprogramming in cancer cells. *Biomedical Reports*. **8**(1), 3–10.

Stünkel, W., Peh, B.K., Tan, Y.C., Nayagam, V.M., Wang, X., Salto-Tellez, M., Ni, B., Entzeroth, M., Wood, J. (2007). Function of the SIRT1 protein deacetylase in cancer. *Biotechnology journal*. **2**(11), 1360–8.

Sweetlove, L.J., Fernie, A.R. (2018). The role of dynamic enzyme assemblies and substrate channelling in metabolic regulation. *Nature Communications*. **9**(1).

Takahashi, K., Yamanaka, S. (2006). Induction of Pluripotent Stem Cells from Mouse Embryonic and Adult Fibroblast Cultures by Defined Factors. *Cell*. **126**(4), 663–676.

Tan, B., Young, D.A., Lu, Z.H., Wang, T., Meier, T.I., Shepard, R.L., Roth, K., Zhai, Y., Huss, K., Kuo, M.S., Gillig, J., Parthasarathy, S., Burkholder, T.P., Smith, M.C., Geeganage, S., Zhao, G. (2013). Pharmacological inhibition of nicotinamide phosphoribosyltransferase (NAMPT), an enzyme essential for NAD<sup>+</sup> biosynthesis, in human cancer cells: Metabolic basis and potential clinical implications. *Journal of Biological Chemistry*. **288**(5), 3500–3511.

Tan, B.T., Park, C.Y., Ailles, L.E., Weissman, I.L. (2006). The cancer stem cell hypothesis: A work in progress. *Laboratory Investigation*. **86**(12), 1203–1207.

Tanida, I., Ueno, T., Kominami, E. (2008). LC3 and autophagy - Methods in Molecular Biology. *Methods in Molecular Biology*. **445**(2), 77–88.

Tanner, K.G., Landry, J., Sternglanz, R., Denu, J.M. (2000). Silent information regulator 2 family of NAD-dependent histone/protein deacetylases generates a unique product, 1-O-acetyl-ADP-ribose. *Proceedings of the National Academy of Sciences of the United States of America*. **97**(26), 14178–14182.

Thakur, B.K., Dittrich, T., Chandra, P., Becker, A., Kuehnau, W., Klusmann, J.H., Reinhardt, D., Welte, K. (2012). Involvement of p53 in the cytotoxic activity of the NAMPT inhibitor FK866 in myeloid leukemic cells. *International Journal of*

*Cancer*. **132**(4), 766–774.

Tissenbaum, H.A., Guarente, L. (2001). Increased dosage of a sir-2 gene extends lifespan in *Caenorhabditis elegans*. *Nature*. **410**(6825), 227–30.

Umemura, K., Kimura, H. (2005). Determination of oxidized and reduced nicotinamide adenine dinucleotide in cell monolayers using a single extraction procedure and a spectrophotometric assay. *Analytical Biochemistry*. **338**(1), 131–135.

Vanhove, K., Derveaux, E., Graulus, G.J., Mesotten, L., Thomeer, M., Noben, J.P., Guedens, W., Adriaensens, P. (2019). Glutamine addiction and therapeutic strategies in lung cancer. *International Journal of Molecular Sciences*. **20**(2).

Vaquero, A., Scher, M., Lee, D., Erdjument-Bromage, H., Tempst, P., Reinberg, D. (2004). Human SirT1 interacts with histone H1 and promotes formation of facultative heterochromatin. *Molecular Cell*. **16**(1), 93–105.

Vaziri, H., Dessain, S.K., Eaton, E.N., Imai, S.I., Frye, R.A., Pandita, T.K., Guarente, L., Weinberg, R.A. (2001). hSIR2/SIRT1 functions as an NAD-dependent p53 deacetylase. *Cell*. **107**(2), 149–159.

Verhaak, R.G.W., Hoadley, K.A., Purdom, E., Wang, V., Qi, Y., Wilkerson, M.D., Miller, C.R., Ding, L., Golub, T., Mesirov, J.P., Alexe, G., Lawrence, M., O’Kelly, M., Tamayo, P., Weir, B.A., Gabriel, S., Winckler, W., Gupta, S., Jakkula, L., Feiler, H.S., Hodgson, J.G., James, C.D., Sarkaria, J.N., Brennan, C., Kahn, A., Spellman, P.T., Wilson, R.K., Speed, T.P., Gray, J.W., Meyerson, M., Getz, G., Perou, C.M., Hayes, D.N. (2010). Integrated Genomic Analysis Identifies Clinically Relevant Subtypes of Glioblastoma Characterized by Abnormalities in PDGFRA, IDH1, EGFR, and NF1. *Cancer Cell*. **17**(1), 98–110.

Vető, B., Szabó, P., Bacquet, C., Apró, A., Hathy, E., Kiss, J., Réthelyi, J.M., Szeri, F., Szüts, D., Arányi, T. (2018). Inhibition of DNA methyltransferase leads to increased genomic 5-hydroxymethylcytosine levels in hematopoietic cells. *FEBS Open Bio*. **8**(4), 584–592.

Vichai, V., Kirtikara, K. (2006). Sulforhodamine B colorimetric assay for

cytotoxicity screening. *Nature Protocols*. **1**(3), 1112–1116.

Vogelstein, B., Lane, D., Levine, A.J. (2000). Surfing the p53 network. *Nature*. **408**(6810), 307–310.

Vyas, S., Chesarone-Cataldo, M., Todorova, T., Huang, Y.H., Chang, P. (2013). A systematic analysis of the PARP protein family identifies new functions critical for cell physiology. *Nature Communications*. **4**.

Wang, J., Qian, Y., Gao, M. (2019). Overexpression of PDK4 is associated with cell proliferation, drug resistance and poor prognosis in ovarian cancer. *Cancer Management and Research*. **11**, 251–262.

Wang, R.H., Sengupta, K., Li, C., Kim, H.S., Cao, L., Xiao, C., Kim, S., Xu, X., Zheng, Y., Chilton, B., Jia, R., Zheng, Z.M., Appella, E., Wang, X.W., Ried, T., Deng, C.X. (2008). Impaired DNA Damage Response, Genome Instability, and Tumorigenesis in SIRT1 Mutant Mice. *Cancer Cell*. **14**(4), 312–323.

Wang, W., Elkins, K., Oh, A., Ho, Y.C., Wu, J., Li, H., Xiao, Y., Kwong, M., Coons, M., Brillantes, B., Cheng, E., Crocker, L., Dragovich, P.S., Sampath, D., Zheng, X., Bair, K.W., O'Brien, T., Belmont, L.D. (2014). Structural basis for resistance to diverse classes of NAMPT inhibitors. *PLoS ONE*. **9**(10).

Warashina, M., Min, K.H., Kuwabara, T., Huynh, A., Gage, F.H., Schultz, P.G., Ding, S. (2006). A Synthetic Small Molecule That Induces Neuronal Differentiation of Adult Hippocampal Neural Progenitor Cells. *Angewandte Chemie International Edition*. **45**(4), 591–593.

Warburg, O. (1956). On the origin of cancer cells. *Science*. **123**(3191), 309–314.

Warburg, O. (1927). The metabolism of tumours in the body. *The Journal of General Physiology*. **8**(6), 519–530.

Watson, M., Roulston, A., Belec, L., Billot, X., Marcellus, R., Bedard, D., Bernier, C., Branchaud, S., Chan, H., Dairi, K., Gilbert, K., Goulet, D., Gratton, M.-O., Isakau, H., Jang, A., Khadir, A., Koch, E., Lavoie, M., Lawless, M., Nguyen, M., Paquette, D., Turcotte, E., Berger, A., Mitchell, M., Shore, G.C., Beauparlant, P.

- (2009). The Small Molecule GMX1778 Is a Potent Inhibitor of NAD<sup>+</sup> Biosynthesis: Strategy for Enhanced Therapy in Nicotinic Acid Phosphoribosyltransferase 1-Deficient Tumors. *Molecular and Cellular Biology*. **29**(21), 5872–5888.
- Weaver, B.A. (2014). How Taxol/paclitaxel kills cancer cells. *Molecular Biology of the Cell*. **25**(18), 2677–2681.
- Weaver, I.C.G., Jerónimo, C., Miranda-Gonçalves, V., Lameirinhas, A., Henrique, R. (2018). Metabolism and Epigenetic Interplay in Cancer: Regulation and Putative Therapeutic Targets EPIGENETIC MECHANISMS IN CANCER: A BRIEF OVERVIEW. *Japan Frontiers in Genetics | www.frontiersin.org*. **9**, 427.
- Wellen, K.E., Hatzivassiliou, G., Sachdeva, U.M., Bui, T. V., Cross, J.R., Thompson, C.B. (2009). ATP-citrate lyase links cellular metabolism to histone acetylation. *Science*. **324**(5930), 1076–1080.
- Weyandt, J.D., Thompson, C.B., Giaccia, A.J., Rathmell, W.K. (2017). Metabolic Alterations in Cancer and Their Potential as Therapeutic Targets. *American Society of Clinical Oncology Educational Book*. **37**, 825–832.
- White, E. (2016). Autophagy and p53. *Cold Spring Harbor Perspectives in Medicine*. **6**(4).
- White, E. (2013). Exploiting the bad eating habits of Ras-driven cancers. *Genes and Development*. **27**(19), 2065–2071.
- Wiechmann, K., Müller, H., König, S., Wielsch, N., Svatoš, A., Jauch, J., Werz, O. (2017). Mitochondrial Chaperonin HSP60 Is the Apoptosis-Related Target for Myrtilone. *Cell Chemical Biology*. **24**(5), 614-623.e6.
- Wilson, J.E. (2003). Isozymes of mammalian hexokinase: Structure, subcellular localization and metabolic function. *Journal of Experimental Biology*. **206**(12), 2049–2057.
- Wise, D.R., Deberardinis, R.J., Mancuso, A., Sayed, N., Zhang, X.Y., Pfeiffer, H.K., Nissim, I., Daikhin, E., Yudkoff, M., McMahon, S.B., Thompson, C.B. (2008). Myc regulates a transcriptional program that stimulates mitochondrial

glutaminolysis and leads to glutamine addiction. *Proceedings of the National Academy of Sciences of the United States of America*. **105**(48), 18782–18787.

Wong, C.C., Qian, Y., Yu, J. (2017). Interplay between epigenetics and metabolism in oncogenesis: Mechanisms and therapeutic approaches. *Oncogene*. **36**(24), 3359–3374.

Wu, J., Hu, L., Wu, F., Zou, L., He, T. (2017). Poor prognosis of hexokinase 2 overexpression in solid tumors of digestive system: A meta-analysis. *Oncotarget*. **8**(19), 32332–32344.

Wurdak, H., Zhu, S., Min, K.H., Aimone, L., Lairson, L.L., Watson, J., Chopiuk, G., Demas, J., Charette, B., Weerapana, E., Cravatt, B.F., Cline, H.T., Peters, E.C., Zhang, J., Walker, J.R., Wu, C., Chang, J., Tuntland, T., Cho, C.Y., Schultz, P.G. (2010). A small molecule accelerates neuronal differentiation in the adult rat. *Proceedings of the National Academy of Sciences of the United States of America*. **107**(38), 16542–16547.

Wurdak, H., Zhu, S., Romero, A., Loriger, M., Watson, J., Chiang, C. yuan., Zhang, J., Natu, V.S., Lairson, L.L., Walker, J.R., Trussell, C.M., Harsh, G.R., Vogel, H., Felding-Habermann, B., Orth, A.P., Miraglia, L.J., Rines, D.R., Skirboll, S.L., Schultz, P.G. (2010). An RNAi Screen Identifies TRRAP as a Regulator of Brain Tumor-Initiating Cell Differentiation. *Cell Stem Cell*. **6**(1), 37–47.

Xiao, M., Yang, H., Xu, W., Ma, S., Lin, H., Zhu, H., Liu, L., Liu, Y., Yang, C., Xu, Y., Zhao, S., Ye, D., Xiong, Y., Guan, K.L. (2012). Inhibition of  $\alpha$ -KG-dependent histone and DNA demethylases by fumarate and succinate that are accumulated in mutations of FH and SDH tumor suppressors. *Genes and Development*. **26**(12), 1326–1338.

Xue, C., Lin, T.Y., Chang, D., Guo, Z. (2017). Thioflavin T as an amyloid dye: Fibril quantification, optimal concentration and effect on aggregation. *Royal Society Open Science*. **4**(1).

Yaku, K., Okabe, K., Hikosaka, K., Nakagawa, T. (2018). NAD metabolism in cancer therapeutics. *Frontiers in Oncology*. **8**(DEC).

Yamamoto, T., Seino, Y., Fukumoto, H., Koh, G., Yano, H., Inagaki, N., Yamada, Y., Inoue, K., Manabe, T., Imura, H. (1990). Over-expression of facilitative glucose transporter genes in human cancer. *Biochemical and Biophysical Research Communications*. **170**(1), 223–230.

Yelamos, J., Farres, J., Llacuna, L., Ampurdanes, C., Martin-Caballero, J. (2011). PARP-1 and PARP-2: New players in tumour development. *American journal of cancer research*. **1**(3), 328–346.

Ying, H., Kimmelman, A.C., Lyssiotis, C.A., Hua, S., Chu, G.C., Fletcher-Sananikone, E., Locasale, J.W., Son, J., Zhang, H., Coloff, J.L., Yan, H., Wang, W., Chen, S., Viale, A., Zheng, H., Paik, J.H., Lim, C., Guimaraes, A.R., Martin, E.S., Chang, J., Hezel, A.F., Perry, S.R., Hu, J., Gan, B., Xiao, Y., Asara, J.M., Weissleder, R., Wang, Y.A., Chin, L., Cantley, L.C., Depinho, R.A. (2012). Oncogenic kras maintains pancreatic tumors through regulation of anabolic glucose metabolism. *Cell*. **149**(3), 656–670.

Yoshida, M., Satoh, A., Lin, J.B., Mills, K.F., Sasaki, Y., Rensing, N., Wong, M., Apte, R.S., Imai, S. ichiro (2019). Extracellular Vesicle-Contained eNAMPT Delays Aging and Extends Lifespan in Mice. *Cell Metabolism*. **30**(2), 329-342.e5.

Younes, M., Lechago, L. V., Somoano, J.R., Mosharaf, M., Lechago, J. (1996). Wide expression of the human erythrocyte glucose transporter Glut1 in human cancers. *Cancer Research*. **56**(5), 1164–1167.

Yu, M., Hon, G.C., Szulwach, K.E., Song, C.X., Zhang, L., Kim, A., Li, X., Dai, Q., Shen, Y., Park, B., Min, J.H., Jin, P., Ren, B., He, C. (2012). Base-resolution analysis of 5-hydroxymethylcytosine in the mammalian genome. *Cell*. **149**(6), 1368–1380.

Zhang, J., Stevens, M.F.G., Bradshaw, T.D. (2012). Temozolomide: mechanisms of action, repair and resistance. *Current molecular pharmacology*. **5**(1), 102–14.

Zhang, N., Xie, T., Xian, M., Wang, Y.J., Li, H.Y., Ying, M.D., Ye, Z.M. (2016). SIRT1 promotes metastasis of human osteosarcoma cells. *Oncotarget*. **7**(48), 79654–79669.

- Zhang, T., Kraus, W.L. (2010). SIRT1-dependent regulation of chromatin and transcription: Linking NAD<sup>+</sup> metabolism and signaling to the control of cellular functions. *Biochimica et Biophysica Acta - Proteins and Proteomics*. **1804**(8), 1666–1675.
- Zhang, W., Liu, Y., Chen, X., Bergmeier, S.C. (2010). Novel inhibitors of basal glucose transport as potential anticancer agents. *Bioorganic and Medicinal Chemistry Letters*. **20**(7), 2191–2194.
- Zhao, G., Cui, J., Zhang, J.G., Qin, Q., Chen, Q., Yin, T., Deng, S.C., Liu, Y., Liu, L., Wang, B., Tian, K., Wang, G.B., Wang, C.Y. (2011). SIRT1 RNAi knockdown induces apoptosis and senescence, inhibits invasion and enhances chemosensitivity in pancreatic cancer cells. *Gene Therapy*. **18**(9), 920–928.
- Zhao, Y., Yang, Y. (2016). Real-time and high-throughput analysis of mitochondrial metabolic states in living cells using genetically encoded NAD<sup>+</sup> /NADH sensors. *Free Radical Biology and Medicine*. **100**, 43–52.
- Zheng, S., Xin, L., Liang, A., Fu, Y. (2013). Cancer stem cell hypothesis: A brief summary and two proposals. *Cytotechnology*. **65**(4), 505–512.
- Zheng, X., Boyer, L., Jin, M., Mertens, J., Kim, Y., Ma, L., Ma, L., Hamm, M., Gage, F.H., Hunter, T. (2016). Metabolic reprogramming during neuronal differentiation from aerobic glycolysis to neuronal oxidative phosphorylation. *eLife*. **5**(JUN2016).
- Zhong, S., Li, Z., Jiang, T., Li, X., Wang, H. (2017). Immunofluorescence Imaging Strategy for Evaluation of the Accessibility of DNA 5-Hydroxymethylcytosine in Chromatins. *Analytical Chemistry*. **89**(11), 5702–5706.
- Zhu, W., DePamphilis, M.L. (2009). Selective killing of cancer cells by suppression of geminin activity. *Cancer Research*. **69**(11), 4870–4877.

## 9. Appendix

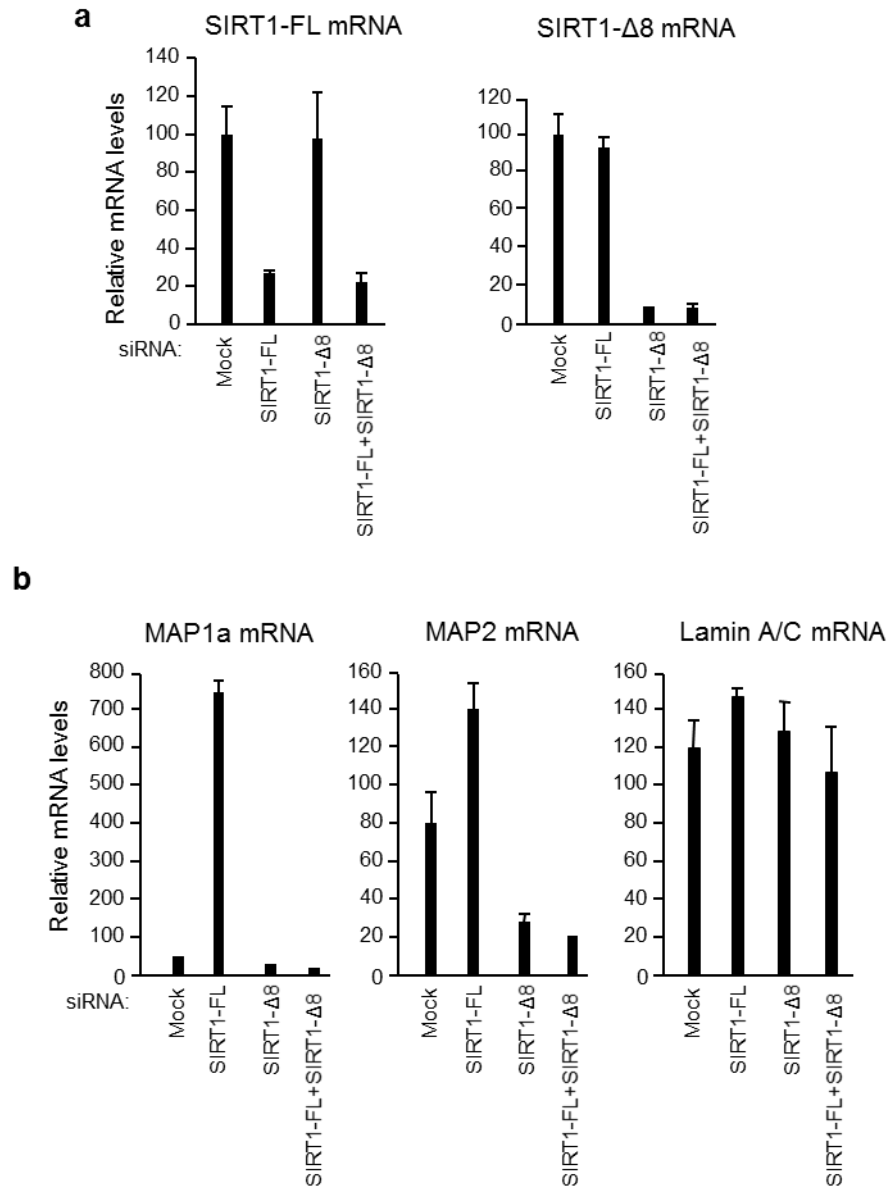


**Figure 9.1: qPCR analysis of SIRT1-FL, SIRT1-Δ8, MAP1a and MAP2 mRNA (data generated by S.J.Allison)**

Relative mRNA levels of SIRT1-FL, SIRT1-Δ8, MAP1a and MAP2 after transfection of ARPE-19 non-cancer cells with SIRT1-FL and SIRT1-Δ8 siRNA alone or in combination for 72 hours. Lamin A/C mRNA levels are shown as the housekeeper gene.

	15% Resolver (20ml)	4% Stack (20ml)
ddH <sub>2</sub> O	6.28ml	13.5ml
Tris	5ml 1.5M pH8.7	2.9ml 1.5M pH8.7
40% acrylamide	7.5ml	2ml
2% bis-acrylamide	0.8ml	1.2ml
10% SDS	200µl	240µl
TEMED	20µl	20µl
APS	200µl	240µl

**Table 9.1: Constituents for 4% and 15% SDS-PAGE gels for Immunoblotting.**

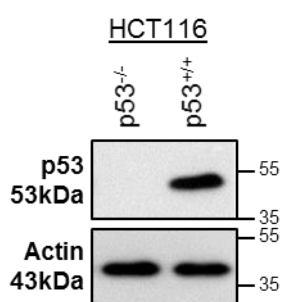


**Figure 9.2: Protein expression of p53 in HCT116 p53<sup>+/+</sup> and HCT116 p53<sup>-/-</sup> cancer cells.** Immunoblot showing differential p53 protein expression in HCT116 p53<sup>+/+</sup> and HCT116 p53<sup>-/-</sup> cancer cells. Actin was used as an endogenous loading control.

Drug	Cell Line	IC <sub>50</sub> (µM)	±SEM
Cisplatin	CP70/A2780cis	10.27	1.77
	A2780	1.47	0.04

**Table 9.2: IC<sub>50</sub> values of cisplatin in CP70/A2780cis and A2780 cancer cells.** Mean IC<sub>50</sub> value ± SEM (n=3 biological repeats) of cisplatin in CP70/A2780cis (cisplatin resistant) and A2780 (cisplatin sensitive) cancer cells after 96 hours continuous drug exposure.

Cell Line	Platinate	IC <sub>50</sub> (μM)	±SEM
CCD 841 CoN	Cisplatin	4.69	0.42
	Oxaliplatin	0.63	0.29
	Carboplatin	69.71	6.50
HCT116 p53 <sup>+/+</sup>	Cisplatin	3.26	0.21
	Oxaliplatin	0.93	0.06
	Carboplatin	32.37	6.43

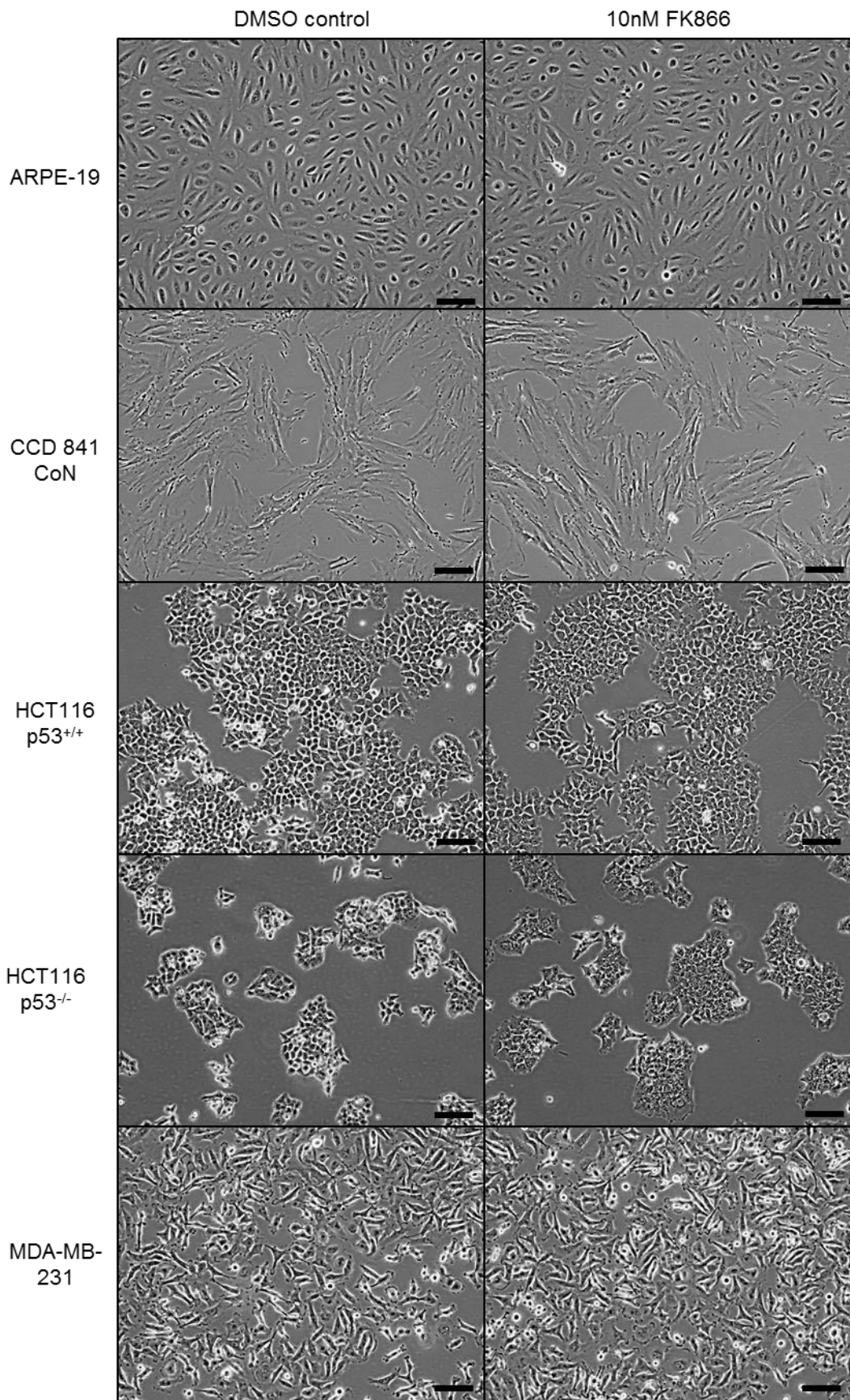
**Table 9.3: IC<sub>50</sub> values of FDA-approved platinates in HCT116 p53<sup>+/+</sup> cancer cells and CCD 841 CoN non-cancer cells.**

Mean IC<sub>50</sub> value ± SEM (n=3 biological repeats) of FDA-approved platinates, Cisplatin, Oxaliplatin and Carboplatin in HCT116 p53<sup>+/+</sup> cancer cells and CCD 841 CoN non-cancer cells after 96 hours continuous exposure.

Drug	Condition	IC <sub>50</sub> (nM)	±SEM
DOX	Normoxic (21% O <sub>2</sub> )	25.75	1.24
	Hypoxic (0.1% O <sub>2</sub> )	42.15	0.90

**Table 9.4: IC<sub>50</sub> values of doxorubicin in HCT116 p53<sup>+/+</sup> cancer cells under normoxic and hypoxic conditions.**

Mean IC<sub>50</sub> value ± SEM (n=3 biological repeats) of doxorubicin (DOX) in HCT116 p53<sup>+/+</sup> cancer cells under normoxic and hypoxic conditions after 96 hours continuous drug exposure.



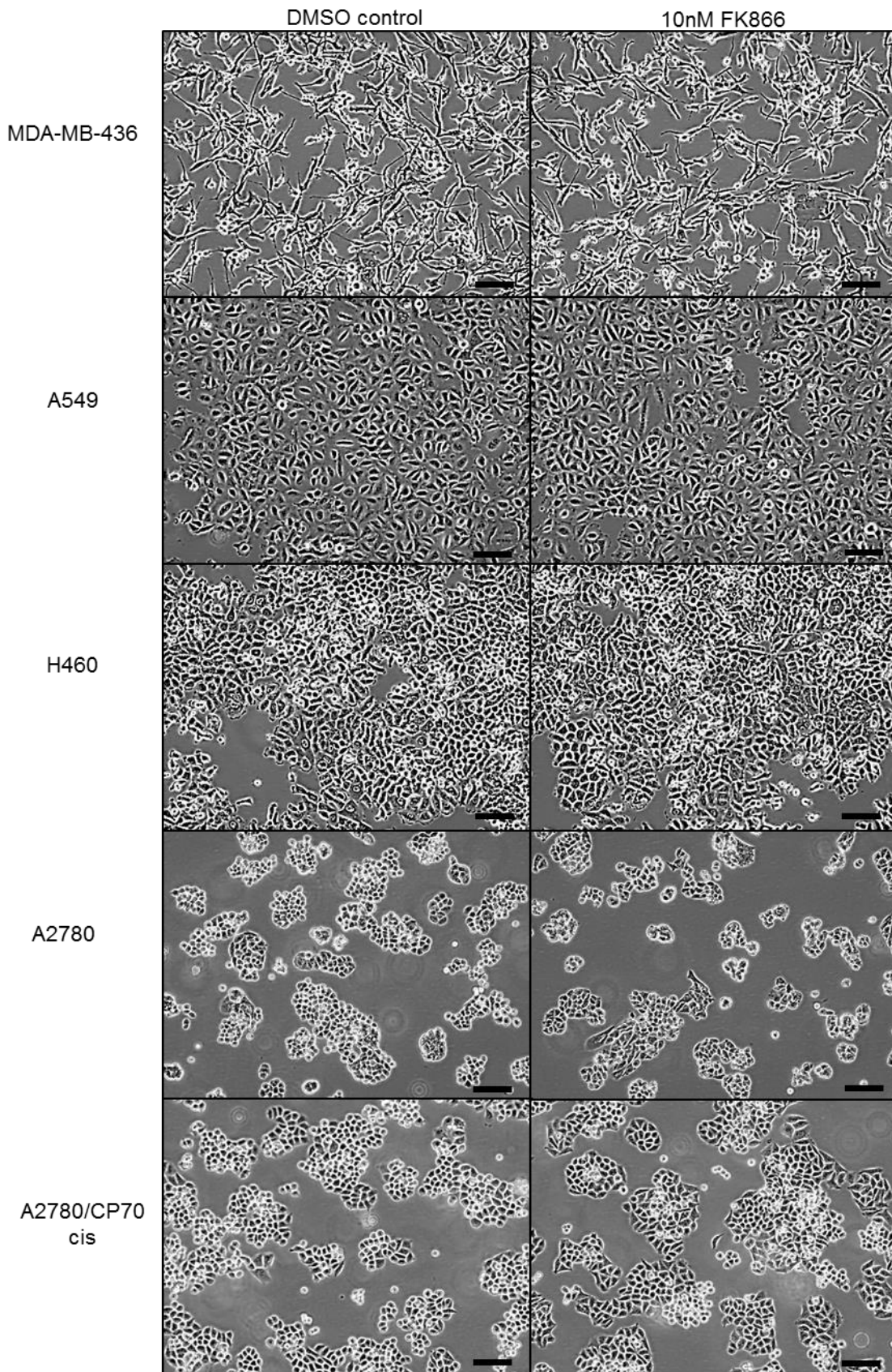


**Figure 9.3: Cell micrographs of non-cancer and cancer cells treated with 10nM FK866 for 24 hours.**

Cell images of the indicated non-cancer and cancer cell lines treated with 10nM FK866 or DMSO control for 24 hours, showing no apparent toxic effects. Images taken with 10x objective and scale bar shown 100µm.

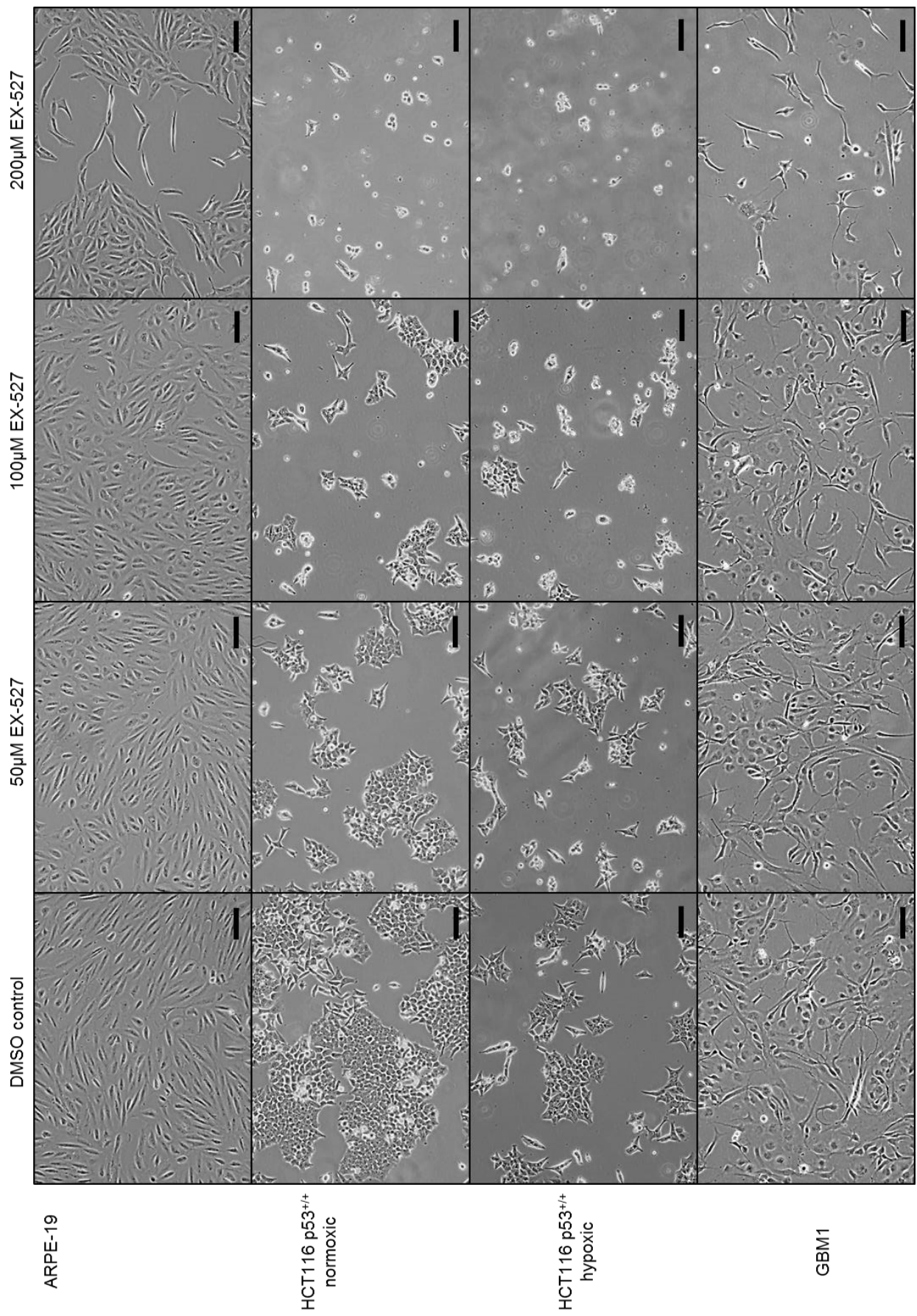


**Figure 9.4: Cell micrographs of ARPE-19 non-cancer cells, HCT116 p53<sup>+/+</sup> cancer cells under normoxic and hypoxic conditions and cancer stem-cell like model GBM1 after EX-527 treatment.**

Cell images of ARPE-19, HCT116 p53<sup>+/+</sup> and GBM1 cells after 48 hours treatment with the indicated EX-527 doses or DMSO control. Images taken with 10x objective and scale bar indicates 100 $\mu$ m.

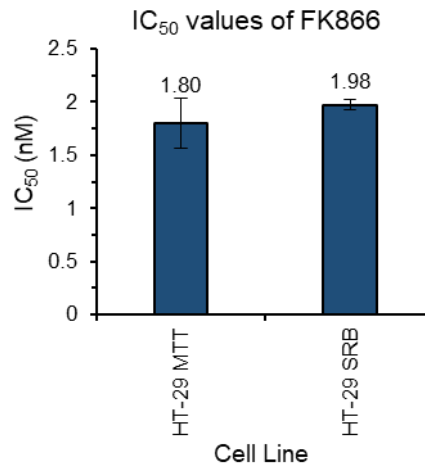


**Figure 9.5: Comparison of IC<sub>50</sub> values of FK866 in HT-29 cancer cells achieved through chemosensitivity assay via SRB or MTT staining.**

Average IC<sub>50</sub> values  $\pm$  SEM, n=3 biological repeats for MTT and n=2 biological repeats for SRB (8 technical replicates per repeat) of FK866 in HT-29 cancer cells.